Spring 5-15-2021

Converting Inorganic Rust to Organic Nanostructured Conducting Polymers: Synthesis and Applications

Yifan Diao
Washington University in St. Louis

WASHINGTON UNIVERSITY IN ST. LOUIS

School of Art and Sciences
Institute of Material Science and Engineering

Dissertation Examination Committee:

Julio M. D'Arcy, Chair
Young-Shin Jun
Vijay Ramani
Bryce Sadtler
Srikanth Singamaneni

Converting Inorganic Rust to Organic Nanostructured Conducting Polymers: Synthesis and Applications

by

Yifan Diao

A dissertation presented to
The Graduate School
of Washington University in
partial fulfillment of the
requirements for the degree
of Doctor of Philosophy

May 2021
St. Louis, Missouri

Contents

List of Figures

List of Tables

List of Abbreviations

AFM	atomic force microscopy
CV	cyclic voltammetry / cyclic voltammogram
CE	counter electrode
CFU	colony-forming unit
CP	conducting polymer
DSSC	dye-sensitized solar cell
EC	electrochemical capacitor
E. coli	Escherichia coli
EDOT	3,4-ethylenedioxythiophene
EDS, EDX	energy dispersive X-ray spectroscopy
EIS	electrochemical impedance spectroscopy
ESR	equivalent series resistances
FF	fill factor
FTIF	Fourier-transform infrared spectroscopy
GC	gas chromatography
GCD	galvanostatic charge-discharge
hcp	hard carbon fiber paper
HVPP	hydrolysis-assisted vapor-phase polymerization
LED	Light-emitting diode
PANi	polyaniline
PEDOT	poly(3,4-ethylenedioxythiophene)
PEDOT:PSS	poly(3,4-ethylenedioxythiophene) polystyrene sulfonate

PVA	polyvinyl alcohol
pXRD	powder X-ray diffraction
PPy	polypyrrole
Py	pyrrole
RVPP	rust-based vapor-phase polymerization
SAED	selected area diffraction
S. aureus	Staphylococcus aureus
SC, μSC	supercapacitor / microsupercapacitor
SEM	scanning electron microscopy / scanning electron micrography
STEM	scanning transmission electron microscopy
TEM	transmission electron microscopy / transmission electron micrography
TGA	thermogravimetric analysis
UPS	ultraviolet photoelectron spectroscopy
UV-vis-NIR	ultraviolet visible infrared spectroscopy
XPS	X-ray photoelectron spectroscopy

Acknowledgments

I am so lucky that I was blessed by many mentors over the years who have shaped the way that I think and interact with the world around me. I am very grateful to Ms. Gu, who is my abecedarian that brings me to the field of Chemistry in middle school. I would like to thank Gangyi Liu and Ms. Liu for introducing me to the Tsinghua winter camp and providing me a chance to start scientific research in high school.

To Julio, it has been a wonderful time for both of us. I really appreciate you and Gen and your support through those fantastic years. I still remember the first presentation in a group meeting that make everyone laughing due to my ignorance and excuses when I was a master student. However, you believe me, encourage me to be your Ph.D. students with that memorable sentence: Other professors bet on their equipment, but I bet on my people. More than a mentor during past years with the help and encouragement in my research, you like a friend. Like Master Yoda and Anakin, I still remember and will never forget the sentence you told me: Yifan, do not try, do it! Thank you for your support of my odd ideas with no restriction. I will never forget the beer we drank, the BBQ we eat, and I will remember Lily, Gen, and Suky (the dog).

Our lab means a lot to me where I spend the best of my youth, enabling me to see the sunrise at 6 AM and the night sky at 3 AM. It's so fulfilling to see old questions answered by new colleagues with fresh perspectives. I want to thank Luciano M. Santino, Yang, Hongmin and Haoru for being both great colleagues and friends. Thank you, Lucky, for being my first mentor in D'Arcy lab. Thank you, Yang, for introducing me to this group. Thank you, Hongmin, for helping me with my first publication. Thank you, Haoru, for the editing and discussion. I would also like to thank the

master student Haozhe Chen who contribute a lot in experiment work and a big thanks to undergraduates that I worked closely with, especially Reagan, your work helped immensely in my research, and I am sure you are going to do great things, whether in medicine or otherwise.

Many people have kept me sane throughout these past few years, especially abroad. I am glad to have found friendship with fellows in Chinese Students and Scholarship Association (CSSA) – Yuqing Liu, Linhua Xu, Zezhong Ye, Hailun, Lan Du, Yiqi Lin, Tracy, Jieni Li, Lin Liu, Yuhao Chen, Jiayu Wang, Zuoxian Hou, Han Xia, Lu Li, Cathy, Sihao Chen, Dai, Zhuqian Feng, Xiangyi Zhu, Yongzhen Liu, Gogoling, Cici, Yiran Zhi, Xinyue Zhang, Qingyuan Meng, Mimi, thanks for your support and bring me countless moments of joy. I would like to thank my roommates Shuai Shuai and Yize Li for their understanding and tolerance, and I will never forget our midnight snack and the traveling experience. I would also thank my friends in the engineering department – Zheyu Wang, Zhaohan Zhang, Qisheng Jiang, Xinsheng Xia, and Li Shan.

St. Louis has helped me grow in ways that different from China, folkway plain and away from the noise allows me to be involved in academics. My first live St. Louisan friend, Lisi Mai and Zheng Qin, who picked me up at Lambert airport at midnight when I first came. I so appreciate it their kindness and cherish our friendship. I would like to thank Tom and Adam for supporting my journal to the entrepreneurship and the patent application.

Above all, thank you to the people who love me, and I bless all the people I love.

Yifan Diao

Washington University in St. Louis

May 2021

Dedicated to my parents and girlfriend

ABSTRACT OF THE DISSERTATION

Converting Inorganic Rust to Organic Nanostructured Conducting Polymers:

Synthesis and Applications

by

Yifan Diao

Doctor of Philosophy in Institute of Materials Science and Engineering

Washington University in St. Louis, 2021

Professor Julio M. D'Arcy, Chair

Iron rust is a type of corrosion product, coming from the chemical reaction between iron and oxygen in the presence of water that first documented ca. 800 BCE. It is a heterogeneous inorganic solid-state material composed of multiple phases and is ubiquitous throughout the universe. Rust species such as Hematite (α-Fe_2O_3), Akaganeite (β-FeOOH), and ferrous hydroxide ($Fe(OH)_2$), make up the solid-state chemical family composed of iron oxides, oxyhydroxides, and hydroxides that are typically recognized as chemical waste. Conducting polymer is a type of organic plastic composed of long chains with repeating subunits that bonding with strong interactions between neighboring molecules. Unlike conventional insulating plastics, conducting polymers possess a unique molecular structure with an electronically conjugated backbone, enabling electron freely to travel interchain and intrachain, and such subject received the Nobel Prize in Chemistry in 2000. This work introduces a unique synthetic strategy that advances the state-of-the-art chemical synthesis of nanostructured conducting polymers by utilizing "waste" material rust, named rust-based vapor-phase polymerization (RVPP). The unique conversion between inorganic rust and organic conducting polymer leads to controlled depositions of poly(3,4-ethylenedioxythiophene) (PEDOT) and polypyrrole (PPy) nanostructures, including fibers, rods, flakes, and thin films.

Owing to the high conductivity, large surface area, and tunable band gap, nanostructured conducting polymers provide promising applications in energy storage, photovoltaics, sensing, CO_2 photoreduction, and antimicrobial field.

Rust (red) / Conducting polymer (blue

Chapter 1

Introduction

This dissertation seeks to build connections between inorganic rust chemistry and modern *in situ* nano and microstructure synthesis of organic conducting polymers. The synthetic strategies presented herein lead not only to novel and elegant nano and microstructures of conducting polymers, but also to distinct molecular structure of polymer chains, affording polymers for applications in energy storage, sensing, CO_2 photoreduction, antimicrobial and photovoltaics.

In this introductory chapter, I will discuss rust chemistry, its history, rust dissolution and iron hydrolysis. I will then discuss the fundamental mechanism by which specific polymers can conduct and store electricity. Finally, I will address the possibility and advantages of converting rust to nanostructured conducting polymers and introduce their potential applications.

In the chapters following, I will describe my own experimental research beginning with synthesizing the conducting polymer PEDOT using rust to produce nanofibers via rust-based vapor-phase polymerization (RVPP). This synthesis opens the avenue of *in-situ* conversion between inorganic solid rust to organic solid conducting polymers, demonstrating the potential of rust for carrying out a chemical synthesis. Inspired by this unique synthesis, various interdisciplinary projects will be described starting with the fabrication of microsupercapacitors by combing RVPP and microelectronic systems (MEMS). 3D nanofibrillar electrodes are

produced from a sputtered Fe_2O_3 layers. I will also describe the deposition of nanofibrillar conducting polymers (PPy, PEDOT) films on Kirigami via RVPP, enabling the fabrication of a stretchable supercapacitor and a humidity dosimeter. The stretchability stems from the mechanical property of Kirigami cuts, and the mechanism for sensing is due to the chemo-resistive response. The RVPP implement layer-by-layer deposition of PEDOT and PPy nanofibers, and the Kirigami sensor is a perfect accessory for the surgical mask. One work also enables the fabrication of PEDOT-coated bricks and tiles that convert sintered Fe_2O_3 to PEDOT nanofibers. Due to the catalytic properties of PEDOT-coated masonry materials, one work demonstrates antimicrobial properties in masonry materials via peroxide generation. PEDOT-coated bricks for store energy is investigated; however, it falls outside of the scope of this dissertation.[1] I will also discuss the photocatalytic property of RVPP-PEDOT for CO_2 photoreduction. Additionally, collaboration with the Biswas lab gives state-of-the-art dye-sensitized solar cells since RVPP-PEDOT nanofibers possess ultra-surface areas that enhance the electrochemical activities. Finally, one work describes controlling nanostructured PEDOT synthesis via pH, solvent, and salts.

I conclude with a discussion of recent advances in conducting polymer and their applications and the perspective of utilizing rust.

1.1 A brief history of rust

Rusting is one of the most widely recognized oxidative processes in the world, and its heterogeneous corrosion product, rust, is ubiquitous throughout the universe. Although rust encompasses a large class of iron oxides, it is most familiar to us as the reddish-brown coating of ferric oxide (Fe_2O_3) that envelops and corrodes iron surfaces as they react with oxygen in the presence of water. Hematite (α-Fe_2O_3), an iron oxide polymorph, is the rusty mineral which gives

Mars its distinctive red hue and is the very reason that the planet was named after the Roman god of war, named the "fire star" by Chinese astronomers, and nicknamed the "Red Planet" by Western ones.[2] Within our solar system, another celestial body influenced by rust is the Moon – the Moon Mineralogy Mapper imaging spectrometer recently found a widespread abundance of hematite at the Moon's lunar poles.[3] The discovery of iron corrosion on the Moon demonstrates that nothing is safe from rust even on a planetary scale.

Here on Earth, rust exists even thriving in the most unlikely climates. In the polar desert of Antarctica, five stories of rusty red saltwater pour out from Taylor Glacier in a striking sight known as "Blood Falls".[4] Buried beneath 400 meters of ice, the anoxic source lake of Blood Falls contains ferrous (Fe^{2+}) iron-rich saltwater that turns blood red upon exposure to the highly oxygenated surface at the outlet of the falls. Although rusting is a natural phenomenon that produce remarkable natural wonders, humankind has long regarded rust as an unwanted pestilence. On an anthropogenic scale, rust represents a persistent problem in all manner of engineering and industrial pursuits. Rust is an inescapable source of chemical waste and has consequently become synonymous with decay and decline in the human psyche. The rusting process is gradual and nondiscriminatory, affecting iron structures of all shapes and sizes, from bridges and buildings to pipelines and wires. Simply exposing iron surfaces to oxygen and water is enough to precipitate the creeping plague of rust and stands as a stark reminder of the ever-present influence of nature.

Corrosion and weakening of iron in factory parts, plane engines, and essential infrastructures such as bridges and water systems necessitates considerable spending on rust prevention and removal techniques. The issue is so pervasive that the National Association of Corrosion Engineers (NACE) estimated the global cost of corrosion to be US$2.5 trillion annually in a study in 2016.[5] The infamous "Rust Belt" is colloquially used to describe regions of the United States

characterized by sharp industrial decline, evoking images of derelict steel factories rusted over from decades of disuse. As a result, rust is commonly regarded as a symptom of deterioration and a physical manifestation of neglect in the eyes of the public. Yet, it is essential to note that even within this 'waste' material, there exists invaluable cultural merit and ample scientific potential.

The color of rust is an iconic aesthetic quality that has long captivated humankind and cemented it as a historical and cultural cornerstone. Shades of rust ranging from fiery red hematite or golden yellow limonite ($FeO(OH)\cdot nH_2O$) to earthy brown goethite ($FeO(OH)$) can be mixed with clay to form intensely colored ochre pigments. Rust pigments have been used since the Middle Stone Ages, from the 73,000-year-old red ochre crayons found in Blombos Cave, South Africa,[6] to the burnt umber streaked throughout Da Vinci's Mona Lisa.[7] Moreover, human utilization of rust is not just limited to painting cave walls and canvases. Ancient Egyptians associated red with life, health, and victory, which led to the common practice of coloring their bodies with red ochre powder during celebrations or women staining their lips and cheeks to brighten their appearances. The practice of adorning bodies with red ochre persists to this day, most notably in the Ovahimba tribe of Namibia. As part of a daily beautification ritual, Himba women slather their bodies, hair, and ornaments with a mixture of red ochre powder and clarified butter known as "otjize".[8]

Red ochre has been found to hold significant photoreceptive capacities under *in vitro* and *in vivo* conditions, demonstrating a positive correlation between iron oxide content and SPF that enables otjize to function as an effective sunscreen. Rust evidently holds immense functional and symbolic value across the boundaries of countless civilizations and appears time and time again throughout the annals of human history. Rust also impacts humans on the most intimate level, coursing through our veins in the hemoglobin of our red blood cells. The *heme* group contains a central ferrous (Fe^{2+}) iron atom that is temporarily oxidized in order to bind with oxygen from the lungs

and deliver it to bodily tissues.[9] Broadly speaking, rusting is a process which is necessary for human survival; to live is to breathe, and to breathe is to rust.

1.2 Characterization of rust

Rust is a corrosion product from the chemical reaction between iron and oxygen in the presence of water. It is a heterogeneous solid-state material composed of multiple phases and is ubiquitous throughout the universe. There are 16 phases of rust, such as oxides, hydroxides and oxyhydroxides (Table 1.1) composed of Fe and O and/or OH.

Oxide–hydroxides and hydroxides	*Oxides*
Goethite α-FeOOH	Hematite α-Fe_2O_3
Lepidocrocite γ-FeOOH	Magnetite Fe_3O_4 ($Fe^{II}Fe_2^{III}O_4$)
Akaganéite β-FeOOH	Maghemite γ-Fe_2O_3
Schwertmannite $Fe_{16}O_{16}(OH)_y(SO_4)_z \cdot n\ H_2O$	β-Fe_2O_3
δ-FeOOH	ε-Fe_2O_3
Feroxyhyte δ′-FeOOH	Wüstite FeO
High pressure FeOOH	
Ferrihydrite $Fe_5HO_8 \cdot 4\ H_2O$	
Bernalite $Fe(OH)_3$	
$Fe(OH)_2$	
Green Rusts $Fe_x^{III}Fe_y^{II}(OH)_{3x+2y-z}(A^-)_z$; $A^- = Cl^-$; ½ SO_4^{2-}	

Table 1.1: All rust phases.[10] Typically, the iron is in the trivalent state with three exceptions, such as FeO, $Fe(OH)_2$ and Fe_3O_4 that contain ferrous ions (Fe^{2+}). Iron oxides consist of close packed arrays of anions (usually in hexagonal (hcp) or cubic close packing (ccp)) in which the interstices are partly filled with divalent or trivalent Fe predominately in octahedral (VI) ($Fe(O, OH)_6$) or tetrahedral (IV) (FeO_4) coordination (Figure 1.1a). The various oxides differ in how the basic structural units are arranged in space via corner, edge and face sharing (Figure 1.1b), resulting in

five polymorphs of FeOOH and four of Fe_2O_3. In some cases, small amounts of anions (Cl^-, SO_4^{2-}, CO_3^{2-}) also participate in the structure.

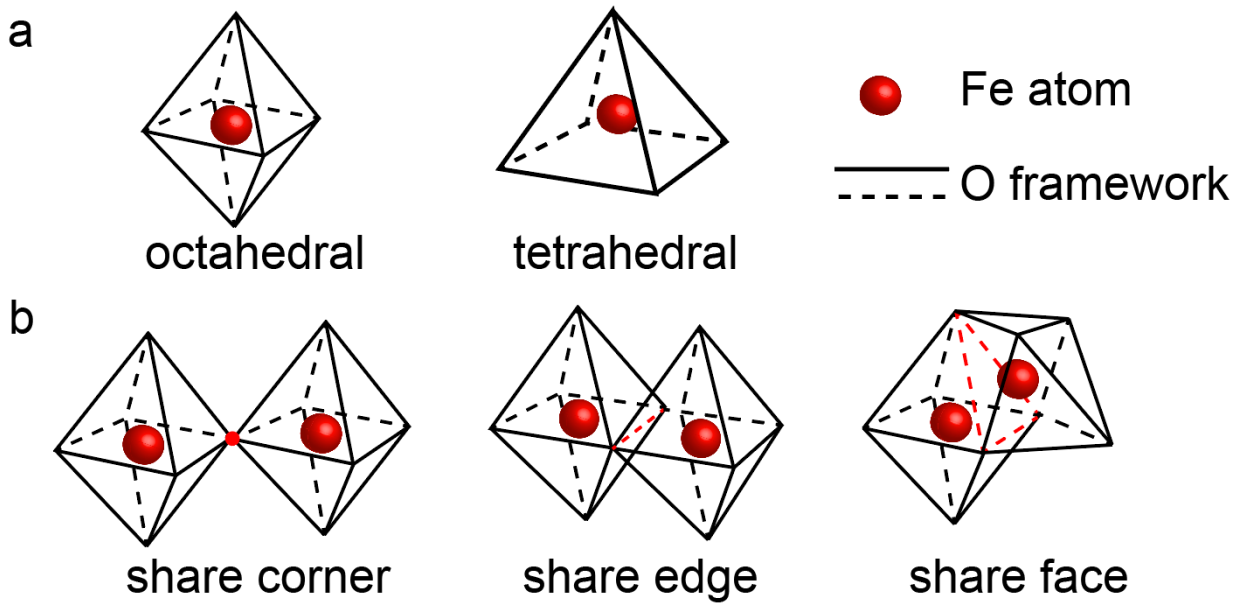

Figure 1.1: (a) Schematic of Fe coordination with octahedra and tetrahedral. (b) Different linkages of octahedral in Fe (III) oxides.

The oxide hydroxide can dehydroxylate to their oxide counterpart because the similarity between the anion frameworks that ensure rearrangement of the cations and loss of OH is often required to effect a transformation. Other characteristics of these compound includes the low solubility (high stability) of ferric oxides the brilliant colors (Figure 1.2), and the partial replacement of Fe in the structure by other cations. Due to the high energy of crystallization, Fe oxides often form minute crystals both in natural environments and industry.

Figure 1.2: Color of Fe (III) oxides.[10]

1.2.1 Rust structures

Goethite (α-FeOOH) (Figure 1.3a) occurs in rocks and throughout the global ecosystem. It possesses the diaspore structure which is based on hexagonal close packing of anions (hcp). Goethite is one of the thermodynamically most stable iron oxides at ambient temperature and is, therefore, either the first oxide to form or the end member among iron oxides transformations. Goethite is a vital pigment that possesses dark brown or black color in massive crystal aggregates and yellow in powder, responsible for the color of natural rocks, soils, and ochre deposits. Notably, goethite was named in 1815 after *Johann Wolfgang von Gethe* (1749-1832), the famous German

poet who was also a scientist and held the position of minister for mines for the Duke of Weimar. Lepidocrocite (γ-FeOOH) (Figure 1.3b), the orange color mineral, is named after its platy crystal shape (lepido = scale) and its orange color (krokus = saffron). It occurs in rocks, soils, biota, and rust and is a common oxidation product of Fe^{2+}. It has the boehmite (γ-AlOOH) structure which is based on cubic close packing (ccp) of anions. Akaganeite (β-FeOOH) (Figure 1.3c) is named after the Akagane mine in Japan, where it was first discovered (Mackay, 1962). It rarely occurs in nature and is found mainly in Cl^- rich environments, such as hot brines, and in rust in marine environments. Unlike the other FeOOH polymorphs, it has a structure based on body-centered cubic packing of anions (bcc) (hollandite structure) and contains chloride or fluoride ions with brown to bright yellow color. Schwertmannite ($Fe_{16}O_{16}(OH)_y(SO_4)_z$)•$nH_2O$ (Figure 1.3d) has the same basic structure as akageneite, however it contains sulfate instead of chloride ions that frequently occurs in nature as an oxidation product of pyrite. The y/z ratio appears to vary, whereas Bigham et al. (1990) noticed a range of 3.3-6 for nature samples. Feroxyhyte (δ-FeOOH) (Figure 1.3e) is reddish-brown, ferrimagnetic compound with poorly crystalline mineral. Their structures are based on hcp anion arrays and differ in the ordering of the cations. Feroxyhyte was first described by Chukhrov et al. in 1976 and it often occurs in various surface environments.

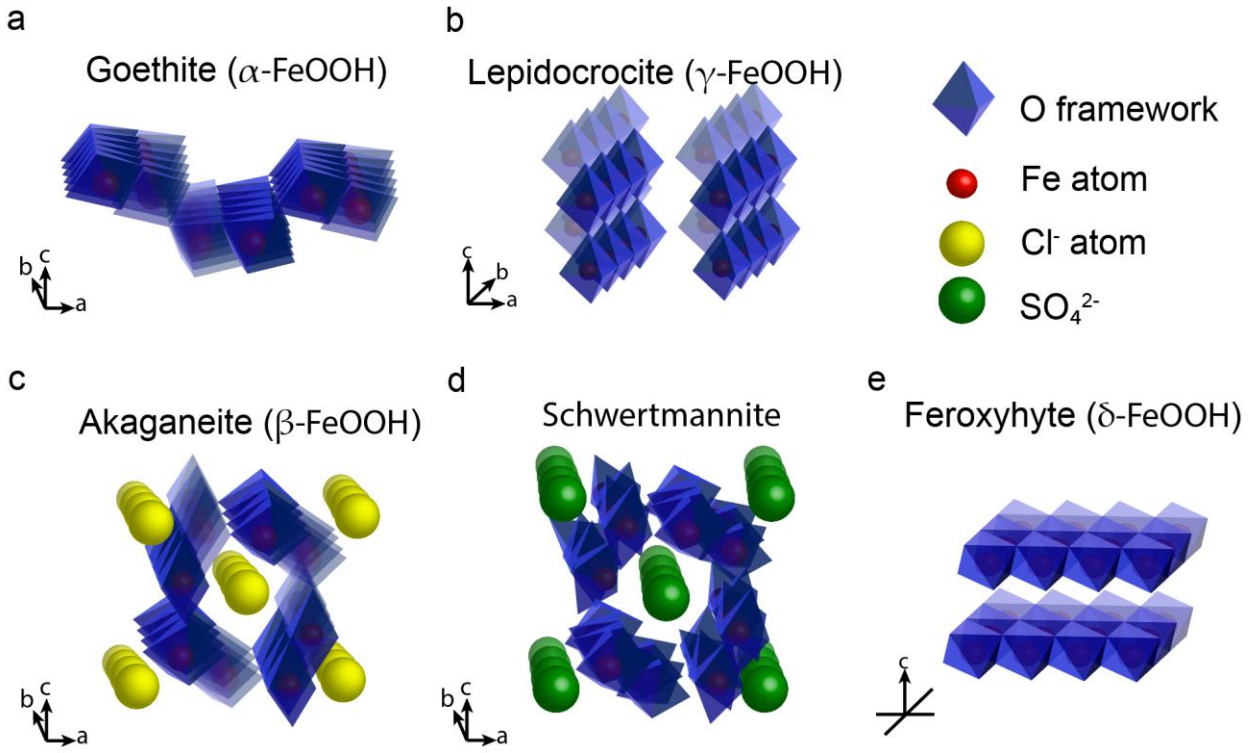

Figure 1.3: Structures of iron oxyhydroxides. (a) Goethite. (b) Lepidocrocite. (c) Akaganeite. (d) Schwertmannite. (e) Feroxyhyte.

The reddish-brown ferrihydrite is widespread in surface environments. It was first described by Chukhrov et al. in 1973. Unlike the other iron oxides, it exists exclusively as nanocrystals and easily transforms with time into the more stable iron oxides. Therefore, ferrihydrite is an important precursor for other more stable iron oxides. Structurally ferrihydrite consists of hcp anions and is a mixture of defect-free and defective structural units. The composition, especially for OH and H_2O, is often recognized as $Fe_5O_8H{\bullet}H_2O$. Bernalite ($Fe(OH)_3$) (Figure 1.4a) is a greenish hydroxide reported by Birch et al. 1993 and Kolitsch 1998, and $Fe(OH)_2$ (Figure 1.4b) is in white color however does not exist as a mineral. The Fe is divalent and its structure is based on an hcp anion array which is similar to brucite. $Fe(OH)_2$ is readily oxidized, upon which it develops into greenish-blue, so-called green rust and further be oxidized to reddish-brown $Fe(OH)_3$ or black magnetite.

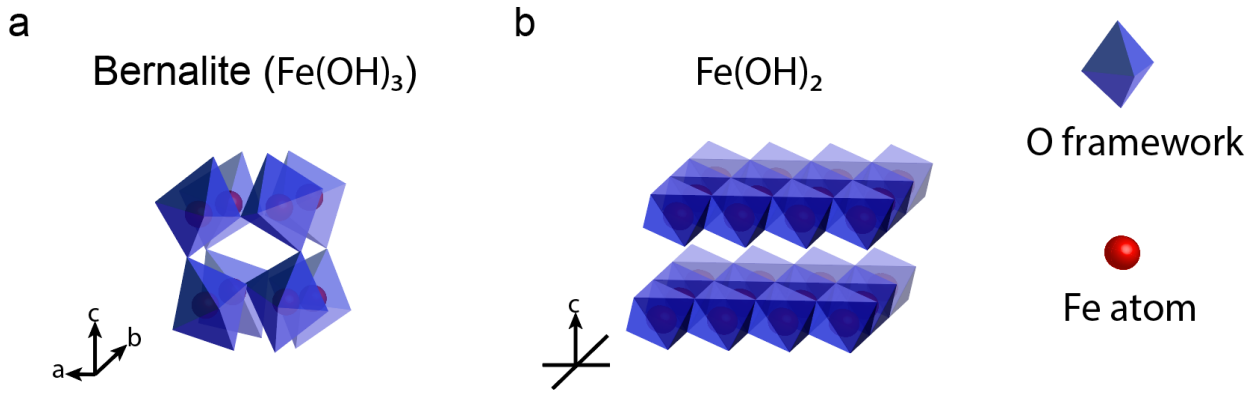

Figure 1.4: Structures of iron hydroxides. (a) Bernalite. (b) $Fe(OH)_2$.

Hematite (α-Fe_2O_3) is the oldest known Fe oxide mineral, first recorded in 800 BCE and widespread in rocks and soils. Its color is blood-red (Greek haima = blood) if finely divided and black or a sparking grey of coarsely crystalline. Hematite has the corundum (α-Al_2O_3) structure which is based on an hcp anion packing and similar to goethite, it is extremely stable and is often the end member of transformations of other iron oxides (Figure 1.5).

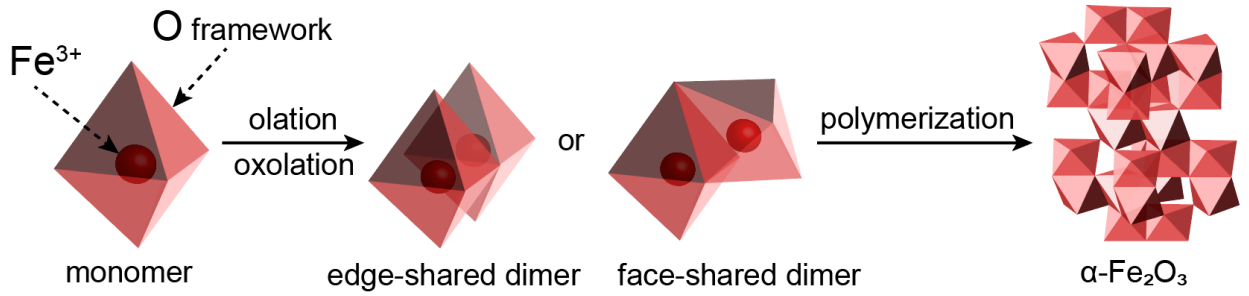

Figure 1.5: Schematic illustration of formation of α-Fe2O3.

Magnetite (Fe_3O_4) is a black ferrimagnetic mineral containing both Fe (II) and Fe (III), possessing an inverse spinel structure known as iron ore. Together with titanomagnetite, it is responsible for

the magnetic properties of rocks, and these are the object of palaeomagnetic studies. Maghemite (γ-Fe_2O_3) is a reddish-brown, ferrimagnetic mineral isostructural with magnetite but with cation deficient sites. It occurs in soils as a weathering product of magnetite or as the product of heating of the Fe oxides, usually in the presence of organic matter. β-Fe_2O_3 and ε-Fe_2O_3 are rare compounds that have been synthesized only in the laboratory. β-Fe_2O_3 (Braun and Gallagher, 1972) is obtained by dehydroxylation of β-FeOOH under a high vacuum at 170 °C. ε-Fe_2O_3 was first reported in 1934 (Forestier and Guillain) and named in 1963 (Schrader and Buttner). It is a dark brown magnetic phase of iron (III) oxide, possessing an orthorhombic noncentral-symmetric structure. High-pressure FeOOH is another rare laboratory compound prepared by hydrothermal conversion of hematite in NaOH at 400 and 8 Gpa. Wustite (FeO) is a black iron oxide that contains only divalent Fe. It is usually non-stoichiometric (O-deficient). The structure is similar to NaCl and is based on ccp anion packing and it is an essential intermediate in the reduction of iron ores. Green rusts are a group of Fe oxides consisting of layers of Fe(II)OH octahedra in which Fe^{3+} replaces some Fe^{2+} and to maintain neutrality, anions, especially Cl^- and SO_4^{2-} are bound between the layers.

1.2.2 Rust dissolution

Rust dissolution refers to ferric ions detached from the solid surface through a redox reaction. The detachment is due to weakening bonds between Fe^{3+} and solid surface, and the rate of dissolution is associated with the electron transfer during the redox process. Rust dissolution effectively reduces iron oxides' harmful effects, such as unclogging the rusty pipe and preventing water contamination. Here, we introduce three major iron dissolution mechanisms, such as proton-mediated dissolution, ligand-mediated dissolution, and reductive dissolution.

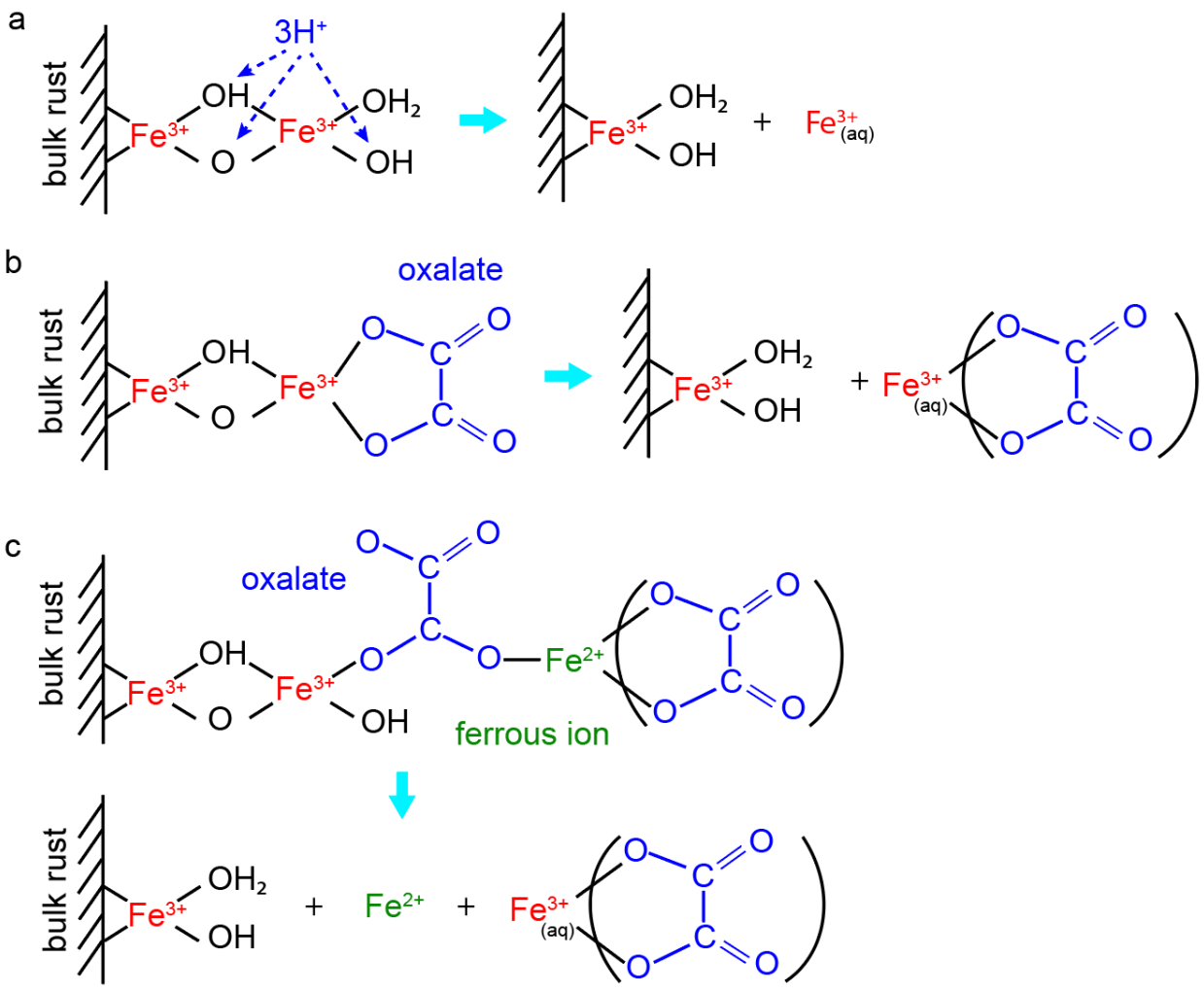

Figure 1.6: Mechanisms of rust dissolution. (a) Proton-mediated dissolution. (b) Ligand-mediated dissolution. (c) Reductive dissolution.

Stumm and Furrer proposed the proton-mediated iron dissolution mechanism (Figure 1.6a), where by three protons are adsorbed per one iron atom to generate a positively charged species.[11] The protonation of several of these groups polarizes and weakens the Fe-O bonds promoting rate-limiting iron detachment from the bulk iron oxide. It is well documented that proton-mediated dissolution is extremely slow compared to ligand-mediated dissolution and reductive dissolution for hematite.[12] This is because protonation alone weakens the Fe-O bond to a lesser extent

compared to the other mechanisms which lead to a higher activation energy thus making it difficult and slower to remove iron (III) atoms from the bulk oxide. Anions that carry protons such as the sulfate ion and the chloride ion from sulfuric acid and hydrochloric acid enhance the kinetics and equilibrium of iron dissolution through anion exchange which further promotes Fe-O bond polarization.[13] Anion exchange also reduces the positive surface charge of the iron oxide in acid and facilitates the proton adsorption.[13] Additionally, increasing the temperature from 15 °C to 35 °C exhibits significantly enchantment of iron dissolution.[14]

The presence of complexing ligands either enhances or inhibits the iron dissolution (Figure 1.6b). For example, ligands form mononuclear complexes promote dissolution while binuclear and trinuclear complexes inhibit iron dissolution.[10] Similar to proton-mediated dissolution, ligand-mediated dissolution involves fast adsorption of atoms onto a surface iron atom (in this case, a ligand) which helps polarize and weaken the Fe-O bond, thus promoting subsequent iron detachment and fast surface protonation. At low pH, the abundance of protons further weakens the Fe-O bond in the presence of complexing ligands resulting in an increased iron dissolution. However, extra protons promote the surface charge of the iron oxide and protonate the complexing ligands impeding iron dissolution via ligand interactions. For example, In the presence of citric acid, hematite dissolution occurs mostly at a pH of 4 (Zhang et al, 1985).[15] In alkaline solutions, Chang and Matijevic demonstrates in the presence of EDTA and hematite, ligand-mediated dissolution involves complexing free iron (III) instead of absorbing onto the surface.[16]

Reductive dissolution is separated into an induction stage followed by autocatalytic dissolution (Figure 1.6c). In the induction stage, an adsorbed reductant, such as ascorbate initiates electron transfer onto a surface Fe (III) atoms which weakens the Fe-O bonds and generates a Fe (II) species, which is subsequently detached. Fe (II) detachment is then assisted by ligand

complexation, which further weakens the Fe-O bonds. The ferrous ligand complexation enables an autocatalytic dissolution since it activates ferrous ions into a better reductant. Stumm and Sulzberger demonstrated photochemistry efficiently facilitates the reductive dissolution since the facile electron transfer from oxalate on hematite.[17] In terms of kinetics, Stumm and Brantwart shown reductive dissolution occurs at a faster rate compared to proton-mediated dissolution and ligand-mediated dissolution of hematite at a pH of 3. This is because iron detachment occurs via a more labile Fe (II) species compared to an Fe (III) species.[17]

1.2.3 Ferric ion hydrolysis

The ferric iron (Fe^{3+}) hydrolysis process includes nucleation and aging (ion exchange and polymerization) that strongly depend on solution pH, reaction temperature, solvent polarity, type of ligands, and iron concentration. Such various conditions enable a multitude of iron precipitates such as iron oxide (Fe_2O_3), hydroxide ($Fe(OH)_3$), and oxyhydroxides (FeOOH).[18]

Typically, monomeric hexa-aqua complexes $[Fe(H_2O)_6]^{3+}$ undergo hydrolyzes, olation and oxolation reaction resulting in ferric hydroxide and oxyhydroxides.[19] The olation and oxolation are condensation reactions, proceed by removing hydrogen and hydroxy ligand to bridge the ferric irons via hydroxy and oxo bridges, respectively (Figure 1.7). This transformation is depended on the binding affinity of ferric metal center and anion that affect by pH and ligands. For example, in acidic condition (pH 0.5-2), the hydrated ferric ion undergoes hydrolysis to form a species with tightly bound hydroxide ions in addition to loosely bound water molecule ligands. For the pH ranges from 0.8-1.8, the predominant aqueous species in solution are expected to be monomers and dimers with zero to two hydroxide ligands per iron atom. If the concentration of these molecules is higher than the saturation concentration, the solution will possess both solid

precipitants and aqueous supernatant. Chloride ligand promotes the formation of tunnel-shape akageneite because the strong binding energy enhances the interaction between Cl^- ions and hydrous iron oxide.

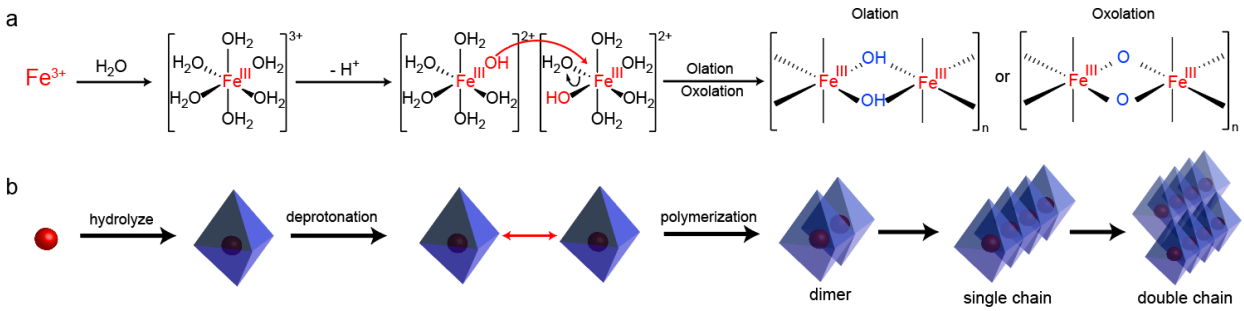

Figure 1.7: Olation and oxolation of ferric ions. (a) Molecular schematic. (b) Iron octahedral schematic.

Hematite (α-Fe_2O_3) is one of the most thermodynamically stable iron oxide phases featuring a hexagonal close-packed (hcp) unit cell composed of octahedral formula units. Each unit cell contains six octahedral units, where each octahedron shares one face with an octahedron and three edges with other octahedra.[10] Notably, due to its stability, hematite is often the product of iron oxide phase transformations, enabling multiple different pathways of hematite formation. For example, feroxyhyte undergoes a phase transformation through thermal dehydroxylation in a vacuum to form hematite.[10] Such phase transformations depend on the precursor and require specific conditions. In nature, hematite exhibits several different morphologies, including round or rhombohedral shapes in hot and dry soil or platy shapes at extremely high temperatures.[20] Synthetically, hematite exhibits rod-shaped morphologies, such as through phase transformations of ferrihydrite when citrate or maltose is present at high pH (10-12),[10] or through the dehydration of akaganeite at high temperatures.[21]

Akaganeite (β-FeOOH) differs from all other iron oxides and hydroxides featuring a body-centered packing (bcp) crystal structure result in a low density.[10] Each monoclinic unit cell is composed of eight octahedron units which are connected on one side through edge sharing to form four pairs of octahedra. These pairs of octahedron units are connected through corner sharing to form a ring-like structure with a tunnel through the center. This tunnel is usually stabilized by chloride ions as well as fluoride ions.[22] Removing the chloride or fluoride ions initiates a phase transformation of akaganeite to either goethite or hematite depending on the acidity of the environment.[23] Synthetically, akaganeite is often formed through the hydrolysis of $FeCl_3$ solution under acidic conditions.[24] Additionally, a study investigating the optimal conditions for akaganeite formation exhibits that akaganeite is the favored product after the oxidation of Fe^{2+} compounds ($[FeCl_2]$ = 1.6 M) when [NaOH] = 0.4 M and the ratio of $[Cl^-]/[OH^-] \geq 8$.[22] Notably, this study found varying the $[Cl^-]/[OH^-]$ ratio determine the formation of α, β, or γ-FeOOH. In nature, akaganeite forms in rust layers in chloride-rich environments, such as volcanoes and marine environments.[25] In summary, different hydrolyzing environments lead to diversified hydrolysis products which are rich in structural chemistry, for example, rod-shape akageneite (β-FeOOH), fiber-shape goethite (α-FeOOH)/lepidocrocite (γ-FeOOH) and spherical and cubic hematite (α-Fe_2O_3).

1.3 A brief history of conducting polymers

Conducting polymers is a type of organic plastic composed of long chains with repeating subunits bonding with strong interactions between neighboring molecules. Unlike conventional insulating

plastics, conducting polymers possess a unique molecular structure with an electronically conjugated backbone, enabling electrons freely to travel interchain and intrachain.

In 1862, the first documented partial conductive compound was synthesized by anodic oxidation of aniline in sulfuric acid, which was probably polyaniline. In the early 1970s, poly(sulfur nitride) (SN)x, the inorganic explosive polymer, exhibited superconductivity at extremely low temperatures (T_c=0.26 K). Meanwhile, many conductive organic compounds were also known, such as those discovered by K. Bechgaard (Copenhagen) together with D. Jerome (Paris) and famous for being superconductive at "high" temperatures (Tc around 10 K). Polyacetylene was the conductive polymer that launched this new field of research. Polyacetylene was known as a black powder and was prepared as a silvery film by Shirakawa and co-workers from acetylene, using a Ziegler-Natta catalyst in 1974; however, despite its metallic appearance, it was not a conductor. In 1977, Shirakawa, MacDiarmid and Heeger discovered polyacetylene films became 109 times more conductive by oxidation via chlorine, bromine or iodine vapor.[26] Such halogen treatment was called "doping" by analogy with the doping of semiconductors. The "doped" polyacetylene had a conductivity of 105 S/m, which was higher than that of any previously known polymer. As a comparison, Teflon has a conductivity of 10^{-16} S/m and silver and copper 108 S/m. The high conductivity found by Heeger, MacDiarmid and Shirakawa opened the field of "plastic electronics".

Other polymers studied extensively since the early 1980s include polypyrrole (PPy), polythiophene (and various polythiophene derivatives, such as poly(3,4ethlenedioxythiophene) (PEDOT)), polyphenylenevinylene (PPV) and polyaniline (PANi). Polyacetylene remains the most crystalline conductive polymer but is not the first commercialized conductive polymer due to its poor environmental stability. Differ from polyacetylene, polypyrrole and polythiophene are

easily synthesized in the doped state and possess physical and chemical stability in the air. Nowadays, poly(3,4-ethylenedioxythiophene) polystyrene sulfonate (PEDOT:PSS) is well-known as the commercialized CPs due to its high conductivity (>1000 S/cm) and simple processibility (solution processible). Due to this remarkable discovery, the 2000 Noble Prize in Chemistry was awarded to Prof. Alan J. Heeger, Prof. Alan G. MacDiarmid, and Prof. Hideki Shirakawa, who have revolutionized the development of electrically conducting polymer.

1.4 Charge transport theory in conducting polymers

Different from inorganic semiconductors that conduct electrons/holes through doping theory, conducting polymers (CPs) possess the intrinsically electrical conductivity due to the delocalized π electrons along the conjugated backbone.[27] To expand the real applications of CPs, we need address the fundamentals of their hydration, microstructure, and carrier-transports.

1.4.1 Hybridization and conjugated π-bonds in conducting polymers

Unlike saturated insulating polymers whose carbon atoms are sp^3 hybridized and all electrons are localized in the form of covalent bonding.[27] CPs possess backbones of contiguous sp^2 hybridized carbon with delocalized electrons.[28] Figure 1.8 illustrates that one 2p electron of a sp^2-hybridized carbon atom is released and the left three remaining electrons that are involved in forming three δ-bond, which constitute the backbones of conductive polymer chains.[29] These 2p electrons are delocalized from carbon atoms forming π-bonds, whose dominant electrical density is located perpendicular to the polymer backbones enabling free charge transfer.[29,30] Compared to saturated chains, conjugated chains exhibit more rigidity since the conjugated π-bonds impede large torsion in the system.[31]

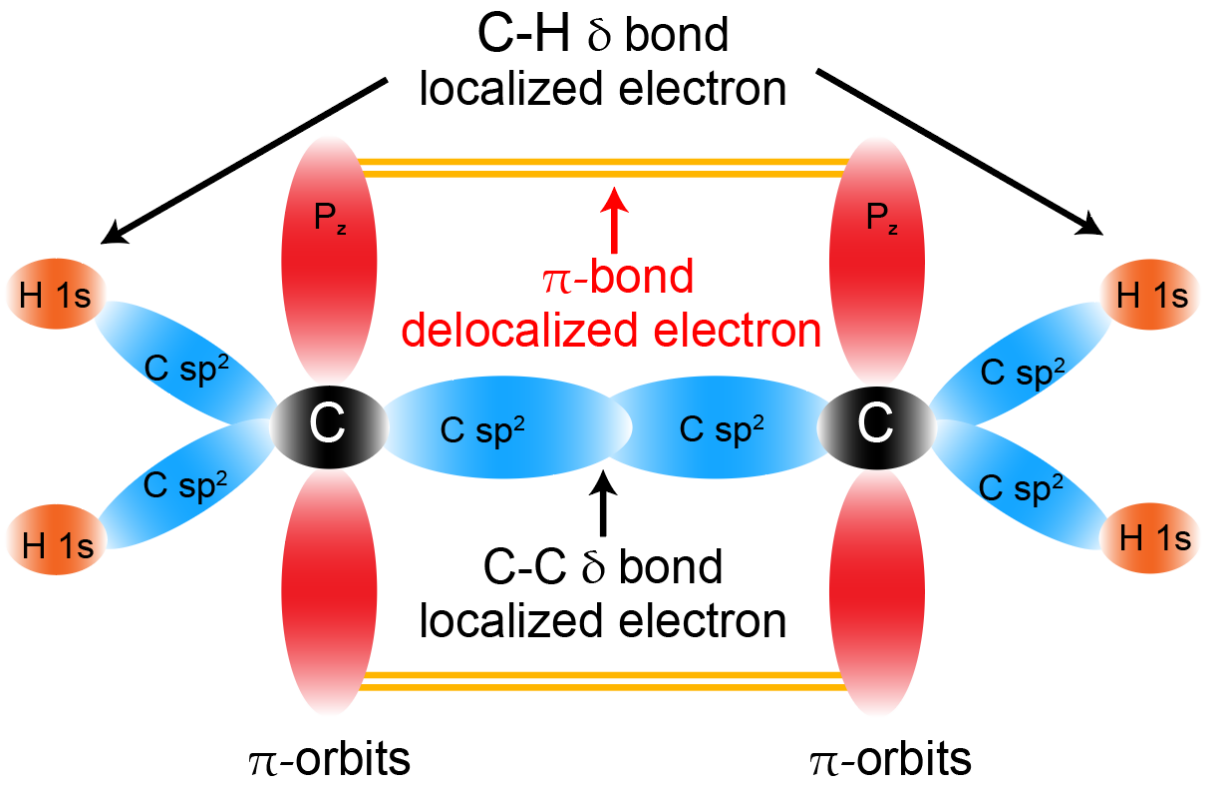

Figure 1.8: Schematic diagram of sp^2 hybridization and conjugated π-bonds in conductive polymers.

1.4.2 Microstructure of conducting polymers

CPs exhibit a random heterogeneous microstructure comprised of crystalline and amorphous domains which is differ from inorganic conductive materials whose structures are generally homogeneous and crystalline.[32] Crystalline domains within CPs possess ordered stacking due to the π-π interaction resulting in rigid conjugated chains. Such crystalline domains enable free-electron transport, while the amorphous domains exhibit refined electron transport.[29, 33] Therefore, CPs is structurally recognized as highly conductive metallic domains surrounded by poorly conductive amorphous matrices.[34] Molecular chains of CPs possess various configurations,

including linear-shaped, crosslinked, branched, and networked structures, leading to the microstructural complexity of CPs.[35]

1.4.3 Charge carriers of conducting polymers – (bi)polarons

Like conventional inorganic semiconductors, intrinsic CPs exhibit low conductivity (δ). Doping treatment effectively improves δ by tuning the number of charge carriers and simultaneously leads to distortion of local structures.[29] Typically, charge carriers in doped conductive polymers exist in the form of polarons or bipolarons.[36]

Doping leads to oxidation or reduction of CPs' backbones through electron transfer. For example, the molecular structure of Cl^- doped PEDOT (Figure 1.9a) presents when one electron is removed from the PEDOT's backbones, a radical cation is generated at the same place, which induces a structural distortion from the benzoid to quinoid structure.[37] Such structural distortion affects several units in the backbones (such as PEDOT with three units) and ultimately leaves an unpaired electron in the backbone recognized as a radical ion (a radical cation for p-type PEDOT). Bipolarons are recognized as a pair of radical ions (dication for p-type PEDOT), and it forms once the unpaired electrons in the polarons are removed. Notably, bipolarons' fomation is related to the Coulomb repulsion, structural distortion, and counterion electrostatic stabilization instead of combining two single polarons.[29, 38] Conjugated π bond in the quinoid structure provides transport orbitals for the electrons of (bi)polarons, making them delocalized within several repeating units.[39]

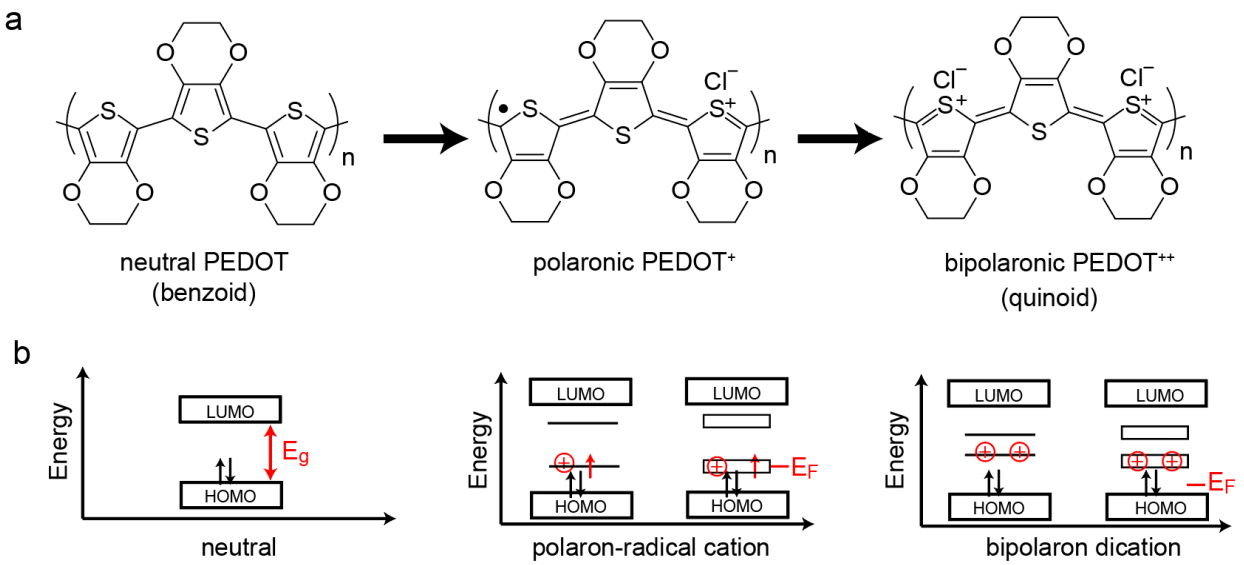

Figure 1.9: (a) Schematic diagram of PEDOT in neutral, polaronic and bipolaronic state. (b) Electronic structure evolution with (bi)polaron generation and doping level, where the LUMO and HOMO represent the lowest unoccupied molecular orbital and the highest occupied molecular orbital, respectively

(Bi)polarons generated by doping create a new electronic state between the conduction band and valence band of CPs, commonly defined as the lowest unoccupied molecular orbital (LUMO) and the highest occupied molecular orbital (HOMO), respectively.[35] For polarons, the remaining unpaired electrons possess higher energy than the paired ones, located at an energy level above the HOMO where electrons are half-filled.[29] Accordingly, a related antibonding level is generated and is located below the LUMO as an empty electronic level as shown in (Figure 1.9b). Removal of the remaining electrons from polarons generates bipolarons with higher electronic energy levels.[36] For example, the energy gap between the bipolaron electronic level and the HOMO band edge is 0.75 eV, while the polaron's energy gap is 0.5 eV.[36] Polaron and bipolarons' binding energies are 0.12 and 0.69 eV, respectively, placing the polaron in a more favorable thermodynamic position by 0.45 eV (0.69-0.12•2). Therefore, bipolarons are less mobile than polarons and contribute only a tiny portion of the electron transport, even with an ambient electric field.[40]

Under low or no doping condition, most (bi)polarons in CPs tend to be localized, resulting in their discontinuous electronic energy levels and isolated energy states within the band structures, and exhibiting insulating.[29] In contrast, at high doping levels, the adjacent (bi)polarons tend to overlap, forming intrachain and interchain (bi)polarons couplings, as shown in (Figure 1.10).[41-42] These overlapping structures create continuous electronic energy levels depicted in electronic energy bands between the LUMO and HOMO, resulting in highly conducting. Such electronic energy bands diminish the bandgap between the LUMO and HOMO enabling the CPs exhibit metal-like electrical properties at room temperature.[43]

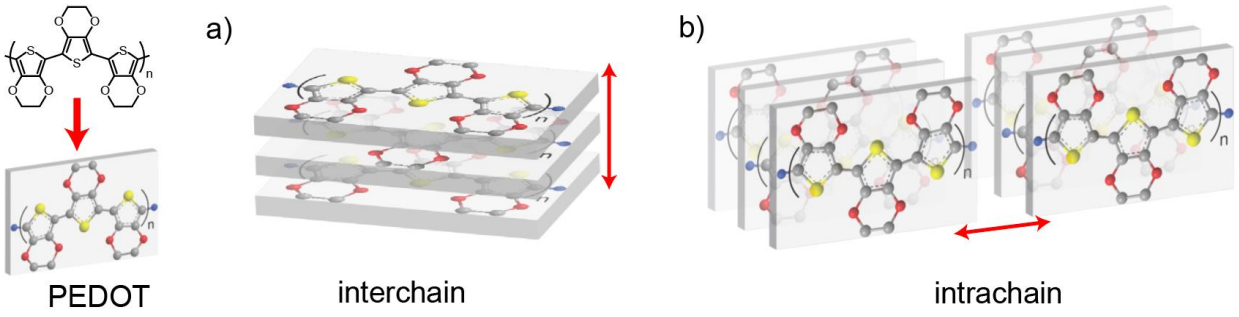

Figure 1.10: Generation of intrachain and interchain (bi)polaron coupling at high doping levels.

1.4.4 Charge carriers transport in conducting polymers

The charge carriers in CPs exhibit a distinct transport mechanism in both ordered crystalline and disordered amorphous domains.[29, 35] Crystalline domains possess a well-ordered structure and exhibit anisotropic carrier-transport behavior both in intrachain and interchain. Intrachain charge carrier transport possesses a high mobility (μ) since the conjugated chains of crystalline domains are connected via covalent bonding. While, intrachain charge carrier transport is limited by the weak π-π interactions, leading to poor μ and anisotropic δ compared with carrier transport within the in-plane direction.[44] Typically, μ of crystalline organic semiconductors (0.1-20 $cm^2/V•s$)[45] is

larger than the amorphous organic materials (< 0.1 $cm^2/V•s$).[46] Charge carrier transport in amorphous domains highly depends on the residence time (τ) of carriers between adjacent chains, and τ is calculated via Equation 1.1.[47]

$$\tau = \frac{h}{W} = \frac{h}{4t} \quad \text{(Equation 1.1)}$$

Where h is the reduced Planck's constant, W is the interchain band induced by π-π interactions, and t is the average electronic coupling or transfer integral.[47] Typically, CPs exhibit t < 0.05 eV which is lower than the crystalline organic semiconductors leading to a large τ. If τ is larger than the vibration (10^{-13} s), local polymer chains possess enough time to relax and adapt their structures and electronic density to trap charge carriers resulting in (bi)polaron formation.[29] These localized (bi)polarons predominately exist in CPs, leading to limited μ. If τ is smaller than the vibration (< 10^{-13} s), polymer chains cannot manage to tune the local structure and electronic density to trap carriers, leading to delocalized carriers. Such delocalized carriers are similar to carriers in single organic crystals, which possess high μ (~ 4.65 $cm^2/V•s$).[48]

1.5 Converting rust to nanostructured conducting polymers

Rust is a thermodynamically stable and its superior stability enables preservation of ancient frescoes resulting in an invaluable cultural merit to the human society.[2] For example, the color of rust is an iconic aesthetic quality that has long captivated humankind and cemented it as a historic and cultural cornerstone.[5] Shades of rust ranging from fiery red hematite or golden yellow limonite ($FeO(OH)·nH_2O$) to earthy brown goethite (FeO(OH)) can be mixed with clay to form intensely colored ochre pigments. From a historical perspective, rust allows us to see those precious cultural

relics; to us, rust is an abundant and stable source of Fe^{3+} ions – a vital chemical reagent, arousing our interest in exploring its function benefiting modern society.

1.5.1 Rust serves as an oxidant for conducting polymers synthesis

Fe^{3+} is a ubiquitous oxidant with a moderate oxidation potential (E_0 = +0.77 V), serving as an ideal oxidant for conjugated polymer synthesis (Figure 1.11 and Figure 1.12).[49-51] Conjugated polymer is a class of organic semiconducting materials possessing both electrical and ionic conductivity. Majority of conjugated polymers are synthesized by oxidative radical polymerization which is initiated via oxidizing monomers into reactive radicals, and the polymer chain grows subsequently via coupling between monomer radicals and neutral monomers, followed by removing excess protons.[52] The presence of oxidant and proton scavenger are thus pivotal throughout the proceeding of the reaction.[18] Nonetheless, using aqueous Fe^{3+} solutions in a polymerization reaction often involves complications, such as liquid surface tension, pH, and the hydrolysis of Fe^{3+}, while powdery and mechanical robust solid phase rust mitigate these constrains.

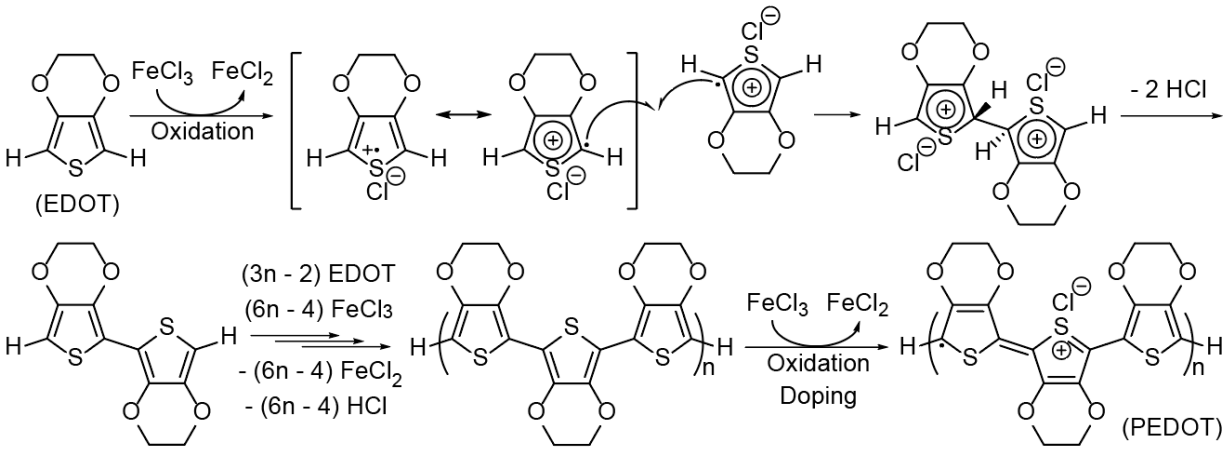

Figure 1.11: Mechanism of PEDOT oxidative radical polymerization

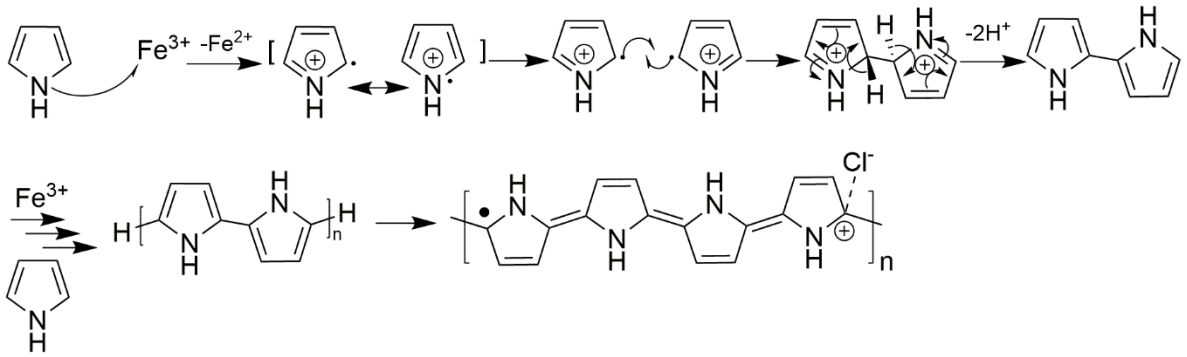

Figure 1.12: Mechanism of PPy oxidative radical polymerization

1.5.2 Rust serves as a template for the formation of conducting polymer nanostructures

Besides oxidative potential, Fe^{3+} ion hydrolysis products provide diversified growing templates due to the rich structural chemistry of rusting process, such as rod-shape akageneite (β-FeOOH), fiber-shape goethite (α-FeOOH)/lepidocrocite (γ-FeOOH) and spherical and cubic hematite (α-Fe_2O_3) (Figure 1.13a-d).[20, 53-54] A high aspect ratio nanostructure is ideal for conjugated polymers to maximize their surface area, benefiting in electrochemical and catalytical performances. Therefore, hard or soft templates are usually employed to guide polymer growth, enabling high aspect ratio nanostructures.[55] Nonetheless, removing these templates are difficult or even impossible. Iron hydrolysis products serve as ideal templates for generating high aspect ratio nanostructured conjugated polymers due to one dimensional growth of hydrolysis nuclei and ease of template removing with mild acid wash.[56] In our strategy, the presence of oxidative radical polymerization changes the course of hydrolysis, captures nanostructured hydrolysis intermediates serving as templates for polymer growth (Figure 1.13e-h). The interplay between iron hydrolysis

and oxidative radical polymerization leads to a highly conductive and various nanostructured conjugated polymers.

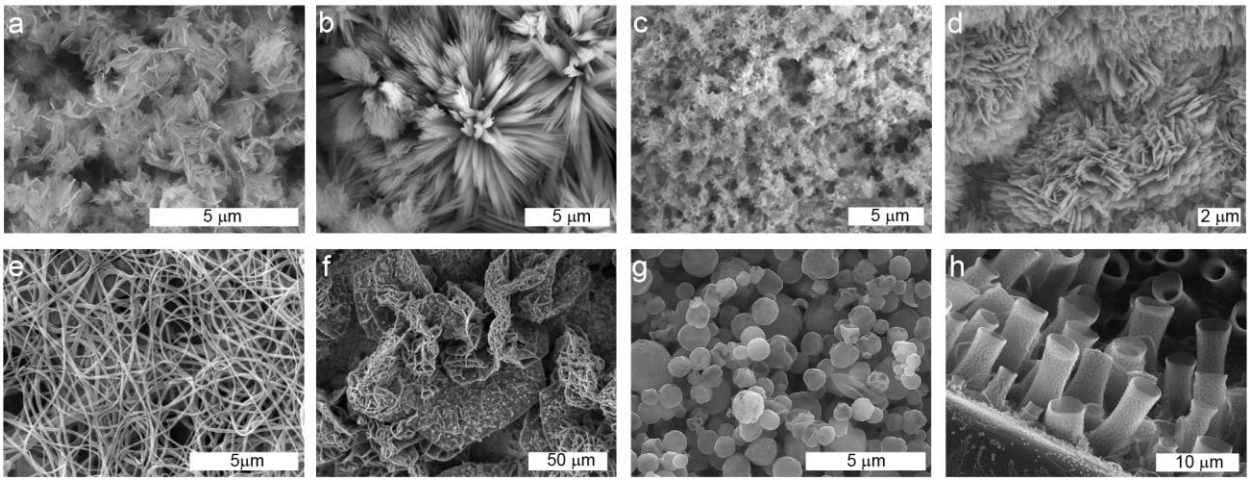

Figure 1.13: Nanostructures of rust and conducting polymers. (a-d) Various rust nanostructures. (e-h) Diversified conducting polymer nanostructures.

1.5.3 Synthesis and methods for converting rust to nanostructured conducting polymers

Conventional synthesis of conducting polymers nanostructures requires hard or soft templates that suffer from costly fabrication and template removal. Here, I introduce our strategy by utilizing products from rust, droplets with rust, and interfaces containing rust to synthesize nanostructured conducting polymer, including rust-based vapor-phase polymerization (RVPP), hydrolysis-assisted vapor-phase polymerization (HVPP).

Rust-based vapor-phase polymerization (RVPP)

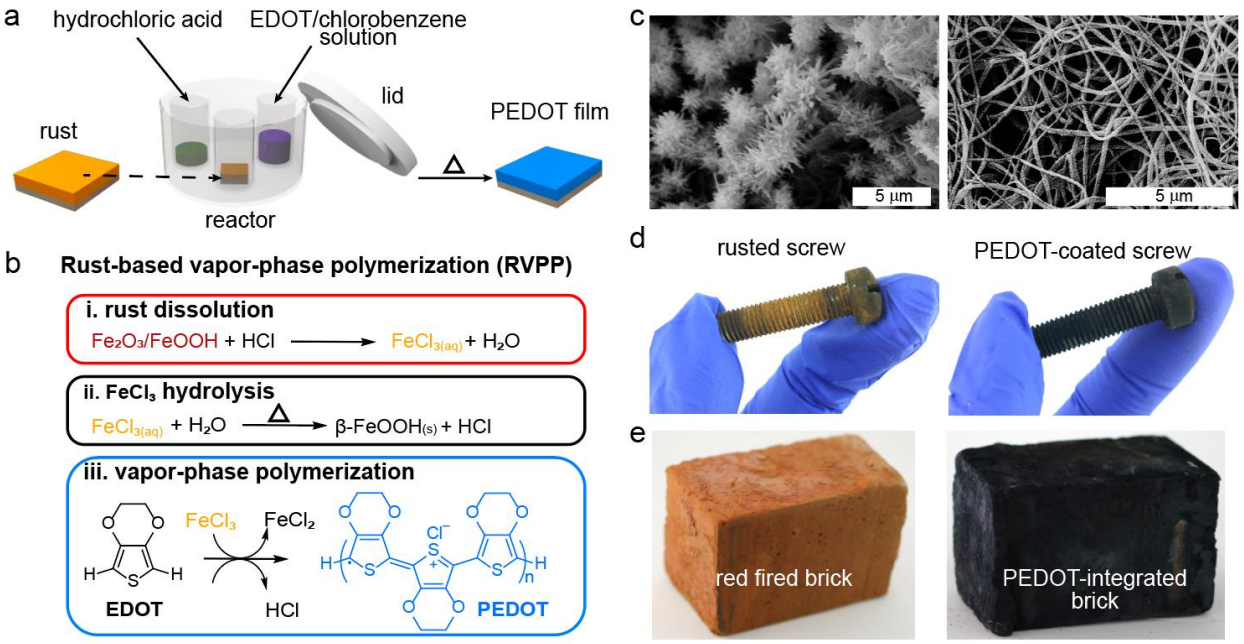

Figure 1.14: (a) Schematic diagram of experimental setup for rust-based vapor-phase polymerization (RVPP) carried out in a sealed vessel. (b) Scheme of RVPP mechanism entailing rust dissolution, Fe^{3+} hydrolysis and oxidative radical polymerization of EDOT monomer resulting in a doped form of PEDOT. (c) Scanning electron micrograph shows the rust possesses sea-urchin like microstructure is converted to a nanofibrillar architecture that possessing a high packing density of high aspect ratio nanofibers. (d-e) Photographs show that a rusted screw and red fired brick serves as a substrate for RVPP leading to a conformal blue texturized PEDOT coating, upon delamination of the polymer coating, adapt from reference 56.

Rust, when treated with an acid, is an ideal source of Fe^{3+} ions that afford an oxidation potential of 0.77 V for oxidizing thiophene-based moieties and for producing conducting polymers characterized by long conjugation lengths.[56] Here, we introduce a strategy that advances the state-of-the-art in chemical synthesis by demonstrating the functionality of this ubiquitous inexpensive inorganic material for depositing freestanding nanofibrillar films of the conducting polymer poly(3,4-ethylenedioxythiophene) (PEDOT) and this synthesis is named rust-based vapor-phase polymerization (RVPP).

A nanofibrillar PEDOT film is deposited through vapor-phase synthesis using a rusted steel sheet in a sealed vessel along with 20 µL of concentrated hydrochloric acid and 200 µL of a 0.0034 M EDOT in chlorobenzene solution (Figure 1.14a). Initially, as temperature is ramped, hydrochloric acid vapor diffuses and dissolves rust. The liberated Fe^{3+} ions simultaneously undergo hydrolysis in an acidic environment and oxidize monomer molecules upon contact (Figure 1.14b). During this oxidative radical polymerization, ferric ions are reduced to ferrous ions (Fe^{2+}) and the monomer 3,4-ethylenedioxythiophene (EDOT) is oxidized to $EDOT^{+\bullet}$ radical cations.[18] The conjugated PEDOT backbone assembles via step growth polymerization as monomer-radical coupling is in concomitant with deprotonation. Finally, the conjugated polymer chain is doped by Cl^- ions present from hydrochloric acid and forms an electronically conductive form of PEDOT that converts sea-urchin like rust to nanofibrillar PEDOT (Figure 1.14c). Since this technique utilizes vapors and a solid-state substrate, a rust-coated three-dimensional substrate is an ideal source of Fe^{3+} ions and as a proof of concept, a corroded metal screw is utilized as a template (Figure 1.14d). Additionally, RVPP is suitable with masonry material and converts a red fired brick to PEDOT nanofiber-integrated brick. This creates opportunity for functionalizing conventional masonry materials (Figure 1.14e).

Hydrolysis-assisted Vapor-phase polymerization (HVPP)

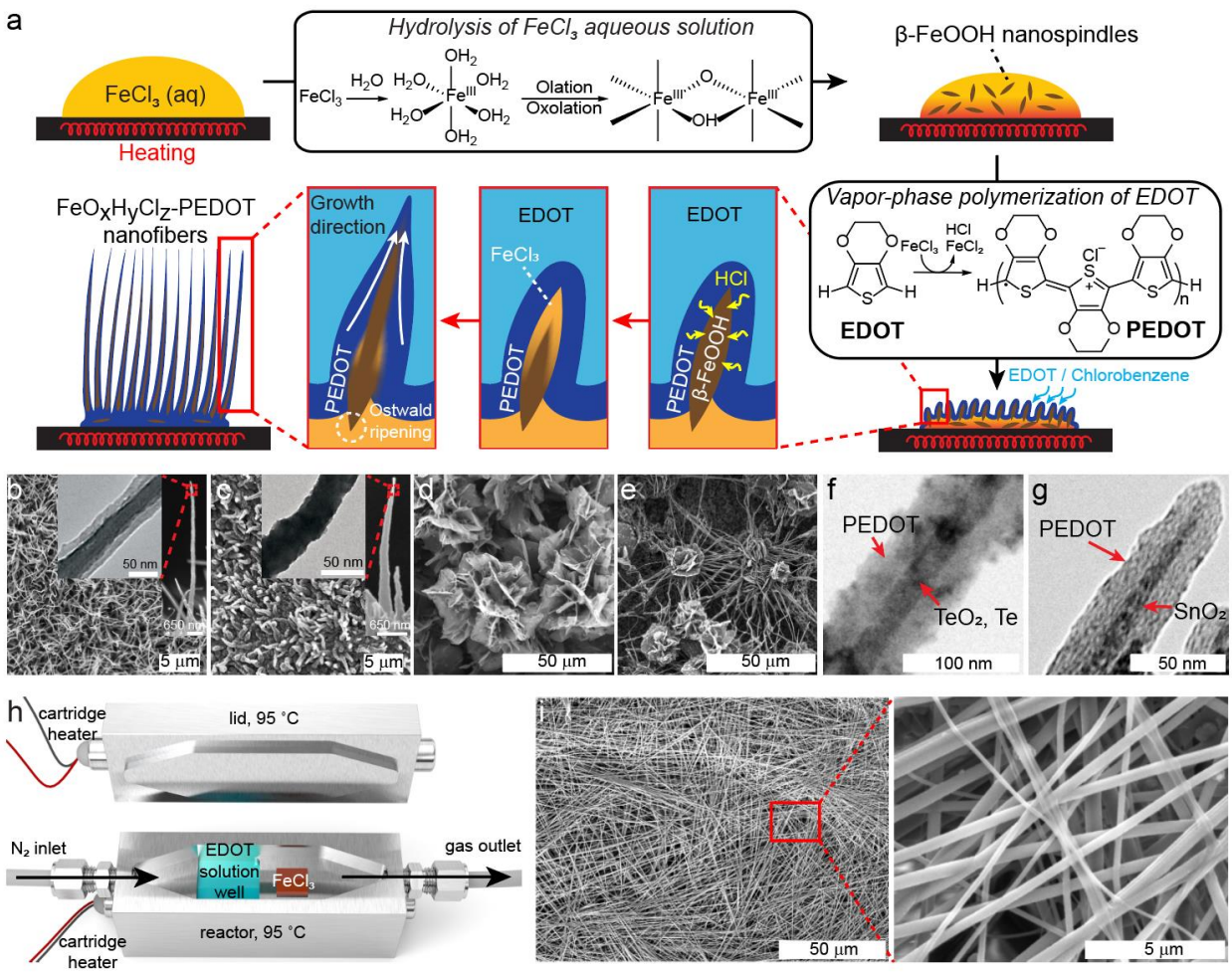

Figure 1.15: (a) Schematic illustration of PEDOT nanofiber growth mechanism including forced hydrolysis of $FeCl_3$ in water into β-FeOOH nanospindles that templates the oxidative radical vapor-phase polymerization of EDOT into PEDOT nanofibers. The polymerization produces Cl^--doped PEDOT and HCl as a byproduct that etches the β-FeOOH core and liberates more $FeCl_3$ for reaction. Control of pH enables the synthesis of (b) $FeO_xH_yCl_z$-PEDOT core-shell nanofibers and (c) monolithic PEDOT nanofibers. (d) Hydrolysis of $FeCl_3$ in organic solvent (ethanol) produces FeOCl 2D nanostructure that templates 2D PEDOT nanoflower synthesis. (e) Addition of 2 vol% water in ethanol results in the formation of 1D + 2D PEDOT nanostructures. Hydrolysis of $TeCl_4$ and $SnCl_4$ lead to (f) TeO_x-PEDOT core-shell nanowires and (g) SnO_2-PEDOT core-shell nanorods. (h) Modification of the reactor adding a N_2 bypass increases mass transport efficiency of EDOT vapor and enables the synthesis at temperatures lower than 130 °C. (i) Horizontally directed PEDOT nanofibers are synthesized with nucleation control and self-assemble into a 3D network mat, adapt from reference 18, 60.

Diverse inorganic compounds form distinct nanostructures from hydrolysis. Hydrolysis-assisted vapor-phase polymerization (HVPP) "hijacks" the formation of nanostructures during hydrolysis of inorganic species and utilize them to template the synthesis of organic conducting polymers such as poly(3,4-ethylenedioxythiophene) (PEDOT). When dissolve ferric chloride in water, hydration of Fe^{3+} produces hexa-aqua complex $[Fe(H_2O)_6]^{3+}$ that undergoes olation and oxolation forming Fe-OH-Fe and Fe-O-Fe bonds, respectively (Figure 1.15a).[57] The Cl^- rich environment and acidic condition contribute to the precipitation of β-FeOOH nanospindles upon forced hydrolysis at an elevated temperature (130 °C). In an atmosphere of vaporized monomer 3,4-ethylenedioxythiophene (EDOT), Fe^{3+} also serves as an ideal oxidant that provides a 0.77 V standard reduction potential to initiate oxidative radical polymerization of EDOT. The product PEDOT attaches to the low aspect ratio β-FeOOH nanospindals (~6) and stabilizes the axial growth, which eventually develops into nanofibers with high aspect-ratio of ~500.

Control of pH, solvent polarity, cation, stoichiometry, temperature, and mass transport enable conducting polymer morphologies from 1D nanofibers to 2D nanoflowers as well as nanostructures from monolithic to core-shell. For example, a higher pH stifles HCl, a byproduct of polymerization from etching the inorganic core and results in $FeO_xH_yCl_z$-PEDOT core-shell nanofibers (Figure 1.15b), while a lower pH leads to monolithic PEDOT nanofibers (Figure 1.15c). The forced hydrolysis of $FeCl_3$ in organic solvents such as ethanol and nitromethane produces FeOCl 2D structures that templates the formation of PEDOT nanoflowers (Figure 1.15d); the mixture of organic solvent with water generates 1D and 2D nanostructures (Figure 1.15e). A two-salt system is developed utilizing $FeCl_3$ as the oxidant for polymerization and the other salt undergoes hydrolysis as a template. The concentration of $FeCl_3$ is reduced to prevent its hydrolysis, and salts more prone to hydrolyze than $FeCl_3$, such as $TeCl_4$ and $SnCl_4$, are introduced in the

reactant solution. Forced hydrolysis of $TeCl_4$ and $SnCl_4$ in water produces TeO_2 nanowires (F Figure 1.15f) and SnO_2 nanorods (Figure 1.15g) serving as cores in inorganic oxide-PEDOT core-shell hybrid nanomaterials.[58-59] Stoichiometry and temperature control the initial nucleation of β-FeOOH that determines the growth direction of PEDOT nanofibers. Under high $FeCl_3$ concentration (saturated) and low temperature (95 °C), hydrolysis is stifled to nucleate β-FeOOH nanospindles in a slow and heterogeneous manner on the substrate. This uncrowded nucleation contributes to the development of nanofibers horizontally directed along the substrate to minimize the overall system energy, eventually self-assembling into a porous mat. Mass transport of EDOT vapor is enhanced with a N_2 gas flow because of the low temperature that diminishes the evaporation of monomer solution (Figure 1.15h).[60] The horizontally directed PEDOT nanofiber shows a high aspect-ratio ~1000 with high packing density and forms 3D network with 23 μm thick (Figure 1.15i).

1.6 Applications of nanostructured conducting polymers

Conducting polymers (CPs) is one of the research hotspots due to their unique electrical, optical, mechanical and biological properties and therefore are widely applied in energy storage and conversion devices, photo/electrocatalysis, chemical/biological sensors and electromagnetic shielding.[61] Unlike bulk CPs, nanostructured CPs exhibit superior electrical conductivity, higher carrier mobility, enhanced electrochemical activity and improved optical property due to their confined nanostructures and ultra-surface areas.[62]

1.6.1 Energy storage

Conducting polymers (CPs) are uniquely suited for energy storage due to their ability to undergo fast and reversible doping and dedoping, as well as reduction and oxidation reactions. Here we will discuss their relevance in electrochemical capacitors (ECs), an important family of energy storage devices that bridge the gap between batteries and capacitors.[63] The ideal energy storage device has the high energy and power density of a combustion engine and would be quickly rechargeable by applying an electrical potential across its electrodes rather than having to refuel to sustain a combustion reaction. Efficiency remains a fundamental drawback of combustion engines. ECs reach 99% efficiency with moderate energy and power densities i.e., these are a compromise between fast (capacitive) storage systems and energy dense (battery-like) systems.[64]

Since 1957, when the first patent was filed,[65] the most common commercially available active material for ECs remains activated carbon; this inexpensive black powder is commonly produced by the combustion of coconut shells. Activated carbon is a porous material that provides a high surface area for ions to adsorb on with applied potential, a mechanism known as electric double layer capacitance. Fabricating active electrodes from activated carbon generally requires the addition of a conductive additive (mostly graphitic carbon black nanoparticles) and a polymer binder. These materials are combined into a slurry, spread on current collectors such as aluminum or copper foil, and lead to an electrochemically active electrode. In a two-electrode geometry device, two of these electrodes are immersed in an electrolyte and with minimal separation to shorten ion diffusion path lengths and avoid a short circuit. This device is charged when electrodes are polarized simultaneously under opposing potentials; as electrolyte ions segregate to the positive and negative electrodes, the charge is balanced and remains stable. Attaching an electrical

load, an LED for example, between these electrodes causes current to flow through the LED as ions desorb from the polarized active material back into solution. Advantages of using carbon allotropes for energy storage include low-cost, high electrical conductivity in some and a wide potential window in organic solvents; moreover, specialized carbons have shown promising energy densities in aqueous media using smaller potential windows.[66] One major limitation of activated carbon ECs is their relatively low energy density caused by non-capacitive additive materials, low redox activity of activated carbons and low material utilization yield.

A promising route to improving the performance and applicability of ECs is to develop new materials for next-generation devices with improved properties. These materials must be able to undergo fast charging and discharging with high efficiency and cycling stability comparable to activated carbon. Some of these promising materials include metal oxides,[67] MXenes,[68-69] small organic molecules[70] and conducting polymers. Composites of these will not be discussed here, though many examples of positive results exist from combining these materials together to improve performance.[71-73] We will focus on the application of conducting polymers for storing electrochemical energy and aim to provide the reader with an accurate depiction of progress made in the last decade. There are many reasons to look at conducting polymers for energy storage; for example, their synthesis is typically inexpensive resulting in nano- and microstructures through self-assembly. Stable conducting polymers have high conductivity, up to 8797 S/cm for PEDOT,[74] with a surprisingly high energy storage density due to a unique redox/doping charge storage mechanism that can also be controlled from the vapor phase, in solution, or via electrochemistry. Advanced polymeric materials synthesized with a focus on molecular structure, engineered into devices that fully consider both the chemical and material limitations of conducting polymers,

have been shown to perform with extraordinarily high cycling stabilities rivaling that of commercialized activated carbons and with a high energy density as well.

1.6.1.1 Theoretical limits of conducting polymers

The amount of charge transferred to or from each monomer unit in the polymer is an important parameter for theoretical capacitance calculation (Equation 1.2). This parameter, α, or doping level, is proportional to the specific capacitance (C_{sp}) of a conducting polymer[75]

$$C_{sp} = \frac{\alpha \cdot F}{\Delta E \cdot M} \qquad \text{(Equation 1.2)}$$

Where F is the Faraday constant, ΔE is the potential range and M is the molecular mass of the monomer unit in the polymer.[76] Generally, analysis of charge-transfer reactions in the conducting polymer is carried out via cyclic voltammetry (CV). The doping level α can be quantified using an electrochemical quartz crystal microbalance (EQCM), by observing the mass of the CP electrode change with repeated electrochemical doping and dedoping of electrolyte ions.[75]

Conducting polymers are semiconductors that undergo conducting/insulating phase transitions during CV i.e., the doping level α varies with the potential window during CV. For example, a ferrocenyl substituted bithiophenic CP cycled under potential windows 0 - 0.8 V, 0.2 - 0.55 V, and 0.55 - 0.7 V exhibits α of 0.93, 0.35 and 0.16, respectively.[77] The specific capacitance is calculated by Equation 1.3.

$$C_{sp} = \frac{Q}{\Delta E \cdot m} \qquad \text{(Equation 1.3)}$$

where m refers to the electrode mass, Q is the total charge transferred in Coulombs, and Q = α•F. Within these potential windows (ΔE), the theoretical capacitances are 505 F/g, 435 F/g, and

464 F/g thereby illustrating the importance of the potential range that is applied. Consideration of the potential window matters when comparing these capacitances, for example, in a 0.8 V window, where 0.0 V represents fully discharged and 0.8 V fully charged, the total % of charge stored differs significantly from 37.3% (0.2 - 0.55 V) down to 17.5% (0.55 - 0.7 V).

Another clear example of the disparity between experiment and theory is found in polyaniline (PANi), a polymer that exhibits the highest theoretical capacitance among all conducting polymers. The theoretical capacitance of PANi is around 2000 F/g while the experimental capacitance of PANI in 1.0 M H_2SO_4 is around 400 F/g – 600 F/g,[78] though some groups have successfully demonstrated capacitances up to 1000 F/g.[79] The cyclic voltammogram of PANi is shown in Figure 1.16.

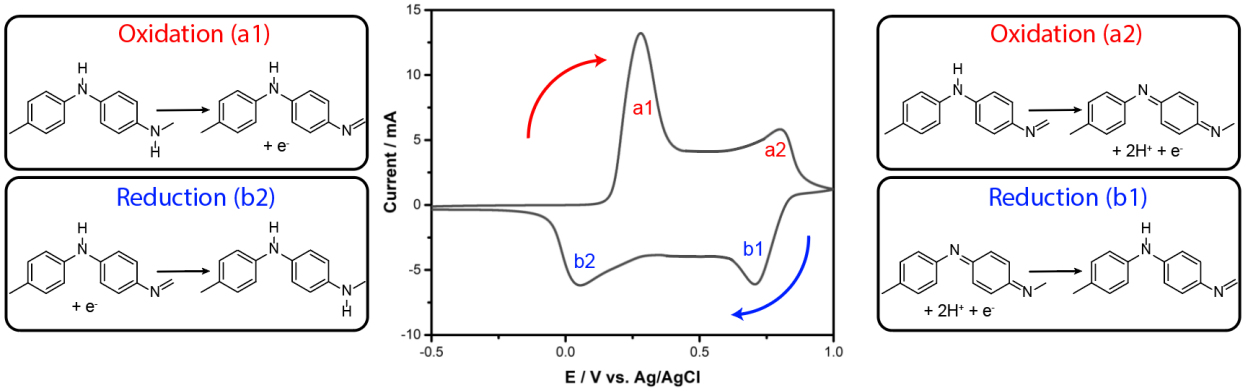

Figure 1.16: Cyclic voltammogram of polyaniline in 1 M aqueous H_2SO_4 shows two redox couples. The direction of potential scan is shown with the arrows and chemical reactions are in boxes.

The cyclic voltammogram shows two oxidation peaks (a1, a2) and two reduction peaks (b1, b2) corresponding to a transition from an insulating to a conducting state; this process is highly reversible without degradation of a polymer when carried out under a constrained potential window. PANi is typically synthesized in the emeraldine oxidation state, observed in the cyclic

voltammogram between fully oxidized pernigraniline (a2) and fully reduced leucoemeraldine (b2). Emeraldine is electronically conducting when doped and an ideal material for electrochemical capacitors; the depth of discharge of a PANi electrode, doping levels, and theoretical capacitance are related to the potential window utilized (Table 1.2).

	ΔE / V	**C_{calc} / F/g**	**% charge**
-0.1 ~ 1.0 V	1.1	825-744	100
-0.1 ~ 0.4 V	0.5	718-648	37.4
0 ~ 0.4 V	0.4	743-670	31.9
0.1 ~ 0.4 V	0.3	719-649	23.5
0.15 ~ 0.5 V	0.35	695-627	25.6
0.15 ~ 0.6 V	0.45	738-665	35.0
0.15 ~ 0.7 V	0.55	747-673	43.4

Table 1.2: Capacitance versus potential window of PANi electrode, adapted from reference [80].

At opposite ends of voltage window, conductivity drops off dramatically, visible as a low current "tail" following a clear redox peak. This also occurs in other conducting polymers, such as polythiophene, poly(3,4-ethylenedioxythiophene) (PEDOT) and polypyrrole (PPy), all of which have insulating states at extreme anodic and cathodic potentials.

The mass of conducting polymer deposited as electrode material needs to be quantitatively determined - an accurate measurement of the mass of activate material is paramount for determining the correct gravimetric capacitance (Equation 1.4):

$$C_{sp} = \frac{I \cdot t}{\Delta E \cdot m} \qquad \text{(Equation 1.4)}$$

Where C_{sp} is the specific capacitance, I is the current, t refers to the discharge time, ΔE is the potential range and m is the mass of electrode.[81] In general, the total mass of PANi coated on a current collector serves as the mass of active material. However, in the case of the PANi nanofibers depicted in Figure 1.17, the mass of electrically accessible active material is constantly in flux depending on charging conditions.

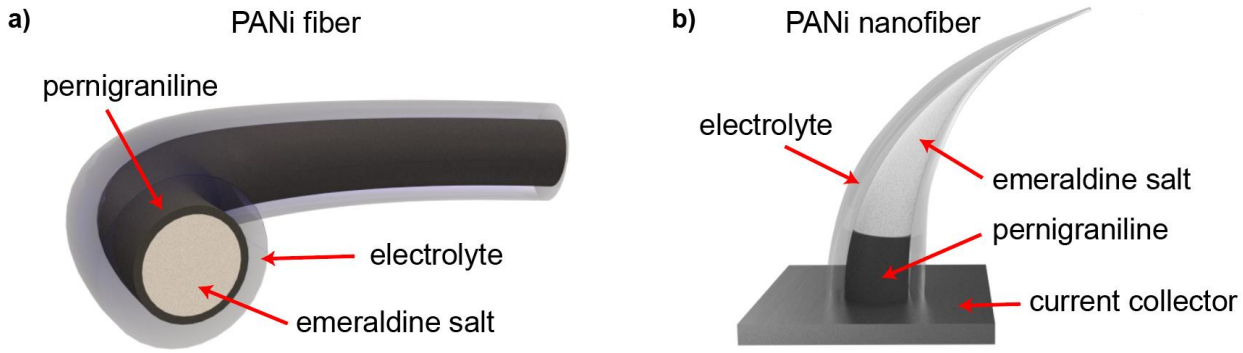

Figure 1.17: Influence of PANi morphology on charging characteristics. (a) Only the outer surface of a low surface-area PANi fiber is doped at high rates, leading to a low gravimetric capacity. (b) The capacitance of a single PANi nanofiber grafted to a current collector is influenced by the kinetics of oxidation of the polymer.

Figure 1.17a depicts a model for an electrochemically oxidized PANi fiber with a significantly large diameter. Dopants can only diffuse to the shell, limiting capacitance at high charging rates. The core does not contribute to charge storage and remains as synthesized, in the emeraldine salt doped state. Given that the large core volume of the PANi nanofiber, the specific capacitance will

be relatively low. A possible way to mitigate this issue is to graft high aspect ratio nanofibers directly on a current collector where the inaccessible core volume is negligible even at high charging rates (Figure 1.17b). Albeit, the nanofibrillar area closest to the current collector may be reduced to an insulating state at a faster rate than the end of the fiber causing break-up of the percolation network and a lower than expected capacitance.

It is important that the relationship between theoretical and experimental capacitance be fully understood before viewing a theoretical capacitance as a "benchmark" or as an unachievable goal. Materials with high theoretical or experimental specific capacitances do not necessarily translate to state-of-the-art energy storage electrodes. However, capacitance can be an incredibly useful metric in the discovery of new materials that may have a lasting impact in energy storage. The level of agreement between theoretical and experimental capacitance allows researchers to elucidate the fundamental mechanisms of charge storage in materials, so that both experimental materials and theoretical models can be improved.

The synthesis of conducting polymers leads to a variety of macromolecular salt structures. Upon initial electrochemical cycling of a material, a conducting polymer electrode undergoes irreversible processes, including conversion of synthesized salt structures to reversible ones and removal of intrinsic dopants. Therefore, it is important not to refer to the initial capacitance loss of a conducting polymer as a loss of reversible charge storage ability. For instance, condensing vapor phase polymerized polypyrrole microtube electrodes purified in 6 M HCl show a high first cycle capacitance in 1 M $LiClO_4$ of over 700 F/g, but quickly fade to a stable capacitance of 350 F/g.[82] Much of the initial charge comes from a large reduction peak present at the lower extent of the potential window. If this initial drop in current were to be included in the calculation of capacitance loss, the polymer would appear to lose 50% of its initial capacitance within the first few cycles.

1.6.1.2 Electrolytes, ions and stability

In CPs, the inherent flexibility of the polymer network causes modulation of pore size during charging and discharging. In rigid materials like activated carbon, electrolyte ions are chosen based on their size compatibility with the pore size in the carbon.[83] Improvement of traditional ECs has involved the production of higher surface area carbon while maintaining acceptable conductivity, combined with distinct ion size matching for maximum double-layer capacitance. The electrolyte ions must also be stable under high potentials and soluble in the chosen solvent.

Aqueous Electrolytes

Aqueous electrolytes such as H_2SO_4, HCl, KOH, and Na_2SO_4 provide a high ionic conductivity compared with other types of electrolyte. Acidic (H_2SO_4) and alkaline (KOH) electrolytes have conductivities up to 1 S/cm, at least an order of magnitude more conductive than salts in organic electrolytes. Thus, ECs using aqueous electrolytes will generally have a higher capacitance and lower internal resistance than ECs based on organic electrolytes.[84] It has been suggested that aqueous acidic electrolytes lead to higher ionic conductivity based on a charge transfer mechanism in water known as the Grotthus mechanism,[85] where protons hop via hydrogen-bonding networks of water molecules on the surface of activated materials, increasing ionic conductivity. Given finite scan rates, this can lead to higher capacitance.[86]

While aqueous electrolytes maintain an advantage of low resistance, they are limited by water decomposition which occurs at a potential of 1.23 V. Voltage window is incredibly important for high energy and power density, shown by Equation 1.5 and Equation 1.6.

$$E = \frac{1}{2} C \Delta V^2 = \frac{Q \Delta V}{2} \qquad \text{(Equation 1.5)}$$

$$P = \frac{1}{4R_s}\Delta V^2 \qquad \text{(Equation 1.6)}$$

where Q denotes the stored total charge in the ECs, ΔV refers to the EC's total voltage window, and R_s stands for the equivalent series resistance of the total packaged EC.[87]

Organic Electrolytes

Compared to aqueous electrolytes, organic electrolytes provide a voltage window as high as 3.5 V. This leads to organic electrolytes being preferred in traditional electrochemical capacitors based on carbon.[84] Among organic electrolytes, acetonitrile (AN) and propylene carbonate (PC) are the most commonly used solvents. Preparation of organic electrolyte ECs is more complicated than their aqueous counterparts. The water content in organic electrolytes must be kept below 3-5 ppm or H_2 and O_2 will be produced by water decomposition at voltages higher than 1.23 V, limiting device lifetime.[84] This often requires solvent distillation, glovebox device fabrication and intricate device sealing mechanisms.

When conducting polymers charge and discharge, in theory, the complete volume of electrode material should contact the electrolyte solution, resulting in a high effective surface area. However, the swelling and shrinking of the polymer chains in organic electrolytes is less pronounced than in aqueous electrolytes, leading to less doping from counter ions because of the constrained space between polymer chains and resulting in high ionic resistance.[88]

Ionic Liquids as Electrolytes

Ionic liquids are solvent-free electrolytes at room temperature; their voltage window stability is thus only driven by the electrochemical stability of the ions.[87] Ionic liquids have many desirable properties that make them promising candidates for CP EC electrolytes, such as low vapor phase

pressure, high thermal as well as chemical stability,[89-90] low flammability, wide electrochemical stability window ranging from 2 to 6 V (typically about 4.5 V). Moreover, ionic liquids anions and counter ions for CPs are often the same, such as PF_6^-, BF_4^-, $CF_3SO_3^-$ or $[(CF_3SO_2)_2N]^-$.[91] In ionic liquids, conducting polymer electrodes show improved performance and greater lifetimes,[92-93] especially in actuators[94] where doping and de-doping of ions into the polymer is required for large-scale morphological changes. Compared with carbon electrodes where ion sorption and desorption is facile, conducting polymers differ by undergoing large volume change in polymer architecture due to the intercalation of doping anions or cations.[91]

However, viscosity remains a problem for ionic liquids. As there is no solvent, the kinetics of ions transfer are low, leading to low ionic conductivity. Ionic liquids can be mixed with small amounts of organic solvents like acetonitrile, nitrobenzene or chloroform, thus decreasing viscosity[95] and increasing ionic conductivity from 20 mS/cm to 70 mS/cm, a value comparable to organic electrolytes.[96]

Solid Gel or Polymer Electrolytes

Compared with using liquid electrolyte in ECs which requires robust encapsulation to prevent leakage and a separator to avoid electrical contact between the electrodes, polymer electrolytes[97-98] offer dual functionality as they combine the separator and the electrolyte into a single layer. This avoids potential leakage since the electrolyte is bound within the polymer matrix and by shortening the distance between two electrodes, the specific capacitance becomes much larger.[98] The performance of gel electrolytes has already been demonstrated to be comparable to its liquid counterparts.[99-100] Flexible devices based on poly(vinyl alcohol)/H_3PO_4 as well have been demonstrated by using-polyaniline and polyaniline composite electrodes.[101-102]

Degradation

Improving the electrochemical cycling stability of CP-based ECs is paramount for their successful implementation in real-world applications. Typically, the electrochemical performance of a CP-based EC decays sharply after only a few thousand charge-discharge cycles, far from the well-established carbon-based ECs that can be cycled up to 1 million times.[84] Two destructive mechanisms during cycling are the causes for CPs' reported low cycling stability: electrochemical and mechanical degradation (Figure 3).

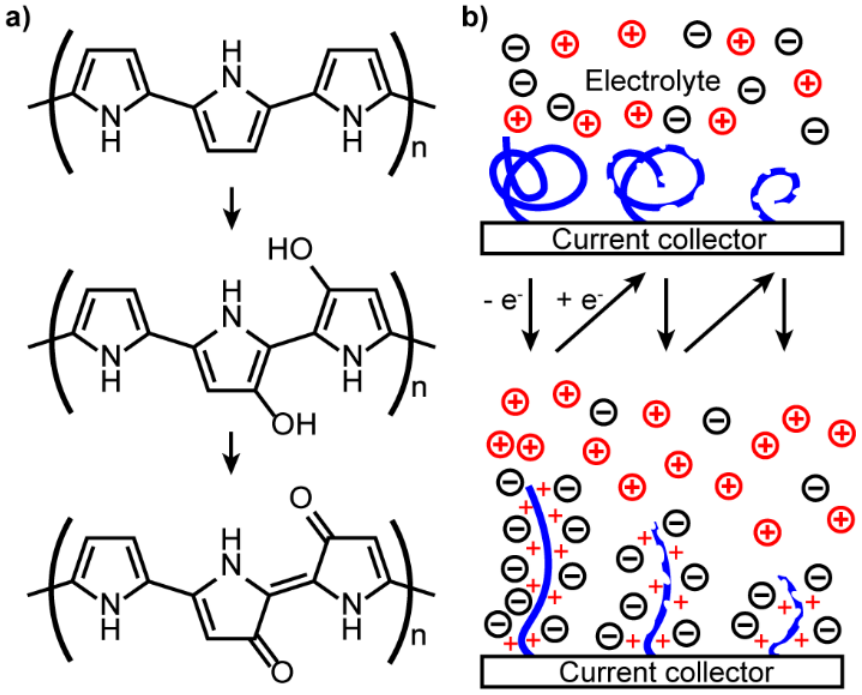

Figure 1.18: A schematic of the electrochemical degradation of CPs. (a) Overoxidation of polypyrrole (chemical degradation); (b) Expansion and contraction of CPs during cycling due to doping and de-doping, resulting in mechanical degradation.

Electrochemical degradation of p-dopable CPs during cycling is related to the over-charging/discharging of polymer backbone and the presence of nucleophiles in the electrolyte (Figure 1.18a). At a more positive potential, chemical bonds in CPs are broken and the polymer chains are irreversibly over-oxidized into fragments; at a more negative potential, the reduced CPs show poor conductivity, resulting in decreased capacitance. For example, both reduced and oxidized states of PANI (leucoemeraldine and pernigraniline, separately) are insulating and result in low current at low and high potentials when charging and discharging.[103]

It is also demonstrated that nucleophile in the electrolyte (e.g. OH^-, Br^-) facilitates the electrochemical degradation of CPs. With OH^- in the electrolyte, it is easy for β-C in PPy to oxidize into C=O and form quinone, disrupting conjugation and leading to low electrochemical performance. Polymer chains also crosslink during the degradation process, creating rigid islands entrapped by insulating points that hinder ionic exchange, deteriorating the capacitance.[104-105] To overcome electrochemical degradation during cycling, both electrochemical processes (voltage window, scan rate, etc.) and cell components (electrolyte, current collector, etc.) need to be carefully selected.[106] Large voltage windows beyond an electrochemically stable range may increase the energy density of a device but will degrade the CP and lead to reversibility issues.

Mechanical degradation is highly related to the volume change of CPs during cycling. When charging and discharging, CPs undergo doping and de-doping processes; counter ions travel toward and away from the polymer backbone, causing repeated expansion and contraction of the material (Figure 1.18b). Unlike in activated carbon, where ion intercalation has little effect on pore structure (Figure 1.19a),[87] there is no accurate model for predicting dopant effects on CP pore structure. Since the solvent shell around ions will undergo partial dissolution when ions penetrate into smaller pores, the effective size of ions can vary.[107] Though the polymer is porous, during the

charge and discharge process, the polymer network will swell and shrink, leading to variable pore size (Figure 1.19b). This can cause irreversible changes in the percolation network, loss of conductivity and reversibility. The correlation between size of electrolyte ion and CP performance is complicated, and electrolyte/CP compatibility is generally determined heuristically.

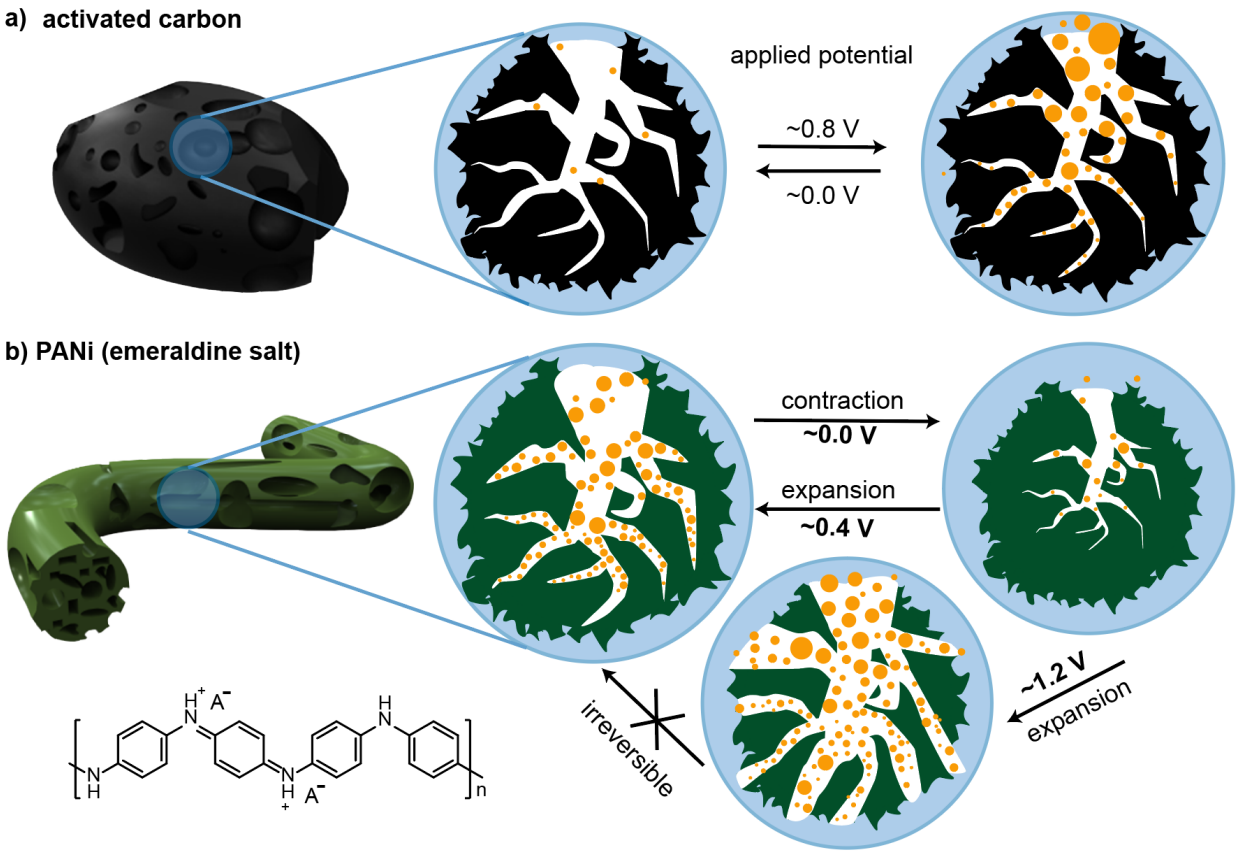

Figure 1.19: Microscale charging mechanisms in rigid materials and soft materials. (a) Porous carbon structure. Inset: Porous carbon structure during charging process in electrolyte. (b) PANi fiber porous structure. Inset: PANi fiber structure during charging process in electrolyte.

Upon doping with ClO_4^-, a PPy film shows radial expansion, causing structural breakdown and decline of electrochemical performance.[84, 105, 108-109] Mechanical degradation of CPs can be minimized by attaching CPs onto porous materials or synthesizing CP nanostructures,[110] allowing more free volume for the material's shrinkage and swelling, while also facilitating electrolyte diffusion. Making composites can also increase the overall mass and volume of the device, decreasing the gravimetric and volumetric capacitance. Moreover, fast diffusion of electrolytes facilitates the self-discharge rate of conducting polymer (higher charge loss rate per unit time at certain cell potential values).[111] Nanostructured CPs with soft architectures are ideal for resisting mechanical degradation while retaining energy density. A homogeneous CP structure and ordered polymer chain alignment help mitigate stress generated during cycling, prevent crack formation when the CPs are shrinking and swelling, and result in extended electrochemical stability.[112-113] For example, control of the electrochemical polymerization of PPy results in ordered molecular alignment that uniformly distributes stress while facilitating charge transfer; the resulting device retains 86% of capacitance after 100,000 charging/discharging cycles.[113] Initial electrochemical cycling under reduced voltage windows is also shown to increase the cycling stability of a CP EC. This "priming" step relaxes the molecular structure gradually, so the electrode architecture experiences less strain after increasing to a larger voltage window. This priming technique enables a PANi based EC to cycle for more than 10,000 cycles with 93% capacitance retained in a voltage window of 0.8 V.[103]

1.6.2 Other applications

1.6.2.1 Biosensors

Biosensors are devices that enable to emulate biological systems and take noninvasive measurements of various functional indicators of the human body.[114] Nanostructured conducting polymers (NCPs) are one of the promising biosensor materials since their conductivities are sensitive to the environment, resulting in a change from an insulating state to an electrically conducting state with chemical or electrochemical doping.[115] There are three advantages of NCPs: first, the properties of NCPs are easily tailored to detect a wide range of chemicals based on the conductivity change versus various dopant ions and doping levels; second, NCPs exhibit enhanced sensitivity compared to the bulk material-based sensors due to their high surface area; third, the NCPs possess faster response time than non-nanostructured sensors since the porosity of the nanostructures enables facile diffusion of gas molecules.[116-117]

1.6.2.2 Electromagnetic interference

Electromagnetic interference (EMI) is receiving increased emphasis due to the extensive utilization of communication equipment, such as phones and radar systems, leading to a negative effect on human health.[118] However, the conventional shielding materials, such as carbon nanotubes, suffer from the reflection, result in incomplete EM waves absorption, and further produce secondary/repeated EMI pollution.[119] Conducting polymers (CPs) are ideal EMI shielding materials due to their high electrical conductivity, low energy optical transitions, low ionization potential, and high electron affinity, enabling both reflection and microwave absorption behavior.[120] To date, CPs-based EMI shielding materials have made significant achievements in

this field through rational design of microstructures and hybridization with different types of materials.[121]

1.6.2.3 Thermoelectric

Thermoelectric materials play a vital role in improving energy conversion efficiency by converting waste heat into electricity.[122] The key parameter of thermoelectric performance is the dimensionless thermoelectric figure-of-merit (ZT), defined as ($ZT = S^2\delta T/\kappa$).[35, 123] Where S is the Seebeck coefficient, δ is the electrical conductivity, T is the absolute temperature, and κ is the thermal conductivity. Conducting polymers (CPs) are well investigated in the thermoelectric field due to their low cost, flexibility, processability and low intrinsic thermal conductivity (0.1-0.5 W/mK).[124] However, the random orientation of the molecular chains in amorphous domains impedes the conductance of CPs, leading to low thermoelectric performance. Recently, considerable enhancements are achieved by nanoscale conducting polymers. The highly ordered polymer chains facilitate the charge carrier mobility result in an improvement in both electrical conductivity and Seebeck coefficient.[125]

References

(1) Wang, H.; Diao, Y.; Lu, Y.; Yang, H.; Zhou, Q.; Chrulski, K.; D'Arcy, J. M., Energy storing bricks for stationary PEDOT supercapacitors. *Nat Commun* **2020,** *11* (1), 3882.

(2) Morris, R. V.; Golden, D. C.; Bell, J. F., Low-temperature reflectivity spectra of red hematite and the color of Mars. *Journal of Geophysical Research: Planets* **1997,** *102* (E4), 9125-9133.

(3) Shuai Li, P. G. L., Abigail A. Fraeman, Andrew R. Poppe, Vivian Z. Sun,Dana M. Hurley,

Peter H. Schultz, Widespread hematite at high latitudes of the Moon. *Science Advances* **2020,** *6* (waba1940).

(4) Jill A. Mikucki, A. P., David T. Johnston, Alexandra V. Turchyn, James Farquhar, Daniel P. Schrag, Ariel D. Anbar, John C. Priscu, Peter A. Lee, A Contemporary Microbially Maintained Subglcial Ferrous "Ocean". *Science* **2009,** *324*.

(5) Koch G, V. J., Thompson N, Moghissi O, Gould M, Payer J, International measures of prevention, application, and economics of corrosion technologies study. Houston: NACE International. **2016**.

(6) Henshilwood, C. S.; d'Errico, F.; van Niekerk, K. L.; Dayet, L.; Queffelec, A.; Pollarolo, L., An abstract drawing from the 73,000-year-old levels at Blombos Cave, South Africa. *Nature* **2018,** *562* (7725), 115-118.

(7) Mady Elias, a. P. C., Multispectral camera and radiative transfer equation used to depict Leonardo's sfumato in Mona Lisa. *APPLIED OPTICS* **2008,** *47* (12).

(8) Rifkin, R. F.; Dayet, L.; Queffelec, A.; Summers, B.; Lategan, M.; d'Errico, F., Evaluating the Photoprotective Effects of Ochre on Human Skin by In Vivo SPF Assessment: Implications for Human Evolution, Adaptation and Dispersal. *PLoS One* **2015,** *10* (9), e0136090.

(9) A. Bianconi, A. C.-C., M. Dell'Ariccia, A. Giovannelli E. Burattini, and P.J. Durham, Increase of the Fe effective charge in hemoproteins during oxygenation process. *Biochemical and biophysical research communications* **1985,** *131* (1).

(10) Cornell, R. M., Schwertmann, U., The Iron Oxides: Structure, Properties, Reactions, Occurrences and Uses. 1st ed. *Wiley-VCH: Weinheim* **2003**.

(11) Stumm, W. a. F., G., The dissolution of oxides and aluminum silicates: Examples of

surface-coordination-controlled kinetics. *In: Stumm, W., (Ed.), Aquatic Surface Chemistry J., Wiley and Sons* **1987**, 197-219.

(12) Banwart, S., Davies, S. and Stumm, W., The role of oxalate in accelerating the reductive dissolution of hematite(α-Fe2O3) by ascorbate. *Colloids and Surfaces* **1989,** *39*, 303-309.

(13) Cornell, R. P., A.; Quirk, J., Kinetics and Mechanisms of the Acid Dissolution of Goethite (α-FeOOH). *Journal of Inorganic and Nuclear Chemistry* **1976,** *38* (3), 563-567.

(14) Salmimies, R.; Mannila, M.; Juha, J.; Häkkinen, A., Acidic Dissolution of Magnetite: Experimental Study on The Effects of Acid Concentration and Temperature. *Clays and Clay Minerals* **2011,** *59* (2), 136-146.

(15) Zhang, Y., Kallay, N. and Matijevic, E., Interactions of Metal Hydrous Oxides with Chelating Agents, VII. Hematite - Oxalic and Citric Acid Systems. *Langmuir* **1985,** *1*, 201-206.

(16) Chang, H. C. a. M., E., Interactions of Metal Hydrous Oxides with Chelating Agents, IV. Dissolution of Hematite. *J. Colloid Interface Sci.* **1983,** *92*, 479-488.

(17) Sulzberger, B., Suter, D., Siffert, C., Banwart, S., Stumm, W., Dissolution of fe(iii)(hydr)oxides in natural waters; laboratory assessment on the kinetics controlled by surface coordination. *Marine Chemistry* **1989,** *28*, 127-144.

(18) Wang, H.; Diao, Y.; Rubin, M.; Santino, L. M.; Lu, Y.; D'Arcy, J. M., Metal Oxide-Assisted PEDOT Nanostructures via Hydrolysis-Assisted Vapor-Phase Polymerization for Energy Storage. *ACS Applied Nano Materials* **2018,** *1* (3), 1219-1227.

(19) Jolivet, J. P.; Chaneac, C.; Tronc, E., Iron oxide chemistry. From molecular clusters to extended solid networks. *Chem Commun (Camb)* **2004,** (5), 481-7.

(20) Jolivet, J.-P.; Tronc, E.; Chanéac, C., Iron oxides: From molecular clusters to solid. A nice example of chemical versatility. *Comptes Rendus Geoscience* **2006,** *338* (6-7), 488-497.

(21) Guo, H.; Barnard, A. S., Naturally occurring iron oxide nanoparticles: morphology, surface chemistry and environmental stability. *J. Mater. Chem. A* **2013,** *1* (1), 27-42.

(22) Rémazeilles, C.; Refait, P., On the formation of β-FeOOH (akaganéite) in chloride-containing environments. *Corrosion Science* **2007,** *49* (2), 844-857.

(23) Bailey, J. K. B., C. J.; Mecartney, M. L., Growth Mechanisms of Iron Oxide Particles of Differing Morphologies from the Forced Hydrolysis of Ferric Chloride Solutions. *J. Colloid Interface Sci.* **1993,** *157*, 1-13.

(24) Zhang, X. C., Y.; Zhao, N.; Liu, H.; Wei, Y, Citrate Modified Ferrihydrite Microstructures: Facile Synthesis, Strong Adsorption and Excellent Fenton-Like Catalytic Properties. *RSC Adv.* **2014,** *4* (41), 21575-21583.

(25) Zhao, J.; Lin, W.; Chang, Q.; Li, W.; Lai, Y., Adsorptive characteristics of akaganeite and its environmental applications: a review. *Environmental Technology Reviews* **2012,** *1* (1), 114-126.

(26) Hideki Shirakawa, E. J. L., Alan G. MacDiarmid, Chwan K. Chinang and Alan J. Heeger, Synthesis of Electronically Conducting Organic Polymers: Halogen Derivatives of Polyacetylene, (CH)x. *J.C.S. Chem. Comm* **1977**.

(27) Inzelt, G., Conducting Polymers: A New Era in Electrochemistry. *Springer-Verlag, Berlin/Heidelberg, Germany* **2008**.

(28) Kamarudin, M. A.; Sahamir, S. R.; Datta, R. S.; Long, B. D.; Mohd Sabri, M. F.; Mohd Said, S., A review on the fabrication of polymer-based thermoelectric materials and fabrication methods. *ScientificWorldJournal* **2013,** *2013*, 713640.

(29) Bubnova, O.; Crispin, X., Towards polymer-based organic thermoelectric generators. *Energy & Environmental Science* **2012,** *5* (11), 9345.

(30) Li, Y., Conducting Polymers. *Organic Optoelectronic Materials, Springer, Cham, Switzerland* **2015**.

(31) Armes, S. P.; Aldissi, M.; Hawley, M.; Beery, J. G.; Gottesfeld, S., Morphology and structure of conducting polymers. *Langmuir* **1991,** *7* (7), 1447-1452.

(32) Dongmin Kang, S.; Jeffrey Snyder, G., Charge-transport model for conducting polymers. *Nat Mater* **2017,** *16* (2), 252-257.

(33) Brown, P. J.; Thomas, D. S.; Köhler, A.; Wilson, J. S.; Kim, J.-S.; Ramsdale, C. M.; Sirringhaus, H.; Friend, R. H., Effect of interchain interactions on the absorption and emission of poly(3-hexylthiophene). *Physical Review B* **2003,** *67* (6).

(34) A. J. Epstein, J. M. G., F. Zuo, H. S. Woo, D. B. Tanner, A. F. Richter, M. Angelopoulos, W. S. Huang, A. G. MacDiarmid, Insulator-to-Metal Transition in Polyaniline: Effect of Protonation in Emeraldine. *Synthetic Metals* **1987,** *21*, 63-70.

(35) Bharti, M.; Singh, A.; Samanta, S.; Aswal, D. K., Conductive polymers for thermoelectric power generation. *Progress in Materials Science* **2018,** *93*, 270-310.

(36) J. L. Bredas, G. B. S., Polarons, Bipolarons, and Solitions in Conducting Polymers. *Acc. Chem. Res* **1985,** *18*, 309-315.

(37) Kroon, R.; Mengistie, D. A.; Kiefer, D.; Hynynen, J.; Ryan, J. D.; Yu, L.; Muller, C., Thermoelectric plastics: from design to synthesis, processing and structure-property relationships. *Chem Soc Rev* **2016,** *45* (22), 6147-6164.

(38) C. Alemán, L. J., Characterization of the Quinoid Structure for the 2,2'-Bithiophene and 2,2',5',2''-Terthiophene Dications. *J. Phys. Chem.* **1996,** *100*, 14661-14664.

(39) Ghosh, R.; Pochas, C. M.; Spano, F. C., Polaron Delocalization in Conjugated Polymer Films. *The Journal of Physical Chemistry C* **2016,** *120* (21), 11394-11406.

(40) Emin, D., Pair breaking in semiclassical singlet small-bipolaron hopping. *Physical Review B* **1995,** *53* (3).

(41) David Beljonne, J. C., Henning Sirringhaus, Peter J. Brown, Maxim Shkunov, Richard H. Friend, and Jean-Luc BrØdas, Optical Signature of Delocalized Polarons in Conjugated Polymers. *Adv. Funct. Mater* **2001,** *11* (3).

(42) Stafstrom, S.; Bredas, J. L.; Epstein, A. J.; Woo, H. S.; Tanner, D. B.; Huang, W. S.; MacDiarmid, A. G., Polaron lattice in highly conducting polyaniline: Theoretical and optical studies. *Phys Rev Lett* **1987,** *59* (13), 1464-1467.

(43) Lee, K.; Cho, S.; Park, S. H.; Heeger, A. J.; Lee, C. W.; Lee, S. H., Metallic transport in polyaniline. *Nature* **2006,** *441* (7089), 65-8.

(44) Nardes, A. M.; Kemerink, M.; Janssen, R. A. J.; Bastiaansen, J. A. M.; Kiggen, N. M. M.; Langeveld, B. M. W.; van Breemen, A. J. J. M.; de Kok, M. M., Microscopic Understanding of the Anisotropic Conductivity of PEDOT:PSS Thin Films. *Advanced Materials* **2007,** *19* (9), 1196-1200.

(45) Podzorov, V.; Pudalov, V. M.; Gershenson, M. E., Field-effect transistors on rubrene single crystals with parylene gate insulator. *Applied Physics Letters* **2003,** *82* (11), 1739-1741.

(46) Shirota, Y., Photo- and electroactive amorphous molecular materials—molecular design, syntheses, reactions, properties, and applications. *J. Mater. Chem.* **2005,** *15* (1), 75-93.

(47) Veaceslav Coropceanu, J. r. m. C., Demetrio A. da Silva Filho, Yoann Olivier, Robert Silbey, and Jean-Luc Bre´das, Charge Transport in Organic Semiconductors. *Chem. Rev.* **2007,** *107*, 926-952.

(48) Lv, A.; Puniredd, S. R.; Zhang, J.; Li, Z.; Zhu, H.; Jiang, W.; Dong, H.; He, Y.; Jiang, L.; Li,

Y.; Pisula, W.; Meng, Q.; Hu, W.; Wang, Z., High mobility, air stable, organic single crystal transistors of an n-type diperylene bisimide. *Adv Mater* **2012,** *24* (19), 2626-30.

(49) DAN LI, J. H., AND RICHARD B. KANER, Polyaniline Nanofibers: A Unique Polymer Nanostructure for Versatile Applications. *Acc. Chem. Res* **2008,** *42* (1), 135-145.

(50) Bhattacharyya, D.; Howden, R. M.; Borrelli, D. C.; Gleason, K. K., Vapor phase oxidative synthesis of conjugated polymers and applications. *Journal of Polymer Science Part B: Polymer Physics* **2012,** *50* (19), 1329-1351.

(51) Lawal, A. T.; Wallace, G. G., Vapour phase polymerisation of conducting and non-conducting polymers: a review. *Talanta* **2014,** *119*, 133-43.

(52) <1-s2.0-S0032386100008004-main.pdf>.

(53) Jean-Yves Bottero, A. M., Frédéric Villieras, and Denise Tchoubar, Structure and Mechanisms of Formation of FeOOH(Cl) Polymers. *Langmuir* **1994,** *10*, 316-319.

(54) Flynn, C. M., Hydrolysis of inorganic iron(III) salts. *Chemical Reviews* **1984,** *84* (1), 31-41.

(55) Julio M. D'Arcy, M. F. E.-K., Pwint P. Khine, Linghong Zhang, Sun Hwa Lee, Nicole R. Davis, David S. Liu, Michael T. Yeung, Sung Yeol Kim, Christopher L. Turner, Andrew T. Lech, Paula T. Hammond, and Richard B. Kaner, Vapor-Phase Polymerization of Nanofibrillar Poly(3,4-ethylenedioxythiophene) for Supercapacitors. *ACS Nano* **2014,** *8* (2), 1500-1510.

(56) Diao, Y.; Chen, H.; Lu, Y.; Santino, L. M.; Wang, H.; D'Arcy, J. M., Converting Rust to PEDOT Nanofibers for Supercapacitors. *ACS Applied Energy Materials* **2019,** *2* (5), 3435-3444.

(57) Tania Henry, K. K., Zaiyuan Ren, Christopher Yerino, and Jung Han, Directed Growth of

Horizontally Aligned Gallium Nitride Nanowires for Nanoelectromechanical Resonator Arrays. *Nano Lett* **2007,** *7* (11), 3315-3319.

(58) Wang, H.; Rogach, A. L., Hierarchical SnO2Nanostructures: Recent Advances in Design, Synthesis, and Applications. *Chemistry of Materials* **2013,** *26* (1), 123-133.

(59) Vayssieres, L.; Graetzel, M., Highly ordered SnO2 nanorod arrays from controlled aqueous growth. *Angew Chem Int Ed Engl* **2004,** *43* (28), 3666-70.

(60) Wang, H.; Santino, Luciano M.; Rubin, M.; Diao, Y.; Lu, Y.; D'Arcy, J. M., Self-woven nanofibrillar PEDOT mats for impact-resistant supercapacitors. *Sustainable Energy & Fuels* **2019,** *3* (5), 1154-1162.

(61) Xue, Y.; Chen, S.; Yu, J.; Bunes, B. R.; Xue, Z.; Xu, J.; Lu, B.; Zang, L., Nanostructured conducting polymers and their composites: synthesis methodologies, morphologies and applications. *Journal of Materials Chemistry C* **2020,** *8* (30), 10136-10159.

(62) Zhao, F.; Shi, Y.; Pan, L.; Yu, G., Multifunctional Nanostructured Conductive Polymer Gels: Synthesis, Properties, and Applications. *Acc Chem Res* **2017,** *50* (7), 1734-1743.

(63) Zhang, Y.; Feng, H.; Wu, X.; Wang, L.; Zhang, A.; Xia, T.; Dong, H.; Li, X.; Zhang, L., Progress of electrochemical capacitor electrode materials: A review. *International Journal of Hydrogen Energy* **2009,** *34* (11), 4889-4899.

(64) Hall, P. J.; Mirzaeian, M.; Fletcher, S. I.; Sillars, F. B.; Rennie, A. J. R.; Shitta-Bey, G. O.; Wilson, G.; Cruden, A.; Carter, R., Energy storage in electrochemical capacitors: designing functional materials to improve performance. *Energy & Environmental Science* **2010,** *3* (9), 1238.

(65) Becker, H. I., Low voltage electrolytic capacitor. **1957**.

(66) Li, Z.; Xu, Z.; Wang, H.; Ding, J.; Zahiri, B.; Holt, C. M. B.; Tan, X.; Mitlin, D., Colossal

pseudocapacitance in a high functionality–high surface area carbon anode doubles the energy of an asymmetric supercapacitor. *Energy Environ. Sci.* **2014,** *7* (5), 1708-1718.

(67) Le Thai, M.; Chandran, G. T.; Dutta, R. K.; Li, X.; Penner, R. M., 100k Cycles and Beyond: Extraordinary Cycle Stability for MnO2 Nanowires Imparted by a Gel Electrolyte. *ACS Energy Letters* **2016,** *1* (1), 57-63.

(68) Lukatskaya, M. R. M., O.; Ren, C. E.; Dall'Agnese, Y.; Rozier, P.; Taberna, P. L.; Naguib, M.; Simon, P.; Barsoum, M. W.; Gogotsi, Y. , Cation Intercalation and High Volumetric Capacitance of Two-Dimensional Titanium Carbide. *Science* **2013,** *341*, 1502-1505.

(69) Ling, Z. R., C. E.; Zhao, M.-Q.; Yang, J.; Giammarco, J. M.; Qiu, J.; Barsoum, M. W.; Gogotsi, Y. , Flexible and conductive MXene films and nanocomposites with high capacitance. . *Science* **2014,** *111*, 16676-16681.

(70) Song, Z.; Zhou, H., Towards sustainable and versatile energy storage devices: an overview of organic electrode materials. *Energy & Environmental Science* **2013,** *6* (8), 2280.

(71) Zhao, M. Q.; Ren, C. E.; Ling, Z.; Lukatskaya, M. R.; Zhang, C.; Van Aken, K. L.; Barsoum, M. W.; Gogotsi, Y., Flexible MXene/carbon nanotube composite paper with high volumetric capacitance. *Adv Mater* **2015,** *27* (2), 339-45.

(72) Liu, T.; Finn, L.; Yu, M.; Wang, H.; Zhai, T.; Lu, X.; Tong, Y.; Li, Y., Polyaniline and polypyrrole pseudocapacitor electrodes with excellent cycling stability. *Nano Lett* **2014,** *14* (5), 2522-7.

(73) Bae, J.; Park, J. Y.; Kwon, O. S.; Lee, C.-S., Energy efficient capacitors based on graphene/conducting polymer hybrids. *Journal of Industrial and Engineering Chemistry* **2017,** *51*, 1-11.

(74) Cho, B.; Park, K. S.; Baek, J.; Oh, H. S.; Koo Lee, Y. E.; Sung, M. M., Single-crystal poly(3,4-

ethylenedioxythiophene) nanowires with ultrahigh conductivity. *Nano Lett* **2014,** *14* (6), 3321-7.

(75) Snook, G. A.; Chen, G. Z., The measurement of specific capacitances of conducting polymers using the quartz crystal microbalance. *Journal of Electroanalytical Chemistry* **2008,** *612* (1), 140-146.

(76) Rudge, A. D., J.; Raistrick, I.; Gottesfeld, S.; Ferraris, J. P. , 1994Conducting polymers as active materials in electrochemical capacitors. *Journal of Power Sources 47*, 89-107.

(77) Peng, C.; Zhou, X.; Chen, G. Z.; Moggia, F.; Fages, F.; Brisset, H.; Roncali, J., Internally referenced analysis of charge-transfer reactions in a new ferrocenyl bithiophenic conducting polymer through cyclic voltammetry. *Chem Commun (Camb)* **2008,** (48), 6606-8.

(78) Li, H.; Wang, J.; Chu, Q.; Wang, Z.; Zhang, F.; Wang, S., Theoretical and experimental specific capacitance of polyaniline in sulfuric acid. *Journal of Power Sources* **2009,** *190* (2), 578-586.

(79) Chen, Z. A., V.; Jia, X.; Xiao, Q.; Dunn, B.; Lu, Y. , High-Performance Sodium-Ion Pseudocapacitors Based on Hierarchically Porous Nanowire Composites. *ACS Nano* **2012,** *6*, 4319-4327.

(80) Peng, C.; Hu, D.; Chen, G. Z., Theoretical specific capacitance based on charge storage mechanisms of conducting polymers: comment on 'Vertically oriented arrays of polyaniline nanorods and their super electrochemical properties'. *Chem Commun (Camb)* **2011,** *47* (14), 4105-7.

(81) Stoller, M. D.; Ruoff, R. S., Best practice methods for determining an electrode material's performance for ultracapacitors. *Energy & Environmental Science* **2010,** *3* (9), 1294.

(82) Santino, L. M.; Hwang, E.; Diao, Y.; Lu, Y.; Wang, H.; Jiang, Q.; Singamaneni, S.; D'Arcy,

J. M., Condensing Vapor Phase Polymerization (CVPP) of Electrochemically Capacitive and Stable Polypyrrole Microtubes. *ACS Appl Mater Interfaces* **2017,** *9* (47), 41496-41504.

(83) Zhang, H.; Cao, G.; Yang, Y.; Gu, Z., Capacitive performance of an ultralong aligned carbon nanotube electrode in an ionic liquid at 60°C. *Carbon* **2008,** *46* (1), 30-34.

(84) Wang, G.; Zhang, L.; Zhang, J., A review of electrode materials for electrochemical supercapacitors. *Chem Soc Rev* **2012,** *41* (2), 797-828.

(85) Agmon, N., The Grotthuss mechanism. *Chemical Physics Letters* **1995,** *244*, 456-462.

(86) Mao, X.; Simeon, F.; Achilleos, D. S.; Rutledge, G. C.; Hatton, T. A., Metallocene/carbon hybrids prepared by a solution process for supercapacitor applications. *Journal of Materials Chemistry A* **2013,** *1* (42), 13120.

(87) Simon, P.; Gogotsi, Y., Materials for electrochemical capacitors. *Nat Mater* **2008,** *7* (11), 845-54.

(88) Inganäs, S. G. a. O., Networks of Electron-Conducting Polymer in Matrices of Ion-Conducting Polymers. *Electrochemical and Solid-State Letters* **2000,** *3* (5), 213-215.

(89) Ohno, H. F., K., Progress in Ionic Liquids for Electrochemical Reaction Matrices. *Electrochemistry* **2007**.

(90) Snook, G. A.; Kao, P.; Best, A. S., Conducting-polymer-based supercapacitor devices and electrodes. *Journal of Power Sources* **2011,** *196* (1), 1-12.

(91) Armand, M. E., F.; MacFarlane, D. R.; Ohno, H.; Scrosati, B., Ionic-liquid materials for the electrochemical challenges of the future. *Nature Materials* **2009,** *8*, 621-629.

(92) Sivakkumar, S. R.; Kim, D.-W., Polyaniline/Carbon Nanotube Composite Cathode for Rechargeable Lithium Polymer Batteries Assembled with Gel Polymer Electrolyte. *Journal of The Electrochemical Society* **2007,** *154* (2), A134.

(93) Sivakkumar, S. R.; MacFarlane, D. R.; Forsyth, M.; Kim, D.-W., Ionic Liquid-Based Rechargeable Lithium Metal-Polymer Cells Assembled with Polyaniline/Carbon Nanotube Composite Cathode. *Journal of The Electrochemical Society* **2007,** *154* (9), A834.

(94) Lu, W. F., A. G.; Qi, B. H.; Smela, E.; Mattes, B. R.; Ding, J.; Spinks, G. M.; Mazurkiewicz, J.; Zhou, D. Z.; Wallace, G. G.; MacFarlane, D. R.; Forsyth, S. A.; Forsyth, M. , Use of ionic liquids for π-conjugated polymer electrochemical devices. *Science* **2002,** *297*, 983-987.

(95) Lewandowski, A.; Olejniczak, A., N-Methyl-N-propylpiperidinium bis(trifluoromethanesulphonyl)imide as an electrolyte for carbon-based double-layer capacitors. *Journal of Power Sources* **2007,** *172* (1), 487-492.

(96) Lewandowski, A.; Olejniczak, A.; Galinski, M.; Stepniak, I., Performance of carbon–carbon supercapacitors based on organic, aqueous and ionic liquid electrolytes. *Journal of Power Sources* **2010,** *195* (17), 5814-5819.

(97) Manuel Stephan, A., Review on gel polymer electrolytes for lithium batteries. *European Polymer Journal* **2006,** *42* (1), 21-42.

(98) Meng, C.; Liu, C.; Chen, L.; Hu, C.; Fan, S., Highly flexible and all-solid-state paperlike polymer supercapacitors. *Nano Lett* **2010,** *10* (10), 4025-31.

(99) Nohara, S. W., H.; Furukawa, N.; Inoue, H.; Morita, M.; Iwakura, C. , Electrochemical characterization of new electric double layer capacitor with polymer hydrogel electrolyte. *Electrochimica Acta* **2003,** *48*, 749-753.

(100) Morita, M.; Qiao, J.-L.; Yoshimoto, N.; Ishikawa, M., Application of proton conducting polymeric electrolytes to electrochemical capacitors. *Electrochimica Acta* **2004,** *50* (2-3), 837-841.

(101) Lin, H.; Li, L.; Ren, J.; Cai, Z.; Qiu, L.; Yang, Z.; Peng, H., Conducting polymer composite

film incorporated with aligned carbon nanotubes for transparent, flexible and efficient supercapacitor. *Sci Rep* **2013,** *3*, 1353.

(102) Wang, K.; Wu, H.; Meng, Y.; Wei, Z., Conducting polymer nanowire arrays for high performance supercapacitors. *Small* **2014,** *10* (1), 14-31.

(103) Santino, L. M.; Lu, Y.; Acharya, S.; Bloom, L.; Cotton, D.; Wayne, A.; D'Arcy, J. M., Enhancing Cycling Stability of Aqueous Polyaniline Electrochemical Capacitors. *ACS Appl Mater Interfaces* **2016,** *8* (43), 29452-29460.

(104) Marchesi, L. F.; Simoes, F. R.; Pocrifka, L. A.; Pereira, E. C., Investigation of polypyrrole degradation using electrochemical impedance spectroscopy. *J Phys Chem B* **2011,** *115* (31), 9570-5.

(105) Johne, C. F., R.; Ignaszak, A., Three-Dimensionally Ordered Polypyrrole Electrode: Electrochemical Study on Capacity and Degradation Process. *Electroanalysis* **2014,** *26*, 1560-1572.

(106) Acharya, S.; Santino, L. M.; Lu, Y.; Anandarajah, H.; Wayne, A.; D'Arcy, J. M., Ultrahigh stability of high-power nanofibrillar PEDOT supercapacitors. *Sustainable Energy & Fuels* **2017,** *1* (3), 482-491.

(107) Salitra, G. S., A.; Eliad, L.; Cohen, Y.; Aurbach, D. , Carbon electrodes for double-layer capacitors - I. Relations between ion and pore dimensions. *Journal of the Electrochemical Society* **2000,** *147*, 2486-2493.

(108) Admassie, S.; Elfwing, A.; Jager, E. W. H.; Bao, Q.; Inganäs, O., A renewable biopolymer cathode with multivalent metal ions for enhanced charge storage. *J. Mater. Chem. A* **2014,** *2* (6), 1974-1979.

(109) Abdelhamid, M. E.; O'Mullane, A. P.; Snook, G. A., Storing energy in plastics: a review on

conducting polymers & their role in electrochemical energy storage. *RSC Advances* **2015,** *5* (15), 11611-11626.

(110) Díaz-Orellana, K. P.; Roberts, M. E., Scalable, template-free synthesis of conducting polymer microtubes. *RSC Advances* **2015,** *5* (32), 25504-25512.

(111) Karlsson, C. N., J.; Evans, D.; Forsyth, M.; Strømme, M.; Sjödin, M.; Howlett, P. C., Stable Deep Doping of Vapor-Phase Polymerized Poly(3,4-ethylenedioxythiophene)/Ionic Liquid Supercapacitors. *ChemSusChem* **2016,** *9*, 2112-2121.

(112) Radtke, M.; McMillan, D. G. G.; Schröter, B.; Höppener, S.; Dietzek, B.; Schubert, U. S.; Ignaszak, A., The effect of 3-amino benzoic acid linker and the reversal of donor–acceptor pairs on the electrochemical performance and stability of covalently bonded poly(pyrrole) nanotubes. *Polymer* **2015,** *77*, 289-296.

(113) Huang, Y.; Zhu, M.; Pei, Z.; Huang, Y.; Geng, H.; Zhi, C., Extremely Stable Polypyrrole Achieved via Molecular Ordering for Highly Flexible Supercapacitors. *ACS Appl Mater Interfaces* **2016,** *8* (3), 2435-40.

(114) Stuart, M. A.; Huck, W. T.; Genzer, J.; Muller, M.; Ober, C.; Stamm, M.; Sukhorukov, G. B.; Szleifer, I.; Tsukruk, V. V.; Urban, M.; Winnik, F.; Zauscher, S.; Luzinov, I.; Minko, S., Emerging applications of stimuli-responsive polymer materials. *Nat Mater* **2010,** *9* (2), 101-13.

(115) Naveen, M. H.; Gurudatt, N. G.; Shim, Y.-B., Applications of conducting polymer composites to electrochemical sensors: A review. *Applied Materials Today* **2017,** *9*, 419-433.

(116) Prajapati, D. G.; Kandasubramanian, B., Progress in the Development of Intrinsically

Conducting Polymer Composites as Biosensors. *Macromol Chem Phys* **2019,** *220* (10), 1800561.

(117) Wang, G.; Morrin, A.; Li, M.; Liu, N.; Luo, X., Nanomaterial-doped conducting polymers for electrochemical sensors and biosensors. *J Mater Chem B* **2018,** *6* (25), 4173-4190.

(118) Cui, C.; Du, Y.; Li, T.; Zheng, X.; Wang, X.; Han, X.; Xu, P., Synthesis of electromagnetic functionalized Fe3O4 microspheres/polyaniline composites by two-step oxidative polymerization. *J Phys Chem B* **2012,** *116* (31), 9523-31.

(119) Wang, Y.; Du, Y.; Xu, P.; Qiang, R.; Han, X., Recent Advances in Conjugated Polymer-Based Microwave Absorbing Materials. *Polymers (Basel)* **2017,** *9* (1).

(120) P. Chandrasekhar, K. N., Broadband microwave absorption and shielding properties of a poly(aniline). *Synthetic Metals* **1999,** *105*, 115-120.

(121) Pang, R.; Hu, X.; Zhou, S.; Sun, C.; Yan, J.; Sun, X.; Xiao, S.; Chen, P., Preparation of multi-shelled conductive polymer hollow microspheres by using Fe(3)O(4) hollow spheres as sacrificial templates. *Chem Commun (Camb)* **2014,** *50* (83), 12493-6.

(122) Gayner, C.; Kar, K. K., Recent advances in thermoelectric materials. *Progress in Materials Science* **2016,** *83*, 330-382.

(123) J. Kim, J.-H. B., J. Hwang, H. Kim, H. Park and W. Kim, *Phys. Status Solidi RRL* **2013**, 1-14.

(124) Shah, K.; Wang, S.-X.; Soo, D.; Xu, J., One-Dimensional Nanostructure Engineering of Conducting Polymers for Thermoelectric Applications. *Applied Sciences* **2019,** *9* (7), 1422.

(125) Zhang, J.; Zhang, K.; Xu, F.; Wang, S.; Qiu, Y., Thermoelectric transport in ultrathin poly(3,4-ethylenedioxythiophene) nanowire assembly. *Composites Part B: Engineering* **2018,** *136*, 234-240.

Chapter 2

Converting Rust to PEDOT Nanofibers for Supercapacitors

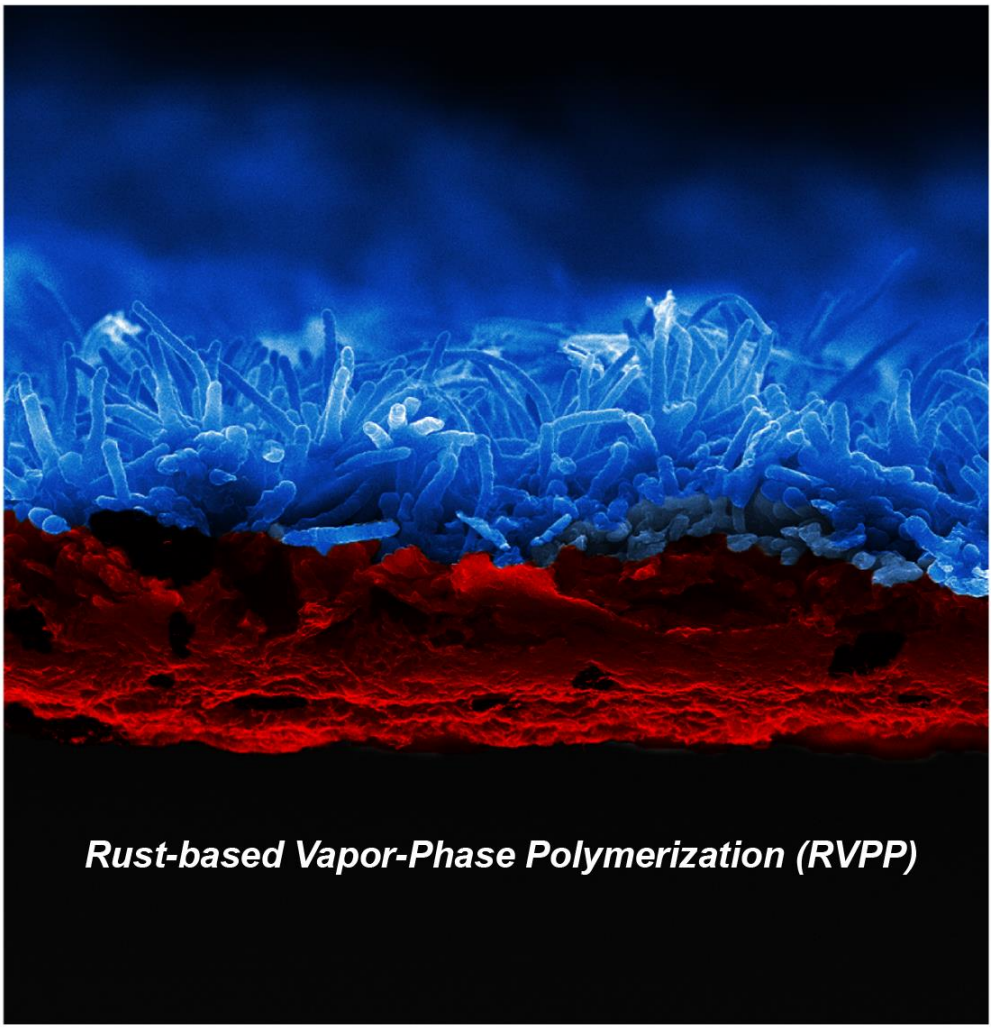

Convert rust (red) to PEDOT nanofibers (blue)

2.1 Introduction

Iron corrosion species such as Hematite (α-Fe_2O_3), Maghemite (γ- Fe_2O_3), Goethite (α-FeOOH) and Lepidocrocite (γ-FeOOH), first documented circa 800 BCE, make up the solid-state chemical family comprised of iron oxides, oxyhydroxides and hydroxides that is known as rust.[1-5] Natural sources of these species are found everywhere in our universe; here, on earth, rust is a byproduct of redox reactions between iron and oxygen in the presence of water and represents a major problem for our anthropogenic engineering endeavors.[6-8] Rust is thermodynamically stable, ubiquitous, inexpensive and contains ferric ions (Fe^{3+}) and therefore serves as an attractive candidate for developing oxidative chemical reactions. The ferric ion, with an oxidation potential of 0.77 V, is a nominal oxidizing agent used in the syntheses of conducting polymers such as poly(3,4-ethylenedioxythiophene) (PEDOT), polythiophene and polypyrrole resulting in doped states and long conjugation lengths.[9-12] PEDOT is a particularly useful heteroaromatic organic electronic possessing excellent chemical and physical stability as well as high electrical conductivity. This polymer is typically synthesized via solution phase reaction, electrochemical oxidation or vapor-phase polymerization.[13,14] Among these, vapor-phase polymerization is a particularly promising strategy that results in conformal coatings of low electrical resistance in a single step.[10,15-18] Polymerization from the vapor phase usually requires a ferric ion-containing salt serving as oxidizing agent. Some ferric ion-containing salts are quite expensive and all ferric ion-containing salts are corrosive requiring safety precautions during handling.[14,19,20] Moreover, Fe^{3+} salts are hygroscopic and chemically unstable undergoing hydrolysis over time which challenges the reproducibility of experiments.[3,4,10]

Here, we present a robust platform for synthesizing PEDOT nanofibers utilizing solid-state rust as a reactant and we introduce rust-based vapor-phase polymerization (RVPP) – a versatile alternative to traditional vapor-phase polymerization. This approach obviates the need of a corrosive salt, affords a nonabsorbent solid-state oxidant source for engineering facile reactions and provides a sustainable approach for the synthesis of organic electronics using what is typically considered chemical waste. The protocol for producing a nanofibrillar PEDOT film requires using hydrochloric acid vapor to dissolve rust and liberate aquated Fe^{3+} ions that initiate polymerization upon contact with monomer vapor. Hydrolysis of Fe^{3+} ions occurs in unison with polymerization resulting in the precipitation of one-dimensional inorganic nanostructured colloidal iron species such as FeOOH. Our approach to synthesis is scalable, producing nanostructured polymer film growth on any rusted surface of any dimension requiring only a sealed vessel for reactant vapors to interact with solid-state rust. Dissolution of rust and hydrolysis of Fe^{3+} ions occur in situ resulting in a conformal coating of inorganic-organic core-shell $FeCl_2$-PEDOT nanofibers. A rust layer on a steel surface plays the role of a versatile solid-state 2D reactant that enables control of polymer patterning and film thickness. Polymerization consumes rust resulting in nanofibrillar PEDOT films that delaminate from the steel. This synthetic strategy results in freestanding nanofibrillar PEDOT films that are ideal for developing energy storage applications possessing an electronic conductivity of 323 S/cm. Our nanofibrillar PEDOT-based supercapacitors exhibit state-of-the-art performance with gravimetric capacitance of 181 F/g at a current density of 3.5 A/g,[10, 21,22] retaining 80% of the original capacitance after 38,000 charge-discharge cycles.

2.2 Experimental methods

2.2.1 Corrosion protocol

α-FeOOH, γ-FeOOH and $FeSO_4$ rust layers were produced as per ASTM A109 protocol by immersing a 2.5 cm × 4 cm low carbon steel sheet in 20 mL of a 0.01 M H_2SO_4 solution for 48 h at 25 °C. Corroded sheets were then rinsed and dried under ambient conditions; thickness of a rust layer is controlled by immersion time ranging between 24 h and 40 h.

2.2.2 Rust-based vapor-phase polymerization (RVPP) of PEDOT

The Teflon liner of a hydrothermal reactor is loaded with: a 7 mm × 7 mm rusted steel substrate, 20 μL of concentrated hydrochloric acid and 200 μL of a 0.0674 M EDOT solution (3.37×10^{-5} mol) in chlorobenzene (4.93×10^{-3} mol). Each of these components is contained in a glass vial. This rector is sealed, heated for 6 h in an oven at 150 °C and then cooled in an ice bath for 15 min. A PEDOT-coated substrate is immersed in water to delaminate the polymer film.

2.2.3 Supercapacitor fabrication

A wet freestanding RVPP-PEDOT film is placed on a hard carbon fiber paper current collector and vacuum dried overnight to enhance adhesion. A platinum foil lead contacts the backside of the current collector and a 25 μm thick Celgard 3501 separator is pre-wetted with a 1 M H_2SO_4 aqueous solution during assembly.

2.2.4 Morphology and structure characterization

Scanning electron micrographs and energy-dispersive X-ray spectrograms were collected using a JEOL 7001LVF FE-SEM. Transmission electron micrographs were obtained in a JEOL 2100 by squeezing a PEDOT film in folding double TEM grid. A Bruker d8 Advanced X-ray diffractometer was utilized to collect powder X-ray diffractograms of pulverized samples at room temperature, with Cu Kα radiation source (λ = 1.5406 Å) and LynxEye XE detector, operating at 40 kV and 40 mA; sample holder was rotated at 30 rpm with a scan step of 0.02°. Ultraviolet–visible–near-infrared absorption spectra were obtained on a Cary 5000 UV-Vis-NIR spectrophotometer using pulverized samples dispersed in 6 M H_2SO_4. Samples were dedoped using concentrated NH_4OH. Fourier-transform infrared spectra were collected on a Bruker ALPHA Platinum-ATR. Thermogravimetric analysis was performed on a Discovery TGA (TA Instruments) with a ramp rate of 2 °C/min. Current-voltage (I-V) curves were obtained using a built-in-house 3D printed probe stating using two gold needles with 1 mm of separation.[56]

2.2.5 Electrochemical measurements

Cyclic voltammetry and electrochemical impedance spectroscopy were performed on a BioLogic VMP3 multi-potentiostat. Three-electrode experiments utilized a platinum mesh lead, affixed to the back side of the working electrode, that was fully covered with polyimide tape. Platinum mesh connected with a platinum wire served as counter electrode. The reference electrode (BASi Ag/AgCl RE-5B) is pointed directly at the working electrode to compensate and minimize solution resistance. A 5 mm × 5 mm PEDOT film serving as working electrode was washed in 6 M HCl and methanol prior to a measurement. A 1 M H_2SO_4 aqueous electrolyte was employed using milli-Q water (18 MΩ) that was degassed for 15 min. Electrochemical impedance spectroscopy was

carried out at the electrode's open circuit potential after obtaining a reversible cyclic voltammogram. Impedance values were recorded using a 10 mV sinusoidal disturbance at frequencies ranging from 100 kHz to 100 mHz.

2.3 Results & discussion

Rust-based vapor-phase polymerization (RVPP) is a synthetic strategy that utilizes rust (Figure 2.1a-c) to produce nanofibrillar freestanding films of the conducting polymer PEDOT (Figure 2.1d-f). Rusted steel serves as substrate and is produced by immersing a steel sheet in a 0.01 M sulfuric acid aqueous solution for 48 h (Figure 2.2); the rust layer possesses a microstructure comprised of two-dimensional platelets and acicular one-dimensional spherulites (Figure 2.1c). Powder X-ray diffraction patterns indicate that these microstructures are α-FeOOH, γ-FeOOH and $FeSO_4$ phases (Figure 2.3). A nanofibrillar PEDOT film (Figure 2.1f) is vapor-phase deposited using a 7 mm × 7 mm rusted steel sheet that is introduced into a sealed vessel along with 20 µL of concentrated hydrochloric acid and 200 µL of a 0.0034 M EDOT solution in chlorobenzene (Figure 2.1g). The reactor is sealed, placed in an oven (150 °C) for 6 hours and subsequently cooled in an ice bath for 15 minutes resulting in a blue colored nanofibrillar PEDOT film that readily delaminates from the steel sheet. Initially, as temperature is ramped, hydrochloric acid vapor diffuses (Figure 2.1h) dissolving rust and liberating Fe^{3+} ions that oxidize monomer vapor upon contact. During this oxidative radical polymerization, ferric ions are reduced to ferrous ions (Fe^{2+}) and the monomer 3,4-ethylenedioxythiophene (EDOT) is oxidized to $EDOT^{+\bullet}$ radical cations (Figure 2.4). The conjugated PEDOT backbone assembles via step growth as radical coupling is concomitant with deprotonation and oligomer formation; protons produced lower the pH of a

reaction.[21] Finally, the conjugated polymer chain is doped by Cl^- ions present from hydrochloric acid resulting in an electronically conductive form of PEDOT.

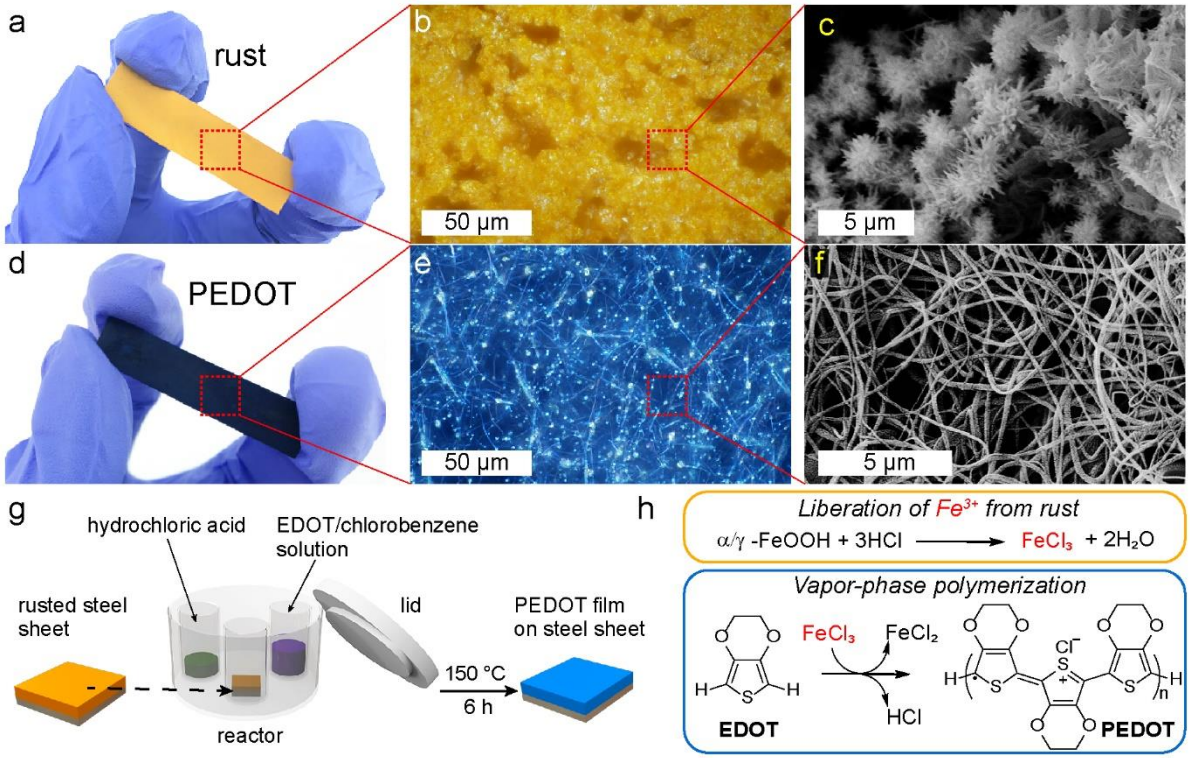

Figure 2.1: Optical and electron microscopy analysis of a nanofibrillar PEDOT film produced from rusted steel. (a) Digital photograph shows a steel sheet coated by a yellow colored rust layer characterized by (b) a texturized porous architecture; (c) scanning electron micrograph shows that the rust layer possesses sea-urchin like microstructure. When this rusted substrate is utilized for vapor phase polymerization, (d) a blue PEDOT coating is deposited comprised of (e) a nanofibrillar architecture possessing (f) a high packing density of high aspect ratio nanofibers. (g) Schematic illustration of rust-based vapor-phase polymerization (RVPP) carried out in a sealed vessel. (h) Scheme of RVPP mechanism entailing dissolution of rust, liberation of Fe3+ ions and oxidative radical polymerization of EDOT monomer resulting in a doped form of PEDOT.

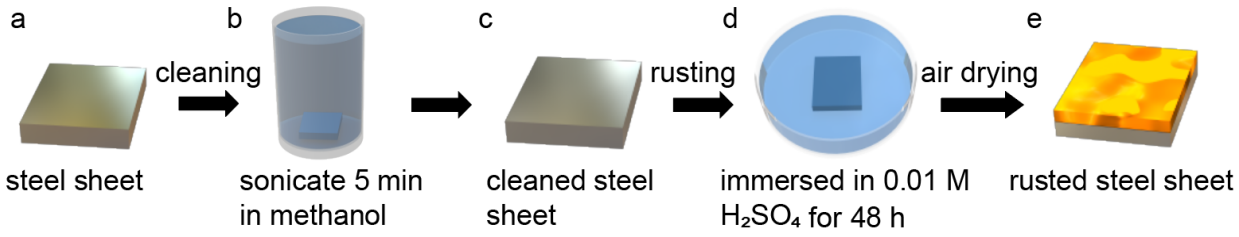

Figure 2.2: Flow process diagram of rust formation.

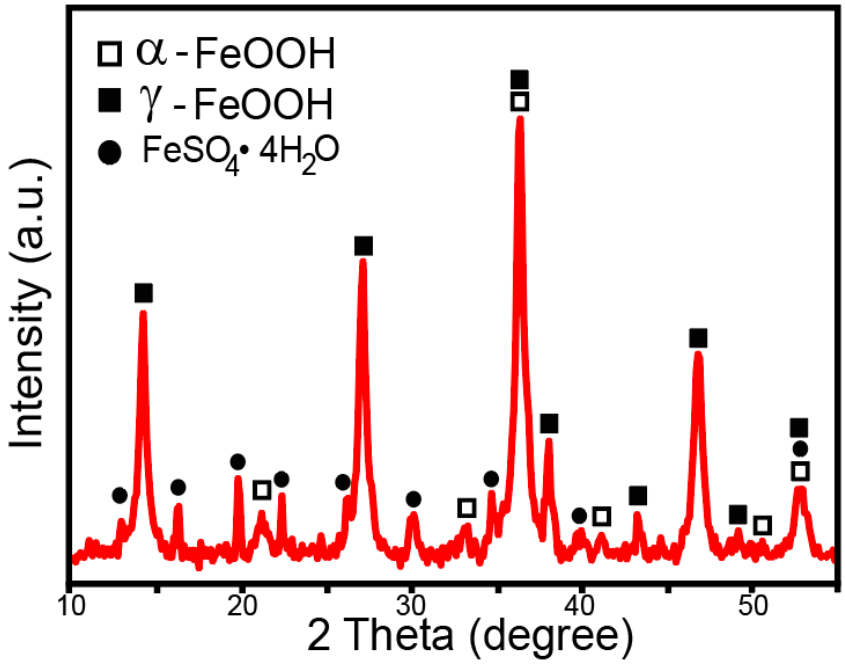

Figure 2.3: Powder X-ray diffraction pattern shows the heterogeneous composition of our rust film.

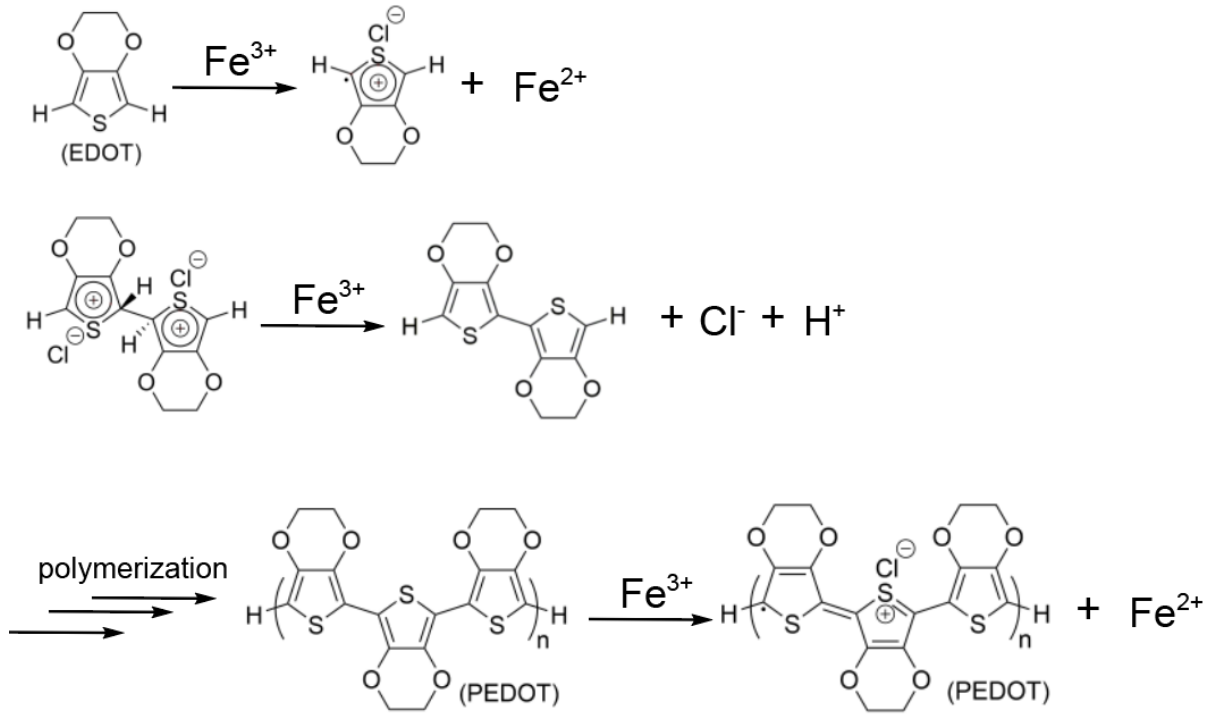

Figure 2.4: Mechanistic scheme of the formation of PEDOT via step growth polymerization.

Mechanistic studies of nanofiber evolution are carried out using microscopy and time-lapse spectroscopy by quenching reactions. Initially, HCl vapor condensation and rust dissolution lead to the collapse of microstructured rust (Figure 2.5a) as proposed in the schematic diagram (Figure 2.5b). After 2 h of reaction, a porous PEDOT skin (Figure 2.5c) forms when aquated Fe^{3+} ions oxidize EDOT monomer vapor, this reaction reduces Fe^{3+} ions and produces the Fe^{2+} ion-containing salt $FeCl_2$ detected via powder X-ray diffraction (PXRD) (Figure 2.6). As the reaction progresses, HCl vapor permeates and diffuses throughout bulk rust increasing the concentration of Fe^{3+}, Cl^- and H^+ aquated ions; dissolution of rust with HCl vapor promotes hydrolysis-driven precipitation of one-dimensional FeOOH nuclei[23-25] detected via PXRD (Figure 2.6). Based on our previous work,[21] these nuclei are responsible for nanofibrillar formation, however, at this early stage of polymerization, nuclei redissolve under the low pH environment (Figure 2.5d). Upon

reaching 3 h of synthesis, the entire rusted surface is coated with a dense PEDOT film visible via scanning electron microscopy (Figure 2.7a). As the reaction continues, HCl vapor is consumed and pH increases thus facilitating hydrolysis and the formation of FeOOH nuclei (Figure 2.6). These inorganic nuclei are unstable and undergo Ostwald ripening by coalescing into more energetically favored larger sized one-dimensional structures.[26-30]

A nanofibrillar morphology is initially observed after 4 h of synthesis and is characterized by low aspect ratio PEDOT microfibers that pierce out of the polymer skin (Figure 2.5e, Figure 2.7b). A one-dimensional PEDOT structure possesses a FeOOH inner scaffold identified by PXRD (Figure 2.6) and as polymerization continues, diffusion of HCl vapor liberates Fe^{3+} ions from this FeOOH inner scaffold promoting polymerization radially inward (Figure 2.5f). Vertical growth of a PEDOT-coated FeOOH nanofiber is driven by hydrolysis, Ostwald ripening and polymerization. Moreover, one-dimensional FeOOH ribbons undergo crystal splitting along the crystal lattice (Figure 2.7c) resulting in extended growth of one-dimensional nanofibers (Figure 2.7d).[31-33] Ferric ions in FeOOH scaffolds are reduced to ferrous ions during oxidative radical polymerization forming a $FeCl_2$ core. This reaction comes to completion after 6 h, resulting in a freestanding polymer film characterized by a high packing density of nanofibers (Figure 2.5e) with a core-shell $FeCl_2$-PEDOT architecture (Figure 2.5h).

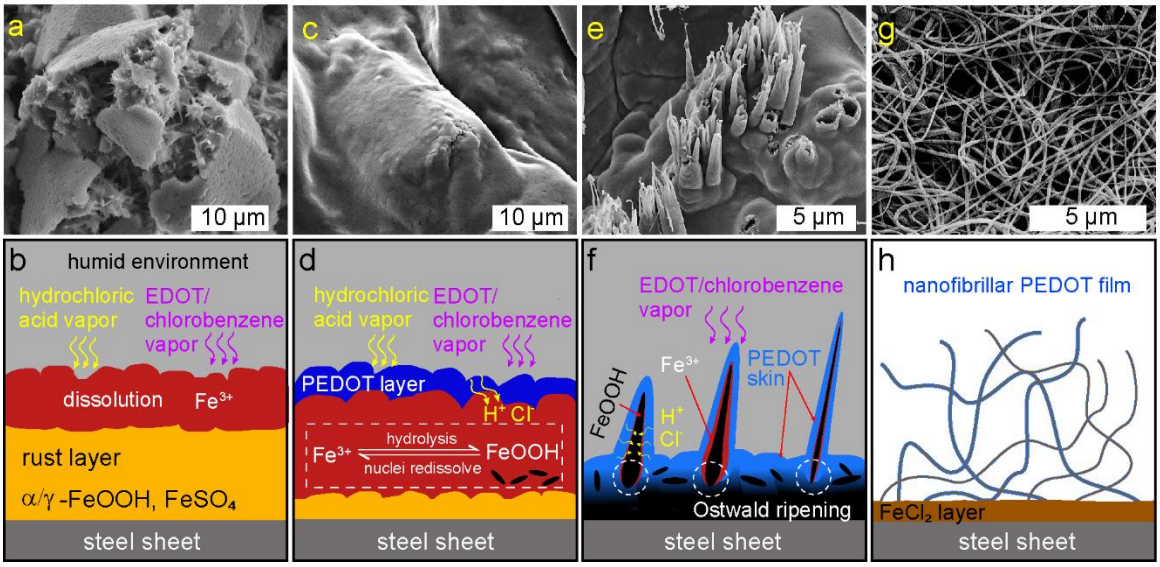

Figure 2.5: Scanning electron micrographs and schematic illustration of rust-based vapor-phase polymerization mechanism. (a) Rust microstructures collapse as HCl vapor dissolves a rust layer promoting the (b) liberation of Fe^{3+} ions from bulk rust (α/γ-FeOOH, $FeSO_4$). (c) A PEDOT skin forms on the surface of rust as Fe^{3+} ions contact EDOT vapor. During this process, water content and Fe^{3+} concentration in the rust bulk increases leading to (d) hydrolysis and the precipitation of FeOOH nuclei. (e) One dimensional microfibers pierce out of the PEDOT skin and as the concentration of hydrolysis products increases, (f) FeOOH nuclei undergo Ostwald ripening forming large one-dimensional microstructures. Upon contact with HCl and EDOT vapor, these microstructures are dissolved and polymerized resulting in one-dimensional core-shell FeOOH-PEDOT microstructures. (g) A high packing density of nanofibers is obtained after a 6 h reaction that reduces ferric ions in the FeOOH core resulting in (h) one-dimensional core-shell $FeCl_2$-PEDOT nanofibers.

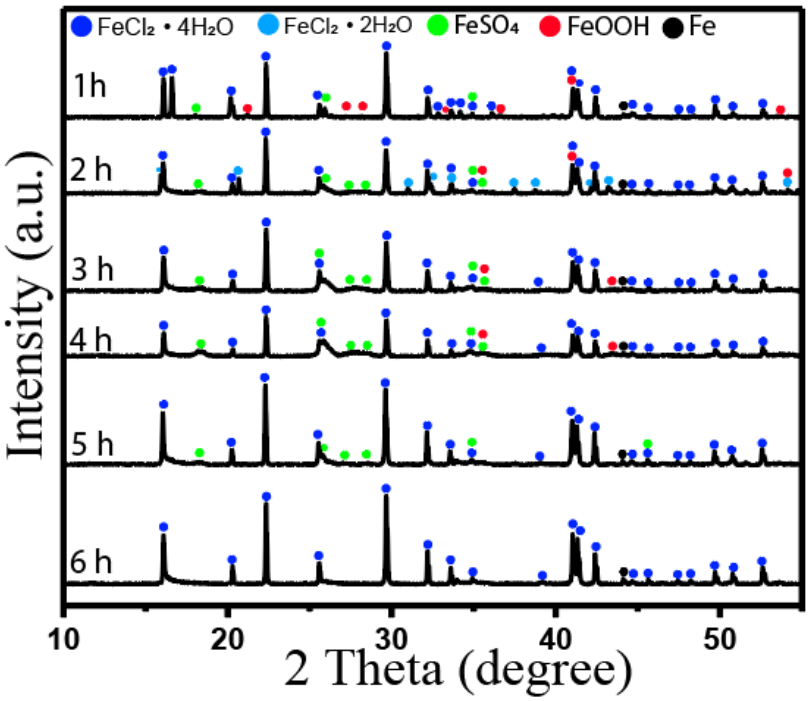

Figure 2.6: Powder X-ray diffraction patterns of quenched experiments during rust-based vapor-phase polymerization.

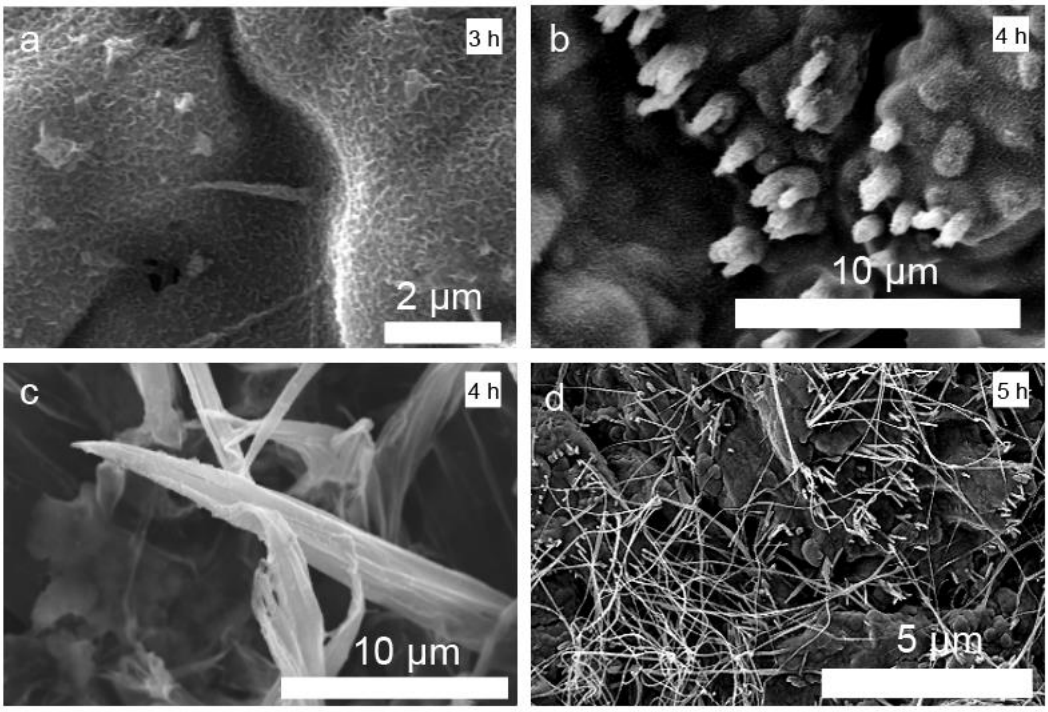

Figure 2.7: Scanning electron micrographs of quenched experiments during rust-based vapor-phase polymerization.

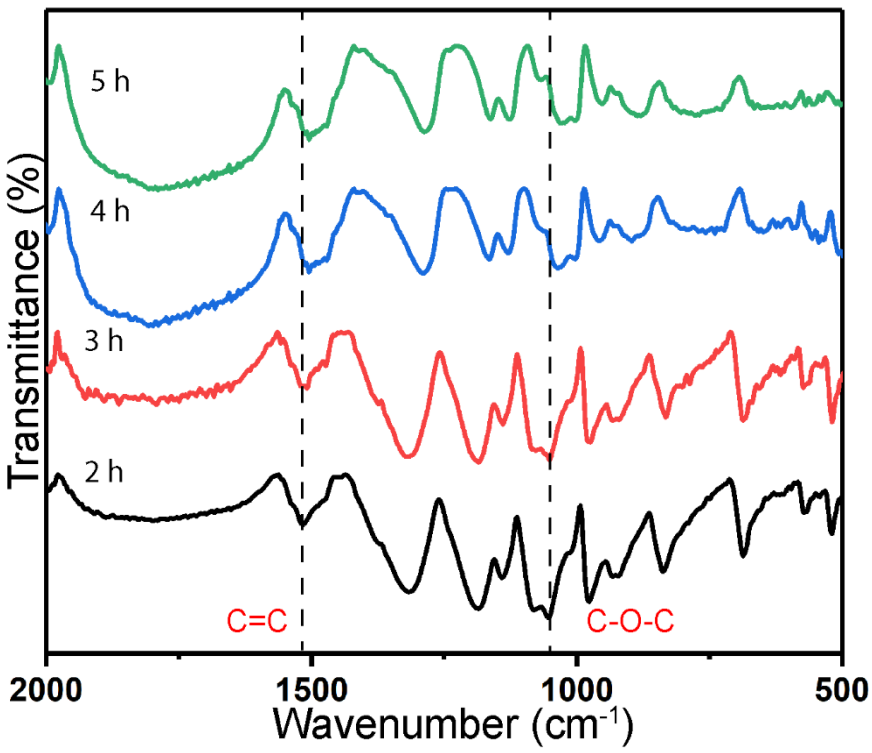

Figure 2.8: Fourier-transform infrared spectrograms of quenched experiments of PEDOT films during rust-based vapor-phase polymerization. The percent of IR transmittance from C=C decreases with respect to C-O-C as the reaction progresses; the conjugation length of the polymer backbone is maximized by 5 h.

The conjugation length of the polymer is studied via Fourier transform infrared spectroscopy (Figure 2.8) and shows the characteristic C=C stretch from the doped quinoid PEDOT structure at 1510 cm^{-1} and the C-O-C vibration peak at 965 cm^{-1} from the ethylenedioxy group.[34] Oxidative doping converts benzoid to quinoid leaving the ethylenedioxy group unaltered, this enables characterization of conjugation length by their relative ratios.[35] The quinoid to ethylenedioxy group ratio is maximized in the 6 h synthesis, resulting in PEDOT nanofibers of long conjugation length.

Our mechanism is tested by obviating HCl vapor from synthesis, this results in suppression of polymerization as indicated by powder X-ray diffraction and electron microscopy (Figure 2.9);

HCl is necessary for rust dissolution, liberation of Fe^{3+} ions and provides a source of water for hydrolysis. A synthesis without EDOT, leads to the collapse of the rust layer and a product void of polymer (Figure 2.10). Nanofibrillar growth requires the use of HCl vapor, EDOT monomer and chlorobenzene as a carrier gas, this organic polar solvent affords a universal surfactant-like solvent for the assembly of oligomers and facile polymer formation (Figure 2.11). Benzene, dichloromethane, nitromethane and 1-butanol also generate nanofibers albeit of low electronic conductivity. Figure 2.12 shows the granular morphology on the underside of a PEDOT film while a rip demonstrates that nanofibers make up the bulk of a cross section of the film.

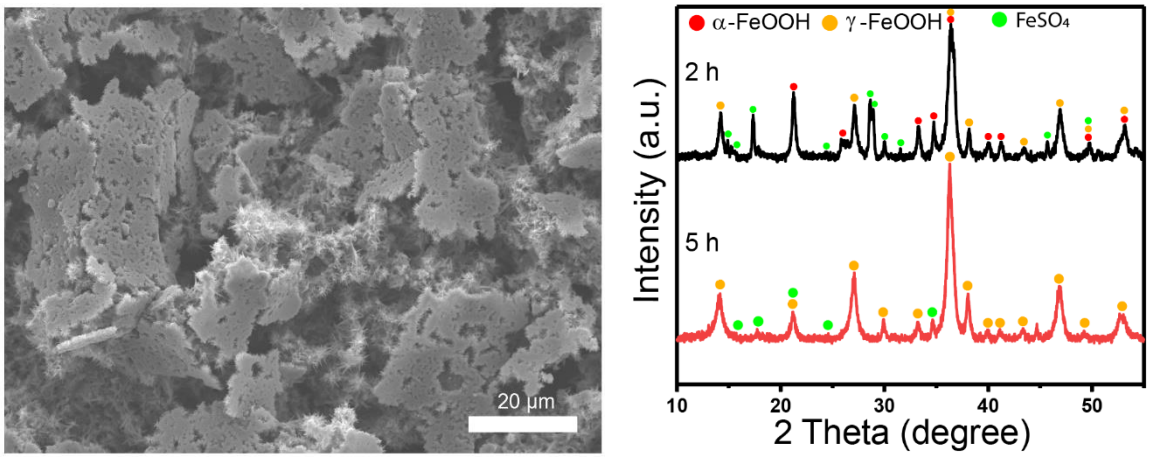

Figure 2.9: Scanning electron micrographs and powder X-ray diffraction patterns of product from rust-based vapor-phase polymerization without HCl vapor.

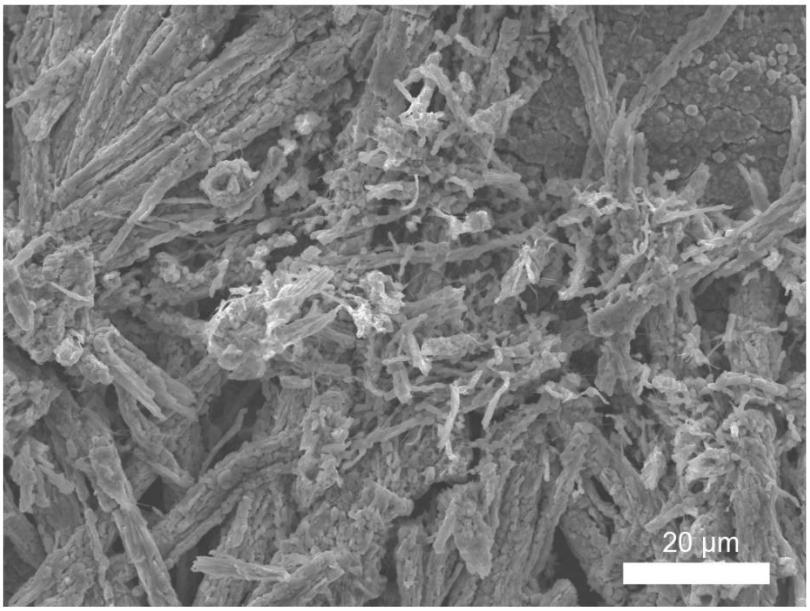

Figure 2.10: Scanning electron micrograph of product from rust-based vapor-phase polymerization without EDOT vapor.

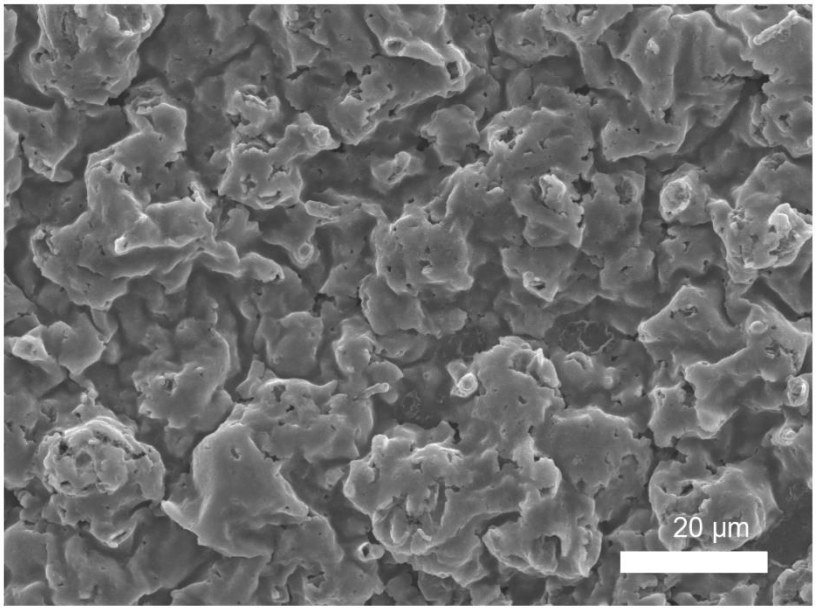

Figure 2.11: Scanning electron micrograph of product from rust-based vapor-phase polymerization without chlorobenzene vapor. Nanofiber growth is stifled plausibly due to chlorobenzene's polar organic structure providing a universal solvent for oligomers and polymer assembly during vapor phase polymerization.

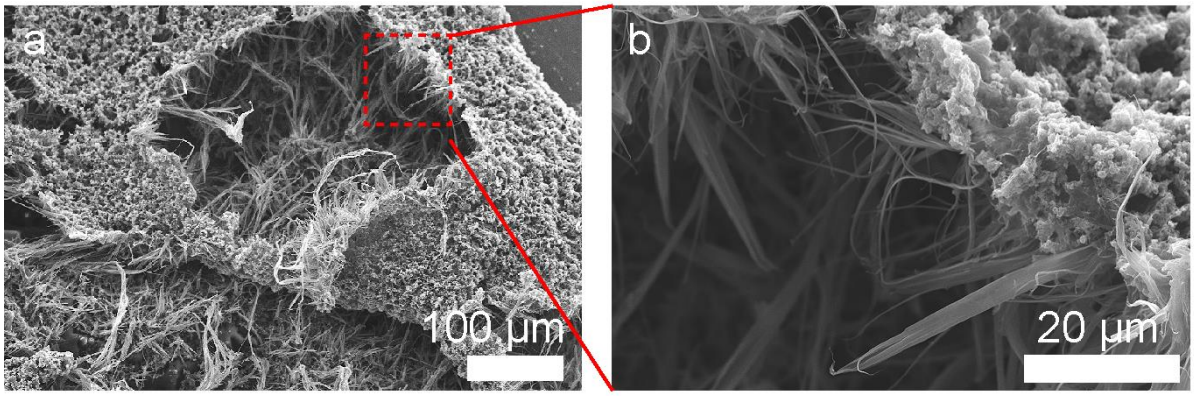

Figure 2.12: Scanning electron micrographs of the underside of a rust-based vapor-phase polymerization PEDOT film.

Rust-based vapor-phase polymerization (RVPP) is scalable due to rust's chemical stability and the ease with which an iron-containing substrate corrodes; the thickness of the rust layer on a substrate is controlled to produce a freestanding PEDOT film that readily delaminates. Figure 2.13a shows a digital picture of a 10 mm × 50 mm delaminated PEDOT film next to its original supporting steel sheet, the thickness of this polymer film is controlled by the thickness of the pre-deposited rust layer. The thickness of a rust layer is optimized by immersing a steel substrate in a 0.01M H_2SO_4 corroding aqueous solution for 24 h, 40 h and 48 h leading to 20 µm, 40 µm and 70 µm rust-layer thickness, respectively (Figure 2.13b–d). These corroded substrates are utilized for RVPP resulting in PEDOT films with thicknesses of 6 µm, 8 µm and 10 µm, respectively (Figure 2.13e–g). A 10 µm thick PEDOT film, produced using a heavily corroded rust layer, possesses a sheet resistance of 2.85 Ω square^{-1} and a conductivity of 323 S cm^{-1}. When a substrate is immersed in a corroding solution for less than 48 h, the rust layer is comprised of a porous architecture that leads to a higher sheet resistance (Figure 2.14).

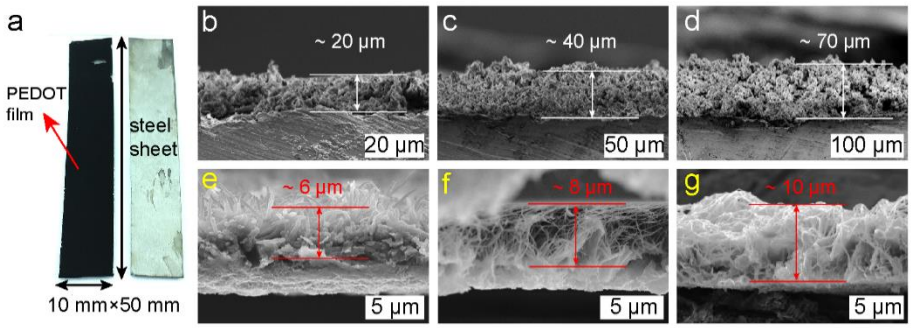

Figure 2.13: RVPP controls the thickness of freestanding PEDOT films. (a) A digital photograph shows a delaminated freestanding PEDOT film next to its original steel substrate. Cross sectional analyses carried out using scanning electron microscopy show rust layers with thicknesses of (b) 20 µm, (c) 40 µm and (d) 70 µm that lead to PEDOT films with thicknesses of (e) 6 µm, (f) 8 µm and (g) 10 µm, respectively.

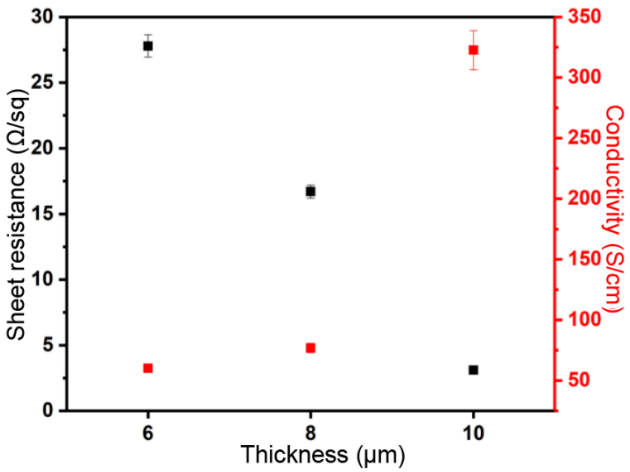

Figure 2.14: Sheet resistance and electrical conductivity of PEDOT film versus film thickness.

Patterning of a PEDOT film is carried out by masking a rusted surface with polyimide tape resulting in selective deposition of an electronically conductive blue colored nanofibrillar PEDOT film (Figure 2.15a–c). In RVPP, a rusted three-dimensional substrate is also an ideal source of Fe^{3+} ions; for example, we utilized a rusted screw as substrate (Figure 2.15d, e). Note that the rust layer on this screw is from natural exposure to environmental moisture and air. A PEDOT coating deposits conformally on a screw via RVPP and delaminates completely by immersion in water leaving the screw surface clean, lustrous and void of rust (Figure 2.15f). In order to ascertain the extent of cleaning attained using our protocol, another rusted screw is cleaned using a commercial rust-removing solution and the surface roughness is characterized before and after via profilometry and scanning electron microscopy. Surface roughness is then compared to that of a cleaned screw after PEDOT delamination (Figure 2.16). The surface roughness of a 2D steel substrate treated with a rust-removing solution exhibits a surface roughness with a 600 nm amplitude in variance after cleaning. When a rusted-steel substrate is utilized for RVPP and rust is removed, its surface roughness exhibits a 400 nm amplitude variance; a steel surface cleaned via RVPP is smoother than steel cleaned by a commercial rust-removing solution. A steel substrate utilized in our synthesis is pre-polished and after synthesis, the surface roughness is comprised of aggregates of iron as determined by powder X-ray diffraction and scanning electron microscopy (Figure 2.17).

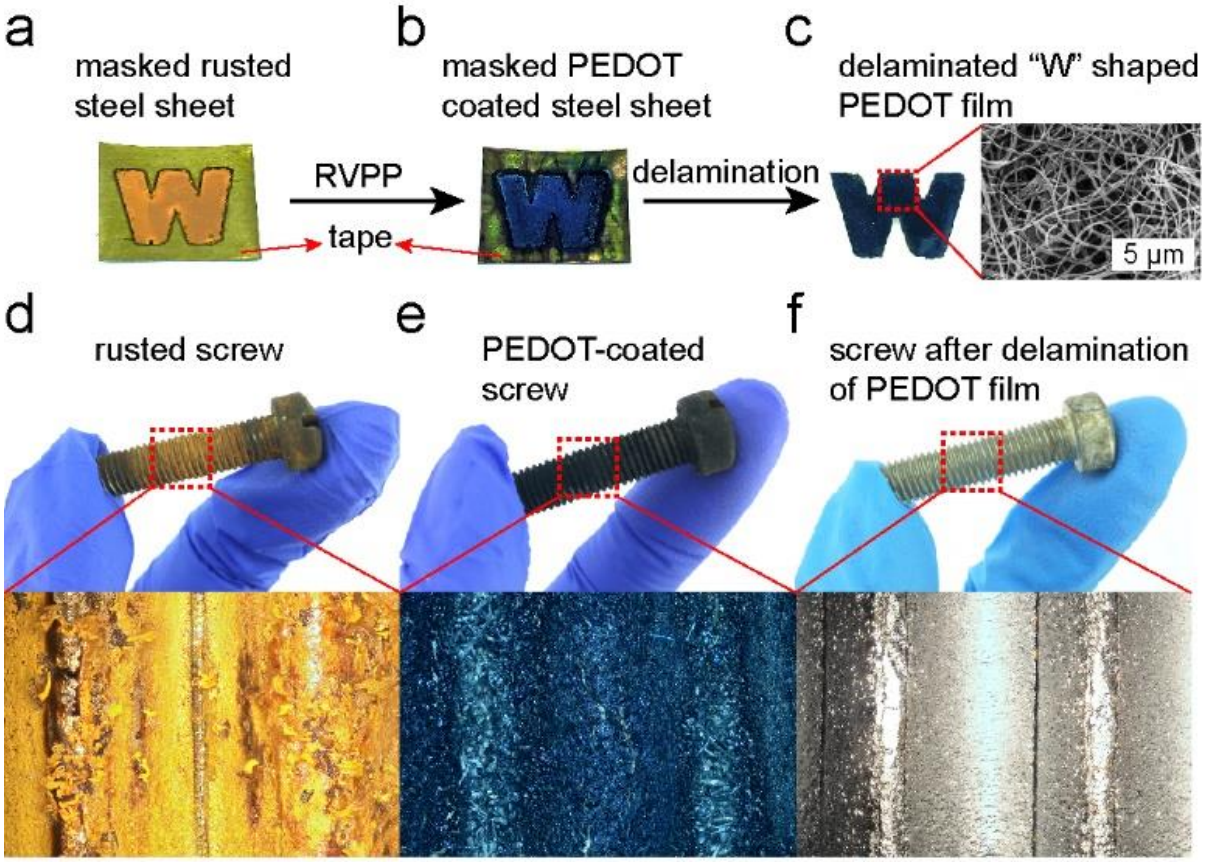

Figure 2.15: RVPP enables patterning of a freestanding PEDOT film as well deposition of a conformal coating on a three-dimensional substrate. (a) Digital photograph shows a rust layer masked by polyimide tape; this substrate is subsequently utilized for RVPP resulting in selective deposition of (b) a blue colored PEDOT film. (c) A patterned delaminated PEDOT film is robust retaining its "W" shaped-pattern and comprised of nanofibers as shown by scanning electron microscopy. (d) Photographs show that a rusted screw also serves as a substrate for RVPP leading to (e) a conformal blue texturized PEDOT coating; upon delamination of the polymer coating, (f) the screw surface is cleaned and void of rust.

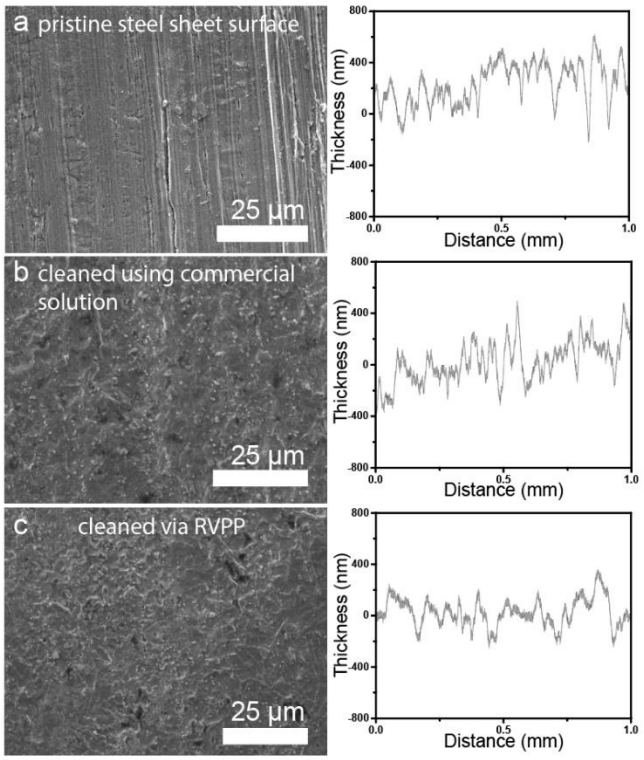

Figure 2.16: Scanning electron micrographs and profilometry measurements for a) pristine steel, b) rusted steel sheet cleaned by commercial solution and c) rusted steel sheet cleaned during rust-based vapor-phase polymerization.

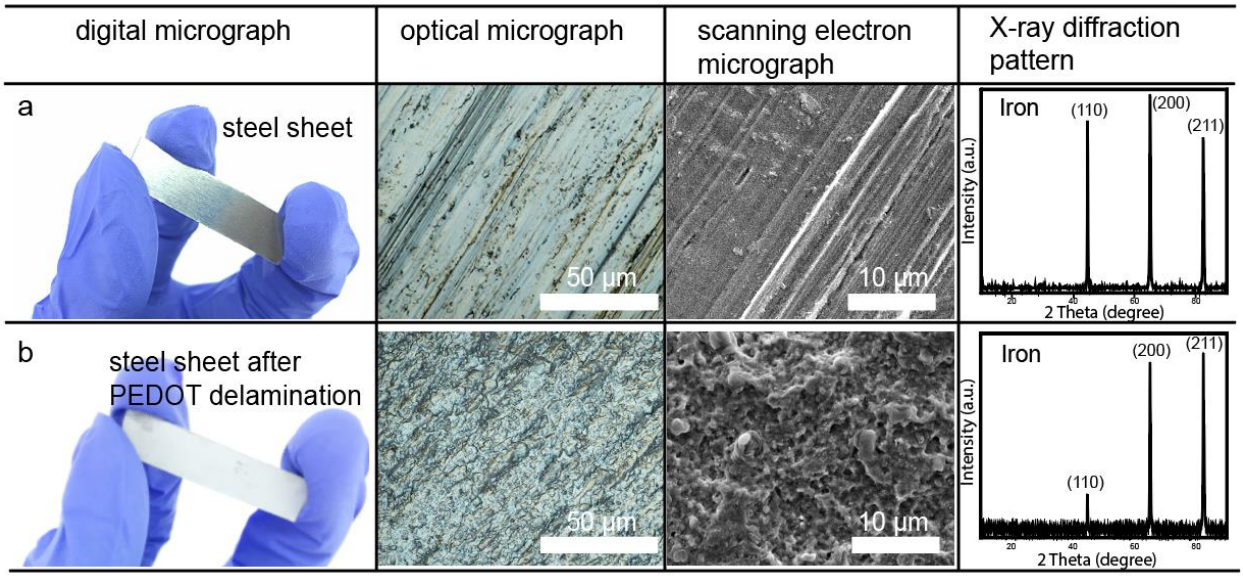

Figure 2.17: Microscopic analysis and X-ray diffraction measurements of a) a pristine steel sheet and b) a rusted-steel sheet cleaned during rust-based vapor-phase polymerization.

A PEDOT film readily delaminates from its substrate by simple immersion in water resulting in a freestanding polymer film, this is because a rust layer lacks chemical coordination to steel (Figure 2.18a). A freestanding RVPP-PEDOT film is characterized by a high packing density of high-aspect ratio core-shell nanofibers as confirmed by high angle annular dark field (HAADF) images collected via scanning transmission electron microscopy (Figure 2.18b). The contrast in these images is roughly proportional to the square of the atomic number enabling characterization of elemental composition.[36,37] These nanofibers have a 20 nm diameter core, 50 nm thick shell (Figure 2.19) and lengths up to 100 μm reaching an aspect ratio of 1000 (Figure 2.20). Energy dispersive X-ray spectroscopy maps show that a PEDOT film possesses an elemental distribution comprised of S and Fe (Figure 2.18c) pertaining to a polymer shell and an inorganic core, respectively. Powder X-ray diffraction confirms the existence of a $FeCl_2$ core (Figure 2.18d); purification in 6 M HCl removes this inorganic core resulting in a hollow nanofiber (Figure 2.21).

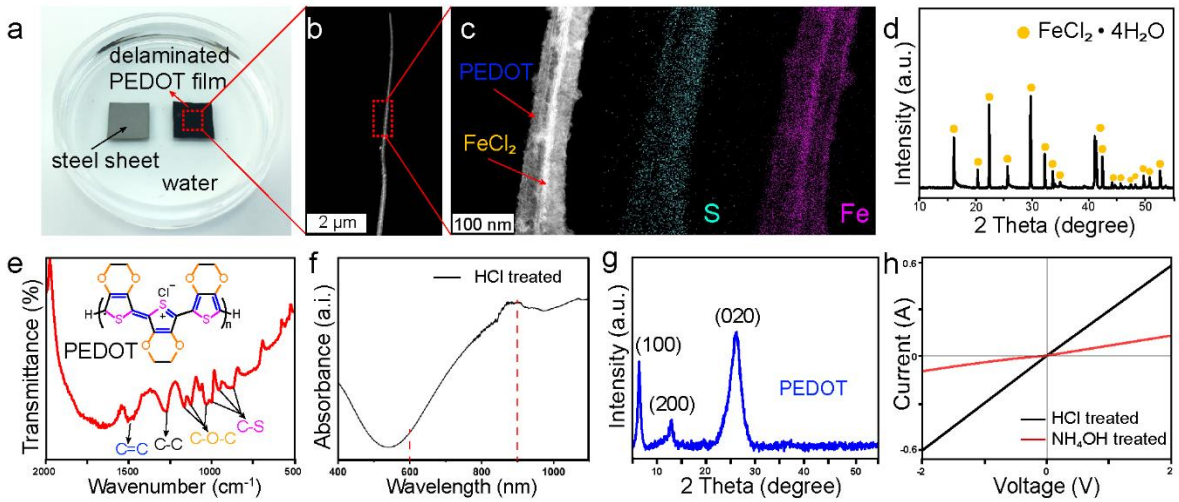

Figure 2.18: Spectroscopic characterization of RVPP-PEDOT. (a) Photograph shows that a PEDOT film retains the substrate's original shape and delaminates by simple immersion in water. (b) A high angle annular dark field (HAADF) scanning transmission electron micrograph for a PEDOT nanofiber. (c) A zoom in image shows its core-shell structure and an elemental composition comprised of a sulfur-containing shell and an iron-containing core. (d) Powder X-ray diffractogram confirms that the core is comprised of ferrous chloride – this salt is the product of reduced ferric ions. (e) FT-IR spectrum shows a doped conjugated backbone. (f) UV-Vis-NIR

spectrum of acid treated PEDOT shows a bipolaronic state and its (g) powder X-ray diffractogram indicates a polycrystalline structure. (h) Current-voltage curve shows that a freestanding PEDOT film is reversibly doped and dedoped by acid and base, respectively.

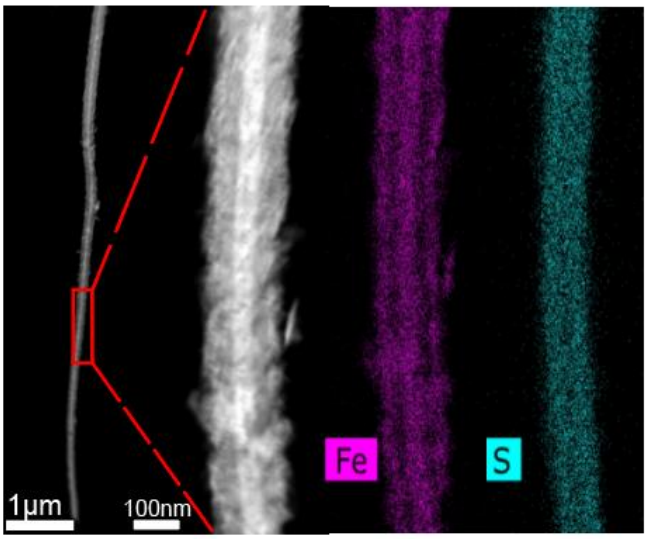

Figure 2.19: High angle annular dark field scanning transmission electron micrographs and energy-dispersive X-ray spectrograms of a PEDOT nanofiber; a polymer nanofiber contains an inorganic Fe core and a sulfur-containing PEDOT shell. Nanofibrillar growth occurs concomitantly as a polymer shell deposits on one-dimensional FeOOH iron (III)-containing crystallites produced from dissolution of rust, hydrolysis and Ostwald ripening.

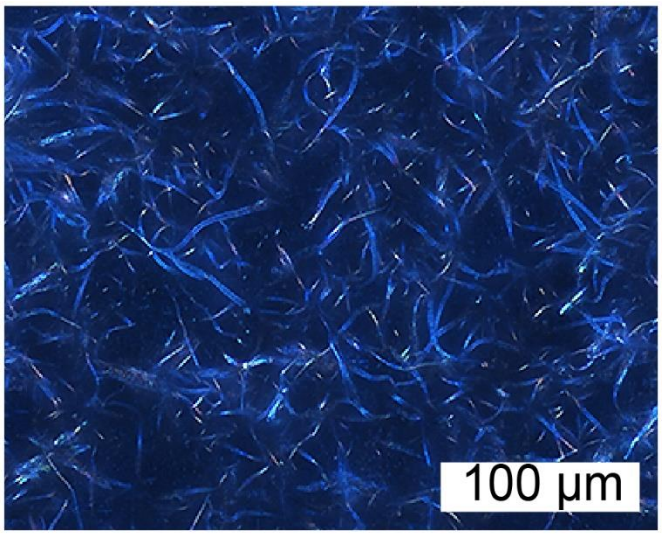

Figure 2.20: Optical micrograph of a PEDOT film shows that the surface of the film is comprised a homogeneous distribution of one-dimensional microstructures

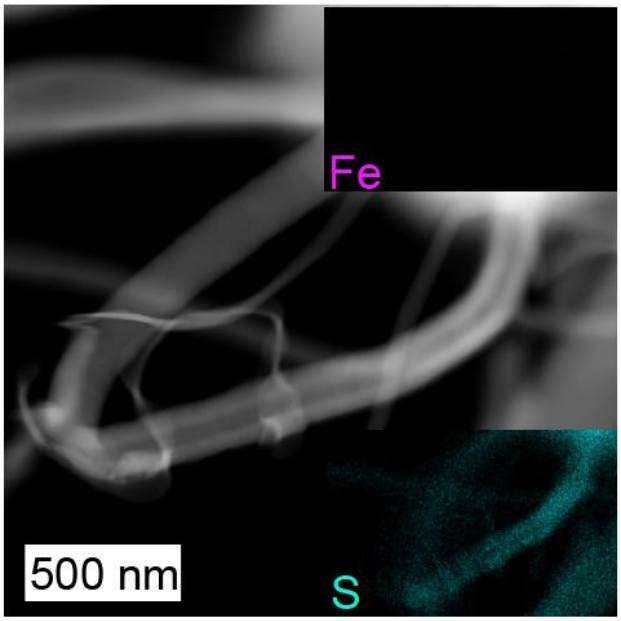

Figure 2.21: High angle annular dark field scanning transmission electron micrographs and energy-dispersive X-ray spectrograms collected after a PEDOT film rinsed in 6 M HCl; note that the acid wash removes the inorganic core resulting in a hollow nanofiber.

The molecular structure of purified RVPP-PEDOT, characterized by Fourier transform infrared spectroscopy (Figure 2.18e), shows an oxidized doped form of PEDOT. The bands at 1510 and 1312 cm^{-1} correspond to aromatic C=C asymmetric stretches in the polythiophene ring and inter-ring C–C stretches, respectively. Bands at 1180, 1135 and 1085 cm^{-1} are assigned to C-O-C stretches in the ethylenedioxy ring whereas the C-S-C stretches in the thiophene ring appear at 962, 903, and 743 cm^{-1}.[38] Ultraviolet-visible-near-infrared absorption spectroscopy aids in probing doping levels and typically, neutral PEDOT produces a broad absorption peak in the visible region (400-600 nm) corresponding to the π-π* transition. The broad absorption above 800 nm corresponds to free charge carriers and a conductive PEDOT state.[17,39] Post-synthetic doping of RVPP-PEDOT using HCl vapor introduces Cl^- ions that increase the doping level and conductivity of the polymer (Figure 2.18f). This post-synthetic doping is detected as a π-π* transition that stifles absorption between 400-600 nm and leads to a broad absorption hump between 800 and 1000 nm

due to the generation of polaronic and bipolaronic states.[10] In order to understand charge transport as a function of a material's structure, a polymer film is examined via powder X-ray diffraction revealing three sharp peaks at 2θ = 6.5°, 13.0° and 26.5° (Figure 2.18g) with peak widths at half height of 0.8, 1.1, 2.7 characteristic of crystalline PEDOT.[10,13] The broad diffraction peak at 2θ = 26.5° due to π-π stacking is assigned to the (020) reflection with an inter-chain spacing distance of ~0.4 nm, a sharp peak for (100) at 2θ = 6.5° and its second-order reflection (200) at 2θ = 13.0° correspond to lateral chain packing; lamellar stacking (100) exhibits a distance of 1.3 nm.[36,40] The selective area electron diffraction pattern of PEDOT shows discrete diffraction spots indicating a preferred polycrystalline orientation (Figure 2.22). Charge transport studied via two-point probe I-V measurements shows linear ohmic behavior for HCl treated PEDOT and a low electrical resistance (Figure 2.18h); treating a PEDOT film with ammonium hydroxide dedopes the polymer resulting in a more negative I-V curve slope. The four-point probe sheet resistance of PEDOT (2.85 Ω square^{-1}) indicates that its electrical conductivity is approximately 323 S cm^{-1} (Figure 2.23) calculated from sheet resistivity.[41] This high electrical conductivity is a function of an ordered crystal structure and a high charge carrier concentration.[36]

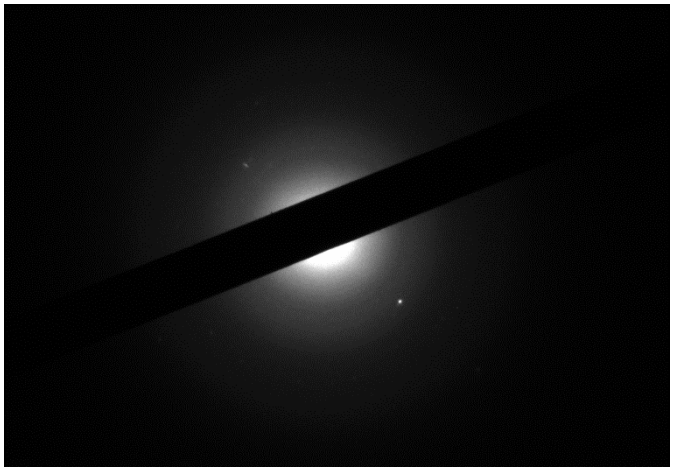

Figure 2.22: Selected area diffraction pattern of purified PEDOT.

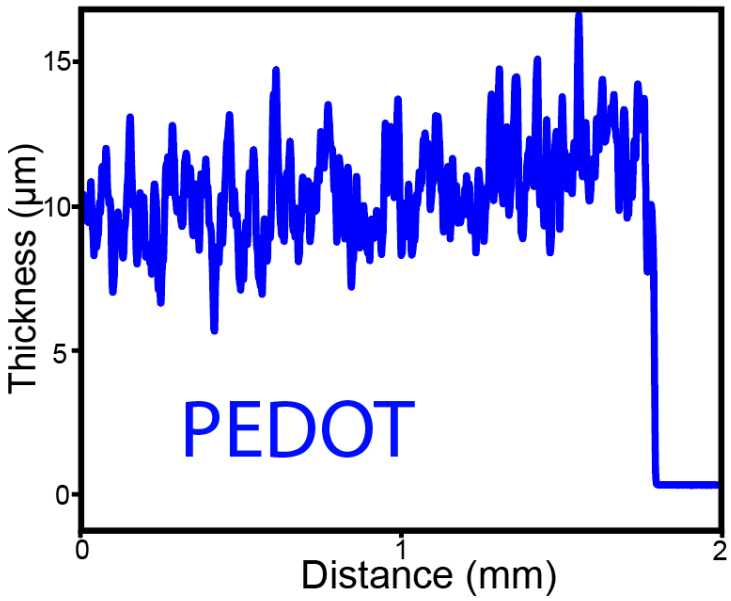

Figure 2.23: Profilometry measurement of a PEDOT film.

The electrochemical properties of a freestanding PEDOT film are studied utilizing a current collector-less three-electrode configuration, platinum lead and a polyimide mask that exposes the polymer to the electrolyte (Figure 2.24a inlet). Cyclic voltammograms demonstrate a high electrochemical stability with nearly rectangular shapes after 500 cycles in 1 M H_2SO_4 at a scan rate of 25 mV s^{-1} (Figure 2.24a). Notably, cyclic voltammograms retain their rectangular shape as the scan rate is increased from 25 mV s^{-1} to 200 mV s^{-1}, this is due to a low electrode resistance and the polymer's high electronic conductivity (Figure 2.24b). Nyquist plots (Figure 2.24c), collected via electrochemical impedance spectroscopy, are carried out at the open circuit potential with a 10 mV sinusoidal perturbation frequency ranging from 0.1 Hz to 100 kHz and show real impedance Z" versus imaginary impedance -Z". A 1.23 Ω internal resistance for the cell is obtained from the x-axis intercept at high-frequency, this represents the aggregated resistances from the electrode material, electrode/electrolyte interface and electrolyte.[42] Low charge-transfer resistance is determined from the nearly 90° angled curve in the low-frequency region of the plot and by

curve shape retention after 500 cycles. The low internal resistance enables reversible facile doping during charging and discharging.[42] PEDOT-RVPP exhibits a state-of-the-art capacitance of 181 F g^{-1} calculated from a discharge curve (Figure 2.24d) at a current density of 3.5 A g^{-1}, moreover, triangular-shaped curves at various current densities indicate facile charge transfer.[43-47] Cyclic voltammetry (Figure 2.24e) and electrochemical impedance spectroscopy (Figure 2.24f) experiments are carried out using 1 M and 6 M H_2SO_4 electrolytes to test the doping effect 4of the SO_4^{2-} counter anion – a commonly used dopant for increasing the conductivity of PEDOT.[48] The Nyquist plots in Figure 2.24f show a large semicircle diameter for 6 M versus 1 M electrolyte stemming from interfacial resistance, poor charge propagation and a low ionic mobility.[49,50]

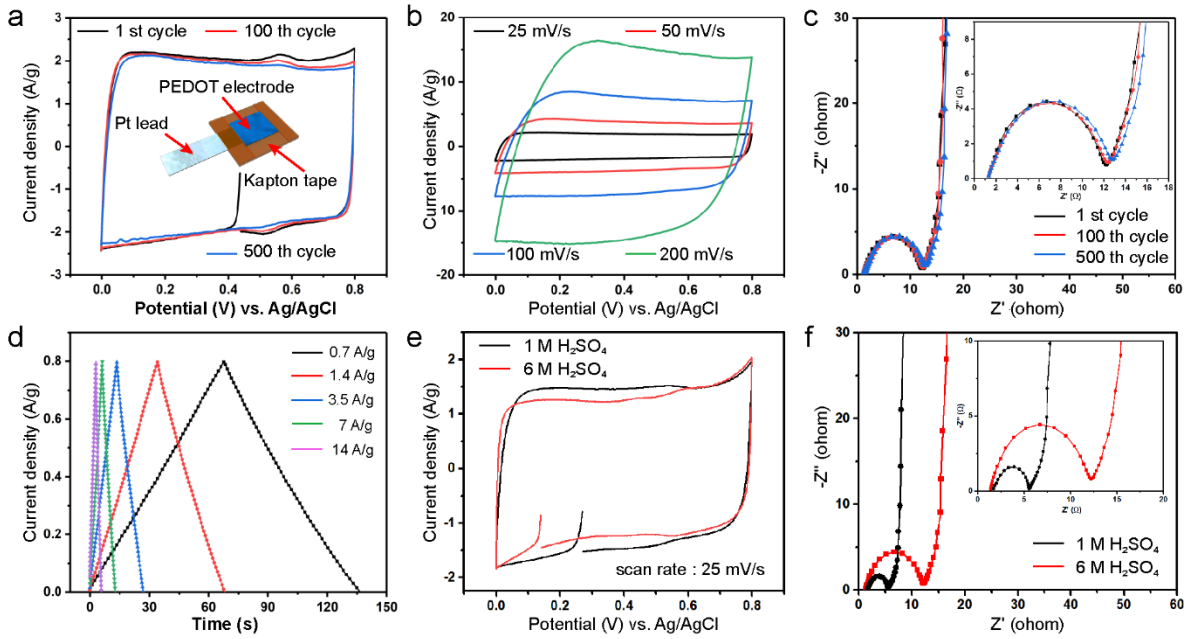

Figure 2.24: Three-electrode electrochemical characterization of a freestanding RVPP-PEDOT film serving as a working electrode. (a) Cyclic voltammograms, collected in the absence of a current collector using a degassed 1 M H_2SO_4 aqueous electrolyte, show rectangular reversibility at a scan rate of 25 mV s^{-1} and (b) as the scan rate increases from of 25 to 200 mV s^{-1}, the polymer remains capacitive. (c) Nyquist plots indicate a mixed pseudocapacitive and capacitive behavior remaining stable throughout 500 cycles. (d) Galvanostatic charge-discharge profiles at 0.7, 1.4, 3.5, 7 and 14 A g^{-1} show retention of triangular symmetry and demonstrate PEDOT's high rate capability. (e) Cyclic voltammograms show similar rectangular curves in 1 M and 6 M H_2SO_4

electrolyte. (f) Electrochemical impedance spectroscopy Nyquist plots display more resistance in 6 M H_2SO_4 from electrolyte ion diffusion.

Supercapacitors are fabricated using RVPP-PEDOT as shown in the flow process diagram of Figure 2.25a, these are developed utilizing a 1 M H_2SO_4 aqueous electrolyte and a hard carbon paper current collector for stable device performance and rapid charging-discharging. A device is encased in polyimide tape to mitigate electrolyte evaporation and retains rectangular-shaped cyclic voltammograms at 25 mV s^{-1} in voltage windows of 0.6 V, 0.8 V, 1V and 1.2 V (Figure 2.25b). After 1000 cycles at a specific scan rate, ranging from 25 mV s^{-1} to 4000 mV s^{-1} (Figure 2.25c, d), electrochemical performance and capacitive behavior remain stable due to a high rate capability.[49] The plot in Figure 2.25e shows that as the scan rate increases, the capacitance decreases from 185 F g^{-1} (25 mV s^{-1}) to 148 F g^{-1} (4000 mV s^{-1}) because of the limited time for electrolyte ions to diffuse to the electrode surface.[51,52] Galvanostatic charge-discharge curves show nearly linear and triangular symmetry (Figure 2.25f) stemming from a low internal resistance and high coulombic efficiency.[53] The highest capacitance attained is 181 F g^{-1} at a current density of 3.5 A g^{-1} with 98.3% coulombic efficiency. Figure 2.25g shows a plot of the ohmic drop versus coulombic efficiency at different current densities, this ohmic drop (ΔU) = I·R stems from stifled ion diffusion due to time constraint. Throughout this test, resistance (R) is held constant and ΔU is proportional to current density (I).[54] The ohmic drop increases with current density as ion diffusion becomes more limited; however, a small initial ohmic drop present at a low current density is due to self-discharge (Figure 2.26). A supercapacitor possesses a self-discharge rate and a charging rate (current density); the effective charging rate is the difference between the set current density and the intrinsic self-discharging rate of a device. Galvanostatic charge-discharge curves show

coulombic efficiencies of 99.1%, 98.3% and 96.5% as a device is charged to 0.6 V, 0.8 V and 1 V respectively, at a current density of 3.5 A g^{-1} (Figure 2.25h).

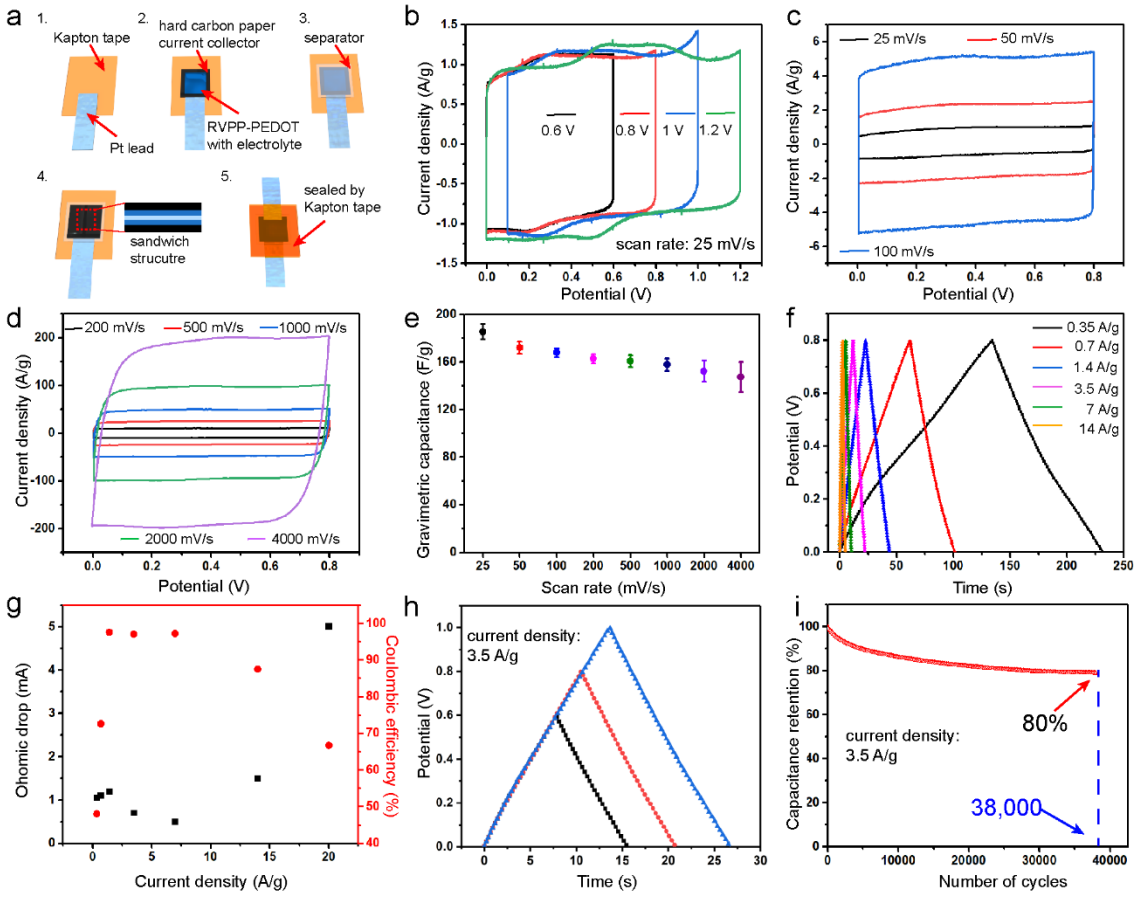

Figure 2.25: Performance characteristics of a two-electrode RVPP-PEDOT symmetric supercapacitors. (a) Flow process diagram of device fabrication. (b) Cyclic voltammograms collected in 1 M H_2SO_4 at a scan rate of 25 mV s^{-1} using varied voltage windows show stable rectangular capacitive behavior. (c, d) A rectangular-shaped curve and stable capacitive behavior is exhibited as the scan rate increases from 25 to 4000 mV s^{-1}; (e) device displays a high rate capability retaining gravimetric capacitance at fast scan rates. (f) Galvanostatic charge-discharge curves at current densities ranging from 0.35 to 14 A g^{-1} show stable profiles with corresponding (g) ohmic drops increasing from 1 to 5 mA as a function of current density. (h) Charge-discharge behavior remains stable as voltage window is widened at a current density of 3.5 A g^{-1} and (i) 80% of original capacitance is retained after 38,000 cycles.

The Nyquist plot in Figure 2.27 shows an equivalent series resistance of 0.43 Ω and an approximate 90° angle at low frequencies. This low aggregated device resistance is characteristic of an electronically conducting nanostructured electrode possessing a large electrode/electrolyte contact area that shortens ion diffusion pathways.[55] An supercapacitor exhibits 80% retention of the original capacitance after 38,000 cycles (Figure 2.25i) buttressed by a nanofibrillar architecture that mitigates the stresses associated with polymer swelling and shrinking during long-term charge and discharge.

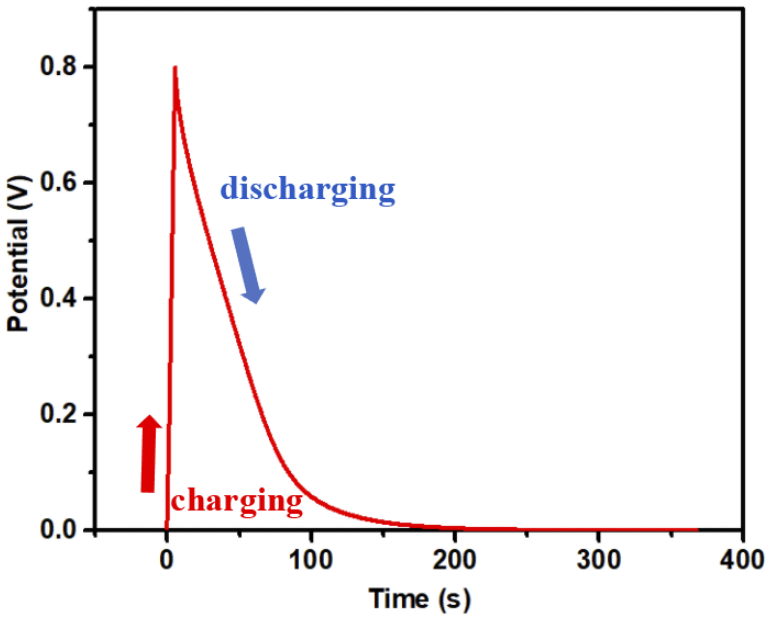

Figure 2.26: Charging and self-discharging curve of a two-electrode symmetric RVPP-PEDOT electrochemical capacitor.

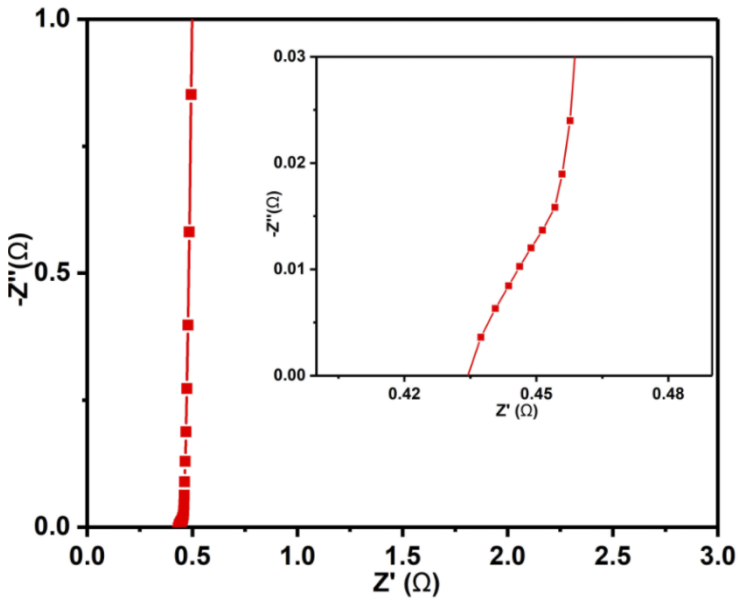

Figure 2.27: Nyquist plot of a two-electrode symmetric RVPP-PEDOT electrochemical capacitor.

2.4 Conclusions

Rust is a ubiquitous byproduct from the corrosion of iron, and when treated with acid, this solid-state material serves as an ideal source of Fe3+ ions for carrying out chemical synthesis. This work demonstrates the advantages of utilizing rust for developing oxidative radical polymerizations from the vapor phase thereby overcoming the hygroscopic and corrosive nature of iron (III) salts that serve as nominal oxidants for synthesizing conducting polymers. Discussions and results presented here address mechanistic steps associated with dissolution of rust during synthesis and introduce a fundamental understanding of a synergistic chemical process that combines polymer growth, hydrolysis, and crystallization. Rust-based vapor-phase polymerization is a novel approach for producing high-performing conducting polymers as proven by the attained high conductivity and high electrochemical stability of our robust freestanding nanofibrillar PEDOT films. In this approach, we advance the fields of conducting polymer synthesis, vapor-phase

chemical deposition, and energy storage through a facile, scalable, and patternable process that enables deposition of electroactive high-surface area electrodes for fabricating state-of-the-art supercapacitors.

References

(1) Jolivet, J.-P.; Tronc, E.; Chanéac, C. Iron Oxides: From Molecular Clusters to Solid. A Nice Example of Chemical Versatility. Comptes Rendus Geoscience 2006, 338 (6-7), 488–497.

(2) Bottero, J. Y.; Manceau, A.; Villieras, F.; Tchoubar, D. Structure and Mechanisms of Formation of Iron Oxide Hydroxide (Chloride) Polymers. *Langmuir* **1994**, *10*, 316–319.

(3) Jolivet, J.-P.; Chaneac, C.; Tronc, E. Iron Oxide Chemistry. From Molecular Clusters to Extended Solid Networks. *Chem. commun.* **2004**, 481-487.

(4) Flynn, JR. C. M. Hydrolysis of Inorganic Iron(III) Salts. *Chem.Rev.* **1984**, *84*, 31-41.

(5) Music´S.; Krehula S.; Popovic´ S.; Skoko Zˇ. Some factors influencing forced hydrolysis of $FeCl_3$ solutions. *Materials Letters.* **2003,** *57*, 1096-1102.

(6) Vaniman, D. T.; Bish, D. L.; Ming, D. W.; Bristow, T. F.; Morris, R. V.; Blake, D. F.; Chipera, S. J.; Morrison, S. M.; Treiman, A. H.; Rampe, E. B.; *et al.* Mineralogy of a Mudstone at Yellowknife Bay, Gale Crater, Mars. *Science* **2014,** *343* (6169), 1243480.

(7) Yoshida, H.; Hasegawa, H.; Katsuta, N.; Maruyama, I.; Sirono, S.; Minami, M.; Asahara, Y.; Nishimoto, S.; Yamaguchi, Y.; Ichinnorov, N.; *et al.* Fe-oxide concretions formed by interacting carbonate and acidic waters on Earth and Mars. *Science Advances* **2018,** *4* (12), eaau0872.

(8) Bibring, J.-P.; Arvidson, R. E.; Gendrin, A.; Gondet, B.; Langevin, Y.; Mouelic, S. L.;

Mangold, N.; Morris, R. V.; Mustard, J. F.; Poulet, F.; *et al.*Coupled Ferric Oxides and Sulfates on the Martian Surface. *Science* **2007**, *317*, 1206–1210.

(9) Yoon, H.; Chang, M.; Jang, J. Formation of 1D Poly(3,4-Ethylenedioxythiophene) Nanomaterials in Reverse Microemulsions and Their Application to Chemical Sensors. *Advanced Functional Materials* **2007**, *17*, 431–436.

(10) D'Arcy, J. M.; El-Kady, M. F.; Khine, P. P.; Zhang, L.; Lee, S. H.; Davis, N. R.; Liu, D. S.; Yeung, M. T.; Kim, S. Y.; Turner, C. L.; *et al.*Vapor-Phase Polymerization of Nanofibrillar Poly(3,4-Ethylenedioxythiophene) for Supercapacitors. *ACS Nano* **2014**, *8*, 1500–1510.

(11) Bhaumik, M.; Maity, A.; Srinivasu, V.; Onyango, M. S. Removal of Hexavalent Chromium from Aqueous Solution Using Polypyrrole-Polyaniline Nanofibers. *Chemical Engineering Journal* **2012**, *181-182*, 323–333.

(12) Pei, J.; Yu, W.-L.; Huang, W.; Heeger, A. J. A Novel Series of Efficient Thiophene-Based Light-Emitting Conjugated Polymers and Application in Polymer Light-Emitting Diodes. *Macromolecules* **2000**, *33*, 2462–2471.

(13) Cho, B.; Park, K. S.; Baek, J.; Oh, H. S.; Lee, Y.-E. K.; Sung, M. M. Single-Crystal Poly(3,4-Ethylenedioxythiophene) Nanowires with Ultrahigh Conductivity. *Nano Letters* **2014**, *14*, 3321–3327.

(14) Lawal, A. T.; Wallace, G. G. Vapour Phase Polymerisation of Conducting and Non-Conducting Polymers: A Review. *Talanta* **2014**, *119*, 133–143.

(15) Bhattacharyya, D.; Howden, R. M.; Borrelli, D. C.; Gleason, K. K., Vapor phase oxidative synthesis of conjugated polymers and applications. *Journal of Polymer Science Part B: Polymer Physics* **2012,** *50* (19), 1329-1351.

(16) Winther-Jensen, B.; Winther-Jensen, O.; Forsyth, M.; Macfarlane, D. R. High Rates of Oxygen Reduction over a Vapor Phase-Polymerized PEDOT Electrode. *Science* **2008**, *321*, 671–674.

(17) Anothumakkool, B.; Soni, R.; Bhange, S. N.; Kurungot, S. Novel Scalable Synthesis of Highly Conducting and Robust PEDOT Paper for a High Performance Flexible Solid Supercapacitor. *Energy & Environmental Science* **2015**, *8*, 1339–1347.

(18) Ren, G.; Lu, X.; Li, Y.; Zhu, Y.; Dai, L.; Jiang, L. Porous Core–Shell Fe_3C Embedded N-Doped Carbon Nanofibers as an Effective Electrocatalysts for Oxygen Reduction Reaction. *ACS Applied Materials & Interfaces* **2016**, *8*, 4118–4125.

(19) Im, S. G.; Gleason, K. K. Systematic Control of the Electrical Conductivity of Poly(3,4-Ethylenedioxythiophene) via Oxidative Chemical Vapor Deposition. *Macromolecules* **2007**, *40*, 6552–6556.

(20) Handy, J. O.; Knote, J. M. Concentration and Purification of Iron Ore, High in Sulphur, by Roasting in a Rotary Kiln. *Journal of Industrial & Engineering Chemistry* **1911**, *3*, 723–730.

(21) Wang, H.; Diao, Y.; Rubin, M.; Santino, L. M.; Lu, Y.; D'Arcy, J. M. Metal Oxide-Assisted PEDOT Nanostructures via Hydrolysis-Assisted Vapor-Phase Polymerization for Energy Storage. *ACS Applied Nano Materials* **2018**, *1*, 1219–1227.

(22) Frackowiak, E.; Khomenko, V.; Jurewicz, K.; Lota, K.; Béguin, F., Supercapacitors based on conducting polymers/nanotubes composites. *Journal of Power Sources* **2006**, *153* (2), 413-418.

(23) Maiti, D.; Devi, P. S. Selective Formation of Iron Oxide and Oxyhydroxide

Nanoparticles at Room Temperature: Critical Role of Concentration of Ferric Nitrate. *Materials Chemistry and Physics* **2015**, *154*, 144–151.

(24) Xu, W.; Wang, M.; Li, Z.; Wang, X.; Wang, Y.; Xing, M.; Yin, Y. Chemical Transformation of Colloidal Nanostructures with Morphological Preservation by Surface-Protection with Capping Ligands. *Nano Letters* **2017**, *17*, 2713–2718.

(25) Luo, W.; Jiang, C.; Li, Y.; Shevlin, S. A.; Han, X.; Qiu, K.; Cheng, Y.; Guo, Z.; Huang, W.; Tang, J. Highly Crystallized α-FeOOH for a Stable and Efficient Oxygen Evolution Reaction. *Journal of Materials Chemistry A* **2017**, *5*, 2021–2028.

(26) Stavila, V.; Whitmire, K. H.; Rusakova, I. Synthesis of Bi_2S_3 Nanostructures from Bismuth(III) Thiourea and Thiosemicarbazide Complexes. *Chemistry of Materials* **2009**, *21*, 5456–5465.

(27) Mondal, C.; Pal, J.; Pal, K. K.; Sasmal, A. K.; Ganguly, M.; Roy, A.; Manna, P. K.; Pal, T. Serendipitous Synthesis of $Ag_{1.92}Mo_3O_{10}\cdot H_2O$ Nanowires from $AgNO_3$-Assisted Etching of Ammonium Phosphomolybdate: A Material with High Adsorption Capacity. *Crystal Growth & Design* **2014**, *14*, 5034–5041.

(28) Eskelsen, J. R.; Phillips, K. J.; Hipps, K. W.; Mazur, U. Hyperbranched Crystalline Nanostructure Produced from Ionic π-Conjugated Molecules. *Chemical Communications* **2015**, *51*, 2663–2666.

(29) Ma, X.; Su, C.; Yang, L.; Li, L.; Wang, K.; Zhou, J.; Yuan, S. Size- and Morphology-Controlled Biomimetic Synthesis of Hierarchical Hollow $BaCO_3$. *CrystEngComm* **2012**, *14*, 8554.

(30) Zhang, M.; Han, D.; Lu, P. PEDOT Encapsulated β-FeOOH Nanorods: Synthesis,

Characterization and Application for Sodium-Ion Batteries. *Electrochimica Acta* **2017**, *238*, 330–336.

(31) Tang, J.; Alivisatos, A. P. Crystal Splitting in the Growth of Bi_2S_3. *Nano Letters* **2006**, *6*, 2701–2706.

(32) Deng, H.; Liu, C.; Yang, S.; Xiao, S.; Zhou, Z.-K.; Wang, Q. Q. Additive-Mediated Splitting of Lanthanide Orthovanadate Nanocrystals in Water: Morphological Evolution from Rods to Sheaves and to Spherulites. *Crystal Growth & Design* **2008,** *8* (12), 4432-4439.

(33) Arumugam, D.; Thangapandian, M.; Mathavan, J. L. J.; Jayaram, A.; Palanichamy, M.; Chandrasekaran, S. S.; Subramanian, U.; Gupta, M.; Okram, G. S.; Jothirajan, M. A.; *et al.*Growth Mechanism of Pine-Leaf-like Nanostructure from the Backbone of $SrCO_3$ Nanorods Using LaMer's Surface Diffusion: Impact of Higher Surface Energy (γ = 38.9 EV/nm^2) {111} Plane Stacking Along ⟨110⟩ (γ = 3.4 EV/nm^2) by First-Principles Calculations. *Crystal Growth & Design* **2017**, *17*, 6394–6406.

(34) Shi, W.; Yao, Q.; Qu, S.; Chen, H.; Zhang, T.; Chen, L. Micron-Thick Highly Conductive PEDOT Films Synthesized via Self-Inhibited Polymerization: Roles of Anions. NPG Asia Materials **2017**, *9* (7), e405.

(35) Im, S. G.; Gleason, K. K. Systematic Control of the Electrical Conductivity of Poly(3,4-Ethylenedioxythiophene) via Oxidative Chemical Vapor Deposition. Macromolecules **2007**, *40* (18), 6552–6556.

(36) Ugur, A.; Katmis, F.; Li, M.; Wu, L.; Zhu, Y.; Varanasi, K. K.; Gleason, K. K. Low-Dimensional Conduction Mechanisms in Highly Conductive and Transparent Conjugated Polymers. *Advanced Materials* **2015**, *27*, 4604–4610.

(37) Chen, Y.-C.; Lu, A.-Y.; Lu, P.; Yang, X.; Jiang, C.-M.; Mariano, M.; Kaehr, B.; Lin, O.; Taylor, A.; Sharp, I. D.; Li, L.-J.; Chou, S. S.; Tung, V. Bioinspired Dimensional Transition: Structurally Deformed MoS2 for Electrochemically Stable, Thermally Resistant, and Highly Efficient Hydrogen Evolution Reaction. *Advanced Materials* **2017**, *29* (44), 1703863.

(38) Winther-Jensen, B.; Chen, J.; West, K.; Wallace, G. Vapor Phase Polymerization of Pyrrole and Thiophene Using Iron(III) Sulfonates as Oxidizing Agents. *Macromolecules* **2004**, *37*, 5930–5935.

(39) Tung, V. C.; Kim, J.; Cote, L. J.; Huang, J. Sticky Interconnect for Solution-Processed Tandem Solar Cells. *Journal of the American Chemical Society* **2011**, *133* (24), 9262–9265.

(40) Wang, X.; Zhang, X.; Sun, L.; Lee, D.; Lee, S.; Wang, M.; Zhao, J.; Shao-Horn, Y.; Dincă, M.; Palacios, T.; *et al.*High Electrical Conductivity and Carrier Mobility in oCVD PEDOT Thin Films by Engineered Crystallization and Acid Treatment. *Science Advances* **2018**, *4* (9), eaat5780.

(41) Smits, F. M. Measurement of Sheet Resistivities with the Four-Point Probe. *Bell System Technical Journal* **1958**, *37*, 711–718.

(42) Rubinson, J. F.; Kayinamura, Y. P. Charge Transport in Conducting Polymers: Insights from Impedance Spectroscopy. *Chemical Society Reviews* **2009,** *38* (12), 3339-3347.

(43) Pal, R. K.; Kundu, S. C.; Yadavalli, V. K. Fabrication of Flexible, F ully Organic, Degradable Energy Storage Devices Using Silk Proteins. *ACS Applied Materials & Interfaces* **2018**, *10*, 9620–9628.

(44) Li, Y.; Ren, G.; Zhang, Z.; Teng, C.; Wu, Y.; Lu, X.; Zhu, Y.; Jiang, L. A Strong and

Highly Flexible Aramid Nanofibers/PEDOT:PSS Film for All-Solid-State Supercapacitors with Superior Cycling Stability. *Journal of Materials Chemistry A* **2016**, *4*, 17324–17332.

(45) Li, Z.; Ma, G.; Ge, R.; Qin, F.; Dong, X.; Meng, W.; Liu, T.; Tong, J.; Jiang, F.; Zhou, Y.; Li, K.; Min, X.; Huo, K.; Zhou, Y., Free-Standing Conducting Polymer Films for High-Performance Energy Devices. *Angewandte Chemie* **2016,** *128* (3), 991-994.

(46) Fong, K. D.; Wang, T.; Kim, H.-K.; Kumar, R. V.; Smoukov, S. K. Semi-Interpenetrating Polymer Networks for Enhanced Supercapacitor Electrodes. *ACS Energy Letters* **2017**, *2*, 2014–2020.

(47) Zhao, D.; Zhang, Q.; Chen, W.; Yi, X.; Liu, S.; Wang, Q.; Liu, Y.; Li, J.; Li, X.; Yu, H. Highly Flexible and Conductive Cellulose-Mediated PEDOT:PSS/MWCNT Composite Films for Supercapacitor Electrodes. *ACS Applied Materials & Interfaces* **2017**, *9*, 13213–13222.

(48) Meen, T.-H.; Chen, K.-L.; Chen, Y.-H.; Chen, W.-R.; Chou, D.-W.; Lan, W.-H.; Huang, C.-J. The Effects of Dilute Sulfuric Acid on Sheet Resistance and Transmittance in Poly(3,4-Thylenedioxythiophene): Poly(Styrenesulfonate) Films. *International Journal of Photoenergy* **2013**, 1–6.

(49) Azman, N. H. N.; Lim, H. N.; Sulaiman, Y. Effect of Electropolymerization Potential on the Preparation of PEDOT/Graphene Oxide Hybrid Material for Supercapacitor Application. *Electrochimica Acta* **2016**, *188*, 785–792.

(50) Si, P.; Ding, S.; Lou, X.-W. (D.; Kim, D.-H. An Electrochemically Formed Three-Dimensional Structure of Polypyrrole/Graphene Nanoplatelets for High-Performance Supercapacitors. *RSC Advances* **2011**, *1*, 1271.

(51) Islam, M. M.; Chidembo, A. T.; Aboutalebi, S. H.; Cardillo, D.; Liu, H. K.;

Konstantinov, K.; Dou, S. X. Liquid Crystalline Graphene Oxide/PEDOT:PSS Self-Assembled 3D Architecture for Binder-Free Supercapacitor Electrodes. *Frontiers in Energy Research* **2014**, *2* (31), 1-11.

(52) Zhang, Q.; Li, Y.; Feng, Y.; Feng, W. Electropolymerization of Graphene Oxide/Polyaniline Composite for High-Performance Supercapacitor. *Electrochimica Acta* **2013**, *90*, 95–100.

(53) Chen, J.; Jia, C.; Wan, Z. The Preparation and Electrochemical Properties of MnO2/Poly(3,4-Ethylenedioxythiophene)/Multiwalled Carbon Nanotubes Hybrid Nanocomposite and Its Application in a Novel Flexible Micro-Supercapacitor. *Electrochimica Acta* **2014**, *121*, 49–56.

(54) Zhou, K.; He, Y.; Xu, Q.; Zhang, Q. E.; Zhou, A. A.; Lu, Z.; Yang, L.-K.; Jiang, Y.; Ge, D.; Liu, X. Y.; *et al.*A Hydrogel of Ultrathin Pure Polyaniline Nanofibers: Oxidant-Templating Preparation and Supercapacitor Application. *ACS Nano* **2018**, *12*, 5888–5894.

(55) Moon, I. K.; Yoon, S.; Oh, J. 3D Highly Conductive Silver Nanowire@PEDOT:PSS Composite Sponges for Flexible Conductors and Their All-Solid-State Supercapacitor Applications. *Advanced Materials Interfaces* **2017**, *4*, 1700860.

(56) Lu, Y.; Santino, L. M.; Acharya, S.; Anandarajah, H.; D'Arcy, J. M. Studying Electrical Conductivity Using a 3D Printed Four-Point Probe Station. *Journal of Chemical Education* **2017**, *94*, 950–955.

Chapter 3

Direct Conversion of Fe_2O_3 to 3D Nanofibrillar PEDOT Microsupercapacitors

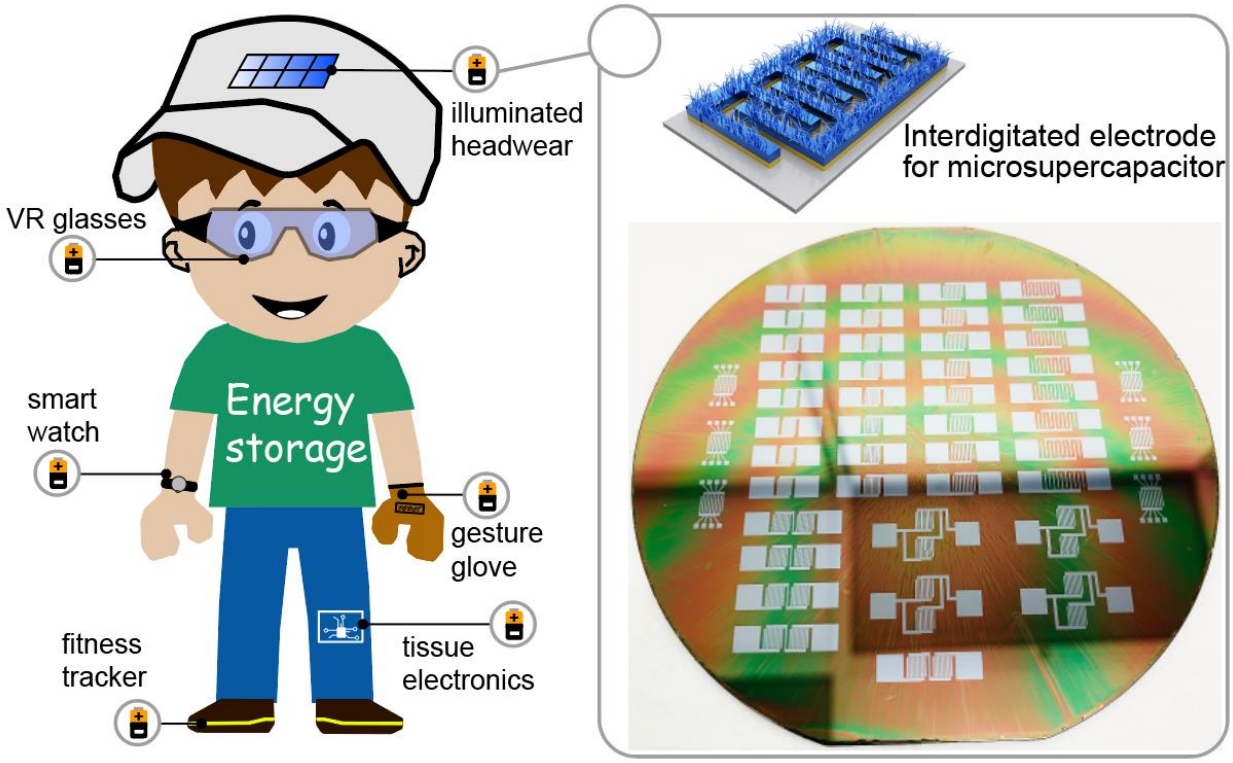

Microsupercapacitor for micro-electronics

3.1 Introduction

The rapidly growing market for autonomous devices, micro-electromechanical systems, micro-robots and radio frequency identification tags creates a demand for high-performing miniaturized electrochemical energy storage.[1-3] Currently, high energy density micro-batteries fulfill the market's needs albeit suffering from diffusion-limited low power density and poor cycling stability that shortens lifespan.[4] Microsupercapacitors (μSCs) are an alternative to micro-batteries affording high charge/discharge rates and high cycling stability[5] for developing power supplies for portable electronics.[5-10] These devices are produced via inkjet printing,[11] laser scribing[12-13] or electrochemistry[14] with a 3D electrode configuration comprised of nanostructures that facilitate ion diffusion and enhance energy density.

Interdigitated electrodes for μSCs are commonly coated by state-of-the-art materials such as capacitive onion-like carbon[15] or carbide-derived carbons[4,16] as well as by pseudocapacitive RuO_2[17,18] or $Ni(OH)_2$.[19] Unfortunately, these carbon allotropes possess low energy density, and metal oxides/hydroxides exhibit low cycling stability as well as poor rate capability due to phase transition and limited ion migration.[20,21] Alternatively, μSCs based on conducting polymers such as polyaniline (PANi),[20,22] polypyrrole (PPy)[23,24] and poly(3,4-ethylenedioxythiophene) (PEDOT)[21, 25-27] show excellent rate capability due to facile charge transport. Moreover, faradic near-surface redox reactions in conducting polymers also afford a pseudocapacitive mechanism for increasing energy density. Among conducting polymers, PEDOT is an ideal electrode material for μSCs due to its high electrical conductivity (reaching 7000 S cm^{-1})[28] and its ability to produce nanofibers,[29] nanowires[30] and nanosheets[31] that increase an electrode's active surface area.

However, integrating 3D PEDOT nanostructures in μSCs is challenging. Current fabrication strategies require pre-fabricated templates that unfortunately possess low packing density and low aspect ratio scaffolds resulting in low surface area.[25, 32-33] Moreover, polymer is typically produced via electrochemical syntheses, that due to an inhomogeneous dristribution of reactants, produce conjugated backbones with structural defects.[2,27,34] These limitations highlight the urgency for advancing current electrode fabrication protocols.

Here, we present a superior low-cost approach for engineering 3D μSCs compatible with conventional micro-fabrication and based on our previously reported rust-assisted vapor-phase polymerization.[35] We produce homogeneous coatings of vertically directed PEDOT nanofibers characterized by an electronic conductivity of 3580 S cm^{-1}; deposition occurs in one step resulting in a high packing density of 1D nanostructures with aspect-ratio of 100. Our electrode engineering protocol utilizes sputtered α-Fe_2O_3 as a ferric ion-containing solid-state oxidant-precursor to induce dissolution, liberation of ferric ions, and Fe^{3+} hydrolysis concomitant with oxidative radical polymerization. The electrode thickness, gap distance and fractal geometry of PEDOT μSCs is controlled resulting in state-of-the-art areal (21.3 mF cm^{-2}) and volumetric (400 F cm^{-3}) capacitances as well as energy density (16.1 mWh cm^{-3}). Such magnitudes exemplify the highest figures of merit for conducting polymer-based μSCs. This work also develops quasi-solid-state μSCs exhibiting extended rate capability (50 V s^{-1}) and high cycling stability (94 % capacitance retention after 10,000 cycles) as well as able to operate efficiently at a temperature of 60 ºC.

3.2 Experimental methods

3.2.1 Fabrication of an interdigitated PEDOT nanofibrillar electrode

1) Micro-fabrication process. An insulating layer of SiO_2 (1.5 μm thick) was deposited on a 4-inch silicon wafer via plasma-enhanced chemical vapor phase deposition (PECVD). To generate a 4 μm thick double layer photoresist on SiO_2, photoresist LOR 10B (Mico Chem) was spun coated at 1500 rpm for 60 s followed by 10 min soft-bake at 195 °C. Subsequently, photoresist AZP 4620 (AZ Electronic Materials) was spun coated at 3000 rpm for 60 s followed by 2 min soft-bake at 115 °C. The photoresist etching was carried out using a Heidelberg Laser Lithography system. After etching, samples were developed in AZ 400 developer solution (AZ Electronic Materials) for 3 min resulting in an interdigitated electrode pattern. Metal layers comprised of 10 nm Cr (adhesion layer) and 50 nm Au (current collector) were sequentially deposited over the patterned photoresist layer via thermal evaporation (Edwards 306 Vacuum Coater). A solid-oxidant precursor, Fe_2O_3, was sputtered over the gold current collector via physical vapor deposition (Kurt J. Lesker PVD 75 RF and DC). 2) Rust-based vapor-phase polymerization. A glass reactor is loaded the Fe_2O_3-coated micro-electrode, and using glass vials, 40 μL of concentrated hydrochloric acid and 200 μL of a 0.674 M EDOT solution in chlorobenzene are also loaded. This rector is sealed and heated in an oven 150 °C / 1.5 hr. A PEDOT-coated substrate is immersed in Remover-PG (Mico Chem) solution and agitated on a shaker for 2 h to induce lift-off.

3.2.2 Spectroscopic characterization of electrode material

Scanning electron micrographs and energy-dispersive X-ray spectra were collected using a JEOL 7001LVF FE-SEM. Transmission electron micrographs were obtained using a JEOL 2100 TEM

by drop-casting a dispersion of PEDOT nanofibers on a TEM grid. Raman spectra were obtained using a Renishaw inVia confocal Raman spectrometer mounted on a Leica microscope with a 20× objective and 785 nm wavelength diode laser serving as an illumination source. A low power was necessary to mitigate heating of PEDOT sample. A Bruker d8 Advanced X-ray diffractometer was utilized to collect powder X-ray diffractograms of pulverized samples at room temperature using a Cu Kα radiation source (λ = 1.5406 Å) and LynxEye XE detector (operating at 40 kV and 40 mA); the sample holder was rotated at 30 rpm with a scan step of 0.02°. Current-voltage (I-V) curves were obtained with a built-in-house 3D printed probe station using two gold needles 1.24 mm apart. A Bruker Multimode 8 Atomic Force Microscope was used to measure the films' surface morphology and thickness. Four-point probe sheet resistance measurements were carried out using a Keithley 2450 SourceMeter with a Signatone SP4 four-point probe head.

3.2.3 Preparation of gel electrolyte

A 1 M H_2SO_4 aqueous electrolyte required milli-Q water (18 MΩ) degassed for 15 min. A 1 M H_2SO_4/polyvinyl alcohol gel electrolyte was prepared by adding 1 g of concentrated H_2SO_4 to 10 mL of deionized water, followed by addition of 1 g of polyvinyl alcohol powder. The whole mixture was heated to 85 °C while stirring until a clear solution was obtained.

3.2.4 Fabrication of PEDOT microsupercapacitor

Platinum foil leads were connected to two gold pads using polyimide sticky tape, and 100 μL of a 1 M H_2SO_4 aqueous electrolyte were added to polymer-coated interdigitated electrodes by drop-casting. For a gel electrolyte, 100 μL of a 1 M H_2SO_4/polyvinyl alcohol mixture were added to interdigitated electrodes by drop-casting followed by drying at 55 °C / 2 h.

3.2.5 Electrochemical characterization of micro-supercapacitor

Cyclic voltammetry and electrochemical impedance spectroscopy were performed on a BioLogic VMP3 multi-potentiostat. Cyclic voltammetry was carried out from 25 mV s^{-1} to 50 mV s^{-1} between 0 V and 1 V. Electrochemical impedance spectroscopy was carried out at the electrode's open circuit potential after obtaining a reversible cyclic voltammogram. Impedance values were recorded using a 10 mV sinusoidal disturbance at frequencies ranging from 100 kHz to 100 mHz.

3.3 Results & discussion

Micro-fabrication requires spin coating photoresist on SiO_2 and photolithography to produce an interdigitated pattern. Typically, microfabrication requires UV-masking protocols. Here, we utilize a laser writer to lower costs and increase versatility enabling us to readily produce interdigitated electrodes, evaluate the gap distance and develop fractal geometries. Chromium, gold and iron oxide (Fe_2O_3) are sequentially deposited serving as an adhesion layer, current collector and oxidant precursor, respectively (Figure 3.1a and Figure 3.2). An Fe_2O_3-coated electrode is introduced into a reaction vessel, heated, and exposed to vapors of 1) concentrated hydrochloric acid (HCl) and 2) 3,4-ethylenedioxythiophene (EDOT) monomer in chlorobenzene to produce PEDOT nanofibers (Figure 3.1b and Figure 3.3). Nanofibers, as previously reported,[35] form via dissolution of an iron (III)-containing solid and hydrolysis of ferric ions concomitant with preferential nucleation of monomer vapor on 1D FeOOH spindles. Polymer grows on partially dissolved spindles via oxidative radical polymerization in a step-growth fashion resulting in the deposition of PEDOT nanofibers on a current collector (Figure 3.1b). After lift-off, PEDOT nanostructures remain intact as interdigitated electrodes adhered to the current collector (Figure 3.1c).

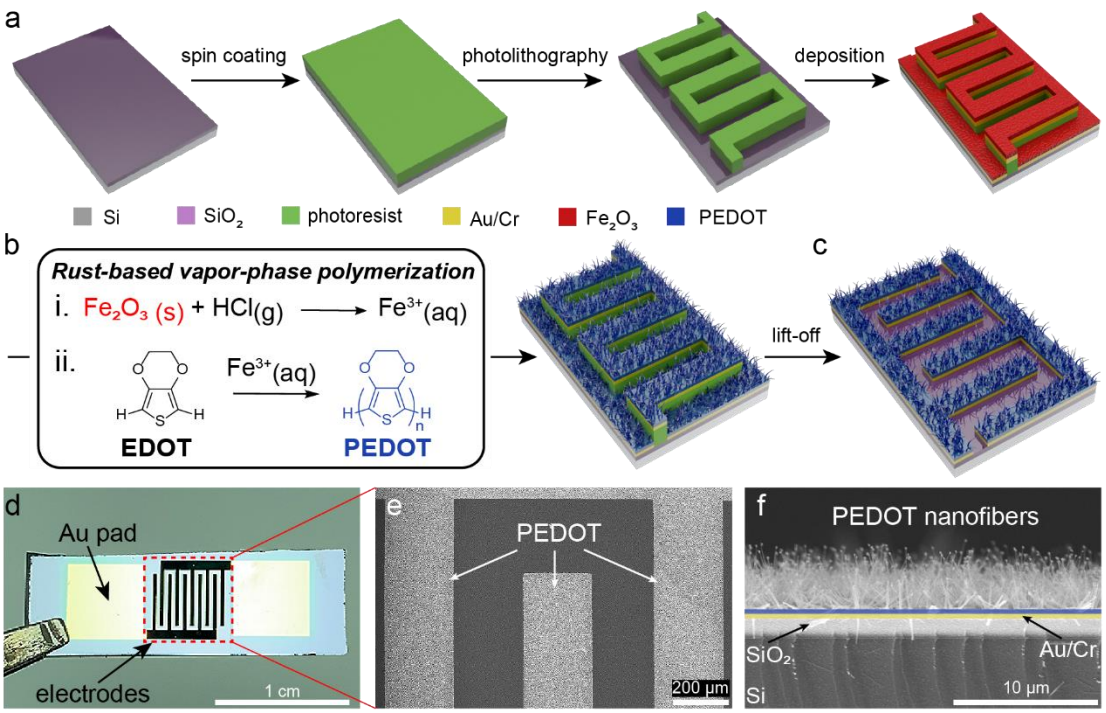

Figure 3.1: Fabrication process and structural characterization of a 3D nanofibrillar PEDOT µSC. a) SiO_2 is deposited on Si wafer, photoresist is spin coated and the interdigitated pattern is produced via laser writer after exposure and development. b) Adhesion layer (Cr), current collector (Au) and oxidant precursor (Fe_2O_3) are deposited sequentially, the latter via sputtering. Chemical conversion is carried out by i) liberating Fe^{3+} from Fe_2O_3 via dissolution using HCl vapor and ii) oxidizing EDOT vapor with Fe^{3+} to produce PEDOT nanofibers. c) A nanofibrillar PEDOT µSC is obtained after lift-off. d) Digital photograph shows the µSC configuration consisting of 2 electrodes with gold pads and each possessing 5 PEDOT-coated fingers. e) A scanning electron micrograph shows a close-up of 200 µm wide polymer-coated fingers and demonstrates a gap void of polymer. f) Cross-sectional electron micrograph captures device layers (augmented by color) and the active polymer coating comprised of a carpet of vertically directed PEDOT nanofibers.

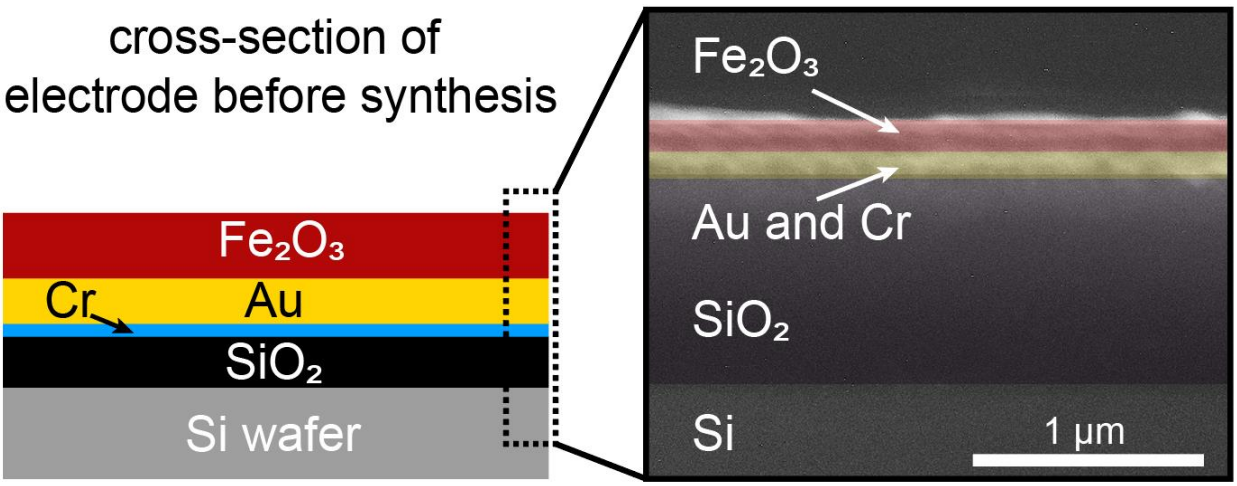

Figure 3.2: Schematic illustration and cross-sectional SEM image shows thickness for each layer in our device including iron oxide (oxidant precursor), gold (current collector), chromium (adhesion layer) and silicon dioxide layer (insulating layer). These have been painted with Photoshop to delineate boundaries.

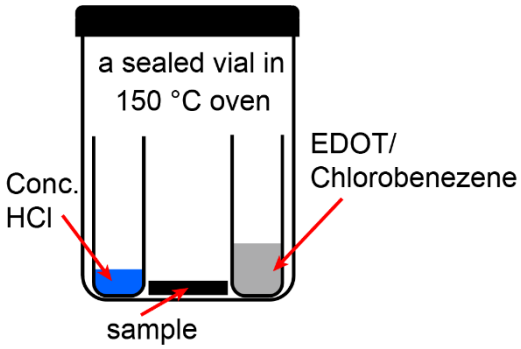

Figure 3.3: Schematic illustration of our rust-based vapor-phase polymerization setup. A glass reactor is loaded with individual containers carrying concentrated hydrochloric acid, EDOT/chlorobenzene, and a micro-fabricated electrode (sample). This glass reactor is then sealed and heat to 150 °C in an oven for 1.5 h.

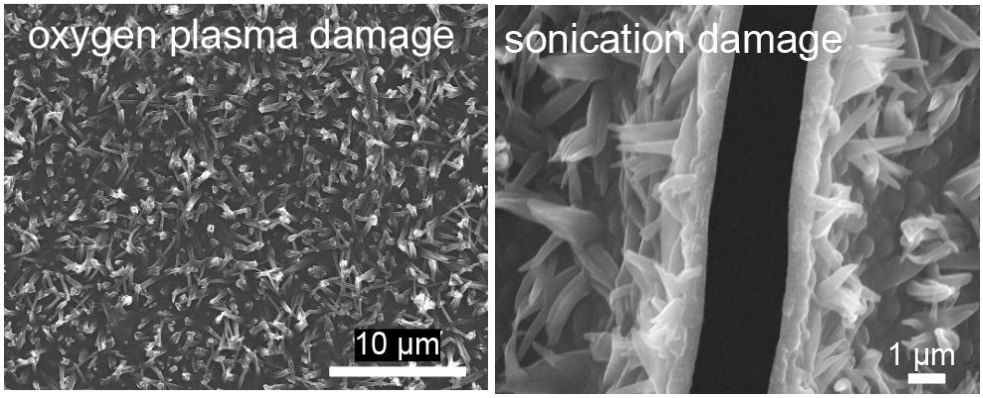

Figure 3.4: Left SEM image show a morphological change on nanofibers after a 5 min oxygen plasma treatment that fused fibers together. Right SEM images shows a rupture in the nanofibrillar polymer film after sonication using a common bath sonicator.

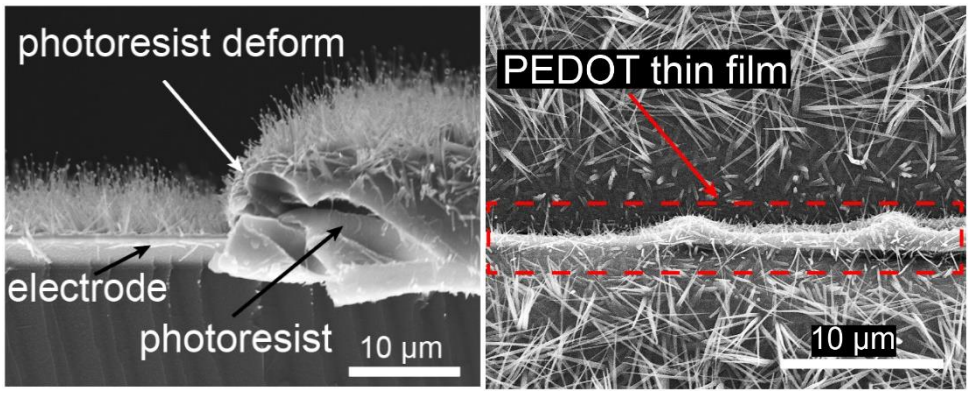

Figure 3.5: Left SEM image shows photoresist deformation during rust-based vapor-phase polymerization. Right SEM image shows the formation of thin PEDOT film over the photoresist at the electrode/gap interface.

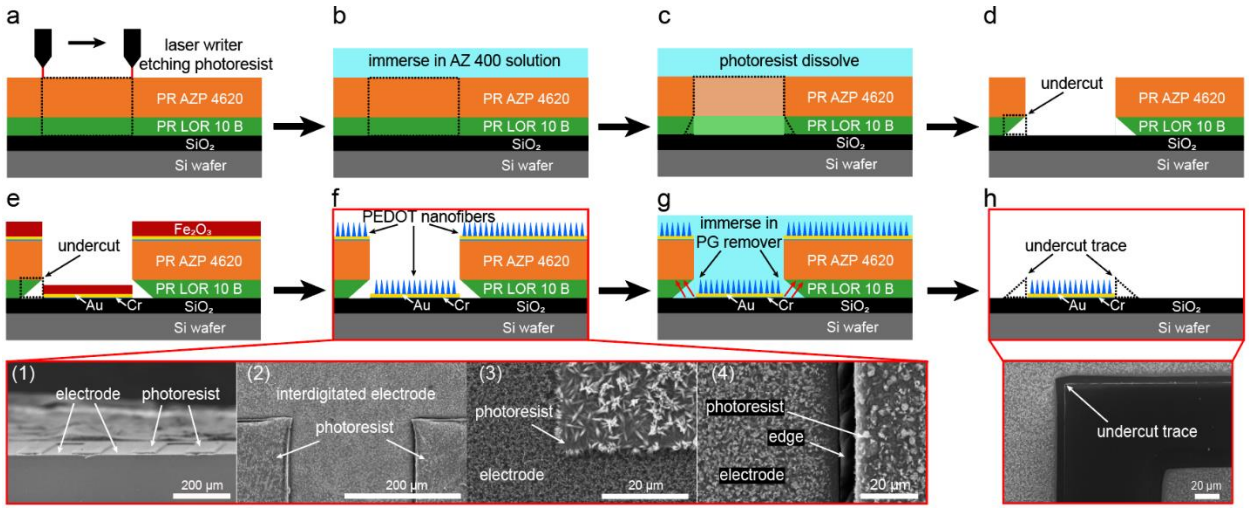

Figure 3.6: Schematic illustration of lift-off process and SEM images show that an undercut, results in a clean lift-off.

The production of this electrode structure is aided by a double-layered photoresist undercut that facilitates lift-off (Figure 3.4-4.6). Lift-off aims to remove photoresist between finger electrodes. Conventionally, oxygen plasma and sonication are two approaches to enhance lift-off, however, these methods damaged our PEDOT morphology resulting in low electronic conductivity (Figure 3.4). Moreover, after EDOT polymerization, we found a thin film forming between electrode and photoresist at the gap interface preventing contact between photoresist and dissolving solution and thus impeding lift-off (Figure 3.5).

To address these problems, we designed a 12 µm-thick double layer photoresist (LOR 10 B and AZP 4620) during spin-coating. The photoresist became soft after laser writer etching (Figure 3.6a) and started dissolving when immersed in AZ 400 solution. Since the dissolution rate of LOR 10 B is faster than AZP 4620, the undercut is obtained by controlling the immersion time as shown in Figure 3.6b-d. The undercut remained after deposition of Cr/Au/Fe_2O_3 layer and synthesis of PEDOT nanofibers (Figure 3.6e). This was confirmed by SEM images as shown in Figure 3.6f1-

f3. The SEM image (Figure 3.6f4**)** exhibits the clear edge between electrode and photoresist thereby enabling clean lift-off (Figure 3.5). The undercut provides more pathways for PG remover solution to dissolve photoresist and the LOR 10 B photoresist is easily lift-off during immersion (Figure 3.6g). Finally, an electrode with a clear gap and an undercut trace is produced as shown in Figure 3.6h.

A µSC is comprised of two five-finger electrodes (Figure 3.1d) homogeneously coated by PEDOT nanofibers; a finger is 200 µm wide and the device's interdigitated gap is 200 µm (Figure 3.1e). Polymer and metal electrodes are strongly adhered as demonstrated after Scotch tape delamination tests and repeated sonication cycles (Figure 3.7). A high packing density of vertically aligned nanofibers is produced, as shown in cross-sectional electron micrograph (Figure 3.1f), plausibly due to confined polymerization[28] within the photoresist trenches.

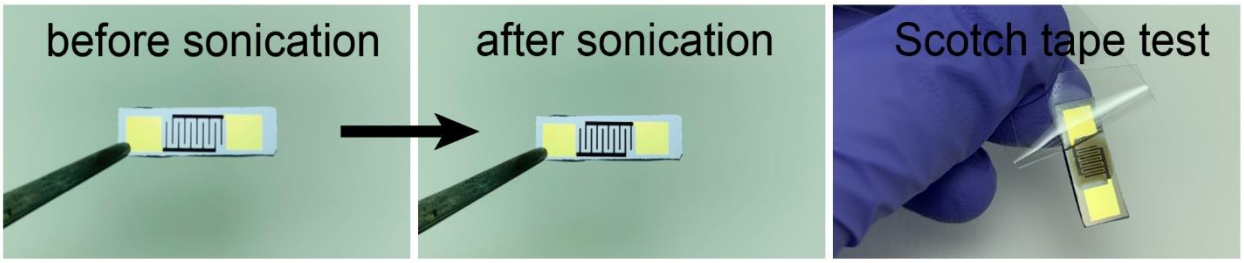

Figure 3.7: Photograph image shows sonication test and Scotch tape test being performed on a micro-supercapacitor.

Understanding intrinsic chemical properties of the electrode material is necessary for advancing µSC engineering and yet few discussions on characterization are present in the literature. Here, we apply microscopy, spectroscopy, current-voltage (I-V) profiles and four-point probe resistivity measurements to probe molecular and solid-state structure. A finger electrode is coated by a high packing density of nanofibers possessing a 10 µm length and 100 nm diameter **(**aspect ratio ~100)

(Figure 3.8a, b and Figure 3.9, 3.10). Each nanofiber possesses a core-shell structure confirmed via high-angle annular darkfield (HAADF) imaging in scanning transmission electron microscopy (Figure 3.8c) where image contrast is roughly proportional to the square of the atomic number.[36] Elemental maps via energy-dispersive X-ray spectroscopy show an iron-containing core and a sulfur-containing shell for a nanofiber (Figure 3.8d and Figure 3.11). This iron core is dissolved in 6 M HCl to produce a hollow 1D polymer nanostructure with an extended surface area[28] and a highly oxidized conjugated backbone; chemical bond resonance signals in Raman spectroscopy (Figure 3.8e) indicate a high doping state.[21]

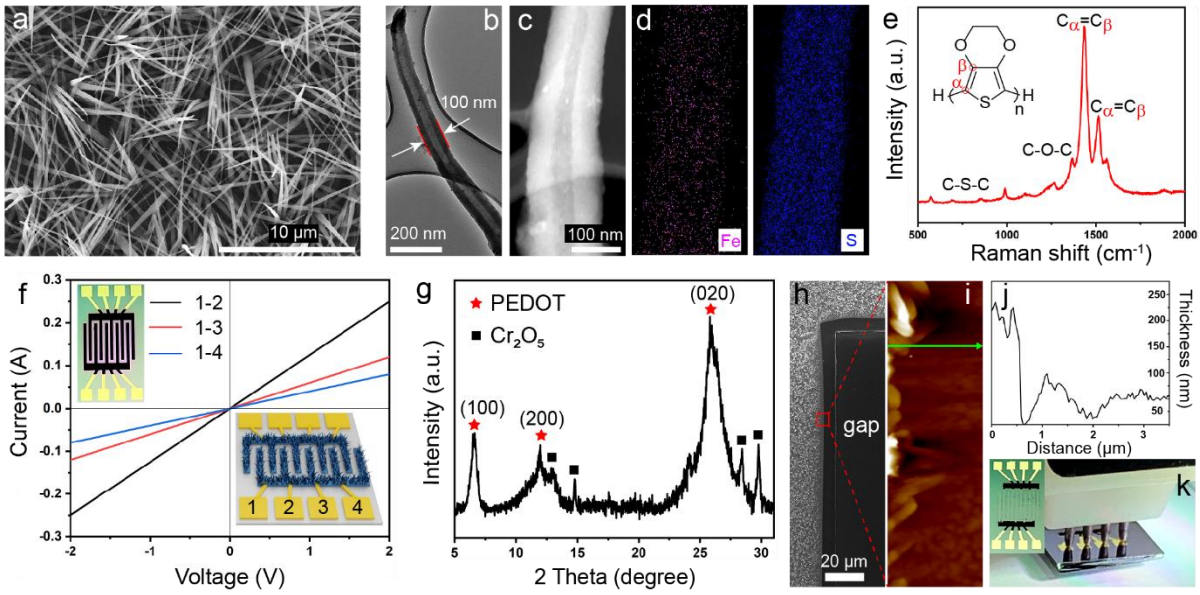

Figure 3.8: Direct characterization on intrinsic properties of a nanofibrillar PEDOT electrode. a) Scanning electron micrograph shows bulk 1D electrode morphology. b) Transmission electron micrograph and c) high-angle annular dark-field STEM image of single fibers confirm a core-shell structure. d) EDX maps for a nanofiber show an elemental composition consisting of Fe and S. e) Raman spectrum is characteristic of an oxidized conjugated backbone possessing high doping. f) I-V curves collected throughout the entire polymer coating (inset) show ohmic behavior indicative of a homogenous percolation network. g) PXRD confirms a polycrystalline structure with three characteristic peaks. h) The electrode/gap interface, probed by i) line scan atomic force microscopy (green arrow), reveals j) a ~250 nm thick polymer coating. k) Four-point probe carried out on a modified electrode (inset), aids in measuring electronic conductivity.

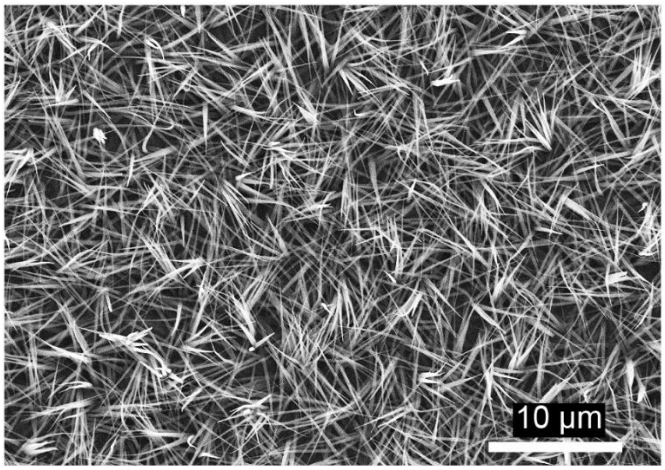

Figure 3.9: Close-up SEM image of a nanofibrillar PEDOT coating on a current collector.

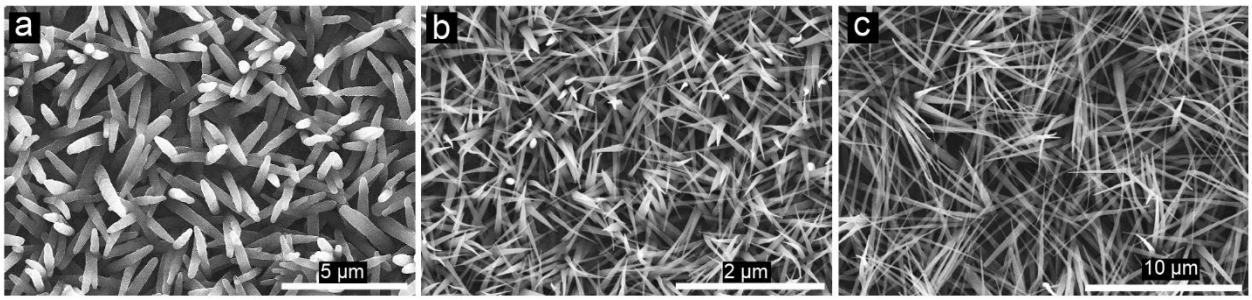

Figure 3.10: SEM images of PEDOT nanofibers synthesized on current collectors possessing aspect ratios of 10 nm (left), 30 nm (middle) and 100 nm (right).

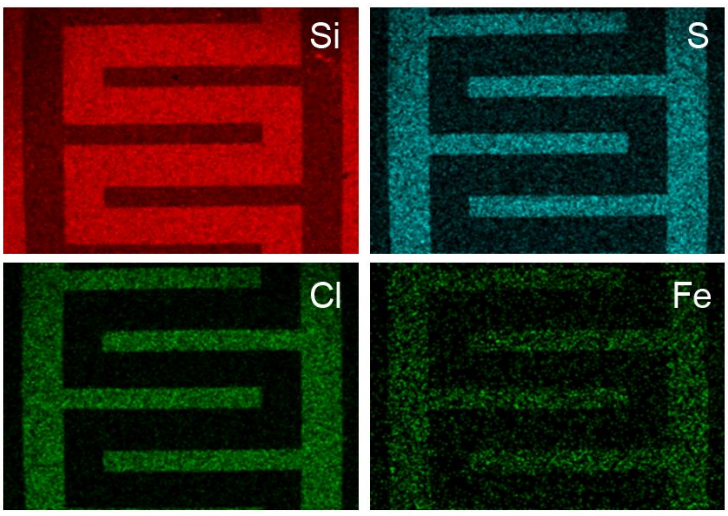

Figure 3.11: Images of EDX maps for a micro-supercapacitor collected after synthesis. Note that purification of polymer was omitted as indicated by iron signal.

Electronic charge transport, plotted by applying a potential and measuring current (Figure 3.8f inset), shows that a PEDOT coating is characterized by ohmic behavior (straight line), low resistance (large slope) (Figure 3.8f) and a small Schottky barrier that facilitates charge transport.[16] We designed a gold micro-electrode using photolithography that possesses identical configuration to our interdigitated micro-supercapacitor electrodes and was connected directly with four (0.8 mm × 0.8 mm) gold pad that fit of four-point-probe station's needles (Figure 3.12). More than 20 devices were fabricated and measured for I-V curve and conductivity measurements.

The line slope decreases linearly and inversely proportional with probe distance because the polymer coating is a homogeneous and continuous percolation network. To probe charge transport as a function of PEDOT's polycrystalline structure, powder X-ray diffraction (Figure 3.8g) is carried out revealing three characteristic peaks at 6.4°, 12.1° and 25.8° corresponding to lateral chain packing of (100), (200) and π- π stacking of (020), respectively. Peaks' widths at half-heights are 0.43, 0.79 and 1.38; these small values indicate a crystalline polymer structure that enhances charge transport.[28] A four-point probe conductivity measurement (Figure 3.8h-k), carried out using a collinear configuration (Figure 3.8k inset), demonstrates an exceedingly high conductivity of 3580 S cm^{-1} stemming both from PEDOT's ordered structure and homogeneous deposition.

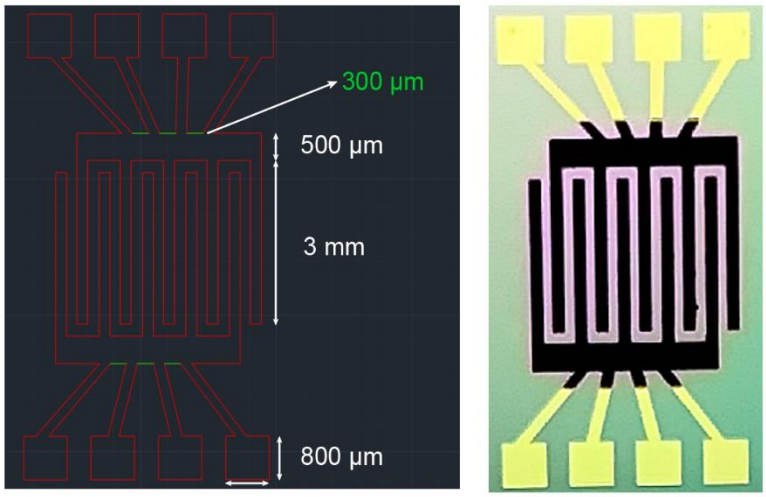

Figure 3.12: AutoCad file (left) and optical photograph (right) of electrode configuration utilized for carrying out I-V and conductivity measurements.

A PEDOT µSC (Figure 3.13a inset) is tested using 1 M H_2SO_4 electrolyte (Figure 3.14) by collecting cyclic voltammograms (CVs) with potential windows of 0.6, 0.8 and 1 V (Figure 3.13a). Single-sided sticky Kapton tape is ideal for connecting potentiostat/galvanostat platinum leads to our device's gold pads; electrical connections are pressed together by hand and remained stable for months and characterized by mechanical robustness (Figure 3.14). Note that soldering leads to the gold pads led to deterioration of the metal layer. These curves exhibit a symmetric rectangular shape due to reversible doping and dedoping during charging and discharging. Free movement of electrolyte ions is facilitated by the ordered nanofibrillar electrode architecture resulting in rectangular CVs under scan rates spanning 1 V/s to 50 V/s throughout 500 cycles (Figure 3.13b). To identify charge transfer and ion diffusion processes, a µSC is cycled 500 times at scan rates of 25 mV s^{-1} and 50 V s^{-1} enabling electrochemical impedance spectroscopy (EIS) studies. Nyquist plots of real impedance Z' (x-axis) versus imaginary impedance -Z" (y-axis) show similar equivalent series resistances (ESR) (x-axis intercept) and capacitive behavior (vertical line), regardless of scan rate (Figure 3.13c). The high rate capability of our µSCs stems from strong

mechanical adhesion between PEDOT and current collector enabling facile electron transfer.[37] The absence of a semicircle at high frequency in Figure 3.13c indicates a low charge transfer resistance as electrolyte readily accesses a nanofibrillar electrode.[21, 38]

Electrode thickness versus electrochemical performance is investigated by developing various PEDOT coatings. Nanofibrillar PEDOT coatings of 250 nm, 500 nm and 900 nm are synthesized from sputtered Fe_2O_3 layers of 60 μm, 120 μm and 180 μm, respectively (Figure 3.15, 3.16). These electrodes lead to areal capacitances of 10.08 mF cm^{-2}, 14.6 mF cm^{-2} and 21.3 mF cm^{-2}, respectively, calculated from galvanostatic charge-discharge (GCD) measurements at a current density of 100 μA cm^{-2} (Figure 3.17). Areal capacitance increases with polymer coating thickness, whereas volumetric capacitance decreases because of limited contact between electrolyte and active electrode surface area.[7] This is shown by an increasing electrolyte resistance (IR drop) and decreasing coulombic efficiency of 99.5%, 97.6% and 94.8% (Figure 3.13d). Notably, a 900 nm thick electrode is well adhered to the current collector and characterized by an areal capacitance of 21.3 mF cm^{-2}, while a thick polymer coating (1 m) exhibits poor adhesion and peels-off during sonication. An electrode thickness of 250 nm leads to a volumetric capacitance of 400 F cm^{-3}. These figures of merit are the highest values among all reported conducting polymer-based μSCs.[2, 8] Cycling stability is evaluated via continuous charging and discharging cycles, at a current density of 100 μA cm^{-2}, demonstrating 90% capacitance retention after 10,000 cycles for all devices regardless of thickness (Figure 3.13e).

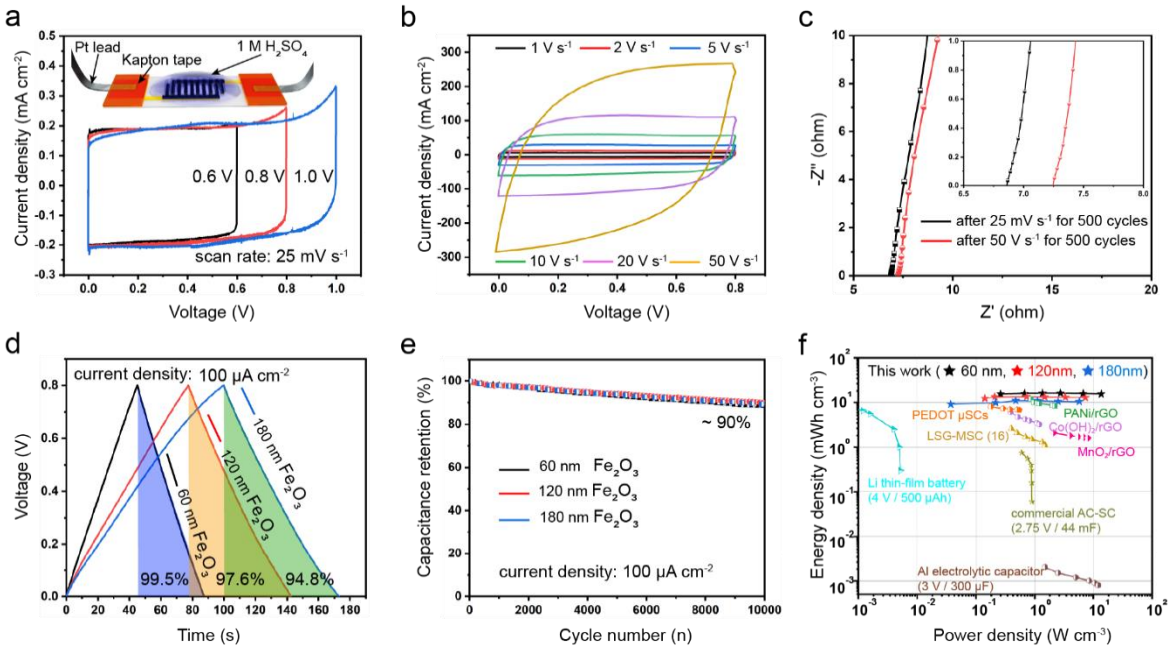

Figure 3.13: Electrochemical performance of nanofibrillar PEDOT µSCs in 1 M H_2SO_4 aqueous electrolyte. a) Cyclic voltammograms, collected at a scan rate of 25 mV s^{-1} and under various voltage windows, show stable capacitive behavior and retain b) a rectangular shape under fast scan rates ranging from 1 to 50 V s^{-1}. c) Nyquist plots show stable ESR and similar capacitive behavior using scan rates of 25 mV s^{-1} and 50 V s^{-1} after 500 cycles. d) Galvanic charge-discharge curves, collected at a current density of 100 µA cm^{-2}, for electrodes generated from 60 nm, 120 nm and 180 nm thick Fe_2O_3 layers show e) a 90% capacitance retention after 10,000 cycles. f) Volumetrically normalized Ragone plot compares our µSCs with 2D lithium film battery, Al electrolytic capacitor, activated carbon commercial supercapacitor as well as 2D PEDOT, PANi/rGO, $Co(OH)_3$/rGO and MnO_2/rGO based micro-supercapacitors.

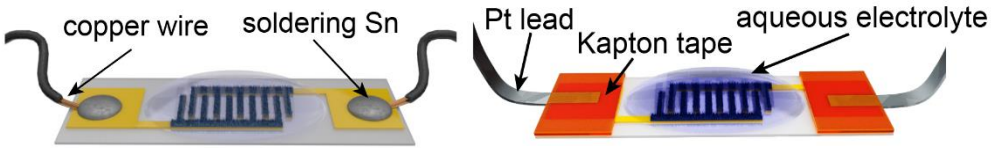

Figure 3.14: Schematic illustrations of two micro-supercapacitor configurations. Left diagram shows copper wires soldered on Au pads for connecting external circuit. Right diagram shows platinum leads stuck on Au pads via adhesive Kapton tape.

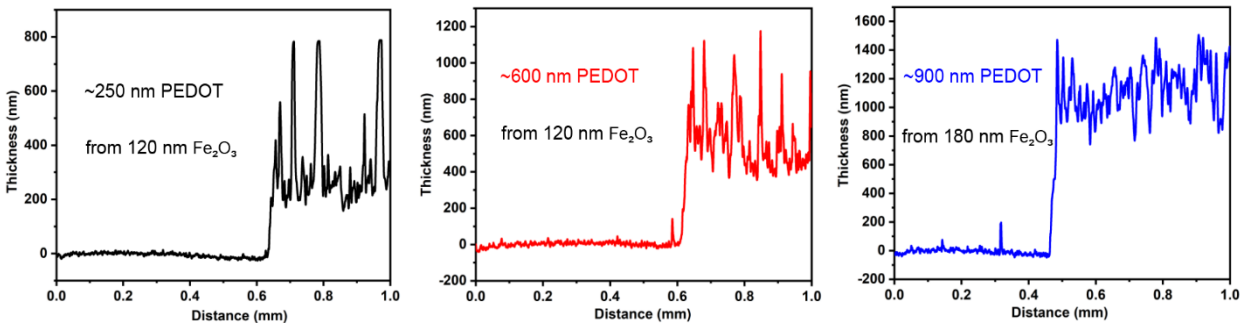

Figure 3.15: Profilometry data for 250 µm (left), 600 µm (middle), and 900 µm (right) thick nanofibrillar PEDOT films generated from 60 nm, 120 nm, and 180 nm thick Fe2O3 layers, respectively.

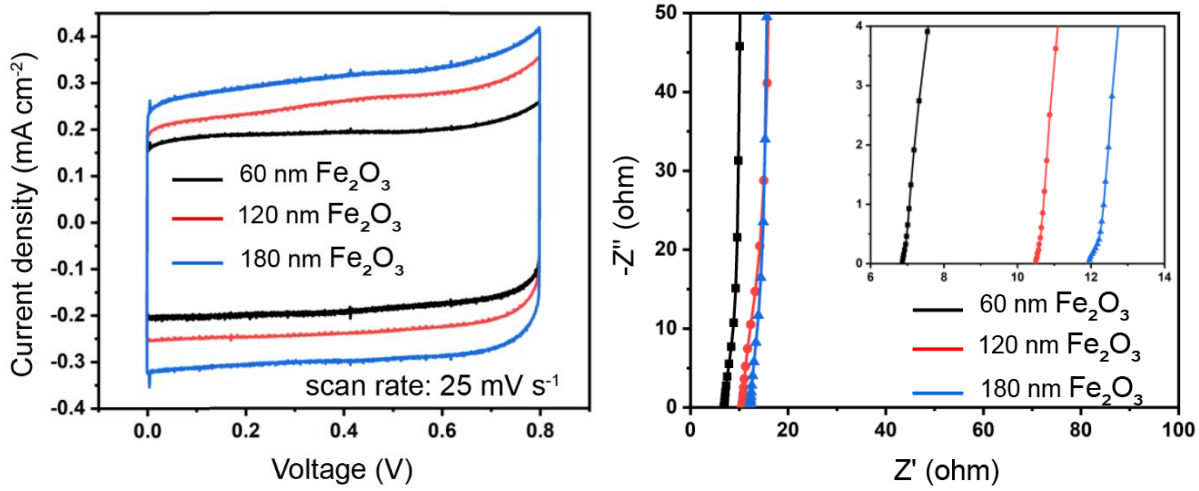

Figure 3.16: Cyclic voltammograms and Nyquist plots for polymer coatings generated from 60 nm, 120 nm and 180 nm thick Fe_2O_3 layers.

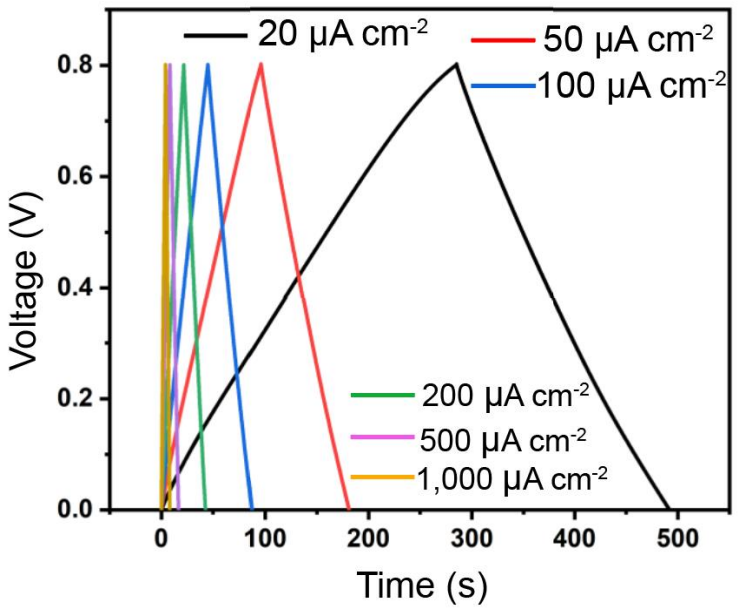

Figure 3.17: Galvanostatic charge and discharge curves for a polymer coating generated using a 60 nm Fe_2O_3 layer – data is collected under different current densities ranging from 20 μA cm^{-2} to 1,000 μA cm^{-2}.

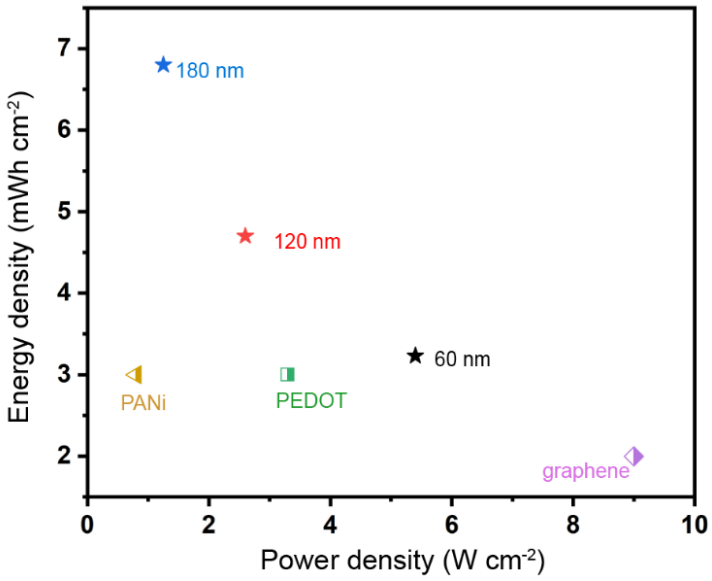

Figure 3.18: Ragone Plot for a PEDOT μSC normalized by area.

A Ragone plot representing the relationship between power density and energy density enables evaluation of energy storage metrics after normalizing figures of merit by volume or area.[39] A 200 nm gap device coated by polymer (250 nm) exhibits a volumetric energy density of 16.1 mWh cm^{-3}, and by increasing coating thickness (900 nm), an areal energy density of 1.9 mWh cm^{-2} is achieved. These values represent the highest performance for conducting polymer-based μSCs surpassing Li-thin film battery metrics (Figure 3.13f and Figure 3.18).[5,15,20,21,40]

Typically, decreasing the gap distance between electrodes results in lower ion diffusion resistance and higher capacitance due to shorter ion diffusion pathways.[38] To evaluate the effect of gap distance we fabricate devices from a 60 nm Fe_2O_3 coating using 200 μm or 500 μm gaps (Figure 3.19a). A device with shorter gap exhibits lower ESR and a more capacitive behavior as demonstrated by a vertical line in Nyquist plots (Figure 3.19b) resulting in a 30% capacitance increase as calculated from CVs (Figure 3.19c). Note that engineering a 100 μm gap is challenging because polymer coating at the gap/electrode interface limits contact between photoresist and lift-off solution (Figure 3.19-3.21).

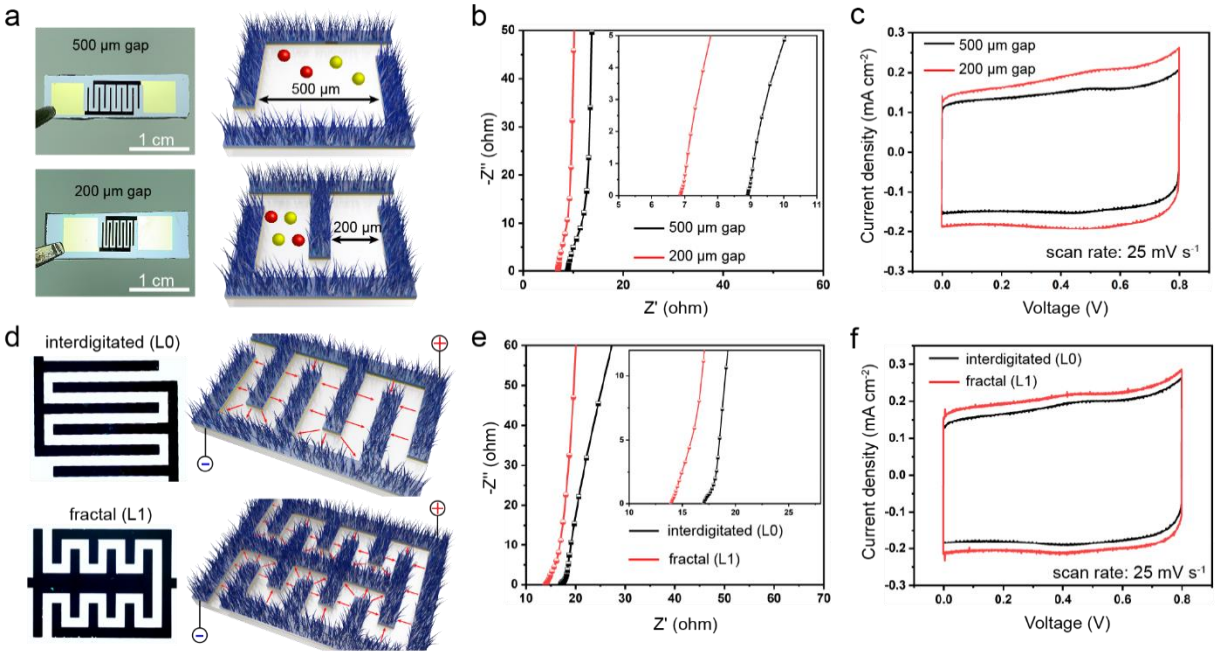

Figure 3.19: Electrochemical performance of PEDOT µSCs, generated from a 60 nm Fe_2O_3 layer, and fabricated with various gap distances and fractal geometries using 1 M H_2SO_4 aqueous electrolyte. a) Photograph and illustrations of Microsupercapacitors with gap distances of 500 µm and 200 µm. b) A Nyquist plot for the 200 µm gap device shows lower impedance and c) its cyclic voltammogram shows higher capacitance. d) Schematic representations of interdigitated (L0) and fractal electrodes (L1) possessing a 200 µm gap. A fractal electrode augments ion diffusion pathways thereby lowering impedance in e) a Nyquist plot and increasing capacitance in f) a CV.

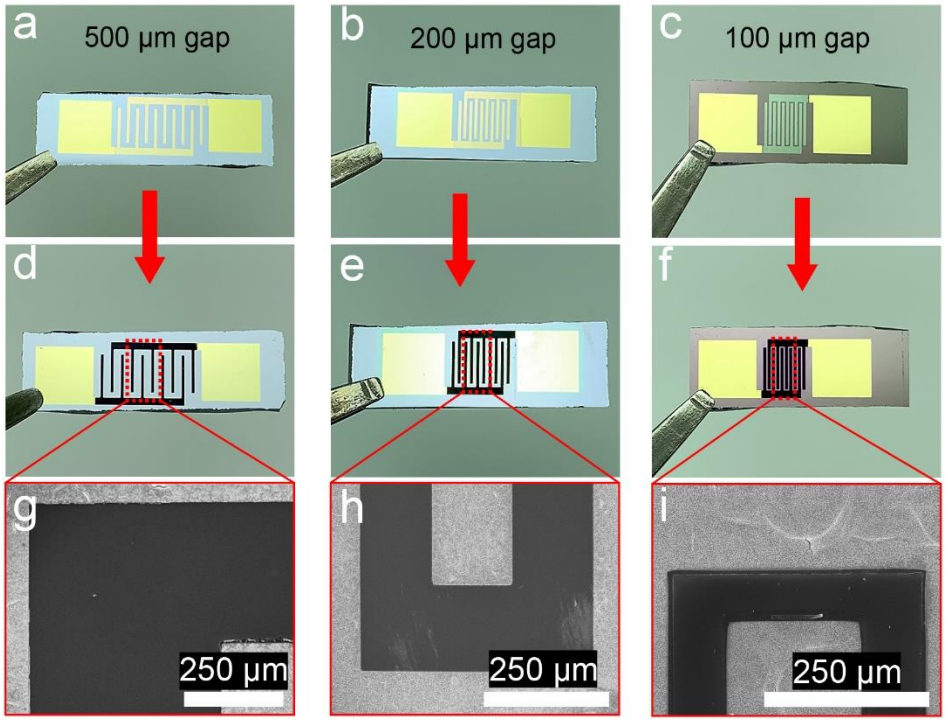

Figure 3.20: Optical images for devices generated from a 60 nm thick Fe_2O_3 layer and with gap distances of 500 µm (a), 200 µm (b), and 100 µm (c). These same devices are then coated with PEDOT nanofibers (d-f) and their corresponding clean gaps (void of polymer) are shown in SEM images (g-i).

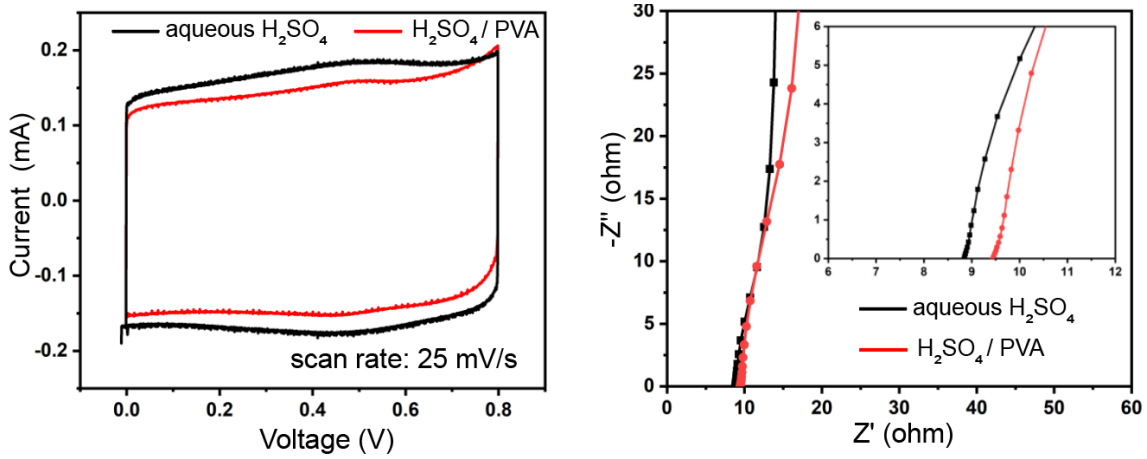

Figure 3.21: Comparison of cyclic voltammograms (left) and Nyquist plots (right) for liquid and quasi-solid-state devices both possessing a 500 µm gap distance.

Fractal electrodes are predicted to enhance electrochemical performance of devices because they maximize 2D active surface area and ion diffusion pathways.[41,42] Here, we demonstrate, for the first time, the effect of a fractal geometry in a 3D μSC architecture by designing interdigitated (L0) and fractal (L1) nanofibrillar PEDOT electrodes (Figure 3.19d). These devices, possessing a 200 μm gap, and generated from a 60 nm Fe_2O_3 layer are characterized by ESRs of ~17 Ω and ~13 Ω, respectively (Figure 3.19e). Unlike 2D electrodes, where ESR increases with complexity in electrode geometry, L1 possesses lower ESR than L0 due to its vertically directed nanofibrillar structure providing accessible ion pathways and resulting in a 10% capacitance increase (Figure 3.19f and Figure 3.22). Our results highlight the synergistic convergence between fractal geometry and a 3D nanofibrillar electrode architecture, demonstrating low impedance, high capacitance and a cost-effective fabrication strategy.

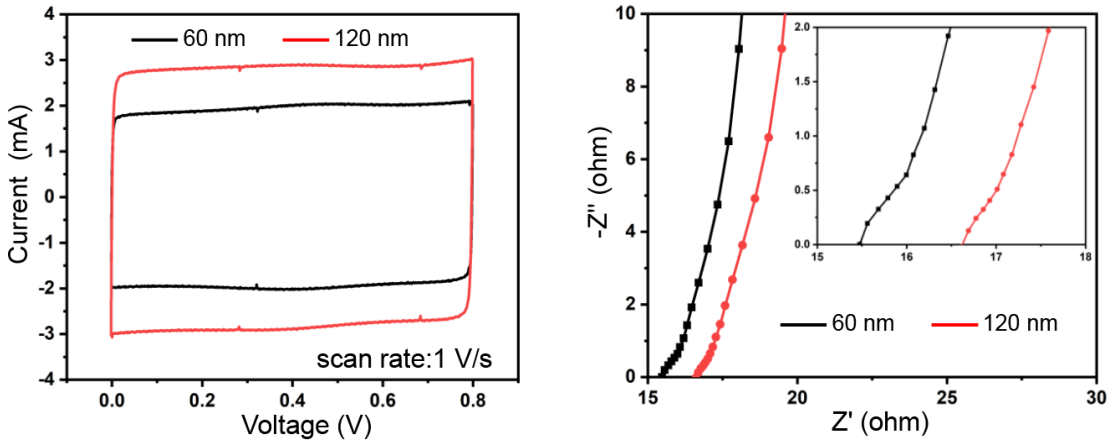

Figure 3.22: Comparison of cyclic voltammograms (left) and Nyquist plots (right) for devices possessing fractal electrodes; polymer coatings were generated from 60 nm and 120 nm thick Fe_2O_3 layers.

Minimization of electrolyte leakage is of paramount importance for developing stable μSCs and is achieved using a gel electrolyte comprised of a viscous hydrated polymer matrix carrying free ions.[39] Micro-supercapacitors, characterized by a 200 μm gap and 1 M H_2SO_4/polyvinyl alcohol (PVA) gel electrolyte (Figure 3.23a inset), exhibit symmetric rectangular CVs due to facile charge transfer processes (Figure 3.23a). Nyquist plots, however, show higher ESR and deviation from capacitive behavior (smaller slope inclination) (Figure 3.23b) due to the electrolyte's high viscosity that stifles ion diffusion.[16] To evaluate the power performance of our quasi-solid-state devices, their frequency response is represented by a Bode plot (Figure 3.23b inset) and analyzed via phase angle and relaxation time studies. Frequency response is evaluated by Bode plot and shows the relationship between phase angle and frequency. As phase angle approaches 90°, the mechanism of energy charge storage is more capacitive because electric double layer capacitance contributions become more significant. The higher phase angle for a liquid electrolyte (82°) versus a gel electrolyte (76°) demonstrates a lower impedance. Further evaluation of frequency response is carried out by comparing the frequency at a phase angle of 45°, also known as the characteristic frequency (f_0), with a relaxation time constant ($\tau_0 = 1/f_0$). The relaxation response time for liquid electrolytes (7 ms) is shorter than for gel electrolytes (11 ms).[37,39,43,44] Our device exhibits 2-4 times faster relaxation time (11 ms) than current state-of-the-art μSCs with a phase angle of 76°.[21] This excellent power performance stems from an extended ordered nanofibrillar surface area as well as low electronic and ionic resistances resulting in a scan rate capability of 50 V s^{-1}. Quasi-solid-state μSCs retain 94% of original capacitance after 10,000 cycles whereas liquid water-based devices retain 90% (Figure 3.23c); a gel electrolyte prevents leakage thus enhancing cycling stability.

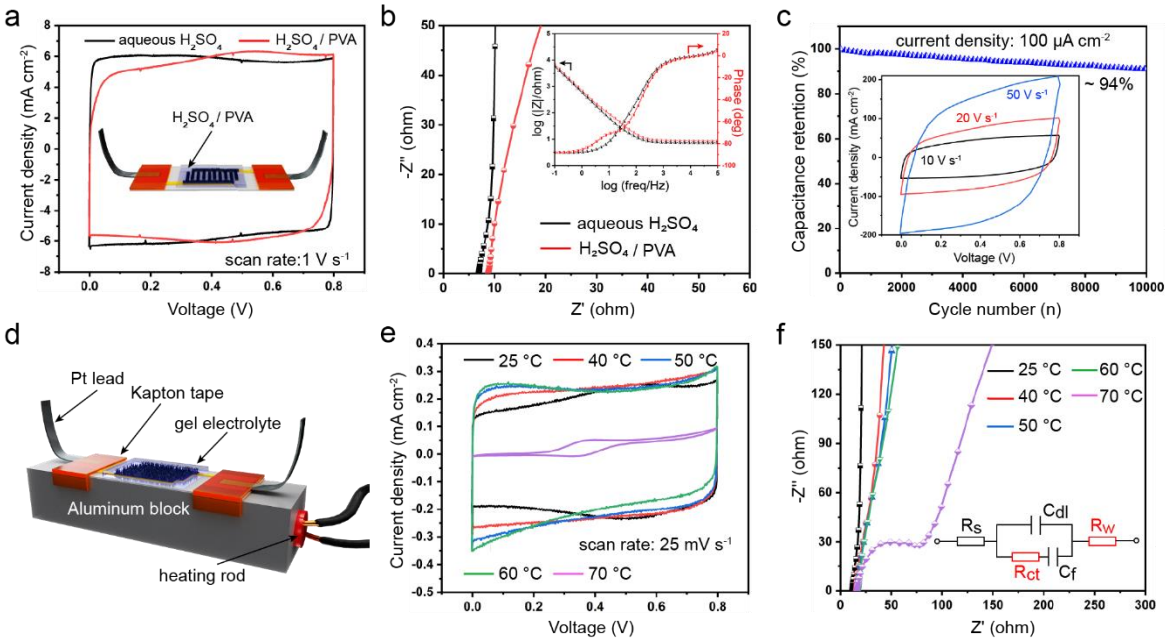

Figure 3.23: Electrochemical performance of quasi-solid-state μSCs in 1 M H_2SO_4/PVA gel electrolyte and its temperature-dependent behavior. a) Cyclic voltammograms compare aqueous and gel electrolytes at a scan rate of 1 V s^{-1}. b) Nyquist plot for aqueous electrolyte exhibits lower impedance and more ideal capacitive behavior versus gel electrolyte; this is also confirmed via Bode plots (inset). c) After 10,000 cycles with a gel electrolyte, 94% of original capacitance is retained and rectangular-shaped cyclic voltammograms are obtained at scan rates of 10 V s^{-1}, 20 V s^{-1} and 50 V s^{-1}. d) Schematic illustration of experimental setup for studying temperature. e) Cyclic voltammograms of a quasi-solid-state μSC show increasing capacitance as temperature rises from 25 °C to 60 °C; note that at 70 °C, capacitance is restricted. f) Nyquist plots exhibit similar ESR between 25 °C – 60 °C, however, as temperature increases, capacitive behavior diminishes resulting in resistive charge transfer (semi-circle) and Warburg impedance as temperature approaches 70 °C.

High-temperature stability is crucial for micro-devices since heat, inevitably generated during energy consumption, imposes thermal stress that leads to current leakage and decreases a device's lifespan.[45] Therefore, the effect of high temperature on quasi-solid-state μSCs is studied and Figure 3.23d shows the experimental setup consisting of a heated aluminum block. We use a large aluminum block to heat our devices using a heating cartridge, thermocouple and PID controller. Through-plane thermal conduction in silicon wafers is excellent thus enabling us to dynamically monitor the effects of temperature on the performance of our devices. The curve area for cyclic

voltammograms expands proportionally as temperature rises from 25 °C to 60 °C and contracts drastically at 70 °C (Figure 3.23e). At the latter temperature, charge storage decline stems from rapid electrolyte evaporation significantly increasing charge transfer resistance as detected by the appearance of a semi-circle and a 45° line (Warburg impedance) in Nyquist plots (Figure 3.23f).[46] Fortunately, chemically and physically stable nanofibrillar PEDOT coatings result in enhanced ion mobilities that boost capacitance in our devices by ~8% at 40 °C, ~10% at 50 °C and ~12% at 60 °C.[35]

3.4 Conclusion

In summary, we demonstrate the integration of chemical synthesis with conventional micro-fabrication producing a streamlined, superior and low-cost electrode engineering strategy for 3D nanofibrillar PEDOT μSCs. This technology leads to 250-nm thick coatings of 3D vertically directed capacitive conducting polymer nanofibers characterized by an electronic conductivity of 3580 S cm $^{-1}$. Our nanofibrillar PEDOT μSCs exhibit areal and volumetric capacitances of 21.3 mF cm^{-2} and 400 F cm^{-3}, respectively, and possess a state-of-the-art energy density of 16.1 mWh cm^{-3} in 1 M H_2SO_4 aqueous electrolyte. Quasi-solid-state μSCs retain 94% of their original capacitance after 10,000 cycles exhibiting high scan rate capability at 50 V s^{-1} and thermostability at 60 °C in 1 M H_2SO_4/PVA gel electrolyte. This work advances electrode characterization in situ and explores electrode thickness, gap distance and fractal geometry to control electrochemical performance. Nanofibrillar PEDOT μSCs are produced using a cost-effective and superior electrode engineering platform enabling in situ deposition of a 3D architecture bridging the energy density gap between micro-batteries and conventional micro-supercapacitors for miniaturized portable electronics.

References

(1) C. Meng, J. Maeng, S. W. M. John, P. P. Irazoqui, Adv. Energy Mater. 2013, 4, 1301269.

(2) N. A. Kyeremateng, T. Brousse, D. Pech, Nat. Nanotechnol. 2016, 12, 7.

(3) Y.-Y. Peng, B. Akuzum, N. Kurra, M.-Q. Zhao, M. Alhabeb, B. Anasori, E. C. Kumbur, H. N. Alshareef, M.-D. Ger, Y. Gogotsi, Energy Environ. Sci. 2016, 9, 2847.

(4) J. Chmiola, C. Largeot, P. L. Taberna, P. Simon, Y. Gogotsi, Science 2010, 328, 480.

(5) M. F. El-Kady, R. B. Kaner, Nat. Commun. 2013, 4, DOI 10.1038/ncomms2446.

(6) H. Zhang, Y. Cao, M. O. L. Chee, P. Dong, M. Ye, J. Shen, Nanoscale 2019, 11, 5807.

(7) C. Lethien, J. L. Bideau, T. Brousse, Energy Environ. Sci. 2019, 12, 96.

(8) D. Qi, Y. Liu, Z. Liu, L. Zhang, X. Chen, Adv. Mater. 2016, 29, 1602802.

(9) D. Yu, K. Goh, H. Wang, L. Wei, W. Jiang, Q. Zhang, L. Dai, Y. Chen, Nat. Nanotechnol. 2014, 9, 555.

(10) C. Yan, X. Wang, M. Cui, J. Wang, W. Kang, C. Y. Foo, P. S. Lee, Adv. Energy Mater. 2013, 4, 1301396.

(11) D. Pech, M. Brunet, P.-L. Taberna, P. Simon, N. Fabre, F. Mesnilgrente, V. Conédéra, H. Durou, J. Power Sources 2010, 195, 1266.

(12) M. F. El-Kady, V. Strong, S. Dubin, R. B. Kaner, Science 2012, 335, 1326.

(13) X. Zang, C. Jian, T. Zhu, Z. Fan, W. Wang, M. Wei, B. Li, M. F. Diaz, P. Ashby, Z. Lu, Y. Chu, Z. Wang, X. Ding, Y. Xie, J. Chen, J. N. Hohman, M. Sanghadasa, J. C. Grossman, L. Lin, Nat. Commun. 2019, 10, DOI 10.1038/s41467-019-10999-z.

(14) X. Lang, A. Hirata, T. Fujita, M. Chen, Nat. Nanotechnol. 2011, 6, 232.

(15) D. Pech, M. Brunet, H. Durou, P. Huang, V. Mochalin, Y. Gogotsi, P.-L. Taberna, P. Simon, Nat. Nanotechnol. 2010, 5, 651.

(16) P. Huang, C. Lethien, S. Pinaud, K. Brousse, R. Laloo, V. Turq, M. Respaud, A. Demortiere, B. Daffos, P. L. Taberna, B. Chaudret, Y. Gogotsi, P. Simon, Simon, Science 2016, 351, 691.

(17) A. Ferris, S. Garbarino, D. Guay, D. Pech, Adv. Mater. 2015, 27, 6625.

(18) T. M. Dinh, K. Armstrong, D. Guay, D. Pech, J. Mater. Chem. A 2014, 2, 7170.

(19) N. Kurra, N. A. Alhebshi, H. N. Alshareef, Adv. Energy Mater. 2014, 5, 1401303.

(20) N. Kurra, Q. Jiang, H. Alshareef, Nano Energy 2015, 16, 1.

(21) N. Kurra, M. Hota, H. Alshareef, Nano Energy 2015, 13, 500.

(22) X. Wang, A. Sumboja, W. L. Foo, C. Y. Yan, K. Tsukagoshi, P. S. Lee, RSC Adv. 2013, 3, 15827.

(23) D. Aradilla, D. Gaboriau, G. Bidan, P. Gentile, M. Boniface, D. Dubal, P. Gómez-Romero, J. Wimberg, T. J. S. Schubert, S. Sadki, J. Mater. Chem. A 2015, 3, 13978.

(24) J. Zang, S.-J. Bao, C. M. Li, H. Bian, X. Cui, Q. Bao, C. Q. Sun, J. Guo, K. Lian, J. Mater. Chem. C 2008, 112, 14843.

(25) D. Aradilla, F. Gao, G. Lewes-Malandrakis, W. Müller-Sebert, P. Gentile, M. Boniface, D. Aldakov, B. Iliev, T. J. S. Schubert, C. E. Nebel, G. Bidan, ACS Appl. Mater. Interfaces 2016, 8, 18069.

(26) L. Zhang, W. Viola, T. L. Andrew, ACS Appl. Mater. Interfaces 2018, 10, 36834.

(27) D. Aradilla, G. Bidan, P. Gentile, P. Weathers, F. Thissandier, V. Ruiz, P. Gómez-Romero, T. J. S. Schubert, H. Sahin, S. Sadki, RSC Adv. 2014, 4, 26462.

(28) B. Cho, K. S. Park, J. Baek, H. S. Oh, Y.-E. K. Lee, M. M. Sung, Nano Lett. 2014, 14, 3321.

(29) J. M. D'Arcy, M. F. El-Kady, P. P. Khine, L. Zhang, S. H. Lee, N. R. Davis, D. S. Liu,

M. T. Yeung, S. Y. Kim, C. L. Turner, A. T. Lech, P. T. Hammond, R. B. Kaner, ACS Nano 2014, 8, 1500.

(30) J. Huang, K. Wang, Z. Wei, J. Mater. Chem. 2010, 20, 1117.

(31) H. Wang, Y. Diao, M. Rubin, L. M. Santino, Y. Lu, J. M. D'Arcy, ACS Appl. Nano Mater 2018, 1, 1219.

(32) M. Beidaghi, C. Wang, Electrochim. Acta. 2011, 56, 9508.

(33) L. Zhang, T. L. Andrew, Adv. Mater. Interfaces 2017, 4, 1700873.

(34) C. J. Zhang, M. P. Kremer, A. Seral-Ascaso, S.-H. Park, N. Mcevoy, B. Anasori, Y. Gogotsi, V. Nicolosi, Adv. Funct. Mater. 2018, 28, 1870059.

(35) Y. Diao, H. Chen, Y. Lu, L. M. Santino, H. Wang, J. M. D'Arcy, ACS Appl. Energy Mater. 2019, 2, 3435.

(36) A. Ugur, F. Katmis, M. Li, L. Wu, Y. Zhu, K. K. Varanasi, K. K. Gleason, Adv. Mater. 2015, 27, 4604.

(37) T. Purkait, G. Singh, D. Kumar, M. Singh, R. S. Dey, Sci. Rep. 2018, 8, DOI 10.1038/s41598-017-18593-3.

(38) Q. Jiang, N. Kurra, H. N. Alshareef, Adv. Funct. Mater. 2015, 25, 5076.

(39) Y. Shao, J. Li, Y. Li, H. Wang, Q. Zhang, R. B. Kaner, Mater. Horiz. 2017, 4, 1145.

(40) M. F. El-Kady, V. Strong, S. Dubin, R. B. Kaner, Science 2012, 335, 1326.

(41) M. K. Hota, Q. Jiang, Y. Mashraei, K. N. Salama, H. N. Alshareef, Adv. Electron. Mater. 2017, 3, 1700185.

(42) K.-H. Huang, C.-T. Lin, Y.-T. Chen, Y.-J. J. Yang, J. Appl. Phys. 2019, 125, 014902.

(43) M. Ganji, A. T. Elthakeb, A. Tanaka, V. Gilja, E. Halgren, S. A. Dayeh, Adv. Funct. Mater. 2017, 27, 1703018.

(44) W. Si, C. Yan, Y. Chen, S. Oswald, L. Han, O. G. Schmidt, Energy Environ. Sci. 2013, 6, 3218.

(45) P. Zhang, J. Wang, W. Sheng, F. Wang, J. Zhang, F. Zhu, X. Zhuang, R. Jordan, O. G. Schmidt, X. Feng, Energy Environ. Sci. 2018, 11, 1717.

(46) Y. Ge, R. Jalili, C. Wang, T. Zheng, Y. Chao, G. G. Wallace, Electrochim. Acta. 2017, 235, 348.

Chapter 4

Kirigami Electrodes of Conducting Polymer Nanofibers for Wearable Humidity Dosimeters and Stretchable Supercapacitors

4.1 Introduction

Wearable healthcare monitors and stretchable power sources are emerging as hotspots in scientific research and engineering innovations due to their expansive applications in medical science and smart electronics.[1-5] Kirigami, the art of paper cutting, is an emerging approach to constructing stretchable 3D architectures out of simply cutting planar sheets. Under external strain, cuts made in thin films undergo in-plane rotation and out-of-plane buckling leading to expanded 3D structures.[6-7] Combining Kirigami with electrode material deposition enables simultaneous achievement of macroscopic robustness, mechanical strength, and high stretchability alongside high electronic performance.[2, 8] These properties are ideally suited to a variety of flexible devices including chemoresistive sensors and supercapacitors. However, these thin film electrodes suffer from limited surface area and are characterized by poor sensitivity and low energy density. The field of Kirigami is consequently experiencing a lack of applications in healthcare-sensing devices and power sources.

Nanofibrillar electrode material deposition offers a promising solution to current challenges in Kirigami thin film-based electrodes. Conducting polymer nanofibers such as poly(3,4-ethylenedioxythiophene) PEDOT,[9] polypyrrole (PPy)[10] and polyaniline (PANi)[11] afford continuous conductive networks for fast electron transfer and a large active surface area. These polymers are highly flexible due to conjugated π-bonding networks and a lack of rigid lattice structures, allowing polymer chains to slide against one another and minimize energy under macroscopic bending forces.[12] However, existing deposition approaches such as solution processing and electrochemistry are incompatible with Kirigami because 1) pre-cut substrates are irregular and impede nanofiber deposition resulting in heterogeneous coatings and 2) laser cutters damage pre-deposited nanofibers.[13-14] Moreover, the low packing density, low yield, and low quantities of nanofibers produced using current established synthetic protocols lead to poor sensitivity and low energy density that hinders practical applications.[15] Given the numerous advantages that Kirigami offers, this gap in the field highlights the necessity for a new synthetic strategy capable of integrating nanofibrillar electrodes and high electroactive performance with stretching, bending and twisting.

Here, we demonstrate precise control over deposition of conducting polymer nanofibers on pre-patterned substrates for humidity dosimeters and supercapacitors via our previously reported rust-assisted vapor-phase polymerization (RVPP).[9] Our electrode engineering protocol utilizes sputtered iron oxide (Fe_2O_3) as a solid-state oxidant-precursor to induce dissolution and hydrolysis of ferric ions (Fe^{3+}) while working in concert with oxidative radical polymerization. Our synthetic approach allows in-situ generation of homogeneous, high packing density coatings of nanofibers that facilitate charge transfer and ion adsorption on the electrode. Our nanofibrillar PEDOT humidity dosimeter exhibits significant sensitivity, showing a 40% resistance change within

seconds when exposed to a new humidity level under 200% stretch. We demonstrate that our humidity dosimeter is an ideal mask accessory for detecting the presence of droplets from coughs or sneezes. Our synthetic strategy affords multi-layer deposition for developing bilayered PPy/PEDOT nanofibrillar composite supercapacitors. This composite supercapacitor exhibits a synergistic effect that elicits a state-of-the-art energy density of 115 μWh/cm^2 at 1 mA/cm^2 and an extended stretched cycle capacitance stability (85% capacitance after 100% elongation over 300 cycles). Assembling the supercapacitor into a planar configuration enables it to light up LEDs at various open voltages and demonstrates its potential as a power supply for wearable electronics.

4.2 Experimental methods

Materials. Pyrrole, 3,4-ethylenedioxythiophene (EDOT, 97%), chlorobenzene (99%), sulfuric acid (98%), hydrochloric acid (37%), lithium perchloride (99.9%), acetonitrile (99.8%), ammonia hydroxide (25%) and hydrazine hydrate (50%) were purchased from Sigma Aldrich and used as received.

4.2.1 Deposition of nanofibrillar Kirigami electrodes

1) Kirigami cut slots were generated via CO_2 laser cutter following a pattern design created in AutoCAD. 2) A solid-oxidant precursor, Fe_2O_3, was sputter deposited over polyethylene terephthalate (PET) films via physical vapor deposition (Kurt J. Lesker PVD 75 RF and DC). 3) For single polymer electrodes, all syntheses were performed at 140 °C for 1.5 h in glass reactors, each containing a substrate, a reservoir for concentrated hydrochloric acid (HCl), and a reservoir for 0.674 M monomer (pyrrole or EDOT) chlorobenzene solution. Various volume combinations of liquid reactants were tested (10~200 μL HCl, 100~200 μL monomer solution) to achieve

conformal coating of polymer on the substrate and to gain optimal electrochemical performance. After 1.5 h, the electrodes were immediately removed from the reactors and cooled at room temperature and purified with 6 M HCl. 4) For PPy/PEDOT composite electrodes, another deposition of Fe2O3 was performed on the purified PEDOT electrodes. The same synthetic procedure was then performed again using concentrated HCl and pyrrole chlorobenzene solution. Composite electrode was purified with 6 M HCl to remove all Fe impurities.

4.2.2 Kirigami electrode characterizations

Scanning electron micrographs and energy-dispersive X-ray spectra were collected using a JEOL 7001LVF FE-SEM. Raman spectra were obtained using a Renishaw inVia confocal Raman spectrometer mounted on a Leica microscope with a 20× objective and 785 nm wavelength diode laser serving as an illumination source. A low power was necessary to mitigate heating of conducting polymer samples. Current-voltage (I-V) curves were obtained with a built-in-house 3D printed probe station using two gold needles 1.24 mm apart. Four-point probe sheet resistance measurements were carried out using a Keithley 2450 SourceMeter with a Signatone SP4 four-point probe head. Stress-strain curves were characterized via INSTRON 5583.

4.2.3 Preparation of gel electrolyte

A 1 M H_2SO_4 and $LiClO_4$ aqueous electrolyte required degassing of milli-Q water (18 MΩ) for 15 min. A 1 M $LiClO_4$/polyvinyl alcohol gel electrolyte was prepared by adding 1 g of concentrated $LiClO_4$ to 10 mL of deionized water, followed by addition of 1 g of polyvinyl alcohol powder. The whole mixture was heated to 85 °C while stirring until a clear solution was obtained.

4.2.4 Fabrication of PEDOT nanofibrillar Kirigami humidity dosimeter

Platinum foil leads were connected to PEDOT film using Kapton tape and attached onto the surgical mask via Scotch tape.

Humidity characterizations. PEDOT nanofibrillar film and PEDOT:PSS granular film were tested via a humidity chamber. Utilizing N_2 gas flow to decrease the humidity and water vapor to increase the humidity.

4.2.5 Fabrication of PPy/PEDOT nanofibrillar Kirigami supercapacitor

Platinum foil leads were connected to PPy/PEDOT film and 100 μL of a 1 M $LiClO_4$ gel electrolyte was added by drop-casting followed by drying at 55 °C / 2 h.

4.2.6 Electrochemical Characterizations

All electrochemical tests were performed on a BioLogic VMP3 multi-potentiostat and each data was selected after testing 5 devices. Cyclic voltammetry was carried out from 25 mV/s to 1000 mV/s between -0.2 V and 0.8 V. Electrochemical impedance spectroscopy was carried out at the electrode's open circuit potential after obtaining a reversible cyclic voltammogram. Impedance values were recorded using a 10 mV sinusoidal disturbance at frequencies ranging from 100 kHz to 100 MHz. After synthesis, the electrodes were soaked in 6 M HCl overnight to remove residual iron compounds from the reaction and then dried at 50 °C. For 3-electrode tests, various electrolytes (1 M H_2SO_4, 1 M $LiClO_4$) were tested against Ag/AgCl reference electrode at room temperature (25 °C). Galvanostatic charging/discharging (GCD) was carried out from 0.1 mA/cm^2 to 2mA/cm^2 between 0 – 1 V.

4.3 Results & discussion

A conformal nanofibrillar coating is produced by sputtering an oxidant precursor (Fe_2O_3) onto a laser cut polyethylene terephthalate (PET) film (Figure 4.1a). The uniformity of the solid-state precursor ensures homogenous polymer deposition and performing synthesis on a pre-cut substrate avoids polymer damage due to CO_2 laser heating. As previously reported, growth of PEDOT nanofibers is initiated by liberating Fe^{3+} ions from Fe_2O_3 via dissolution using HCl vapor at 140 °C (Figure 4.1bi).[9, 16] PEDOT nanofiber deposition stems from the preferential nucleation of monomer vapor on one-dimensional FeOOH spindles produced in situ during concomitant Fe^{3+} hydrolysis (Figure 4.1bii). Pyrrole has a similar oxidant potential which makes the synthesis of PPy nanofibers possible (Figure 4.1biii).[10] Scanning electron micrographs (SEM) in Figure 4.1c-d show homogeneous PEDOT (blue) and PPy (black) thin films with nanofibers growing up to an aspect ratio of 50. These nanofibers deposit with a high packing possessing a higher surface area than a granular film.

Although the polymerization mechanism between PEDOT and PPy is similar, the stoichiometry of acid required for obtaining nanofibrillar morphology varies. SEM images of PEDOT films only show nanofibrillar structures when a small volume of HCl (10-20 µL) is used during synthesis, as larger quantities of acid lead to the formation of ferrous chloride crystals and granular morphology of the polymer. This is because the excess HCl creates a more acidic environment inside the reactor, enhancing dissolution of iron oxides but suppressing the hydrolysis of Fe^{3+} ions as well as the formation and growth of FeOOH spindles. The consequent lack of nucleation sites and templates for PEDOT growth results in an undesirable granular morphology (Figure 4.2).

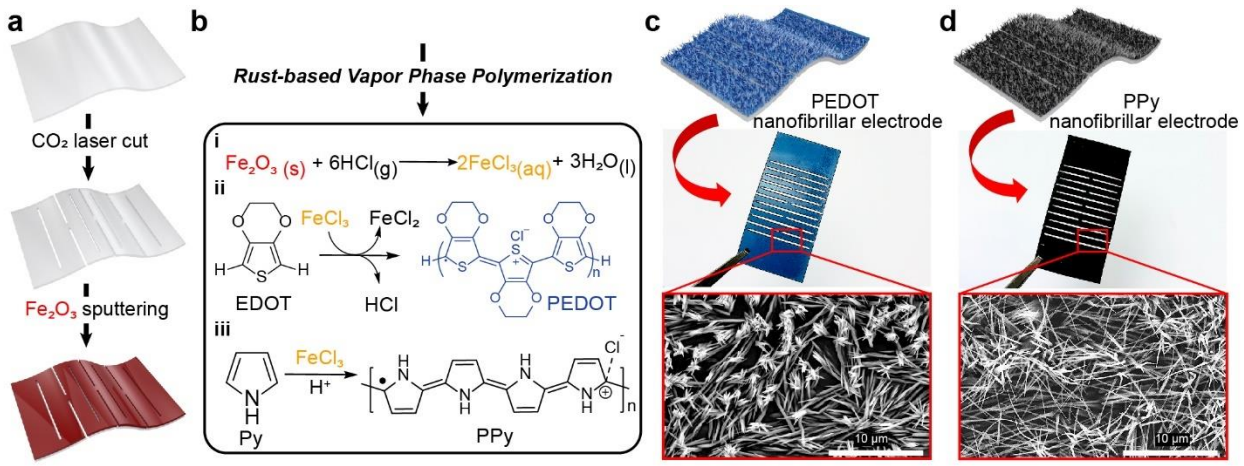

Figure 4.1: Schematic diagram shows deposition of conducting polymer nanofibrillar coatings on Kirigami sheets. a) PET sheet is laser cut and subsequently sputtered with a 60 nm Fe_2O_3 layer. b) Rust-based vapor phase polymerization results in PEDOT and PPy nanofibers by i) liberating Fe^{3+} from Fe_2O_3 thus triggering oxidative polymerization of ii) EDOT and iii) Py. The resulting nanofibrillar coatings are homogeneous as shown by c) blue PEDOT and (d) black PPy.

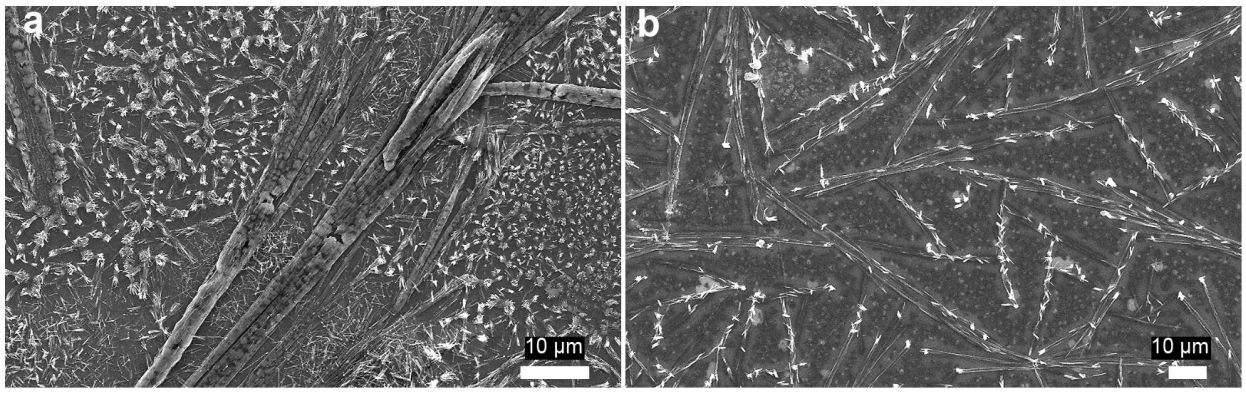

Figure 4.2: SEM images of ferrous chloride crystals and granular morphology of PEDOT.

In comparison, PPy synthesis requires much larger volumes of HCl (100-150 µL) to produce a nanofibrillar morphology. We propose that this phenomenon arises from the difference in polymerization mechanisms of PEDOT and PPy; although both polymers form via an oxidative radical polymerization mechanism, their initiation steps differ. Pyrrole molecules are more prone

to protonation due to the nitrogen atom in the heterocycle, and this initial protonation step facilitates the formation of a cationic radical (Figure 4.3), whereas EDOT is readily oxidized and forms cationic radicals without protonation.[17] Previous work also indicates that PPy synthesis requires the presence of a much higher concentration of Fe^{3+} ions than PEDOT synthesis.[10] Thus, to generate a nanofibrillar morphology during PPy synthesis, greater volumes of HCl are required to account for protonation as well as for the large amount of Fe^{3+} liberated by dissolution. Here, we develop PEDOT (~7 Ω, 15 µL-HCl) and PPy (~15 Ω, 120 µL-HCl) nanofibrillar films to serve as electrodes for further characterization and application.

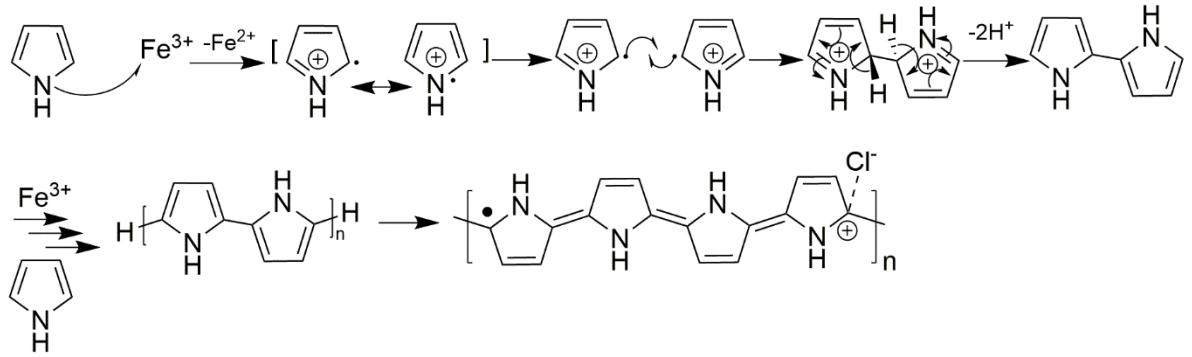

Figure 4.3: Step growth mechanism for PPy via oxidative radical polymerization.

Characterizing the intrinsic chemical properties of nanofibrillar conducting polymer electrodes is necessary to deepen understanding of their potential applications. Raman spectroscopy provides insight into the impact of doping on chemical bonding within our materials. Raman peaks of PEDOT (Figure 4.4a) at 1261 and 1357 cm^{-1} correspond to C_α-C_α, and C_β-C_β, bonds, respectively, while peaks at 1437 and 1510 cm^{-1} correspond to symmetric and asymmetric C_α=C_β stretching.[18] The symmetric C_α=C_β stretching band shifts towards 1426 cm^{-1} after doping with HCl vapor. This shift towards higher wavenumbers corresponds to greater doping levels due to an increased ratio

of quinoid vs. benzenoid structure in PEDOT, and is consistent with previously reported behavior of electrochemically synthesized PEDOT samples.[19-20] Similar information is derived from the Raman analysis of PPy that shows peaks at 1345 and 1573 cm^{-1} associated with C=C bonds at higher intensity (Figure 4.5). The behavior of the PEDOT and PPy samples indicates that Cl^- is an efficient dopant due to its small size and single negative charge as a counter anion.[21]

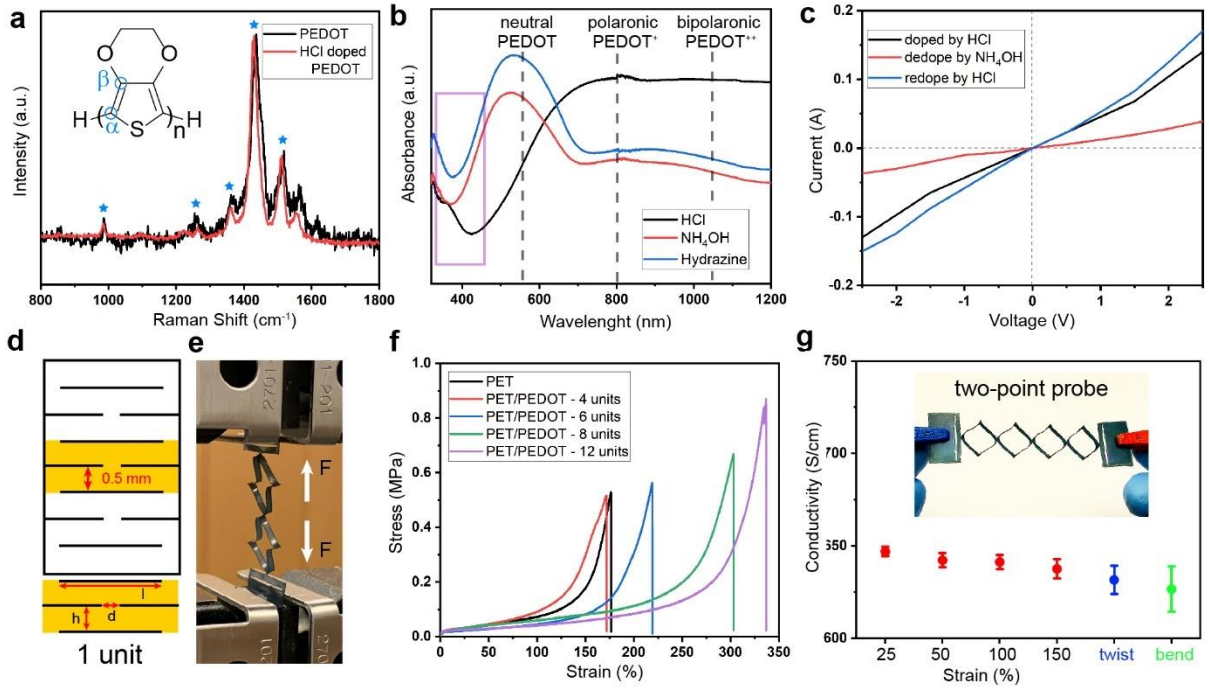

Figure 4.4: Spectroscopic and mechanical characterization of conducting polymer coatings. a) Raman spectra shows PEDOT's oxidized conjugated backbone. b) UV-vis spectra prove that both a reducing agent and base partially convert polaronic PEDOT to its neutral state. c) I-V curves for a PEDOT-coated substrate demonstrate ohmic behavior stemming from a homogenous percolation network. d) Schematic illustration of a Kirigami unit cell. e) Stress tests of PEDOT-coated Kirigami sheet yield f) stress-strain curves that show increasing elongation proportional with increasing unit cells. g) Electronic conductivity remains stable throughout the entire stretching process.

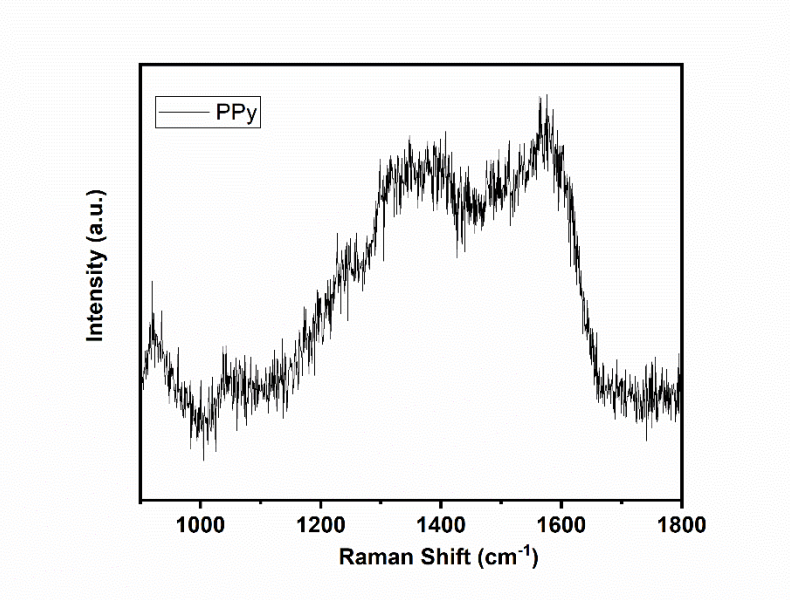

Figure 4.5: Raman spectra of the oxidized conjugated backbone of PPy.

Ultraviolet-Visible-near-IR spectroscopy (UV-Vis-NIR) is utilized to assess charge carrier density as a function of chemical structure and determine changes in molecular structure due to doping. The UV-Vis-NIR spectra of PEDOT (Figure 4.4b) is divided into three regimes: neutral, polaronic, and bipolaronic.[22] A larger absorbance in the polaronic and bipolaronic regimes for the HCl vapor-doped PEDOT sample vs. the ammonia hydroxide (NH_4OH) and hydrazine hydrate dedoped samples is observed because doping increases the charge carrier density of the polymer chain, resulting in enhanced conductivity. This behavior also emerges in the UV-Vis-NIR spectra of HCl vapor-doped PPy (Figure 4.6a).[23] Notably, this doping process is reversible and controlled by charge carrier concentration as evidenced by Figure 4.6b. Electronic charge transport of the PEDOT film is probed via I-V measurement showing ohmic behavior (straight line) and low resistance (large slope) (Figure 4.4c) signifying a homogeneous and continuous percolation network that facilitates charge transport.[24] The line slope decreases when the sample is de-doped

with NH_4OH due to the reduction of charge carriers thus showing reversibility that is consistent with UV-Vis spectra.

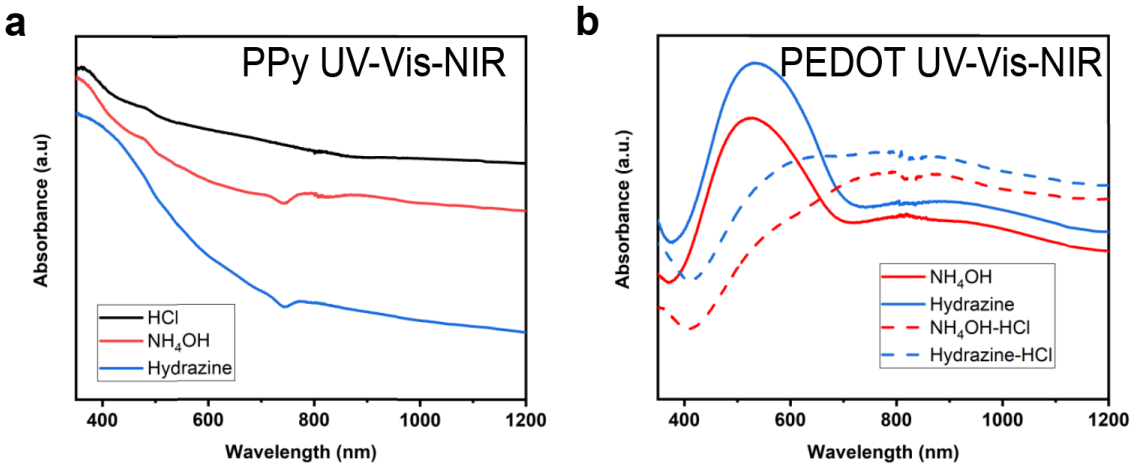

Figure 4.6: (a) UV-Vis-NIR spectra of PPy doped by HCl and dedoped by NH_4OH and hydrazine. (b) UV-Vis-NIR spectra of PEDOT dedoped by NH_4OH and hydrazine and subsequently re-doped by HCl.

The stretchable electrode is highly dependent on mechanical properties and strong adhesion between active material and substrate. Strain-stress and two/four-point probe measurements examine the relationship between mechanical deformation and conductivity. Kirigami is an engineering solution to a chemistry problem that overcomes the intrinsic stretch limits of conducting polymers by redirecting applied strain onto the substrate instead. We pattern unit cells with a cut geometry of length l (18 mm), horizontal spacing d (0.2 mm), and vertical spacing h (0.5 mm), enabling PET-based films to stretch up to 350% strain before rupturing (Figure 4.4d). As mechanical strain is first applied, the cuts open, enhancing the in-plane stretching capacity of the substrate. Additional strain causes the initial planar structure to deform and the unit cells begin bending out-of-plane to redistribute stress concentrations to the vertices of the cuts (Figure 4.4e).[25] This structural response allows the substrate to accommodate increased stretching and maintain

low stress growth by minimizing the strain felt by individual nanofibers. We conformally coat PET substrates with active materials to fabricate electrodes, establishing adhesion strength as a critical factor in the ability to withstand bending while retaining capacitance. Conducting polymers exhibit strong interfacial adhesion to the PET substrate due to covalent interactions. This is facilitated by Friedel-Crafts catalysts that covalently graft PEDOT onto aromatic polymer substrates.[26] Our synthesis utilizes this mechanism by providing reaction conditions that enable simultaneous formation of radical cations on monomer vapor and aromatic PET substrate using chlorobenzene carrier gas. Adhesion strength between PEDOT and PET is clearly demonstrated by bending, scotch tape and sonication tests (Figure 4.7) revealing minimal delamination of active material. In comparison, pristine PPy electrodes exhibit cracking and delamination when bent, revealing weaker adhesion with PET attributed to the lack of covalent interactions (Figure 4.8).[26]

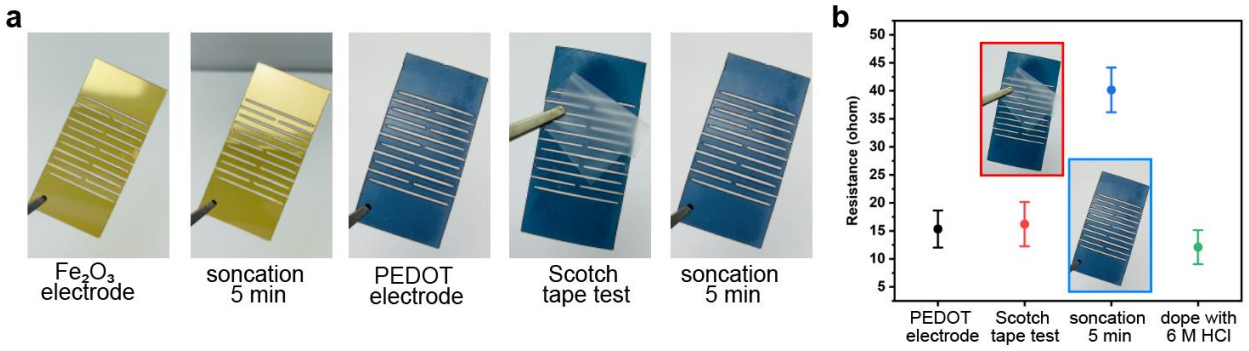

Figure 4.7: (a) Adhesion strength of PEDOT electrode demonstrated after sonication, scotch tape tests and via (b) resistance characterization.

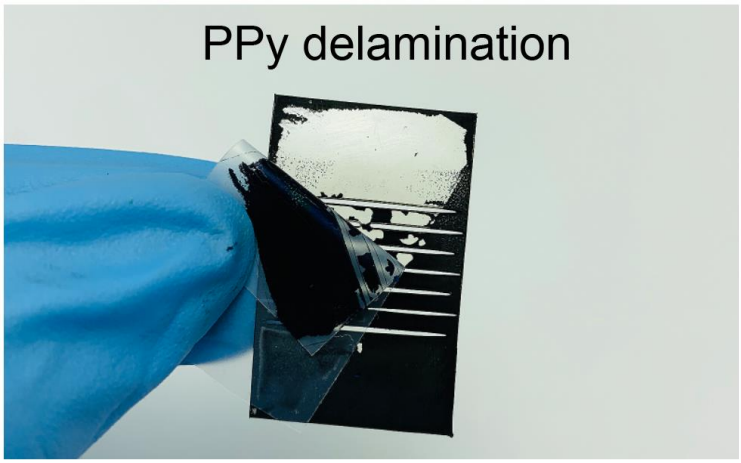

Figure 4.8: PPy film delaminate from Kirigami sheet.

Increasing the number of Kirigami unit cells (Figure 4.9) further extends the maximum elongation of the film. Additional unit cells can delay the point of fracture as demonstrated by the gradual decoupling of the stress-strain curves in Figure 4.4f. Similar curves obtained for PET and PEDOT/PET indicate that the PEDOT coating is strongly adhered while the mechanical properties for a substrate remain intact. Under increasing external strain, yielding initiates from the innermost cut and propagates outwards until the peripheral cuts reach their maximum stress load and the electrode ruptures.[27] Besides buffering the transmission of strain to outer regions of the film, extra unit cells also lessen the overall load felt by each cut, significantly enhancing the fracture strain.[4, 28] The nanofibrillar electrodes demonstrate excellent electrical stability stemming from their ability to withstand complex deformation without rupturing the conductive polymer layer. Conductivity-strain curves (Figure 4.4g) confirm that electrode conductivity is not significantly affected by increasing strain. Localization of strain on the corners of the cuts allows the substrate to stretch without disrupting the conductive nanofibrillar network.[29] Preservation of conducting pathways allows the electrode to retain a high degree of electrical conductivity (95%) under different mechanical tensile strains (0-150%). Other modes of mechanical deformation, such as bending

and twisting, exert low stress on the film allowing the structural and electrical properties of the active material layer to also remain unchanged.[30] These characterizations indicate that our synthetic strategy generates high packing density, highly conductive, stretchable nanofibrillar electrodes with great feasibility for sensing and energy storage applications.

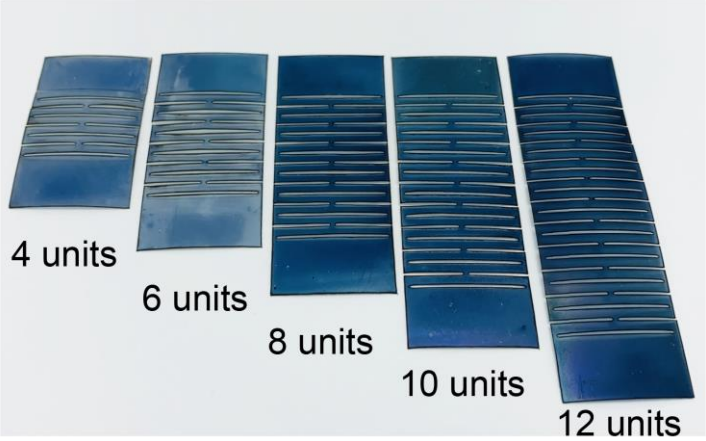

Figure 4.9: Nanofibrillar PEDOT Kirigami sheets with increasing number of unit cells.

The global outbreak of COVID-19 is significantly affecting economic and human health, and recent studies have demonstrated that surgical masks can efficiently prevent virus transmission from airborne aerosols.[31-32] However the ability to detect whether the outer surface of a mask has been exposed to respiratory droplets from coughing or sneezing, is also of considerable importance since the mask will lose function once it faces extreme humidity. Also, touching or handling a contaminated mask carries the risk of transmitting infections (Figure 4.10a).[33] Our nanofibrillar PEDOT film serves as a flexible chemoresistive sensor by monitoring the relative humidity change on the mask to detect droplet attachment. The stretchable 2D film is easily integrated onto the 2D mask via platinum lead, Kapton tape and a multimeter (Figure 4.10b) and shows clear compatibility with the mechanical requirements of wearing surgical masks due to the 3D tunable

mechanical properties generated by Kirigami. Notably, the electrode is only 0.5 mm thick and weighs only 0.16 g making it easy to assemble on the mask (Figure 4.10c).

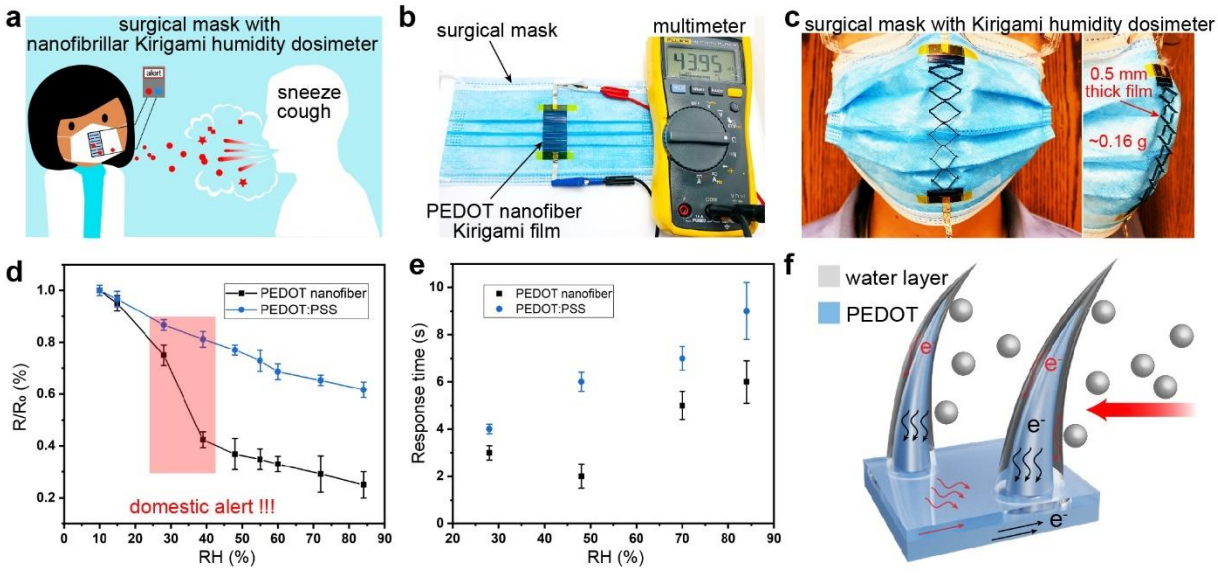

Figure 4.10: Nanofibrillar PEDOT coatings for Kirigami humidity dosimeters. a) Schematic illustration shows our humidity dosimeter detecting droplets that originate from sneezes and coughs. b) Photograph of humidity dosimeter in its 2D state attached to a surgical mask. c) Front and side view of our device stretching to accommodate 3D deformation from surgical mask. d) Resistance change and e) response time in dosimeters comprised of PEDOT nanofibers vs. PEDOT:PSS and as a function of relative humidity. f) Schematic illustration shows water droplets spreading on PEDOT nanofibers and enhancing charge transfer processes.

To explore the relationship between sensitivity and electrode morphology, we introduce our nanofibrillar PEDOT electrode and compare it against PEDOT:PSS thin film electrodes for testing humidity levels. Figure 4.10d shows that the resistance decreases with increasing humidity for both electrodes due to 1) polymer swelling-induced electron transfer through conjugation length, and 2) formation of a water layer that induces electron hopping and facilitates electron transfer. Importantly, the nanofibrillar PEDOT film exhibits remarkable decrease in resistance at the initial humidity range (around 40% relative humidity) and exhibits faster response (<2s) in comparison to the PEDOT:PSS thin film (Figure 4.10e).[34] The heightened response of our electrode is a

consequence of the larger surface area generated by high aspect ratio nanofibers that provide more accessible pathways for water vapor to traverse.[35] This is congruent with the porous nature of nanofiber films, in which gas molecules or aerosol droplets can rapidly diffuse in and out of the nanofibers (Figure 4.10f).[36] Our PEDOT nanofibrillar humidity dosimeter exhibits better performance in both sensitivity and response time than conventional PEDOT:PSS films as well as commercial humidity sensors, qualifying it as an ideal humidity-sensing dosimeter accessory for surgical masks.

Our synthetic strategy utilizes a solid-state precursor that allows us to deposit nanofibers layer-by-layer providing a solution to issues stemming from a low packing density or low nanofibrillar mass. We engineer a composite electrode to circumvent delamination by polymerizing PPy directly on the surface of an initial PEDOT layer (Figure 4.11a). SEM images show that the composite electrode surface is comprised of a carpet of PPy/PEDOT nanofibers. The hierarchical configuration suggests that the preceding PEDOT layer acts as a barrier to the diffusion of HCl vapor. Hydrochloric acid is prevented from initiating PPy polymerization on the PET substrate and PEDOT nanofibers therefore serve as the preferential nucleation site for PPy growth.[10, 37] This sequential deposition of conducting polymer layers allows grafting of PPy onto the PEDOT layer affording a novel synthetic approach for depositing electroactive composites and engineering electrodes (Figure 4.11b).

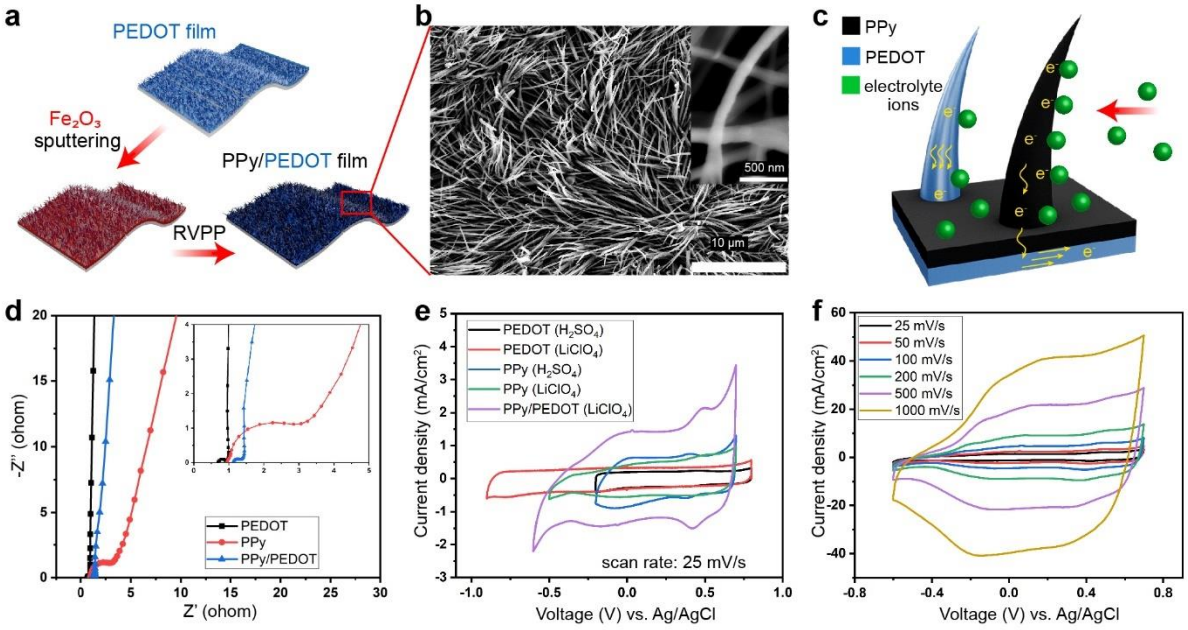

Figure 4.11: Nanofibrillar Polypyrrole and PEDOT composites for Kirigami electrodes. a) Schematic illustration shows deposition strategy where a nanofibrillar PEDOT-coated PET substrate is sputtered with oxidant precursor (Fe_2O_3) and utilized for synthesis (RVPP) producing a nanofibrillar polypyrrole film on top of PEDOT nanofibers. These bi-layered PPy/PEDOT Kirigami electrodes b) possess a high packing density of nanofibers as shown by SEM with a 150 nm diameter (inset). c) Schematic illustration shows a PPy/PEDOT composite electrode charging in the electrolyte where PPy serves as a highly capacitive material with active redox sites and PEDOT serves as a conductive layer providing facile charge transfer. d) EIS of PEDOT, PPy, and PPy/PEDOT electrodes show that the latter exhibits lower ESR due to the conductive PEDOT layer and low ion transfer resistance suggesting an ideal structure for ion penetration. e) CVs of PEDOT, PPy, and PPy/PEDOT composite electrodes at 25 mV/s show a larger CV area for the latter indicating a higher capacitance in the composite. f) Scan rate capability of the PPy/PEDOT composite electrode from 25 to 1000 mV/s in $LiClO_4$ aqueous electrolyte.

The composite electrodes possess a bilayer architecture that capitalizes on the high conductivity of PEDOT (1000 S/cm) through intimate contact and chemical bonding at the electrode/current collector interface. Moreover, the PPy layer (nanofibers) possesses higher pseudo-capacitance and is more sensitive to ion adsorption at the electrode/electrolyte interface than PEDOT (Figure 4.11c). To prove this model, we introduce EIS to compare the electron and ion transfer resistance of the single electrode against the composite electrode (Figure 4.11d). Nyquist data for PEDOT and PPy electrodes reveal that PEDOT possesses a lower ESR (intercept of x axis), lower ion

diffusion resistance (small semicircle) and superior capacitive behavior (large slope) than PPy that is consistent with the literature.[16] In comparison, EIS results for the composite electrode produce a Nyquist plot with a smaller semicircle. A smaller radius compared to PEDOT indicates less contact resistance between electrolyte ions and the electrode and low diffusion resistance for adsorption/desorption of electrolyte ions.[38] The enhanced diffusion and adsorption of ions stems from the grafting process generating mechanically stable nanofibers that readily withstand expansion and contraction during doping and dedoping, respectively.

Three-electrode cyclic voltammetry (CV) provides fundamental understanding of electrochemical processes that occur during charging and discharging of the composite electrode. Figure 4.11e shows the CV curves for PEDOT, PPy and PPy/PEDOT electrodes immersed in 1 M aqueous solutions of various electrolytes. Unlike PEDOT, where both acidic and neutral electrolytes are suitable, the most rectangular and reversible curve for PPy is achieved using $LiClO_4$ as an electrolyte (Figure 4.12). Interestingly, the composite electrode performs better in $LiClO_4$ which typically generates a neutral environment that weakens the charge storage performance of PEDOT. This behavior is offset by the high capacitance of PPy enhancing charge storage and diffusion of electrolyte ions to yield a greater enclosed CV area vs. single active material electrodes. The composite electrode exhibits superior electrochemical performance demonstrating that a synergistic effect exists between PEDOT and PPy. Synergy is generally regarded as the cooperative interaction of multiple components producing a greater collective effect than the sum of the individuals.[39] In our composite material, PEDOT's electronic charge transport and PPy's pseudo-capacitance interact and enhance the electrode's electrochemical performance. Cyclic voltammograms remain mostly undistorted at high scan rates (1000 mV/s) as the open electrode

nanofibrillar architecture creates free volume and accessible electroactive sites; fast redox reactions in our devices enable high-rate charging that is ideal for supercapacitors (Figure 4.11f).

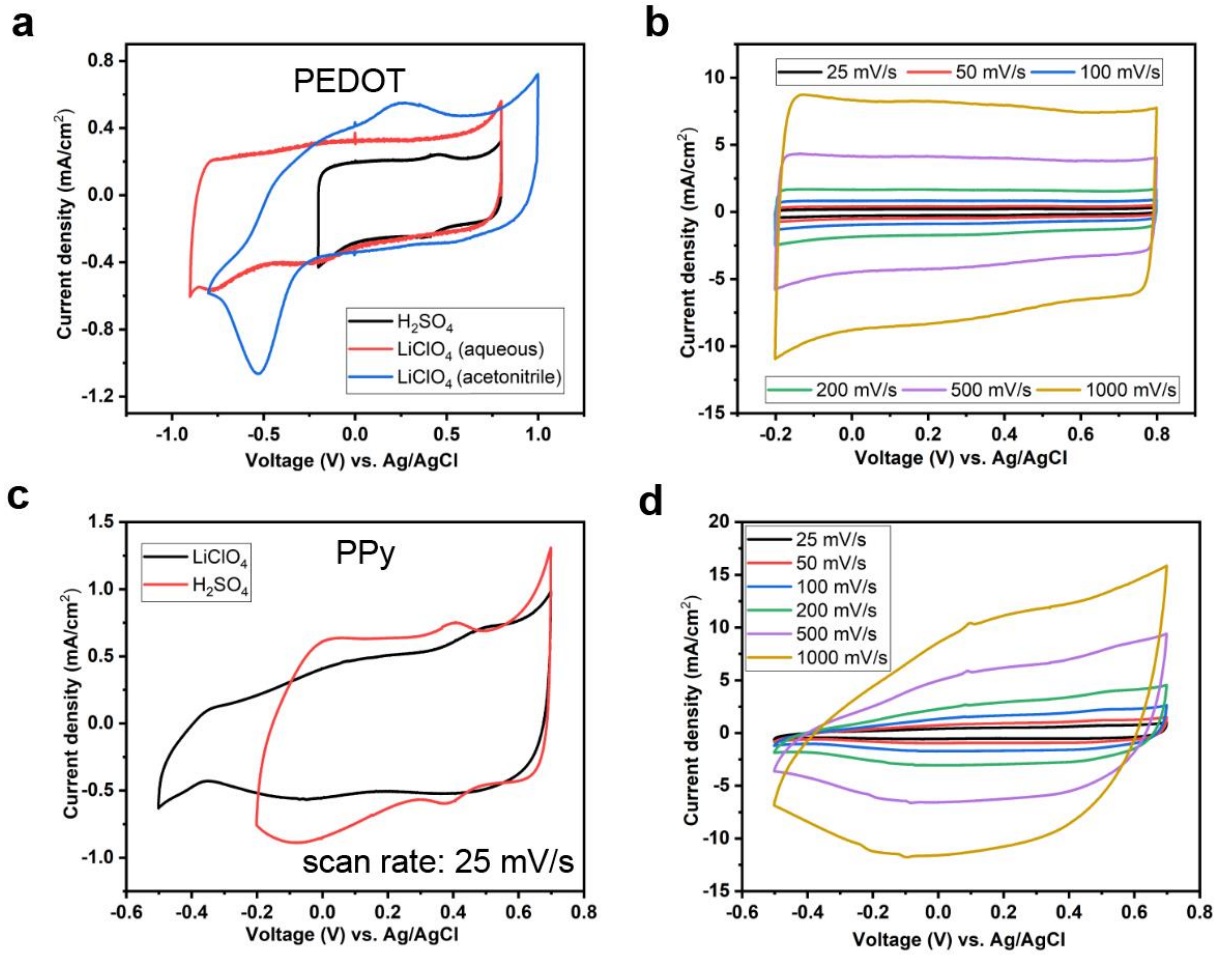

Figure 4.12: (a) CV scans of PEDOT in 1M H_2SO_4, 1M aqueous $LiClO_4$ and 1M $LiClO_4$ in acetonitrile. (b) Rectangular CV response of PEDOT in 1M H_2SO_4 electrolyte under scan rates ranging from 25 to 1000 mV/s. (c) CV scans of PPy in $LiClO_4$ and H_2SO_4 aqueous electrolyte. (d) CV response of PPy in 1M $LiClO_4$ aqueous electrolyte under scan rates ranging from 25 to 1000 mV/s.

Our PPy/PEDOT nanofibrillar electrodes excel at charge transfer processes that are of paramount importance in enhancing electrochemical performance for supercapacitors. Electrochemical

capacitance is characterized via galvanostatic charging/discharging (GCD) and cyclic voltammetry (CV) techniques. The sandwich configuration supercapacitor is comprised of two electrodes and 1M $LiClO_4$ gel electrolyte (Figure 4.13a). GCD curves (Figure 4.13b) for the composite electrode exhibit symmetric triangular shapes under current densities (0-1 V) indicating a reversible redox charge storage mechanism.[40] The linearity of the GCD curves together with minimized IR-drop at a fast discharging rate stems from a low internal resistance promoting capacitive behavior.[41] Cyclic voltammograms exhibit a rectangular shape proportional to the reversibility of doping/dedoping by electrolyte ions. The PPy/PEDOT composite electrode is characterized by a fast charge/discharge capability producing symmetric rectangular cyclic voltammograms under scan rates ranging from 5 mV/s to 50 mV/s and larger area compared with pristine PEDOT and PPy electrodes (Figure 4.14).[42] Areal capacitance calculations from CV curves are summarized in Figure 4.13c. The PPy/PEDOT composite supercapacitor possesses state-of-the art areal capacitance of 378 F/g due to its bilayered nanofibrillar morphology. Moreover PPy nanofibers provide a large surface area for storing charge and PEDOT nanofibers provide conductive networks that facilitate electron transfer.[43] This result further confirms the synergistic effect between the two nanofibrillar polymers in our composite electrode.

Maintaining electrical performance under mechanical deformation is a crucial parameter for stretchable power sources. Our PPy/PEDOT nanofibrillar supercapacitor shows only a slight change in capacitance during stretching (378 F/g at 0% stretch, 373 F/g at 50% stretch, 368 F/g at 100% stretch, 363 F/g at 50% stretch), twisting (369 F/g at 50% stretch) and bending (372 F/g at 50% stretch) (Figure 4.13d**)** demonstrating superior energy storage performance under mechanical

strain. Our composite supercapacitor is stable exhibiting 99% and 85% capacitance retention after a 1 and 300 cycles (100% stretch), respectively (Figure 4.13e). An areal-normalized Ragone plot

graphing the relationship between power density and energy density shows the state-of-the-art performance among carbon allotropes and metal oxides, as well as a metal-organic framework, MXene, and transition metal dichalcogenide (Figure 4.13f).[44-48] Among these, our composite supercapacitor exhibits the highest areal energy density of 115 μWh/cm^2. This result confirms the synergistic effect of our bilayered composite electrode characterized by highly conductive PEDOT, capacitive PPy and a large surface area.

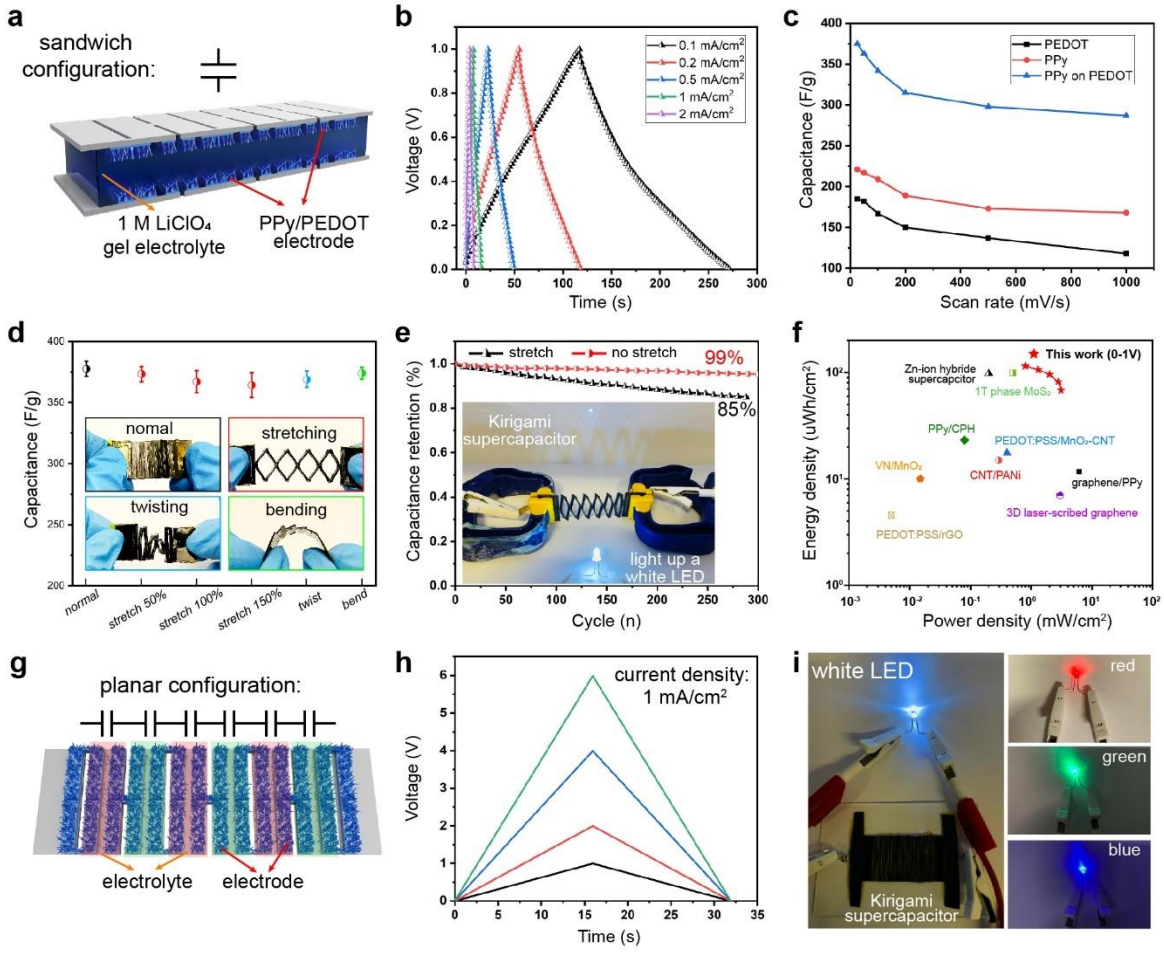

Figure 4.13: Nanofibrillar PPy/PEDOT Kirigami supercapacitors. a) Schematic diagram shows our 2-electrode (sandwich configuration) supercapacitor comprised of a 1 M $LiClO_4$ gel electrolyte. b) Symmetric triangular GCD curves at current densities ranging from 0.1 mA/cm^2 to 2 mA/cm^2 demonstrate reversible charging and discharging. c) The PPy/PEDOT composite possesses higher capacitance than pristine PEDOT or PPy across all scan rates due to synergistic interactions between capacitive PPy and conductive PEDOT. d) Capacitance in our supercapacitors is stable during mechanical deformation such as stretching, twisting, and bending.

e) Comparison of capacitance retention without stretching versus stretching demonstrates an 85% capacitance retention after 300 stretching cycles; an LED is powered using 3 stretched supercapacitors connected in series (inset). f) Areal normalized Ragone plot compares our PPy/PEDOT composite device against graphene/PPy, CNT/PANI, PEDOT:PSS/MnO_2/CNT, RuO_2/PEDOT:PSS, PPy/CPH, 10% rGO-PEDOT:PSS, and PEDOT/rGO thin-film polymer-based supercapacitors. g) Schematic diagram of planar configuration of multiple supercapacitors connected in series for high voltage generation. h) GCD curves collected at 1 mA/cm^2 show 1 V (black), 2 V (red), 4 V (blue) and 6 V (green) plots with increasing number of units of PPy/PEDOT supercapacitors. i) Photograph shows our Kirigami supercapacitor module in its planar configuration powering various colored LEDs.

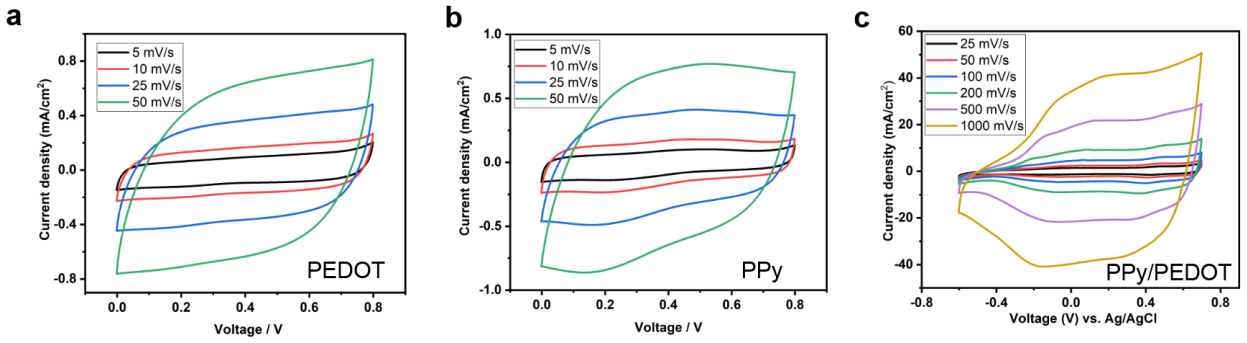

Figure 4.14: CV scans of (a) PEDOT, (b) PPy and (c) PPy/PEDOT in 1M $LiClO_4$ electrolyte under various scan rates**.**

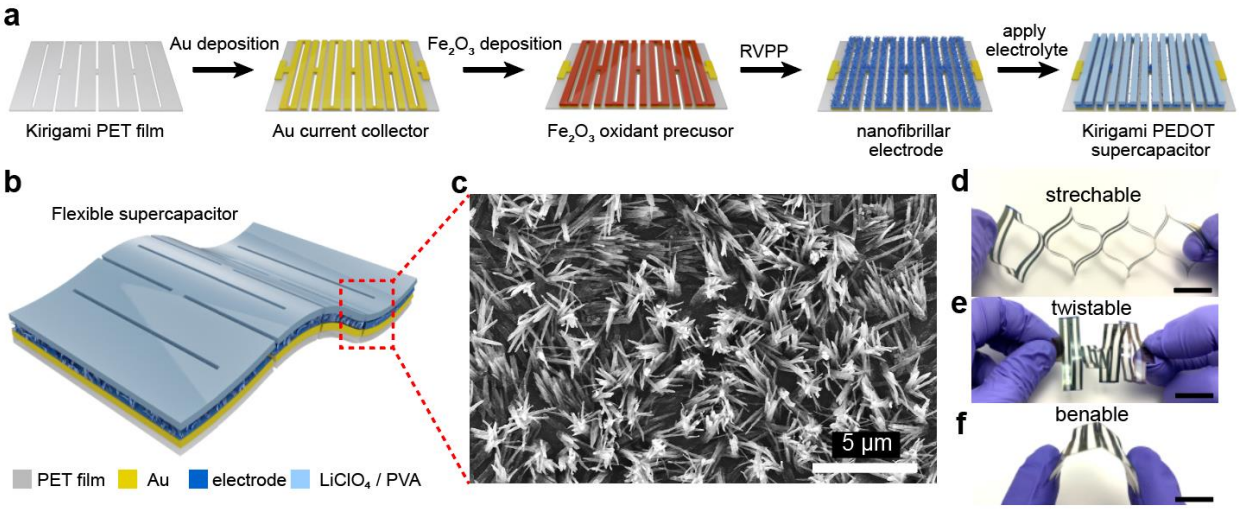

Figure 4.15: (a) Fabrication process of a nanofibrillar PEDOT Kirigami-based supercapacitor in a planar configuration. (b) Schematic diagram of flexible supercapacitor (c) possessing a high packing density of 1D nanostructures. The supercapacitor withstands complex deformation including (d) stretching, (e) twisting and (f) bending.

Supercapacitor units are assembled both in series and in parallel to meet specific energy needs or open circuit voltages making it a versatile choice for various applications. Figure 4.13g and **F** Figure 4.15 illustrates the geometric details of the planar configuration comprised of 6 units of PPy/PEDOT supercapacitors (labeled in red and green) connected in parallel. The capacitance performance is confirmed via GCD curves collected at 1 mA/cm^2 for 1V (black), 2V (red), 4V (blue) and 6V (green). This functional device lights up LEDs of different colors demonstrating the advantage of a planar configuration and highlighting its potential applications for stretchable electronics.

4.4 Conclusion

We advance stretchable electrodes and Kirigami-based engineering by developing a synthetic strategy that produces electroactive nanofibrillar films of conducting polymer composites. Our approach directly grafts polymer onto a PET substrate in situ during synthesis producing a high packing density of various conducting polymer nanofibers. We develop a Kirigami humidity dosimeter using PEDOT nanofibers that exhibits superior performance both in sensitivity (40% change) and response time (<2s) over conventional PEDOT:PSS films and commercial humidity sensors. This work demonstrates how to apply our layer-by-layer technique via consecutive depositions to produce nanofibrillar PPy/PEDOT composite-based supercapacitors possessing state-of-the-art energy density (115 μWh/cm^2 at 1 mA/cm^2) and capacitance (85% capacitance retention after 300 stretching cycles). This work overcomes current challenges associated with nanostructure deposition on pre-cut substrates by generating stretchable electrodes that enhance

both sensitivity and energy density in Kirigami-based wearable healthcare monitors and stretchable power sources.

References

(1) Z. Huang, Y. Hao, Y. Li, H. Hu, C. Wang, A. Nomoto, T. Pan, Y. Gu, Y. Chen, T. Zhang, W. Li, Y. Lei, N.Kim, C. Wang, L. Zhang, J. W. Ward, A. Maralani, X. Li, M. F. Durstock, A. Pisano, Y. Lin, S. Xu, *Nat. Electronics* **2018,** *1* (8), 473-480.

(2) C. Yang, H. Zhang, Y. Liu, Z. Yu, X. Wei, Y. Hu, *Adv Sci* **2018,** *5* (12), 1801070.

(3) Z. Song, X. Wang, C. Lv, Y. An, M. Liang, T. Ma, D. He, Y. J. Zheng, S. Q. Huang, H. Yu, H. Jiang, *Sci Rep* **2015,** *5*, 10988.

(4) Y. S. Guan, H. Li, F. Ren, S. Ren, *ACS Nano* **2018,** *12* (8), 7967-7973.

(5) H. Guo, M. H. Yeh, Y. C. Lai, Y. Zi, C. Wu, Z. Wen, C. Hu, Z. L. Wang, *ACS Nano* **2016,** *10* (11), 10580-10588.

(6) R. Zhao, S. Lin, H. Yuk, X. Zhao, *Soft Matter* **2018,** *14* (13), 2515-2525.

(7) Y. Tang, Y. Li, Y. Hong, S. Yang, J. Yin, *Proc Natl Acad Sci USA* **2019**.

(8) Y. S. Guan, Z. Zhang, Y. Tang, J. Yin, S. Ren, *Adv. Mater* **2018,** *30* (20), e1706390.

(9) Y. Diao, H. Chen, Y. Lu, L. M. Santino, H. Wang, J. M. D'Arcy, *ACS Appl. Energy Mater* **2019,** *2* (5), 3435-3444.

(10) L. M. Santino, S. Acharya, J. M. D'Arcy, *J. Mater. Chem. A* **2017,** *5* (23), 11772-11780.

(11) L. M. Santino, Y. Lu, S. Acharya, L. Bloom, D. Cotton, A. Wayne, J. M. D'Arcy, *ACS Appl Mater Interfaces* **2016,** *8* (43), 29452-29460.

(12) S. E. Root, S. Savagatrup, A. D. Printz, D. Rodriquez, D. J. Lipomi, *Chem Rev* **2017,** *117* (9), 6467-6499.

(13) R. Xu, A. Zverev, A. Hung, C. Shen, L. Irie, G. Ding, M. Whitmeyer, L. Ren, B. Griffin, J. Melcher, L. Zheng, X. Zang, M. Sanghadasa, L. Lin, *Microsyst Nanoeng* **2018,** *4*, 36.

(14) S. Huang, Y. Liu, Y. Zhao, Z. Ren, C. F. Guo, *Adv. Funct. Mater.* **2018,** *29* (6), 1805924.

(15) E. Pomerantseva, F. Bonaccorso, X. Feng, Y. Cui, Y. Gogotsi, *Science* **2019,** *366* (6468).

(16) Y. Diao, Y. Lu, H. Yang, H. Wang, H. Chen, J. M. D'Arcy, *Adv. Funct. Mater.* **2020,** *30* (32), 2003394.

(17) L. M. Santino, Y. Diao, H. Yang, Y. Lu, H. Wang, E. Hwang, J. M. D'Arcy, *Nanoscale* **2019,** *11* (25), 12358-12369.

(18) B. R. Pistillo, K. Menguelti, N. Desbenoit, D. Arl, R. Leturcq, O. M. Ishchenko, M. Kunat, P.

K. Baumann, D. Lenoble, *J. Mater. Chem. C* **2016,** *4* (24), 5617-5625.

(19) J. Yang, F. Zeng, Z. S. Wang, C. Chen, G. Y. Wang, Y. S. Lin, F. Pan, *J. Mater. Chem. A* **2011,** *110* (11), 114518.

(20) Y. Wang, C. Zhu, R. Pfattner, H. Yan, L. Jin, S. Chen, F. Molina-Lopez, F. Lissel, J. Liu, N. I. Rabiah, Z. Chen, J. W. Chung, C. Linder, M. F. Toney, B. Murmann, Z. Bao, *Sci. Adv.* **2017,** *3* (e1602076).

(21) M. Setka, R. Calavia, L. Vojkuvka, E. Llobet, J. Drbohlavova, S. Vallejos, *Sci Rep* **2019,** *9* (1), 8465.

(22) T. A. Yemata, Y. Zheng, A. K. K. Kyaw, X. Wang, J. Song, W. S. Chin, J. Xu, *RSC Adv.* **2020,** *10* (3), 1786-1792.

(23) W. Zhao, Y. Wang, A. Wang, *Mater. Sci. Applications* **2017,** *08* (11), 774-783.

(24) P. Huang, C. L., S. Pinaud, K. Brousse, R. Laloo, V. Turq, M. Respaud, A. Demortière, B. Daffos, P. L. Taberna, B. Chaudret, Y. Gogotsi, P. Simon1, *Sci. Adv.* **2016,** *351* (6274).

(25) T. V. Manen, S. Janbaz, M. Ganjian, A. A. Zadpoor, *Mater. Today* **2020,** *32*, 59-67.

(26) S. G. Im, P. J. Yoo, P. T. Hammond, K. K. Gleason, *Adv. Mater.* **2007,** *19* (19), 2863-2867.

(27) Y. Tang, G. Lin, L. Han, S. Qiu, S. Yang, J. Yin, *Adv Mater.* **2015,** *27* (44), 7181-90.

(28) C. Wu, X. Wang, L. Lin, H. Guo, Z. L.Wang, *ACS Nano* **2016,** *10* (4), 4652-9.

(29) J. Kim, H. Park, S.-H. Jeong, *J. Industrial Eng. Chem* **2020,** *82*, 144-152.

(30) H. Li, W. Wang, Y. Yang, Y. Wang, P. Li, J. Huang, J. Li, Y. Lu, Z. Li, Z. Wang, B. Fan, J. Fang, W. Song, *ACS Nano* **2020,** *14* (2), 1560-1568.

(31) C. Sohrabi, Z. Alsafi, N. O'Neill, M. Khan, A. Kerwan, A. Al-Jabir, C. Iosifidis, R. Agha, *Int J Surg* **2020,** *76*, 71-76.

(32) N. H. L. Leung, D. K. W. Chu, E. Y. C. Shiu, K. H. Chan, J. J. McDevitt, B. J. P. Hau, H. L. Yen, Y. Li, D. K. M. Ip, J. S. M. Peiris, W. H. Seto, G. M. Leung, D. K. Milton, B. J. Cowling, *Nat. Med* **2020,** *26* (5), 676-680.

(33) L. Huang, S. Xu, Z. Wang, K. Xue, J. Su, Y. Song, S. Chen, C. Zhu, B. Z. Tang, R. Ye, *ACS Nano* **2020**.

(34) H. Françon, Z. Wang, A. Marais, K. Mystek, A. Piper, H. Granberg, A. Malti, P. Gatenholm, P. A. Larsson, L. Wågberg, *Adv. Funct. Mater.* **2020,** *30* (12), 1909383.

(35) M. Panapoy, W. Singsang, B. Ksapabutr, *Physica Scripta* **2010,** *T139*, 014056.

(36) J. Huang, S. Virji., B. H. Weiller, R. B. Kaner, *J. Am. Chem. Soc.***2003,** *125*, 314-315.

(37) H. Wang, Y. Diao, M. Rubin, L. M. Santino, Y. Lu, J. M. D'Arcy, *ACS Appl. Nano Mater* **2018,** *1* (3), 1219-1227.

(38) S. Jiao, A. Zhou, M. Wu, H. Hu, *Adv Sci* **2019,** *6* (12), 1900529.

(39) H. U. Lee, C. Park, J. H. Jin, S. W. Kim, *J. Power Sources* **2020,** *453*, 227898.

(40) J. S. M. Lee, M. E. Briggs, C. C. Hu, A. I. Cooper, *Nano Energy* **2018,** *46*, 277-289.

(41) K. Dong, Y. C. Wang, J. Deng, Y. Dai, S. L. Zhang, H. Zou, B. Gu, B. Sun, Z. L. Wang, *ACS Nano* **2017,** *11* (9), 9490-9499.

(42) Z. Pan, J. Yang, L. Li, X. Gao, L. Kang, Y. Zhang, Q. Zhang, Z. Kou, T. Zhang, L. Wei, Y. Yao, J. Wang, *Energy Storage Mater.* **2020,** *25*, 124-130.

(43) S. Khan, A. Majid, R. Raza, *J. Mater. Sci: Mater. in Electron* **2020,** *31* (16), 13597-13609.

(44) Y. Wang, Y. Ding, X. Guo, G. Yu, *Nano Research* **2019,** *12* (9), 1978-1987.

(45) H. Zhu, M. Li, D. Wang, S. Zhou, C. Peng, *J. Electrochemi. Soc.* **2017,** *164* (9), A1820-A1825.

(46) Y. Ma, Q. Wang, X. Liang, D. Zhang, M. Miao, *J. Mater. Sci* **2018,** *53* (20), 14586-14597.

(47) H. Zhou, G. Han, *Electrochim. Acta* **2016,** *192*, 448-455.

(48) N. Wang, X. Wang, Y. Zhang, W. Hou, Y. Chang, H. Song, Z. hao, G. Han, *J. Alloys Compd.* **2020,** *835*, 155299.

Chapter 5

PEDOT-integrated Masonry Materials for Antimicrobial Application

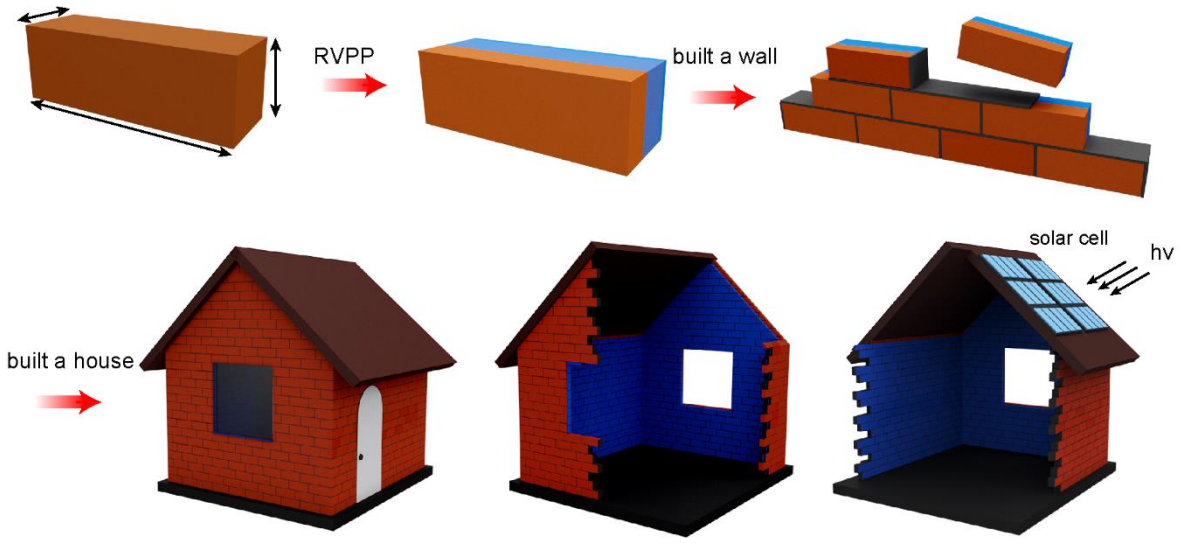

Future sustainable house with PEDOT masonry materials

5.1 Introduction

Demand for antimicrobial surfaces is rapidly increasing due to heightened public awareness regarding home hygiene and stringent regulations across the healthcare industry.[1,2] Antimicrobial solutions are frequently used to disinfect surfaces such as sinks, tables and walls.[3] However, overuse of antimicrobials has led to the development of antibiotic-resistant microbes resulting in less effective or completely ineffective antibiotic treatments.[1,4] In 2019, the CDC reported over 2.8 million individuals had infections caused by antibiotic-resistant bacteria and fungi.[5] Antibiotic resistant infections lead to prolonged hospital stays, higher medical costs, and an increase in mortality.[6,7] Common infectious diseases are becoming more difficult to treat with emerging resistance mechanisms. It is therefore essential that new technologies be developed to limit the use of antibiotics, thereby limiting the evolution of resistance.[7] Non-antimicrobial cleansers have also been developed, but there is concern that frequent exposure to chemical cleansers can have detrimental health effects, and with any cleansers there is the possibility for accidental ingestion by children and pets. Traditionally, microbes settle on surfaces and are allowed to proliferate, where they potentially acquire resistance, and are later removed by periodic application of disinfectant cleansers. Ideally, new technologies ought to prevent infections by reducing our exposure to microbes without requiring the use of harmful cleansers and antibiotics.[8] A strategy for accomplishing these goals would integrate antimicrobial agents within the microstructure of masonry materials, such as brick and tile. This concept is a promising approach for sterilizing commonly contacted surfaces without exacerbating the rise of microbial resistance. Therefore, developing antimicrobial masonry materials is an imperative step towards preventing antibiotic-resistant infections.

Researchers have made numerous attempts to develop antimicrobial masonry materials by introducing additives that possess antimicrobial properties for sterilization.[9,10] For example, ZnO-cement composite possesses effective antibacterial and antifungal activities under dark and solar light due to nanosized ZnO particles that are hazardous to bacteria via ROS generation.[11,12] Concrete containing TiO_2 nanoparticles kills bacteria under light by provoking inflammation, cytotoxicity and DNA damage in bacterial cells.[13,14] Nanostructures have been shown to also kill bacteria by affecting their uptake through cell membranes, stimulating phagocytosis, as well as endogenous ROS generation.[15] Unfortunately, these strategies suffer from complicated synthesis, coating delamination and metal ion contamination.[16] Furthermore, each of these strategies would be complicated to translate to a format amenable to household use.

Here, we demonstrate a new class of antimicrobial masonry materials by integrating conducting polymer poly(3,4-ethylenedioxythiophene) (PEDOT) nanofibers within the microstructure of conventional brick and tile. We find that a network of nanofibers, extending from the surface to the pores inside masonry materials, has efficient antimicrobial properties when a weak external electric voltage is applied. These antimicrobial properties are notable even on the external glazed surface of tiles. Brick and tile are cost-effective, mechanically robust, and ubiquitous in today's masonry construction. Inspired by our previous work,[17] we transform Fe_2O_3 in brick and tile to initiate rust-based vapor-phase polymerization (RVPP)[18] resulting in the nanofibrillar conducting polymer PEDOT characterized by high environmental stability and low electrical resistance (5 Ω/sq). PEDOT-integrated masonry materials such as a PEDOT-tile and PEDOT-brick possesses highly conductive surface results in peroxide generation upon application of an external voltage, eliciting a strong antimicrobial effect against *Escherichia coli*, *Saccharomyces cerevisiae*, and *Staphylococcus aureus*. This common *E. coli* bacteria is

responsible for food-poisoning[19] while *S. aureus*, a pathogenic bacteria, readily acquires resistance leading to methicillin resistant staph infections (MRSA).[20,21] *S. cerevisiae* (harmless baker's yeast) serves as a model fungi to assess the likelihood that this method could prove effective against other fungi such as *Stachybotrys chartarum* (black mold) and *Candida albicans* (cause of ringworm/athlete's foot).[22,23] A high packing density of PEDOT nanofibers ensures significant peroxide production (large inhibition zone). Integration of PEDOT with brick and tile results in robust organic-inorganic composites that withstand wear and tear. Notably, coating PEDOT onto the back face of tile also produces an antimicrobial effect on the front surface enabling construction of antimicrobial glazed tile walls, floors and counters.

5.2 Experimental methods

Materials. Chlorobenzene (99%), 3,4-ethylenedioxythiophene (97%), poly(vinyl alcohol) (Mw 89,000–98,000, 99+% hydrolyzed), methanol (≥99.8%), and hydrochloric acid (37%) were purchased from Sigma-Aldrich; sulfuric acid (AR) was purchased from Macron. All chemicals were used without further purification. Platinum foil (0.025mm thick, 99.9%) was purchased from Alfa Aesar and utilized for engineering electrode leads and Celgard 3501 membrane was used as a separator. Fired bricks were purchased from local hardware stores: The Home Depot Inc. (type 1 brick, https://www.homedepot.com, Internet #100323015, Model #RED0126MCO, Store SKU #393134), Lowe's Inc. Floor tiles are purchased from local hardware stores: Internet #305322621, Model #NRETBLA3X6INBEV, Store SKU #1003235709, Store SO SKU #1003190599.

5.2.1 Synthesis of nanofibrillar PEDOT-integrated masonry materials

Brick and tile were cut using a diamond saw (±0.03 cm error) into the 2.00 cm × 1.00 cm × 1.00 cm. A brick is thrice washed with deionized water to remove surface dust then dried at 140 °C for 1 h and cooled to room temperature. Reaction was carried out in a glass reactor (12.30 cm× 8.55 cm× 11.30 cm) using 100 µL of 12M HCl and 200 mL of a 0.675M EDOT in chlorobenzene solution at 140 °C for 1.5 h.

5.2.2 Material characterization

Scanning electron micrographs and energy-dispersive X-ray spectra were collected with a JEOL 7001LVF FE-SEM. Two-point probe resistance measurements were carried out using a Fluke 177 True RMS digital multimeter with 3 mm distance between two probes. Current–voltage tests were performed on a 3D printed two-point probe station with two gold probes separated by 2mm.

5.2.3 Microbial strains and growth

XL10 gold *E. coli* cells (Agilent) were used for this study. The bacterial stocks were stored at -80˚C in glycerol stocks. The cells were thawed on ice and then 50 µL of cells were mixed with 200 µL of fresh SOC medium before being plated on LB agar plates (Figure 5.3h). A similar process was performed with the SH1000 *S. aureus* cells (gifted from Petra Levin) that were stored at -80˚C in glycerol stocks. These cells were thawed on ice, then 50 µL of cells were mixed with 200 µL of fresh LB medium, then all 250 µL were plated on LB agar plates (Figures 3F, 3J). The *S. cerevisiae* cells were thawed from -80˚C glycerol stocks and diluted with SD-HU medium and plated on SD-HU plates (Figure 3I). The media has been supplemented with 2% glucose.

5.2.4 Percent cell survival assay

The *E. coli* cells were grown overnight at 37˚C rotating in sterilized LB media. On the second day, the overnight culture was diluted so the optical density at 600 nm went from ~1.0 to 0.3. Two samples of the XL10 gold *E. coli* cells were diluted by a factor of 10^{3}, 10^{4}, and 10^{5} into fresh SOC media and plated on LB agar plates (Figure 5.3a). These plates were incubated overnight at 37˚C and imaged the following day (Figure 5.3b). The number of colonies on each plate were counted manually for three replicates (Figure 5.3c).

5.2.5 Real scenario test

After performing the 1:5 dilution of the *E. coli* glycerol stocks, 200 µL of the sample was plated on the LB agar plate, and then 25 µL of the sample was split and plated atop each of the tiles. The plates were left overnight at room temperature and treated with 3V (Figure 4b). The tiles were swabbed the following day and plated directly on LB agar plates and incubated overnight at 37˚C. The tiles were swabbed again after 48 hours following the same protocol. The plates were imaged after incubating at 37˚C.

5.3 Results & discussion

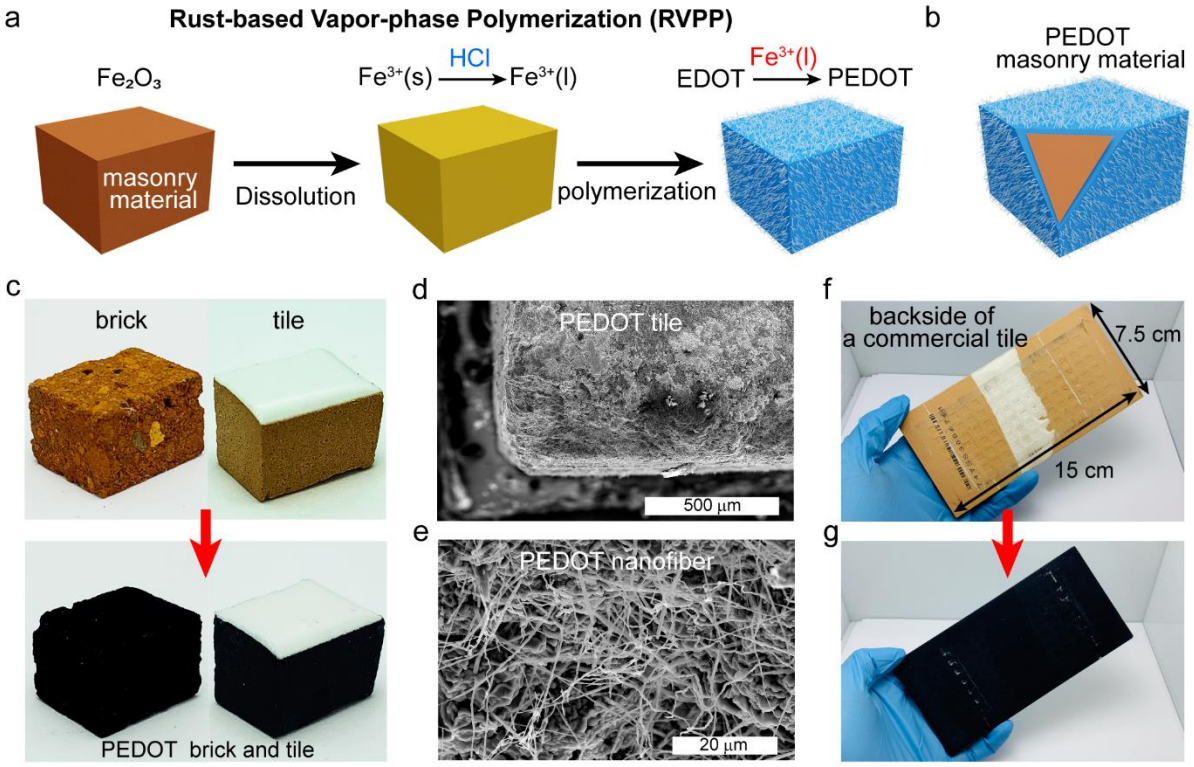

Figure 5.1: Deposition of PEDOT nanofibers on brick and tile. (a) Schematic illustration of rust-based vapor-phase polymerization (RVPP) shows that the final product is (b) a polymer-coated masonry material. (c) Photographs show the color change of a brick and tile (2 cm × 1 cm × 1 cm) as Fe_2O_3 (red) is converted to PEDOT (dark blue). (d-e) Scanning electron micrographs show complete conformal coverage of a masonry material by PEDOT nanofibers. f-g Synthesis is scalable to the decimeter scale as demonstrated by a coat on the back side of a commercial tile.

PEDOT nanofiber synthesis is initiated by partially dissolving a masonry material's hematite (α-Fe_2O_3) using HCl vapor (140 °C) thereby liberating Fe^{3+} ions from their solid-state environment. Liberated ferric ions spontaneously undergo hydrolysis forming 1D FeOOH spindles that serve as preferential nucleation sites for polymerizing EDOT vapor and promoting the growth of PEDOT nanofibers (Figure 5.1a). We advance previous findings by demonstrating that rust-based vapor-phase polymerization is a versatile synthesis suitable for both brick and tile (Figure 5.1b).[17,18] The

inorganic oxide matrix structure of a substrate, comprise of SiO_2 and Al_2O_3, remains pristine after synthesis enabling robust integration with polymer nanofibers (Figure 5.1c). Scanning electron micrographs (SEM) show that nanofibers (aspect ratio = 50) generate a high surface area and high packing density (Figure 5.1d); polymerization imparts high electronic conductivity and is scalable (Figure 5.1e).

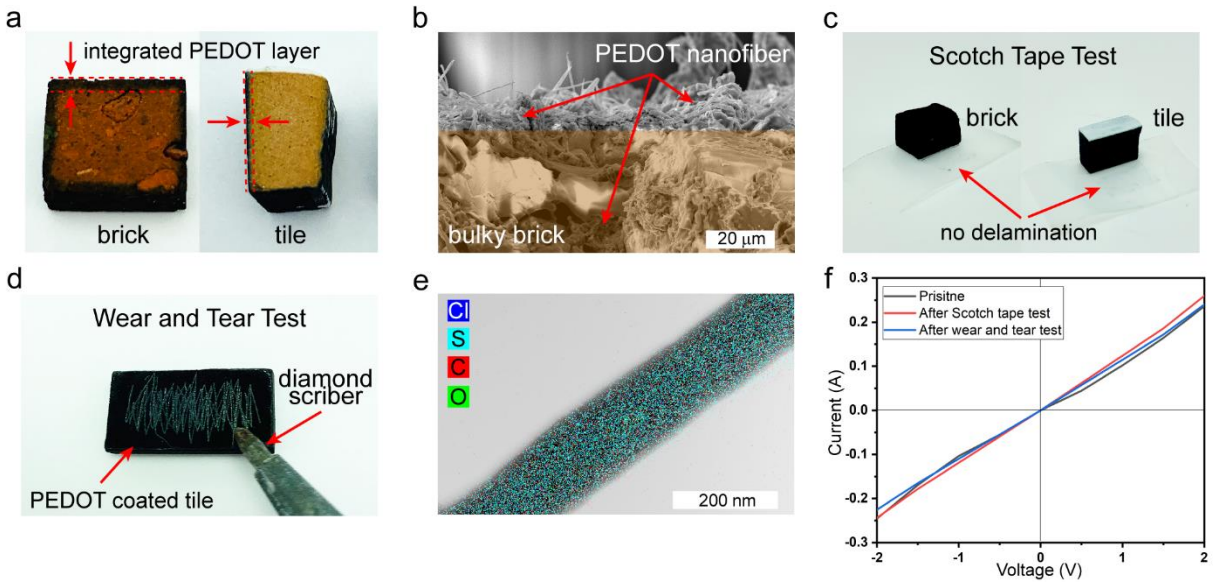

Figure 5.2: Characterization of a nanofibrillar PEDOT coating integrated in masonry materials. (a) Cross-sectional photograph of brick and tile show PEDOT integration. (b) SEM confirms that PEDOT nanofibers penetrate the brick bulk forming a conformal coating (~20 µm-thick). (c) A Scotch tape test fails to delaminate a polymer coating from brick and tile. Moreover, (d) a scratch test using a diamond scriber proves that polymer remains integrated within the inorganic matrix. (e) Energy-dispersive X-ray elemental map for a PEDOT nanofiber shows overlapping Cl, S, C and O signals. (f) Linear current–voltage curves show ohmic behavior after Scotch tape test and wear and tear test indicating a stable electronic performance for the nanofibrillar polymer coating.

In contrast to conventional coating technologies that only deposit a surface layer, our synthetic strategy enables integration of PEDOT nanofibers within the porous microstructure of a masonry material (Figure 5.2a); cross-sectional SEM shows that nanofibers penetrate the brick microstructure resulting in a 20 µm-thick coating (Figure 5.2b). During synthesis, the vapor

diffusion of reactants leads to a nanofibrillar surface coating and integration of a nanofibrillar network within bulk of the substrate. Coatings on brick and tile exhibit strong adhesion, are impervious to delamination under Scotch tape tests (Figure 5.2c) and withstand wear and tear after scratch tests using a diamond scriber (Figure 5.2d). Elemental maps obtained via energy-dispersive X-ray spectroscopy for a single fiber (Figure 5.2e) show overlapping Cl, S, C and O signals indicating a homogeneous PEDOT composition.[25] Electronic transport for a polymer film, probed using current–voltage measurements, shows ohmic behavior (straight line) and low resistance (large slope, ~5 Ω/sq) (Figure 5.2f) due to a continuous percolation network that facilitates charge transport.[26] PEDOT-tiles and PEDOT-bricks exhibit stable electrical resistance after adhesion tests because our synthetic strategy achieves significant mechanical robustness suitable for masonry surface coating applications.

To study the antimicrobial effects of a PEDOT-integrated tile, we carried out solution experiments with *Escherichia coli* (*E. coli*) and studied cell growth upon treatment with external voltage at room temperature.[11] Here, *E.coli* cultures were grown to logarithmic phase to reach an OD_{600} of 0.3. PEDOT-integrated tiles were then added to the tubes and an external voltage (3 V) was applied to the tile overnight (Figure 5.3a). As a control, we included a second culture where we added a PEDOT-integrated tile without applying voltage. Following overnight treatment, cultures were diluted and plated to quantify cell survival. The treated (3 V) sample displays strongly diminished growth as compared to the untreated (no voltage) sample (Figure 5.3b). Quantification of cell survival indicates that 70% of *E. coli* are killed upon treatment with external voltage (Figure 5.3c) confirming PEDOT's antimicrobial effect.

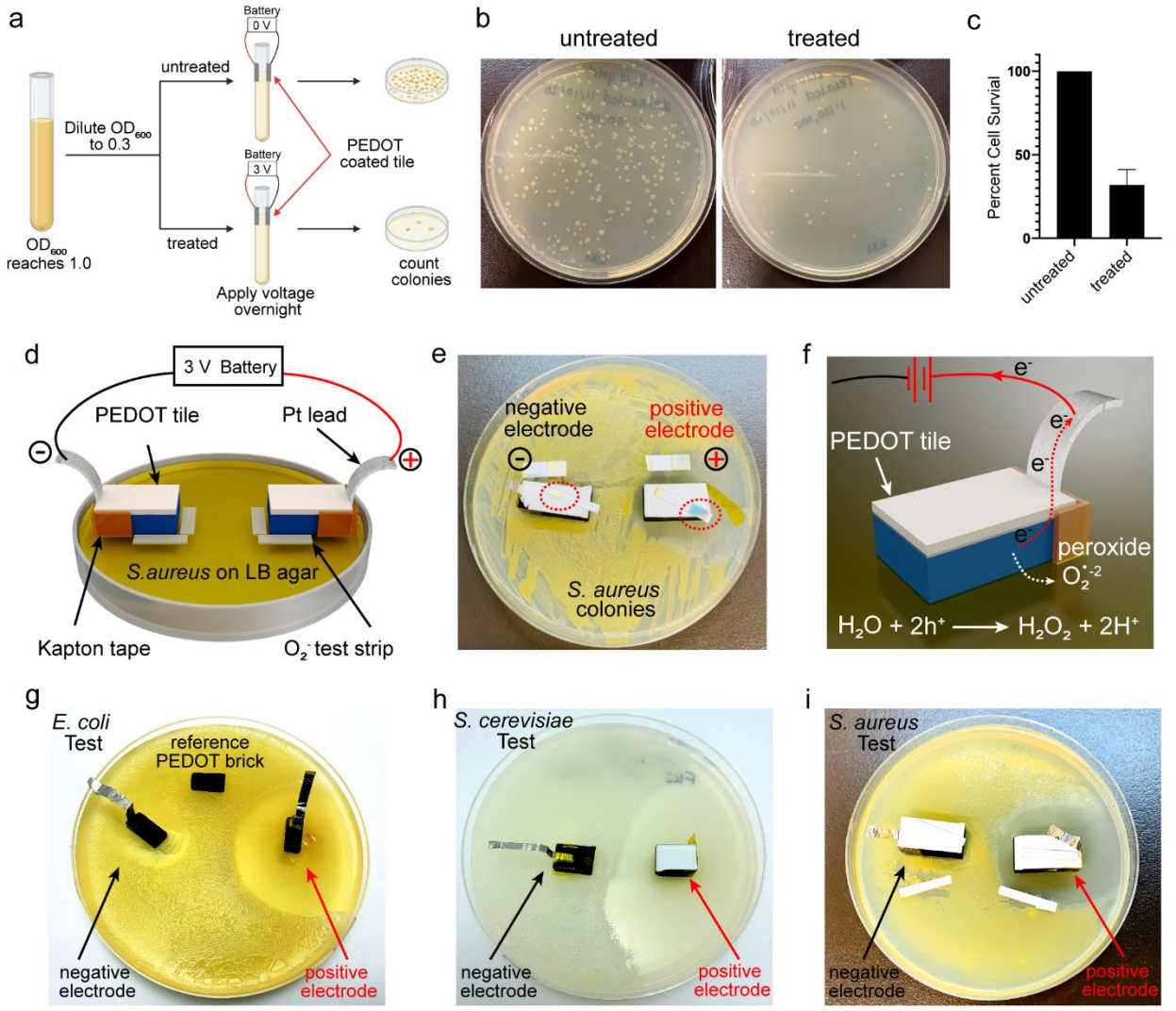

Figure 5.3: Antimicrobial effects of PEDOT tiles. (a) *E. coli* was cultured to logarithmic phase until the OD_{600} reached 1.0 at which point the culture was diluted and a low voltage (3 V) treatment was applied overnight. Equal volumes from each culture were plated to compare colony growth. (b) Growth is compared from a culture with voltage applied (treated) and without an applied voltage (untreated). (c) Colonies from b were counted to determine percent cell survival. Values represent means +/- SEM, n=3. (d) Schematic showing experimental setup comprised of two PEDOT tiles, external 3 V battery and O_2^- test strip. (e) Upon applying voltage, O_2^- test strip at the positive electrode turns blue signaling the generation of O_2^- as demonstrated. (f) Schematic depicting generation of O_2^-. (g-i) Experiments were performed as depicted in part D on plates of freshly streaked with *E. coli* (g), *S. cerevisiae* (h), and *S. aureus* (i). To demonstrate that voltage is required for antimicrobial effects, an additional PEDOT reference brick that was not connected to an electrode was included in (g). In each instance, a region with no microbial growth is noted surrounding the positive electrode.

Antimicrobial properties based on hydrophobicity, electrostatic repulsion and cathodic peroxide generation have been reported for a similar conducting polymer (PEDOT:PSS), unfortunately, these studies suffer from minimal antimicrobial effect and polymer coatings prone to delamination.[27-30] To more closely investigate our polymer and its antimicrobial mechanism, we modified our setup to monitor growth on agar plates and included a test strip next to a PEDOT-tile to detect peroxide generation (Figure 5.3d). Notably, the test strip turns blue at the positive electrode after voltage is applied for 2 h confirming peroxide production, while the negative electrode lacks peroxide (test trip color remains unchanged) (Figure 5.3e). Unlike conventional metal oxide electrodes (WO_3, $BiVO_4$ and Al_2O_3) commonly used for anodic H_2O oxidation, [30,31] this is the first time that PEDOT has been demonstrated to generate anodic peroxide. We propose that this mechanism is driven by anodic oxidation of water, where electrons (serving as charge carriers in the closed circuit) transfer to the anode, leaving holes to coordinate with H_2O to produce peroxide (Figure 5.3f).[32]

We next assessed the versatility of our strategy by testing for efficacy against not just gram-negative *E. coli*, but also gram-positive *S. aureus* bacteria, and yeast *S. cerevisiae* strains. Two PEDOT bricks were attached to either a positive or negative electrode and applied to plates of freshly streaked microbes. A third brick was included without an applied voltage to serve as an additional control (Figure 5.3g). After applying 3 V for 24 h, the *E. coli* plates shows no growth in the region surrounding the positive electrode, whereas the regions surrounding the negative electrode and the reference brick (no voltage) display normal growth. Antimicrobial effects on *S. cerevisiae* (Figure 5.3h) were tested under the same conditions using a PEDOT brick and PEDOT tile. Notably, we again observe no growth in the region surrounding the positive electrode. Similar results were achieved against *S. aureus* (Figure 5.3i). We noted what appeared to be more mild

effects against *S. aureus* compared to E. coli. This observation could be due to the thick peptidoglycan layers that make S. aureus harder to kill.[33,35] Antimicrobial effects are observed against all three microbes, indicating that our strategy yields materials with antimicrobial properties suitable for various types of masonry materials (brick and tile).

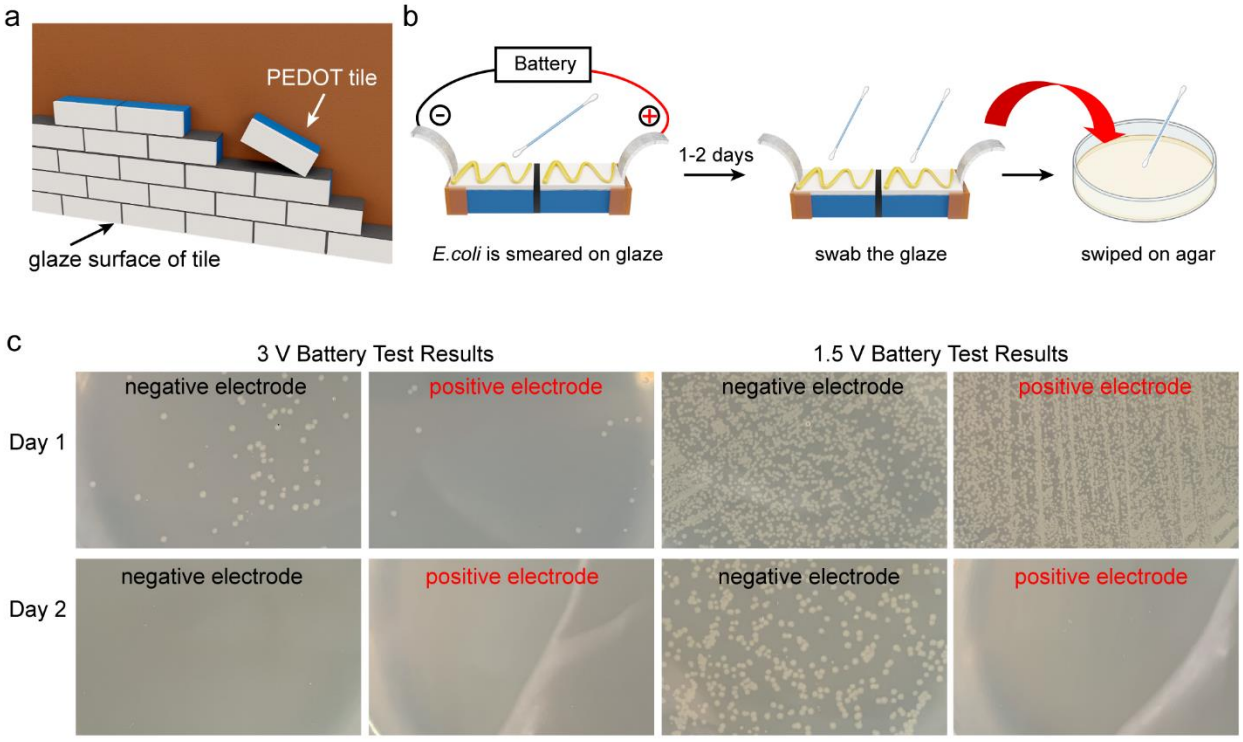

Figure 5.4: Real-world scenario test based on a "tile wall". (a) Schematic illustration of potential application of PEDOT-coated tiles to construct a bathroom wall. (b) *E. coli* was smeared on a glazed tile surface and a 3 V battery was applied. (c) After 1 (top) or 2 (bottom) days of applied voltage, the tiles were swiped and allowed to outgrow on an agar plate.

To test the applicability of antimicrobial masonry materials in real-world scenarios such as bathroom or kitchen tile walls, floors, and counters, we examined whether a PEDOT-integrated tile exhibits antimicrobial effects on the glazed surface that is exposed to bacteria (Figure 5.4a). Two tiles are connected by 1 M H_2SO_4/PVA gel and an external 3 V battery is applied as illustrated

in Figure 5.4b. *E. coli* is applied onto the glazed surface. A 3 V or 1.5 V battery is then applied. Following application of voltage for 1 day or 2 days, the surface of the tiles was swabbed and streaked onto agar plates. When a 3 V battery is applied (Figure 5.4c), just a few colonies were noted in the positive electrode region following one day of applied voltage. In the region surrounding the negative electrode, more colonies were noted after one day of applied voltage. These results are consistent with our earlier findings suggesting that peroxide is generated from anodic oxidation (Figure 5.3). Antimicrobial effects are observed on the uncoated face of the tile as peroxide diffuses (in vapor phase) or penetrates (in liquid phase) up to the glazed surface. To determine if this antimicrobial activity persists, we next applied voltage to the tiles for 2 days. Interestingly, following two days of treatment we observe no *E. coli* colonies on either plate. This suggests that either the peroxide generation is sufficiently strong to reach the region near the negative electrode, or that both electrodes possess antimicrobial properties. We propose that the delayed antimicrobial effect exhibited by the negative electrode is due to the restrained oxygen diffusion as is typically seen in fuel cell systems. A 1.5 V battery test was carried out to probe the energy consumption required to observe an antimicrobial effect. The results exhibit *E. coli* survival in both electrodes after 1 day, while antimicrobial effect is observed on both electrodes (less *E. coli* colonies on negative electrode and clear Agar on positive electrode) after 2 days suggesting low voltage (1.5 V) takes longer time to achieve the same antimicrobial effect. These results demonstrate that the magnitude of the external voltage affects the rate of antimicrobial effect and provide a reference for future customized design.

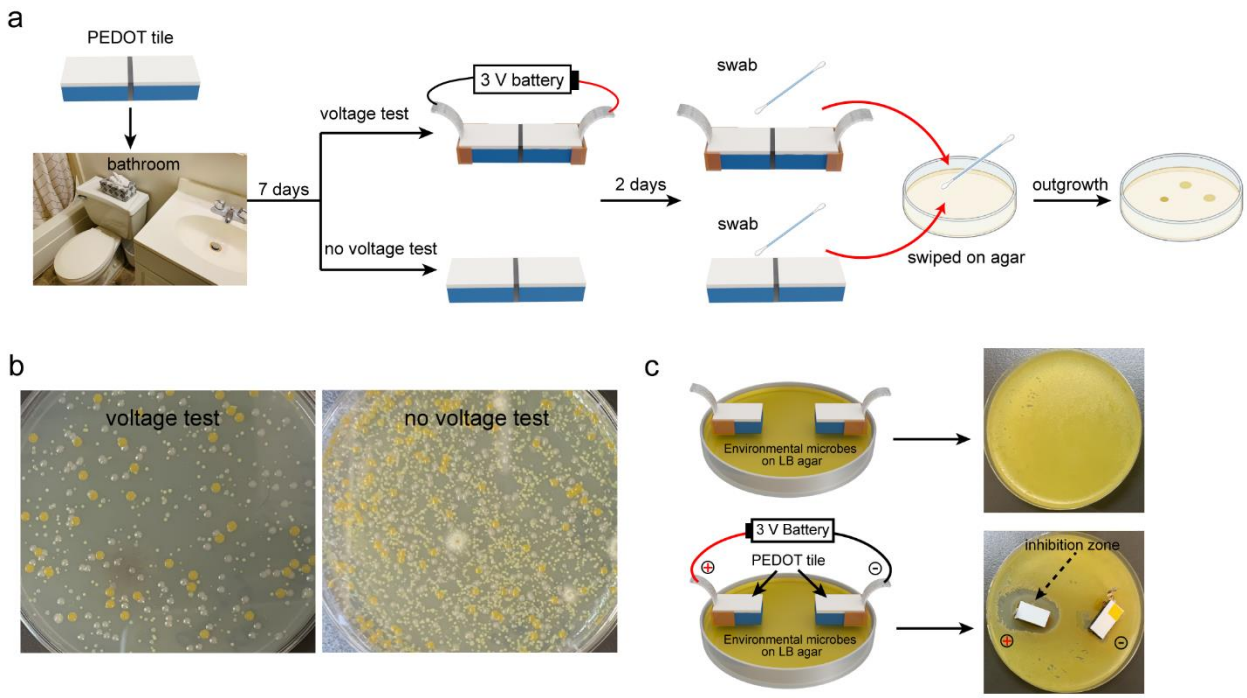

Figure 5.5: Testing PEDOT against environmental microbes. (a) Flow process diagram of placing PEDOT tiles in a bathroom. Environmental microbe experiments are introduced on tiles' glaze surface with voltage test and no voltage test. (b) Optical images of voltage test and no voltage test results. (c) Schematic diagram and optical images of environmental microbes' experiment on LB agar.

Since tiles are encountered in a household setting, to probe whether our products possess efficacy against environmental microbes, we place PEDOT tiles in a bathroom to experience home conditions. Two groups (voltage test and no voltage test) of tiles are placed in bathroom for 7 days, enabling environmental microbes to naturally accumulate on the glaze side of the tiles (Figure 5.5a). 3 V is applied on the tiles in the voltage test group for 2 days while no voltage to the other group. Each group of tiles is swabbed and streaked onto agar plates to assess outgrowth. An increased growth of microbes is obtained versus the laboratory strains of microbes (Figure 5.5b). Notably, a significant decrease in voltage test is observed compared with no voltage test, demonstrating our PEDOT tiles possess an efficient antimicrobial property against environmental microbes.

To confirm whether any of these microbes were resistant to our approach, we introduce another experiment by introducing the environmental microbes' mixture onto a fresh LB plate and repeated the experiments using the same method as the inhibition assays in Figure 3g-i (Figure 5.5c). Strikingly, we observe a clear boundary of growth in a region around the positive electrode for the environmental microbes, similar to our laboratory strain experiments. Therefore, we conclude that the PEDOT tiles enable preventing the growth of all environmental microbes.

5.4 Conclusion

This work demonstrates that rust-based vapor-phase polymerization produces composites comprised of PEDOT nanofibers and conventional masonry materials possessing antimicrobial properties. The state-of-the-art is advanced by our synthetic technology resulting in a superior antimicrobial effect against *E. coli*, *S. cerevisiae*, *S. aureus* and other environmental microbes. Here, vapor polymerization utilizes the structural stability and open microstructure of bricks and tiles producing a mechanically robust integrated polymer structure impervious to mechanical degradation such as delamination. PEDOT's antimicrobial properties, arising from the release of peroxide triggered by an external anodic voltage, represent a new electrochemical mechanism. In comparison to traditional cleaning products, this new class of smart masonry materials removes and prevents the growth of microbes thereby obviating the need for hazardous chemicals that propagate resistance to antibiotics. Interestingly, the dual nature of these smart masonry materials affords energy storing functionality (previously demonstrated) and antimicrobial properties for developing the next generation of multifunctional sustainable infrastructures.

References

(1) Zaman, S. B. *et al.* A Review on Antibiotic Resistance: Alarm Bells are Ringing. *Cureus* **9**, e1403, doi:10.7759/cureus.1403 (2017).

(2) Ardal, C. *et al.* Antibiotic development - economic, regulatory and societal challenges. *Nat Rev Microbiol* **18**, 267-274, doi:10.1038/s41579-019-0293-3 (2020).

(3) Jaesang Lee, S. M., and Pedro J. J. Alvarez. Nanomaterials in the Construction Industry: A Review of Their Applications and Environmental Health and Safety Considerations. *ACS Nano* **4** (2010).

(4) Cassidy, S. S. *et al.* Antimicrobial surfaces: A need for stewardship? *PLoS Pathog* **16**, e1008880, doi:10.1371/journal.ppat.1008880 (2020).

(5) ANTIBIOTIC RESISTANCE THREATS IN THE UNITED STATES 2019. *U.S. Department of Health and Human Services*, doi:10.15620/cdc:82532 (2019).

(6) Antibiotic resistance. *World Health Organization* (2020).

(7) Dadgostar, P. Antimicrobial Resistance: Implications and Costs. *Infect Drug Resist* **12**, 3903-3910, doi:10.2147/IDR.S234610 (2019).

(8) Lee, C. R., Cho, I. H., Jeong, B. C. & Lee, S. H. Strategies to minimize antibiotic resistance. *Int J Environ Res Public Health* **10**, 4274-4305, doi:10.3390/ijerph10094274 (2013).

(9) Gomez-Carretero, S., Nybom, R. & Richter-Dahlfors, A. Electroenhanced Antimicrobial Coating Based on Conjugated Polymers with Covalently Coupled Silver Nanoparticles Prevents Staphylococcus aureus Biofilm Formation. *Adv Healthc Mater* **6**, doi:10.1002/adhm.201700435 (2017).

(10) Brinkman, C. L. *et al.* Exposure of Bacterial Biofilms to Electrical Current Leads to Cell Death Mediated in Part by Reactive Oxygen Species. *PLoS One* **11**, e0168595, doi:10.1371/journal.pone.0168595 (2016).

(11) Venkata Rao Krishnamurthi, A. R., Janet Peifer, Isabelle I. Niyonshuti, Jingyi Chen, Yong Wang. Microampere Electric Current Causes Bacterial Membrane Damage and Two-Way Leakage in a Short Period of Time. *Applied and Environmental Microbiology* **86**, e01015-01020, doi:10.1128/AEM (2020).

(12) Sirelkhatim, A. *et al.* Review on Zinc Oxide Nanoparticles: Antibacterial Activity and Toxicity Mechanism. *Nanomicro Lett* **7**, 219-242, doi:10.1007/s40820-015-0040-x (2015).

(13) W. Zhu, P. J. M. B. a. A. P. Application of nanotechnology in construction Summary of a state-of-the-art report. *37*, 649-658 (2004).

(14) Hanna L. Karlsson, P. C., Johanna Gustafsson, and Lennart Mo¨ller. Copper Oxide Nanoparticles Are Highly Toxic: A Comparison between Metal Oxide Nanoparticles and Carbon Nanotubes. *Chem, Res, Toxicol* **21**, 1726-1732 (2008).

(15) J. L. DEL POZO, M. S. R., and R. PATEL. Bioelectric effect and bacterial biofilms. A systematic review. *Int J Artif Organs* **31**, 786-795 (2008).

(16) Tuson, H. H. & Weibel, D. B. Bacteria-surface interactions. *Soft Matter* **9**, 4368-4380, doi:10.1039/C3SM27705D (2013).

(17) Wang, H. *et al.* Energy storing bricks for stationary PEDOT supercapacitors. *Nat Commun* **11**, 3882, doi:10.1038/s41467-020-17708-1 (2020).

(18) Diao, Y. *et al.* Converting Rust to PEDOT Nanofibers for Supercapacitors. *ACS Applied Energy Materials* **2**, 3435-3444, doi:10.1021/acsaem.9b00244 (2019).

(19) E. coli. *World Health Organization* (2018).

(20) Chambers, H. F. & Deleo, F. R. Waves of resistance: Staphylococcus aureus in the antibiotic era. *Nat Rev Microbiol* **7**, 629-641, doi:10.1038/nrmicro2200 (2009).

(21) Piechota, M., Kot, B., Frankowska-Maciejewska, A., Gruzewska, A. & Wozniak-Kosek, A. Biofilm Formation by Methicillin-Resistant and Methicillin-Sensitive Staphylococcus aureus Strains from Hospitalized Patients in Poland. *Biomed Res Int* **2018**, 4657396, doi:10.1155/2018/4657396 (2018).

(22) Facts about Stachybotrys chartarum. *Centers for Disease Control and Prevention, National Center for Environmental Health* (2019).

(23) Ringworm. Centers for Disease Control and Prevention, National Center for Emerging and Zoonotic Infectious Diseases (NCEZID), Division of Foodborne, Waterborne, and Environmental Diseases (DFWED) (2020).

(24) Wang, H. *et al.* Metal Oxide-Assisted PEDOT Nanostructures via Hydrolysis-Assisted Vapor-Phase Polymerization for Energy Storage. *ACS Applied Nano Materials* **1**, 1219-1227, doi:10.1021/acsanm.7b00382 (2018).

(25) Diao, Y. *et al.* Direct Conversion of Fe2O3 to 3D Nanofibrillar PEDOT Microsupercapacitors. *Advanced Functional Materials* **30**, 2003394, doi:10.1002/adfm.202003394 (2020).

(26) Lu, Y. *et al.* Synthesis of Submicron PEDOT Particles of High Electrical Conductivity via Continuous Aerosol Vapor Polymerization. *ACS Appl Mater Interfaces* **11**, 47320-47329, doi:10.1021/acsami.9b15625 (2019).

(27) Sanchez-Jimenez, M. *et al.* Antimicrobial activity of poly(3,4-ethylenedioxythiophene) n-doped with a pyridinium-containing polyelectrolyte. *Soft Matter* **15**, 7695-7703, doi:10.1039/c9sm01491h (2019).

(28) Kangkamano, T. *et al.* Product-to-intermediate relay achieving complete oxygen reduction reaction (cORR) with Prussian blue integrated nanoporous polymer cathode in fuel cells. *Nano Energy* **78**, 105125, doi:10.1016/j.nanoen.2020.105125 (2020).

(29) Talikowska, M., Fu, X. & Lisak, G. Application of conducting polymers to wound care and skin tissue engineering: A review. *Biosens Bioelectron* **135**, 50-63, doi:10.1016/j.bios.2019.04.001 (2019).

(30) Perry, S. C. *et al.* Electrochemical synthesis of hydrogen peroxide from water and oxygen. *Nature Reviews Chemistry* **3**, 442-458, doi:10.1038/s41570-019-0110-6 (2019).

(31) Xia, C. *et al.* Confined local oxygen gas promotes electrochemical water oxidation to hydrogen peroxide. *Nature Catalysis* **3**, 125-134, doi:10.1038/s41929-019-0402-8 (2020).

(32) Mitraka, E. *et al.* Electrocatalytic Production of Hydrogen Peroxide with Poly(3,4-ethylenedioxythiophene) Electrodes. *Advanced Sustainable Systems* **3**, 1800110, doi:10.1002/adsu.201800110 (2019).

(33) Khan, S. & Narula, A. K. Bio-hybrid blended transparent and conductive films PEDOT:PSS:Chitosan exhibiting electro-active and antibacterial properties. *European Polymer Journal* **81**, 161-172, doi:10.1016/j.eurpolymj.2016.06.005 (2016).

(34) BEVERIDGE, T. J. Structures of Gram-Negative Cell Walls and Their Derived Membrane Vesicles. *Journal of Bacteriology* **181**, 4725-4733 (1999).

(35) Gerondakis, S. & Siebenlist, U. Roles of the NF-kappaB pathway in lymphocyte development and function. *Cold Spring Harb Perspect Biol* **2**, a000182, doi:10.1101/cshperspect.a000182 (2010).

Chapter 6

Single PEDOT Catalyst Boosts CO_2 Photoreduction Efficiency

6.1 Introduction

Excessive fossil fuel combustion has drastically increased net global carbon dioxide (CO_2) flux into Earth's atmosphere, inducing climate change and worsening air quality, human health, and energy security.[1-2] The critical need for mankind to counteract increasing atmospheric greenhouse gas concentrations elicits intensive research to develop processes that attenuate CO_2 emissions.[3] Photoreduction of CO_2 is one promising approach wherein abundant and sustainable solar energy is utilized with the aid of semiconductor photocatalysts to reduce CO_2 into chemical fuels.[4-5] In a photocatalytic system, electrons/holes generated by light absorption migrate towards catalytically active sites where they react with adsorbed CO_2 molecules. Catalytic efficiency relies on generation and separation of photogenerated charge carriers while minimizing recombination as well as on efficient CO_2 adsorption and light absorption.[6-7] Numerous efforts have optimized structure and composition of photocatalysts by increasing surface area, creating surface defects on graphene, introducing nanocrystals to enhance visible light absorption and applying metal/metal oxide co-catalysts such as Ni, TiO_2 and ZnO to facilitate charge separation. However, these co-catalysts suffer from recombination of charge carriers and band gap mismatch leading to poor

conversion efficiencies.[8-9] As opposed to a single catalyst, delivery of photogenerated charge carriers between co-catalysts of different band gaps must overcome the high energy barrier of out-of-plane Ohmic or Schottky contact during an intramolecular cascade.[10] Although researchers have modified co-catalyst systems by tuning the ratio of components to precisely match the band gap, costly fabrication techniques and low yields highlight the importance of developing a more favorable single catalyst alternative.

Among all single catalysts, conducting polymers (CPs) are a new class of organic semiconductors primed to become the next generation of multifunctional photocatalysts; this is because the π-conjugation backbone in CPs enhances CO_2 adsorption via π-π interactions with delocalized p-conjugated electrons from CO_2 molecules. As semiconductors, CPs possess a wide light absorption range and photostability in the Ultraviolet-Visible-near-IR (UV-Vis-NIR) region that is easily controlled by doping/de-doping treatments and further enhanced by wide-ranging nanostructures.[11] Growing interest in CPs has prompted recent studies on CO2 photoreduction using polyaniline (PANi) and polypyrrole (PPy), [12-13] unfortunately the low electrical conductivity of these polymers results in low photoreduction efficiency. Poly(3,4-ethylenedioxythiophene) (PEDOT) exhibits high mobility of photogenerated electrons/holes[14] and is widely recognized as the most stable conductive CP (7600 S/cm) thus potentially serving as an ideal CO2 photoreduction catalyst. To the best of our knowledge, there is an absence of reports in the current literature regarding its CO_2 photoreduction catalytic properties.

Here, for the first time, we demonstrate that a nanofibrillar PEDOT film is an ideal single catalyst for CO_2 photoreduction. This film is deposited via our previously reported rust-based vapor-phase polymerization[15] resulting in a homogeneous PEDOT coating of high surface area possessing a nanofibrillar morphology and characterized by a high electronic conductivity (1200 S/cm). The

CO2 adsorption and light absorption properties are controlled by the polymer's band gap via chemical doping and de-doping treatments using an acid (HCl) and base (NH4OH or hydrazine), respectively. Our single catalyst results in a state-of-the-art CO yield rate (3000 μmolg-1 h-1) with 100% CO yield under a stable regime (> 10h) representing two orders of magnitude higher than the best single catalyst reported and surpassed by only three other co-catalyst systems.

6.2 Experimental methods

Materials. Fluoropore™ membrane was purchased from MilliporeSigma. 3,4-ethylenedioxythiophene (EDOT, 97%), chlorobenzene (99%), hydrochloric acid (37%), ammonia hydroxide (25%) and hydrazine hydrate (50%) were purchased from Sigma Aldrich and used as received.

6.2.1 Deposition of nanofibrillar PEDOT film

A solid-oxidant precursor, Fe_2O_3, was sputter deposited over polytetrafluoroethylene (PTFE) membrane via physical vapor deposition (Kurt J. Lesker PVD 75 RF and DC). All syntheses were performed at 140 °C for 1.5 h in glass reactors, each containing a substrate, a reservoir with 20 μL concentrated hydrochloric acid (HCl) and a reservoir with 200 μL of a 1.56 M EDOT/chlorobenzene solution. After 1.5 h, the electrodes were immediately removed from the reactors and cooled at room temperature and purified with 6 M HCl.

6.2.2 PEDOT Characterizations

Scanning electron micrographs and energy-dispersive X-ray spectra were collected using a JEOL 7001LVF FE-SEM. Transmission electron micrographs were obtained using a JEOL 2100 TEM

by drop-casting a dispersion of PEDOT nanofibers on a TEM grid. Raman spectra were obtained using a Renishaw inVia confocal Raman spectrometer mounted on a Leica microscope with a 20× objective and 785 nm wavelength diode laser serving as an illumination source. A low power was necessary to mitigate heating of conducting polymer samples. A Bruker d8 Advanced X-ray diffractometer was utilized to collect powder X-ray diffractograms of pulverized samples at room temperature using a Cu Kα radiation source (λ = 1.5406 Å) and LynxEye XE detector (operating at 40 kV and 40 mA); the sample holder was rotated at 30 rpm with a scan step of 0.02°. Current-voltage (I-V) curves were obtained with a built-in-house 3D printed probe station using two gold needles 1.24 mm apart. Four-point probe sheet resistance measurements were carried out using a Keithley 2450 SourceMeter with a Signatone SP4 four-point probe head.[16] Ultraviolet−Visible−near infrared (UV-Vis-NIR) spectra were collected on a Cary 5000 UV−Vis−NIR spectrophotometer. Solid PEDOT films were dispersed in HCl (37%), NH_4OH and hydrazine. X-ray photoelectron spectroscopy (XPS) was conducted on solid samples using a PHI 5000 Versaprobe II with an Al 1486.6 eV Mono-X-ray source at 51.3 W, a beam diameter of 100−200 μm and a 1 V neutralizer at 15 μA. Ultraviolet photoemission spectroscopy (UPS) measurements required a Physical Electronics 5000 VersaProbe II Scanning ESCA Microprobe and were performed to determine the valence band, conduction band and Fermi level position. He I (21.2 eV) ultraviolet source was used, and a 5 V bias was applied to the sample to observe a clear secondary electron edge.

6.2.3 Evaluation of PEDOT films for CO_2 photoreduction

Photocatalytic activity of the synthesized PEDOT films was evaluated using a photoreduction analysis system (Figure 6.5D) which was explained in our previous publications.[17-18] The

photoreduction analysis system contains a lab-built continuous flow reactor, Xe arc lamp (Oriel 66021, Newport Co.) and gas chromatograph (GC, 6895N, Agilent Technologies, Inc.). For testing samples, the PEDOT film was deposited glass and placed in a lab-built continuous flow reactor. High purity compressed CO_2 was used as the source gas and its flow rate was fixed at 20 ml min^{-1} by a mass flow controller (OMEGA engineering Inc.). The gas stream continuously passed through a water bubbler to generate a mixed flow of CO_2 and water vapor. Then, the mixed flow was introduced into the continuous flow reactor and a quartz window enables positioning a sample vertically to face the light (inset photo of Figure 6.5D). The PEDOT film was illuminated by the Xe arc lamp which was operated at 400 W with UV-vis-NIR wavelength region (250-950 nm). The compositions in the gas streams were continuously measured by the GC equipped with a porous layer open tubular (PLOT) capillary column (Supelco Carboxen-1010) and a thermal conductivity detector (TCD); helium was used as a carrier gas for the GC. In all experiments, the Xe arc lamp was initiated after the system was stabilized and approximately 3 ml min^{-1} of gas stream was introduced to the GC. All experiments were performed at least in duplicates.

6.3 Results & discussion

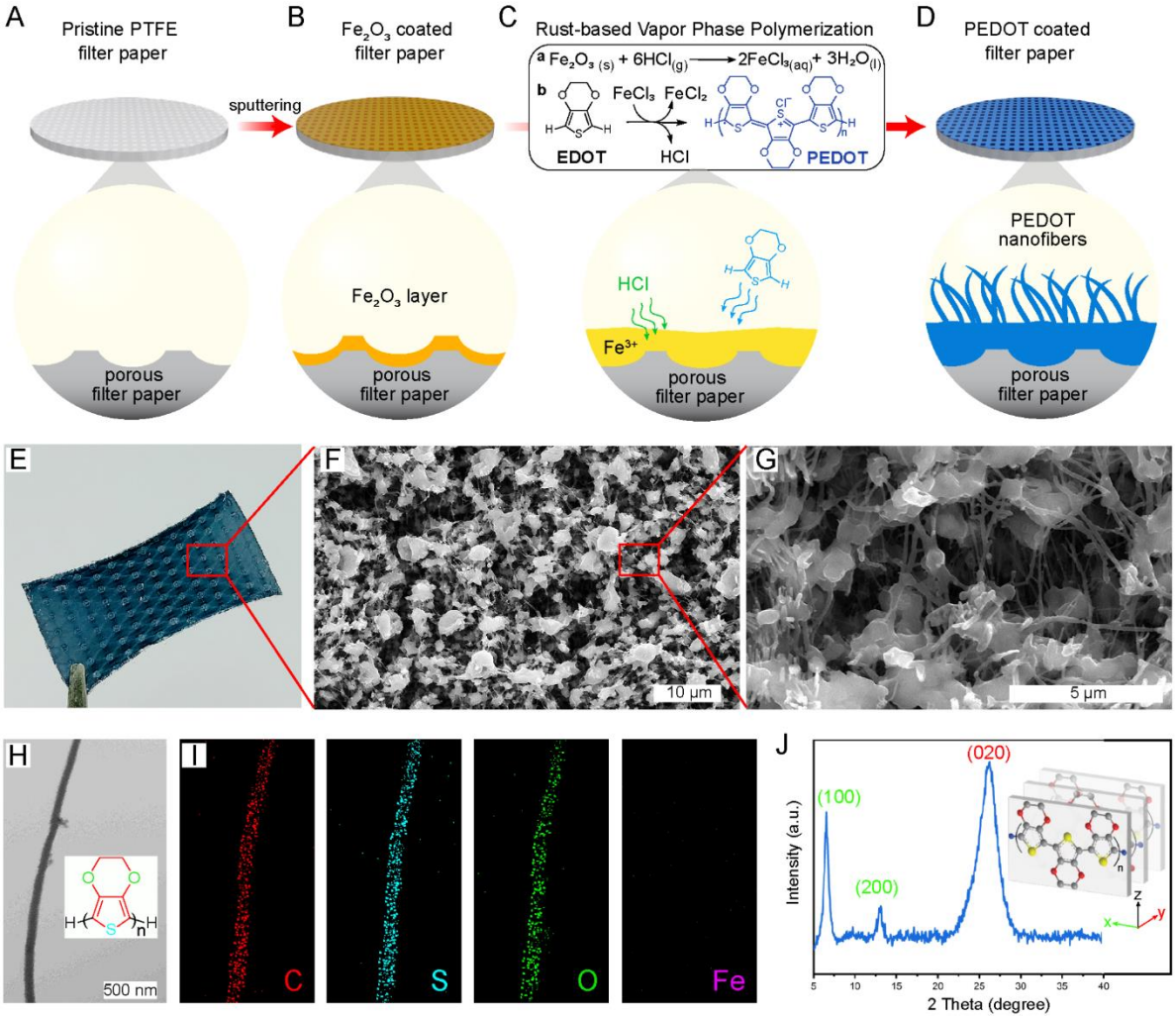

Figure 6.1: Schematic diagram of PEDOT nanofiber deposition on PTFE membrane and microscopy/spectroscopy characterization of nanofibrillar PEDOT film. (A) Pristine porous PTFE membrane is sputtered with a 60 nm Fe_2O_3 layer (B). (C) Rust-based vapor phase polymerization results in PEDOT nanofibers by a) liberating Fe^{3+} from Fe_2O_3 and triggering oxidative polymerization of b) EDOT. (D) Homogenous PEDOT nanofibrillar coating supported on a membrane. (E) Optical image of a PEDOT-coated PTFE membrane. (F) Scanning electron micrograph (SEM) shows bulk homogeneous PEDOT coating. (G) Close-up SEM reveals the free volume architecture between nanofibers. (H) Transmission electron micrograph (TEM) of a single nanofiber (aspect ratio ~50). (I) EDX maps of nanofiber show an elemental composition consisting of C, S, O and Fe. (J) PXRD confirms a polycrystalline structure with three characteristic peaks.

A conformal PEDOT nanofibrillar coating is produced via rust-based vapor-phase polymerization[15] by initially sputtering a 60 nm coating of Fe_2O_3 oxidant precursor onto a robust polytetrafluoroethylene (PTFE) membrane (Figure 6.1A). A conformally packed oxide coating exhibits a yellow color in the solid state (Figure 6.1B) and its dissolution controls oxidant concentration resulting in the homogenous deposition of a PEDOT coating. Polymer deposition is initiated by dissolving Fe_2O_3 at 140 °C using HCl vapor to dissolve inorganic oxide, liberate Fe^{3+} ions (Figure 6.1C) and promote the hydrolysis of ferric ions. Monomer vapor, induced by heating a liquid EDOT reservoir, preferentially nucleates on 1-D FeOOH spindles produced during Fe3+ hydrolysis resulting in PEDOT nanofibers (Figure 6.1D). This templated vapor-phase synthetic strategy is scalable, enabling deposition of a homogenous nanofibrillar PEDOT coating on a superhydrophobic substrate.

Photocatalyst morphology, surface area, and intrinsic chemical properties are vital parameters for CO_2 adsorption, light absorption and CO_2 reduction efficiency. The molecular and solid-state structure of a blue PEDOT-coated PTFE film (2 cm × 5 cm) (Figure 6.1E) is characterized via microscopy and spectroscopy. The polymer is uniformly integrated within the PTFE membrane (Figure 6.2) and scanning electron micrographs (SEM) of low (Figure 6.1F) and high magnification (Figure 6.1G) reveal a free volume web-like architecture composed of spherical aggregates interconnected by nanofibers. This open nanofibrillar structure possesses a high surface area that enhances absorption of both light and CO_2; transmission electron micrograph (TEM) shows a 100 nm mean nanofiber diameter with an aspect ratio of 50 (Figure 6.1H). Elemental mapping via energy-dispersive X-ray spectroscopy (Figure 6.1I) shows a uniform distribution and strong signals for C, O, and S corresponding to PEDOT's ethylenedioxy and thiophene ring whereas Fe signal disappears once PEDOT is purified using 6 M HCl. Current-voltage (I-V)

measurements, carried out to probe the electronic charge transport of a PEDOT film, demonstrate ohmic behavior (linear relationship) and a low resistance (large positive slope) (Figure 6.3) characteristic of a homogeneous and continuous percolation network that facilitates charge transport. Powder X-ray diffraction patterns (Figure 6.1J) further elucidate PEDOT's charge transport as a function of its polycrystalline structure. Three characteristic peaks are observed at 6.4°, 13.1° and 26.3° corresponding to lattice planes (100), (200) and (020), respectively. The first and second planes stem from lateral chain packing (x-axis) and the third is due to π–π stacking (y-axis). Low peak width values at half-height (0.4, 0.7, and 1.4) indicate a crystalline polymer structure responsible for enhanced charge transport.[19] Four-point probe conductivity measurements (Figure 6.4) show a high conductivity (1200 S/cm) stemming from the homogeneous deposition of an ordered PEDOT structure.

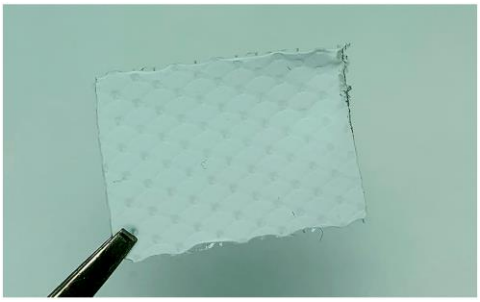

Figure 6.2: Photograph of a pristine PTFE film shows its macroscale morphology.

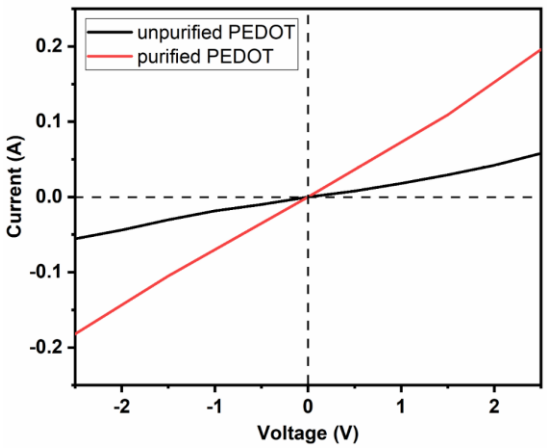

Figure 6.3: I-V curves of unpurified and purified PEDOT films (purification is carried out via repeated washes in concentrated HCl).

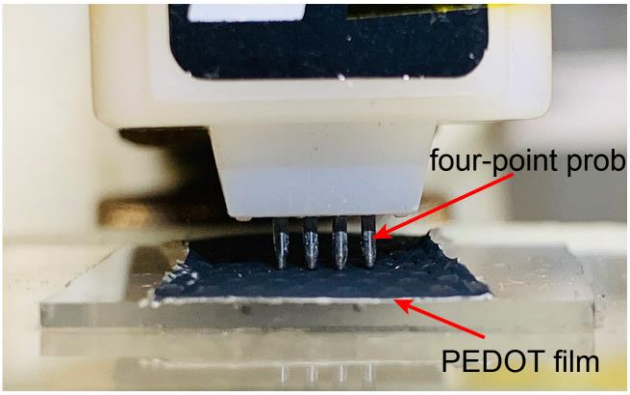

Figure 6.4: Conductivity measurement is carried out using a four-point probe station.

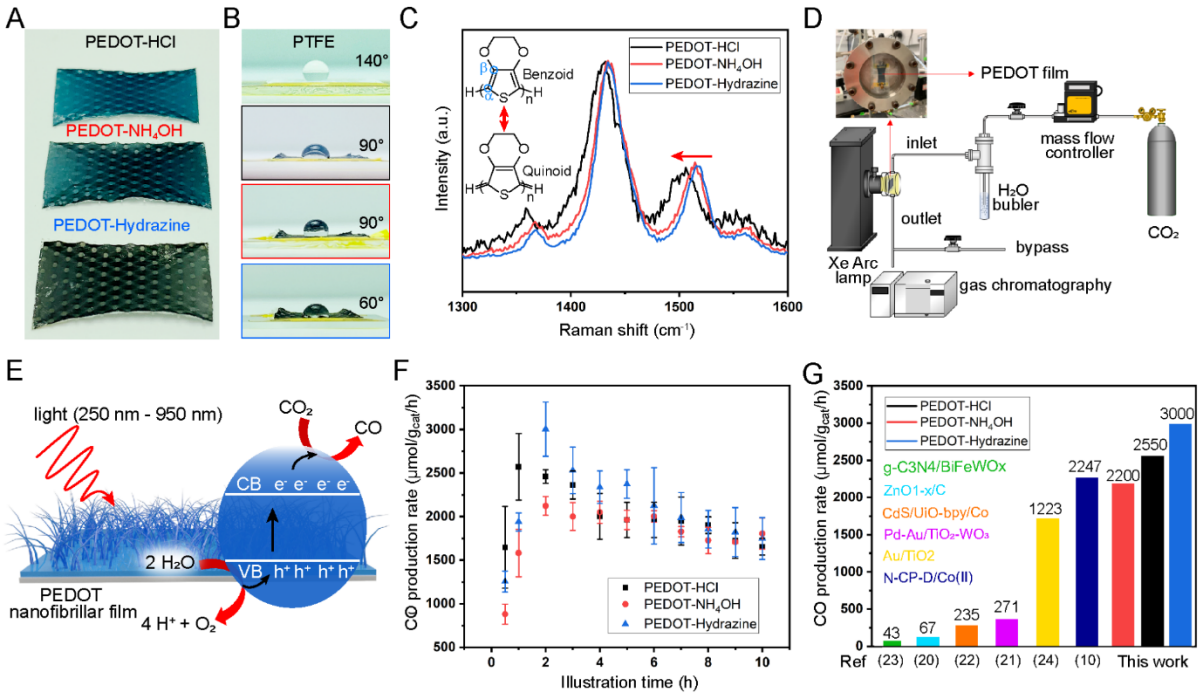

Figure 6.5: Doping/de-doping treatment of PEDOT catalyst and CO_2 photoreduction characterization. (A) Optical image of PEDOT-coated PTFE treated with HCl (doping), NH_4OH (de-doping) and hydrazine (de-doping). (B) Contact angle data show the decreasing surface energy via de-doping. (C) Raman spectra demonstrate two interchangeable polymer backbones i.e., benzoic and quinoid controlled by de-doping and doping, respectively. (D) Illustration of gas-phase CO_2 photoreduction set-up and (E) insight process of light absorption, photogeneration and charge carrier transportation. (F) Time-dependent production rate of CO versus PEDOT-HCl, PEDOT-NH_4OH and PEDOT-Hydrazine catalysts under illumination (250 nm – 950 nm). (G) Our catalysts exhibit state-of-the-art performance among multiple conventional photocatalysts.

PEDOT's CO_2 adsorption capacity is enhanced by doping/de-doping treatments with acid, base and reducing agents that alter its surface energy.[20] We investigate this property utilizing HCl (37%), NH_4OH (30%) and hydrazine to dope/de-dope a PEDOT film resulting in PEDOT-HCl (light blue), PEDOT-NH_4OH (purple) and PEDOT-hydrazine (black) samples (Figure 6.5A). Contact-angle measurements are carried out to study surface energy revealing that all PEDOT coatings decrease PTFE surface energy while the hydrazine-treated PEDOT film exhibits the wetting degree angle at 60° (Figure 6.5B). PEDOT-coated membranes promote water molecule permeability confirmed by water content using TGA (Figure 6.6), SEM (Figure 6.7) and EDX

(Figure 6.8); we suspect this is due to charged dopant effects. We gain insight into the impact of doping on chemical bonding within our materials using Raman spectroscopy. PEDOT's peak (Figure 6.5C) at 1357 cm^{-1} correspond to C_β-C_β bonds, while peaks at 1437 and 1510 cm^{-1} correspond to symmetric and asymmetric C_α=C_β stretching. The symmetric C_α=C_β stretching band shifts towards 1426 cm^{-1} after doping with HCl.[21] This shift towards higher wavenumbers corresponds to greater doping levels due to an increased ratio of quinoid vs. benzenoid structures in PEDOT and is consistent with previously reported behavior of other PEDOT films.[22]

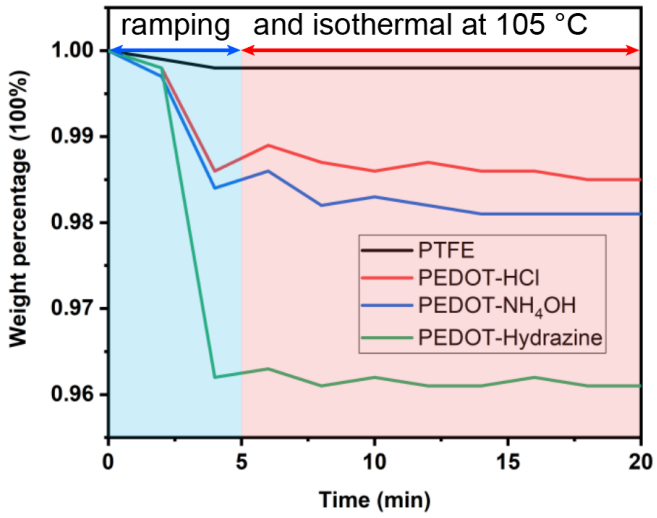

Figure 6.6: TGA of pristine PTFE and PEDOT-coated PTFE.

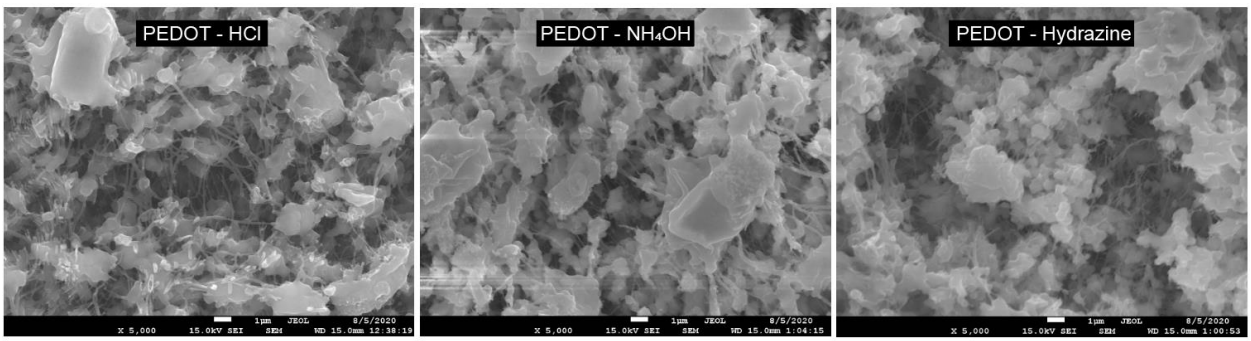

Figure 6.7: Scanning electron micrographs of PEDOT catalyst after treatment of HCl, NH_4OH, and hydrazine.

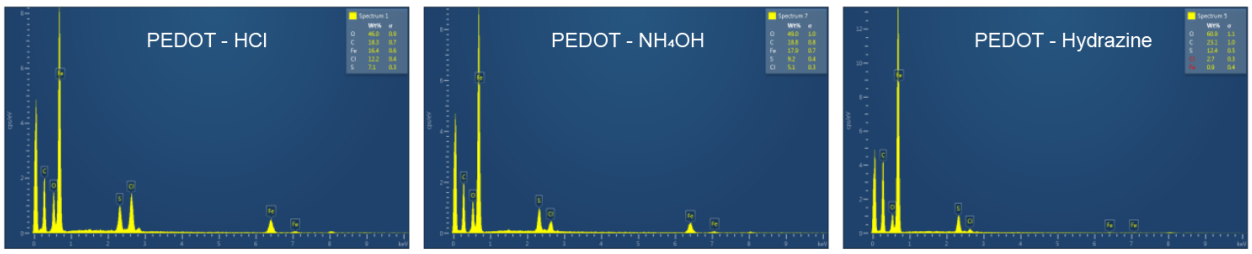

Figure 6.8: Energy-dispersive X-ray spectroscopy of PEDOT after treatment of HCl, NH_4OH, and hydrazine.

The CO_2 photoreduction properties of PEDOT films are evaluated using a photoreduction analysis system under atmospheric pressure and room temperature (Figure 6.5D). Three initial control tests are performed to establish the source of the reduction products: the first test is conducted with He as the source gas instead of CO_2, the second test is performed in the absence of PEDOT, and the third test is carried out under a lack of illumination. Carbonaceous product is absent from all three control test results demonstrating that catalysis is unfeasible in the absence of CO_2, PEDOT film or light illumination. Notably, our gas-solid interface-based photoreduction system produces nearly 100% CO as the main product because CO formation is kinetically favorable, requiring only a minimal number of electrons and protons for CO_2 reduction. Electrons and holes generated by UV-Vis-NIR light (250 - 950 nm) arrive at the photoactive PEDOT film interface (Figure 6.5E) facilitating simultaneous reduction of CO_2 (electrons) and oxidation of H_2O (holes). The PEDOT nanofibrillar morphology boosts light-harvesting because internal reflection of light is multiplied within the fibrillar nanostructure. Figure 6.5F shows the production rates of CO using three PEDOT films as a function of illumination time, initially starting after 30 min of excitation, and reaching a maximum after one or two hours. PEDOT-hydrazine exhibits the highest CO_2 photoreduction activity (3000 µmol g_{cat}^{-1} h^{-1}) followed by PEDOT-HCl (2550 µmol g_{cat}^{-1} h^{-1}) and PEDOT-NH_4OH (2200 µmol g_{cat}^{-1} h^{-1}). Thereafter production rates gradually decrease and

converge to approximately 2000 µmol g_{cat}^{-1} h^{-1} due to PEDOT photocorrosion as confirmed by UV absorption (Figure 6.9). All CO production rates decrease after reaching their maxima and remain stable for 10 h thus demonstrating excellent catalytic stability. Maximum (3000 µmol $gcat^{-1}$ h^{-1}) and average (2350 µmol $gcat^{-1}$ h^{-1}) activity rates over 10 h for the hydrazine-treated PEDOT catalyst are state-of-the-art.[23-24] Our performance is two orders of magnitude higher than the top-rated single catalyst and is surpassed by only three other co-catalyst systems (Figure 6.5G). [1, 10, 18, 25-30]

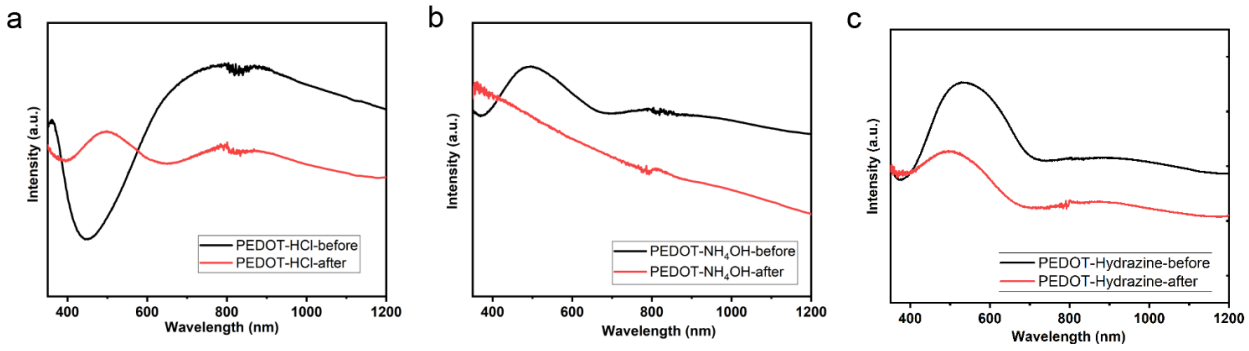

Figure 6.9: UV-vis-NIR measurement data after CO_2 photoreduction.

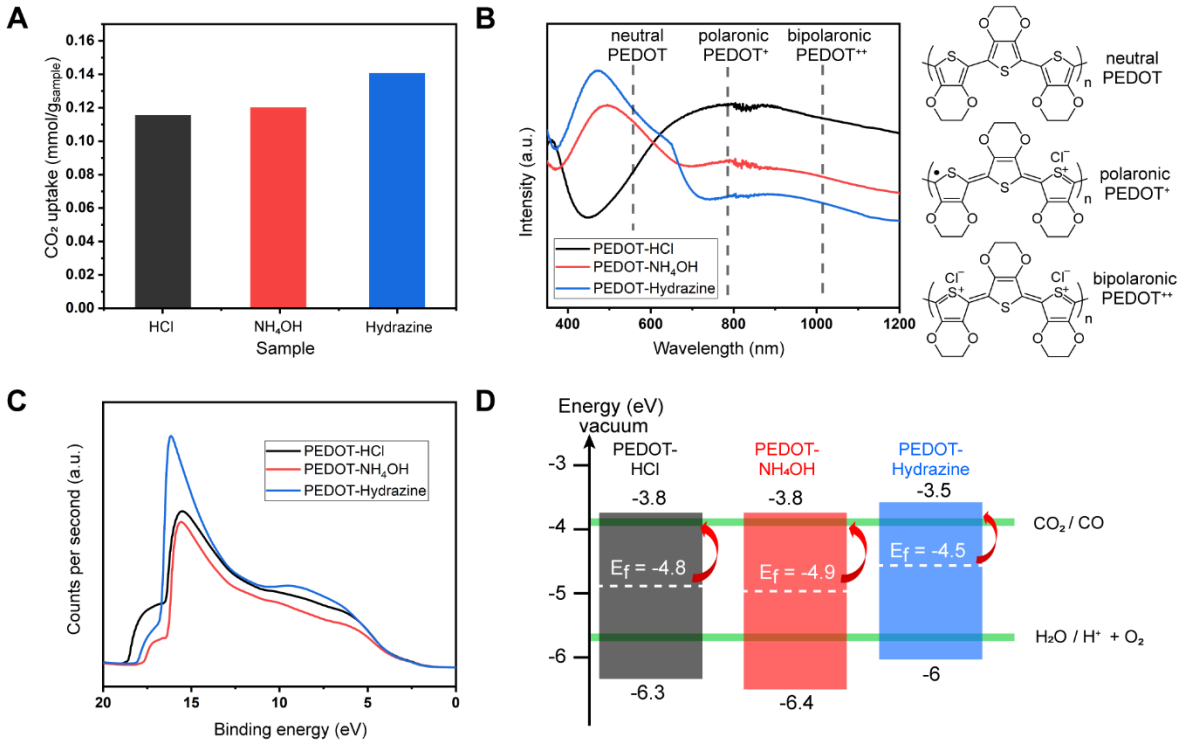

Figure 6.10: PEDOT mechanism for CO_2 photoreduction. (A) CO_2 adsorption capabilities of PEDOT-HCl, PEDOT-NH_4OH and PEDOT-Hydrazine at 80 °C. (B) UV-Vis-NIR spectra prove that both a reducing agent and base can enhance the light absorption at visible region and can partially convert polaronic PEDOT to its neutral state. (C) Ultraviolet photoelectron valence band spectra for PEDOT-HCl, PEDOT-NH_4OH and PEDOT-Hydrazine predict the secondary electron edge and onset of the density of states. (D) Proposed mechanism of charge separation/transfer and LUMO/HOMO band gap for PEDOT-HCl, PEDOT-NH_4OH and PEDOT-Hydrazine photocatalysts under a range of wavelengths (250 nm – 950 nm).

To study reduction rates among our catalysts, we investigate CO_2 adsorption, light harvesting properties and band gap structure through CO_2 uptake data, UV-Vis-NIR and ultraviolet photoelectron spectroscopy (UPS). Adsorption of CO_2 on the catalytic surface is the first step of the photocatalytic reaction, marking it as an important parameter for catalyst evaluation. The CO_2 uptake data evaluated from TGA measurements (Figure 6.10A and Figure 6.11), show the following trend: PEDOT-hydrazine (0.15) > PEDOT-NH_4OH (0.113) ≈ PEDOT-HCl (0.12), confirming that low surface energy enhances CO_2 adsorption. The π-conjugated structure of

PEDOT attracts delocalized p-conjugated electrons from CO_2 molecules prompting CO_2 uptake on catalytic surface sites.[31] The enhanced CO_2 uptake capacity exhibited by PEDOT-hydrazine may arise from increased interactions between quadrupolar CO_2 (Lewis acid) and depolarized oxygen of the ethylenedioxy ring (Lewis base) leading to greater CO_2 solubility and permeability in PEDOT-coated membranes.[32]

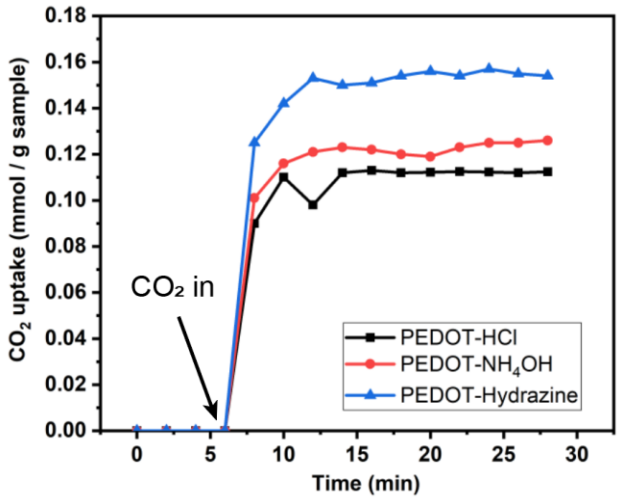

Figure 6.11: TGA isotherm for CO_2 adsorption

Another key factor for improving CO_2 photoreduction efficiency is light absorption as photons act as the energy source for photoreduction. UV-Vis-NIR spectroscopy is utilized to assess charge carrier density as a function of chemical structure and characterize changes in molecular structure caused by doping. The UV-Vis-NIR spectra of PEDOT (Figure 6.10B) is divided into three regimes i.e., neutral, polaronic and bipolaronic.[33] The wavelengths chosen for CO_2 reduction (250 nm – 950 nm) lead to higher absorbance for de-doped PEDOT-hydrazine and PEDOT-NH_4OH thereby promoting photogeneration of charge carriers as well as enhanced photocatalytic activity.

Larger absorbance in the polaronic and bipolaronic regimes for the PEDOT-HCl samples is observed because doping ions (Cl^-) help delocalization of electron cloud thereby increasing electrical conductivity.

To understand the effect of doping on charge carrier density and mobility for enhanced CO_2 photoreduction, UPS is employed to determine the valence band (VB), conduction band (CB), and Fermi level of the PEDOT catalyst (Figure 6.10C). Long tails in the VB spectrum of each PEDOT sample indicate different convoluted peaks and PEDOT-hydrazine in particular exhibits clear steps suggesting the presence of multiple hybridized states between VB and CB.[18] The work function (Fermi level energy) of the PEDOT is determined by calculating the difference between the secondary electron cutoff and the energy of an incident photon. The gap between the Fermi level and the VB maximum is the onset of photoemission of valence electrons and the CB is calculated from the VB maxima, Fermi level and band gap. An energy level diagram shows that the CB level for all PEDOT catalysts meets CO_2 reduction requirements by lying at potentials wider than that of CO_2 redox couples (Figure 6.10D). PEDOT catalysts are excited by absorbing energetic photons and produce electron-hole pairs as opposed to conventional inorganic catalysts which only allow direct excitation of electrons from the VB to the CB. The doping process introduces various hybridized middle states into PEDOT enabling electrons to jump from the sub-band to the VB. Further study is required to determine whether doping or de-doping changes the charge carrier density or charge carrier mobility. Based on our results, PEDOT-hydrazine possesses a narrower band gap requiring less excitation energy and a higher Fermi level promoting facile excitation. Moreover, the higher Fermi level also prevents the recombination process of photo-excited electrons and holes thereby facilitating photocatalytic activity.

6.4 Conclusion

In summary, we present PEDOT nanofibers as a novel single catalyst for CO_2 photoreduction and a synthetic strategy enabling conformal deposition on a superhydrophobic PTFE membrane thereby affording both high surface area and high electronic conductivity. The hydrazine-treated PEDOT catalyst demonstrates the highest CO production rate under 250 nm – 950 nm wavelengths. We achieve a state-of-the-art CO yield rate (3000 μmol g_{cat}^{-1} h^{-1}) with 100% CO yield under a stable regime (> 10h) surpassing the top performing single catalyst system by two orders of magnitude. This work overcomes challenges associated with co-catalyst systems and opens up a new avenue for CO_2 photoreduction utilizing nanofibrillar conducting polymers. Our single catalyst system represents a novel material serving as the next generation building block for developing co-catalyst systems with the potential to catapult catalytic efficiencies to new levels.

References

(1) Kaiyang Niu, Y. X., Haicheng Wang, Rong Ye, Huolin L. Xin, Feng Lin, Chixia Tian, Yanwei Lum, Karen C. Bustillo, Marca M. Doeff, Marc T. M. Koper, Joel Ager, Rong Xu, Haimei Zheng, A spongy nickel-organic CO_2 reduction photocatalyst for nearly 100% selective CO production. *Science Advances* **2017,** *3* (e1700921).

(2) Thompson, W. A.; Sanchez Fernandez, E.; Maroto-Valer, M. M., Review and Analysis of CO_2 Photoreduction Kinetics. *ACS Sustainable Chemistry & Engineering* **2020,** *8* (12), 4677-4692.

(3) Halime Coskun, A. A., Phil De Luna, Dominik Farka, Theresia Greunz, David Stifter,

Mahmut Kus, Xueli Zheng, Min Liu, Achim W. Hassel, Wolfgang Schöfberger, Edward H. Sargent, Niyazi Serdar Sariciftci, Philipp Stadler, Biofunctionalized conductive polymers enable efficient CO2 electroreduction. *Science Advances* **2017,** *3* (e1700686).

(4) Wang, Y.; Liu, X.; Han, X.; Godin, R.; Chen, J.; Zhou, W.; Jiang, C.; Thompson, J. F.; Mustafa, K. B.; Shevlin, S. A.; Durrant, J. R.; Guo, Z.; Tang, J., Unique hole-accepting carbon-dots promoting selective carbon dioxide reduction nearly 100% to methanol by pure water. *Nat Commun* **2020,** *11* (1), 2531.

(5) Chen, C.; Khosrowabadi Kotyk, J. F.; Sheehan, S. W., Progress toward Commercial Application of Electrochemical Carbon Dioxide Reduction. *Chem* **2018,** *4* (11), 2571-2586.

(6) Wang, S.; Xu, M.; Peng, T.; Zhang, C.; Li, T.; Hussain, I.; Wang, J.; Tan, B., Porous hypercrosslinked polymer-TiO2-graphene composite photocatalysts for visible-light-driven CO_2 conversion. *Nat Commun* **2019,** *10* (1), 676.

(7) Chang, X.; Wang, T.; Gong, J., CO2 photo-reduction: insights into CO2 activation and reaction on surfaces of photocatalysts. *Energy & Environmental Science* **2016,** *9* (7), 2177-2196.

(8) Dai, W.; Xu, H.; Yu, J.; Hu, X.; Luo, X.; Tu, X.; Yang, L., Photocatalytic reduction of CO_2 into methanol and ethanol over conducting polymers modified Bi_2WO_6 microspheres under visible light. *Applied Surface Science* **2015,** *356*, 173-180.

(9) Lee, S.; Kim, S.; Park, C.; Moon, G.-h.; Son, H.-J.; Baeg, J.-O.; Kim, W.; Choi, W., Nafion-Assisted Noncovalent Assembly of Molecular Sensitizers and Catalysts for Sustained Photoreduction of CO_2 to CO. *ACS Sustainable Chemistry & Engineering* **2020,** *8* (9), 3709-3717.

(10) Wang, S.; Hai, X.; Ding, X.; Jin, S.; Xiang, Y.; Wang, P.; Jiang, B.; Ichihara, F.; Oshikiri, M.; Meng, X.; Li, Y.; Matsuda, W.; Ma, J.; Seki, S.; Wang, X.; Huang, H.; Wada, Y.; Chen, H.; Ye, J., Intermolecular cascaded pi-conjugation channels for electron delivery powering CO2 photoreduction. *Nat Commun* **2020,** *11* (1), 1149.

(11) Jianwei Nai, S. W., Xiong Wen (David) Lou, Ordered colloidal clusters constructed by nanocrystals with valence for efficient CO_2 photoreduction. *Science Advances* **2019,** *5* (eaax5095).

(12) Hursan, D.; Kormanyos, A.; Rajeshwar, K.; Janaky, C., Polyaniline films photoelectrochemically reduce CO_2 to alcohols. *Chem Commun (Camb)* **2016,** *52* (57), 8858-61.

(13) Darkwah, W. K.; Teye, G. K.; Ao, Y., Graphene nanocrystals in CO_2 photoreduction with H_2O for fuel production. *Nanoscale Advances* **2020,** *2* (3), 991-1006.

(14) Cho, B.; Park, K. S.; Baek, J.; Oh, H. S.; Koo Lee, Y. E.; Sung, M. M., Single-crystal poly(3,4-ethylenedioxythiophene) nanowires with ultrahigh conductivity. *Nano Lett* **2014,** *14* (6), 3321-7.

(15) Diao, Y.; Chen, H.; Lu, Y.; Santino, L. M.; Wang, H.; D'Arcy, J. M., Converting Rust to PEDOT Nanofibers for Supercapacitors. *ACS Applied Energy Materials* **2019,** *2* (5), 3435-3444.

(16) Lu, Y.; Santino, L. M.; Acharya, S.; Anandarajah, H.; D'Arcy, J. M., Studying Electrical Conductivity Using a 3D Printed Four-Point Probe Station. *Journal of Chemical Education* **2017,** *94* (7), 950-955.

(17) Wang, W.-N.; Park, J.; Biswas, P., Rapid synthesis of nanostructured Cu–TiO2–SiO2

composites for CO_2 photoreduction by evaporation driven self-assembly. *Catalysis Science & Technology* **2011,** *1* (4), 593.

(18) Lin, L.-Y.; Kavadiya, S.; Karakocak, B. B.; Nie, Y.; Raliya, R.; Wang, S. T.; Berezin, M. Y.; Biswas, P., ZnO_{1-x}/carbon dots composite hollow spheres: Facile aerosol synthesis and superior CO_2 photoreduction under UV, visible and near-infrared irradiation. *Applied Catalysis B: Environmental* **2018,** *230*, 36-48.

(19) Diao, Y.; Lu, Y.; Yang, H.; Wang, H.; Chen, H.; D'Arcy, J. M., Direct Conversion of Fe_2O_3 to 3D Nanofibrillar PEDOT Microsupercapacitors. *Advanced Functional Materials* **2020,** *30* (32), 2003394.

(20) Arif, M.; Barifcani, A.; Lebedev, M.; Iglauer, S., Impact of Solid Surface Energy on Wettability of CO2-brine-Mineral Systems as a Function of Pressure, Temperature and Salinity. *Energy Procedia* **2017,** *114*, 4832-4842.

(21) Krieg, L.; Meierhofer, F.; Gorny, S.; Leis, S.; Splith, D.; Zhang, Z.; von Wenckstern, H.; Grundmann, M.; Wang, X.; Hartmann, J.; Margenfeld, C.; Manglano Clavero, I.; Avramescu, A.; Schimpke, T.; Scholz, D.; Lugauer, H. J.; Strassburg, M.; Jungclaus, J.; Bornemann, S.; Spende, H.; Waag, A.; Gleason, K. K.; Voss, T., Toward three-dimensional hybrid inorganic/organic optoelectronics based on GaN/oCVD-PEDOT structures. *Nat Commun* **2020,** *11* (1), 5092.

(22) Yue Wang, C. Z., Raphael Pfattner, Hongping Yan, Lihua Jin, Shucheng Chen, Francisco Molina-Lopez, Franziska Lissel, Jia Liu, Noelle I. Rabiah, Zheng Chen, Jong Won Chung, Christian Linder, Michael F. Toney, Boris Murmann, Zhenan Bao, A highly stretchable, transparent, and conductive polymer. *Science Advances* **2017,** *3* (e1602076).

(23) Di, J.; Zhu, C.; Ji, M.; Duan, M.; Long, R.; Yan, C.; Gu, K.; Xiong, J.; She, Y.; Xia, J.;

Li, H.; Liu, Z., Defect-Rich Bi12 O17 Cl2 Nanotubes Self-Accelerating Charge Separation for Boosting Photocatalytic CO2 Reduction. *Angew Chem Int Ed Engl* **2018,** *57* (45), 14847-14851.

(24) Yu, X.; Yang, Z.; Qiu, B.; Guo, S.; Yang, P.; Yu, B.; Zhang, H.; Zhao, Y.; Yang, X.; Han, B.; Liu, Z., Eosin Y-Functionalized Conjugated Organic Polymers for Visible-Light-Driven CO2 Reduction with H2 O to CO with High Efficiency. *Angew Chem Int Ed Engl* **2019,** *58* (2), 632-636.

(25) Zhu, Z.; Huang, W.-R.; Chen, C.-Y.; Wu, R.-J., Preparation of Pd–Au/TiO2–WO3 to enhance photoreduction of CO2 to CH4 and CO. *Journal of CO2 Utilization* **2018,** *28*, 247-254.

(26) Chen, C.; Wu, T.; Wu, H.; Liu, H.; Qian, Q.; Liu, Z.; Yang, G.; Han, B., Highly effective photoreduction of CO2 to CO promoted by integration of CdS with molecular redox catalysts through metal-organic frameworks. *Chem Sci* **2018,** *9* (47), 8890-8894.

(27) Wang, Y.; Zeng, Y.; Wan, S.; Cai, W.; Song, F.; Zhang, S.; Zhong, Q., In Situ Fabrication of 3D Octahedral g-C3N4/BiFeWOx Double-Heterojunction for Highly Selective CO2 Photoreduction to CO Under Visible Light. *ChemCatChem* **2018,** *10* (20), 4578-4585.

(28) Tahir, M., Synergistic effect in MMT-dispersed Au/TiO2 monolithic nanocatalyst for plasmon-absorption and metallic interband transitions dynamic CO2 photo-reduction to CO. *Applied Catalysis B: Environmental* **2017,** *219*, 329-343.

(29) Gao, C.; Meng, Q.; Zhao, K.; Yin, H.; Wang, D.; Guo, J.; Zhao, S.; Chang, L.; He, M.;

Li, Q.; Zhao, H.; Huang, X.; Gao, Y.; Tang, Z., Co3 O4 Hexagonal Platelets with Controllable Facets Enabling Highly Efficient Visible-Light Photocatalytic Reduction of CO2. *Adv Mater* **2016,** *28* (30), 6485-90.

(30) Zhong, W.; Sa, R.; Li, L.; He, Y.; Li, L.; Bi, J.; Zhuang, Z.; Yu, Y.; Zou, Z., A Covalent Organic Framework Bearing Single Ni Sites as a Synergistic Photocatalyst for Selective Photoreduction of CO2 to CO. *J Am Chem Soc* **2019,** *141* (18), 7615-7621.

(31) Lee, J. H.; Jung, J. P.; Jang, E.; Lee, K. B.; Hwang, Y. J.; Min, B. K.; Kim, J. H., PEDOT-PSS embedded comb copolymer membranes with improved CO2 capture. *Journal of Membrane Science* **2016,** *518*, 21-30.

(32) Hong, J. Y.; Huh, S., Hollow S-doped carbon spheres from spherical CT/PEDOT composite particles and their CO(2) sorption properties. *J Colloid Interface Sci* **2014,** *436*, 77-82.

(33) Lu, Y.; Kacica, C.; Bansal, S.; Santino, L. M.; Acharya, S.; Hu, J.; Izima, C.; Chrulski, K.; Diao, Y.; Wang, H.; Yang, H.; Biswas, P.; Schaefer, J.; D'Arcy, J. M., Synthesis of Submicron PEDOT Particles of High Electrical Conductivity via Continuous Aerosol Vapor Polymerization. *ACS Appl Mater Interfaces* **2019,** *11* (50), 47320-47329.

Chapter 7

Highly Conductive PEDOT Film with Enhanced Catalytic Activity for Dye-Sensitized Solar Cells

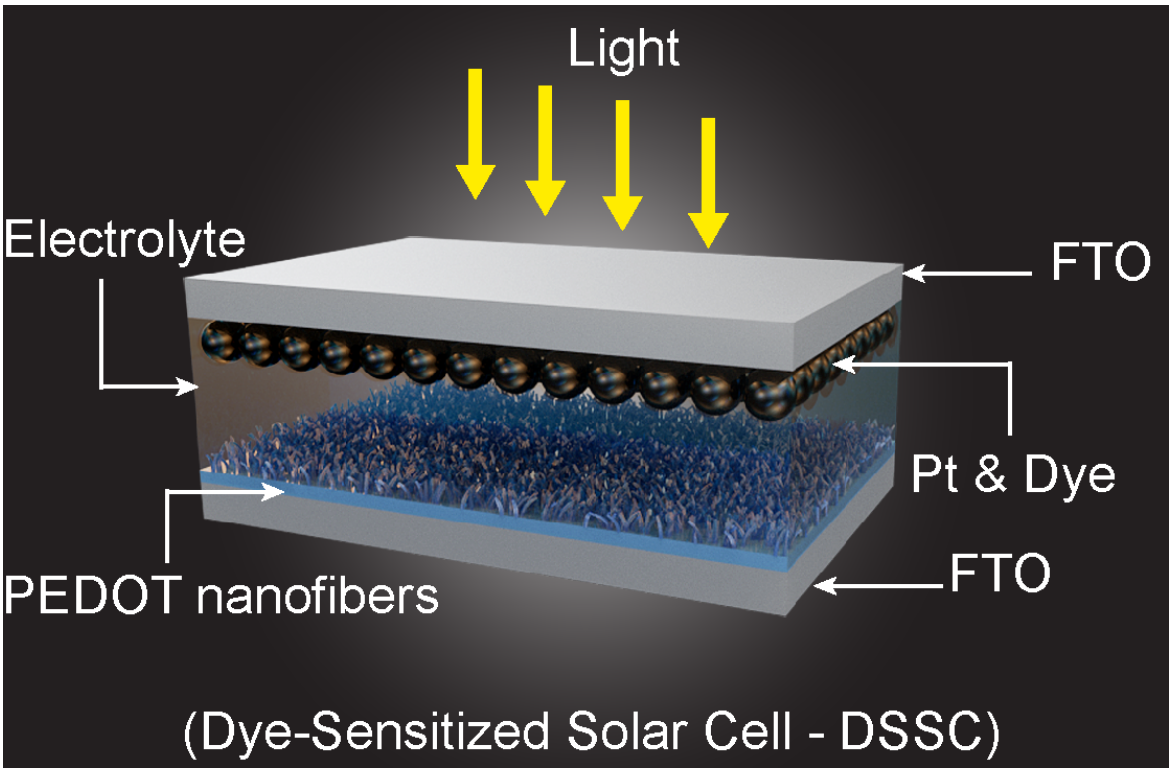

PEDOT nanofiber-based counter electrode DSSC

7.1 Introduction

Dye-sensitized solar cells (DSSCs) are low cost and simple to make, and they have a relatively high conversion efficiency of ~12%.[1] Generally, DSSCs consist of a porous TiO_2 electrode sensitized with an absorbing layer, an electrolyte, and a platinum (Pt) counter electrode (CE). In DSSCs, CE are used to reduce an oxidized redox couple, to collect and transmit the electrons back into the cell, and to reflect unabsorbed light back to the cell, enhancing the utilization of solar energy. To ensure an efficient redox reaction in the electrolyte, an ideal CE should possess high conductivity, high electrochemical and mechanical stability, and high catalytic activity. Pt, because of its high conductivity and excellent catalytic activity toward I_3^- (iodide) reduction, is the most nearly ideal CE in DSSC.[2] However, large-scale use of Pt is limited by its low stability in the redox electrolyte, as well as by its high cost and rarity.[3-5] An alternative CE is highly desirable, one with low-cost fabrication, easy scalability, high photocorrosion stability, and relatively high conversion efficiency. To this end, many works have carried out to substitute Pt with suitable alternatives, such as carbonaceous material,[3-4, 6-7] metal oxide,[8-10] and polymers.[11-12] Among these alternatives, polymers are advantageous for their low cost and high catalytic activity.[13-17] Polypyrrole (PPy), polyaniline (PANI),[15] and poly (3,4 ethylenedioxythiophene) (PEDOT)[18] are commonly used as conductive polymer CEs in DSSC or as hole transporting materials in perovskite solar cells.[19-23] Amongst them, PEDOT is attractive as it possesses the highest transparency, stability, and catalytic activity.[24] Its conductivity, 300–600 S/cm, is also much higher than those of PANI (~5 S/cm) and PPy (~50 S/cm).[18, 25-28] However, the existing conductivity can be increased by various methods, such as by annealing at elevated temperatures,[29] acid treatment, adding co-solvents,[30-31] and doping to enhance the crystallization of the films.[32-33] Zhang et al.[24] used cyclic voltammetry (a three-

electrode system) to deposit three different CEs with different carbon doped polymers to fabricate a DSSC with C160 ruthenium dye. PEDOT + carbon black (C) exhibited the highest efficiency, 7.6%, compared to PANI + C and PPY + C with efficiencies of ~ 5.2%, prepared under the same experimental condition. Typically, PEDOT films are generated via electrochemical polymerization under constant voltage or constant current, which results in low electrical conductivity.[24, 34-35] For example, Li et al.[36] report a PEDOT/rGO composite film possessing a conversion efficiency of 7.115%; however, their electrochemical method requires a potentiostat, a three-electrode system, and refined control of voltage, all of which decrease the film's reproducibility. Alternatively, toluenesulfonate, ClO, poly(styrenesulfonate) (PSS),[31] TsO;[37] and polyoxometalate (POM)) are frequently employed as dopants to increase the solubility or electrical conductivity of PEDOT. The water solubility and simple fabrication process of PEDOT:PSS make it an interesting industrial polymer. G. T. Yue et al.[31] deposited PEDOT:PSS/carbon on an fluorine doped tin oxide (FTO) glass with a scratch method under infrared light irradiation and used it as a CE for DSSC. They achieved the highest reported conductivity for a PEDOT:PSS/carbon electrode, 173 S/cm, and a resulting cell efficiency of 7.6%. Another synthesis approach is oxidative vapor phase polymerization (VPP) using various oxidants such as $MoCl_5$,[38] $Fe(ClO_4)_3$,[39] and FeCl.[40-42] However, these oxidants require fabrication in a controlled environment.[43] Bjorn et al. synthesized a PEDOT film via chemical vapor deposition (CVD) by controlling the humidity and pressure, achieving a PEDOT conductivity of only 1000 S/cm.[43] It is worth noting that single-crystal PEDOT has a reported electrical conductivity as high as 8797 S/cm, which is significantly higher than that observed in the thin films desired for electronic devices.[44] These limitations highlight the urgency of advancing current PEDOT film fabrication protocols so that they are facile, cheap, and yield high conductivity. Several methods have been proposed, mainly using VPP

with $FeCl_3$ as an oxidant, but to the best of our knowledge our method has never been applied in DSSC. Herein, we present a low-cost approach for engineering superior quality PEDOT films on FTO glass, using iron oxide (rust) -based vapor-phase polymerization (RVPP).[45] We used Fe_2O_3 (rust) as an oxidant because it is the cheapest and most thermodynamically stable Fe phase. The electronic conductivity of the films is reported. The film as synthesized was used as a CE in a Pt-free DSSC.

7.2 Experimental methods

7.2.1. Counter electrode preparation

FTO glass substrates (TEC™ 7) were purchased from MSE supplies LLC, USA. First, the FTO glass substrates were washed via ultrasonic baths in acetone and then in isopropyl alcohol for 20 min, each. Then they were treated under UV-ozone for 30 min to remove remaining organic impurities. Next, a solid-oxidant precursor, 20-nm thick Fe_2O_3, was sputtered over the FTO via physical vapor deposition (Kurt J. Lesker PVD 75 RF and DC). A glass reactor was loaded with the Fe_2O_3-coated FTO, 40 μL of HCl, and 200 μL of a 0.674 M EDOT solution in chlorobenzene, then sealed and heated in an oven at 140 ◦C for 1.5 hr. The samples were purified via 6 M HCl overnight to remove iron impurities (Figure 7.1). The sputtered α-Fe2O3 was used as a ferric ion-containing solid-state oxidant precursor to induce dissolution, liberation of ferric ions, and Fe^{3+} hydrolysis concomitant with oxidative radical polymerization.

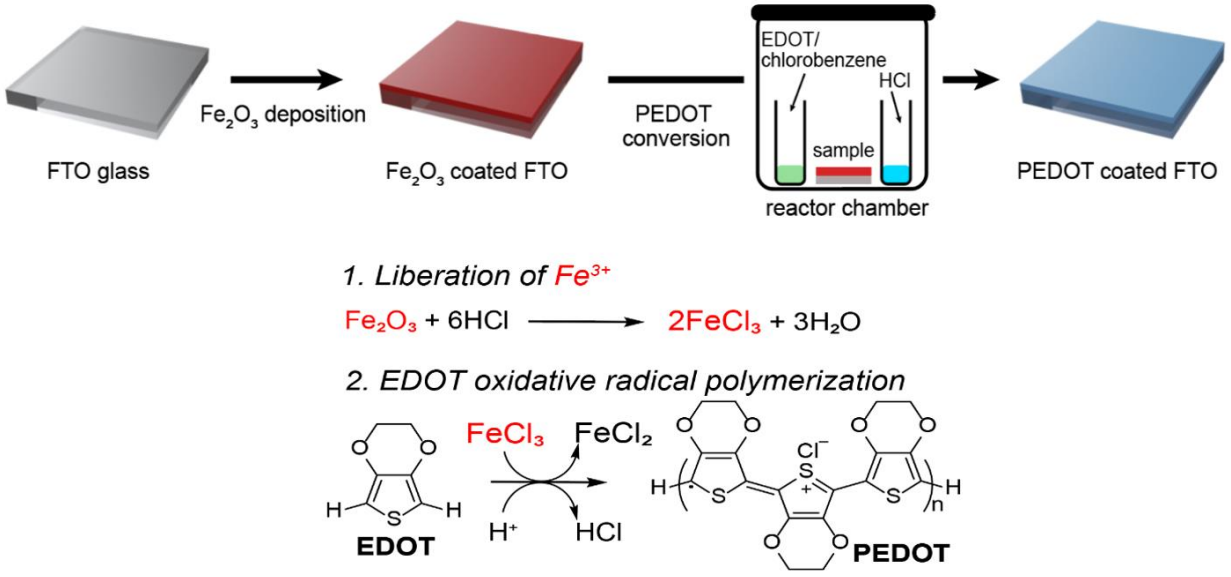

Figure 7.1: Schematic diagram of PEDOT/FTO fabrication and its Mechanistic scheme for the liberation of Fe^{3+} and formation of PEDOT via step-growth polymerization.

7.2.2. Solar cell materials and device fabrication process

A working electrode was made of two layers of screen printed TiO_2 nanoparticles (transparent TiO_2 and a reflective TiO_2) treated with $TiCl_4$, resulting in an overall thickness of 12–16 μm. The final TiO_2 film was then annealed at 450 °C for 30 min before immersing it in a dye solution of N719, 20 mg/mL in ethanol. The working electrode was soaked in the dye solution after being cooled to 70 °C. After 12 h, it was rinsed with ethanol, and dried. The Pt electrode was made by drop casting Plastisol T/SP precursor solution on the FTO glass and was used as the reference CE. Finally, both the CE and the working electrode were clipped together and filled with Iodolyte AN-50 (Solaronix, Aus) electrolyte. Then the cell was tested under ambient conditions (30–50% relative humidity) and AM1.5 illumination.

7.2.3. Characterization

To investigate their crystal structure, PEDOT films were characterized with an X-ray diffractometer (XRD, Bruker D8 ADVANCE, Bruker, USA) configured with a 1.5418 Å Cu X-ray operating at 40 kV. Field emission scanning electron microscopy (FE-SEM, Nova NanoSEM 230) also used to investigate the surface morphology of the PEDOT films on the FTO substrate. Four-point probe measurements were carried out using a Keithley 2450 SourceMeter with a Signatone SP4 four-point probe head. Cyclic voltammetry (CV) analysis and electro impedance spectroscopy (EIS) were conducted using a BioLogic VMP3 multipotentiostat. CV was carried out with three-electrode configurations at a scan rate of 50 mV/s. Ag/AgCl (3 M KCl) was used as a reference electrode, Pt and PEDOT films were the working electrodes, and Pt wire was the CE, in an acetonitrile solution containing LiI (10 mM), I_2 (1 mM), and $LiClO_4$ (0.1 M) as supporting electrolytes. The surface area of the CEs was 1 cm^2. EIS characterization was carried out using a symmetric cell, which consisted of two same CEs facing each other (Pt-Pt and PEDOT-PEDOT), and the space between the CEs was filled with the same electrolyte as used in full DSSC. EIS was operated at open circuit voltage using an ac perturbation of 10 mV and a frequency range 100 kHz to 0.1 Hz. The spectra were then analyzed by fitting the arc observed at the highest frequency in Nyquist plots to the equivalent circuit, which contained the series resistance (Rs), charge transfer resistance (RCT), and constant phase element (CPE).

7.3 Results & discussion

7.3.1. Morphology and crystal structure of PEDOT CE

Figure 7.2a shows a SEM image of a PEDOT film on an FTO glass substrate. The film consists of bundles and nanofibers that result from, respectively, the removal of iron crystals formed during iron hydrolysis and EDOT oxidative radical polymerization through RVPP.[45-46]

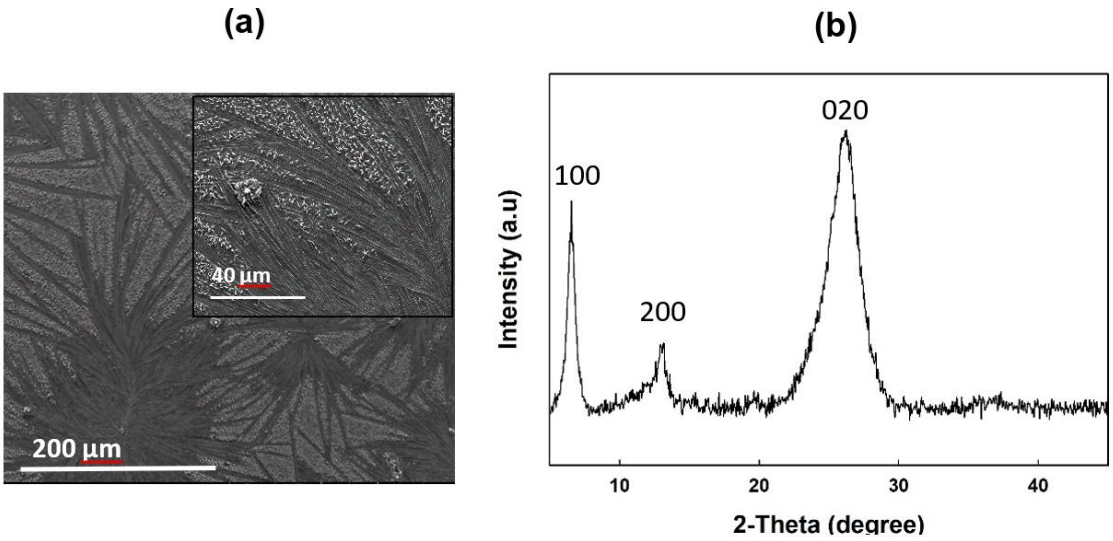

Figure 7.2: (a) SEM image of a PEDOT film on an FTO substrate (b) XRD spectra of a PEDOT film on a glass substrate.

Figure 7.2b shows XRD patterns of the same PEDOT film on a glass substrate. Three characteristic peaks are centered at 6.5 °, 13.0 °, and 26.5 °. The wide diffraction peak at 26.5 ° corresponds to the (020) reflection, which is due to π-π stacking, whereas the sharp peaks at 6.5 ° and 13.0 ° are assigned to (200) and (100) reflections, respectively, and correspond to lateral chain packing. A four-point probe conductivity measurement was also carried out and demonstrated an exceedingly high conductivity of 1120 S/cm, mainly the result of the PEDOT crystal structure and its high

charge carrier concentration.[47] The thickness of the PEDOT film is around 200 nm, measured using a profilometer (Figure 7.3).

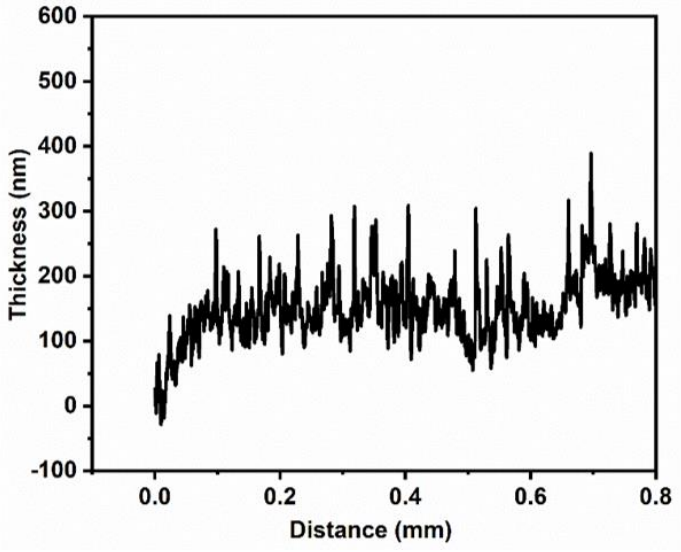

Figure 7.3: Profilometer data of PEDOT thin film

7.3.2. Electrochemical properties of PEDOT CE

The electrocatalytic activities of the PEDOT CEs were evaluated by CV to quantify the electrocatalytic activities of the CEs in the electrolyte. The Pt CE was also prepared under the same experimental conditions for comparison. In CV analysis, the oxidation of I- and the reduction of I_3^- are the major redox reactions, corresponding to the anodic (J_{pa}) and cathodic (J_{pc}) peak current densities, respectively.

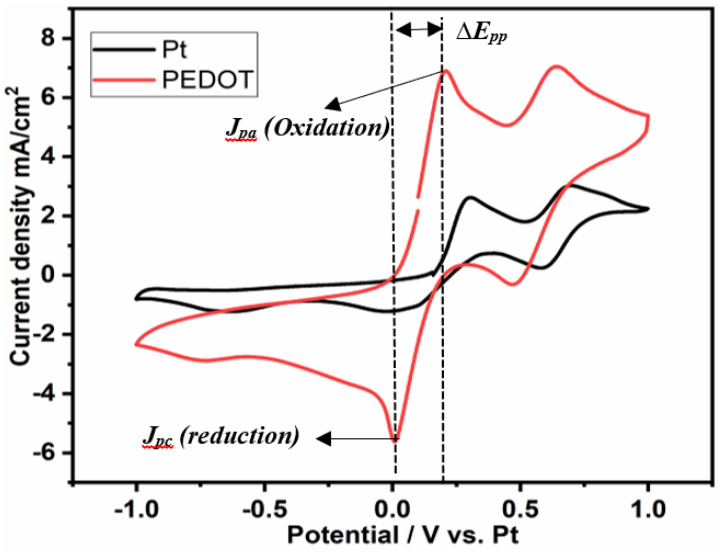

Figure 7.4: Cyclic voltammograms of Pt and PEDOT film as counter electrode for DSSC at a scan rate of 50 mV/s.

These peaks are labeled in Figure 7.4, which shows the CV diagrams of PEDOT and Pt CEs. J_{pa} in CV is not important to us, because the main role of a CE is to prompt the reduction of I3- in the DSSC. Therefore, J_{pc} and the potential difference between the J_{pa} and J_{pc} (ΔE_{pp}) are our focuses in this graph. The very high *Jpc* value of PEDOT (6.0 mA/cm^2), compared to Pt electrode with a J_{pc} of 2.7 mA/cm^2, indicates the outstanding electrocatalytic activity of the PEDOT CE in the I^{3-} reduction reaction.[48] The lower peak potential separation (ΔE_{pp}) for PEDOT film also shows a quicker reaction rate for the reduction of I3- to I-. Both factors together result in higher values of the short-current density (J_{SC}) and fill factor (*FF*) in a complete cell, owing to higher charge transfer through the electrolyte and CE interface and a lower recombination rate at the electrolyte and working electrode interface, respectively.

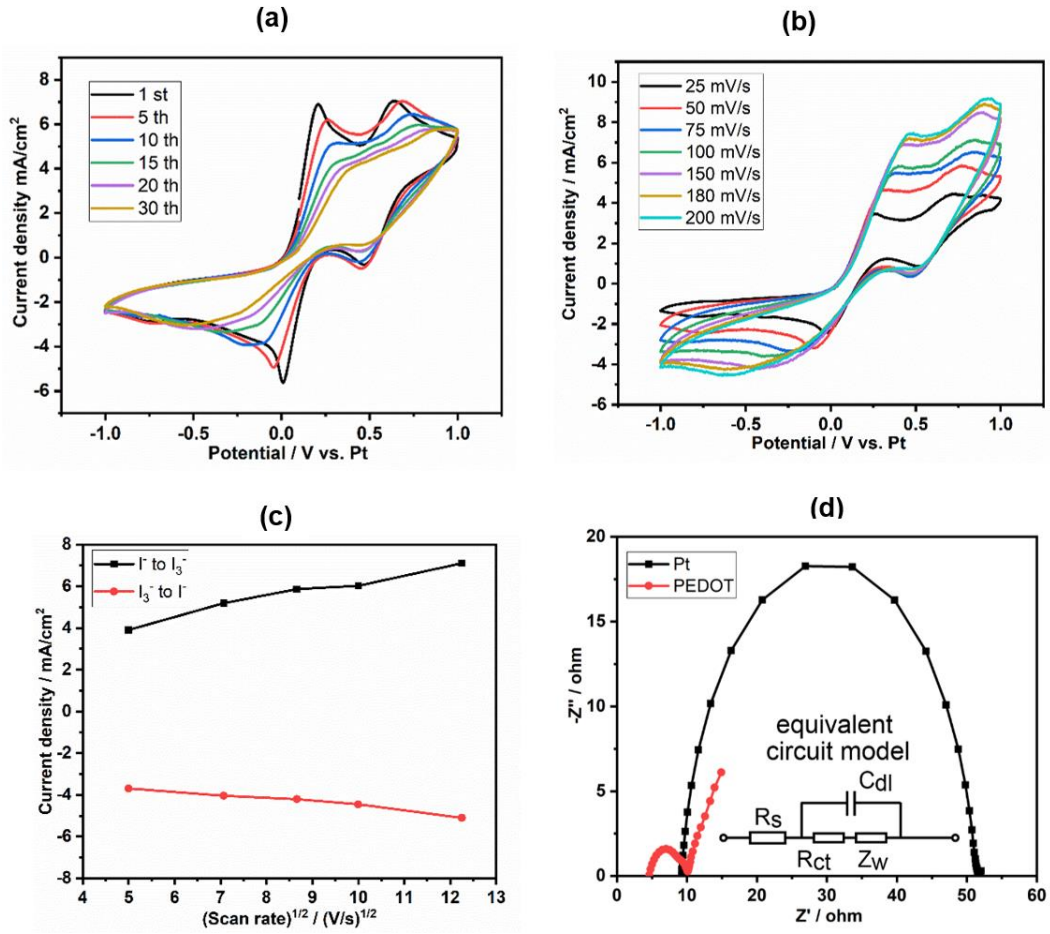

Figure 7.5: CV of Pt and PEDOT film using acetonitrile solution containing 0.1 M of $LiClO_4$, 10 mM of LiI, 1 mM of I_2 as supporting electrolyte, (a) at fix scan rate of 50 mV/s, cycle times = 30; (b) with different scan rates (from inner to outer: 25, 50, 75. . .200 mV/s) ;(c) and the redox peaks current versus square root of scan rate at different scan rates from 25 mV/s to 200 mV/s ; (d) Nyquist plots of the symmetric CE-CE cells and the equivalent circuit models for I^-/ I_3^- reaction. Rs: series resistance; R_{ct}: charge-transfer resistance at CE/electrolyte interface; C_{dl}: double layer capacitance; W: diffusion resistance.

Figure 7.5a shows 30 successive scan cycles of the PEDOT CE at a fixed scan rate. The peak current densities change with the change in scan rate, while the potential remains unchanged, which indicates that the PEDOT film possesses good chemical stability and is firmly coated on the FTO substrate.[31] Figure 7.5b displays the CVs of the PEDOT at scan rates ranging from 25 mV/s to 200 mV/s. As the scan rate is increased, the cathodic and anodic peaks slowly shift in the

negative and positive directions, respectively. In addition, Figure 7.5c shows a linear relationship between the current density and the square root of the scan rate, indicating that the reduction reaction of the redox couples at the PEDOT CE is controlled by ionic diffusion of iodide species within the electrolyte, and accordingly follows the Randles-Sevcik equation.[49-50] We further investigated the electrochemical features of the CEs by EIS measurements in a symmetric cell in which the iodine electrolyte solution was filled in the interspaces of two facing identical CEs to eliminate the effect of the photoanode. A fixed electrode area of 1 cm^2 was used for these measurements. Figure 7.5d shows the Nyquist plot of the real impedance, Z', on the x-axis versus the imaginary impedance, -Z", on the y-axis for Pt and PEDOT cells. The intercept of the high frequency (100 kHz) semicircle on the x-axis represents the series resistance (R_s). The diameter of the high-frequency semicircle equals both the charge transfer resistance (R_{ct}) at the CE/electrolyte interface as well as the redox species (I^-/I_3^-) diffusion resistance (Z_w) in the electrolyte. The equivalent RC circuit model is also given in inset (d) of Figure 7.5 and was used to obtain the EIS parameters (R_S, R_{ct}, Z_w) by fitting the impedance spectra to the equivalent model. The R_s value, known as the equivalent series resistances (ESR: x-axis intercept), which is mainly associated with the contact between current collector and CE, the resistance of CE as well as the electrolyte resistance at CE surface. The Nyquist plot of our PEDOT CE possess much lower ESR (4.3 Ω) compare to PT (9.2 Ω). The value of R_{ct} for the PEDOT film (7 Ω) is similarly six times lower than that for the Pt film (42 Ω), indicating a higher charge transfer process at the electrolyte and PEDOT CE interface. This difference can be associated with the high conductivity and catalytic activity of the PEDOT, which facilitate the transmission of the electrons across the PEDOT film/FTO interface. Therefore, we can expect higher photovoltaic performance from a DSSC using a PEDOT CE. Bode phase plot of the Pt and PEDOT CEs is also provided in Figure 7.6.

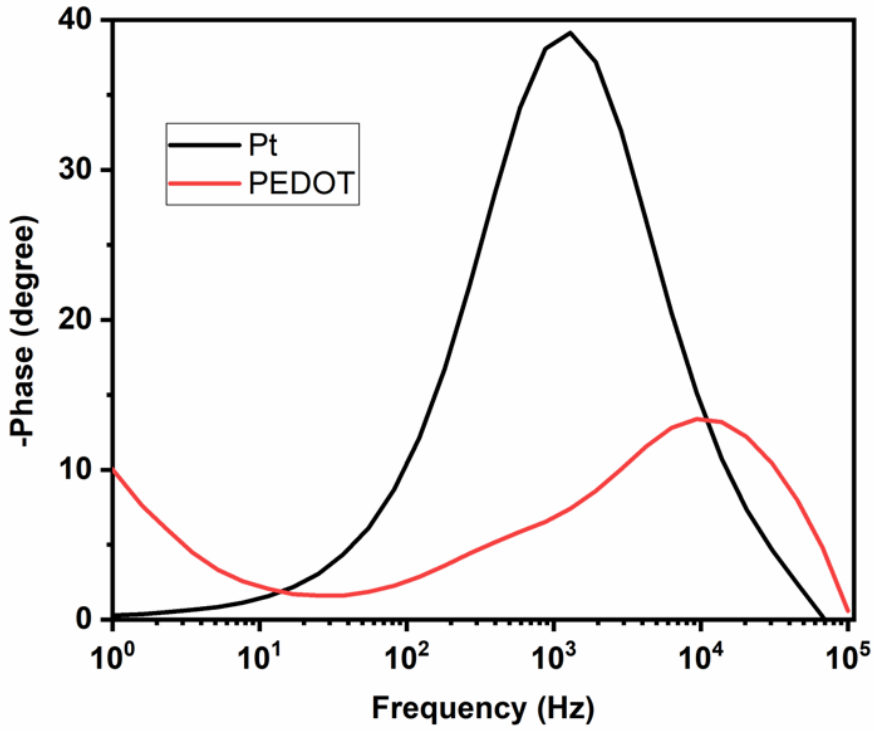

Figure 7.6: Bode plot for PEDOT and Pt counter electrode

Typically, the high-frequency peak in the bode phase plots are reflecting the Rct (charge transfer), and a smaller peak phase or higher frequency often indicates lower R_{ct}.[51] Our PEDOT CE possess a peak around 13 ° which is smaller than the Pt CE (39 °) at higher frequency that suggesting our PEDOT CE exhibits lower charge transfer resistance. Furthermore, obvious shift in the characteristic response peaks at high-frequency regime implies a faster electron transfer at the interface between PEDOT and electrolyte when compare to Pt CE.[52-53]

7.3.3. Photovoltaic performance of PEDOT CE in DSSC

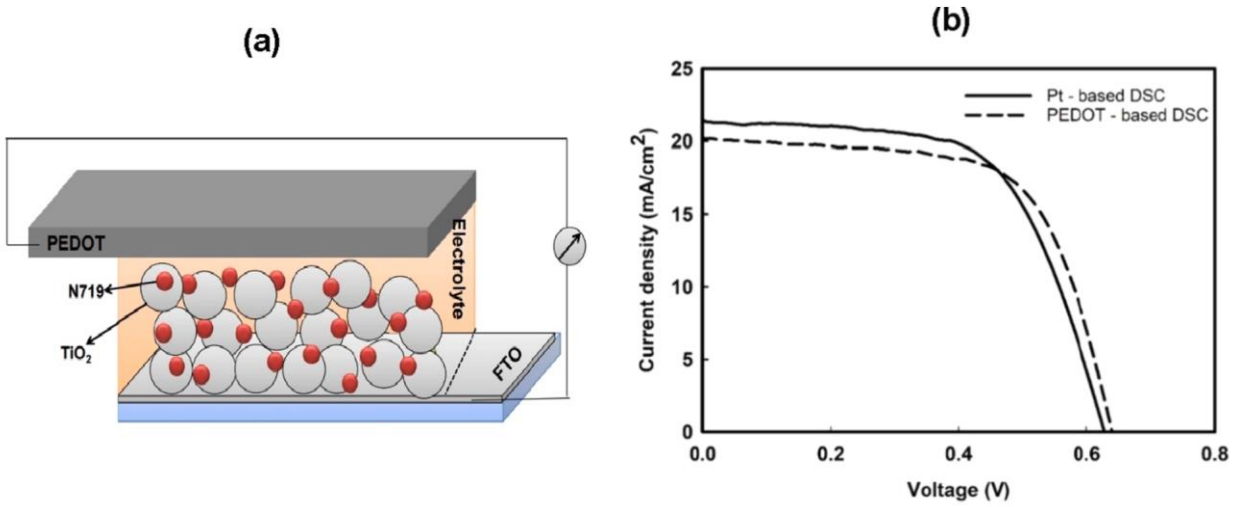

Figure 7.7: (a) Schematic diagram of a DSSC using a PEDOT film as a CE and (b) Photocurrent-voltage characteristics of DSSCs with the PEDOT and Pt CEs under the illumination of AM 1.5 G.

Table 7.1: photovoltaic parameters of the DSSCs assembled with PEDOT and Pt CEs under the illumination of AM 1.5.

Cell name	J_{sc} **(mA/cm^2)**	V_{oc} **(V)**	***FF* (%)**	**η (%)**
PEDOT-based DSSC	20.24	0.64	0.65	8.42
Pt-based DSSC	21.47	0.64	0.61	8.38

The photovoltaic performances of DSSCs with PEDOT and Pt CEs were evaluated under ambient conditions. Figure 7.7a is a schematic of the full cell, using FTO/TiO_2 as the working electrode and PEDOT as the CE. For comparison, Figure 7.7b plots the photocurrent density–photovoltage (*J*–*V*) of DSSCs using PEDOT and Pt as CEs, and Table 7.1 lists their photovoltaic parameters. The open-circuit voltage (V_{OC}) values of both CEs, as listed in Table 7.1, are the same because we used the same TiO_2 as the working electrode for both cells. The DSSC with a PEDOT CE presents

a high J_{sc} of 20.24 mA/cm^2, which is slightly lower than the Pt electrode due to the higher intrinsic electrical conductivity of the Pt. However, a higher FF value is observed for the PEDOT film, which we attribute to its low R_{ct} and excellent electrochemical catalytic activity. Moreover, the comparably high J_{sc} and *FF* values can be originated from the improved contact area between the PEDOT CE and the electrolyte.[54] In general, high performance of the CE originates due to three factors, (i) the intrinsic electrocatalytic activity of CE, (ii) large contact area between the CE and the electrolyte, and (iii) the good adhesion between the CE and the substrate.[55] Here in this study, good contact area between the CE and the electrolyte can be seen from high catalytic activity of the PEDOT CE to reduce iodine to triiodide as evidence by CV analysis shown in Figure 7.4, while good adhesion of PEDOT to the substrate can be confirmed from Figure 7.5a showing 30 successive CV of PEDOT electrode in an iodine containing electrolyte solution. Moreover, the porous structure of the PEDOT film (Figure 7.2a) can further improve the contact area between CE and electrolyte by providing more surface area for the electrolyte to react with the CE. As a result, the PEDOT-based cell achieved an efficiency of 8.4%, among the highest of values reported in the literature, some of which are listed in Table 7.2. Notably, our synthesis approach is facile and cheap because we use a rust layer as the oxidant and the reaction occurs in a simple glass vial at a low temperature.

Table 7.2: PEDOT films with different fabrication strategies, taken from the references

CE	Conductivity (S/cm)	Reaction condition	Efficiency (%)	Reference
PEDOT	**1120**	**Rust-based vapor-phase polymerization**	**8.4**	**(this work)**

PEDOT/rGO[a]	----	Potentiostat (three-electrode system) with applied voltage	7.1	[36]
PEDOT	---	Oxidative molecular layer deposition using $MoCl_5$ as an oxidant	7.2	[38]
PEDOT	357	Humidify chamber with low pressure and gas purge system using $Fe(ClO_4)_3$ as an oxidant	6.1	[39]
PEDOT/CNT[b]	45.2	$FeCl_3$	4.62	[34]
PEDOT	195	Potentiostat (three-electrode system) with applied voltage	7.8	[49]
Graphene/ PEDOT:PSS	6.24	Electrospray using applied voltage	8.3	[18]
Carbon +PEDOT	----	Potentiostat (three-electrode system) with applied voltage	7.6	[24]
PEDOT:PSS	172	Scratch method under infrared light irradiation	7.6	[31]

[a]Reduced graphene oxide, [b]Single wall carbon nanotube;

7.4. Conclusion

Highly conductive and low-cost PEDOT films were successfully deposited on an FTO glass substrate via rust-based vapor-phase polymerization (RVPP) and used as the CE in a DSSC. CV and EIS measurements revealed a highly efficient electrochemical catalysis of the PEDOT CE, accelerating the triiodide to iodide reduction and ensuring fast electron transport at the CE/electrolyte interface. The PEDOT CE also showed a high *FF* (65%) and conversion efficiency (8.4%), slightly outperforming Pt CEs. Compared to costly and rare Pt-based CEs, the inexpensive and simple fabrication method of our PEDOT CE, in addition to its high conductivity and excellent efficiency, make it a promising candidate for large scale DSSC applications.

References

(1) GRATZEL, M., Recent Advances in Sensitized Mesoscopic Solar Cells. *Accounts of Chemical Research* **2009,** *42* (11).

(2) Briscoe, J.; Dunn, S., The Future of Using Earth-Abundant Elements in Counter Electrodes for Dye-Sensitized Solar Cells. *Adv Mater* **2016,** *28* (20), 3802-13.

(3) Kouhnavard, M.; Ludin, N. A.; Ghaffari, B. V.; Sopian, K.; Ikeda, S., Carbonaceous materials and their advances as a counter electrode in dye-sensitized solar cells: challenges and prospects. *ChemSusChem* **2015,** *8* (9), 1510-33.

(4) Kouhnavard, M.; Ahmad Ludin, N.; Vazifehkhah Ghaffari, B.; Sopian, K.; Abdul Karim, N.; Miyake, M., An Efficient Metal-Free Hydrophilic Carbon as a Counter Electrode for Dye-Sensitized Solar Cells. *International Journal of Photoenergy* **2016,** *2016,* 1-7.

(5) Espen Olsen, G. H., Sten Eric Lindquist, Dissolution of platinum in methoxy propionitrile containing LiI/I2. *Solar Energy Materials & Solar Cells* **2000,** *63*, 267-273.

(6) Ren, H.; Shao, H.; Zhang, L.; Guo, D.; Jin, Q.; Yu, R.; Wang, L.; Li, Y.; Wang, Y.; Zhao, H.; Wang, D., A New Graphdiyne Nanosheet/Pt Nanoparticle-Based Counter Electrode Material with Enhanced Catalytic Activity for Dye-Sensitized Solar Cells. *Advanced Energy Materials* **2015,** *5* (12), 1500296.

(7) Zheng, X.; Deng, J.; Wang, N.; Deng, D.; Zhang, W. H.; Bao, X.; Li, C., Podlike N-doped carbon nanotubes encapsulating FeNi alloy nanoparticles: high-performance counter electrode materials for dye-sensitized solar cells. *Angew Chem Int Ed Engl* **2014,** *53* (27), 7023-7.

(8) Guo, W.; Zhang, X.; Yu, R.; Que, M.; Zhang, Z.; Wang, Z.; Hua, Q.; Wang, C.; Wang, Z. L.; Pan, C., CoS NWs/Au Hybridized Networks as Efficient Counter Electrodes for Flexible Sensitized Solar Cells. *Advanced Energy Materials* **2015,** *5* (11), 1500141.

(9) Ahn, S. H.; Manthiram, A., Edge-Oriented Tungsten Disulfide Catalyst Produced from Mesoporous WO_3 for Highly Efficient Dye-Sensitized Solar Cells. *Advanced Energy Materials* **2016,** *6* (3), 1501814.

(10) Zhang, X.; Chen, X.; Zhang, K.; Pang, S.; Zhou, X.; Xu, H.; Dong, S.; Han, P.; Zhang, Z.; Zhang, C.; Cui, G., Transition-metal nitride nanoparticles embedded in N-doped reduced graphene oxide: superior synergistic electrocatalytic materials for the counter electrodes of dye-sensitized solar cells. *Journal of Materials Chemistry A* **2013,** *1* (10), 3340.

(11) Ghani, S.; Sharif, R.; Bashir, S.; Zaidi, A. A.; Rafique, M. S.; Ashraf, A.; Shahzadi, S.; Rafique, S.; Kamboh, A. H., Polypyrrole thin films decorated with copper nanostructures as counter electrode for dye-sensitized solar cells. *Journal of Power Sources* **2015,** *282,* 416-420.

(12) Lu, C.-Y.; Tsai, C.-H.; Tsai, Y.-T.; Hsu, C.-J.; Chang, C.-H.; Wu, C.-C., Spontaneous Formation of Nanofibrillar and Nanoporous Structures in High-Conductivity Conducting Polymers and Applications for Dye-Sensitized Solar Cells. *Advanced Energy Materials* **2015,** *5* (6), 1401738.

(13) Jeon, S. S.; Kim, C.; Ko, J.; Im, S. S., Spherical polypyrrole nanoparticles as a highly efficient counter electrode for dye-sensitized solar cells. *Journal of Materials Chemistry* **2011,** *21* (22), 8146.

(14) Park, J. W.; Jang, J., Fabrication of graphene/free-standing nanofibrillar PEDOT/P(VDF-HFP)

hybrid device for wearable and sensitive electronic skin application. *Carbon* **2015,** *87*, 275-281.

(15) Qidong Tai, B. C., Feng Guo, Sheng Xu, Hao Hu, Bobby Sebo, and Xing-Zhong Zhao, In Situ Prepared Transparent Polyaniline Electrode and Its Application in Bifacial Dye-Sensitized Solar Cells. *ACS NANO* **2011,** *5* (5).

(16) Tang, Z.; Wu, J.; Zheng, M.; Tang, Q.; Liu, Q.; Lin, J.; Wang, J., High efficient PANI/Pt nanofiber counter electrode used in dye-sensitized solar cell. *RSC Advances* **2012,** *2* (10), 4062.

(17) Zhou, L.; Yu, M.; Chen, X.; Nie, S.; Lai, W.-Y.; Su, W.; Cui, Z.; Huang, W., Screen-Printed Poly(3,4-Ethylenedioxythiophene):Poly(Styrenesulfonate) Grids as ITO-Free Anodes for Flexible Organic Light-Emitting Diodes. *Advanced Functional Materials* **2018,** *28* (11), 1705955.

(18) Kim, J. C.; Rahman, M. M.; Ju, M. J.; Lee, J.-J., Highly conductive and stable

graphene/PEDOT:PSS composite as a metal free cathode for organic dye-sensitized solar cells. *RSC Advances* **2018,** *8* (34), 19058-19066.

(19) Liu, X.; Wang, M.; Wang, F.; Xu, T.; Li, Y.; Peng, X.; Wei, H.; Guan, Z.; Zang, Z., High-Performance Photodetectors With X-Ray Responsivity Based on Interface Modified Perovskite Film. *IEEE Electron Device Letters* **2020,** *41* (7), 1044-1047.

(20) Wang, M.; Zang, Z.; Yang, B.; Hu, X.; Sun, K.; Sun, L., Performance improvement of perovskite solar cells through enhanced hole extraction: The role of iodide concentration gradient. *Solar Energy Materials and Solar Cells* **2018,** *185*, 117-123.

(21) Wang, M.; Wang, H.; Li, W.; Hu, X.; Sun, K.; Zang, Z., Defect passivation using ultrathin PTAA layers for efficient and stable perovskite solar cells with a high fill factor and eliminated hysteresis. *Journal of Materials Chemistry A* **2019,** *7* (46), 26421-26428.

(22) Zeng, X.; Zhou, T.; Leng, C.; Zang, Z.; Wang, M.; Hu, W.; Tang, X.; Lu, S.; Fang, L.; Zhou, M., Performance improvement of perovskite solar cells by employing a CdSe quantum dot/PCBM composite as an electron transport layer. *Journal of Materials Chemistry A* **2017,** *5* (33), 17499-17505.

(23) Zhou, T.; Wang, M.; Zang, Z.; Fang, L., Stable Dynamics Performance and High Efficiency of ABX3-Type Super-Alkali Perovskites First Obtained by Introducing H5O2 Cation. *Advanced Energy Materials* **2019,** *9* (29), 1900664.

(24) Zhang, J.; Long, H.; Miralles, S. G.; Bisquert, J.; Fabregat-Santiago, F.; Zhang, M., The combination of a polymer-carbon composite electrode with a high-absorptivity ruthenium dye achieves an efficient dye-sensitized solar cell based on a thiolate-disulfide redox couple. *Phys Chem Chem Phys* **2012,** *14* (19), 7131-6.

(25) Yung-Hoon Ha, N. N., Steven K. Pollack, John Mastrangelo, Brett D. Martin, Towards a

Transparent, Highly Conductive Poly(3,4-ethylenedioxythiophene). *Advanced Functional Materials* **2004,** *14* (6).

(26) Wei Wei, H. W., Yun Hang Hu, A review on PEDOT-based counter electrodes for dyr-sensitized solar cells. *International Journal of Energy Research* **2014,** *38* (9), 1099-1111.

(27) Hou, W.; Xiao, Y.; Han, G.; Lin, J. Y., The Applications of Polymers in Solar Cells: A Review.

Polymers (Basel) **2019,** *11* (1).

(28) Wu, J.; Lan, Z.; Lin, J.; Huang, M.; Huang, Y.; Fan, L.; Luo, G.; Lin, Y.; Xie, Y.; Wei, Y., Counter electrodes in dye-sensitized solar cells. *Chem Soc Rev* **2017,** *46* (19), 5975-6023.

(29) Lee, S.; Paine, D. C.; Gleason, K. K., Heavily Doped poly(3,4-ethylenedioxythiophene) Thin Films with High Carrier Mobility Deposited Using Oxidative CVD: Conductivity Stability and Carrier Transport. *Advanced Functional Materials* **2014**, n/a-n/a.

(30) Wei, Q.; Mukaida, M.; Naitoh, Y.; Ishida, T., Morphological change and mobility enhancement in PEDOT:PSS by adding co-solvents. *Adv Mater* **2013,** *25* (20), 2831-6.

(31) Yue, G.; Wu, J.; Xiao, Y.; Lin, J.; Huang, M.; Fan, L.; Yao, Y., A dye-sensitized solar cell based on PEDOT:PSS counter electrode. *Chinese Science Bulletin* **2013,** *58* (4-5), 559-566.

(32) Gueye, M. N.; Carella, A.; Massonnet, N.; Yvenou, E.; Brenet, S.; Faure-Vincent, J.; Pouget, S.; Rieutord, F.; Okuno, H.; Benayad, A.; Demadrille, R.; Simonato, J.-P., Structure and Dopant Engineering in PEDOT Thin Films: Practical Tools for a Dramatic Conductivity Enhancement. *Chemistry of Materials* **2016,** *28* (10), 3462-3468.

(33) Rudd, S.; Franco-Gonzalez, J. F.; Kumar Singh, S.; Ullah Khan, Z.; Crispin, X.; Andreasen, J. W.; Zozoulenko, I.; Evans, D., Charge transport and structure in semimetallic polymers. *J Polym Sci B Polym Phys* **2018,** *56* (1), 97-104.

(34) Trevisan, R.; Döbbelin, M.; Boix, P. P.; Barea, E. M.; Tena-Zaera, R.; Mora-Seró, I.; Bisquert, J., PEDOT Nanotube Arrays as High Performing Counter Electrodes for Dye Sensitized Solar Cells. Study of the Interactions Among Electrolytes and Counter Electrodes. *Advanced Energy Materials* **2011,** *1* (5), 781-784.

(35) Lin, Y.-F.; Li, C.-T.; Ho, K.-C., A template-free synthesis of the hierarchical hydroxymethyl PEDOT tube-coral array and its application in dye-sensitized solar cells. *Journal of Materials Chemistry A* **2016,** *4* (2), 384-394.

(36) Li, Y.-C.; Jia, S.-R.; Liu, Z.-Y.; Liu, X.-Q.; Wang, Y.; Cao, Y.; Hu, X.-Q.; Peng, C.-L.; Li, Z., Fabrication of PEDOT films via a facile method and their application in Pt-free dye-sensitized solar cells. *Journal of Materials Chemistry A* **2017,** *5* (17), 7862-7868.

(37) Yasuteru Saito, T. K., Yuji Wada, and Shozo Yanagida, Application of Poly(3,4-ethylenedioxythiophene) to Counter Electrode in Dye-Sensitized Solar Cells. *Chemistry Letters* **2002,** *31* (10).

(38) Kim, D. H.; Atanasov, S. E.; Lemaire, P.; Lee, K.; Parsons, G. N., Platinum-free cathode for dye-sensitized solar cells using poly(3,4-ethylenedioxythiophene) (PEDOT) formed via oxidative molecular layer deposition. *ACS Appl Mater Interfaces* **2015,** *7* (7), 3866-70.

(39) Anothumakkool, B.; Agrawal, I.; Bhange, S. N.; Soni, R.; Game, O.; Ogale, S. B.; Kurungot, S., Pt- and TCO-Free Flexible Cathode for DSSC from Highly Conducting and Flexible PEDOT Paper Prepared via in Situ Interfacial Polymerization. *ACS Appl Mater Interfaces* **2016,** *8* (1), 553-62.

(40) Kim, J.; Kim, E.; Won, Y.; Lee, H.; Suh, K., The preparation and characteristics of conductive poly(3,4-ethylenedioxythiophene) thin film by vapor-phase polymerization. *Synthetic Metals* **2003,** *139* (2), 485-489.

(41) Jo, S.-H.; Lee, Y.-K.; Yang, J.-W.; Jung, W.-G.; Kim, J.-Y., Carbon nanotube-based flexible transparent electrode films hybridized with self-assembling PEDOT. *Synthetic Metals* **2012,** *162* (13-14), 1279-1284.

(42) Xiaoxue Wang, X. Z., Lei Sun, Dongwook Lee, Sunghwan Lee, Minghui Wang, Junjie Zhao, Yang Shao-Horn, Mircea Dinc, Tom Palacios, Karen K. Gleason, High electrical conductivity and carrier mobility in oCVD PEDOT thin films by engineered crystallization and acid treatment. *Science Advances* **2018,** *4* (eaar5780).

(43) West, B. W.-J. a. K., Vapor-Phase Polymerization of 3,4-Ethylenedioxythiophene: A Route to Highly Conducting Polymer Surface Layers. *Macromolecules* **2004,** *37*, 4538-4543.

(44) White, M. S.; Kaltenbrunner, M.; Głowacki, E. D.; Gutnichenko, K.; Kettlgruber, G.; Graz, I.; Aazou, S.; Ulbricht, C.; Egbe, D. A. M.; Miron, M. C.; Major, Z.; Scharber, M. C.; Sekitani, T.; Someya, T.; Bauer, S.; Sariciftci, N. S., Ultrathin, highly flexible and stretchable PLEDs. *Nature Photonics* **2013,** *7* (10), 811-816.

(45) Diao, Y.; Chen, H.; Lu, Y.; Santino, L. M.; Wang, H.; D'Arcy, J. M., Converting Rust to PEDOT Nanofibers for Supercapacitors. *ACS Applied Energy Materials* **2019,** *2* (5), 3435-3444.

(46) Wang, H.; Diao, Y.; Rubin, M.; Santino, L. M.; Lu, Y.; D'Arcy, J. M., Metal Oxide-Assisted PEDOT Nanostructures via Hydrolysis-Assisted Vapor-Phase Polymerization for Energy Storage. *ACS Applied Nano Materials* **2018,** *1* (3), 1219-1227.

(47) Ugur, A.; Katmis, F.; Li, M.; Wu, L.; Zhu, Y.; Varanasi, K. K.; Gleason, K. K., Low-Dimensional Conduction Mechanisms in Highly Conductive and Transparent Conjugated Polymers. *Adv Mater* **2015,** *27* (31), 4604-10.

(48) V. N. Prigodin, A. J. E., Nature of insulator-metal transition and novel mechanism of charge

transport in the metallic state of highly doped electronic polymers. *Synthetic Metals* **2002,** *125*, 43-53.

(49) Huicheng Sun, Y. L., Yiduo Zhang, Dongmei Li, Zhexun Yu, Kexin Li, and Qingbo Meng, In Situ Preparation of a Flexible Polyaniline/Carbon Composite Counter Electrode and Its Application in Dye-Sensitized Solar Cells. *J. Phys. Chem. C* **2010,** *114*, 11673-11679.

(50) Yue, G.; Wang, L.; Zhang, X. a.; Wu, J.; Jiang, Q.; Zhang, W.; Huang, M.; Lin, J., Fabrication of high performance multi-walled carbon nanotubes/polypyrrole counter electrode for dye-sensitized solar cells. *Energy* **2014,** *67*, 460-467.

(51) Hyunkook Kim, H. C., Sookhyun Hwang, Youngjoo Kim and Minhyon Jeon, Fabrication and characterization of carbon-based counter electrodes prepared by electrophoretic deposition for dye-sensitized solar cells. *Nanoscale Research Letters* **2012,** *7* (53).

(52) Cheng, M.; Yang, X.; Chen, C.; Zhao, J.; Zhang, F.; Sun, L., Dye-sensitized solar cells based on hydroquinone/benzoquinone as bio-inspired redox couple with different counter electrodes. *Phys Chem Chem Phys* **2013,** *15* (36), 15146-52.

(53) Hao, F.; Dong, P.; Luo, Q.; Li, J.; Lou, J.; Lin, H., Recent advances in alternative cathode materials for iodine-free dye-sensitized solar cells. *Energy & Environmental Science* **2013,** *6* (7), 2003.

(54) Yi Li, H. S., Masatoshi Sakairi, Kazuhiro Shigyo, Hideaki Takahashi and Masahiro Seo, Formation and Breakdown of Anodic Oxide Films on Aluminum in Boric Acid/Borate Solutions. *J. Electrochem. Soc* **1997,** *144* (3).

(55) Sining Yun, A. H., Counter Electrodes for Dye-Sensitized and Perovskite Solar Cells. *John Wiley & Sons* **2019,** *2*.

Chapter 8

Hydrolysis-Assisted Vapor-Phase Polymerization (HVPP) on PEDOT Nanostructures

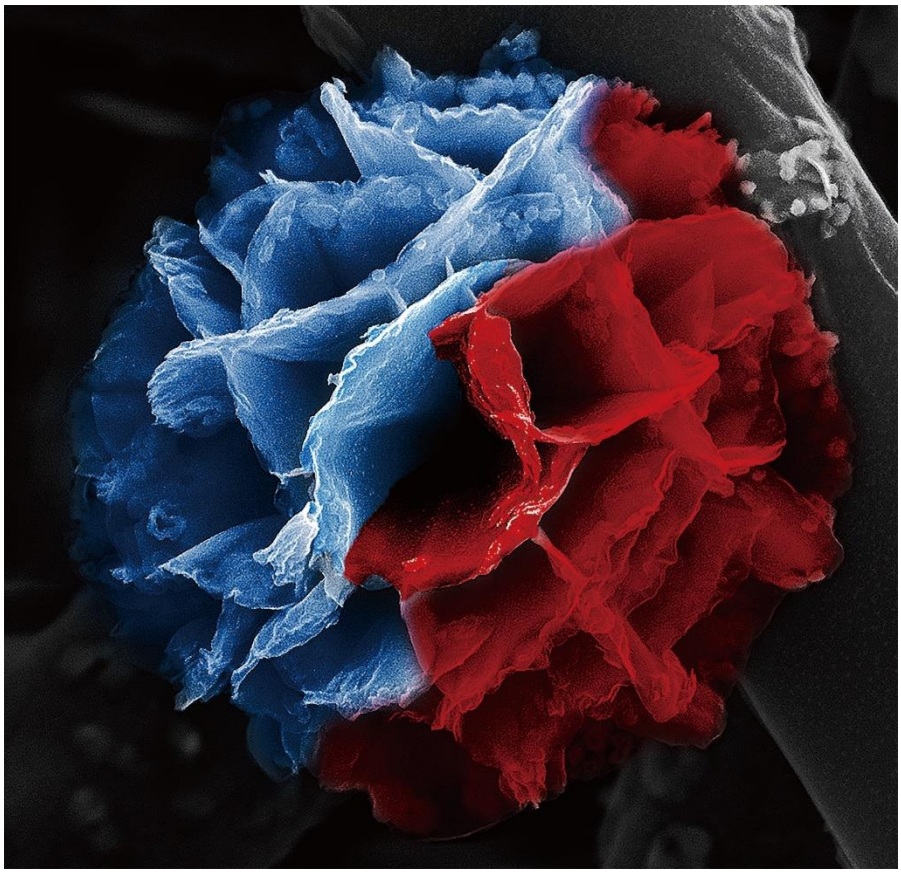

Conducting polymer (blue) / Rust (red)

8.1 Introduction

When ferric chloride dissolves in water, the result is a thermodynamically unstable aqueous solution that readily hydrolyzes under standard conditions and at room temperature. This kinetically controlled reaction yields a multitude of iron precipitates such as oxides, hydroxides, and oxyhydroxides, with various crystal growth mechanisms.[1-3] Initially, a hexaaqua complex $[Fe(H_2O)_6]^{3+}$ hydrolyzes to produce ferric hydroxides $[Fe(H_2O)_5(OH)]^{2+}$,[4-7] then olation and oxolation connect iron centers *via* hydroxo and oxo bridges,[5, 8] finally condensing into ferric hydroxides or oxyhydroxides.[5-10] The pH of solution, electronegativity of ions, reaction temperature, and solvent properties control hydrolysis product, crystal structure and nanostructure morphology. The binding affinity of an anion to a ferric metal center is pH dependent. Under acidic conditions, Cl^- and SO_4^{2-} bind stronger leading to the precipitation of β-FeOOH (akaganeite) nanorods, while a weak binding affinity in ClO_4^- and NO_3^- results in $(Fe^{3+})_2O_3{\cdot}0.5H_2O$ (ferrihydrite) nanosheets.[8, 11] Moreover, β-FeOOH and 6-line ferrihydrite are the main products of hydrolysis at high temperatures (90-100 °C) and high Cl^- concentration (> 0.2 M).[5-6, 12]

Interestingly, this unstable ferric chloride aqueous solution is an ideal oxidant for synthesizing a plethora of conjugated polymer nanostructures and plays the role of a dopant by providing a Cl^- counter anion that stabilizes charge during polymerization.[13] The synthesis and doping of a semiconducting polymer via oxidative polymerization requires oxidation of monomer resulting in oligomers and a final conjugated polymer backbone.[14] Oxidation strategies include electrochemical, solution and vapor-phase techniques, the last two share common chemical oxidizing agents such as $FeCl_3$ (0.77 V), $Fe(OTs)_3$, (0.77 V), $Fe_3(SO_4)_2$ (0.77 V), ammonium persulfate (2.01 V), H_2O_2 (1.78 V), $CuCl_2$ (0.32 V).[15-17] Among these synthetic routes, the vapor-

phase is particularly appealing when using $FeCl_3$ to oxidize a monomer such as 3,4-ethylenedioxythiophene (EDOT) because it results in poly(3,4-ethylenedioxythiophene) (PEDOT) conformal coatings of high chemical and physical stability and low electrical resistance in a single step.[13, 18-20] For example, vapor-phase polymerization (VPP) using $FeCl_3$ in a liquid-bridge-mediated nanotransfer printing process, deposits crystal PEDOT nanowires with conductivities ranging between 3000 and 8000 S/cm.[21] $FeCl_3$ is a mild inexpensive oxidant highly soluble both in both water and polar protic organic solvents making it an ideal oxidant for solution processing.

Here, we combine VPP with *in situ* hydrolysis of a ferric chloride aqueous solution by introducing a liquid droplet that contains hydrolyzable inorganic salts into a CVD reactor and develop a system that allows us to control both hydrolysis and polymerization. This approach results in conformal coatings of 1D or 2D $FeO_xH_yCl_z$-PEDOT core-shell nanostructures via a hydrolysis-assisted vapor-phase polymerization (HVPP) (Figure 8.1). Our evaporative approach to material synthesis utilizes dewetting to produce homogenous nanostructures; dewetting serves as a universal and versatile platform in the literature for controlling nanostructure formation *in situ*.[22-23] Hybrid inorganic-organic 1D nanofibers, nanowires and nanorod as well as 2D nanoleaves and nanoflowers are deposited in bulk quantities in a single step from the vapor phase. A mechanism for the formation of nanostructures is proposed whereby kinetics of hydrolysis and polymerization are controlled *in situ* during synthesis, this universal approach to core-shell nanostructures is tested by depositing other oxide composites such as TeO_2-PEDOT and SnO_2-PEDOT. The capacitance of these PEDOT nanostructures is then measured for energy storage applications in electrochemical capacitors with structure-property relationship discussed.

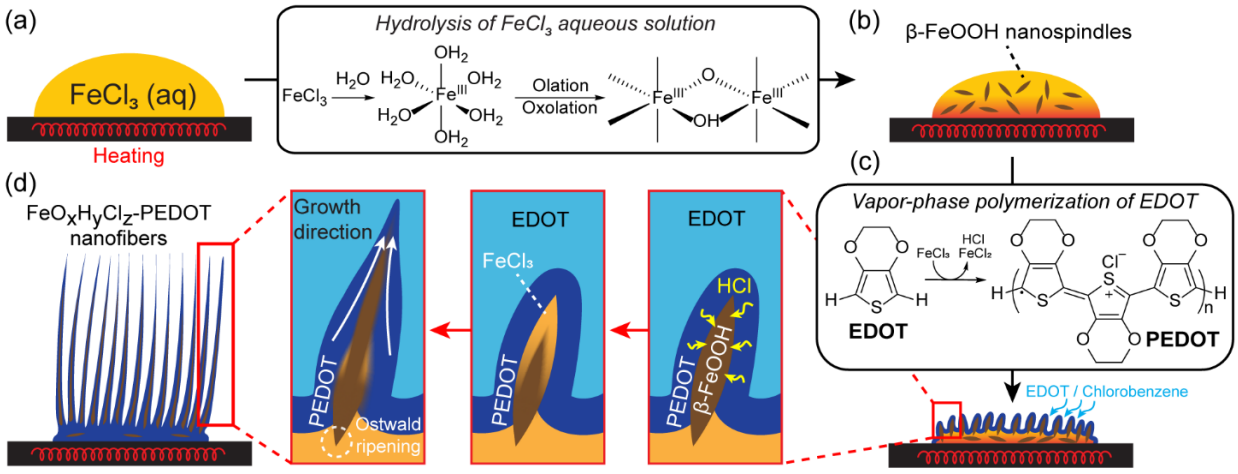

Figure 8.1: The mechanism for HVPP PEDOT core-shell nanofibrillar growth. (a) the hydrolysis of $FeCl_3$ and results in (b) the precipitation of β-FeOOH nanospindles. (c) Polymerization is initiated when EDOT monomer vapors contact the oxidant producing HCl as a byproduct. Upon contact with HCl, β-FeOOH nanospindles are transformed to $FeCl_3$; this oxidant localizes polymerization to the spindle surface, and as hydrolysis continues, Ostwald ripening of β-FeOOH nanospindle promotes (d) nanofibrillar growth.

8.2 Experimental methods

8.2.1 Preparation of PEDOT via hydrolysis-assisted vapor-phase polymerization (HVPP) protocol.

A flow process diagram of synthesis is shown in Figure 8.2. In a CVD chamber, a droplet of 150 µL 0.266 M $FeCl_3$ (3.99×10^{-5} mol) is placed on a substrate, and 500 µL of a 0.0674 M EDOT (3.37×10^{-5} mol) / chlorobenzene (4.93×10^{-3} mol) solution is loaded in two separate reservoirs. Controlled by a PID controller, the temperature ramps from 30 °C to 130 °C in 10 min (rate = 10 °C/min) and holds at 130 °C for 50 min, then the obtained material on glass is annealed in air at 130 °C for 10 min.

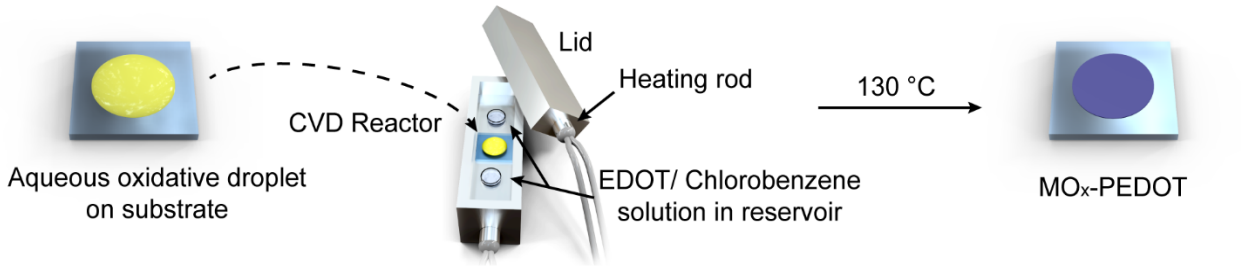

Figure 8.2: Schematic illustration of HVPP synthesis protocol.

8.2.2 Reaction substrate preparation.

A glass substrate is cleaned via sonication in soapy water, followed by washing in deionized water and methanol. The substrate is immersed in piranha solution (concentrated H_2SO_4 : 30% H_2O_2 = 3 : 1) at room temperature overnight, then rinsed with water and immersed in 0.025 M HCl isopropanol solution at room temperature overnight for the control of surface energy. For synthesis, the pre-treated substrates are dried in air and cut into 2.5 cm × 2.5 cm pieces. In nitromethane-HVPP and ethanol-HVPP, the surface energy of the substrate is modified using 3% trichlorododecylsilane (by volume) in dry toluene. Typically, glass is soaked for 2 h at room temperature followed by washing in dry toluene (2 h). This surface-modified substrate is immersed in isopropanol for 2 h at room temperature and then dried in air. For electrochemical characterization of PEDOT, 0.5 inch × 0.5 inch hard carbon paper is placed on a glass slide as the substrate.

8.2.3 Synthesis of metal oxide-PEDOT nanostructures.

All syntheses follow a common HVPP protocol. For H_2O-HVPP, urea-HVPP and NH_4OH-HVPP, 150 µL 0.266 M $FeCl_3$ (3.99×10^{-5} mol) aqueous solution only, or the mixture with 0.266 M urea

(3.99×10^{-5} mol) or diluted aqueous ammonia (5.6 ~ 6.0%) are used as the oxidative droplet. For $TeCl_4$-HVPP, 150 μL aqueous solution with 0.0266 M $FeCl_3$ (3.99×10^{-6} mol), 0.2394 M $TeCl_4$ (3.59×10^{-5} mol) and 1.08 M HCl (1.62×10^{-4} mol) is used as the oxidant droplet. For $SnCl_4$-HVPP, 150 μL aqueous solution with 0.0399 M $FeCl_3$ (5.99×10^{-6} mol) and 0.2261 M $SnCl_4$ (3.39×10^{-5} mol) is used as the oxidant droplet. For solvent controlled synthesis, 150 μL nitromethane (or ethanol/H_2O) solution with 0.266 M $FeCl_3$ (3.99×10^{-5} mol) is used as the oxidant droplet. PEDOT is purified by soaking thrice in 6 M HCl at 70 °C (1 hr/soak) and methanol at 25 °C (10 min/soak) and is dried in air; this process removes all inorganic species.

8.2.4 Characterization

pH of the solution is measured with a Mettler Toledo Inlab Micro pH probe combined with a F20 pH meter. Scanning electron micrographs (SEM) and energy-dispersive X-ray spectroscopy (EDXS) data is collected using a JEOL 7001LVF FE-SEM, Transmission electron micrographs (TEM) data is obtained in a FEI Spirit TEM; samples are dropcast from hexafluoroisopropanol onto TEM grids. A Bruker d8 advance X-ray diffractometer is utilized to collect powder X-ray diffraction spectrum (PXRD) of pulverized sample s at room temperature, with Cu Kα radiation source (λ = 1.5406 Å) and LynxEyeXE detector, operating at 40 kV and 40 mA with sample holder rotate at 30 rpm/min at a scan step of 0.02°. The composition of the hybrid material and the mass of PEDOT in PEDOT/HCP electrode is determined by Discovery thermogravimetric analysis (TGA) from TA Instruments. To characterize the composition of the sample, samples are heated from 30 °C to 600 °C with a ramping rate of 2 °C / min. For determining the mass of PEDOT in PEDOT/HCP electrode, temperature is ramped to 100 °C under N_2 and held isothermally for 30 min to drive off water, then ramped to 600 °C with a ramping rate of 20 °C / min and held

isothermally for 60 min; after that, the purging gas is exchanged to dry air to induce the rapid decomposition of PEDOT. Ultraviolet-visible-near infrared absorption spectra (UV-Vis-NIR) are collected on a SHIMADZU UV-1800 spectrophotometer with pulverized samples that are dispersed in concentrated H_2SO_4. Fourier-transform infrared spectra (FT-IR) is collected on a Bruker ALPHA Platinum-ATR.

Cyclic voltammetry (CV) and electrochemical impedance spectroscopy (EIS) are performed on a BioLogic VMP3 multi-potentiostat. For three-electrode CV characterization, a platinum mesh lead is affixed to the back side of the working electrode and fully covered with a polyimide tape. A bundled length of platinum mesh with a platinum wire lead serves as counter electrode. The reference electrode (BASi Ag/AgCl RE-5B) is pointed directly at the working electrode surface to minimize solution resistance. All the as-synthesized working electrodes are washed in 6M HCl and methanol to remove any excess solvent or reduced oxidant, and are cut to 5 mm × 5 mm square shape. The electrolyte in all cases is 1M H_2SO_4 in milli-Q water (18 MΩ). EIS is carried out at the electrodes' open circuit potential after obtaining a reversible cyclic voltammogram. Impedance values are recorded with a 10 mV sinusoidal disturbance at frequencies ranging from 100 kHz to 100 mHz. 4-point probe resistance is measured by a Keithley 2450 SourceMeter with a 5 mA current; the resistance of each sample is measured for 10 times on different spots then averaged. Resistance data is recorded after continuously adding pressure on the probe until a stable reading (Ω) to two decimal places is achieved. Current-voltage (I-V) curves are measured with a convertible 2/4 point probe station built in-house, with two gold probes held at 1 mm in distance.[24]

8.3 Results & discussion

Hydrolysis-assisted vapor-phase polymerization is a synthetic strategy that utilizes a droplet of an aqueous solution of $FeCl_3$ to carry out two reactions simultaneously: 1) forced hydrolysis and 2) oxidative radical polymerization. This droplet is placed inside a chemical vapor deposition chamber and rapidly heated under an atmosphere of monomer vapor (Figure 8.2). An aqueous solution of ferric chloride is thermodynamically unstable and readily hydrolyzes resulting in the precipitation of various inorganic colloidal phases. The pH of hydrolysis enables selective precipitation of iron hydroxides (β-FeOOH, pH ≤ 1.80), oxides (α-Fe_2O_3, pH = 4.20 – 4.40) and mixtures thereof (α-FeOOH/α-Fe_2O_3, pH = 6.00 – 6.50).[1] The pH is controlled using a base, either inorganic (sodium hydroxide, ammonium hydroxide) or organic (urea, urotropine).[1, 25-27] At elevated temperatures, urea decomposes into NH_4^+ and OH^-, buffering the solution, resulting in the precipitation of ferric hydroxide and oxide nanostructures of uniform shape and size.[25-27] The effect of urea and ammonium hydroxide in the synthesis is therefore investigated for producing metal oxide-conducting polymer composite nanostructures of uniform shape and size.

Figure 8.3a shows the pH change in droplets as they undergo the synthesis with (urea-HVPP and NH_4OH-HVPP) and without a pH controlling additive (H_2O-HVPP). The initial pH for a urea-treated droplet is 1.47. After 7 min of forced hydrolysis, pH smoothly decays down to 1.26. Urea buffers this reaction by continuously releasing NH_3, neutralizing HCl produced during hydrolysis and polymerization.[27] The pH profile for an ammonium hydroxide-treated droplet resembles that of urea during the first 6 minutes, however, by minute 7, complete evaporation of NH_3 at 90 °C triggers a sharp drop in pH down to 0.87. The omission of a base or buffer results in abrupt fluctuations in pH, starting at 1.33 and decreasing to 0.92.

This low pH approximates that of an ammonium hydroxide treated droplet at minute 7. The erratic variations in pH are due to competing reactions during synthesis i.e., the rapid evaporation of HCl byproduct from step-growth polymerization increases pH, whereas droplet evaporation elevates ferric chloride concentration, promoting hydrolysis and decreasing pH.[27-28] Quenching experiments aid in determining the identity of colloidal phases throughout the synthesis. After 8 min of heating, PXRD and TEM show that β-FeOOH nanospindles precipitate out of a droplet; these 1D nanostructures are 150 nm in length and 25 nm in diameter and are a common product of $FeCl_3$ hydrolysis[1, 7, 27, 29-31] (Figure 8.3b). Addition of urea or ammonium hydroxide produces a high concentration of β-FeOOH nanospindles due to an increase in OH^- ions, promoting precipitation (Figure 8.4).

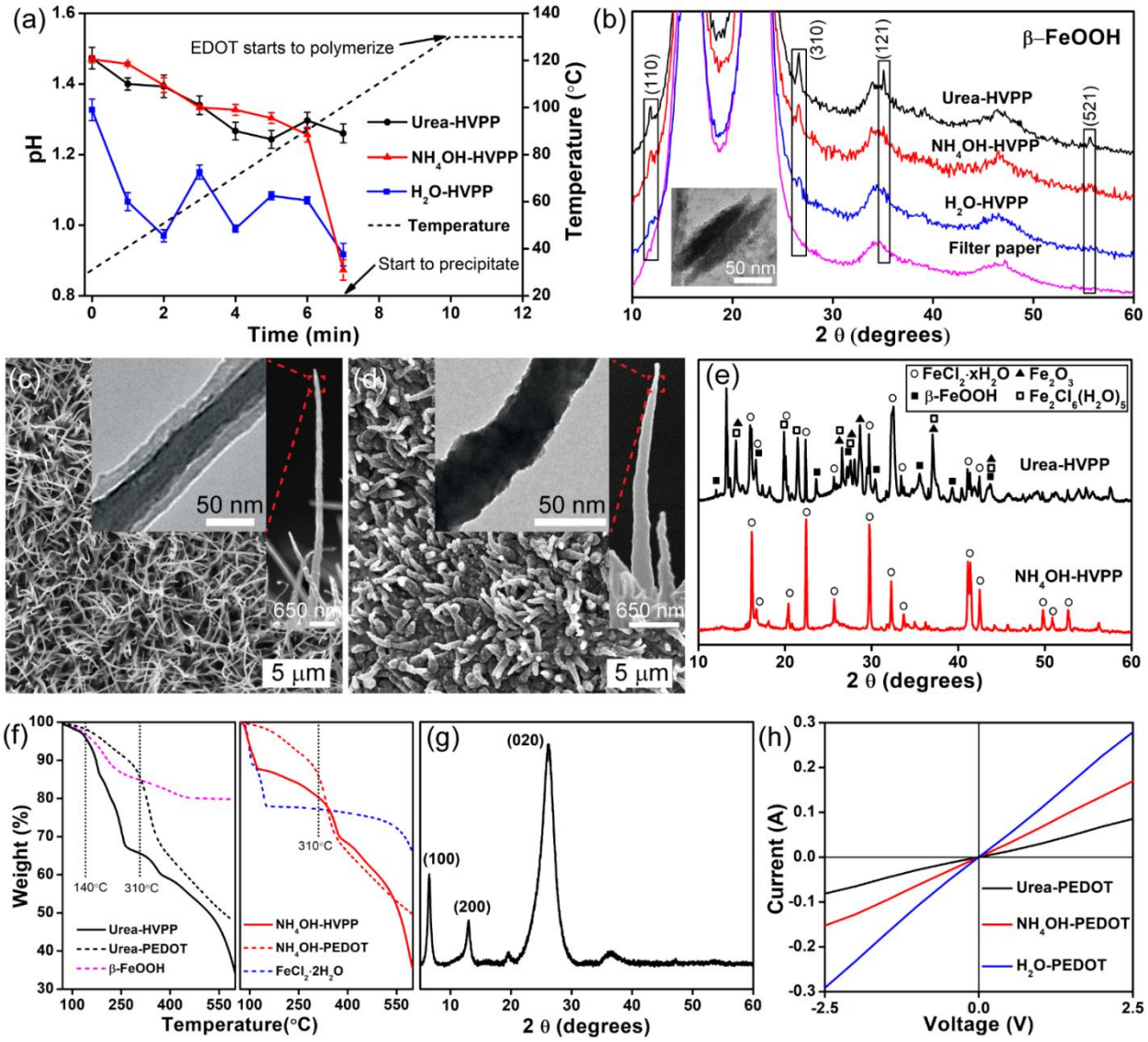

Figure 8.3: Characterization of pH controlled PEDOT synthesis from HVPP. (a) pH and temperature change for all the three syntheses during first 12 min of reaction. (b) PXRD of the suspension at 8 min after drop-casting on filter paper (inset at the bottom is the TEM of the precipitate from all the syntheses). Morphology of PEDOT under SEM: (c) Urea-HVPP and (d) NH_4OH-HVPP. (e) PXRD and (f) TGA for the synthesized product. (g) PXRD and (h) I-V for the PEDOT samples after removal of inorganic species.

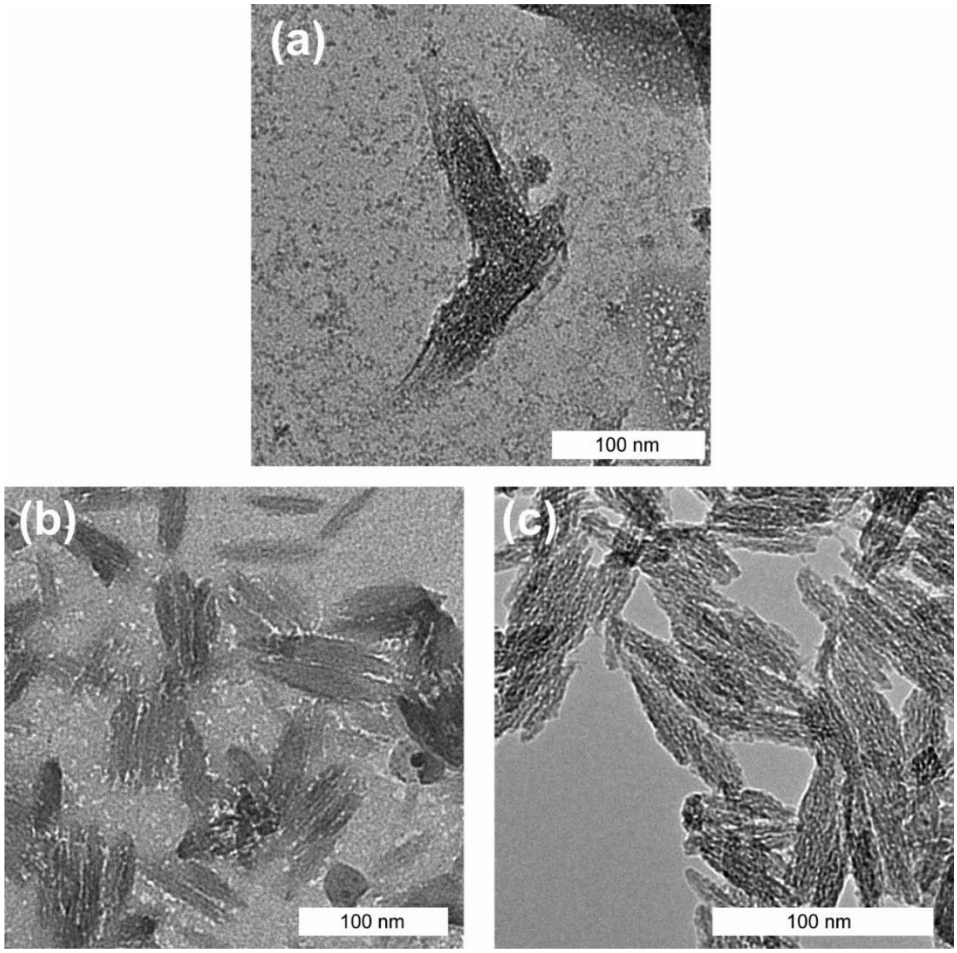

Figure 8.4: TEM of quenched synthesis at 8 min showing the density of distribution of β-FeOOH nanospindles for (a) H_2O-HVPP, (b) urea-HVPP and (c) NH_4OH-HVPP.

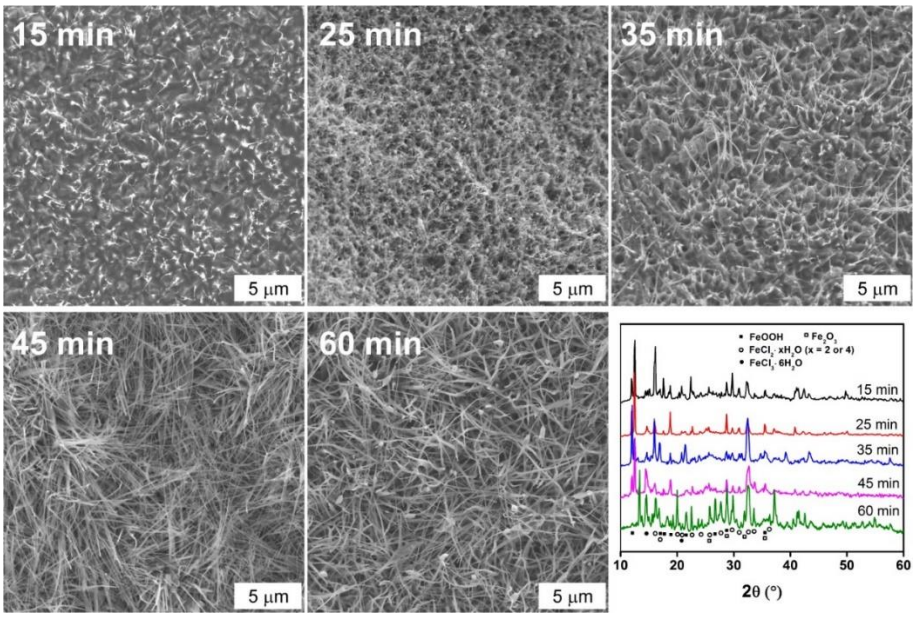

Figure 8.5: SEM and PXRD spectra show the morphology and composition of urea-HVPP quenched at 15, 25, 35, 45 and 60 min after ramping from 30 °C.

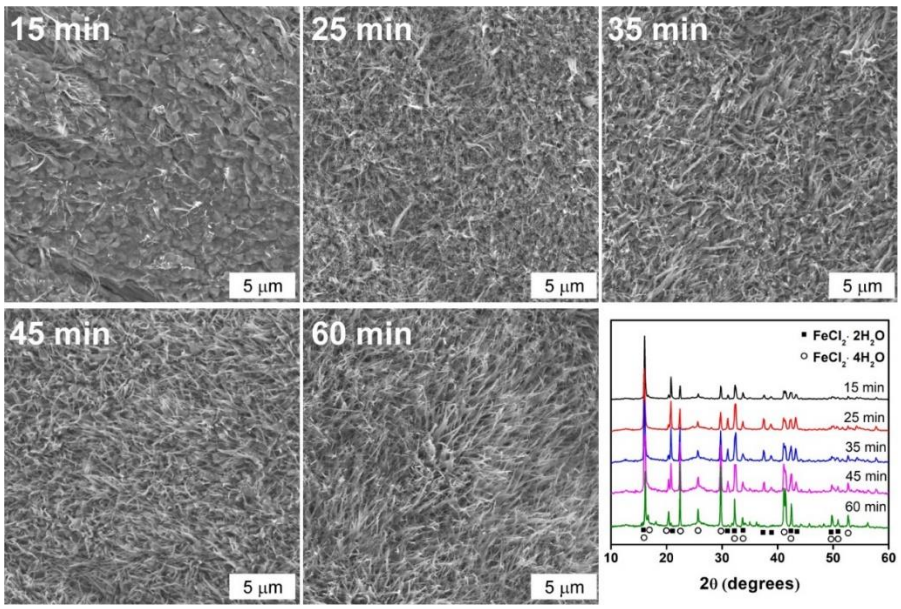

Figure 8.6: SEM and PXRD spectra show the morphology and composition of NH_4OH-HVPP quenched at 15, 25, 35, 45 and 60 min after ramping from 30 °C.

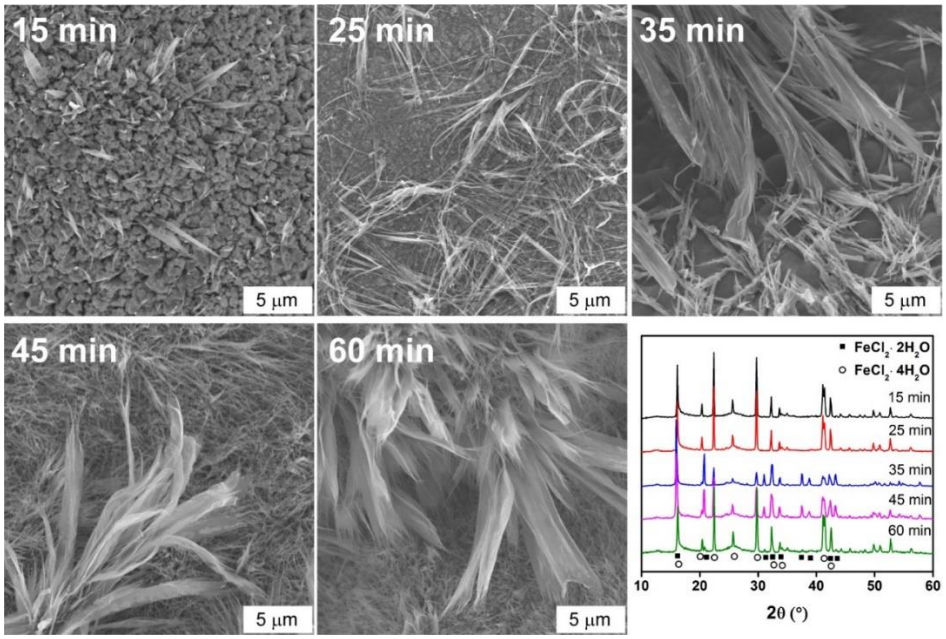

Figure 8.7: SEM and PXRD spectra show the morphology and composition of H2O-HVPP quenched at 15, 25, 35, 45 and 60 min after ramping from 30 °C.

After 15 minutes, a blue colored disc-shaped polymer coating covers the droplet area and PXRD shows the presence of $FeCl_2 \cdot xH_2O$, a byproduct of vapor-phase polymerization from the reduction of $FeCl_3$ (Figure 8.5-8.7). When EDOT vapor is oxidized by $FeCl_3$, radical coupling is promoted resulting in the formation of a conjugated backbone. During assembly of PEDOT, unstable intermediates such as low molecular weight oligomers are produced that require deprotonation. Water serves as a proton scavenger that stabilizes oligomers and enables step-growth polymerization; these scavenged protons react with chloride ions in solution forming HCl *in situ*. SEM of unpurified PEDOT after 60 minutes of polymerization show that both urea-HVPP and NH_4OH-HVPP deposit bulk quantities of homogeneous nanofibers of approximately 5 µm in length (Figure 8.3c-d) (Figure 8.8-8.9). When pH is not controlled, a striking difference in polymer morphology is observed, i.e., nanofibers are heterogeneous in length and range between 3 and 20 µm (Figure 8.10).

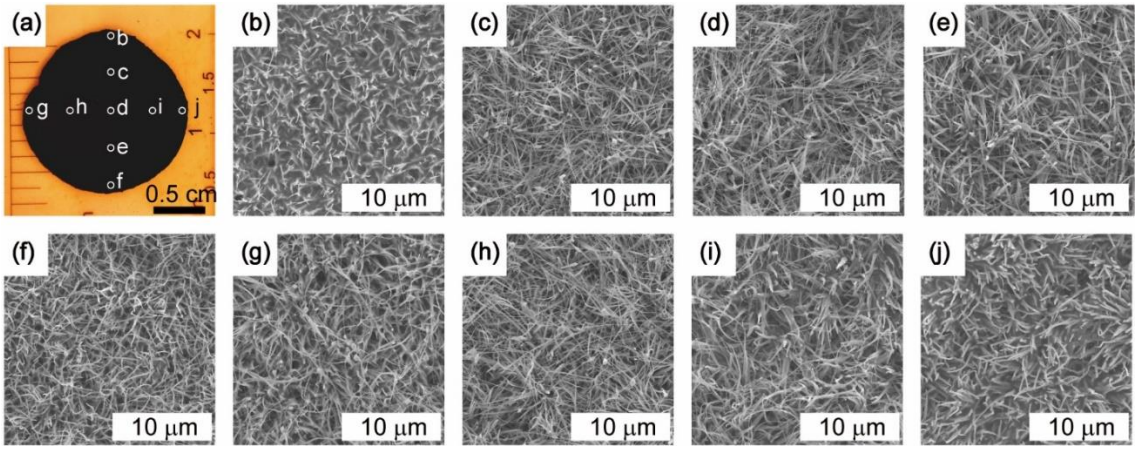

Figure 8.8: (a) As-synthesized PEDOT disk from urea-HVPP. (b-j) SEM of different regions on the disk showing controlled homogeneous morphology.

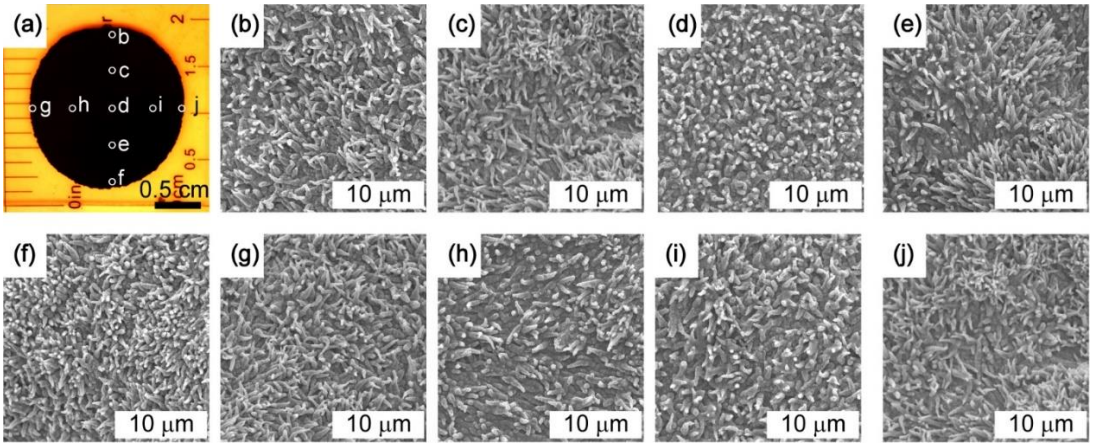

Figure 8.9: (a) As-synthesized PEDOT disk from NH_4OH-HVPP. (b-j) SEM of different regions on the disk showing controlled homogeneous morphology.

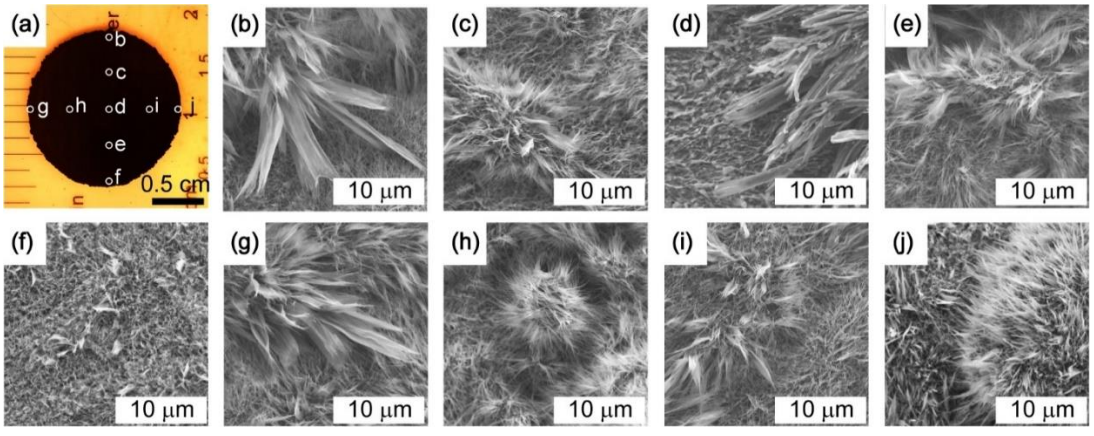

Figure 8.10: (a) As-synthesized PEDOT disk from H_2O-HVPP. (b-j) SEM of different regions on the disk showing heterogeneous morphology.

The difference in fiber length distribution is possibly caused by two different nucleation types: instantaneous nucleation and progressive nucleation.[32] When bases are added, more β-FeOOH is produced at the initial stage of the reaction (Figure 8.4) serving as nucleation sites, then nanostructures homogeneously grow based on the initial nucleation sites, i.e., "instantaneous" nucleation. For the synthesis without a base, new nucleation sites keep emerging during the reaction because of both a small number of initial nucleation sites, as well as a relatively high concentration of $FeCl_3$ (due to less transformation into β-FeOOH initially with low pH). As a result, the growing time for each nucleation sites are different, leading to the heterogeneous nanostructure formation, i.e., "progressive" nucleation. Atomic-resolution chemical mapping using EDXS shows these nanofibers are composed of the elements S, Fe, C, Cl, and O (Figure 8.11-8.13). TEM reveals a difference in their nanofibrillar structure where urea-HVPP leads to $FeO_xH_yCl_z$-PEDOT core-shell nanofibers with a 35 nm core diameter and an 18 nm thick polymer shell (Figure 8.3c inset). NH_4OH-HVPP nanofibers have a monolithic polymer architecture and a diameter of 40 nm (Figure 8.3d inset). PXRD patterns prove the presence of β-FeOOH, Fe_2O_3 and $Fe_2Cl_6(H_2O)_5$ for urea-HVPP, and $FeCl_2 \cdot xH_2O$ (x = 2 or 4) for both urea-HVPP and NH_4OH-HVPP (Figure 8.3e). TGA confirms the major degradable inorganic species as β-FeOOH for urea-HVPP (degrade at 140 °C) and $FeCl_2 \cdot xH_2O$ for NH_4OH-HVPP (degrade below 100 °C) (Figure 8.3f); purified PEDOT nanofibers degrade at 310 °C.

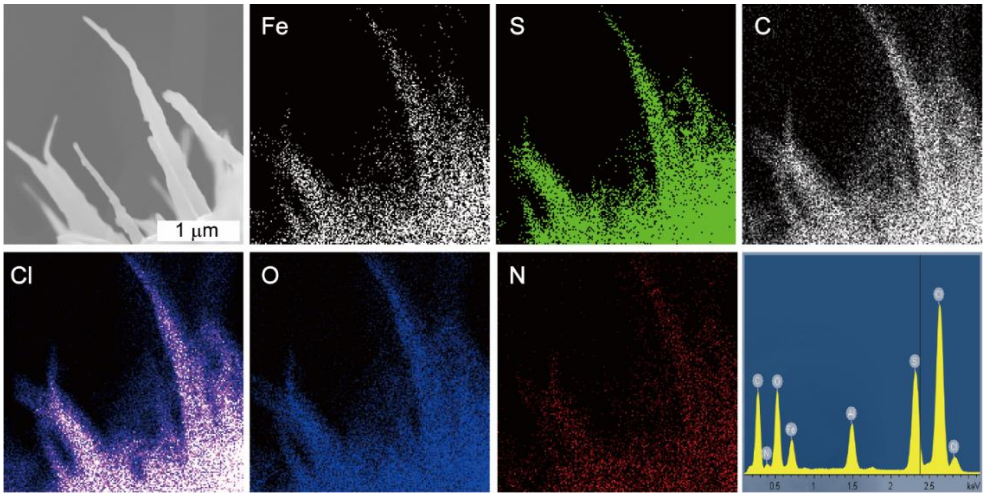

Figure 8.11: EDXS mapping and spectrum of as-synthesized PEDOT from urea-HVPP.

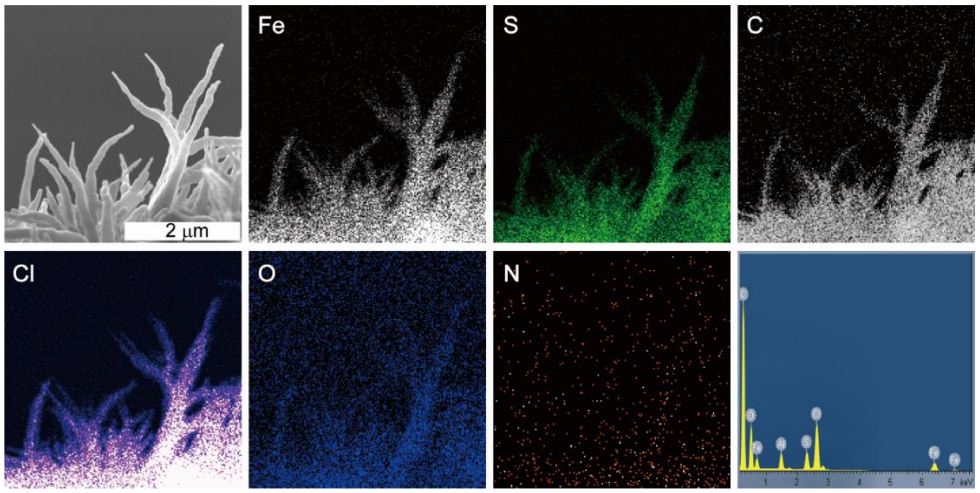

Figure 8.12: EDXS mapping and spectrum of as-synthesized PEDOT from NH4OH-HVPP.

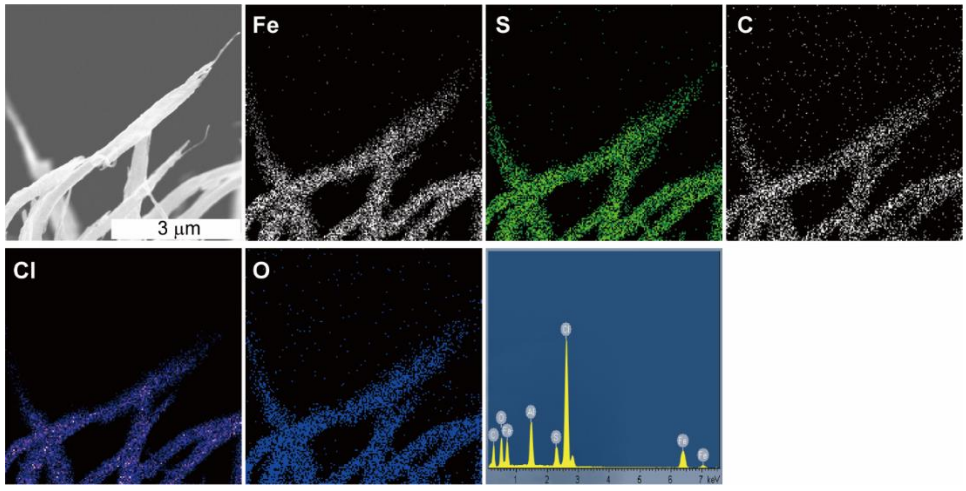

Figure 8.13: EDXS mapping and spectrum of as-synthesized PEDOT from H_2O-HVPP.

PEDOT is permeable to both organic and aqueous solvents and is purified by extended immersion in 6 M HCl to remove iron species. A PXRD pattern of the purified polymer shows a sharp peak for (100) at 2θ = 6.5° and its second-order reflection for (200) at 2θ = 13.0°. These low angle reflections correspond to edge-on packing, a lamella stacking with (100) distance in the range of 1.33 - 1.39 nm for Cl^- doped PEDOT. The (020) peak at 2θ = 26.2° is characteristic of face-to-face packing, an interchain planar ring-stacking with distance of 0.3 – 0.4 nm (Figure 8.3g and 8.14).[33-35] PEDOT's polycrystallinity leads to ohmic behavior during I-V measurements under an applied voltage ranging between -2.5 and 2.5 V (Figure 8.3h); the sheet resistance for urea-HVPP PEDOT is 4.6 Ω / square. Note that when no pH controlling additive is used (H_2O-HVPP), the polymer layer has a lower electrical resistance as indicated by the more positive I-V slope (Figure 8.3h). This is because under pH controlled conditions, $FeCl_3$ is consumed during hydrolysis whereas when no additive is used, preferred oxidation of the monomer leads to an increased layer thickness and a possibly longer conjugation length.[36]

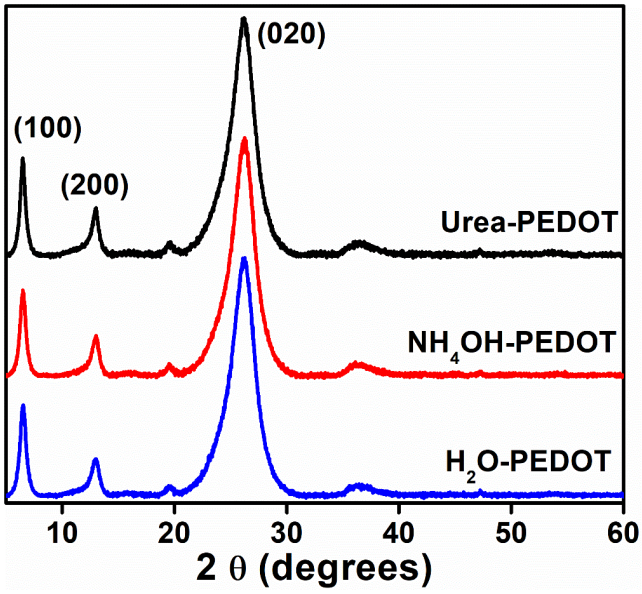

Figure 8.14: EDXS mapping and spectrum of as-synthesized PEDOT from H_2O-HVPP.

Evolution of nanofibrillar morphology is observed between minutes 15 and 60 of the synthesis. Initially, low aspect ratio tapered nanofibers appear, and by minute 60, growth ceases (Figure 8.5-8.7). Tapering of fiber tips, presenting at initial and final stages of nanostructure formation, indicates a top-down growth process, a common growth mechanism for inorganic nanostructures where the bottom of a nanofiber serves as the active growing site.[37-39] A proposed mechanism for nanofibrillar growth in HVPP is shown in the red boxes in Figure 8.1. Initial precipitation of β-FeOOH nanospindles (Figure 8.1a-b) and oxidation of EDOT vapor lead to deposition of a disc-shaped polymer film that coats β-FeOOH spindles (Figure 8.1c). As polymerization proceeds, water and EDOT vapor permeate the polymer film. During step-growth polymerization protons are released and scavenged by water molecules leading to *in situ* formation of hydrochloric acid that, upon reaction with β-FeOOH, regenerates $FeCl_3$. This in situ regeneration of the oxidant promotes preferential nucleation of polymer at the nanospindle surface, combined with the growth of nanospindle bottom cause by Ostwald ripening,[40] resulting in the deposition of $FeO_xH_yCl_z$-PEDOT nanofibers (Figure 8.1d). When the kinetics of consumption and Ostwald ripening of β-FeOOH are controlled, core-shell or monolithic structures are formed. For example, the addition of urea increases the pH (Figure 8.2) that facilitates the hydrolysis of $FeCl_3$ and Ostwald ripening, resulting in an enhanced growth rate of β-FeOOH that leads to the core-shell nanofiber, with β-FeOOH remaining as the core. For NH_4OH-HVPP and H_2O-HVPP, a lower pH after 7 min (Figure 8.1a) results in a slower Ostwald ripening rate, enabling the complete conversion of β-FeOOH to $FeCl_3$ that promotes polymerization, leading to a monolithic PEDOT structure.

The polymer morphology is controlled by $FeCl_3$ present during the synthesis (Figure 8.15-8.17). A low $FeCl_3$ concentration (0.050 M) leads to a rough amorphous polymer surface while a high concentration (0.266 M) leads to nanofibers. A concentrated solution (0.4 M) causes aggregation

of β-FeOOH nanospindles into raft-shaped somatoids[29-30] resulting in nanofibrillar bundles and microribbons of PEDOT (Figure 8.16e, 8.17c, d, e). Assemblies of β-FeOOH also form star-shaped twined crystals[31] that lead to radially aligned PEDOT superstructures (Figure 8.18). Polymer morphology is also affected by EDOT vapor concentration. Decreasing the concentration of a vaporizable EDOT solution from 0.067 M to 0.022 M stifles nanofibrillar growth in both NH_4OH-HVPP and H_2O-HVPP, and results in a heterogeneous polymer morphology in urea-HVPP. This indicates that a critical mass of polymer is required to support the growth of homogenous nanostructures during $FeCl_3$ hydrolysis (Figure 8.19). Vapor-phase polymerization is crucial for the synergistic growth of inorganic crystal and polymer, because the combination of solution-phase PEDOT polymerization with *in situ* hydrolysis of $FeCl_3$ produces low aspect ratio β-$FeO_xH_yCl_z$-PEDOT nanospindles between 250 – 390 nm long and 60 – 120 nm wide.[41]

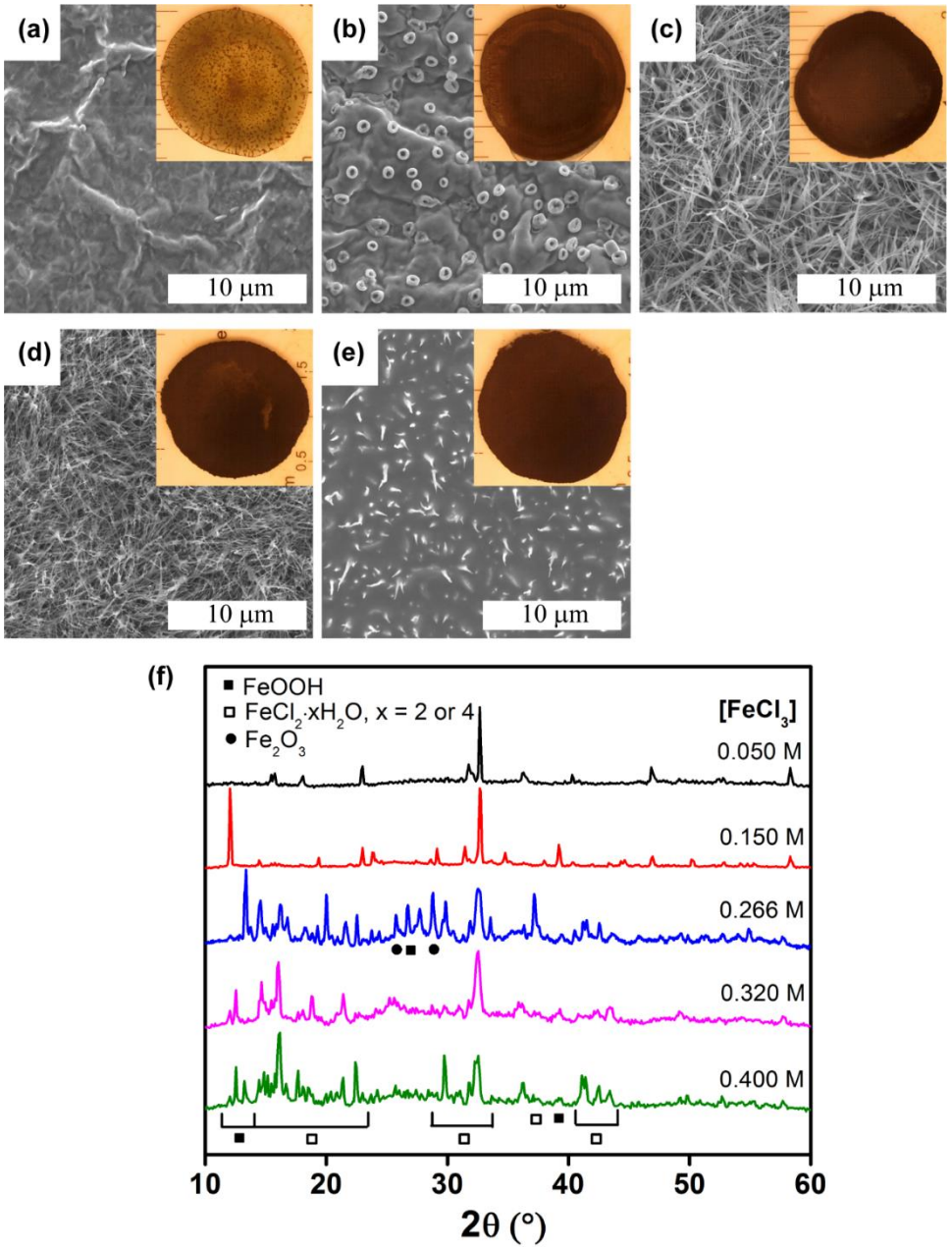

Figure 8.15: SEM and PXRD of urea-HVPP carried with $FeCl_3$ concentration of (a) 0.050 M, (b) 0.015 M, (c) 0.266 M, (d) 0.320 M and (e) 0.400 M.

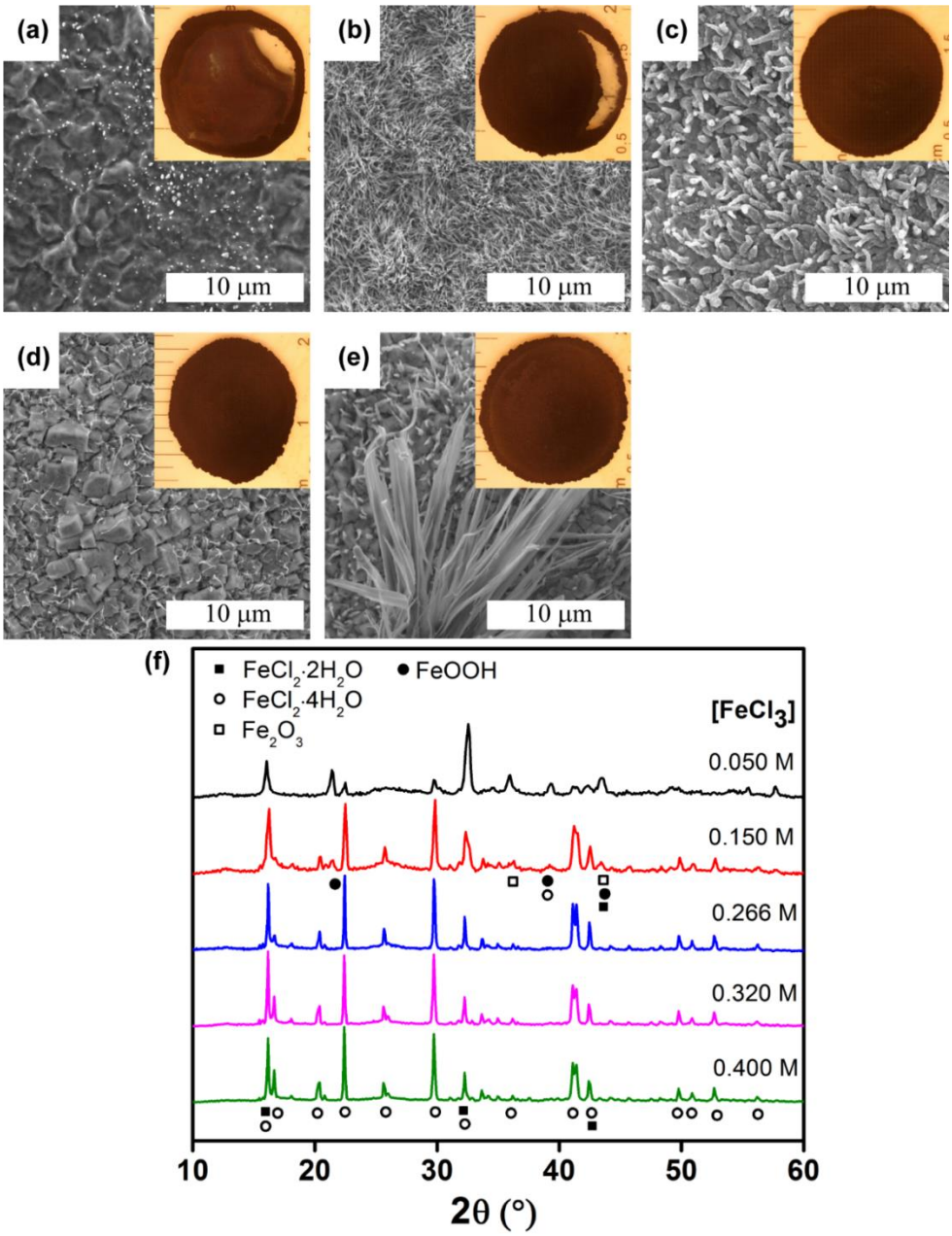

Figure 8.16: SEM and PXRD of NH_4OH-HVPP carried with $FeCl_3$ concentration of (a) 0.050 M, (b) 0.015 M, (c) 0.266 M, (d) 0.320 M and (e) 0.400 M.

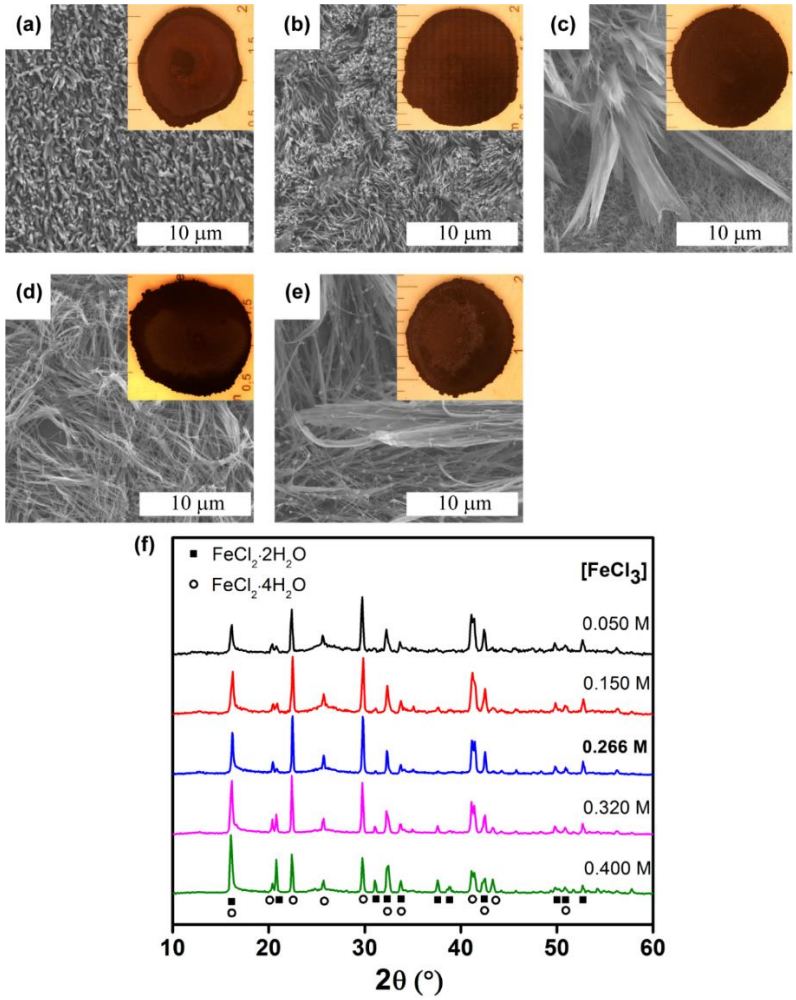

Figure 8.17: SEM and PXRD of H_2O-HVPP carried with $FeCl_3$ concentration of (a) 0.050 M, (b) 0.015 M, (c) 0.266 M, (d) 0.320 M and (e) 0.400 M.

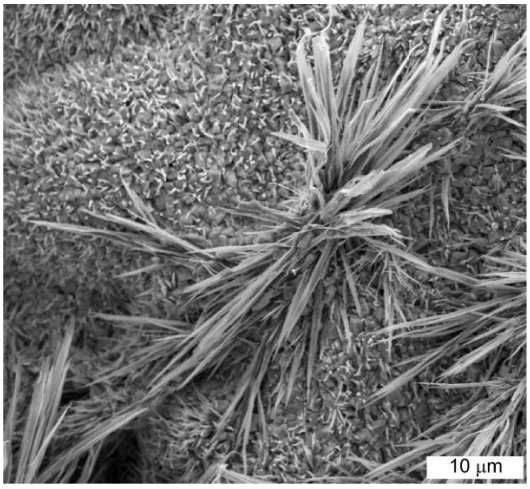

Figure 8.18: SEM of radially aligned nanofiber superstructures from NH_4OH-HVPP with $FeCl_3$ concentration of 0.4 M.

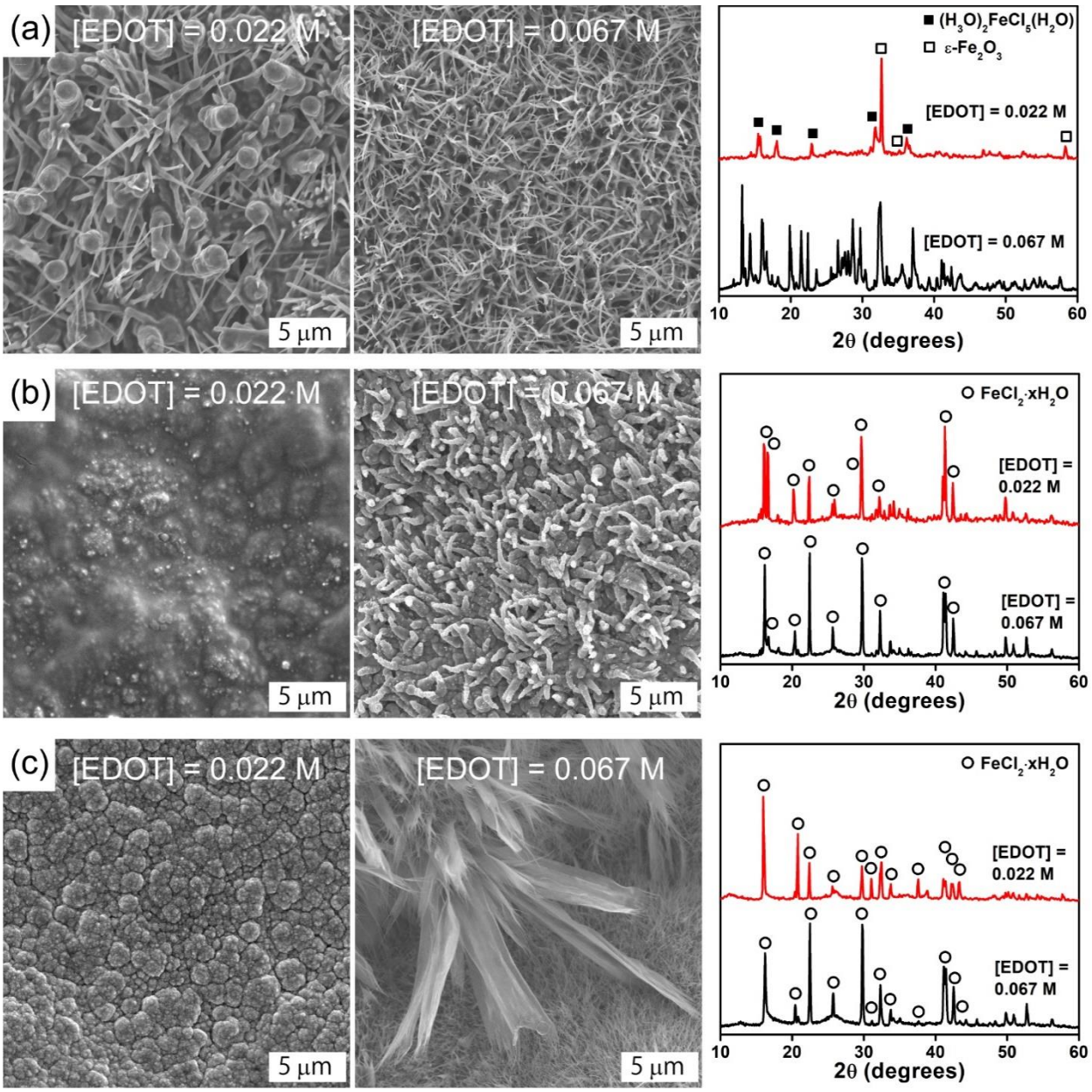

Figure 8.19: SEM and PXRD of (a) urea-HVPP, (b) NH_4OH-HVPP and (c) H_2O-HVPP with EDOT concentration of 0.022 M and 0.067 M.

Solvent polarity plays a pivotal role in $FeCl_3$ hydrolysis, for example, in a polar protic solvent α-Fe_2O_3 precipitates, while in an aprotic solvent such as dimethylformamide, this phase transforms into γ-Fe_2O_3.[42-43] Among non-aqueous protic and aprotic solvents, both ethanol and nitromethane solubilize $FeCl_3$, promote assembly of PEDOT and result in a polymer with low electrical resistance. The hydrolysis of $FeCl_3$ in nitromethane initially produces 2-line ferrihydrite ($Fe_2O_3 \cdot 0.5H_2O$), an intermediate that reacts with $FeCl_3$ under thermolysis to generate FeOCl. Nitromethane-HVPP results in the deposition of FeOCl-PEDOT core-shell 2D nanostructures that resemble nanoleaves as confirmed by SEM, TEM, and PXRD (Figure 8.20a-c, 8.21). EDXS mapping shows the expected overlap between iron and sulfur signals (Figure 8.22). PEDOT's FT-IR spectrum indicates an oxidized doped polymer state and shows vibration bands at 1485 and 1285 cm^{-1} due to C–C and C=C stretching in the quinoidal structure of the thiophene ring. The characteristic C-S bond stretching bands are present (961, 907 and 742 cm^{-1}) as well as C-O-C stretching bands from the ethylenedioxy ring (1166, 1129 and 1045 cm^{-1}) (Figure 8.20d).[44-45] FeOCl is an oxidant with lamellar structure for the polymerization of conducting polymers such as polyaniline[46] and polypyrrole[47], it is possible for PEDOT to intercalate through FeOCl structure. For this reason, the core-shell structure of FeOCl-PEDOT is further investigated by removing PEDOT from the composite at 250°C (in air) in a TGA instrument. After the completion of degradation indicated by TGA (Figure 8.23a, b), samples are taken out for TEM. As a result, a structure with a width of around 200 nm is observed (Figure 8.23c), compatible with the diameter of FeOCl in FeOCl-PEDOT, indicating that the shape of the FeOCl core remains after burning. High-resolution TEM (HRTEM) shows a clear and continuous boundary of the structure with lattice fringes (Figure 8.23d), indicating a solid instead of porous core structure. After heated to 800 °C, the structure is deformed and transformed into granules (Figure 8.23e). Electron energy

loss spectroscopy (EELS) measurement for the sample burnt at 250 °C shows low S content (Figure 8.23f), combing with TGA confirms the complete degradation of PEDOT. Based on these experiments, we believe a clear boundary between PEDOT and FeOCl is present, with limited PEDOT intercalation through FeOCl.

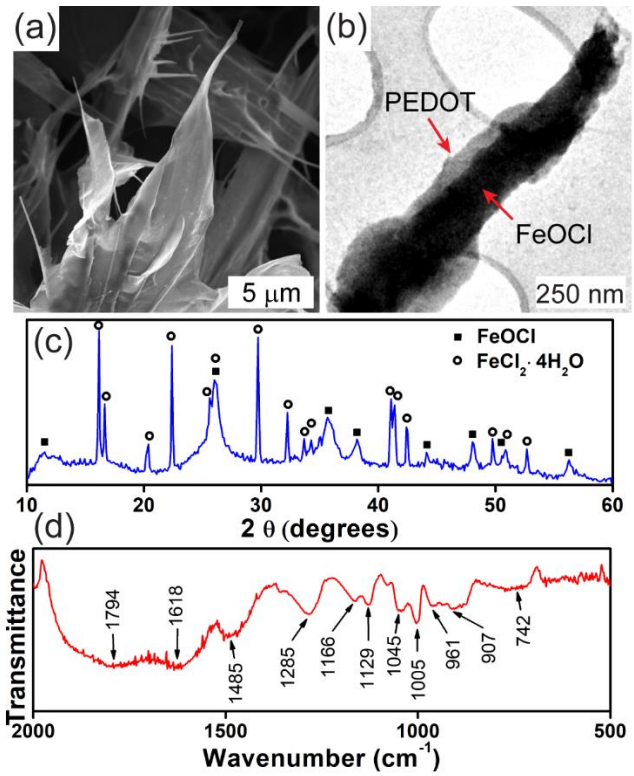

Figure 8.20: Characterization of FeOCl-PEDOT core-shell nanoleaves produced from nitromethane-HVPP. (a) SEM, (b) TEM and (c) PXRD of as-synthesized FeOCl-PEDOT core-shell nanoleaves, and (d) FT-IR after removal of FeOCl.

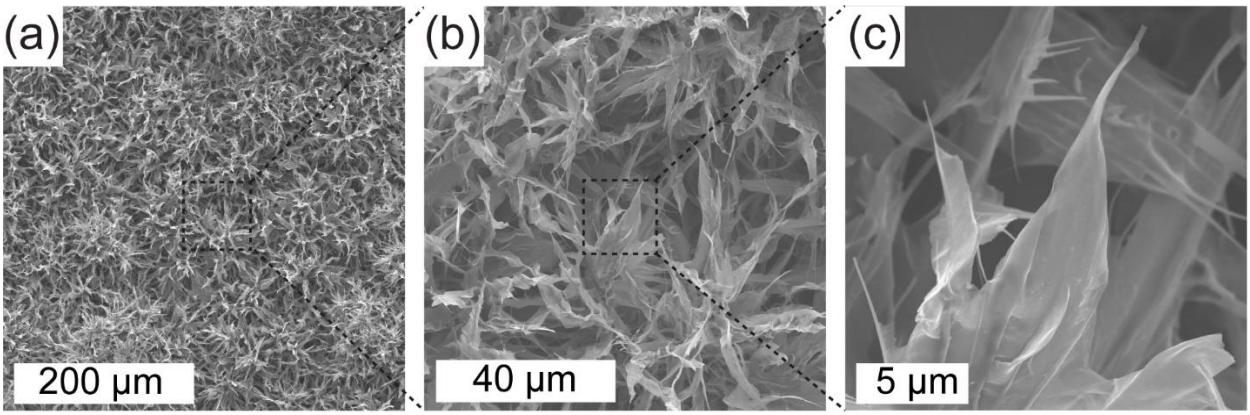

Figure 8.21: (a-c) Close-up SEM of as-synthesized nitromethane-HVPP PEDOT nanoleaves.

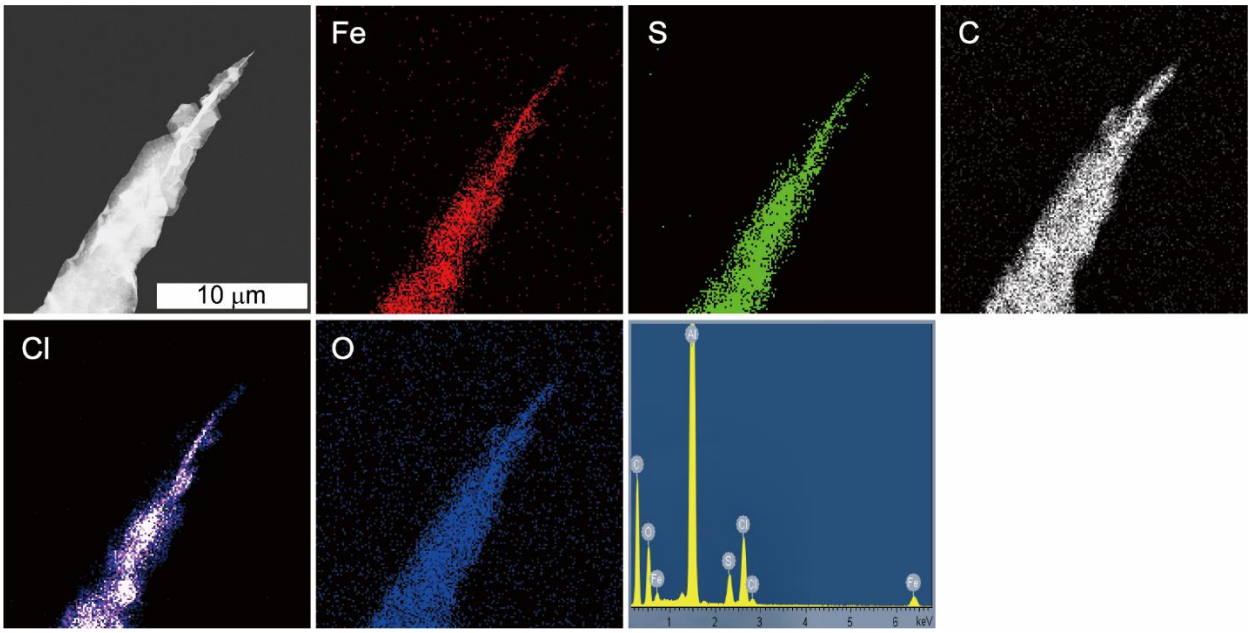

Figure 8.22: EDXS mapping and spectrum of as-synthesized nitromethane-HVPP PEDOT nanoleaves.

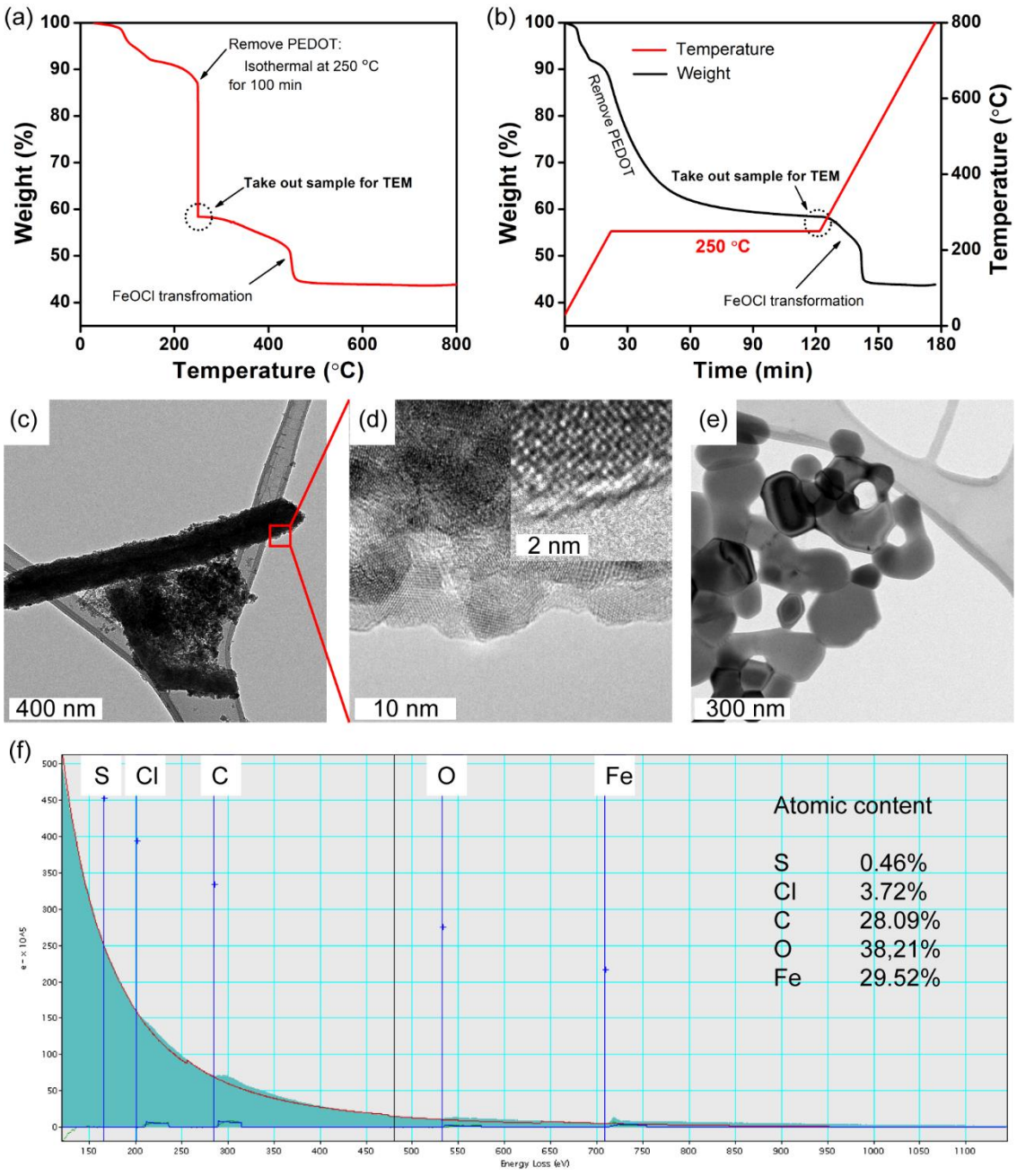

Figure 8.23: Core-shell relationship research in nitromethane-HVPP. (a). temperature based and (b). time based TGA curve for burning off PEDOT at 250°C for 100 min. Close-up (c). TEM and (d). HR-TEM of sample burns at 250°C; (e). TEM of sample burns at 800°C. (f). EELS of sample burns at 250°C.

Ethanol-HVPP results in monolithic PEDOT nanoflowers comprised of 2D nanoplates (Figure 8.24a, 8.25) and reduced oxidant $FeCl_2 \cdot H_2O$ (Figure 8.26). If the monomer is omitted from synthesis, PXRD shows that FeOCl, Fe_2O_3 and $FeCl_2 \cdot 4H_2O$ are produced ($FeCl_2 \cdot 4H_2O$ is produced from the reduction of Fe^{3+} by ethanol[48]) (Figure 8.27). The presence of the single inorganic species $FeCl_2 \cdot H_2O$ when using a monomer, indicates facile polymerization kinetics that outcompete hydrolysis. Addition of water to anhydrous ethanol leads to selective deposition of 1D PEDOT nanostructures (Figure 8.24b-c, 8.28); this selectivity is proportional with water concentration, and above 30%, nanofibers are deposited in bulk quantities (Figure 8.29). Two-probe I-V measurements after removal of inorganic species demonstrate that using a mixture of ethanol and water results in PEDOT exhibiting ohmic behavior (Figure 8.24d). An increasing slope with water content indicates a lower electrical resistance[49] that conforms well with the 4-point probe sheet resistance of 4.78 Ω / square, 4.42 Ω / square and 2.81 Ω / square for ethanol-PEDOT, ethanol-PEDOT(2% H_2O) and ethanol-PEDOT(30% H_2O), respectively. This is possibly due to water's superior proton scavenging ability that promotes step-growth polymerization and produces polymer of longer conjugation length.[50] UV-Vis-NIR shows a broad absorption band starting at 450 nm and extending to over 800 nm (Figure 8.24d inset), indicating a π-π^* transition associated with the conductive metallic state of PEDOT.[51] Absorption above 800 nm and the peak at 980 nm is due to bipolarons, dopant counter anions and an extended polymer chain conformation resulting in a free carrier tail characteristic of doped PEDOT.[52]

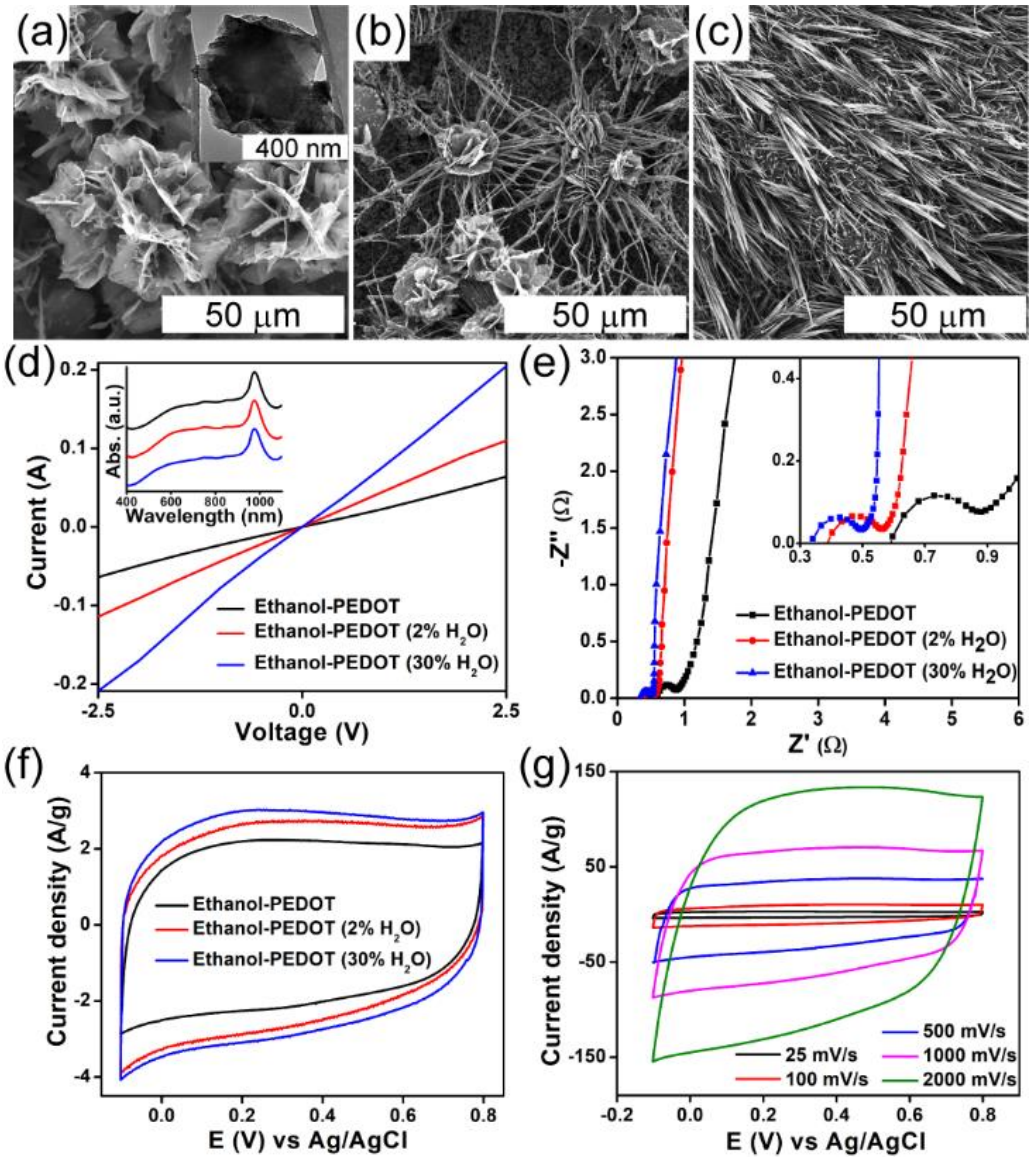

Figure 8.24: Characterization of PEDOT synthesized with ethanol as the solvent. SEM of as-synthesized PEDOT from ethanol-HVPP with H_2O addition of (a) 0%, (b) 2% and (c) 30% by volume. (d-g) Characterization of ethanol-PEDOT after removal of inorganic species. (d) I-V (inset: UV-Vis-NIR), (e) Nyquist plot of impedance response (inset shows the high frequency region), (f) cyclic voltammogram at 100th cycle with scan rate of 25 mV/s and (g) cyclic voltammogram of PEDOT nanofibers cycled at varying scan rates from 25 mV/s to 2000 mV/s.

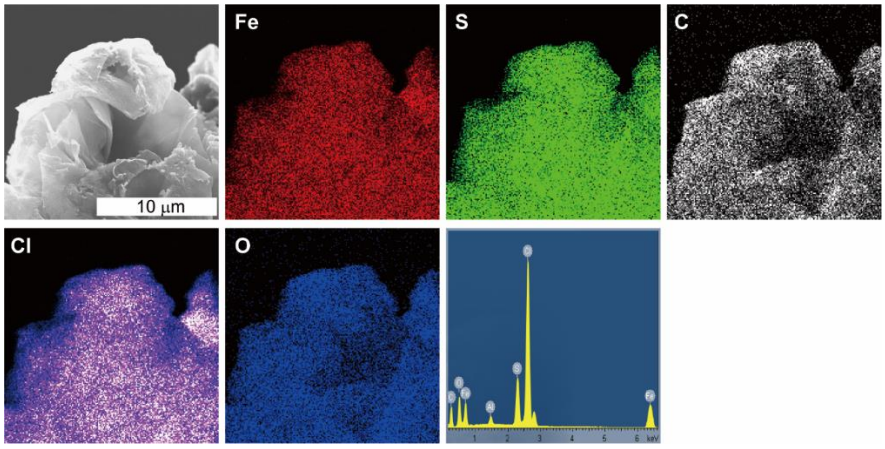

Figure 8.25: EDXS mapping and spectrum of as-synthesized ethanol-HVPP PEDOT nanoflakes.

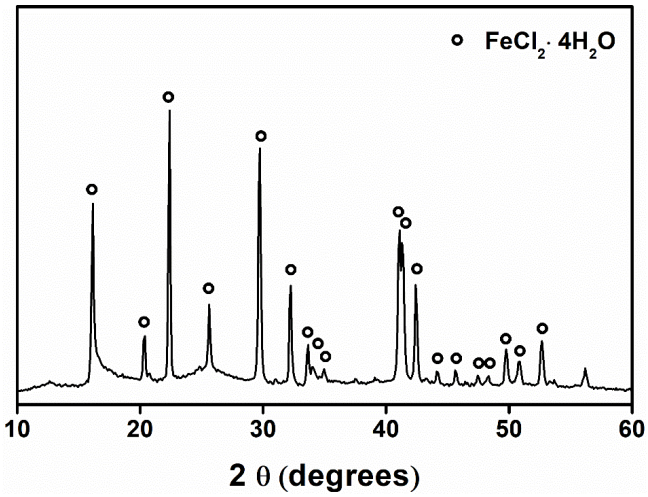

Figure 8.26: PXRD spectrum of as-synthesized product *via* ethanol-HVPP.

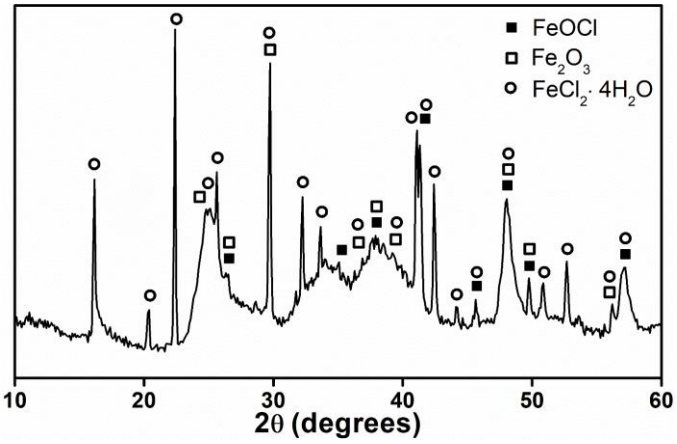

Figure 8.27: PXRD spectrum of product from synthetic procedure of ethanol-HVPP without EDOT.

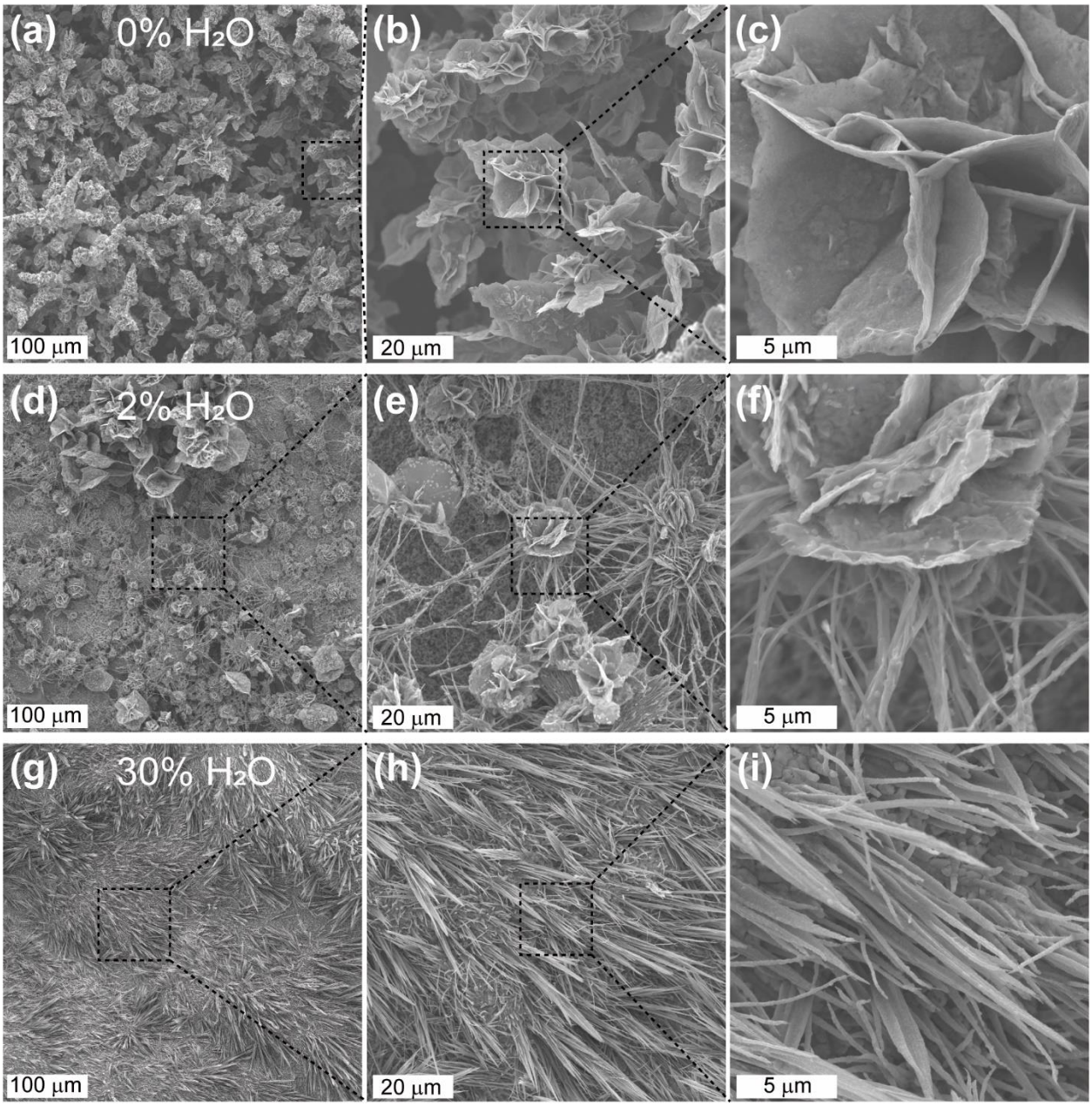

Figure 8.28: Close-up sequence of SEM of (a-c) PEDOT nanoflakes obtained from ethanol-controlled synthesis, (d-f) PEDOT nanoflowers obtained from ethanol controlled synthesis with 2% (by volume) of H_2O, and (g-i) PEDOT nanofibers obtained from ethanol controlled synthesis with 30% H_2O.

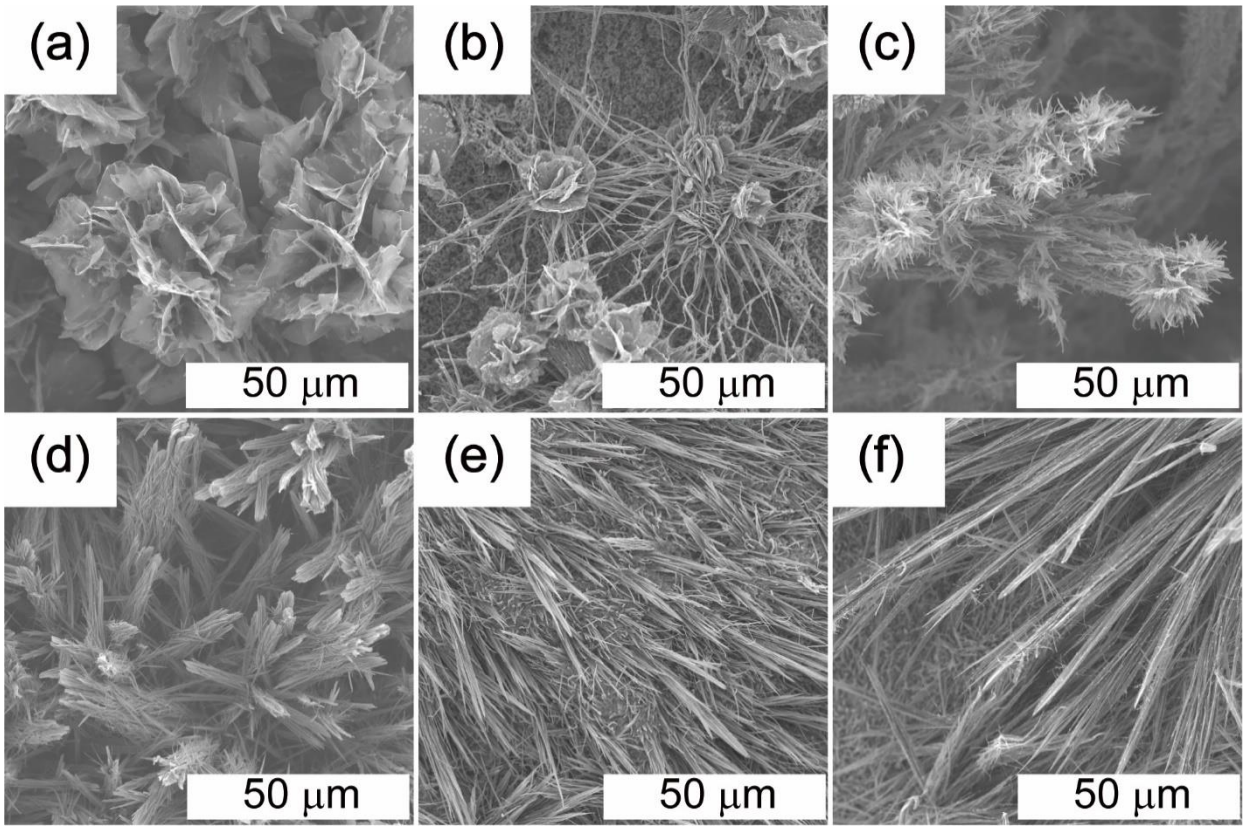

Figure 8.29: SEM of morphology evolution of H_2O affected ethanol-HVPP, from nanoflakes to nanoflowers to nanofibers. The water content in ethanol is (a) 0%, (b) 2%, (c) 10%, (d) 20%, (e) 30% and (f) 40%.

Inspired by the diversity of synthesized PEDOT nanostructures, we tested PEDOT nanoplates, nanofibers and their mixture as electrodes for electrochemical capacitors. Three-electrode cyclic voltammograms of HVPP-PEDOT-coated electrodes, collected at 25 mV/s in a 1M H_2SO_4 aqueous electrolyte, show a rectangular shape indicative of facile charge transfer kinetics with capacitance values of 90.2 F/g, 125.5 F/g and 185 F/g for synthesis with pure ethanol, 2% water in ethanol and 30% water in ethanol (Figure 8.24f). This capacitance is comparable to the nanofibrillar PEDOT electrodes synthesized with similar protocols around 180 F/g.[18, 35] Notably, PEDOT synthesized from 30% water retains a rectangular shape at a high sweep voltage of 2000 mV/s, indicating a good conjugation network and electrolyte contact (Figure 8.24g). The difference in capacitance is

caused by more than electrode material resistance, for example, ethanol-PEDOT and ethanol-PEDOT (2% H_2O) share similar sheet resistance (4.78 Ω / square and 4.42 Ω / square) however with a large difference in capacitance (90.2 F/g and 125.5 F/g). Morphology of the electrode material is another important factor that affects charge transfer events and capacitive behavior, as probed via EIS[53] with Nyquist plots spanning frequencies ranging from 100 mHz to 100 kHz (Figure 8.24e). The high frequency intercept of the semicircle with the x-axis represents the internal resistance from the electrode, the electrode/electrolyte interface, the electrolyte, and the components' contact,[54] that are 0.59 Ω (for synthesis with pure ethanol), 0.38 Ω (2% water in ethanol) and 0.34 Ω (30% water in ethanol). A higher water content during the synthesis (higher in fibrillar morphology content) results in a lower internal resistance. Synthesis with 2% and 30% water in ethanol produce PEDOT showing small semicircle radius on the Nyquist plot, combining with a nearly 90° angle at low-frequency region indicating low charge-transfer resistance and facile doping. For ethanol-PEDOT, the deviation of low-frequency curve from 90° indicates that the charge transfer process is limited by ion diffusion.[55] The EIS research suggests that 1D fibrillar morphology enhances the capacitance performance by increasing the electrolyte diffusion kinetics, resulting in a facile doping and de-doping of PEDOT during charging and discharging, leading to a lower internal resistance and higher capacitance compared to a 2D planar morphology.

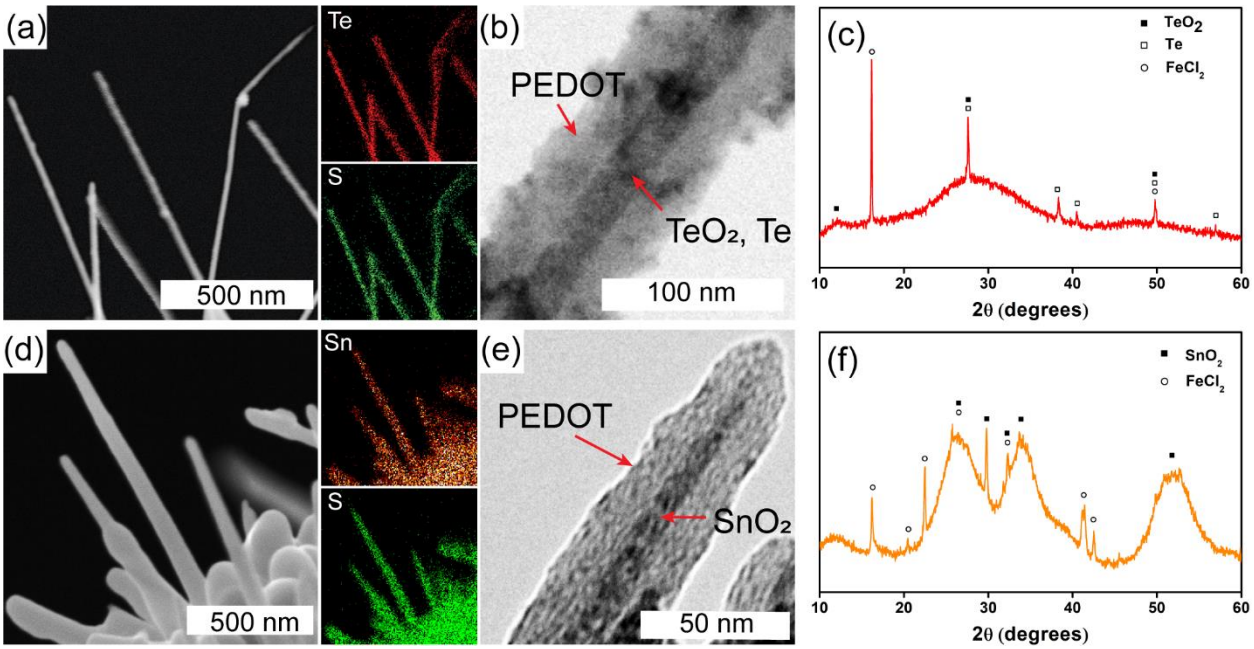

Figure 8.30: Characterization of metal oxides-PEDOT core-shell nanostructures. SEM, EDXS mapping, TEM and PXRD spectrum for (a-c) PEDOT nanowires from $TeCl_4$ templated synthesis ($TeCl_4$-HVPP), and (d-f) PEDOT nanorods from $SnCl_4$ templated synthesis ($SnCl_4$-HVPP).

Hydrolysis is a versatile strategy for mixing hydrolysable salts, where $FeCl_3$ serves as the oxidant, and a second salt plays the role of a template. This two-salt system strategy enables deposition of various metal oxide-PEDOT core-shell nanostructures. In this approach $FeCl_3$ is used in reduced concentration; approximately 90% of the salt mixture is comprised of a templating salt such as $TeCl_4$ or $SnCl_4$. The hydrolysis of $TeCl_4$ into $Te(OH)_4$ ($K_{sp} = 3 \times 10^{-54}$) and $SnCl_4$ into $Sn(OH)_4$ ($K_{sp} = 1 \times 10^{-56}$) is preferred over the hydrolysis of $FeCl_3$ into $Fe(OH)_3$ ($K_{sp} = 4 \times 10^{-38}$). During hydrolysis of $TeCl_4$ and $SnCl_4$, the continuous drop of pH caused by the production of H^+ stifles the hydrolysis of $FeCl_3$. As a result, $TeCl_4$ and $SnCl_4$ hydrolyze to form nanostructures while $FeCl_3$ only serve as the oxidant. At 130 °C, $Te(OH)_4$ and $Sn(OH)_4$ dehydrate forming TeO_2 and SnO_2, and in air, TeO_2 decomposes spontaneously to Te metal.[56] The hydrolysis of $TeCl_4$ and $SnCl_4$

results in TeO_2 nanowires[56] and SnO_2 nanorods[57-58] serving as templating structures for polymer growth. Electron microscopy shows that these salts lead to the deposition of TeO_x-PEDOT core-shell nanowires and SnO_2-PEDOT core-shell nanorods (Figure 8.30, 8.31). EDXS mapping confirms overlap of sulfur and metal signals (Figure 8.30a and 8.30d) and the presence of Fe, S, C, Cl, O and Te or Sn (Figure 8.32-8.33). A TeO_x-PEDOT core-shell nanowire has a 25 nm core diameter and a 33 nm thick polymer shell, PXRD indicates the presence of Te in the core as well (Figure 8.30b-c), while a SnO_2-PEDOT core-shell nanorod possesses a 10 nm core diameter and a 15 nm thick polymer shell (Figure 8.30e-f). Purification in DI-water selectively removes Fe byproducts and retains the Te and Sn nanofibrillar core (Figure 8.33-8.35).

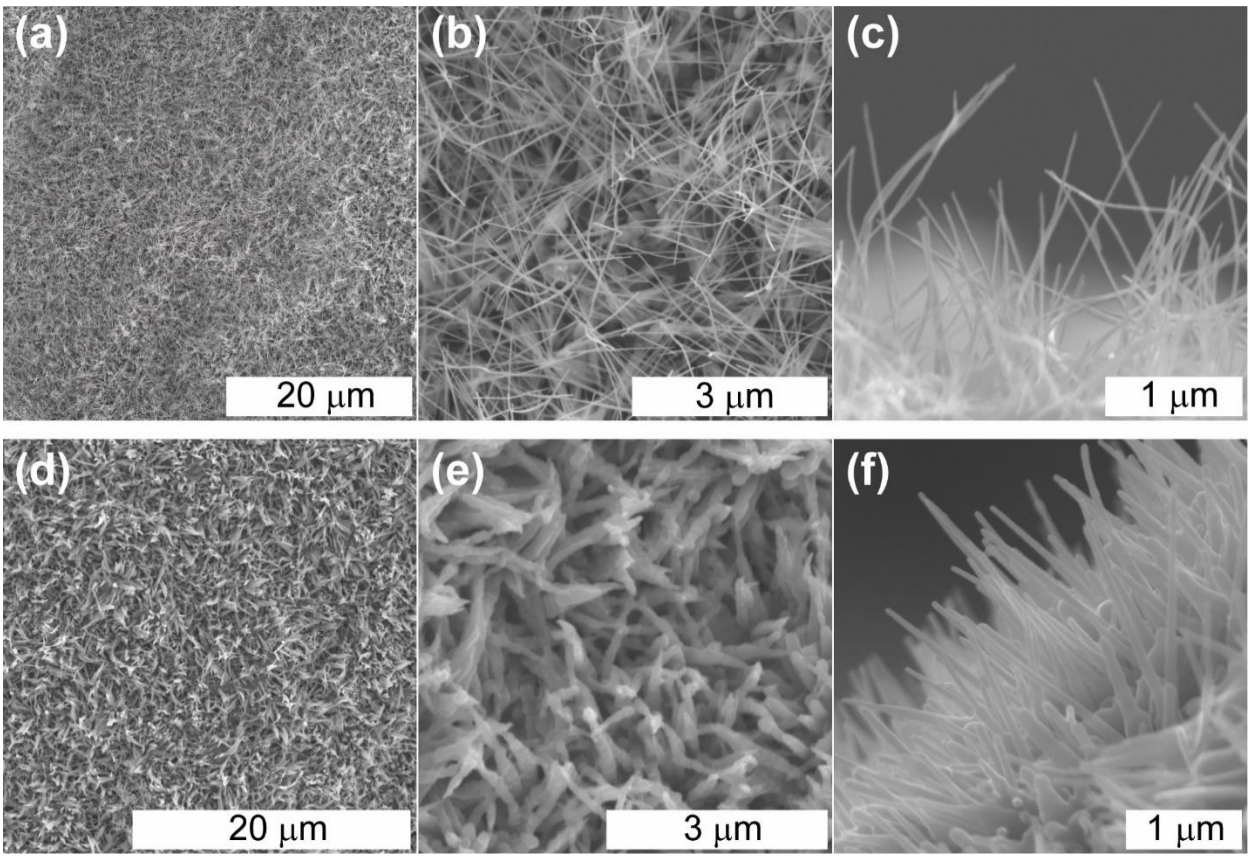

Figure 8.31: Close-up sequence of SEM of (a-c) TeO_x-PEODT nanowires from $TeCl_4$-HVPP and (d-f) PEDOT nanorods from $SnCl_4$-HVPP.

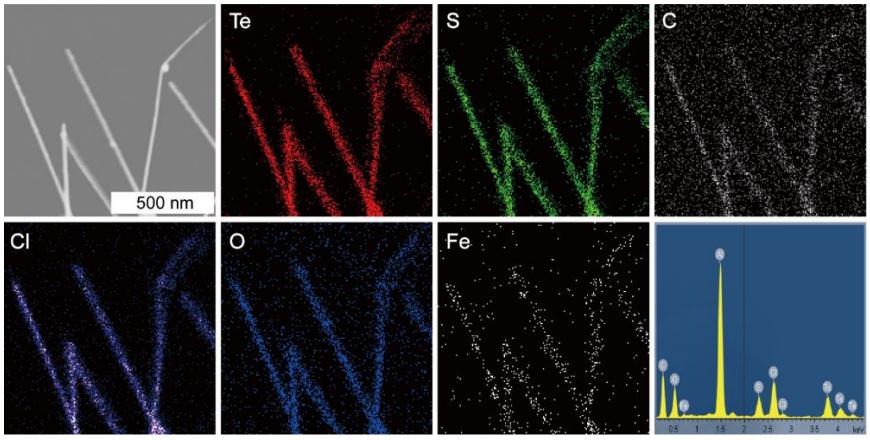

Figure 8.32: EDXS mapping and spectrum of as-synthesized nanowires from $TeCl_4$-HVPP.

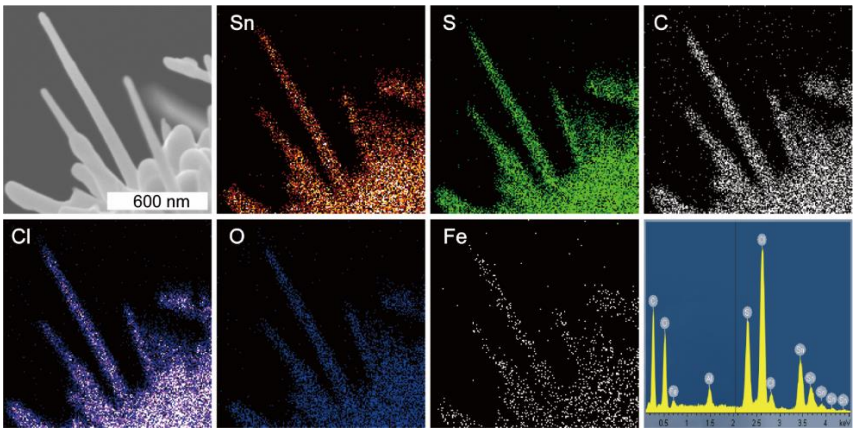

Figure 8.33: EDXS mapping and spectrum of as-synthesized nanorods from $SnCl_4$-HVPP.

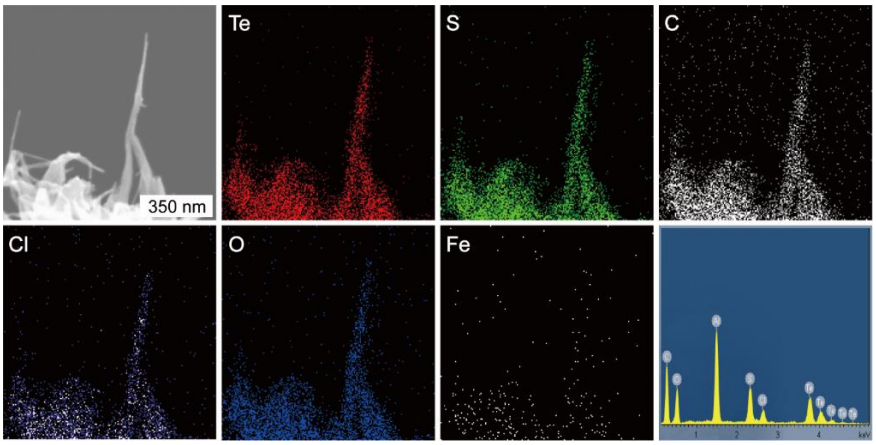

Figure 8.34: EDXS mapping and spectrum of PEDOT nanowires from $TeCl_4$-HVPP after washed with 0.1M HCl for 30 min at room temperature, then rinsed with deionized water and acetone thrice each in sequence and dried at 60 °C for 10 min.

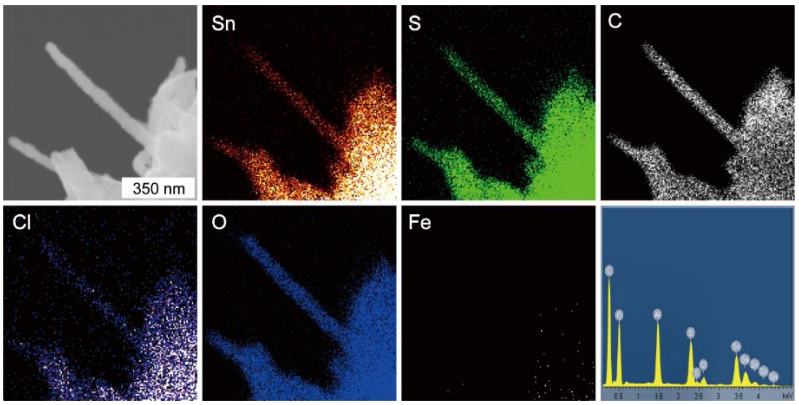

Figure 8.35: EDXS mapping and spectrum of PEDOT nanorods from $SnCl_4$-HVPP after washed with deionized water for 30 min at room temperature, then rinsed with deionized water and acetone thrice each in sequence and dried at 60 °C for 10 min.

8.4 Conclusions

In conclusion, a new one-step protocol for synthesizing nanostructured PEDOT and its metal-oxide composites is developed. A hydrolysis-assisted vapor-phase polymerization strategy is demonstrated whereby control of the hydrolysis of an inorganic salt with simultaneous polymerization of a conducting polymer drives the growth of hybrid nanostructures. Control of parameters such as pH, solvent type, and the nature of the hydrolyzable salt leads to homogeneous formation of inorganic−organic hybrid materials such as 1D FeOxHyClz/ PEDOT core−shell nanofibers, TeOx/PEDOT core−shell nanowires, and SnO2/PEDOT core−shell nanorods as well as 2D FeOCl/PEDOT nanoflowers. For energy storage application, the structure−property relationship is discussed based on the capacitance of PEDOT with different morphologies: 1D fibrillar structure enables facile electrolyte ion diffusion kinetics compared to 2D structure, resulting in a higher capacitance. The synergistic connection established between hydrolysis and polymerization enables the future development of nanostructured inorganic, polymeric, and inorganic−organic hybrid materials with large diversity. This work provides a synthetic route for

enabling various applications using hybrid composites that are ideal for energy storage applications.

References

(1) Saric, A.; Music, S.; Nomura, K.; Popovic, S., Microstructural Properties of Fe-Oxide Powders Obtained by Precipitation from $FeCl_3$ Solutions. *Materials Science and Engineering B* **1998,** *56* (1), 43-52.

(2) Penn, R. L.; Li, D.; Soltis, J. A., A Perspective on the Particle-Based Crystal Growth of Ferric Oxides, Oxyhydroxides, and Hydrous Oxides. In *New Perspectives on Mineral Nucleation and Growth: From Solution Precursors to Solid Materials*, Van Driessche, A. E. S.; Kellermeier, M.; Benning, L. G.; Gebauer, D., Eds. Springer International Publishing: Cham, **2017**, pp 257-273.

(3) Schwertmann, U.; Cornell, R. M., The Iron Oxides. In *Iron Oxides in the Laboratory*, Wiley-VCH Verlag GmbH: **2007**, pp 5-18.

(4) Jolivet, J.-P.; Tronc, E.; Chanéac, C., Iron Oxides: From Molecular Clusters to Solid. A Nice Example of Chemical Versatility. *C. R. Geoscience* **2006,** *338* (6-7), 488-497.

(5) Jolivet, J. P.; Chaneac, C.; Tronc, E., Iron Oxide Chemistry. From Molecular Clusters to Extended Solid Networks. *Chem. Commun.* **2004,** (5), 481-487.

(6) Bottero, J. Y.; Manceau, A.; Villieras, F.; Tchoubar, D., Structure and Mechanisms of Formation of Iron Oxide Hydroxide (Chloride) Polymers. *Langmuir* **1994,** *10* (1), 316-319.

(7) Flynn, C. M., Hydrolysis of Inorganic Iron(III) Salts. *Chem. Rev.* **1984,** *84* (1), 31-41.

(8) Bailey, J. K.; Brinker, C. J.; Mecartney, M. L., Growth Mechanisms of Iron Oxide Particles of Differing Morphologies from the Forced Hydrolysis of Ferric Chloride Solutions. *J. Colloid Interface Sci.* **1993,** *157* (1), 1-13.

(9) Collins, R. N.; Rosso, K. M.; Rose, A. L.; Glover, C. J.; David Waite, T., An in Situ XAS Study of Ferric Iron Hydrolysis and Precipitation in the Presence of Perchlorate, Nitrate, Chloride and Sulfate. *Geochim. Cosmochim. Acta* **2016,** *177*, 150-169.

(10) Wang, W.; Howe, J. Y.; Gu, B., Structure and Morphology Evolution of Hematite (α-Fe2O3) Nanoparticles in Forced Hydrolysis of Ferric Chloride. J. Phys. Chem. C 2008, 112 (25), 9203-9208.

(11) Zhang, X.; Chen, Y.; Zhao, N.; Liu, H.; Wei, Y., Citrate Modified Ferrihydrite Microstructures: Facile Synthesis, Strong Adsorption and Excellent Fenton-Like Catalytic Properties. *RSC Adv.* **2014,** *4* (41), 21575-21583.

(12) Jambor, J. L.; Dutrizac, J. E., Occurrence and Constitution of Natural and Synthetic Ferrihydrite, a Widespread Iron Oxyhydroxide. *Chem. Rev.* **1998,** *98* (7), 2549-2586.

(13) Brooke, R.; Cottis, P.; Talemi, P.; Fabretto, M.; Murphy, P.; Evans, D., Recent Advances in the Synthesis of Conducting Polymers from the Vapour Phase. *Prog. Mater. Sci.* **2017,** *86*, 127-146.

(14) Malinauskas, A., Chemical Deposition of Conducting Polymers. *Polymer* **2001,** *42* (9), 3957-3972.

(15) Li, D.; Huang, J. X.; Kaner, R. B., Polyaniline Nanofibers: A Unique Polymer Nanostructure for Versatile Applications. *Acc. Chem. Res.* **2009,** *42* (1), 135-145.

(16) Bhattacharyya, D.; Howden, R. M.; Borrelli, D. C.; Gleason, K. K., Vapor Phase Oxidative Synthesis of Conjugated Polymers and Applications. *J. Polym. Sci., Part B:*

Polym. Phys. **2012,** *50* (19), 1329-1351.

(17) Lawal, A. T.; Wallace, G. G., Vapour Phase Polymerisation of Conducting and Non-Conducting Polymers: a Review. *Talanta* **2014,** *119*, 133-143.

(18) Acharya, S.; Santino, L. M.; Lu, Y.; Anandarajah, H.; Wayne, A.; D'Arcy, J. M., Ultrahigh Stability of High-Power Nanofibrillar PEDOT Supercapacitors. *Sustainable Energy Fuels* **2017,** *1* (3), 482-491.

(19) Kim, J.; Kim, E.; Won, Y.; Lee, H.; Suh, K., The Preparation and Characteristics of Conductive Poly(3,4-ethylenedioxythiophene) Thin Film by Vapor-Phase Polymerization. *Synth. Met.* **2003,** *139* (2), 485-489.

(20) Tung, T. T.; Castro, M.; Feller, J.-F.; Kim, T. Y.; Suh, K. S., Hybrid Film of Chemically Modified Graphene and Vapor-Phase-Polymerized PEDOT for Electronic Nose Applications. *Org. Electron.* **2013,** *14* (11), 2789-2794.

(21) Cho, B.; Park, K. S.; Baek, J.; Oh, H. S.; Koo Lee, Y. E.; Sung, M. M., Single-Crystal Poly(3,4-ethylenedioxythiophene) Nanowires with Ultrahigh Conductivity. *Nano Lett.* **2014,** *14* (6), 3321-3327.

(22) D'Arcy, J. M.; Tran, H. D.; Tung, V. C.; Tucker-Schwartz, A. K.; Wong, R. P.; Yang, Y.; Kaner, R. B., Versatile Solution for Growing Thin Films of Conducting Polymers. *PNAS* **2010,** *107* (46), 19673-19678.

(23) Chen, Y.-C.; Lu, A.-Y.; Lu, P.; Yang, X.; Jiang, C.-M.; Mariano, M.; Kaehr, B.; Lin, O.; Taylor, A.; Sharp, I. D.; Li, L.-J.; Chou, S. S.; Tung, V., Structurally Deformed MoS_2 for Electrochemically Stable, Thermally Resistant, and Highly Efficient Hydrogen Evolution Reaction. *Adv. Mater.* **2017,** *29* (44), 1703863.

(24) Lu, Y.; Santino, L. M.; Acharya, S.; Anandarajah, H.; D'Arcy, J. M., Studying Electrical

Conductivity Using a 3D Printed Four-Point Probe Station. *J. Chem. Educ.* **2017,** *94* (7), 950-955.

(25) Subrt, J.; Bohacek, J.; Stengl, V.; Grygar, T.; Bezdicka, P., Uniform Particles with a Large Surface Area Formed by Hydrolysis of $Fe_2(SO_4)_3$ with Urea. *Mater. Res. Bull.* **1999,** *34* (6), 905-914.

(26) Music, S.; Maljkovic, M.; CzakoNagy, I., Effect of Urea on the Hydrolysis of Fe^{3+} Ions in Aqueous Solutions at Elevated Temperature. *Mater. Lett.* **1997,** *31* (1-2), 43-48.

(27) Kajiyama, A.; Nakamura, T., Hydrothermal Synthesis of β-FeO(OH) Rod-Like Particles with Uniform Size Distribution. *Colloids and Surfaces A: Physicochem. Eng. Aspects* **2000,** *163* (2-3), 301-307.

(28) Chen, K.; Chen, X.; Xue, D., Hydrothermal Route to Crystallization of FeOOH Nanorods via $FeCl_3 \cdot 6H_2O$: Effect of Fe^{3+} Concentration on Pseudocapacitance of Iron-Based Materials. *CrystEngComm* **2015,** *17* (9), 1906-1910.

(29) Pu, Z.; Cao, M.; Yang, J.; Huang, K.; Hu, C., Controlled Synthesis and Growth Mechanism of Hematite Nanorhombohedra, Nanorods and Nanocubes. *Nanotechnology* **2006,** *17* (3), 799-804.

(30) Mackay, A. L., β-Ferric Oxyhydroxide-Akaganeite. *Mineral. Mag.* **1962,** *33* (259), 270-280.

(31) Mackay, A. L., β-Ferric Oxyhydroxide. *Mineral. Mag.* **1960,** *32* (250), 545-557.

(32) Penner, R. M., Mesoscopic metal particles and wires by electrodeposition. *J. Phys. Chem. B* **2002,** *106* (13), 3339-3353.

(33) Ugur, A.; Katmis, F.; Li, M.; Wu, L.; Zhu, Y.; Varanasi, K. K.; Gleason, K. K., Low-

Dimensional Conduction Mechanisms in Highly Conductive and Transparent Conjugated Polymers. *Adv. Mater.* **2015,** *27* (31), 4604-10.

(34) Tamburri, E.; Guglielmotti, V.; Matassa, R.; Orlanducci, S.; Gay, S.; Reina, G.; Terranova, M. L.; Passeri, D.; Rossi, M., Detonation Nanodiamonds Tailor the Structural Order of PEDOT Chains in Conductive Coating Layers of Hybrid Nanoparticles. *J. Mater. Chem. C* **2014,** *2* (19), 3703-3716.

(35) D'Arcy, J. M.; El-Kady, M. F.; Khine, P. P.; Zhang, L.; Lee, S. H.; Davis, N. R.; Liu, D. S.; Yeung, M. T.; Kim, S. Y.; Turner, C. L.; Lech, A. T.; Hammond, P. T.; Kaner, R. B., Vapor-Phase Polymerization of Nanofibrillar Poly(3,4-ethylenedioxythiophene) for Supercapacitors. *ACS Nano* **2014,** *8* (2), 1500-1510.

(36) Song, M.-K.; Kim, Y.-T.; Kim, B.-S.; Kim, J.; Char, K.; Rhee, H.-W., Synthesis and Characterization of Soluble Polypyrrole Doped with Alkylbenzenesulfonic Acids. *Synth. Met.* **2004,** *141* (3), 315-319.

(37) Henry, T.; Kim, K.; Ren, Z.; Yerino, C.; Han, J.; Tang, H. X., Directed Growth of Horizontally Aligned Gallium Nitride Nanowires for Nanoelectromechanical Resonator Arrays. *Nano Lett.* **2007,** *7* (11), 3315-3319.

(38) Guo, Y. B.; Liu, H. B.; Li, Y. J.; Li, G. X.; Zhao, Y. J.; Song, Y. L.; Li, Y. L., Controlled Core-Shell Structure for Efficiently Enhancing Field-Emission Properties of Organic-Inorganic Hybrid Nanorods. *J. Phys. Chem. C* **2009,** *113* (29), 12669-12673.

(39) Liu, F.; Su, Z.; Li, L.; Mo, F.; Jin, S.; Deng, S.; Chen, J.; Shen, C.; Gao, H.; Xu, N., Effect of Contact Mode on the Electrical Transport and Field-Emission Performance of Individual Boron Nanowires. *Adv. Funct. Mater.* **2010,** *20* (12), 1994-2003.

(40) Zhang, M.; Han, D.; Lu, P., PEDOT Encapsulated β-FeOOH Nanorods: Synthesis,

Characterization and Application for Sodium-Ion Batteries. *Electrochim. Acta* **2017,** *238*, 330-336.

(41) Mao, H.; Lu, X.; Chao, D.; Cui, L.; Li, Y.; Zhang, W., Preparation and Characterization of PEDOT//β-$Fe^{3+}O$(OH,Cl) Nanospindles with Controllable Sizes in Aqueous Solution. *J. Phys. Chem. C* **2008,** *112* (51), 20469-20480.

(42) Mou, F.; Guan, J.; Xiao, Z.; Sun, Z.; Shi, W.; Fan, X.-a., Solvent-Mediated Synthesis of Magnetic Fe_2O_3 Chestnut-Like Amorphous-Core/γ-Phase-Shell Hierarchical Nanostructures with Strong As(V) Removal Capability. *J. Mater. Chem.* **2011,** *21* (14), 5414-5421.

(43) Gash, A. E.; Tillotson, T. M.; Satcher, J. H.; Poco, J. F.; Hrubesh, L. W.; Simpson, R. L., Use of Epoxides in the Sol−Gel Synthesis of Porous Iron(III) Oxide Monoliths from Fe(III) Salts. Chem. Mater. 2001, 13 (3), 999-1007.

(44) Xiao, Y.; Lin, J.-Y.; Tai, S.-Y.; Chou, S.-W.; Yue, G.; Wu, J., Pulse Electropolymerization of High Performance PEDOT/MWCNT Counter Electrodes for Pt-Free Dye-Sensitized Solar Cells. *J. Mater. Chem.* **2012,** *22* (37), 19919-19925.

(45) Winther-Jensen, B.; Chen, J.; West, K.; Wallace, G., Vapor Phase Polymerization of Pyrrole and Thiophene Using Iron(III) Sulfonates as Oxidizing Agents. *Macromolecules* **2004,** *37* (16), 5930-5935.

(46) Wu, C. G.; DeGroot, D. C.; Marcy, H. O.; Schindler, J. L.; Kannewurf, C. R.; Bakas, T.; Papaefthymiou, V.; Hirpo, W.; Yesinowski, J. P., Reaction of Aniline with FeOCl. Formation and Ordering of Conducting Polyaniline in a Crystalline Layered Host. *J. Am. Chem. Soc.* **1995,** *117* (36), 9229-9242.

(47) Kanatzidis, M. G.; Tonge, L. M.; Marks, T. J.; Marcy, H. O.; Kannewurf, C. R., In Situ

Intercalative Polymerization of Pyrrole in FeOCl: a New Class of Layered, Conducting Polymer-Inorganic Hybrid Materials. *J. Am. Chem. Soc.* **1987,** *109* (12), 3797-3799.

(48) Martín, S. E.; Suárez, D. o. F., Catalytic Aerobic Oxidation of Alcohols by $Fe(NO_3)_3$–$FeBr_3$. *Tetrahedron Lett.* **2002,** *43* (25), 4475-4479.

(49) Zhang, L.; Jamal, R.; Zhao, Q.; Wang, M.; Abdiryim, T., Preparation of PEDOT/GO, PEDOT/MnO_2, and PEDOT/GO/MnO_2 Nanocomposites and Their Application in Catalytic Degradation of Methylene Blue. *Nanoscale Res. Lett.* **2015,** *10*, 148-156.

(50) Fabretto, M.; Zuber, K.; Hall, C.; Murphy, P., High Conductivity PEDOT Using Humidity Facilitated Vacuum Vapour Phase Polymerisation. *Macromol. Rapid Commun.* **2008,** *29* (16), 1403-1409.

(51) Kim, T.-W.; Woo, H.-Y.; Jung, W.-G.; Ihm, D.-W.; Kim, J.-Y., On the Mechanism of Conductivity Enhancement in Plasma Treated Poly(3,4-ethylenedioxythiophene) Films. *Thin Solid Films* **2009,** *517* (14), 4147-4151.

(52) Zhao, Q.; Jamal, R.; Zhang, L.; Wang, M.; Abdiryim, T., The Structure and Properties of PEDOT Synthesized by Template-Free Solution Method. *Nanoscale Res. Lett.* **2014,** *9* (1), 557-557.

(53) Rubinson, J. F.; Kayinamura, Y. P., Charge Transport in Conducting Polymers: Insights from Impedance Spectroscopy. *Chem. Soc. Rev.* **2009,** *38* (12), 3339-47.

(54) Yeh, M.-H.; Lee, C.-P.; Chou, C.-Y.; Lin, L.-Y.; Wei, H.-Y.; Chu, C.-W.; Vittal, R.; Ho, K.-C., Conducting Polymer-based Counter Electrode for a Quantum-Dot-Sensitized Solar Cell (QDSSC) with a Polysulfide Electrolyte. *Electrochim. Acta* **2011,** *57* (Supplement C), 277-284.

(55) Antiohos, D.; Folkes, G.; Sherrell, P.; Ashraf, S.; Wallace, G. G.; Aitchison, P.; Harris,

A. T.; Chen, J.; Minett, A. I., Compositional Effects of PEDOT-PSS/Single Walled Carbon Nanotube Films on Supercapacitor Device Performance. *J. Mater. Chem.* **2011,** *21* (40), 15987-15994.

(56) Arab, F.; Mousavi-Kamazani, M.; Salavati-Niasari, M., Synthesis, Characterization, and Optical Properties of Te, Te/TeO_2 and TeO_2 Nanostructures via a One-Pot Hydrothermal Method. *RSC Adv.* **2016,** *6* (75), 71472-71480.

(57) Wang, H.; Rogach, A. L., Hierarchical SnO_2 Nanostructures: Recent Advances in Design, Synthesis, and Applications. *Chem. Mater.* **2014,** *26* (1), 123-133.

(58) Vayssieres, L.; Graetzel, M., Highly Ordered SnO_2 Nanorod Arrays from Controlled Aqueous Growth. *Angew. Chem. Int. Ed.* **2004,** *43* (28), 3666-3670.

Chapter 9

Advances in conducting polymers and their applications

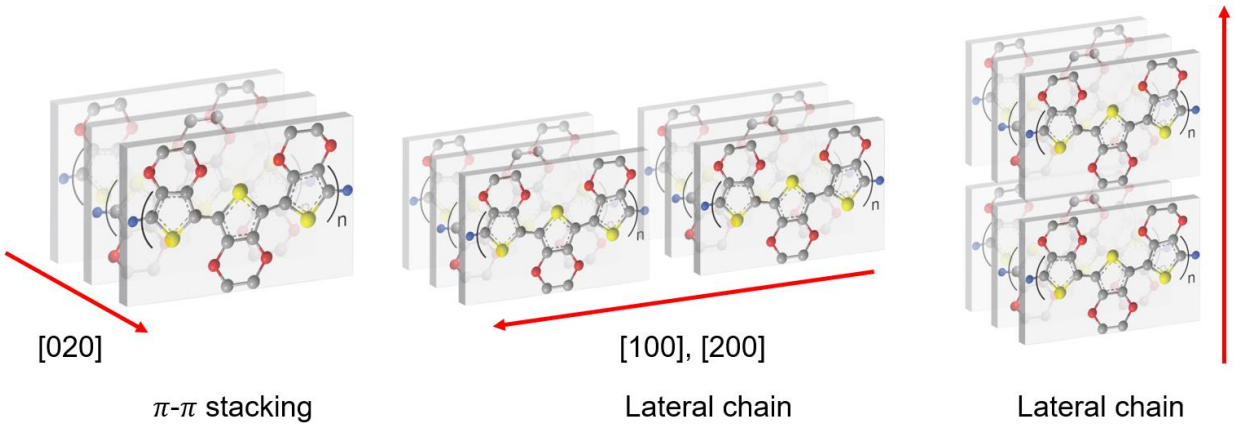

PEDOT configuration

9.1 Conducting polymer configuration

9.1.1. Background

Conducting polymers are of widespread interest for enabling high-performance, low-cost electronic devices due to their excellent conductivity.[1] Optimal device performance for high-end technologies requires a fundamental comprehension of charge transfer mechanism and polymer chain configuration.[2] However, the understanding of conduction mechanisms remains incomplete even after several decades of intensive investigation.[3]

Recent researches shed light on complicated microscale conduction pathways from different aspects.[4] Charge carriers in conducting polymers, such as polaron and bipolaron, is one of the directions that highly depended on various dopants, such as Cl^-, tosylate and polystyrenesulfonate.[5] Besides, charge transfer is another critical factor that affects the conductivity associated with the degree of crystallinity.[6] Currently, there is a debate on charge transfer in conducting polymers, which neither fully crystalline nor completely amorphous and different models are introduced (Dudel model and Mott and Efros–Shklovskii model).[7-8] Charge-carrier mobility depends not only on polymer chain alignment (crystallinity) and crystallite orientation at the nanoscale, but also on the connection or defects between crystalline and amorphous domains at the macroscale.[9] For example, single-crystal PEDOT exhibit the highest conductivity (~8000S/cm) due to the well-aligned polymer chains, the absence of grain boundaries.[10] However, the crystalline order of PEDOT and its derivatives is limited in amorphous domains, leading to scattering, trapping at defects, and localization of charge carriers.[11]

Highly crystalline domains are vital for superior conductivity since the close-pack π-π stacking facilitates the charge transfer associated with optimized crystal morphology and degree of

crystallinity.[12] Therefore, the configuration of conducting polymers is essential for research, and here, we utilize poly(3,4-ethylenedioxythiophene) (PEDOT) as an example to construct a configuration.

To better understand PEDOT configuration, we introduce glass transition temperature, degradation temperature, and melting temperature as the critical parameters to a polymer structure. Glass transition temperature (T_g) is a property of the amorphous materials or the amorphous portion of semicrystalline materials, referring to the temperature at which 30-50 carbon chains start to move.[13] Unfortunately, PEDOT as a semicrystalline polymer possesses no observable glass transition temperatures due to its unsolvable property. Similar to T_g, PEDOT exhibit no melting temperature since the polymer chains undergo degradation at 160°C in the atmosphere and 200°C in N_2.[14] However, based on other soluble or chemically stable conducting polymers, there is a trend suggesting that the T_g and melting temperature for highly crystalline polymer possess higher T_g due to the enhanced interaction between polymer chains.[15] After summarizing previous works, we propose a model for the PEDOT configuration possessing a tertiary structure.

9.1.2. Experimental Methods

The Teflon liner of a hydrothermal reactor is loaded with: a 7 mm × 7 mm rusted steel substrate, 20 μL of concentrated hydrochloric acid and 200 μL of a 0.0674 M EDOT solution (3.37×10^{-5} mol) in chlorobenzene (4.93×10-3 mol). Each of these components is contained in a glass vial. This rector is sealed, heated for 6 h in an oven at 150 °C and then cooled in an ice bath for 15 min. A PEDOT-coated substrate is immersed in water to delaminate the polymer film.

Scanning electron micrographs and energy-dispersive X-ray spectrograms were collected using a JEOL 7001LVF FE-SEM. Transmission electron micrographs were obtained in a JEOL 2100 by squeezing a PEDOT film in folding double TEM grid. A Bruker d8 Advanced X-ray diffractometer was utilized to collect powder X-ray diffractograms of pulverized samples at room temperature, with Cu Kα radiation source (λ = 1.5406 Å) and LynxEye XE detector, operating at 40 kV and 40 mA; sample holder was rotated at 30 rpm with a scan step of 0.02°.

9.1.3. Discussion

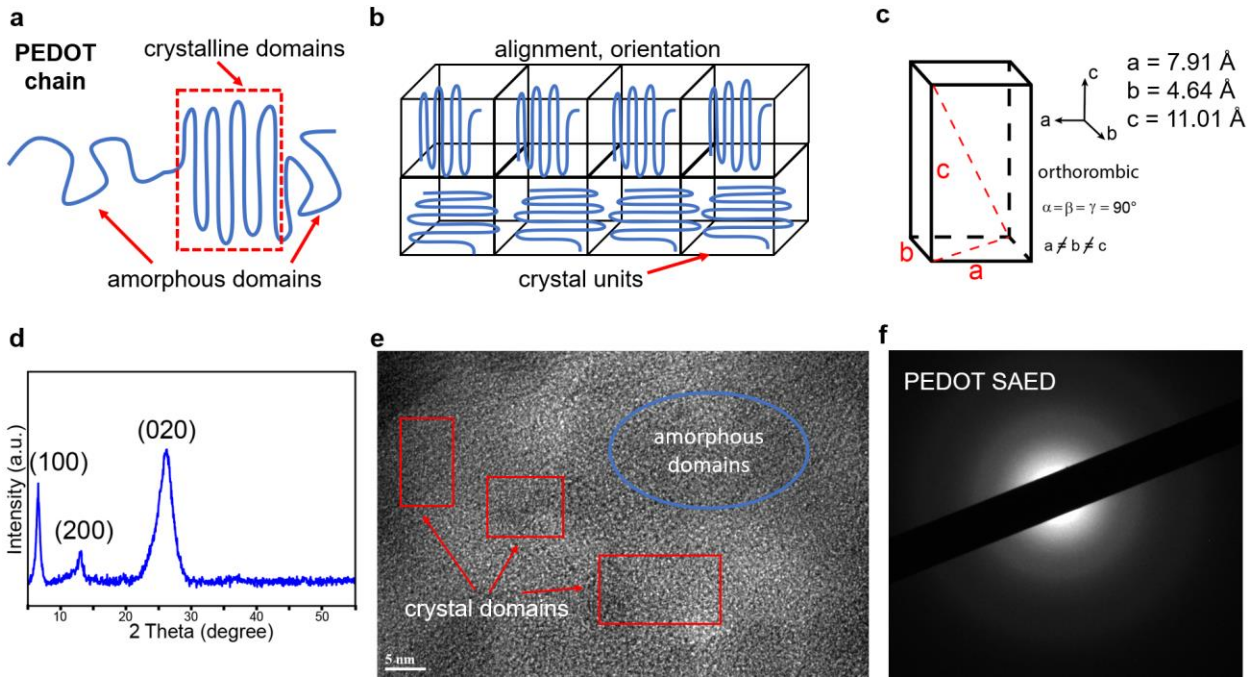

Figure 9.1: (a) Schematic of RVPP-PEDOT chain. (b) Schematic of PEDOT crystalline domains. (c) Orthorhombic crystal unit. (c) pXRD of PEDOT. (e) HRTEM exhibit crystal domains and amorphous domains of PEDOT. (f) SAED of PEDOT

PEDOT exhibits a random heterogeneous microstructure comprised of crystalline and amorphous domains, which differ from inorganic conductive materials whose structures are generally homogeneous and crystalline (Figure 9.1a).[11, 16] Unlike the well-ordered inorganic unit cell, PEDOT's unit cell consists of polymer chains and crystal (Figure 9.1b). Based on the single crystal PEDOT research, RVPP-PEDOT exhibits an orthorhombic crystal unit cell (Figure 9.1c) with lattice constants of a = 11.01 Å, b = 4.64 Å, and c = 7.91 Å and that it forms along the [010] direction on the substrate, coinciding with the (100) projection from XRD results (Figure 9.1d).[10] A high-resolution transmission electro-micrograph (HRTEM) (Figure 9.1e) exhibits both crystal and amorphous domains. The crystalline structures of the RVPP-PEDOT are characterized by

selective-area electron diffraction (SAED). A SAED pattern of the RVPP-PEDOT (Figure 9.1f) presents various continuous haloes that confirming the semi-crystal structure.[17-18]

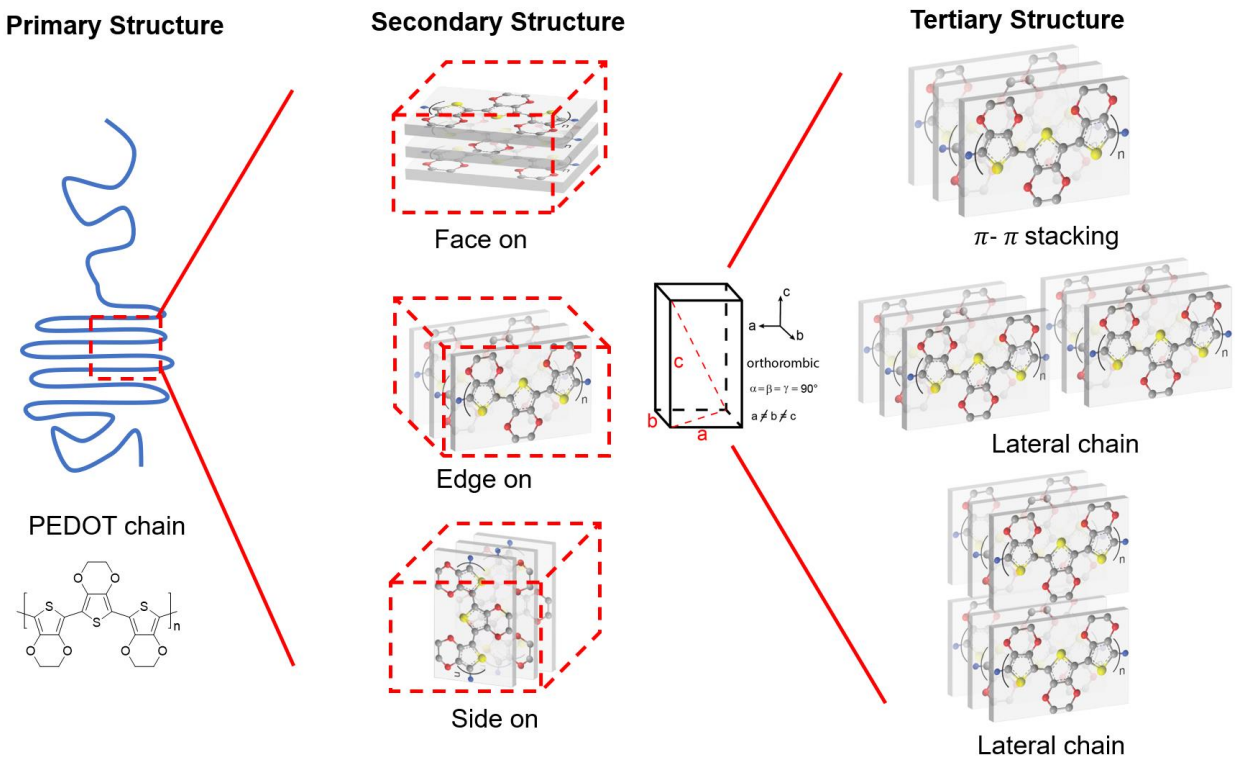

Figure 9.2: Schematic of PEDOT's configuration.

Similar to protein structures, PEDOT configuration consists of multiple levels of structures. The primary structure exhibit that RVPP-PEDOT chain is semicrystalline composed of crystal domains and amorphous domains.[2] The secondary structure is associate with the orientation between polymer chain and substrate, consisting of face-on, edge-on and side-on.[19-20] The tertiary structure is based on the molecular chains' location, including π-π stacking and lateral chains.[4] Therefore, accurate control of PEDOT configuration enables refining the charge transfer, thus enhance the PEDOT electrical conductivity.

9.2 Synthesis and processing of conducting polymers for energy storage

During charging and discharging, CP ECs undergo two major processes simultaneously: ions diffuse through the electrolyte into the vicinity of CP backbones and electrons are either added or removed. Thus, more accommodation of electrolyte ions and lower resistance of ion and electron migration in the system lead to both high energy density and power density. The former requires ionically porous CP electrodes with large ion accessible areas, invoking ideas of nano/microstructural design, while the latter calls for highly conductive, crystalline CP electrodes in which all active material is utilized and connected to the same conjugated network. In the past decade, significant progress has been made *via* improved synthetic techniques and advances in electrode processing.

Synthesis controls the molecular structure of CPs by manipulation of reaction kinetics. When polymerization is carried out too quickly, uncontrollable reactions deteriorate the conjugation length and packing of CP chains by introducing defects and side reactions, rendering CP electrodes with low conductivity. On a larger scale, poor polymerization conditions result in dense and non-porous CP films, blocking accessible surface area and hindering ion diffusion, both of which are critical for advancing energy storage. Not accounting for expansion in these electrodes leads to mechanical delamination during charging and discharging and thus low cycling stability.[21-22] Researchers have developed a myriad of ways to mitigate these issues. In general, the synthesis of any conducting polymer needs only monomer and oxidant. Creatively introducing these two components has been a large contributor to the progress in polymer science over the past decade. The most common method is chemical (solution phase) polymerization, where monomer and

oxidant are both in liquid form. Electrochemical polymerization of CPs is also a universal strategy, where a potentiostat is used in lieu of a chemical oxidant. CPs retain their conjugation network and conductivity during synthesis, whereas electropolymerization of non-conjugated polymers leads to a huge drop in current and slowing of the polymerization process as the conductive electrode is coated with an insulator. A variety of strategies have also been developed where oxidant and/or monomer are reacted in the vapor phase; moreover, interfacial synthesis and templating routes have led to many exquisite CP morphologies. Advances in synthesis seek to confine the reaction rate and selectivity of polymerization to generate highly conductive CP electrodes characterized by high crystallinity, long conjugation length, high conductivity and well-ordered nano/micro architectures.

9.2.1. Solution-based chemical polymerization

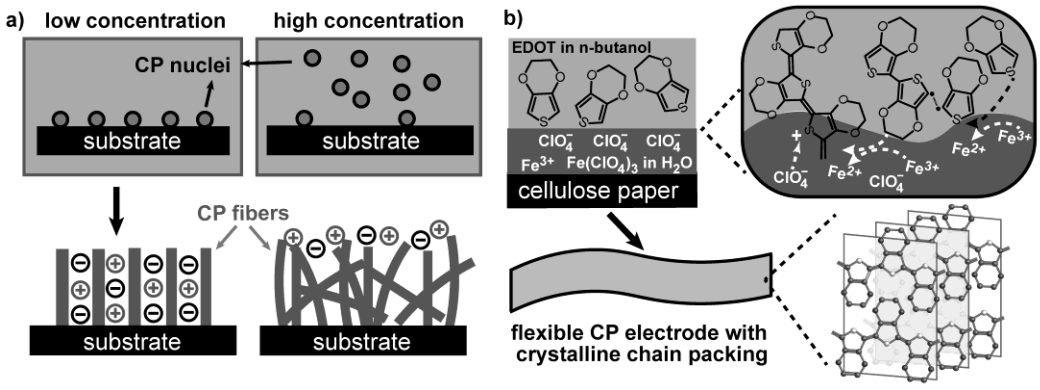

Figure 9.3: Control of polymerization conditions leads to molecular ordering of CP electrodes. (a) In chemical synthesis (solution phase), low concentration of reactants forces preferential deposition of polymer on the substrate with directional growth, netting a high aspect ratio architecture beneficial to charge storage. Using too high a concentration of reactants results in disordered nuclei forming in solution, reducing electrode performance. (b) If the oxidant and monomer solutions are immiscible, polymerization will be restricted to their interface, lowering reaction kinetics. CP films synthesized inter-facially show a high crystallinity, conductivity, and capacitance.

Solution-based chemical polymerization refers to mixing oxidant and monomer in solution; this method is simple and results in bulk quantities of solution-processable active material with minimal effort. A purification step, commonly carried out via filtration, centrifugation or dialysis, is often required to remove excess oxidant, monomer and reaction side-products. This ensures a stable and reversible charge storage performance during electrochemical testing of a conducting polymer electrode. Solid-state polymer powder samples can also be obtained by filtration or lyophilization protocols; these powders are processable, similar to activated carbon.

Direct deposition of CPs onto substrates and current collectors remains a challenge in solution-based chemical polymerization. It has been shown that immersing a substrate in a dilute mixture of oxidant and monomer solution results in fast nucleation of polymer on solid surfaces, favoring CP growth on the substrate.[23] Lowering reagent concentration slows down the polymerization speed, resulting in oriented nano and micro-morphologies. An array of needle-like PANi nanowires is synthesized on graphitized carbon fiber by immersing the substrate in a mixed solution of ammonium persulfate (oxidant) and aniline (monomer); the length of a nanowire increases with aniline concentration. The nanowires become disordered when aniline concentration exceeds 0.3 M, attributed to a high concentration of PANi nuclei in solution (Figure 9.3a).[24] Variability in PANi nanowire length and degree of alignment affects the charge storage ability i.e., short nanowires synthesized from 0.1 M aniline possess a capacitance of 546 F/g, longer nanowires from 0.3 M aniline reach 976.5 F/g, and disordered PANi nanowires (0.5 M aniline) show a capacitance of 573.5 F/g. Aligned high aspect ratio nanowires exhibit the highest performance due to well-defined ion diffusion channels that result in high capacitance and high charging rate electrodes for ECs.[24]

Another strategy for coating substrates from solution is to apply reagents directly on a substrate. For example, alternating coats of immiscible oxidant and monomer solutions on flexible cellulose paper confine polymerization at the monomer/oxidant interface, slow the rate of polymer growth, and lead to an ordered CP molecular packing that enhances the conductivity of the electrode. This interfacially synthesized PEDOT is characterized by high crystallinity and high electrical conductivity (375 S/cm), whereas similar monophasic solution-based PEDOT exhibits lower conductivity (30 S/cm) (Figure 9.3b).[25] A capacitance of 115 F/g coupled with electrochemical stability even after 4000 bending cycles, makes this EC an ideal example of a flexible device.[25]

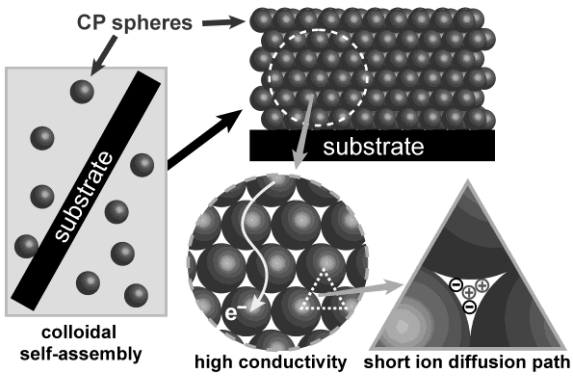

Figure 9.4: Size controllable CP colloidal synthesis is a promising direction to explore, as a highly conductive electrode self-assembles with ordered pores that accommodate a large volume of ions with short diffusion paths, optimum for high energy density and power density ECs.

Size and shape controllable syntheses create CP nanoparticles that serve as building blocks for EC electrodes. When particles are of a monodispersed spherical shape, their self-assembly will result in an electrode consisting of close-packed microspheres on a substrate.[26] The close-packed architecture presents a high electrical conductivity derived from many contact points between neighboring spheres. Ordered microporous vacancies between the spheres facilitate ion migration,

and lead to high energy, power and rate EC electrodes (Figure 9.4).[26] Theoretically, the smaller the particles are, the higher the surface area should be, however, a recent study shows that small spherical CP particles lack sufficient charge carriers to serve as active material in an EC electrode. Moderate sized (80 nm) particles lead to ECs with the highest specific capacitance.[27] Optimized particle size and shape with refined self-assembly conditions will lead to solution processable, high performance EC electrodes ready for commercialization.

9.2.2. Electrochemical polymerization

Electrochemical polymerization of CPs, first reported in 1979,[28] allows for fine control of synthetic parameters rather than relying on limited oxidation potentials and chemical oxidants. Typically, a potentiostat is programmed to pulse current and cycle through potentials, leading to a broad variety of polymer nano/microstructures and molecular packing. There are several challenges in the electropolymerization of high-performance CP electrodes for ECs requiring careful optimization of reaction conditions. Uncontrolled electrochemical polymerization of CPs, as in solution-based chemical polymerization, commonly leads to dense films that block ion diffusion pathways.[29-31] Electrochemical polymerization is a surface localized process and as the thickness of a deposited conducing polymer film grows, its molecular structure changes due to increased electrode resistance and hindered ion migration; unregulated polymer growth also leads to a high concentration of defects, hindering conductivity.[31-32] Electrochemical oxidation requires a working electrode typically coupled to a conducting current collector that pulls electrons away from a monomer in solution. Deposition of CPs on insulating substrates is also important for developing flexible and transparent EC electrodes and is carried out electrochemically by pre-patterning of a substrate with a conductive coating, albeit at a high cost.[31]

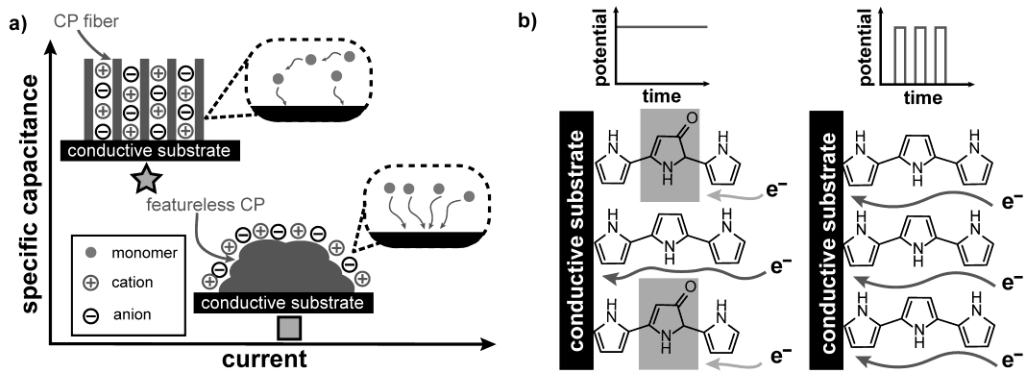

Figure 9.5: (a) In electrochemical synthesis, low current results in aligned CP fibers; high current leads to a thick, featureless film due to uncontrolled reaction kinetics. The aligned conformation exhibits higher performance due to its superior structure promoting ion accommodation. b) Pulsed potential in electrochemical polymerization significantly reduces the defects on polymer chains due to constrained reaction speed, increasing conjugation length, and enhancing specific capacitance.

The nano or microscale morphology of an electropolymerized CP is controlled by polymerization kinetics in situ during synthesis using an applied voltage and/or current; this method is versatile and enables the synthesis of a plethora of template-free nanoscale morphologies.[31] For example, an array of vertically aligned polyaniline (PANi) nanowires of 50 nm in diameter is synthesized galvanostatically using a constant current. Initial polymer nucleation minimizes interfacial surface energy as monomer radicals nucleate repeatedly on a surface site resulting in preferential directional growth, whereas uncontrolled reaction kinetics result in a disordered dense polymer architecture via a branched growth process.[23] Aligned nanowires (Figure 9.5a) provide a short ion diffusion path and a large accessible surface area resulting in ECs with a specific capacitance of 950 F/g at 1 A/g; this pure PANi electrode also exhibits a high rate capability with an 82% capacitance retention at 40 A/g.

Direct on/off switching of polymerization with pulses of current further steers polymer chain alignment and packing, leading to CPs with high conjugation length and low defects. Decreasing

the current pulse time from 50 ms to 5 ms leads to a near doubling of electrode specific capacitance at 1100 F/g. Shorter pulse times lead to CP electrodes with a low density of backbone defects like carbonyl groups and high electronic conductivity. Carbonyl bonds are due to oxidation of hydroxyl groups at the β position of pyrrole, as water molecules react with monomer radicals. Short pulses suppress the kinetics of this process and minimize defect density in the final molecular structure. A longer pulse-off interval (~100 ms) allows the growing polymer chains to relax in the direction of conjugation before further growth, leading to ordered films with high conjugation length (Figure 9.5b). ECs made from pulse electropolymerized PPy films demonstrate a high capacitance of 400 F/g with a charging/discharging stability of 10 000 cycles at 5 mA/cm^2.[32]

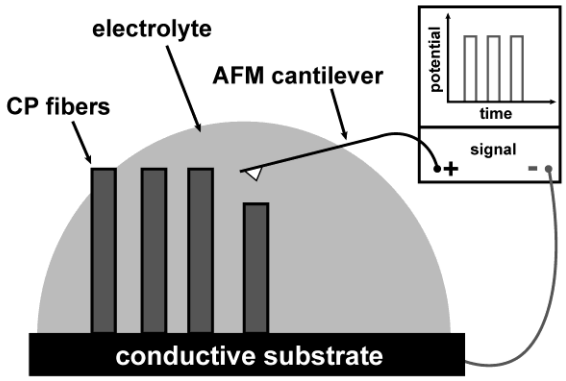

Figure 9.6: Atomic force microscope (AFM) based electrochemical synthesis. A pulsed potential is applied to the conductive tip, guiding the polymer formation in an electrolyte. This method has high resolution in 3-dimensions, ideal for design and fabrication of a hierarchical EC electrode.

Electrochemical polymerization also offers precise deposition and simultaneous patterning of a polymer architecture via Atomic Force Microscopy (AFM) using a cantilever tip as working electrode and a gold coated-counter electrode.[31] Polymer growth at the electrolyte/substrate interface occurs when a substrate is immersed in an electrolyte containing monomer and a pulse of current is applied to the cantilever. The small dimension of the tip provides highly localized

current for polymerization. An ultrashort pulsing of current is essential in achieving a well confined morphology because it limits current dispersion (Figure 9.6). This technique offers excellent patterning in both lateral (353 nm-3.37 μm) and vertical dimensions (2.0-88.3 nm) and enables continuous fabrication of CP electrodes with well controlled nano/micro architectures.[33]

9.2.3. Vapor-phase polymerization

Several synthetic methods fall under the umbrella of vapor-phase polymerization (VPP), generally, involving the oxidative polymerization reaction between monomer vapor and a chemical oxidant resulting in the deposition of a solid-state polymer film. Using a pre-patterned oxidant-coated substrate is a particularly successful form of VPP that leads to PEDOT films of high electrical conductivity when additives such as base inhibiters (pyridine) and triblock copolymers (PEG-PPG-PEG) are added to the oxidant; these species slow down reaction kinetics and reduce acidic side reactions.[34] Ultrahigh electronic conductivity of 8797 S/cm (Figure 9.7a) has been reported for VPP-PEDOT single-crystal nanowires deposited inside 10 nm deep channels[35] that constrain polymer growth and plausibly slow down reaction kinetics.

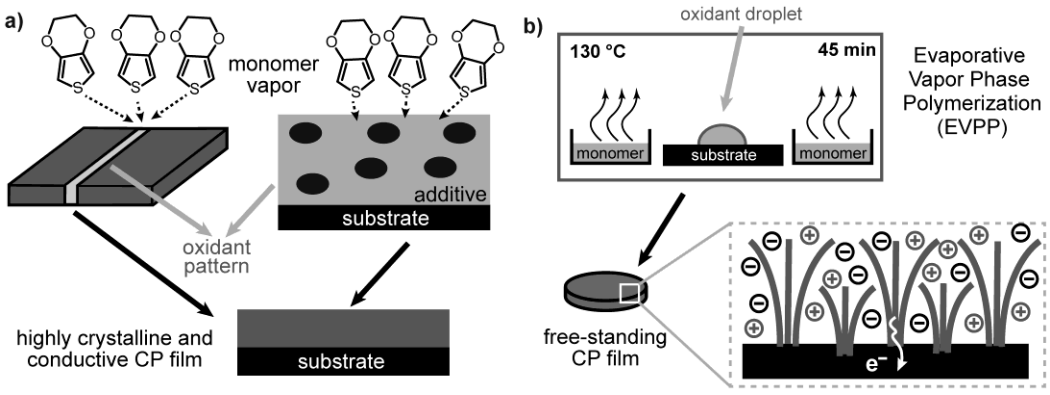

Figure 9.7: Vapor phase polymerization. (a) Dimensional constraint or polymerization inhibiting additives help lower reaction rates, leading to highly crystalline and conductive CP films. (b) Evaporative Vapor Phase Polymerization (EVPP) is a facile technique that results in a highly conductive CP film with ordered high aspect ratio nanostructures.

In traditional VPP the resulting CP film is typically a thin smooth layer deposited on a substrate; this flat polymer architecture results in a low areal energy density not favorable for standard ECs,[34] albeit favorable for in-plane microsupercapacitors. To increase areal energy density, oxidant is commonly applied directly on a porous substrate of high surface area, this strategy aims to produce a conformal polymer coating that increases material utilization yield.

Our own efforts in this field have produced one-dimensional nanostructures via evaporative vapor phase polymerization without the use of templates leading to nanofibrillar electrodes that increase areal and gravimetric energy density. This strategy is rapid and occurs when monomer vapor reacts with a heated droplet of an aqueous solution of iron (III) chloride; as the droplet evaporates, a freestanding disc shaped PEDOT film deposits. This film is characterized by a nanofibrillar architecture (Figure 9.7b) and electrical conductivity of 130 S/cm; deposition of on carbon fiber paper current collectors enables fabrication of ECs with a capacitance of 160 F/g at 1A/g. Increasing the current density 1000-fold results in 9% loss of capacitance – this minimal loss is due to a nanofibrillar morphology that maximizes free volume of the electrode architecture thus enhancing ionic conductivity and resulting in a high rate capability. [36] Polypyrrole nanofibers deposit possessing similar morphology under these conditions.[37] Evaporative vapor phase polymerization also grafts PEDOT nanofibers on aromatic rings present on the carbon-based current collector's graphitic surface. This is accomplished via Friedel-Crafts alkylation during in situ vapor phase polymerization, using nitromethane as a catalyst activator and $FeCl_3$ Friedel-Crafts as catalyst; grafting imparts outstanding electrochemical stability and contributes to a capacitance retention of 90 % after 350,000 cycles.[38]

9.2.3. Summary

The electrical conductivity of a CP, controlled via crystal structure, solid-state packing, conjugation length and doping levels, can be improved during synthesis, generally, by slowing down polymerization rates. For example, during electrochemical polymerization, lowering the magnitude of the applied current and concentration of chemical species increases the packing order due to a polymer structure possessing few numbers of defects. Using immiscible solvents and chemical inhibitors in chemical polymerization and vapor phase polymerization, respectively, lead to a high degree of crystallinity. This, in turn, facilitates intrachain, interchain and interdomain electronic transport and[39] results in conductive bulk electrodes.

Ordered CP architectures with well-defined ion migration channels are ideal for high energy density and high-rate capability electrochemical electrodes. In solution-based polymerization, a low concentration of monomer leads to a low polymerization rate that favors ordered polymer nucleation and growth that enables template-free protocols for producing nanostructured CPs. These polymer architectures are readily applied in electrochemical capacitors due to their high conductivity, ordered micro/nano morphologies, accessible surface area and robust electrochemical stability.

Among various synthetic techniques, vapor phase polymerization is a promising route for producing PEDOT electrodes for symmetric ECs reaching a 300 F/g capacitance.[40] Polymerization rate controlled by mass transport of reactant vapors under steady state kinetics results in high electronic conductivity. Our own investigations in this area are focused on the interface between a resting oxidant liquid droplet and monomer vapor; we envision precise deposition of CP hierarchical architectures using oxidant aerosols and a modified 3D printer (Figure 9.8).

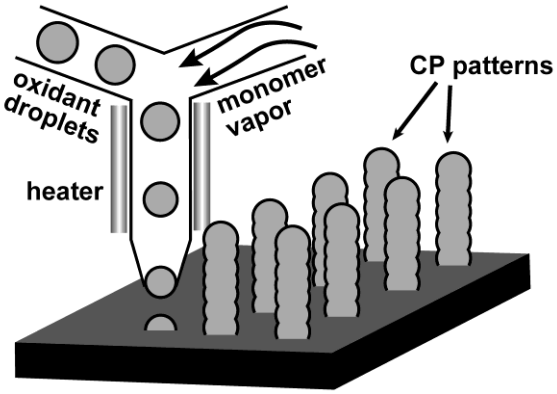

Figure 9.8: An idealized 3D printing strategy to controlling droplet/vapor interface and polymerization kinetics.

9.3 Materials and electrochemical capacitor engineering

PEDOT and PANi based ECs exceed 100,000 cycles and exhibit a high capacitance retention[38, 41] thus serving as promising soft organic materials for developing stable electrochemical cells possessing extended shelve lives. This high cycling stability is achieved by innovation in material synthesis and rational engineering. For example, ordered CP nanostructures characterized by aligned polymer chains are ideal synthetic targets that when directly grafted onto current collectors, result in efficient charge transport as well as highly accessible surface area electrodes.

9.3.1. Types of electrochemical capacitors

A CP based electrochemical capacitor typically consists of two electrodes, anode and cathode,[42] that undergo fast redox reactions within a controlled potential window while immersed in an electrolyte. A CP that attains stability in positively charged oxidized state is p-dopable, and conversely, n-dopable when stability is gained in a negatively charged reduced state; most CPs are

p-type solid-state organic semiconductors given that a negatively charged carbon backbone is highly reactive toward water and oxygen from ambient atmosphere and electrolyte.[43] Electrodes in CP based ECs are therefore usually categorized as p-dopable or p/n dopable; based on the symmetry and doping mechanism of the two electrodes, ECs are commonly segregated as Type I, Type II, Type III or Type IV devices. These four types of ECs have theoretical energy densities proportional to the maximum extractable charge and highest achievable voltage window. A detailed explanation of types of CP-based ECs can be found in the previous edition of this Handbook[44] as well as in a perspective recently published by our group.[45] Briefly, a Type I EC contains two identical p-dopable CP electrodes and the cell voltage is restricted to one of the electrode's p-doping potential window ($\Delta V = 0.5 \sim 0.75$ V). Charging creates a neutral negative electrode and a fully doped positive electrode; discharging brings both electrodes back to a partially doped state. This releases only half of the total charge stored and thus restricts the energy density of a Type I device. A Type II device utilizes two different types of p-dopable CP electrodes e.g., PANi and PEDOT that offer complementary stable potential windows for increasing both cell voltage ($\Delta V = 1 \sim 1.25$ V) and extractable charge resulting in high energy density. Type III and Type IV ECs utilize ambipolar p/n electrodes where the negative electrode is negatively doped, and the positive electrode is positively doped, this engineering strategy expands the maximum charging voltage ($\Delta V = \sim 3$ V). Full discharging brings the device's electrodes to a neutral state and therefore Type III and IV devices often exhibit significantly higher energy densities than Type I or Type II devices.[46] Unlike a Type III device that uses two identical p/n dopable CPs, a Type IV device combines two different p/n dopable CPs. This results in two active materials, each with different stable potential window. In a Type IV, polymers electrodes are selected that match the

maximum voltage window for an electrolyte; this idealized geometry leads to the highest energy density among all four devices.[44]

Type III and Type IV ECs are rarely reported due to a lack of stable n-dopable CPs - this challenge, previously brought up in the last edition[44] remains today a significant barrier for advancing conducting polymer ECs.[47-48] Many advances in n-doping of CP electrodes have taken place over the last decade however, however, Type III and Type IV ECs remain mostly unexplored.[11] The addition of an electron from a donating dopant leads to instability in the CP conjugated backbone as this electron is readily lost in the presence of oxygen or water given that it resides in a dopant band of higher energy level than the LUMOs of ambient air (O_2 and water) (Figure 9.9a).[43] In ECs, aqueous electrolytes and air stability are a major concern. An aqueous electrolyte is often favored over organics because it results in a device possessing a low equivalent circuit resistance (ESR) originating from higher ionic conductivity,[49] moreover, water leads to a reduced cost in packaging and sealing due to its non-flammable nature. Surprisingly, no water-stable n-dopable CP ECs have been reported in the literature.

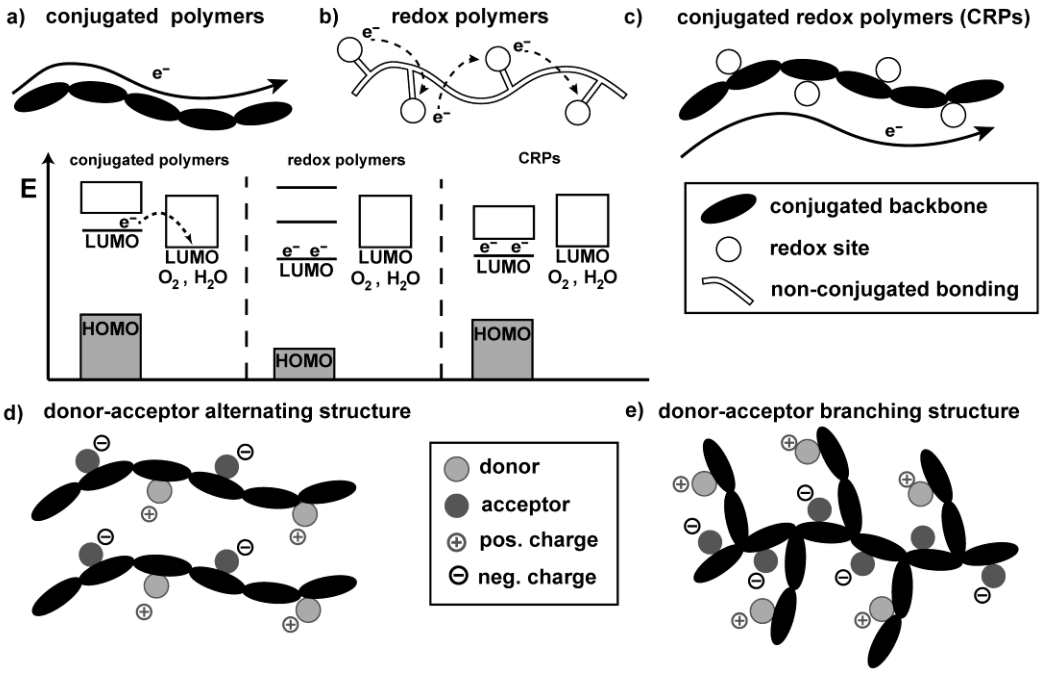

Figure 9.9: Stability of n-doped CPs. (a) CPs have conjugated backbones that enable electronic conductivity due to a continuous conduction band arising from delocalized charge, however, the higher LUMO causes electrons to be easily lost to ambient oxygen or water, making n-doping unstable. (b) Redox polymers have redox sites that stabilize electrons, but the electron transfer is hindered due to non-conjugated bonding, which leads to discrete energy level instead of a conduction band. (c) A combination of conjugated CP and redox polymer sites both increase the charge stabilization and charge transport, making stable n-dopable CP possible. (d) Alternating chain structure of acceptor and donor CRPs. (e) Branched structure of acceptor and donor CRPs. Adapted from reference.[77]

For a CP electrode to be stable in its n-doped state, electrons injected into the backbone need to be stabilized by electron accepting groups.[50] Some non-conjugated redox polymers have electron accepting groups that stabilize the negatively charged carbanion chain from donating electrons to water and air by significantly lowering the polymer's LUMO, however, the lack of conjugation makes the use of these polymers difficult for high-power energy storage. These suffer from a poor electronic conductivity that originates from discrete energy levels that localize charge in acceptor sites (Figure 9.9b).[50] Combining the redox active moieties with a conjugated backbones forms what is referred to as "conjugated redox polymers" (Figure 9.9c).[50] Lowering of polymer LUMO

stabilizes n-doping and decreases the band gap by increasing the HOMO due to electron richness, while charge transport is facilitated by a continuous conduction band in the conjugated backbone.[51] In organic electrolytes, poly[N,N'-bis(2-octyldodecyl)-1,4,5,8-naphthalenedicarboximide-2,6-diyl]-alt-5,5'-(2,2'-bithiophene), shortened to P(NDI2OD-T2), is a polymer that presents stable and reversible n-dopability at a high doping level while retaining 100% capacitance over 3,000 cycles. Its structure is shown in Figure 9.10. Further investigation reveals that electron accommodation on the redox groups has little effect on backbone electronic transport, suggesting great versatility in the continuous tuning of conjugated redox polymer structure and performance.[50] Alternating acceptor and donor units can also be incorporated in the conjugated backbone imparting ambipolar character. During charging and discharging cycles, the donor and acceptor units will stabilize and release charges on the backbone, contributing to the energy storage and output.

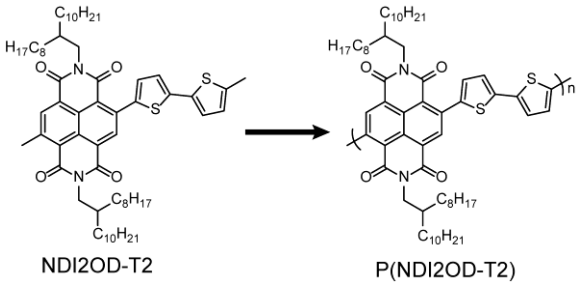

Figure 9.10: Molecular structure of monomer NDI2OD-T2 and its corresponding polymer P(NDI2OD-T2).

Poly[6,6'-bis(ethylene-3,4-dioxythien-2-yl)]N,N'-dialkylisoindigo (PBEDOT-iI) (Figure 9.11) is an ambipolar conjugated redox polymer for a Type III device where if only the p-doping voltage window is utilized (0.5 – 0.75 V), a specific energy of 0.5 Wh/kg with 80% retention over 10 000 cycles is obtained. On the other hand, when the operating voltage is increased to 2.5 V, both

electrodes become fully doped and the specific energy jumps to 15 Wh/kg as both p- and n-doping potential windows are utilized. Electrochemical stability, however, is poor with a 50% capacitance loss within 100 cycles and nearly 100% lost after 200 cycles.[52] Another Type III EC based on poly(4Cz−4Cl−PBI) (Figure 9.12) exhibits an energy density of 22.1 mWh/cm^3.[48]

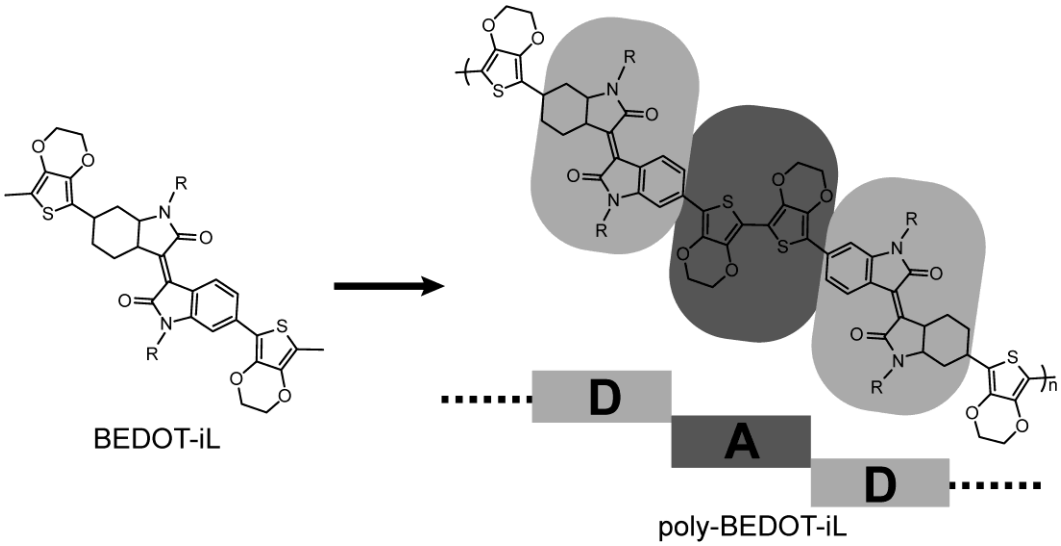

Figure 9.11: Molecular structure of monomer BEDOT-iL and its corresponding polymer poly-BEDOT-iL. "D" represents an electron donating functional group, which is p-dopable, while "A" represents an acceptor functional group, which is n-dopable.

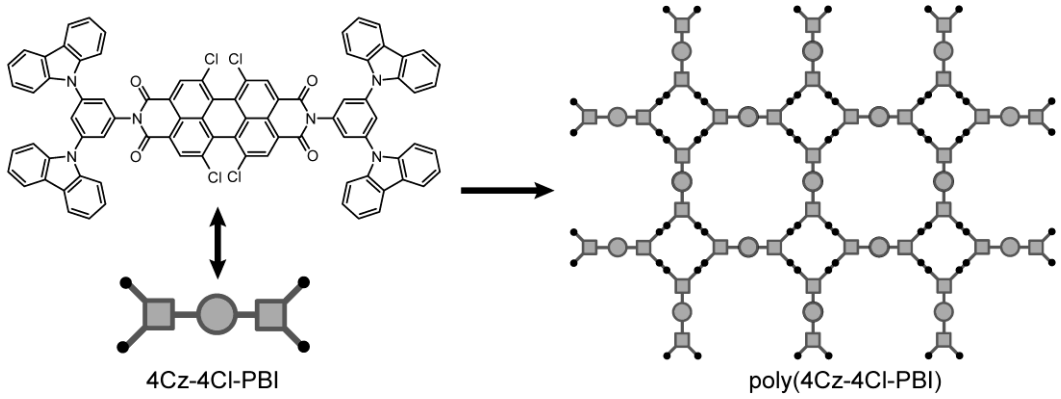

Figure 9.12: Chemical structure of 4Cz-4Cl-PBI and its polymerized form poly(4Cz-4Cl-PBI). Shapes are used to illustrate how a monomer connects to four neighboring units, making a polymer. Adapted from reference.[76]

Unfortunately, conjugated redox polymer-based ECs suffer from a low cyclability with poor-reversible n-doping, even in organic electrolytes. During n-doping, these polymers become less conductive than in their p-doped form, due to more delocalized electrons in electron accepting groups. Some irreversibly trapped charges remain unreleased during discharging due to poor electron transfer, this leads to degradation of device performance in energy retention.[47] One effective strategy to address this is by tuning the conformation of the polymer chain with the spatial distribution of the redox active groups. The performance differences of conjugated redox polymer electrodes based on donor-acceptor-donor unbranched structures (Figure 9.9d) and branched structures (Figure 9.9e) are compared. Branching shows a better cyclability with 83% retention over 2,000 cycles (56% for linear polymer). The branched structure possesses extended conjugation, a more open morphology and attains a high doping level, contributing to a high conductivity when n-doped. This relieves the charge trapping effect and enhances the device's reversibility and cyclability. Type III ECs made with alternating linear and branched structures show a maximum energy density of 29.1 Wh/kg and 19.5 Wh/kg. The alternating structure has a higher bandgap than the branched structure, expanding its maximum charging voltage to 2.4 V, while branched structure Type III devices are limited to 2.0 V.[47]

The realization of commercial Type III and Type IV ECs is highly dependent on the development of stable p/n-dopable electrodes. The understanding of n-dopable CPs for ECs still lags far behind p-dopable CPs. More investigation is needed to increase substantially the electrode specific energy and cyclability. The structure of conjugated redox polymers is rather complex compared to p-dopable CPs, and their synthesis is mostly restricted to electrochemical polymerization. Finding low mass and stable n-dopable CP structures will increase active material utilization yield[50] and enhance energy density in Type III and Type IV devices.[55]

9.3.2. Novel types of polymer electrochemical capacitors

9.3.2.1 Flexible and Stretchable Polymeric Electrochemical Capacitors

Recent developments in material science and engineering boost the strong market demand for flexible electronics including roll-up displays, sensory skins and smart textiles, as well as flexible power sources with high energy and power density. CPs are the most promising active material for flexible energy storage due to inherent flexibility brought by 1D polymer chains that bend and slide past each other opposed only by van der Waals' forces; subsequently, flexible ECs based on CPs are well established.[53-55]

Apart from flexibility, which refers to bending in most cases, stretchability that requires extension is another important parameter for future wearable electronics. Desirable properties of stretchable electronics include low modulus and stiffness, high crack-onset strain, low thickness and high elasticity that is comparable to human skin.[56] Serving as an active layer, thin films of CPs maximize device specific capacitance by minimizing the device mass and volume, meanwhile facilitating electron and charge transfer. Unfortunately, this film architecture hardly bears mechanical loads (low crack-onset strain). Furthermore, CPs are stiffer than other organic polymers (larger forces needed for unit strain) due to the strong π-π interaction between polymer chains, presenting an intrinsic challenge for fabrication of stretchable CP based ECs.

To overcome CPs' mechanical loading limitation in ECs, several strategies include synthesizing CPs with porous architecture and depositing CPs uniformly onto a substrate. Porous CP networks accommodate a certain degree of strain and increase the EC's mechanical cycling stability. For example, combining a porous PANi nanofiber network with multiwalled carbon nanotubes and poly(dimethylsiloxane), leads to a stretchable electrode. The device capacitance is 150 F/g with

volumetric capacitance of 2.0 F/cm^3 at 10 mV/s scan rate, which drops to 1.38 F/cm^3 when stretched by 50% strain. Dynamically stretching and releasing the EC to 50% strain for 500 cycles decreases the volumetric capacitance by only 4.4%, indicating a good mechanical cycling stability.[57]

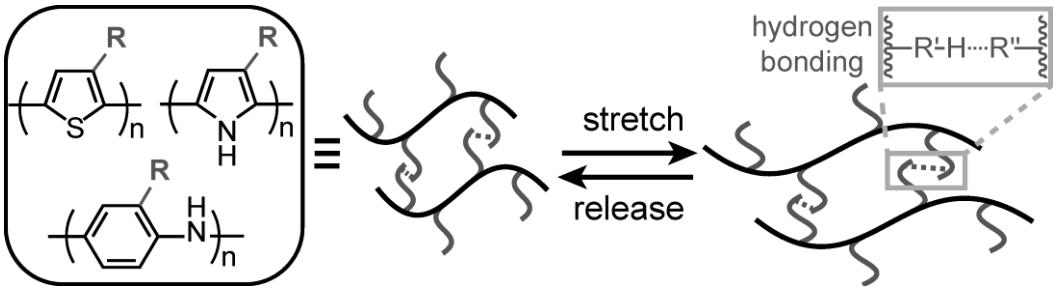

Figure 9.13: Enhancing the stretchability of CPs by grafting functional groups that noncovalently cross-link polymer chains via hydrogen bonding.

A uniform CP coating also shows high electronic and mechanical cycling stability due to low number of surface defects. For example, when PEDOT is polymerized from 2,5-dibromo-3,4-ethylenedioxythiophene onto a polyester fabric substrate using vacuum, the resulting material shows high areal (0.64 F/cm^2) and volumetric (5.12 F/cm^3) capacitance with good cycling stability. After 50,000 cycles or when stretched by 100% strain, the capacitance is nearly unchanged.[58]

Introduction of interchain hydrogen bonding by grafting functional side groups is an effective way to enhance the stretchability of CPs, this compensates for stress during stretching via noncovalent cross-linking (Figure 9.13).[59] Incorporation of ionic additives in PEDOT:PSS improves the conductivity and stretchability by softening the PSS domains, promoting the connectivity and crystallinity of PEDOT regions and providing dopant.[60] Stretchable materials obtained from these strategies are generally applied to fields such as field-effect transistors and strain sensors instead

of flexible ECs, so more investigation is needed to determine if they are useful for energy storage purposes. In terms of device fabrication, other strategies that improve the stretchability and capacitance include using superelastic substrates,[61] stretchable and self-healing electrolytes[62] and other pseudocapacitive materials.[63]

9.3.2.2 Transparent Electrochemical Capacitors

The emergence of transparent electronic devices including speakers,[64] diodes[65] and transistors[66] requires the design of transparent power sources, accordingly, transparent CP based ECs are in development. Thin layers of CPs are semi-transparent. When designing transparent ECs, a high transmittance always means a low concentration or low thickness of CP that has decreased capacitance. In this case a balance needs to be achieved between transmittance and capacitance by controlling the CP layer concentration or thickness. Apart from CP layers, the selection of electrode substrate and separator with high transmittance is also important, affecting the overall transmittance of the device.

The most common CPs used for transparent ECs are PANI, PEDOT and PPy, deposited as a thin layer on a transparent substrate and then incorporated into a device. Because of the thin film structure, most of the ECs are both transparent and flexible. The substrate or incorporated material includes single/multi-walled carbon nanotubes,[67-68] graphene,[69-70] cellulose nanofibers,[71-72] PET film,[73] RuO_2[74] and metal nanowires.[75] A high surface area of the substrate ensures a high capacitance while retaining a thin device for high transparency. For example, when using 15 nm thick transparent films composed of single-walled carbon nanotubes (10.0 µg/cm^2) as the substrate for electrochemically depositing PANI (59 wt%), the transmittance is 70% at 500 nm while the capacitance is 55.0 F/g at a current density of 2.6 A/g.[67] The capacitance is enhanced to 233 F/g when using aligned multi-walled carbon nanotubes at 1 A/g, with PANI loading of 70 wt% and

transmittance of 70% in a wavelength range of 300 – 900 nm; loss of alignment decreases capacitance when testing randomly dispersed nanotubes under the same condition.[68] Graphene and reduced graphene oxide, possessing good transparency, high theoretical specific area and good electrical conductivity are easily combined with PANI for fabricating transparent ECs. Through a one-pot liquid-liquid interfacial synthesis, PANI/graphene nanocomposite thin film is synthesized from benzene and aniline, and shows 83.7% transmittance at 550 nm with 88 nm in thickness; after supported by PET film, the fabricated device shows a capacitance of 95.5 F/cm^3.[69]

Exquisite molecular control is achieved in aqueous solvents via Layer-by-layer assembly of PANI, graphene oxide and PEDOT:PSS on cellulose nanofibrillar paper for transparent ECs; cellulose nanofibers have a net negative charge in aqueous solution that facilitates assembly process. As a result, the device fabricated by PANI and graphene oxide shows a transmittance of 30.6% at 550 nm, with areal capacitance of 5.86 mF/cm^2 at a current density of 0.0043 mA/cm^2, while the device fabricated by PANI and PEDOT:PSS shows 47.1% transmittance and 4.22 mF/cm^2 under the same conditions.[69] Aerosol-jet spraying is used to produce RuO_2/PEDOT:PSS hybrid thin films with high transparency, good conductivity and high capacitance. RuO_2 is both pseudocapacitive and conductive, resulting in a thin film with areal capacitance of 1.2 mF/cm^2 at a high transmittance of 93%.[74]

The development of transparent CP based ECs enables engineering new functionalities in energy storage technologies, for example, an electrochromic EC is a type of smart EC that indicates the level of stored energy via color or contrast change. This requires incorporation of two electrochromic materials into one device i.e., PANi as the active electrode under positive potentials during anodic oxidation and $W_{18}O_{49}$ as the active electrode under negative potentials during cathodic reduction. PANI is bleached at -0.2V and colored at 0.8 V, while $W_{18}O_{49}$ is bleached at

0V and colored at -0.6V; selective deposition of PANI and $W_{18}O_{49}$ results in a device that only shows PANI's pattern at 0.8 V, and $W_{18}O_{49}$'s at -0.5 V.[76] PANI itself also has multiple oxidative states that show different colors, among them yellow, green and blue that can be observed by naked eye, so the transparent ECs using PANI as the active material also indicate charged states (Figure 9.14).[77]

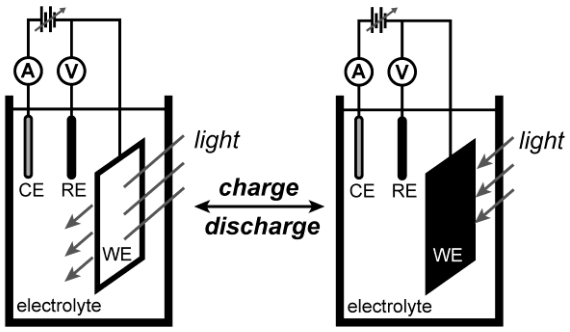

Figure 9.14: Schematic representation of a smart electrochromic-EC electrode that shows different color at different charged states.

9.4 PEDOT-based electrochromic device

9.4.1 Background

Electrochromic is a reversible optical change in materials upon redox reaction in the presence of external potential.[78] Electrochromic devices (ECD), made of electrochromic materials, are widely used in smart windows, electrochromic displays, anti-glare rearview mirrors, and military camouflage.[79-80] Inorganic electrochromic materials, such as WO_3, MoO_3, NiO and V_2O_5 are commercialized in the last several years; however, they suffer from slow response time, high cost and complex fabrication.[81] Currently, conducting polymers attract much attention due to their excellent optical contrast ratio, rapid response and low applied potential. PEDOT is a promising

material due to its simple synthesis, low-cost fabrication, tunable properties and high environmental stability.[82]

Previous reports demonstrate PEDOT's nanostructures enable enhancement in electrochromic performance, such as nanoparticles,[83] nanotubes[84] and nanowires[85]. However, the poor optical contrast, low cycle stability and unsatisfied response time impede their practical applications. Recent research focuses on hybridization between organic and inorganic components, enhancing charge transfer via metal additives to solve those issues.[86-87]

9.4.2 Experimental Methods

FTO glass substrates (TEC™ 7) were purchased from MSE supplies LLC, USA. First, the FTO glass substrates were washed via ultrasonic baths in acetone and then in isopropyl alcohol for 20 min, each. Then they were treated under UV-ozone for 30 min to remove remaining organic impurities. Next, a solid-oxidant precursor, 20-nm thick Fe_2O_3, was sputtered over the FTO via physical vapor deposition (Kurt J. Lesker PVD 75 RF and DC). A glass reactor was loaded with the Fe_2O_3-coated FTO, 30 μL of HCl, and 200 μL of a 0.674 M EDOT solution in chlorobenzene, then sealed and heated in an oven at 140 ◦C for 1.5 hr. The samples were purified via 6 M HCl overnight to remove iron impurities. The sputtered α-Fe_2O_3 was used as a ferric ion-containing solid-state oxidant precursor to induce dissolution, liberation of ferric ions, and Fe^{3+} hydrolysis concomitant with oxidative radical polymerization.

9.4.3 Discussion

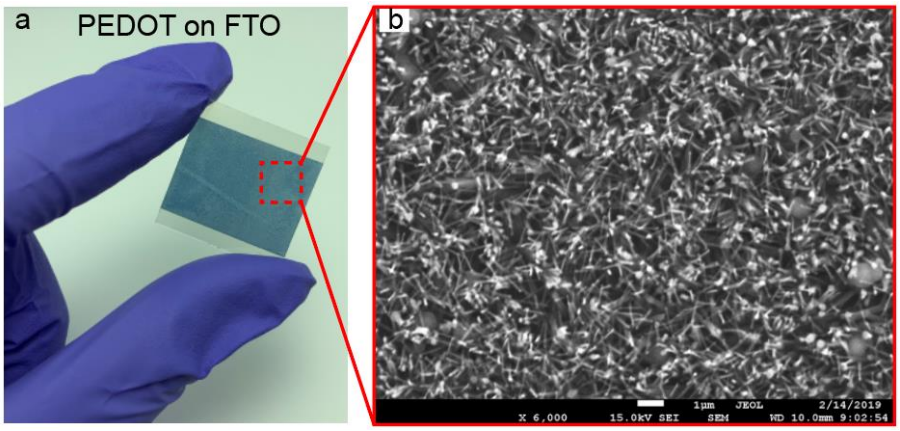

Figure 9.15: (a) A photograph of PEDOT coated FTO. (b) The SEM of PEDOT film exhibit nanofibrillar morphology.

A light blue color PEDOT film (Figure 9.15a) is deposited on FTO glass substrate (2.5 cm × 2 cm) via rust-based vapor phase polymerization (RVPP).[88-89] Figure 9.15b exhibits conformal PEDOT nanofibers suggest high surface area.

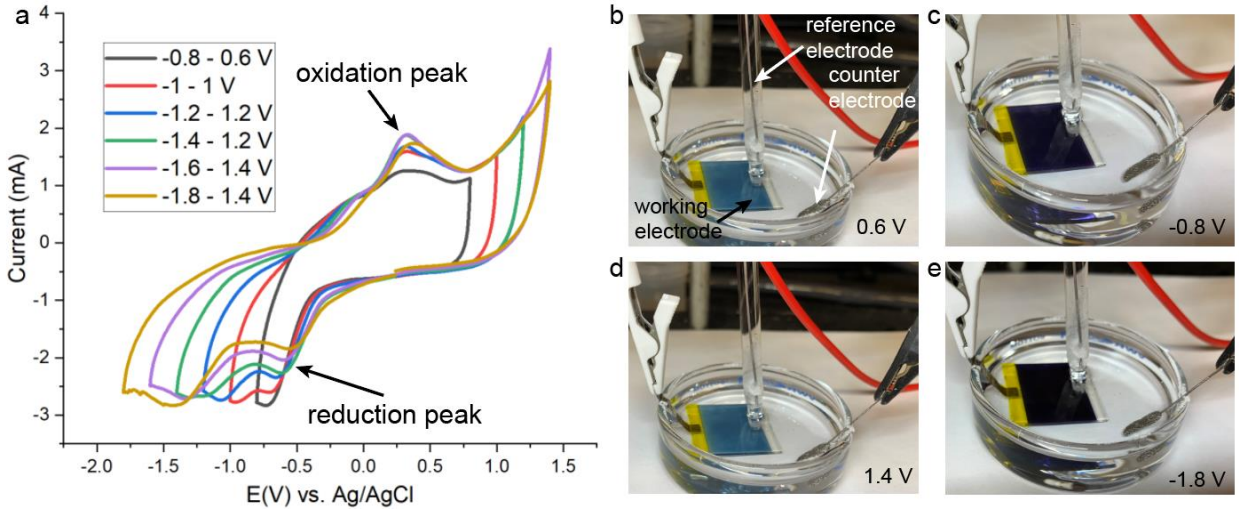

Figure 9.16: (a) Cyclic voltammagrams of PEDOT on FTO (working electrode) with reference electrode of Ag/AgCl and counter electrode of platnium mesh in 1 M $LiClO_4$ acetonitrile

electrolyte, showing PEDOT oxidation peak and reductionpeak. (b-c) The color change during cycling from 0.6 V (blue) to -0.8 V (purple). (d-e) The color change during cycling from 1.4 V (light blue) to -1.8 V (dark purple).

Electrochromic performance is evaluated via a three-electrode electrochemical cell using 1 M $LiClO_4$ acetonitrile electrolyte under different potential varying from 1.4 V to -1.8 V (vs. Ag/AgCl). The CVs (Figure 9.16a) exhibits characteristic peaks of PEDOT at 0.5 V and -1.5 V, and the PEDOT electrode possesses cycle stability between 1.4 V and 1.8 V. The color of the PEDOT film (Figure 9.16b) changed from blue to purple at -0.8 V corresponding to reduced-state, and the color change back to blue -0.6 V corresponding to oxidized-state. Such color change is due to the various dopant that affects the conductivity of PEDOT.[90] The electrical conductivity varies by order of magnitude between the oxidized (high conductivity) and reduced (low conductivity) state. The low conductivity contains neutral segments that contribute to strong absorption of visible light centered around 600 nm, forming a purple tint. Charging the polymer by electrochemical oxidation minimizes this absorption, making the same film transparent to visible light exhibiting blue tint.[91-92] Notably, the extended voltage window from 1.4 V to -1.8 V possesses similar color contrast.

9.5 Iron-based electrode for battery applications

9.5.1. Introduction

The critical need for high energy density batteries has drastically elicited intensive research to develop next-generation batteries due to the rapid development of electronic devices and electric vehicles. There are two promising battery systems that potentially meet this requirement, lithium-ion battery[93] and metal-air battery.[94]

The next-generation lithium-ion batteries are the key to a revolution in electronic devices, electric vehicles, and implantable medical devices.[95-96] The ideal batteries require inexpensive electrode materials, high energy density, and environmentally friendly materials. Therefore, iron oxides as anode materials serve as a promising option since iron enables lithium reaction to give metal nanoparticles through conversion reactions.[97] This concept of hematite (α-Fe_2O_3) with metallic Li is demonstrate in the earlier 1980s,[98] and reignited by research on hematite electrodes with a theoretical capacity of 1007 mAh/g in 2000.[99] However, the hematite anode suffers from rapid capacity loss during the first cycle when operating at voltages, enabling complete reduction to metallic iron. Recently, significant progress in cyclability is reported with magnetite/carbon composites with a stable capacity of 600 mAh/g at a rate of 10 C.[100]

Metal-air batteries are the other promising battery system due to their high energy density and potential application in grid energy storage.[101-102] There are multiple anode material candidates, such as iron,[103] zinc[104] and aluminum,[105] and iron-air battery received considerable attention due to their high electrochemical and thermal stability, low cost, and environmental safety.[106] However, the iron-air battery suffers from electrode passivation caused by iron hydroxide generation during discharge, preventing further anodic utilization. Notably, a porous iron electrode possesses a low hydrogen overpotential, limiting its application in commercial batteries.[106]

9.5.2. Results and Discussion

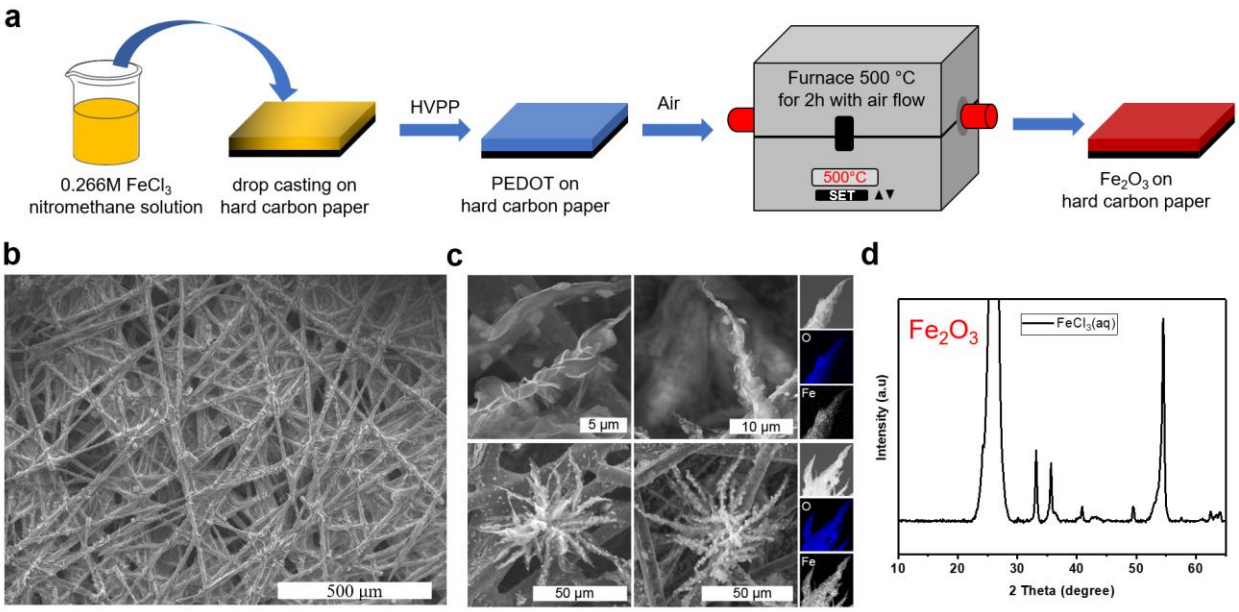

Figure 9.17: (a) Flow process diagram of α-Fe_2O_3 electrode fabrication. (b) SEM of Fe_2O_3 coated hard carbon paper electrode. (c) Close-up SEM and EDX of Fe_2O_3 electrode. (d) pXRD pattern of α-Fe_2O_3 electrode.

Fe_2O_3 electrode is obtained from PEDOT electrode through combustion: 1) 0.266 M FeCl3 nitromethane solution is drop cast on a piece of hard carbon paper (HCP) (1 cm × 1cm). 2) a uniform PEDOT nanofibrillar coating is deposited on HCP via HVPP synthesis. 3) a homogeneous nanostructured Fe_2O_3 electrode is obtained after combustion at 500 °C with 2 h airflow (Figure 9.17a). Figure 9.17b exhibits the Fe_2O_3 layer conformally deposit on HCP, and Fe_2O_3 electrode possesses aggregated nanoflake morphology suggesting the high surface area (Figure 9.17c). Elemental maps via energy-dispersive X-ray spectroscopies show a uniform distribution and solid signals for Fe and O corresponding to Fe_2O_3. Powder X-ray diffraction (Figure 9.17d) is carried out and reveals three characteristic peaks at 33°, 35.5°, 42°, 50°, 54° corresponding to (104), (110), (113), (024), (116) lattice planes, respectively, that confirms the α-Fe_2O_3 configuration.[107]

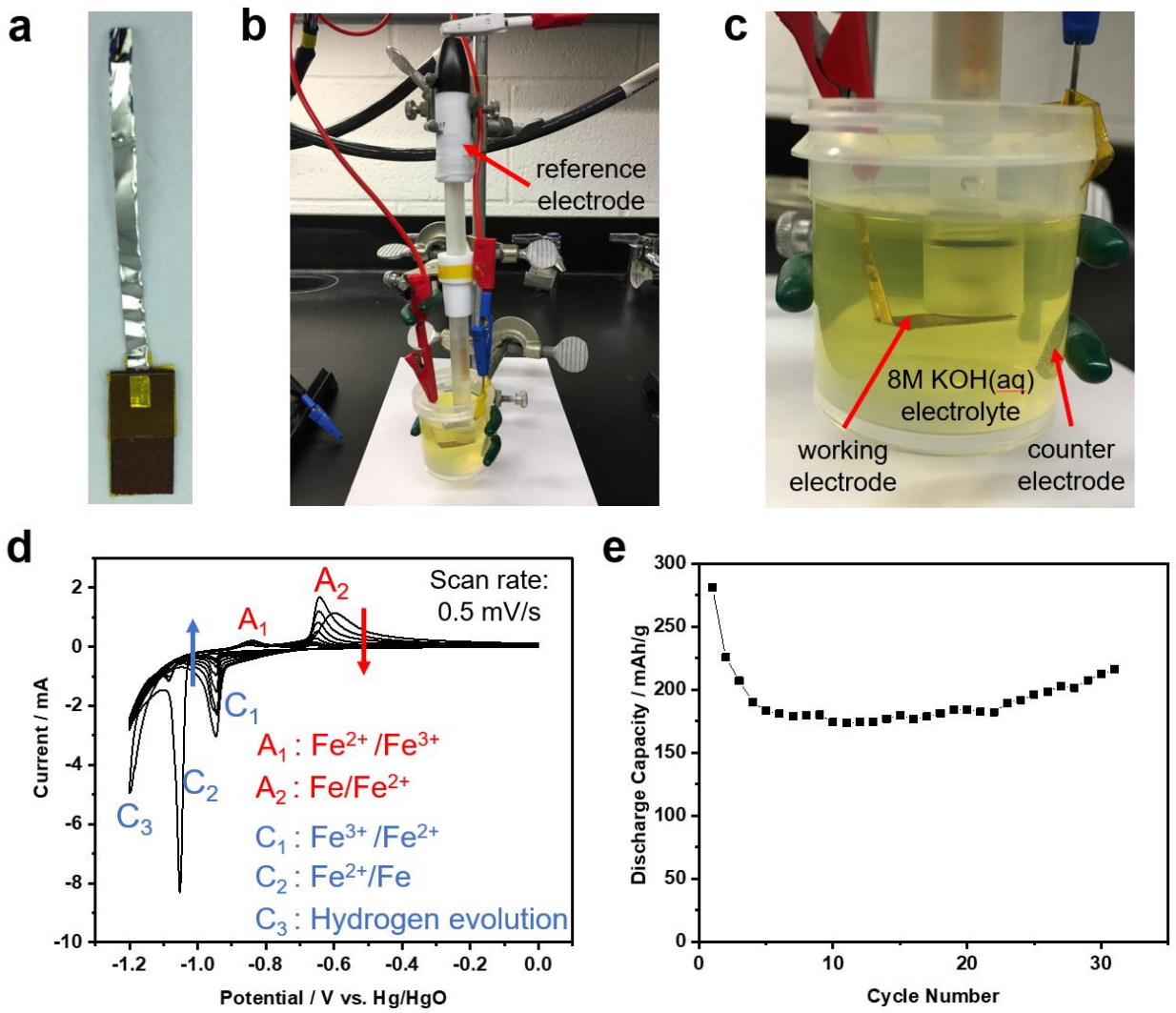

Figure 9.18: (a) Photograph of a single α-Fe_2O_3/HCP electrode connected with Pt lead. (b-c) Three electrode setup of a single α-Fe_2O_3/HCP electrochemical characterization, including Hg/HgO reference electrode, α-Fe_2O_3/HCP working electrode, Pt mesh counter electrode and 8 M KOH aqueous electrolyte. (d) CVs of α-Fe_2O_3/HCP electrode with a scan rate of 0.5 mV/s under voltage window of -1.2 V - 0 V. (e) Cycle performance of α-Fe_2O_3/HCP electrode.

Nanostructured α-Fe_2O_3/HCP electrode is sealed with Pt lead via Kapton tape (Figure 9.18a). Three electrode system is investigated to probe the electrochemical property of a single α-Fe_2O_3/HCP electrode. Typically, the setup for iron electrode characterization consists of a working electrode (α-Fe_2O_3/HCP), a counter electrode (Pt mesh), and a specific reference electrode (Hg/HgO) to accurate probe the electrochemical performance under alkaline solution (8 M KOH)

(Figure 9.18b). Cyclic voltammogram (CV) curves of α-Fe_2O_3/HCP electrode (Figure 9.18c) exhibit Fe/Fe (II) and Fe (II)/Fe (III) redox couples. The oxidation of Fe (II)/Fe (III) occurs at -0.62 V (a2) and the corresponding reduction peak is at around -0.98 V (c1), whereas a Fe/Fe (II) redox couple occurs at around -0.9V (a1) and -1.1 V (c2), respectively.[108] The redox current for the Fe/Fe (II) couple is smaller than the Fe (II)/Fe (III) couple and hydrogen evolution (c3) occurs at -1.2 V, suggesting the nanostructured α-Fe_2O_3/HCP electrode possess a small overpotential of Fe/Fe(II) redox couple resulting in a separation of hydrogen evolution.[109]

Notably, a significant current drop occurs after the first cycle associated with the irreversible conversion between $Fe(OH)_3$ to FeOOH or $Fe(OH)_2$, resulting in passivation of the electrode. The cycle performances (Figure 9.18d) exhibit good stability within 30 cycles and possess a capacity of 200 mAh/g, which is one-third of the state-of-the-art performance,[94] and further work is necessary to surpass the hydrogen evolution, restrain the passivation of the electrode, and increase the surface area and stability of the iron electrode.

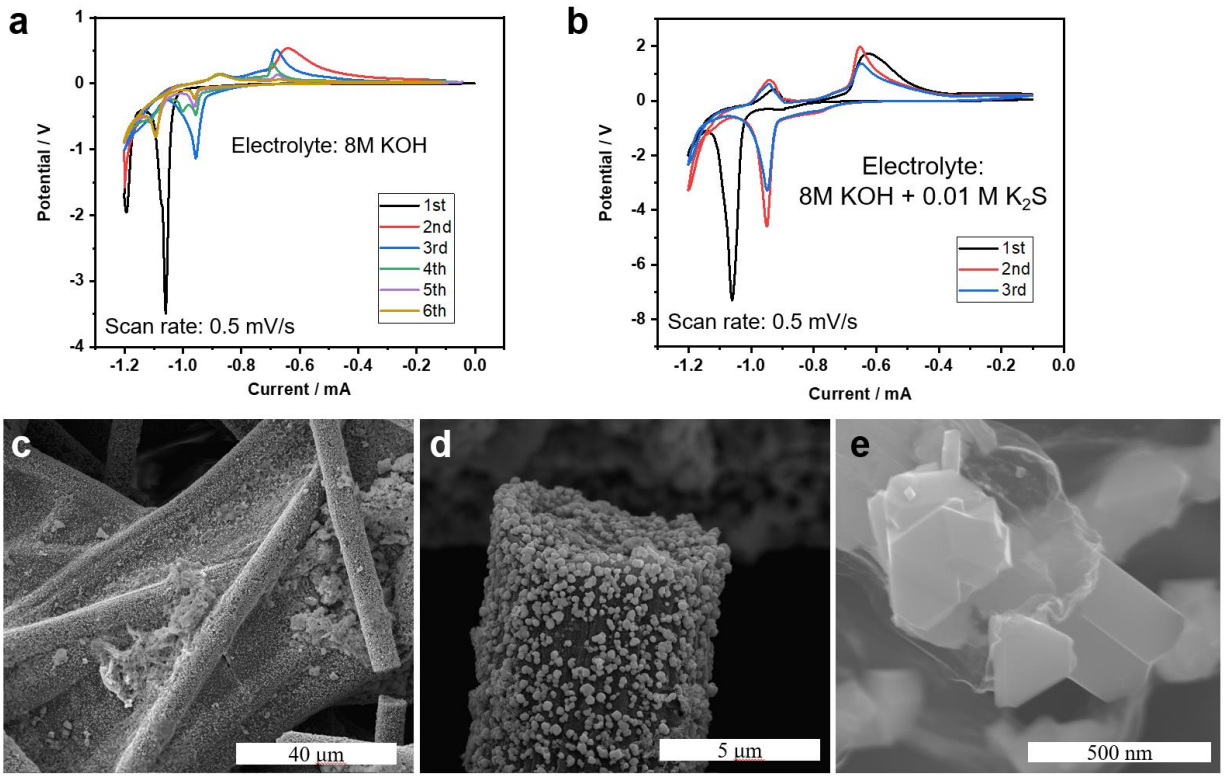

Figure 9.19: (a-b) CVs of α-Fe_2O_3/HCP electrode in 8 M KOH and 8 M KOH/0.01 M K_2S with a scan rate of 0.5 mV/s. (c-e) SEM of α-Fe_2O_3/HCP electrode after 30 cycles.

To improve the α-Fe_2O_3/HCP electrode's capacity, we add 0.01 M K_2S additive to the electrolyte. Metal sulfide additives, such as K_2S, FeS, Bi_2S_3, are common additives for iron-based battery systems since they are effective in suppressing hydrogen evolution, enhancing the ionic conductivity of the electrolyte, impeding passivation of the electrode, and promoting the dissolution of iron.[110-111] CVs of α-Fe_2O_3/HCP electrode in 8 M KOH/0.01 M K_2S electrolyte exhibit a more significant current compare with 8 M KOH electrolytes, confirming the sulfide additives improve the capacity (Figure 9.19a-b). Notably, the overlapping of CVs suggests the excellent reversibility and stability of the electrochemical reaction.[107]

To understand the change of α-Fe_2O_3/HCP electrode after the 30 cycles at a scan rate of 0.5 mV/s. SEMs is introduced to compare the structure of the electrodes before and after cycling (Figure 9.19c-e). Before cycling, the α-Fe_2O_3 in the iron electrode is nanoflakes (Figure 9.17), while after continuous cycling, they transfer to a prismatic shape with the size of the particles from 200 nm to 500 nm (Figure 9.19). Such Fe_2O_3 particle is generated via dissolution-precipitation ripening of the Fe_2O_3.[112] The phase transition from nanoflakes to nanoparticles leads to less surface area and detachment from HCP, resulting in gradual passivation of the iron electrode that impedes the electrochemical reaction.

Reference

(1) Bed Poudel, Q. H., Yi Ma, Yucheng Lan, Austin Minnich, Bo Yu, Xiao Yan, Dezhi Wang, Andrew Muto, Daryoosh Vashaee, Xiaoyuan Chen, Junming Liu, Mildred S. Dresselhaus, Gang Chen, Zhifeng Ren, High-Thermoelectric Performance of Nanostructured Bismuth Antimony Telluride Bulk Alloys. *Science* **2008,** *320*.

(2) Takano, T.; Masunaga, H.; Fujiwara, A.; Okuzaki, H.; Sasaki, T., PEDOT Nanocrystal in Highly Conductive PEDOT:PSS Polymer Films. *Macromolecules* **2012,** *45* (9), 3859-3865.

(3) Sariciftci, N. S.; Heeger, A. J.; Cao, Y., Paramagnetic susceptibility of highly conducting polyaniline: Disordered metal with weak electron-electron interactions (Fermi glass). *Physical Review B* **1994,** *49* (9), 5988-5992.

(4) Ugur, A.; Katmis, F.; Li, M.; Wu, L.; Zhu, Y.; Varanasi, K. K.; Gleason, K. K., Low-Dimensional Conduction Mechanisms in Highly Conductive and Transparent Conjugated Polymers. *Adv Mater* **2015,** *27* (31), 4604-10.

(5) L. Bert Groenendaal, F. J., Dieter Freitag, Harald Pielartzik, and John R. Reynolds, Poly(3,4-

ethylenedioxythiophene) and Its Derivatives: Past, Present, and Future. *Adv Mater* **2000,** *12* (7).

(6) McCulloch, I.; Heeney, M.; Bailey, C.; Genevicius, K.; MacDonald, I.; Shkunov, M.; Sparrowe, D.; Tierney, S.; Wagner, R.; Zhang, W.; Chabinyc, M. L.; Kline, R. J.; McGehee, M. D.; Toney, M. F., Liquid-crystalline semiconducting polymers with high charge-carrier mobility. *Nature Materials* **2006,** *5* (4), 328-333.

(7) Kang, S. D.; Snyder, G. J., Charge-transport model for conducting polymers. *Nature Materials* **2016,** *16* (2), 252-257.

(8) Heng Liu, A. P., and Philippe Guyot-Sionnest, Mott and Efros-Shklovskii Variable Range Hopping in CdSe Quantum Dots Films. *ACS Nano* **2010,** *9*, 5211-5216.

(9) Jui-Fen Chang, B. S., Dag W. Breiby, Martin M. Nielsen, Theis I. So¨lling, Mark Giles, Iain McCulloch, and Henning Sirringhaus, Enhanced Mobility of Poly(3-hexylthiophene) Transistors by Spin-Coating from High-Boiling-Point Solvents. *Chem. Mater.* **2004,** *16*, 4772-4776.

(10) Cho, B.; Park, K. S.; Baek, J.; Oh, H. S.; Koo Lee, Y. E.; Sung, M. M., Single-crystal poly(3,4-ethylenedioxythiophene) nanowires with ultrahigh conductivity. *Nano Lett* **2014,** *14* (6), 3321-7.

(11) Su, K.; Nuraje, N.; Zhang, L.; Chu, I. W.; Peetz, R. M.; Matsui, H.; Yang, N. L., Fast Conductance Switching in Single-Crystal Organic Nanoneedles Prepared from an Interfacial Polymerization-Crystallization of 3,4-Ethylenedioxythiophene. *Advanced Materials* **2007,** *19* (5), 669-672.

(12) Zhou, S.; Qiu, Z.; Strømme, M.; Wang, Z., Highly Crystalline PEDOT Nanofiber Templated

by Highly Crystalline Nanocellulose. *Advanced Functional Materials* **2020,** *30* (49), 2005757.

(13) L.Throne, R. J. C., Rotational Molding Technology. *Plastics Design Library* **2002**, 19-68.

(14) Stepien, L.; Roch, A.; Tkachov, R.; Leupolt, B.; Han, L.; van Ngo, N.; Leyens, C., Thermal operating window for PEDOT:PSS films and its related thermoelectric properties. *Synthetic Metals* **2017,** *225*, 49-54.

(15) Liu, D.; Osuna Orozco, R.; Wang, T., Deviations of the glass transition temperature in amorphous conjugated polymer thin films. *Phys Rev E Stat Nonlin Soft Matter Phys* **2013,** *88* (2), 022601.

(16) Kim, J. Y.; Kwon, M. H.; Min, Y. K.; Kwon, S.; Ihm, D. W., Self-Assembly and Crystalline Growth of Poly(3,4-ethylenedioxythiophene) Nanofilms. *Advanced Materials* **2007,** *19* (21), 3501-3506.

(17) K.E. Aasmundtveit, E. J. S., O. Ingan¨as, L.A.A. Pettersson, T. Johansson, S. Ferrer, Structural aspects of electrochemical doping and dedoping of poly3,4-ethylenedioxythiophene/. *SYnthetic Metals* **2000,** *113*, 93-97.

(18) Zuber, K.; Fabretto, M.; Hall, C.; Murphy, P., Improved PEDOT Conductivity via Suppression of Crystallite Formation in Fe(III) Tosylate During Vapor Phase Polymerization. *Macromolecular Rapid Communications* **2008,** *29* (18), 1503-1508.

(19) Xiaoxue Wang, X. Z., Lei Sun, Dongwook Lee, Sunghwan Lee, Minghui Wang, Junjie Zhao, Yang Shao-Horn4,6,7, Mircea Dincă, Tomás Palacios, Karen K. Gleason, High electrical conductivity and carrier mobility in oCVD PEDOT thin films by engineered crystallization and acid treatment. *Science Advances* **2018,** *4*, eaat5780.

(20) Gleason, K. K., CVD Polymers, Fabrication of Organic Surface and Devices. *Wiley-VCH*,

Verlag GmbH & Co. KGaA **2015**.

(21) Ng, C. A.; Camacho, D. H., Polymer electrolyte system based on carrageenan-poly(3,4-ethylenedioxythiophene) (PEDOT) composite for dye sensitized solar cell. *IOP Conference Series: Materials Science and Engineering* **2015,** *79*, 012020.

(22) Yan, B.; Wu, Y.; Guo, L., Recent Advances on Polypyrrole Electroactuators. *Polymers* **2017,** *9* (9), 446.

(23) Chiou, N. R.; Lu, C.; Guan, J.; Lee, L. J.; Epstein, A. J., Growth and alignment of polyaniline nanofibres with superhydrophobic, superhydrophilic and other properties. *Nature Nanotechnology* **2007,** *2* (6), 354-7.

(24) He, S.; Hu, X.; Chen, S.; Hu, H.; Hanif, M.; Hou, H., Needle-like polyaniline nanowires on graphite nanofibers: hierarchical micro/nano-architecture for high performance supercapacitors. *J. Mater. Chem.* **2012,** *22* (11), 5114.

(25) Anothumakkool, B.; Soni, R.; Bhange, S. N.; Kurungot, S., Novel scalable synthesis of highly conducting and robust PEDOT paper for a high performance flexible solid supercapacitor. *Energy & Environmental Science* **2015,** *8* (4), 1339-1347.

(26) Kim, S. K.; Jung, E.; Goodman, M. D.; Schweizer, K. S.; Tatsuda, N.; Yano, K.; Braun, P. V., Self-assembly of monodisperse starburst carbon spheres into hierarchically organized nanostructured supercapacitor electrodes. *ACS applied materials & interfaces* **2015,** *7* (17), 9128-33.

(27) Zhou, Y.; Wang, P.; Hu, M.; Tian, X., Charge carrier related superior capacitance of the precisely size-controlled polypyrrole nanoparticles. *Electrochim. Acta* **2017,** *249*, 290-300.

(28) Diaz, A. F.; Kanazawa, K. K.; Gardini, G. P., Electrochemical Polymerization of Pyrrole. *J. Chem. Soc., Chem. Commun.* **1979,** (14), 635-636.

(29) Liang, L.; Liu, J.; Windisch, C. F.; Exarhos, G. J.; Lin, Y. H., Direct assembly of large arrays of oriented conducting polymer nanowires. *Angew Chem Int Edit* **2002,** *41* (19), 3665-3668.

(30) Peshoria, S.; Narula, A. K., Study and explanation about the morphological, electrochemical and structural properties of differently synthesized polypyrrole. *Journal of Materials Science: Materials in Electronics* **2017**.

(31) Li, C.; Bai, H.; Shi, G., Conducting polymer nanomaterials: electrosynthesis and applications. *Chem. Soc. Rev.* **2009,** *38* (8), 2397-409.

(32) Sharma, R. K.; Rastogi, A. C.; Desu, S. B., Pulse polymerized polypyrrole electrodes for high energy density electrochemical supercapacitor. *Electrochem. Commun.* **2008,** *10* (2), 268-272.

(33) Nam, K.; Lee, G.; Jung, H.; Park, J.; Kim, C. H.; Seo, J.; Yoon, D. S.; Lee, S. W.; Kwon, T., Single-step electropolymerization patterning of a polypyrrole nanowire by ultra-short pulses via an AFM cantilever. *Nanotechnology* **2011,** *22* (22), 225303.

(34) Brooke, R.; Cottis, P.; Talemi, P.; Fabretto, M.; Murphy, P.; Evans, D., Recent advances in the synthesis of conducting polymers from the vapour phase. *Prog. Mater Sci.* **2017,** *86*, 127-146.

(35) Cho, B.; Park, K. S.; Baek, J.; Oh, H. S.; Lee, Y.-E. K.; Sung, M. M., Single-Crystal Poly(3,4-ethylenedioxythiophene) Nanowires with Ultrahigh Conductivity. *Nano Lett.* **2014,** *14*, 3321-3327.

(36) Julio M.D'Arcy, M. F. E.-K., Pwint P.Khine, Linghong Zhang, Sun Hwa Lee, Nicole R. Davis, David S. Liu, Michael T.Yeung, Sung Yeol Kim, Christopher L. Turner, Andrew T. Lech, Paula T. Hammond, and Richard B. Kaner, Vapor-Phase Polymerization of Nanofibrillar Poly(3,4-ethylenedioxythiophene) for Supercapacitors. *ACS Nano* **2014,** *8* (2), 1500-1510.

(37) Santino, L. M.; Acharya, S.; D'Arcy, J. M., Low-temperature vapour phase polymerized polypyrrole nanobrushes for supercapacitors. *Journal of Materials Chemistry A* **2017,** *5* (23), 11772-11780.

(38) Acharya, S.; Santino, L. M.; Lu, Y.; Anandarajah, H.; Wayne, A.; D'Arcy, J. M., Ultrahigh stability of high-power nanofibrillar PEDOT supercapacitors. *Sustain Energ Fuels* **2017,** *1* (3), 482-491.

(39) Dai, L.; Winkler, B.; Mau, A. W. H., Construction of oriented and patterned conjugated polymers. In *Semiconductive Polymers*, Hsieh, B.; Galvin, M.; Wei, Y., Eds. ACS: Washington, D.C., 1999.

(40) Karlsson, C.; Nicholas, J.; Evans, D.; Forsyth, M.; Strømme, M.; Sjödin, M.; Howlett, P. C.; Pozo-Gonzalo, C., Stable Deep Doping of Vapor-Phase Polymerized Poly(3,4-ethylenedioxythiophene)/Ionic Liquid Supercapacitors. *ChemSusChem* **2016,** *9* (16), 2112-2121.

(41) Santino, L. M.; Lu, Y.; Acharya, S.; Bloom, L.; Cotton, D.; Wayne, A.; D'Arcy, J. M., Enhancing Cycling Stability of Aqueous Polyaniline Electrochemical Capacitors. *ACS applied materials & interfaces* **2016**.

(42) Faraday, M., Experimental Researches in Electricity-Seventh Series. *Philos. Trans. R. Soc. London* **1834,** *124*, 77-122.

(43) Di Pietro, R.; Fazzi, D.; Kehoe, T. B.; Sirringhaus, H., Spectroscopic Investigation of Oxygen- and Water-Induced Electron Trapping and Charge Transport Instabilities in n-type Polymer Semiconductors. *J. Am. Chem. Soc.* **2012,** *134* (36), 14877-14889.

(44) Irvin , J. A.; Irvin, D. J.; Stenger-Smith, J. D., Electroactive Polymers for Batteries and

Supercapacitors. In *Handbook of Conjugated Polymers: Processing and Applications* 3rd ed.; Skotheim, T. A.; Reynolds, J. R., Eds. CRC Press: Boca Raton, FL, 2007.

45) Bryan, A. M.; Santino, L. M.; Lu, Y.; Acharya, S.; D'Arcy, J. M., Conducting Polymers for Pseudocapacitive Energy Storage. *Chem. Mater.* **2016,** *28* (17), 5989-5998.

(46) Andy Dudge, J. D., Ian Raistrick, Shimshon Gottesfeld and John P. Ferraris Conducting Polymers as active material in electrochemicasl capacitors. *J. Power Sources* **1994,** *47*, 89-107.

(47) Zhang, H.; Yao, M.; Wei, J.; Zhang, Y.; Zhang, S.; Gao, Y.; Li, J.; Lu, P.; Yang, B.; Ma, Y., Stable p/n-Dopable Conducting Redox Polymers for High-Voltage Pseudocapacitor Electrode Materials: Structure-Performance Relationship and Detailed Investigation into Charge-Trapping Effect. *Advanced Energy Materials* **2017,** *7* (21), 1701063.

(48) Qin, L.; Ma, W.; Hanif, M.; Jiang, J.; Xie, Z.; Ma, Y., Donor–Node–Acceptor Polymer with Excellent n-Doped State for High-Performance Ambipolar Flexible Supercapacitors. *Macromolecules* **2017,** *50* (9), 3565-3572.

(49) Wang, G.; Zhang, L.; Zhang, J., A review of electrode materials for electrochemical supercapacitors. *Chem. Soc. Rev.* **2012,** *41* (2), 797-828.

(50) Liang, Y.; Chen, Z.; Jing, Y.; Rong, Y.; Facchetti, A.; Yao, Y., Heavily n-Dopable pi-Conjugated Redox Polymers with Ultrafast Energy Storage Capability. *J. Am. Chem. Soc.* **2015,** *137* (15), 4956-9.

(51) Thomas, C. A.; Zong, K.; Abboud, K. A.; Steel, P. J.; Reynolds, J. R., Donor-Mediated Band Gap Reduction in a Homologous Series of Conjugated Polymers. *J. Am. Chem. Soc.* **2004,** *126* (50), 16440-16450.

(52) Estrada, L. A.; Liu, D. Y.; Salazar, D. H.; Dyer, A. L.; Reynolds, J. R., Poly[Bis-EDOT-

Isoindigo]: An Electroactive Polymer Applied to Electrochemical Supercapacitors. *Macromolecules* **2012,** *45* (20), 8211-8220.

(53) Nyholm, L.; Nystrom, G.; Mihranyan, A.; Stromme, M., Toward flexible polymer and paper-based energy storage devices. *Advanced materials* **2011,** *23* (33), 3751-69.

(54) Shown, I.; Ganguly, A.; Chen, L.-C.; Chen, K.-H., Conducting polymer-based flexible supercapacitor. *Energy Science & Engineering* **2015,** *3* (1), 2-26.

(55) Huang, Y.; Li, H. F.; Wang, Z. F.; Zhu, M. S.; Pei, Z. X.; Xue, Q.; Huang, Y.; Zhi, C. Y., Nanostructured Polypyrrole as a flexible electrode material of supercapacitor. *Nano Energy* **2016,** *22*, 422-438.

(56) Root, S. E.; Savagatrup, S.; Printz, A. D.; Rodriquez, D.; Lipomi, D. J., Mechanical Properties of Organic Semiconductors for Stretchable, Highly Flexible, and Mechanically Robust Electronics. *Chem. Rev.* **2017,** *117* (9), 6467-6499.

(57) Yu, M.; Zhang, Y.; Zeng, Y.; Balogun, M. S.; Mai, K.; Zhang, Z.; Lu, X.; Tong, Y., Water surface assisted synthesis of large-scale carbon nanotube film for high-performance and stretchable supercapacitors. *Advanced materials* **2014,** *26* (27), 4724-9.

(58) Yu, X.; Su, X.; Yan, K.; Hu, H.; Peng, M.; Cai, X.; Zou, D., Stretchable, Conductive, and Stable PEDOT-Modified Textiles through a Novel In Situ Polymerization Process for Stretchable Supercapacitors. *Advanced Materials Technologies* **2016,** *1* (2), 1600009.

(59) Baek, P.; Aydemir, N.; An, Y.; Chan, E. W. C.; Sokolova, A.; Nelson, A.; Mata, J. P.; McGillivray, D.; Barker, D.; Travas-Sejdic, J., Molecularly Engineered Intrinsically Healable and Stretchable Conducting Polymers. *Chem. Mater.* **2017,** *29* (20), 8850-8858.

(60) Wang, Y.; Zhu, C.; Pfattner, R.; Yan, H.; Jin, L.; Chen, S.; Molina-Lopez, F.; Lissel, F.; Liu,

J.; Rabiah, N. I.; Chen, Z.; Chung, J. W.; Linder, C.; Toney, M. F.; Murmann, B.; Bao, Z., A highly stretchable, transparent, and conductive polymer. *Science Advances* **2017,** *3* (3).

(61) Zhang, Z.; Deng, J.; Li, X.; Yang, Z.; He, S.; Chen, X.; Guan, G.; Ren, J.; Peng, H., Superelastic supercapacitors with high performances during stretching. *Advanced materials* **2015,** *27* (2), 356-62.

(62) Huang, Y.; Zhong, M.; Huang, Y.; Zhu, M.; Pei, Z.; Wang, Z.; Xue, Q.; Xie, X.; Zhi, C., A self-healable and highly stretchable supercapacitor based on a dual crosslinked polyelectrolyte. *Nature communications* **2015,** *6*, 10310.

(63) Tang, Q.; Chen, M.; Yang, C.; Wang, W.; Bao, H.; Wang, G., Enhancing the energy density of asymmetric stretchable supercapacitor based on wrinkled CNT@MnO_2 cathode and CNT@polypyrrole anode. *ACS applied materials & interfaces* **2015,** *7* (28), 15303-13.

(64) Xiao, L.; Chen, Z.; Feng, C.; Liu, L.; Bai, Z. Q.; Wang, Y.; Qian, L.; Zhang, Y. Y.; Li, Q. Q.; Jiang, K. L.; Fan, S. S., Flexible, Stretchable, Transparent Carbon Nanotube Thin Film Loudspeakers. *Nano Lett.* **2008,** *8* (12), 4539-4545.

(65) Kim, R. H.; Bae, M. H.; Kim, D. G.; Cheng, H.; Kim, B. H.; Kim, D. H.; Li, M.; Wu, J.; Du, F.; Kim, H. S.; Kim, S.; Estrada, D.; Hong, S. W.; Huang, Y.; Pop, E.; Rogers, J. A., Stretchable, transparent graphene interconnects for arrays of microscale inorganic light emitting diodes on rubber substrates. *Nano Lett.* **2011,** *11* (9), 3881-6.

(66) Liang, J.; Li, L.; Chen, D.; Hajagos, T.; Ren, Z.; Chou, S. Y.; Hu, W.; Pei, Q., Intrinsically stretchable and transparent thin-film transistors based on printable silver nanowires, carbon nanotubes and an elastomeric dielectric. *Nature communications* **2015,** *6*, 7647.

(67) Ge, J.; Cheng, G.; Chen, L., Transparent and flexible electrodes and supercapacitors using

polyaniline/single-walled carbon nanotube composite thin films. *Nanoscale* **2011,** *3* (8), 3084- 8.

(68) Lin, H.; Li, L.; Ren, J.; Cai, Z.; Qiu, L.; Yang, Z.; Peng, H., Conducting polymer composite film incorporated with aligned carbon nanotubes for transparent, flexible and efficient supercapacitor. *Scientific reports* **2013,** *3*, 1353.

(69) Souza, V. H. R.; Oliveira, M. M.; Zarbin, A. J. G., Bottom-up synthesis of graphene/polyaniline nanocomposites for flexible and transparent energy storage devices. *J. Power Sources* **2017,** *348*, 87-93.

(70) Chen, F.; Wan, P.; Xu, H.; Sun, X., Flexible Transparent Supercapacitors Based on Hierarchical Nanocomposite Films. *ACS applied materials & interfaces* **2017,** *9* (21), 17865-17871.

(71) Wang, X.; Gao, K.; Shao, Z.; Peng, X.; Wu, X.; Wang, F., Layer-by-Layer assembled hybrid multilayer thin film electrodes based on transparent cellulose nanofibers paper for flexible supercapacitors applications. *J. Power Sources* **2014,** *249*, 148-155.

(72) Devarayan, K.; Lei, D.; Kim, H.-Y.; Kim, B.-S., Flexible transparent electrode based on PANi nanowire/nylon nanofiber reinforced cellulose acetate thin film as supercapacitor. *Chem. Eng. J.* **2015,** *273*, 603-609.

(73) Higgins, T. M.; Coleman, J. N., Avoiding Resistance Limitations in High-Performance Transparent Supercapacitor Electrodes Based on Large-Area, High-Conductivity PEDOT:PSS Films. *ACS applied materials & interfaces* **2015,** *7* (30), 16495-506.

(74) Zhang, C.; Higgins, T. M.; Park, S.-H.; O'Brien, S. E.; Long, D.; Coleman, J. N.; Nicolosi, V., Highly flexible and transparent solid-state supercapacitors based on RuO_2/PEDOT:PSS conductive ultrathin films. *Nano Energy* **2016,** *28*, 495-505.

(75) Moon, H.; Lee, H.; Kwon, J.; Suh, Y. D.; Kim, D. K.; Ha, I.; Yeo, J.; Hong, S.; Ko, S. H., Ag/Au/Polypyrrole Core-shell Nanowire Network for Transparent, Stretchable and Flexible Supercapacitor in Wearable Energy Devices. *Scientific reports* **2017,** *7*, 41981.

(76) Tian, Y.; Cong, S.; Su, W.; Chen, H.; Li, Q.; Geng, F.; Zhao, Z., Synergy of $W_{18}O_{49}$ and polyaniline for smart supercapacitor electrode integrated with energy level indicating functionality. *Nano Lett.* **2014,** *14* (4), 2150-6.

(77) Chen, X.; Lin, H.; Chen, P.; Guan, G.; Deng, J.; Peng, H., Smart, stretchable supercapacitors. *Advanced materials* **2014,** *26* (26), 4444-9.

(78) Xu, Z.; Kong, L.; Wang, Y.; Wang, B.; Zhao, J., Tuning band gap, color switching, optical contrast, and redox stability in solution-processable BDT-based electrochromic materials. *Organic Electronics* **2018,** *54*, 94-103.

(79) Thakur, V. K.; Ding, G.; Ma, J.; Lee, P. S.; Lu, X., Hybrid materials and polymer electrolytes for electrochromic device applications. *Adv Mater* **2012,** *24* (30), 4071-96.

(80) Wang, Z.; Zhu, M.; Gou, S.; Pang, Z.; Wang, Y.; Su, Y.; Huang, Y.; Weng, Q.; Schmidt, O. G.; Xu, J., Pairing of Luminescent Switch with Electrochromism for Quasi-Solid-State Dual-Function Smart Windows. *ACS Appl Mater Interfaces* **2018,** *10* (37), 31697-31703.

(81) Reynolds, P. M. B. a. J. R., Color Control in π-Conjugated Organic Polymers for Use in Electrochromic Devices. *Chem. Rev* **2010,** *110*, 268-320.

(82) Chang-Jian, C.-W.; Cho, E.-C.; Yen, S.-C.; Ho, B.-C.; Lee, K.-C.; Huang, J.-H.; Hsiao, Y.-S., Facile preparation of WO 3 /PEDOT:PSS composite for inkjet printed electrochromic window and its performance for heat shielding. *Dyes and Pigments* **2018,** *148*, 465-473.

(83) Augusto, T.; Teixeira Neto, É.; Teixeira Neto, Â. A.; Vichessi, R.; Vidotti, M.; de Torresi, S.

I. C., Electrophoretic deposition of Au@PEDOT nanoparticles towards the construction of high-performance electrochromic electrodes. *Solar Energy Materials and Solar Cells* **2013,** *118*, 72-80.

(84) Seung Il Cho, D. H. C., Sang-Ho Kim, and Sang Bok Lee, Electrochemical Synthesis and Fast Electrochromics of Poly(3,4-ethylenedioxythiophene) Nanotubes in Flexible Substrate. *Chem. Mater.* **2005,** *17*, 4564-4566.

(85) Kateb, M.; Safarian, S.; Kolahdouz, M.; Fathipour, M.; Ahamdi, V., ZnO–PEDOT core–shell nanowires: An ultrafast, high contrast and transparent electrochromic display. *Solar Energy Materials and Solar Cells* **2016,** *145*, 200-205.

(86) Zhen, S.; Xu, J.; Lu, B.; Zhang, S.; Zhao, L.; Li, J., Tuning the optoelectronic properties of polyfuran by design of furan-EDOT monomers and free-standing films with enhanced redox stability and electrochromic performances. *Electrochimica Acta* **2014,** *146*, 666-678.

(87) Cai, G. F.; Tu, J. P.; Zhou, D.; Zhang, J. H.; Wang, X. L.; Gu, C. D., Dual electrochromic film based on WO3/polyaniline core/shell nanowire array. *Solar Energy Materials and Solar Cells* **2014,** *122*, 51-58.

(88) Diao, Y.; Chen, H.; Lu, Y.; Santino, L. M.; Wang, H.; D'Arcy, J. M., Converting Rust to PEDOT Nanofibers for Supercapacitors. *ACS Applied Energy Materials* **2019,** *2* (5), 3435-3444.

(89) Wang, H.; Diao, Y.; Rubin, M.; Santino, L. M.; Lu, Y.; D'Arcy, J. M., Metal Oxide-Assisted PEDOT Nanostructures via Hydrolysis-Assisted Vapor-Phase Polymerization for Energy Storage. *ACS Applied Nano Materials* **2018,** *1* (3), 1219-1227.

(90) Kawahara, J.; Ersman, P. A.; Engquist, I.; Berggren, M., Improving the color switch contrast in PEDOT:PSS-based electrochromic displays. *Organic Electronics* **2012,** *13* (3), 469-474.

(91) Mitraka, E.; Jafari, M. J.; Vagin, M.; Liu, X.; Fahlman, M.; Ederth, T.; Berggren, M.; Jonsson, M. P.; Crispin, X., Oxygen-induced doping on reduced PEDOT. *J Mater Chem A Mater* **2017,** *5* (9), 4404-4412.

(92) Berggren, M.; Crispin, X.; Fabiano, S.; Jonsson, M. P.; Simon, D. T.; Stavrinidou, E.; Tybrandt, K.; Zozoulenko, I., Ion Electron-Coupled Functionality in Materials and Devices Based on Conjugated Polymers. *Adv Mater* **2019,** *31* (22), e1805813.

(93) Tartaj, P.; Morales, M. P.; Gonzalez-Carreno, T.; Veintemillas-Verdaguer, S.; Serna, C. J., The iron oxides strike back: from biomedical applications to energy storage devices and photoelectrochemical water splitting. *Adv Mater* **2011,** *23* (44), 5243-9.

(94) Bui Thi Hang, D. H. T., Nguyen Tuyet Nga, Phan Thi Le Minh, and Eiji Kobayashie, Nanoparticle Fe2O3-Loaded Carbon Nanofibers as Iron-Air Battery Anodes. *Journal of The Electrochemical Society* **2013,** *160* (9), A1442-A1445.

(95) Tarascon, M. A. a. J.-M., Building better batteries. *Nature* **2008,** *451* (652).

(96) CHENG, J. C. A. F., Combination of Lightweight Elements and Nanostructured Materials for Batteries. *Accounts of chemical research* **2009,** *42* (6), 713-723.

(97) Cheng, F.; Liang, J.; Tao, Z.; Chen, J., Functional materials for rechargeable batteries. *Adv Mater* **2011,** *23* (15), 1695-715.

(98) Coetzer, M. M. T. a. J., A PRELIMINARY INVESTIGATION OF THE ELECTROCHEMICAL PERFORMANCE OF a-Fe203 AND Fe304 CATHODES IN HIGHTEMPERATURE CELLS. *Mat. Res. Bull* **1981,** *16,* 591-597.

(99) P. Poizot, S. L., S. Grugeon, L. Dupont & J-M. Tarascon, Nano-sized transition-metaloxidesas negative-electrode materials for lithium-ion batteries. *Nature* **2000,** *407*.

(100) Ban, C.; Wu, Z.; Gillaspie, D. T.; Chen, L.; Yan, Y.; Blackburn, J. L.; Dillon, A. C.,

Nanostructured Fe(3)O(4)/SWNT electrode: Binder-free and high-rate li-ion anode. *Adv Mater* **2010,** *22* (20), E145-9.

(101) Reddy, D. L. a. T. B., Handbook of Batteries, 3rd ed. *McGraw-Hill, New York* **2002**.

(102) Hayashi, H. A. a., Encyclopedia of Electrochemical Power Sources, fourth ed. *Elsevier B.V., Amsterdam* **2009**, 347.

(103) CARLSSON, L. J. a. L., AN IRON-AIR VEHICLE BATTERY. *Jounral of Power Sources* **1977-1978,** *2*, 287-296.

(104) Ma, M.; Tu, J. P.; Yuan, Y. F.; Wang, X. L.; Li, K. F.; Mao, F.; Zeng, Z. Y., Electrochemical performance of ZnO nanoplates as anode materials for Ni/Zn secondary batteries. *Journal of Power Sources* **2008,** *179* (1), 395-400.

(105) Qingfeng Li, N. J. B., Aluminum as anode for energy storage and conversion: a review. *journal of Power Sources* **2002,** *110*, 1-10.

(106) Salking, S. V. F. a. A. J., Alkaline Storage Batteries. *Wiley, New York* **1969,** *1*.

(107) Gu, H.; Zhang, Y.; Huang, M.; Chen, F.; Yang, Z.; Fan, X.; Li, S.; Zhang, W.; Yang, S.; Li, M., Hydrolysis-Coupled Redox Reaction to 3D Cu/Fe3O4 Nanorod Array Electrodes for High-Performance Lithium-Ion Batteries. *Inorg Chem* **2017,** *56* (14), 7657-7667.

(108) Sun, Y.; Hu, X.; Luo, W.; Xia, F.; Huang, Y., Reconstruction of Conformal Nanoscale MnO on Graphene as a High-Capacity and Long-Life Anode Material for Lithium Ion Batteries. *Advanced Functional Materials* **2013,** *23* (19), 2436-2444.

(109) Hiroki Kitamura, L. Z., Bui Thi Hang, Shigeto Okada, and Jun-ichi Yamakib,, Effect of Charge Current Density on Electrochemical Performance of Fe/C Electrodes in Alkaline Solutions. *Jounral of Electrochemical Society* **2012,** *159* (6), A720-724.

(110) Hang, B. T.; Yoon, S.-H.; Okada, S.; Yamaki, J.-i., Effect of metal-sulfide additives on

electrochemical properties of nano-sized Fe2O3-loaded carbon for Fe/air battery anodes. *Journal of Power Sources* **2007,** *168* (2), 522-532.

(111) Hang, B. T.; Watanabe, T.; Egashira, M.; Watanabe, I.; Okada, S.; Yamaki, J.-i., The effect of additives on the electrochemical properties of Fe/C composite for Fe/air battery anode. *Journal of Power Sources* **2006,** *155* (2), 461-469.

(112) H. A. Figueredo-Rodr´ıguez, R. D. M., M. Insausti, A. Garcia Luis, C. Ponce de Le´on, C. Alegre, V. Baglio, A. S. Aric`o, and F. C. Walsh, A Rechargeable, Aqueous Iron Air Battery with Nanostructured Electrodes Capable of High Energy Density Operation. *Jounral of Electrochemical Society* **2017,** *164* (6), A1148-A1157.

Chapter 10

Conclusions

The similarity of the fine nano/micro-structures in rust and conducting polymers inspires us to think about bridging this "waste" inorganic material and this promising organic material. Fortunately, the chemistry of rust (natural Fe^{3+} source) and nanostructured conducting polymers (Fe^{3+} as an essential oxidant for synthesis) provides a fundamental understanding of the synthesis versus structure versus property relationship for developing novel synthesis and state-of-the-art devices in energy storage, sensing, electro/photocatalysis, and mixed ionic-electronic electronics. Clearly, such a combination will raise a revolution in rust utilization and synthesis of nanostructure conducting polymers.

Over the course of this dissertation, we have introduced various concepts for producing nanostructured conducting polymers by utilizing rust via rust-based vapor phase polymerization (RVPP). It should be reiterated that rust is a ubiquitous byproduct from the corrosion of iron, and a solid-state material serving as an ideal source of Fe^{3+} ions for carrying out chemical synthesis via its 0.77 V oxidant potential. The emergence of RVPP overcomes the traditional challenge of utilizing hygroscopic and corrosive iron (III) salts for synthesizing conducting polymers. It also creates an approach that enables conducting polymer synthesis from any solid-state materials, such as on masonry materials and even possibly on rust-containing soil on other planets. Besides the oxidative property, rust also provides various nanostructured templates that enable multiple

nanostructured conducting polymers, such as nanofibers, nanoflakes, nanowires, nanotubes, and microparticles.

Conducting polymers exhibit unique properties - they are soft materials assembling into nanostructures held by weak intermolecular electrostatic and van der Waals bonds; they are versatile materials and possess high surface area, enabling applications in energy storage, sensing, CO_2 photoreduction, antimicrobial, and photovoltaics. Conducting polymers accommodate solvated ions impregnation without structural degradation and provides ultra-surface area, leading to an outstanding electrochemical performance in energy storage under various electrochemical circumstances. Conducting polymers are responsive to external stimuli, such as humidity, temperature, and acidity, due to their large active surface area and sensitive electrical properties, leading to a chemoresisitve sensor. Conducting polymer PEDOT is an ideal photocatalysis for CO_2 photoreduction and H_2O_2 evolution due to its suitable band gap for CO_2/CO and H_2O/H_2O_2 conversion and facile charge carrier mobility. The band gap is controlled by doping treatment, such as acid, base, oxidized and reduced agents enabling various doping levels for performance optimization. Notably, PEDOT also investigated in photovoltaics and light-emitting diodes as a charge collection or charge injection layer, such as a hole transfer layer in dye-sensitized solar cells and perovskite solar cells.

Unlike ordered inorganic crystal structures, conducting polymers possess both crystalline and amorphous domains that affect the charge transfer. To better understand the conduction mechanism in polycrystalline conducting polymers, we describe a PEDOT configuration of tertiary structures. Almost all conducting polymers exhibit electrochromism when electrochemically oxidized or reduced, such as PEDOT transfer from light blue (oxidized state) to dark purple (reduced state), enabling applications in smart windows and electrochromic displays.

We detail a deposition of PEDOT nanofibers on FTO, leading to an enhancement of electrochromic stability. The research for next-generation batteries remains a significant area of discovery. Lithium-iron batteries and iron-air batteries receive intensive attention due to their inexpensive, high energy density, and environmentally friendly properties. We offer a novel approach to iron electrode deposition via combustion on RVPP-PEDOT, enabling nanoflakes and nanofibers morphologies.

Appendix A Rust formation and RVPP reactions

A.1 Remove impurity ions from glass reactors

Since ions have effect on the hydrolysis synthesis, it is necessary to keep away all impurities among reactors. 1) Utilize Aqua regia (concentrated HCl:concentrated nitic acid = 3:1) to wash all glass reactors, such as beakers, containers and pipets. 2) Utilize plastic reactors and pipets is an alternative approach. 3) Utilize MilliQ water for hydrolysis synthesis making sure there is no impurities.

A.2 Immersion methods

Rust layers are produced as per ASTM A109 protocol by immersing a 4 cm × 4 cm low-carbon steel sheet in 20 mL of a 0.01 M H_2SO_4 solution for 24 h at 25 °C. Corroded sheets were then rinsed and dried under ambient conditions. The thickness of a rust layer is controlled by immersion time ranging between 18 and 24 h.

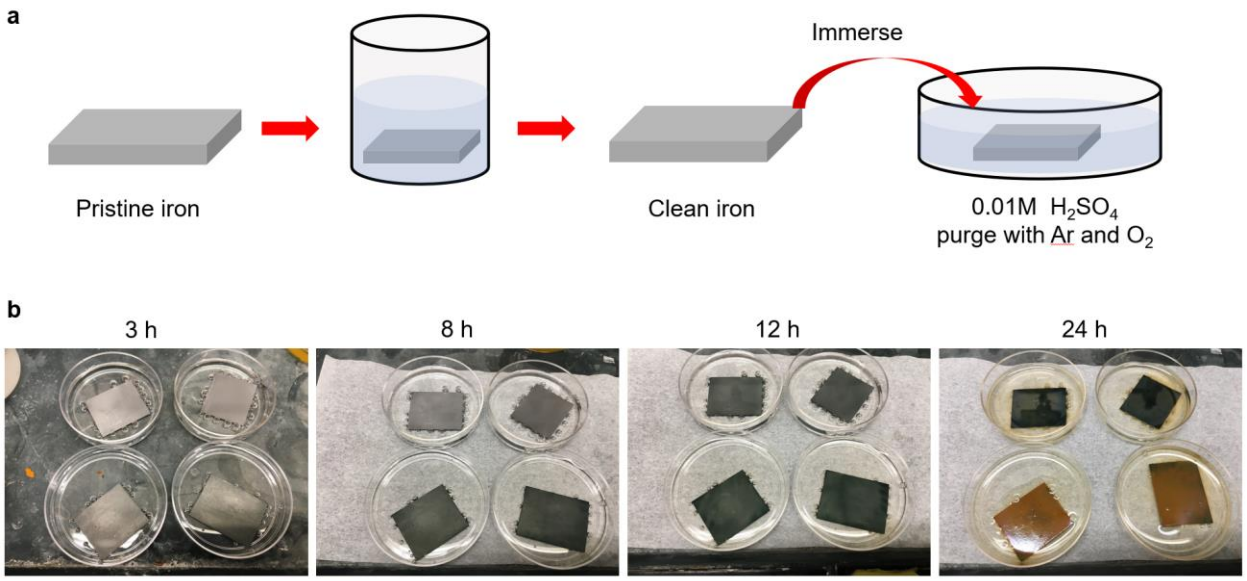

A.1: Immersion method for rust film production.

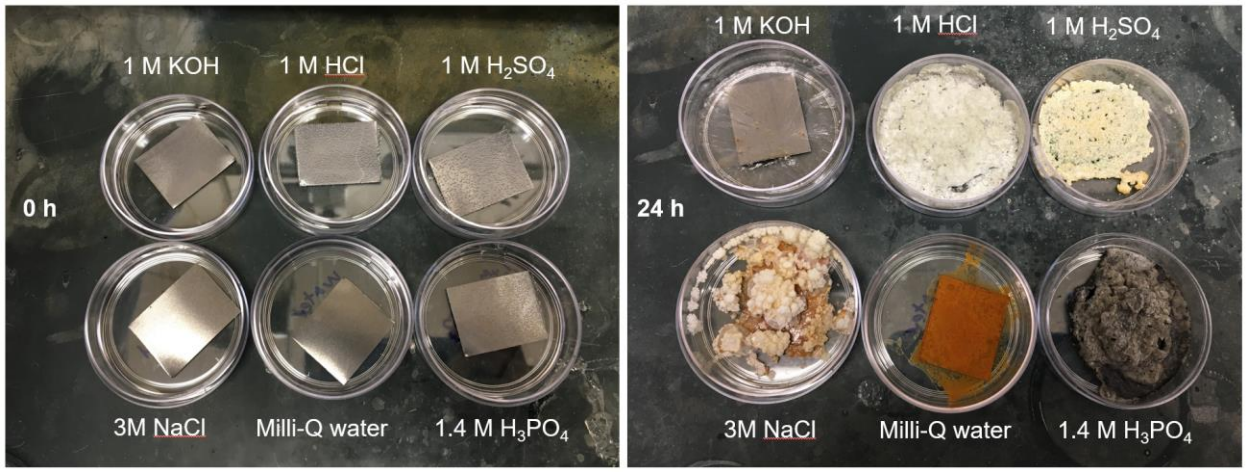

A.2: Synthesis rust from 1 M KOH, 1 M HCl, 1 M H_2SO_4, 3 M NaCl, MilliQ water, and 1.4 M H_3PO_4.

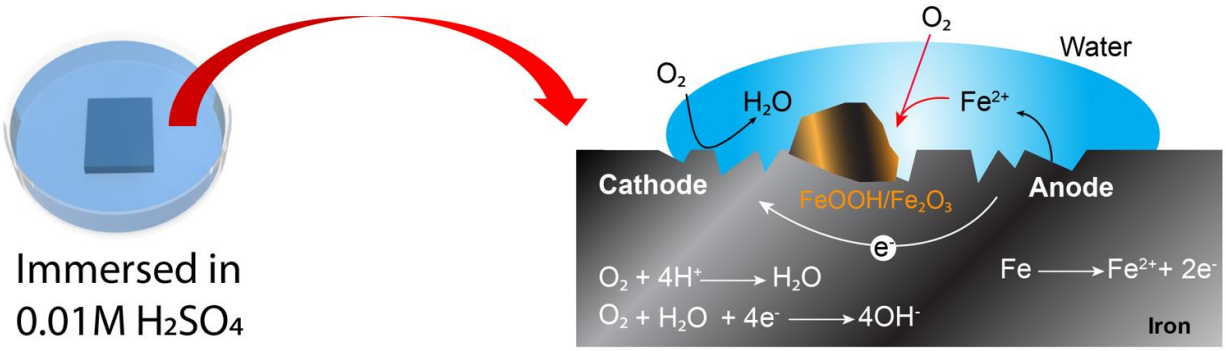

A.3: Mechanism of rust formation in 0.01 M H_2SO_4.

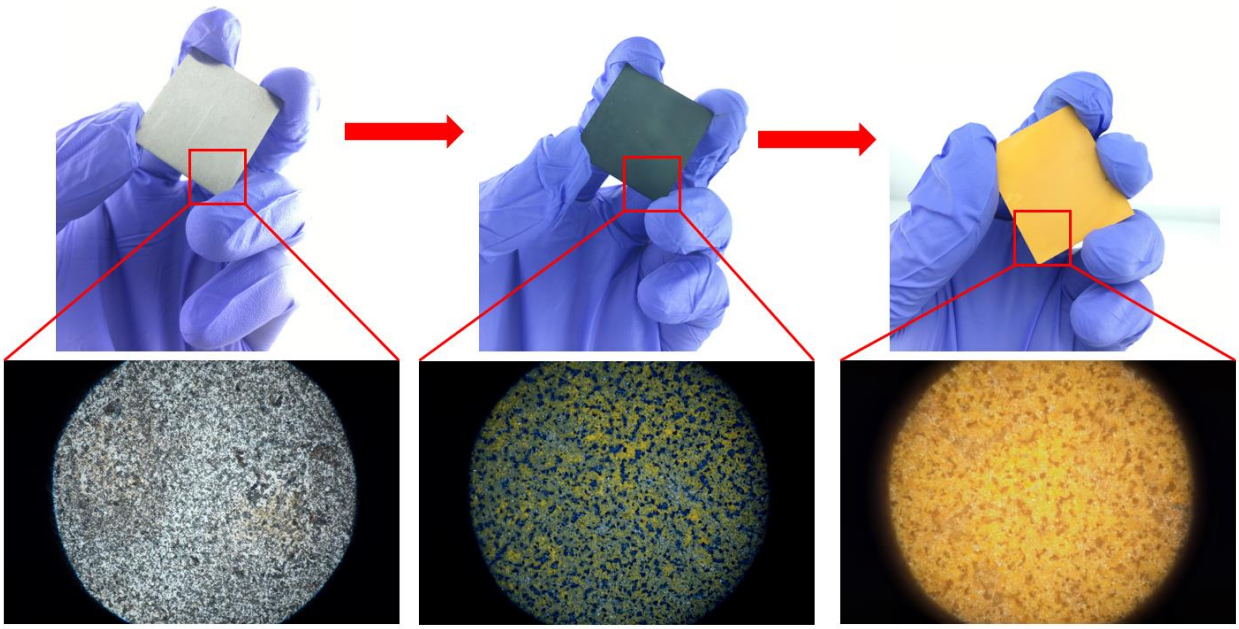

A.4: Optical photographs of pristine iron, green rust, and yellow rust.

A.3 RVPP reactions

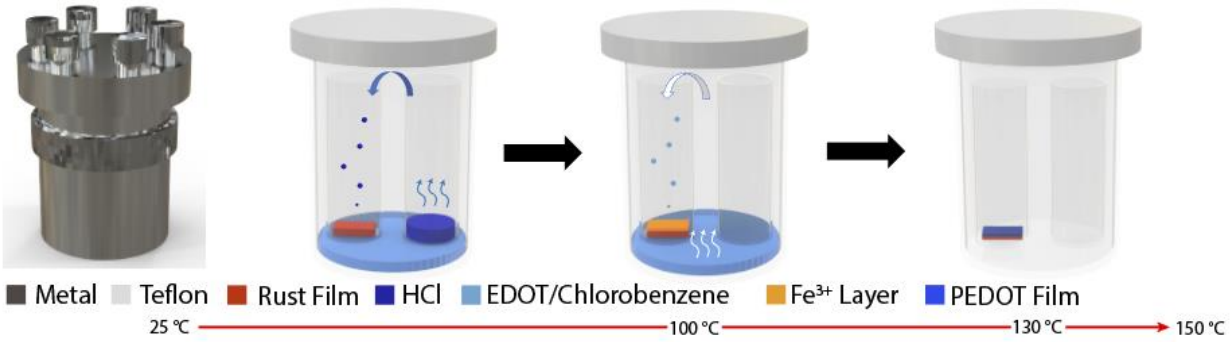

A.5: Schematic illustration of rust-based vapor phase polymerization (RVPP).

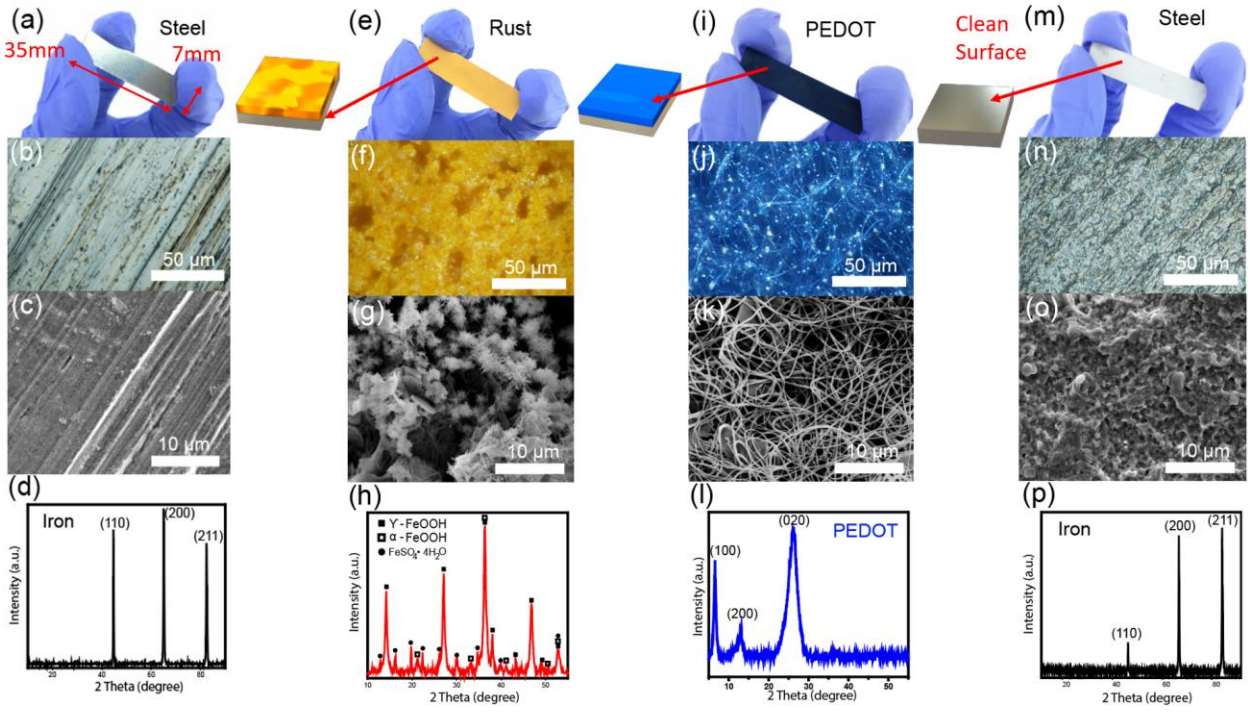

A.6: Flow process diagram of rust-based vapor phase polymerization (RVPP). (a-d) Pristine iron piece rusted to (e-h) α-FeOOH and γ-FeOOH layer via immersion method. (i-l) PEDOT nanofibers deposited on the iron substrate after RVPP. (m-p) The PEDOT layer detached from the iron substrate resulting in a clean and smooth iron surface.

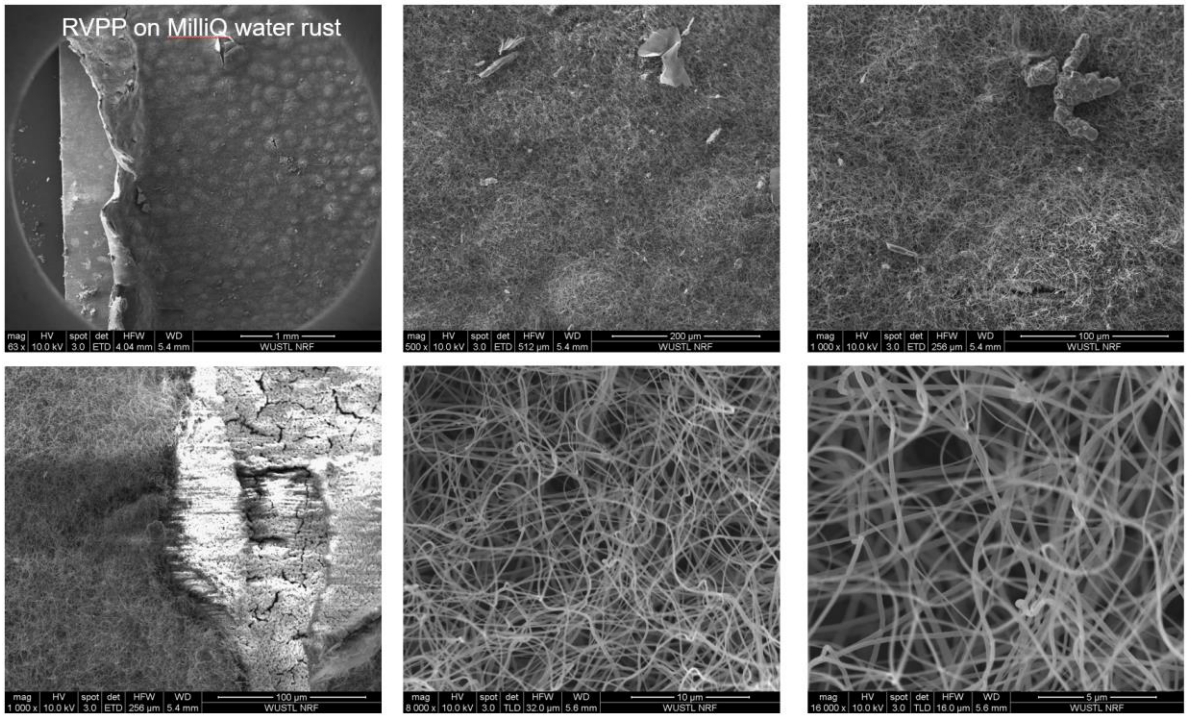

A.7: SEMs of RVPP-PEDOT synthesized from MilliQ water rust.

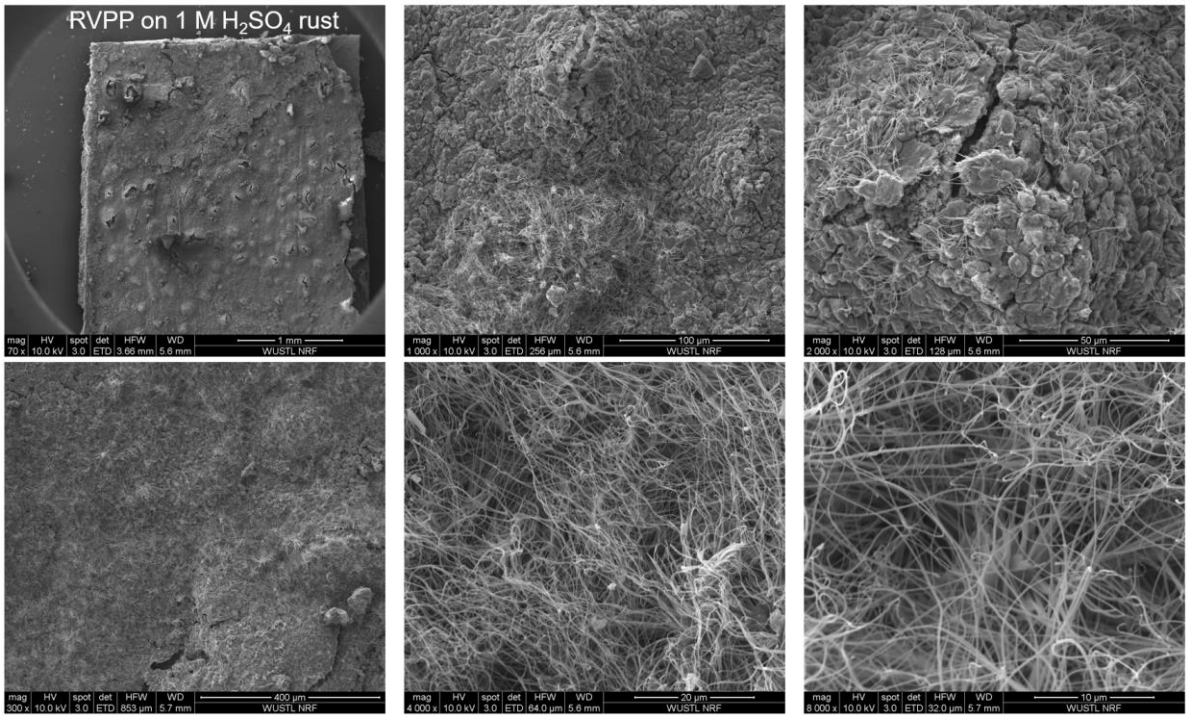

A.8: SEMs of RVPP-PEDOT synthesized from 1 M H_2SO_4 rust.

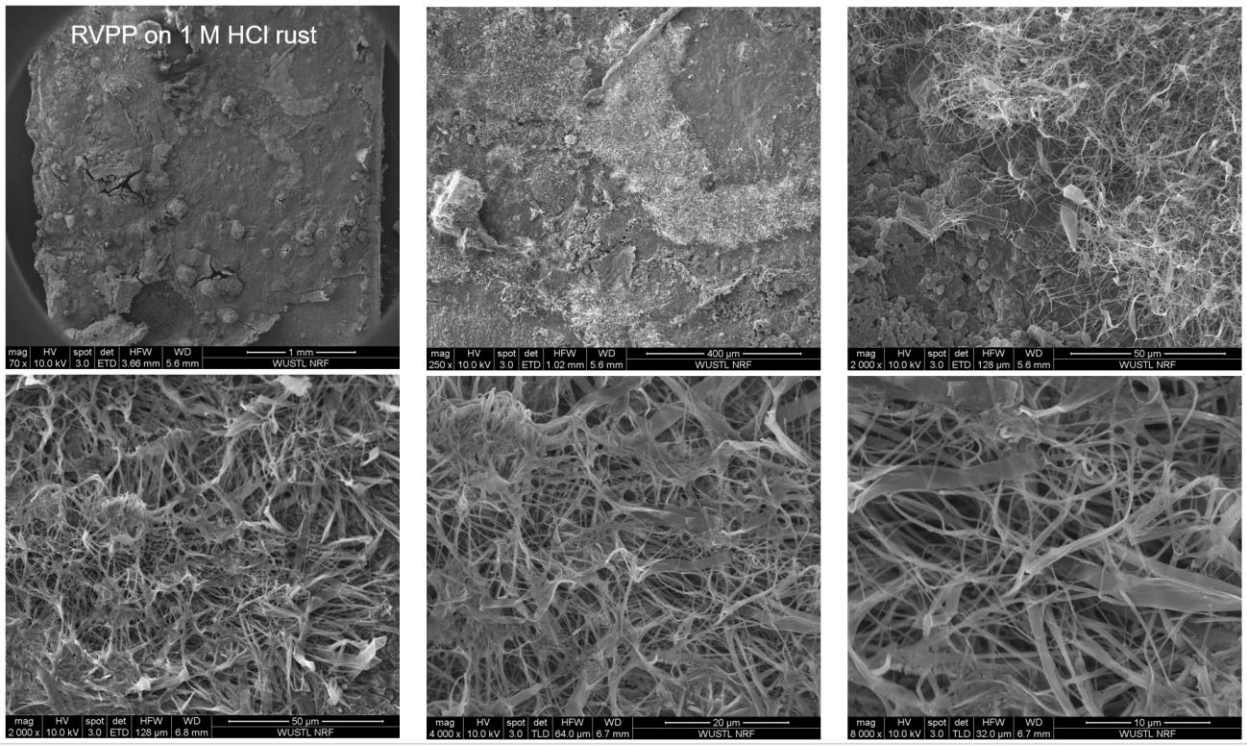

A.9: SEMs of RVPP-PEDOT synthesized from 1 M HCl rust.

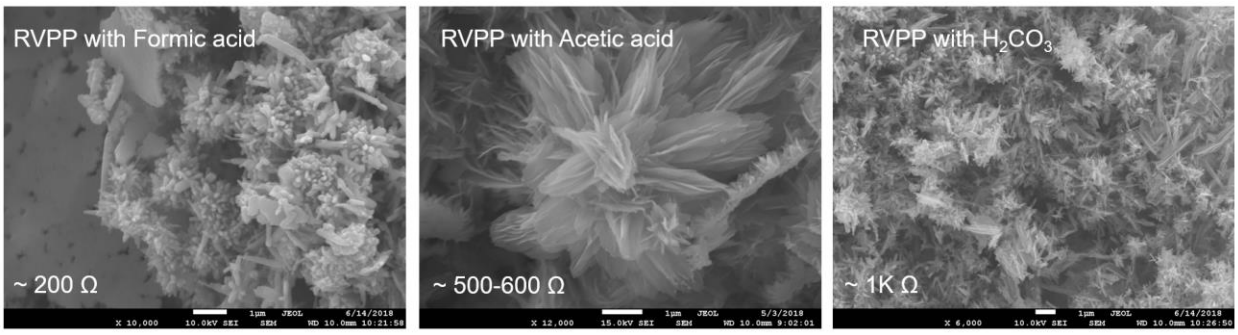

A.10: SEMs of RVPP-PEDOT synthesized from 1 M H_2SO_4 rust via formic acid, acetic acid and carbonic acid.

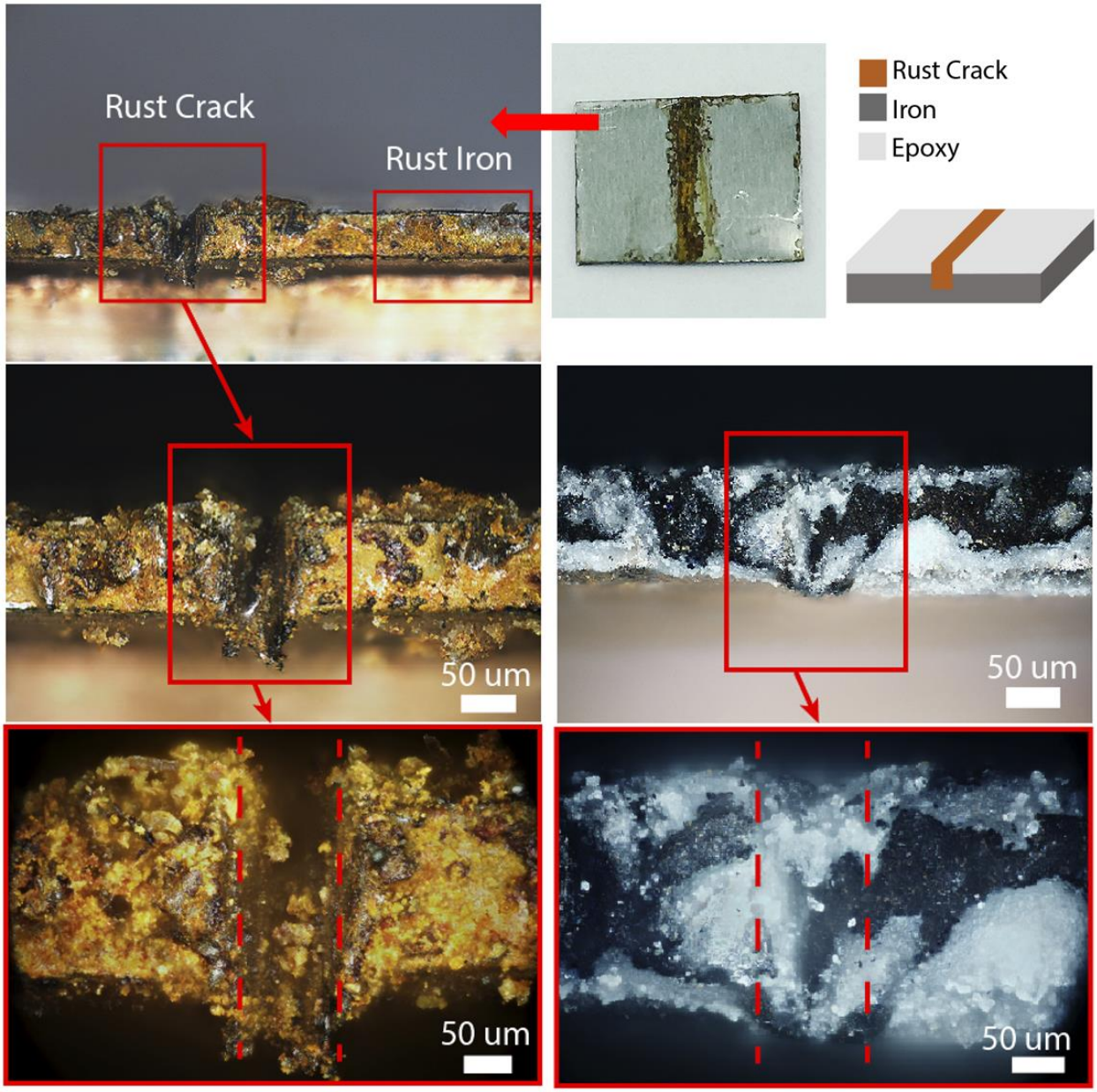

A.11: Optical photographs demonstrate that RVPP enables crack recover.

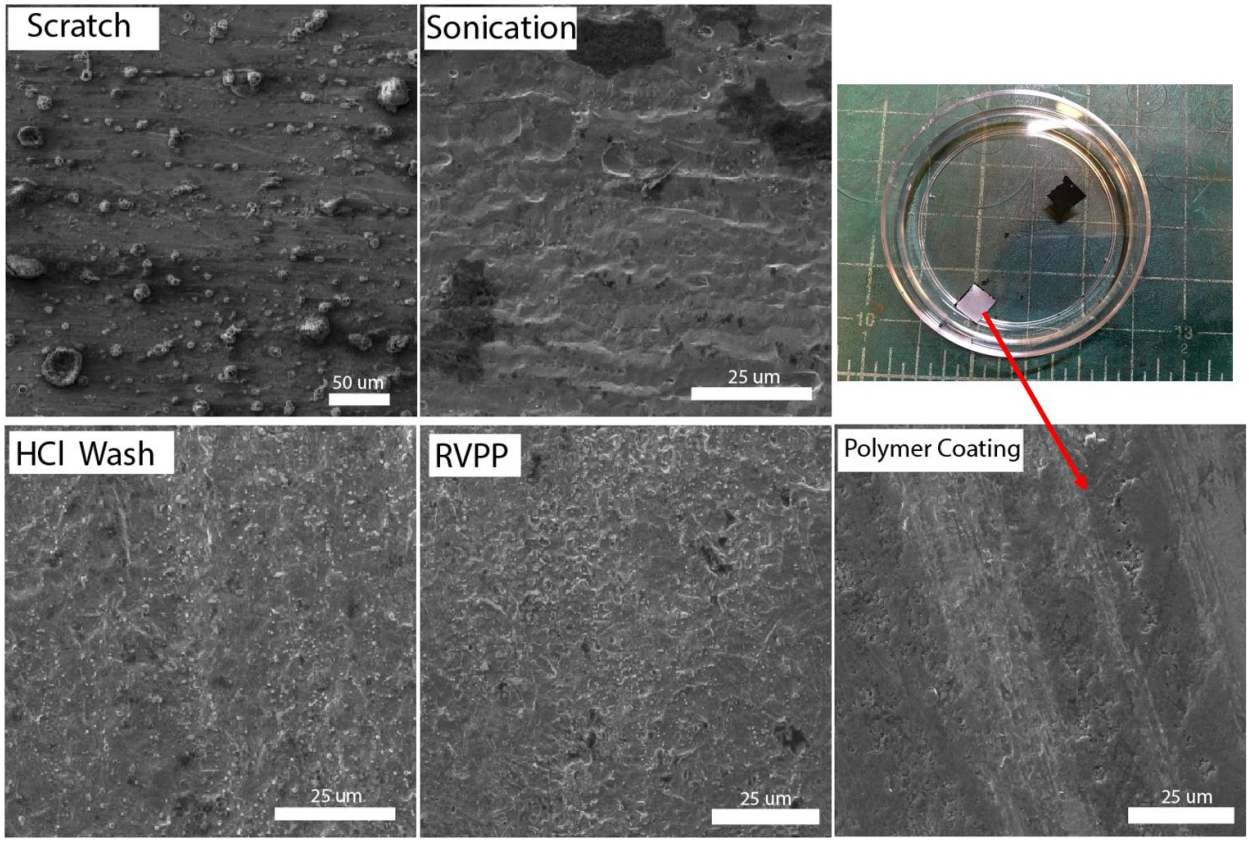

A.12: Comparation of rust cleaning between scratch, sonication, HCl wash, and RVPP via SEMs.

Appendix B Hydrothermal synthesis for β-FeOOH

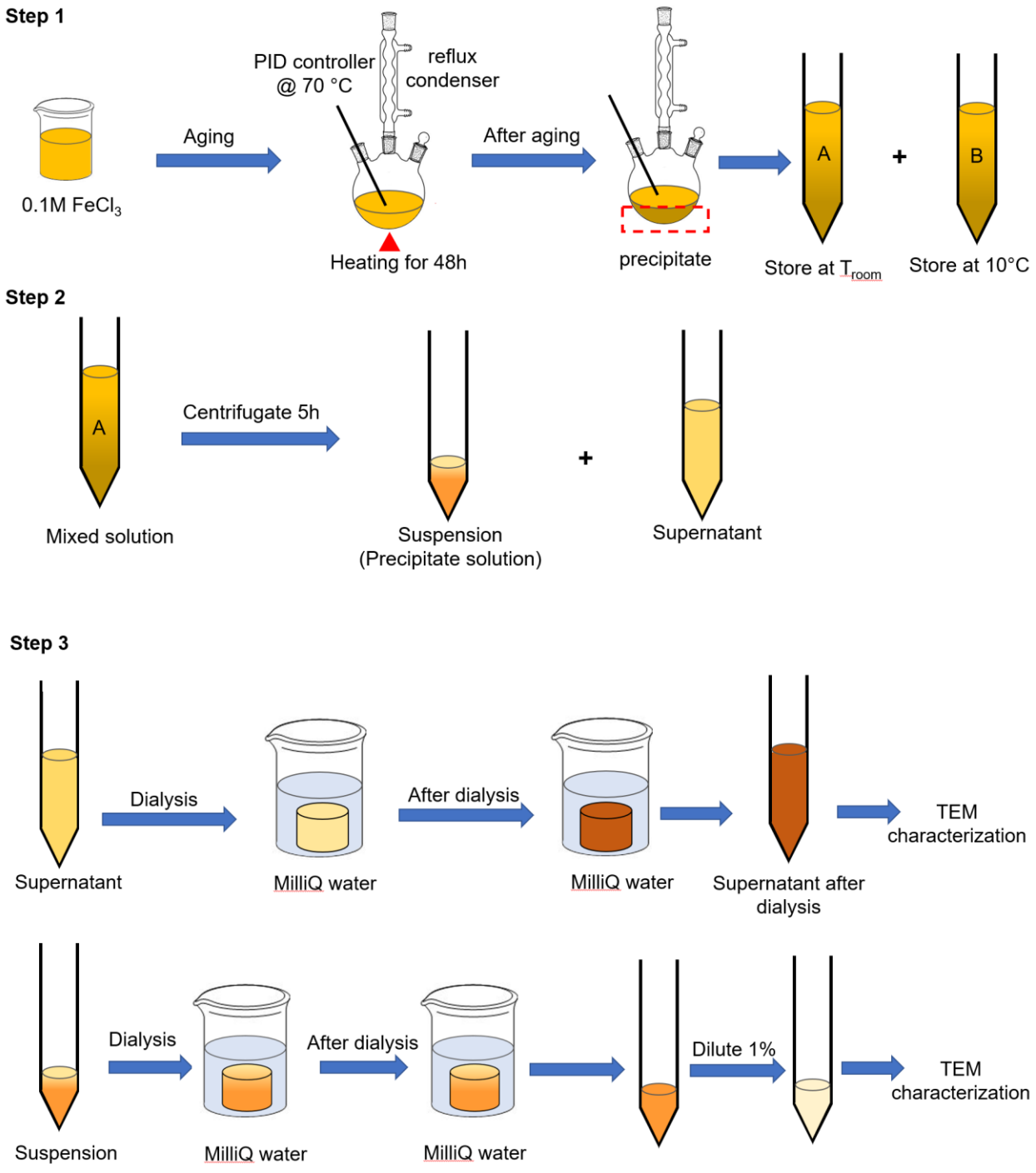

B.1: Schematic of β-FeOOH hydrothermal synthesis.

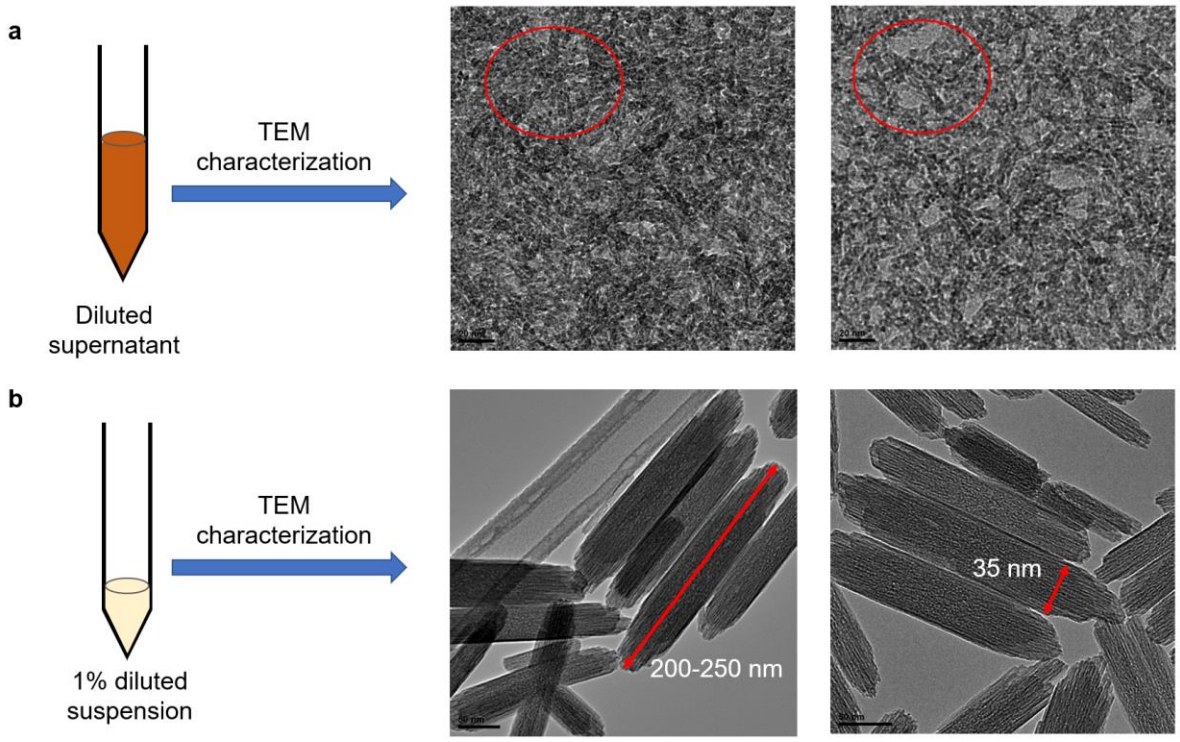

B.2: TEM characterization of β-FeOOH.

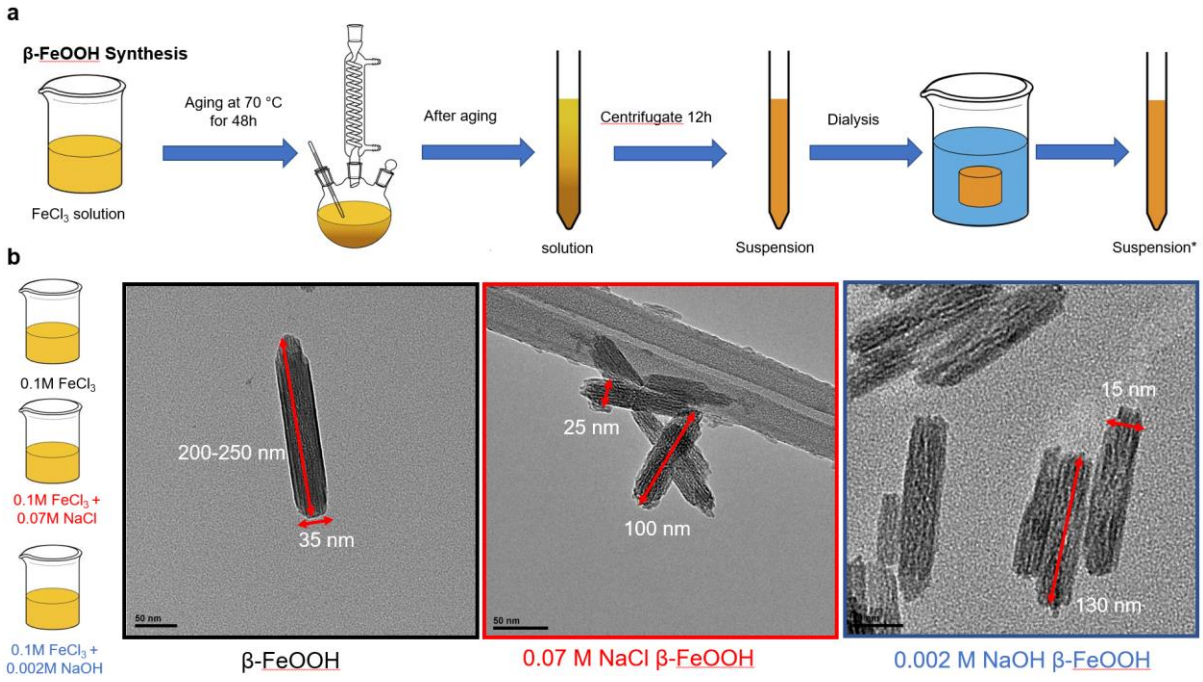

B.3: Schematic and TEM characterization of β-FeOOH hydrothermal synthesis under different conditions.

Appendix C Stoichiometry experiments on HVPP

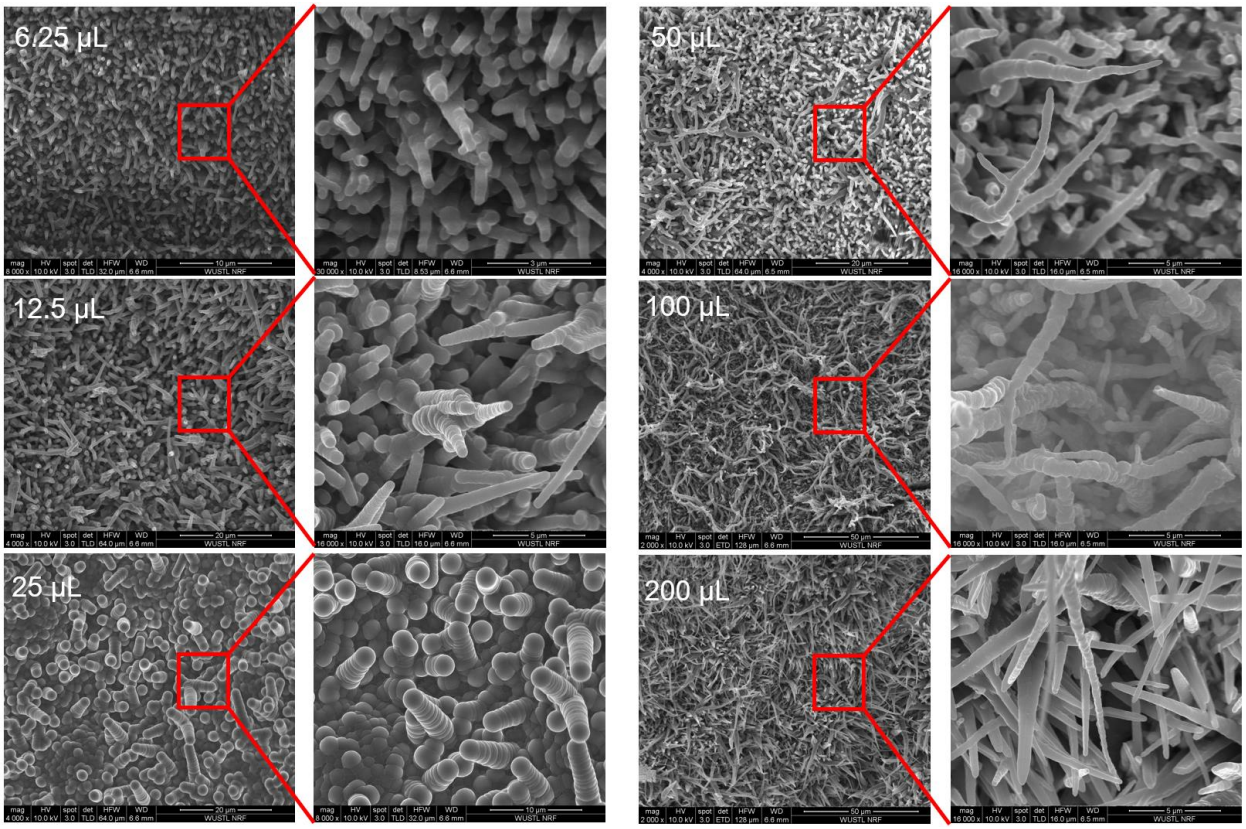

C.1: Stoichiometry of chlorobenzene. HVPP reactions in 0.266 M $FeCl_3$ and 0.0674 M EDOT/chlorobenzene solution with different amount of chlorobenzene.

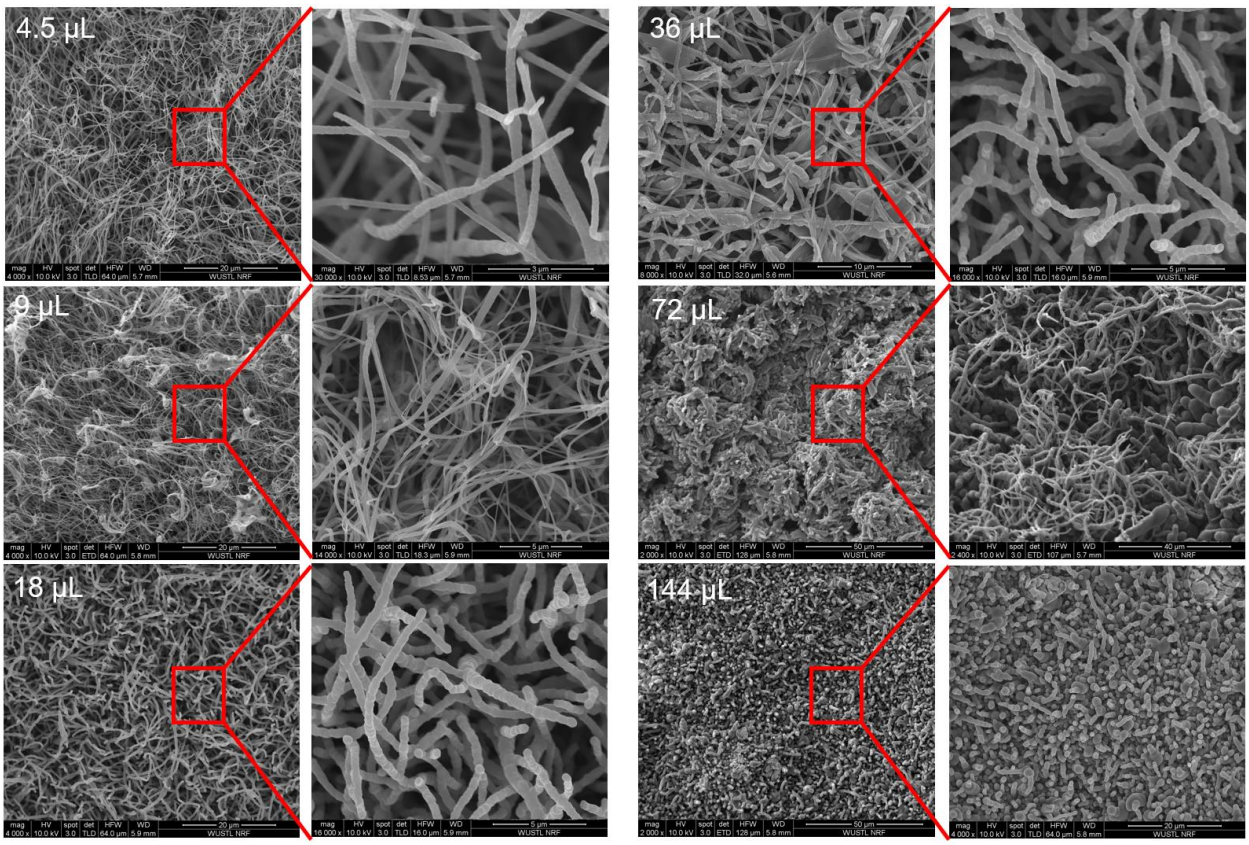

C.2: Stoichiometry of EDOT. HVPP reactions in 0.266 M $FeCl_3$ and 200 mL EDOT/chlorobenzene solution with different amount of EDOT.

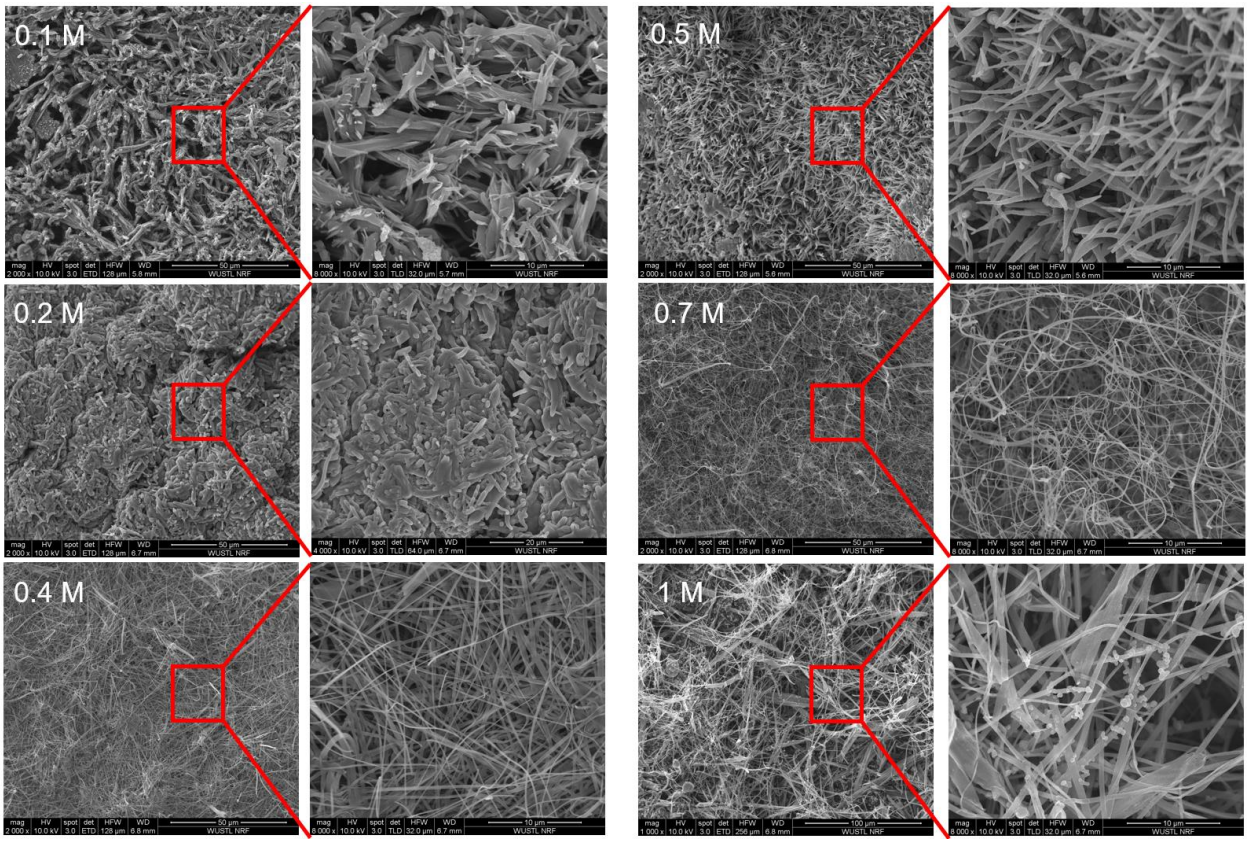

C.3: Stoichiometry of $FeCl_3$. HVPP reactions in 200 mL 0.0674 M EDOT/chlorobenzene solution with different amount of $FeCl_3$ solution.

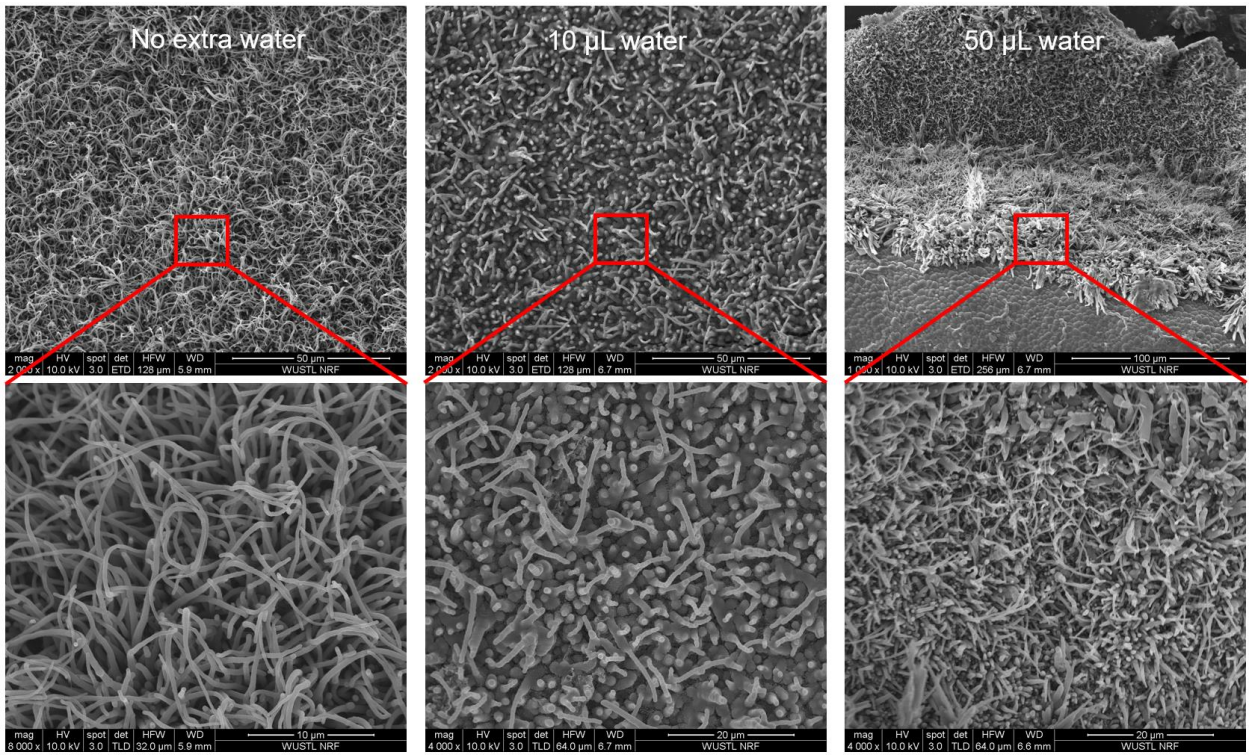

C.4: Stoichiometry of water content. HVPP reactions in in 0.266 M $FeCl_3$ and 200 mL 0.0674 M EDOT/chlorobenzene solution with different amount of water content.

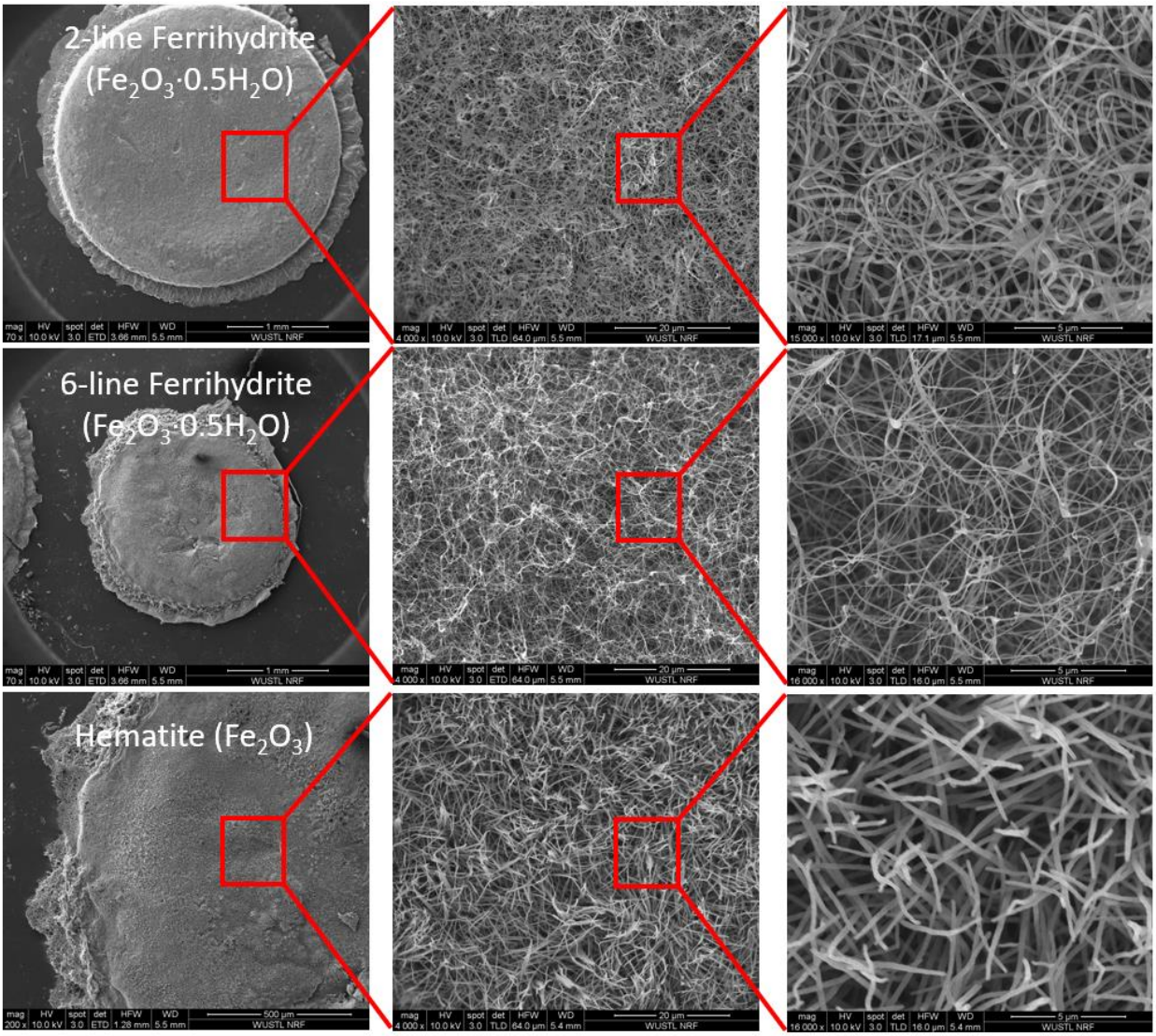

C.5: HVPP reactions in 200 mL 0.0674 M EDOT/chlorobenzene solution with different iron nanoparticles.

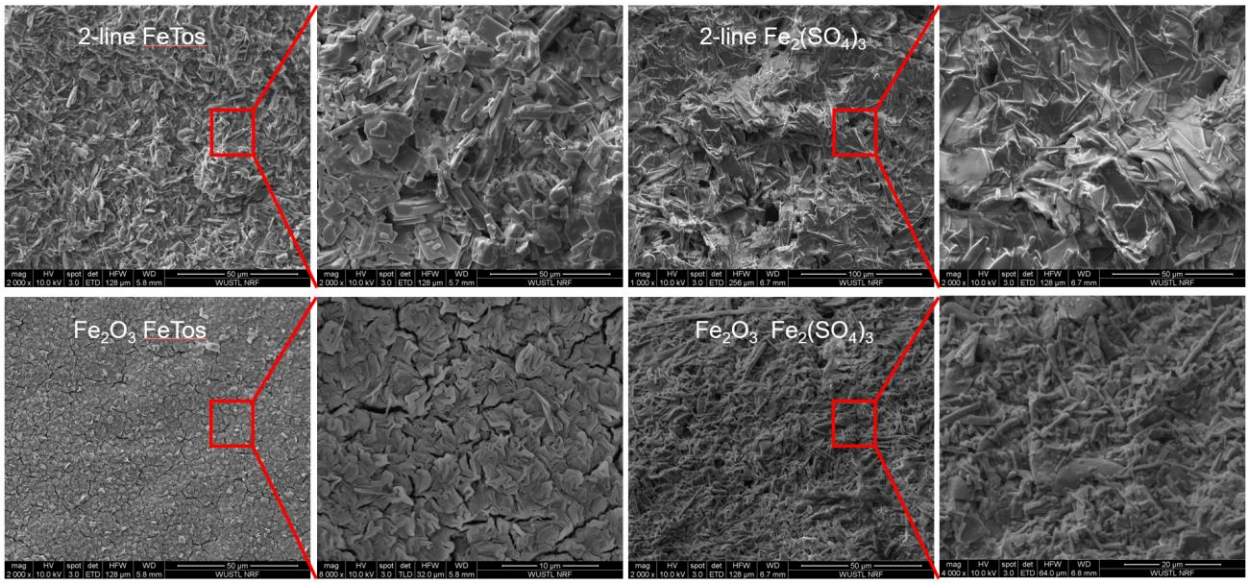

C.6: HVPP reactions in 200 mL 0.0674 M EDOT/chlorobenzene solution with different iron nanoparticles.

Appendix D Three electrode system for electrochemical characterization

D.1 Schematic and mechanism of three electrode system

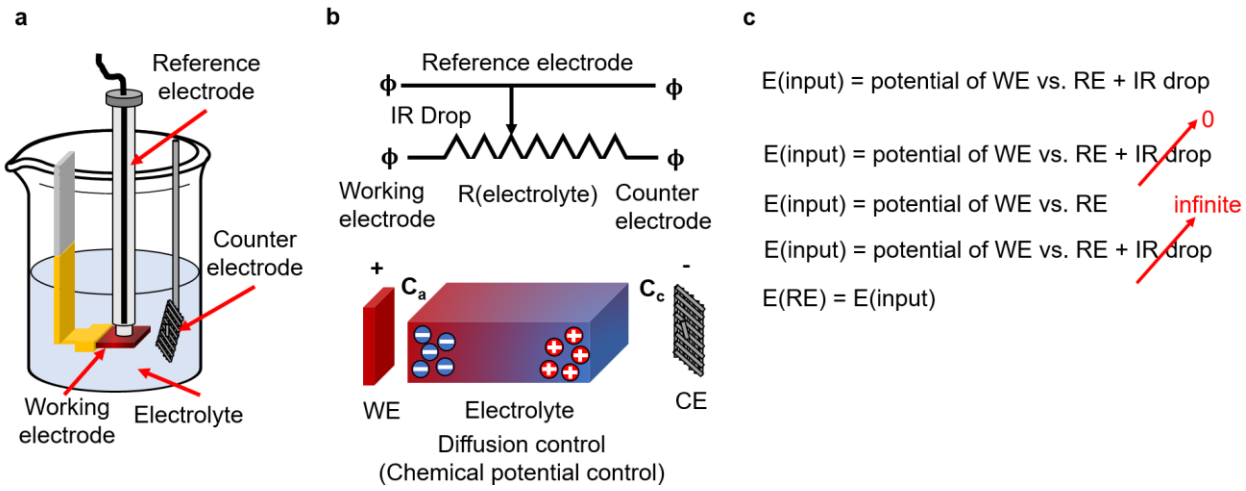

D.1: (a) Schematic illustration of three electrode system. (b) Mechanism of reference electrode. (c) Equations for input potential calculation.

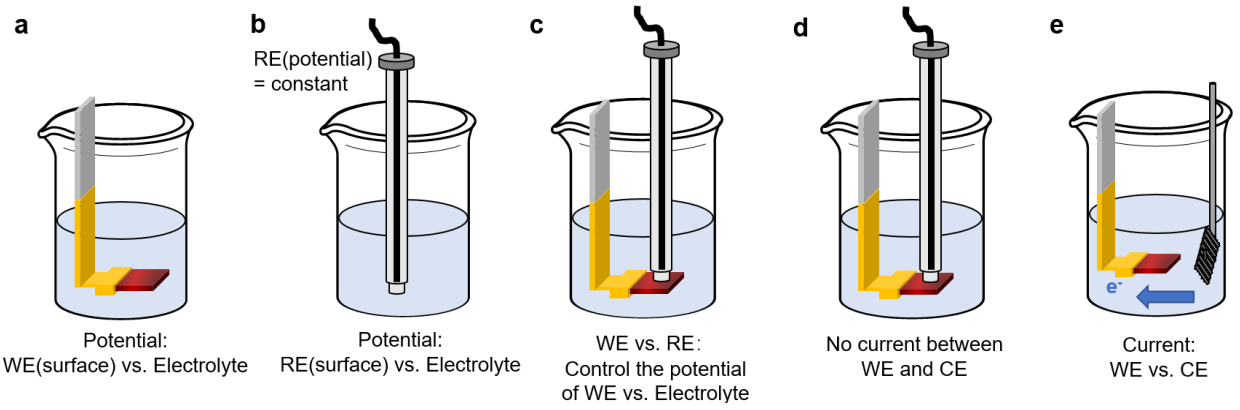

D.2: Schematic of potential and current flow in three electrode system.

D.2 Electrochemical impedance spectroscopy

Electrochemical impedance spectroscopy (EIS) is a technique that can detect the ion transfer during electrochemical process including Nyquist plot and Bode plot.

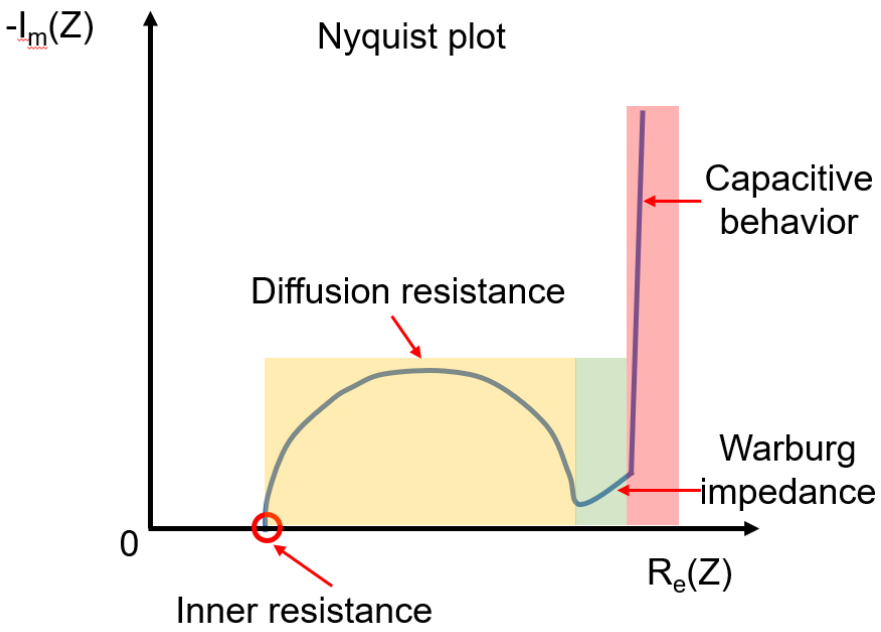

D.3: Schematic of Nyquist plot.

Potential

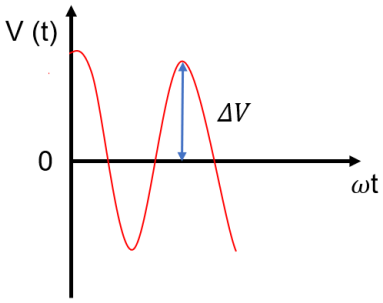

$V(t) = \Delta V cos(\omega t)$

Current

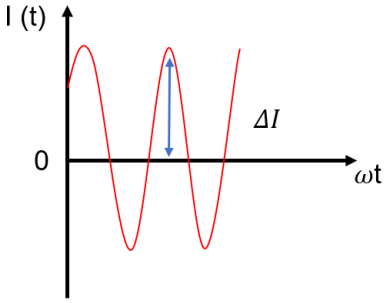

$I(t) = \Delta I cos(\omega t + \varphi)$

Ohm's Law

$$R(t) = \frac{V(t)}{I(t)} = \frac{\Delta V cos(\omega t)}{\Delta I cos(\omega t + \varphi)}$$

Ohm's Law:

$$R(t) = \frac{V(t)}{I(t)} = \frac{\Delta V cos(\omega t)}{\Delta I cos(\omega t + \varphi)}$$

Euler's Formula: $e^{i\theta} = \cos\theta + i \sin\theta$

- $i = (-1)^{0.5}$ - imaginary number

$$Z(t) = \frac{\widetilde{V(t)}}{\widetilde{I(t)}} = \frac{\Delta V e^{i\omega t}}{\Delta I e^{i(\omega t+\varphi)}} = \frac{V(t)}{I(t)} e^{-i\varphi}$$

Impedance (real part + imaginary part)

$$Y = \frac{1}{Z} = \frac{I(t)}{V(t)} e^{i\varphi}$$

Conductance

EX 1. A pure resistor (R)

$I = V/R$

$$\widetilde{V(t)} = \Delta V e^{i\omega t} \qquad \widetilde{I(t)} = \frac{\widetilde{V(t)}}{R} = \frac{\Delta V}{R} e^{i\omega t}$$

$$Z(R) = \frac{\widetilde{V(t)}}{\widetilde{I(t)}} = R$$

EX 2. A pure capacitor (C)

$$Q = CV \qquad \frac{dQ}{dt} = I = C\frac{dV}{dt}$$

$$\widetilde{V(t)} = \Delta V e^{i\omega t} \qquad \widetilde{I(t)} = \frac{\widetilde{dV(t)}}{dt} C = C\, i\omega\, \Delta V e^{i\omega t}$$

$$Z(C) = \frac{\widetilde{V(t)}}{\widetilde{I(t)}} = \frac{1}{i\omega C} = 0 - \frac{i}{\omega C}$$

real imaginary

D.4: Mathematic model of EIS.

EX 3. A series circuit

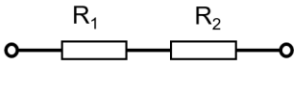

$R_{total} = R_1 + R_2$

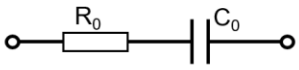

$Z_R = R_0 \qquad Z_C = \frac{1}{i\omega C_0}$

$Z = R_0 + \frac{1}{i\omega C_0} = R_0 - \frac{i}{\omega C_0}$

Nyquist plot for RC circuit

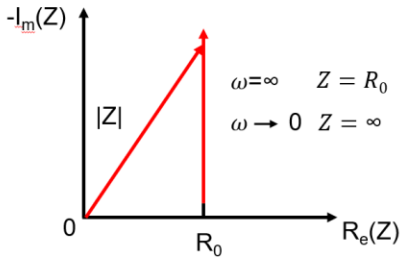

Bode plot for RC circuit

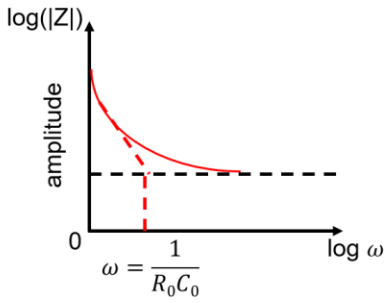

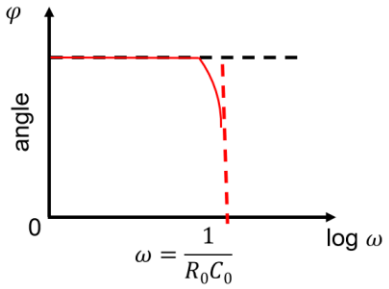

D.5: Mathematic model of a series RC circuit.

EX 4. a parallel RC circuit

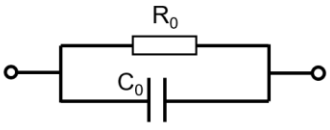

$\frac{1}{Z} = \frac{1}{Z_R} + \frac{1}{Z_C}$

$Z = \frac{Z_R Z_C}{Z_R + Z_C} = \frac{R_0/i\omega C_0}{R_0 + i\omega C_0} = \frac{R_0}{1 + i\omega R_0 C_0}$

Nyquist plot

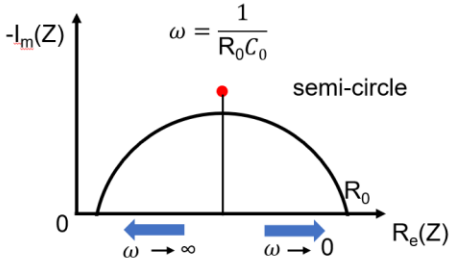

EX 5. ideal metal electrode

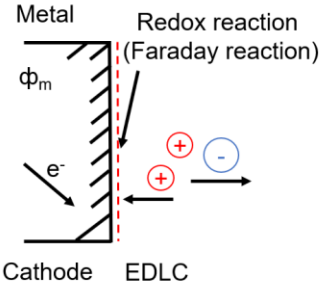

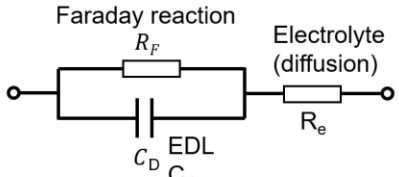

$Z_1 = RF \quad Z_2 = \frac{1}{i\omega CD} \quad Z_3 = Re$

$Z = \frac{Z_1 Z_2}{Z_1 + Z_2} + Z_3 = \frac{R_F}{1 + i\omega C_D R_F} + R_e$

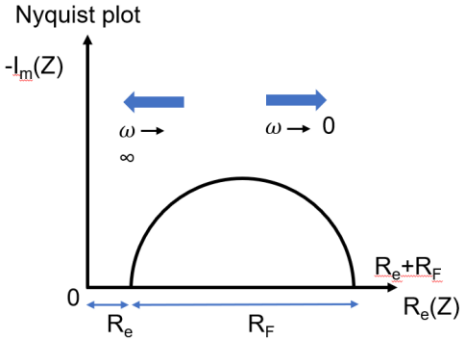

D.6: Mathematic model of a parallel RC circuit.

EX 6. ideal blocking electrode (no Faraday reaction)

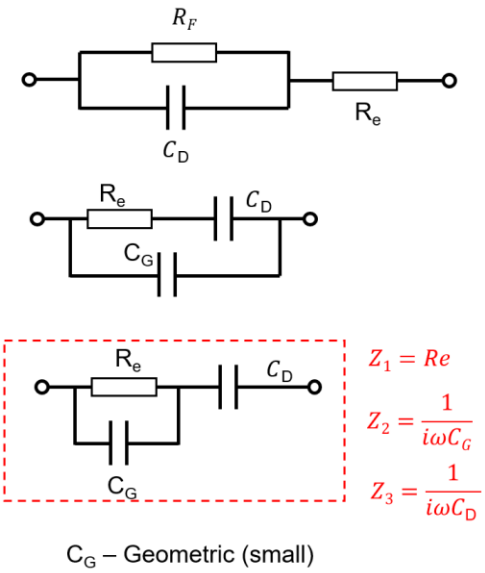

$$Z = \frac{Z_1 Z_2}{Z_1 + Z_2} + Z_3 = \frac{R_e}{1 + i\omega R_e C_G} + \frac{1}{i\omega C_D}$$

$$\tilde{Z} = Z/R_e = \frac{1}{1 + i\omega R_e C_G} + \frac{1}{i\omega R_e C_D} \qquad C_G << C_D$$

1) $\omega R_e C_D << 1$ $\tilde{Z} = \infty$

2) $\omega R_e C_G >> 1$ $\tilde{Z} = 0$

3) $\omega R_e C_G << 1 << \omega R_e C_D$ $\tilde{Z} = \frac{1}{1 + i\omega R_e C_D}$

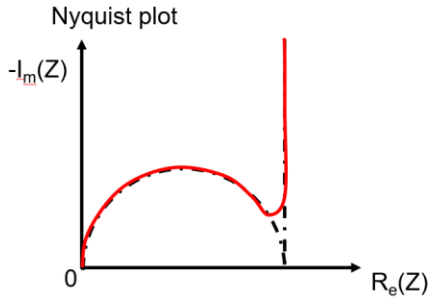

D.7: Mathematic model of an ideal blocking electrode circuit.

EX 7. Pseudo-capacitor (EDLC + additional capacitance from faraday reaction)

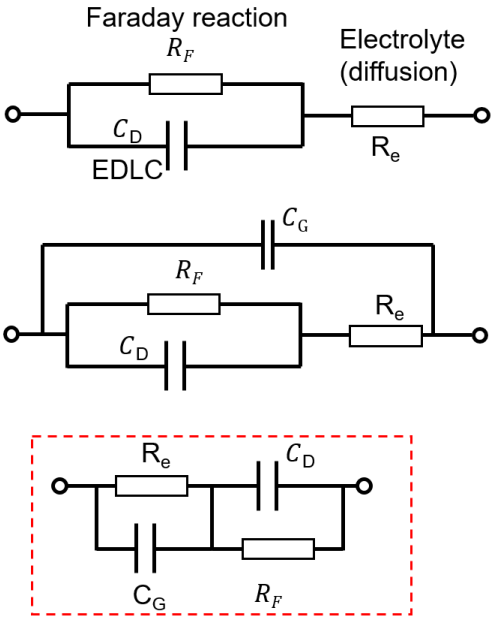

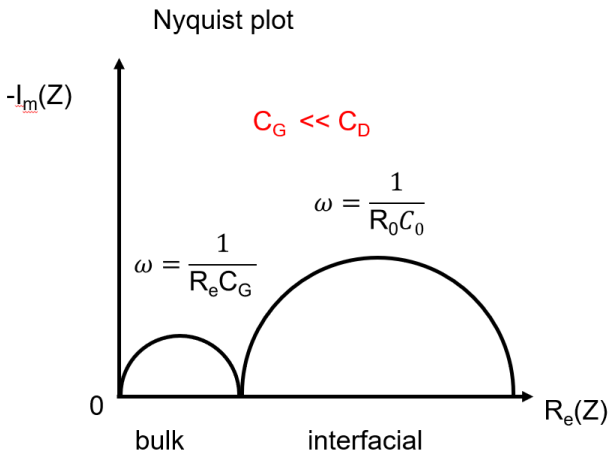

D.8: Mathematic model of a pseudocapactive electrode circuit.

EX 8. Porous electrode

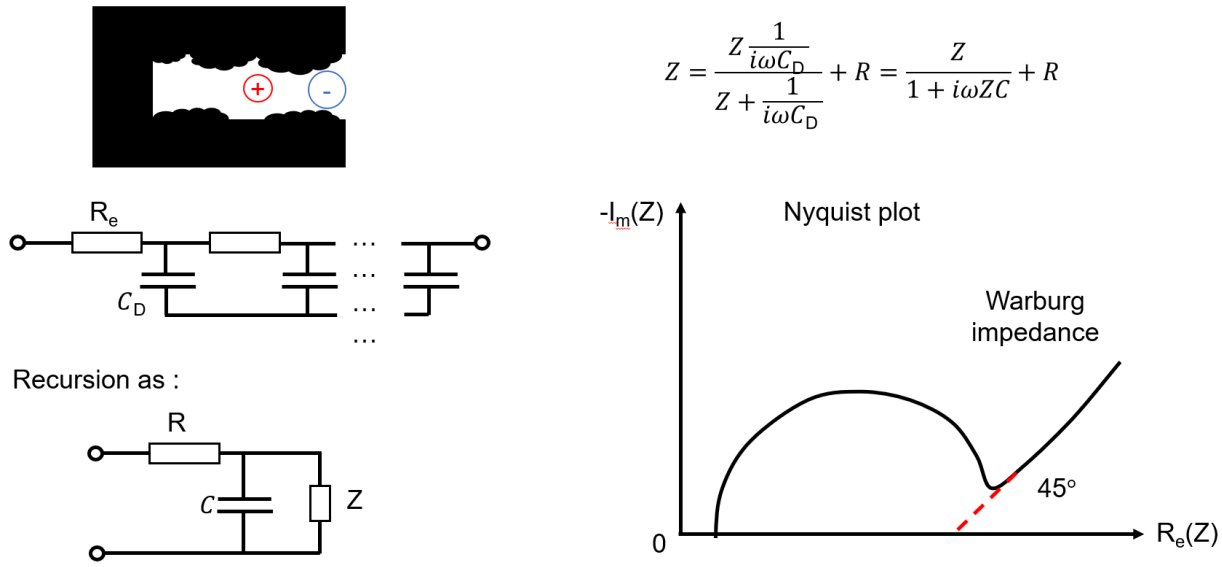

$$Z = \frac{Z\frac{1}{i\omega C_D}}{Z + \frac{1}{i\omega C_D}} + R = \frac{Z}{1 + i\omega ZC} + R$$

D.9: Mathematic model of a porous electrode circuit.

Appendix E Smart masonry material for future sustainable living

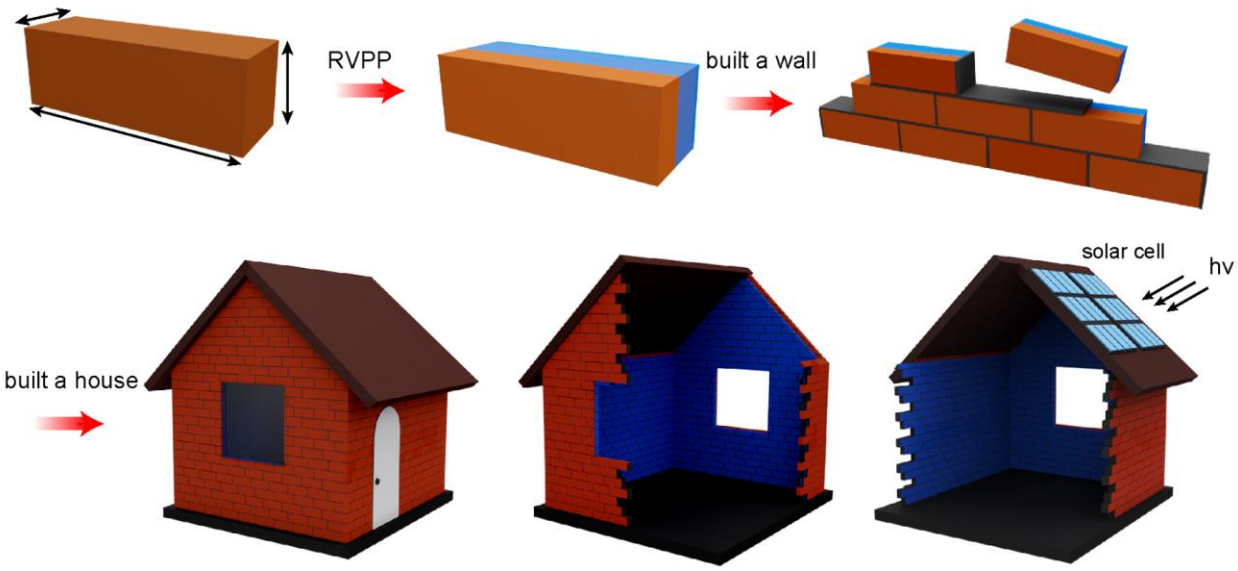

E.1: Schematic illustration of conductive brick for sustainable living.

E.2: Schematic illustration of conductive brick for energy storage application

Appendix F Mechanism of solar cell

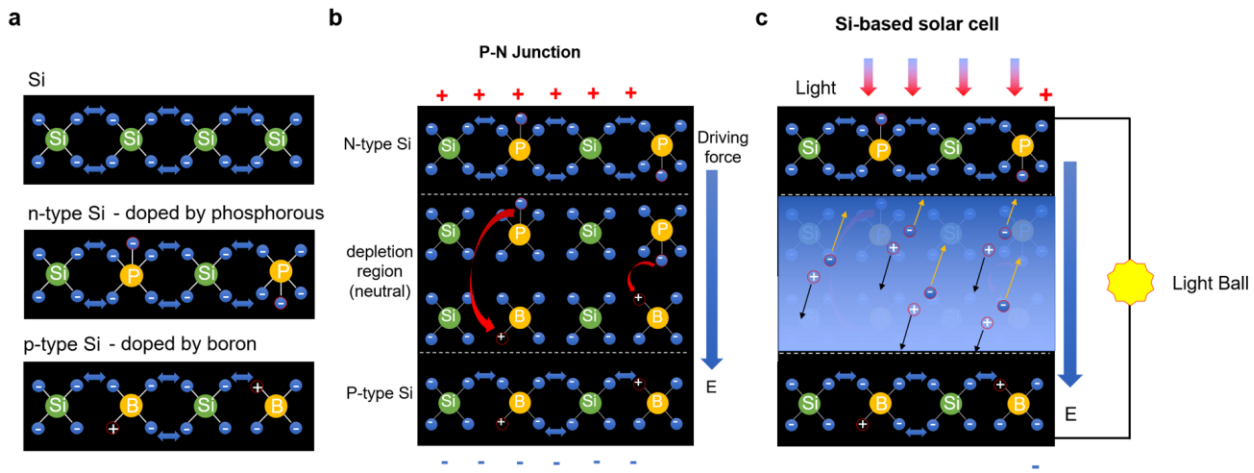

F.1: Schematic illustration of solar cell mechanism.

Appendix G AutoCAD of microsupercapacitor patterns

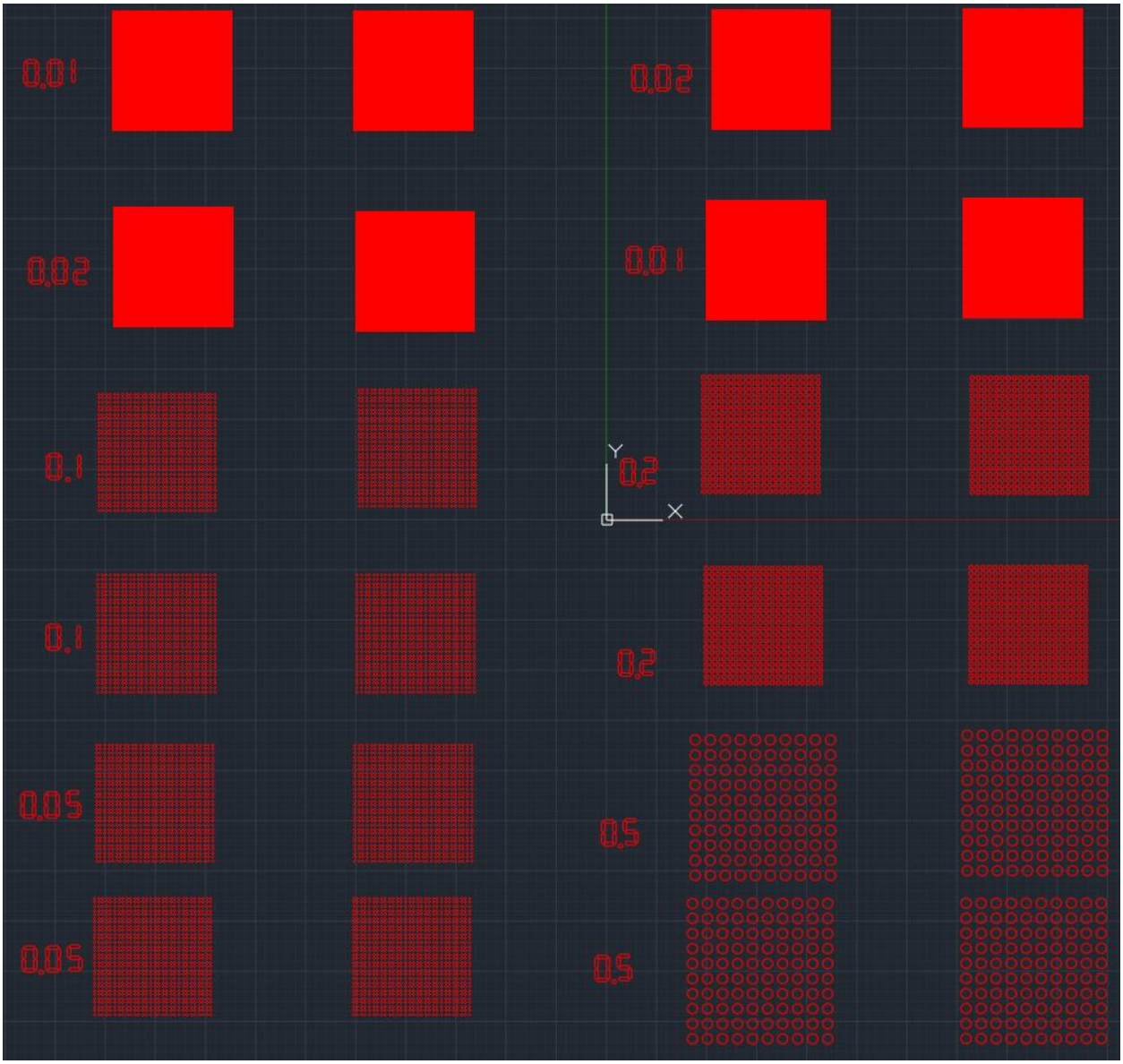

G.1: AutoCAD of dots array electrode.

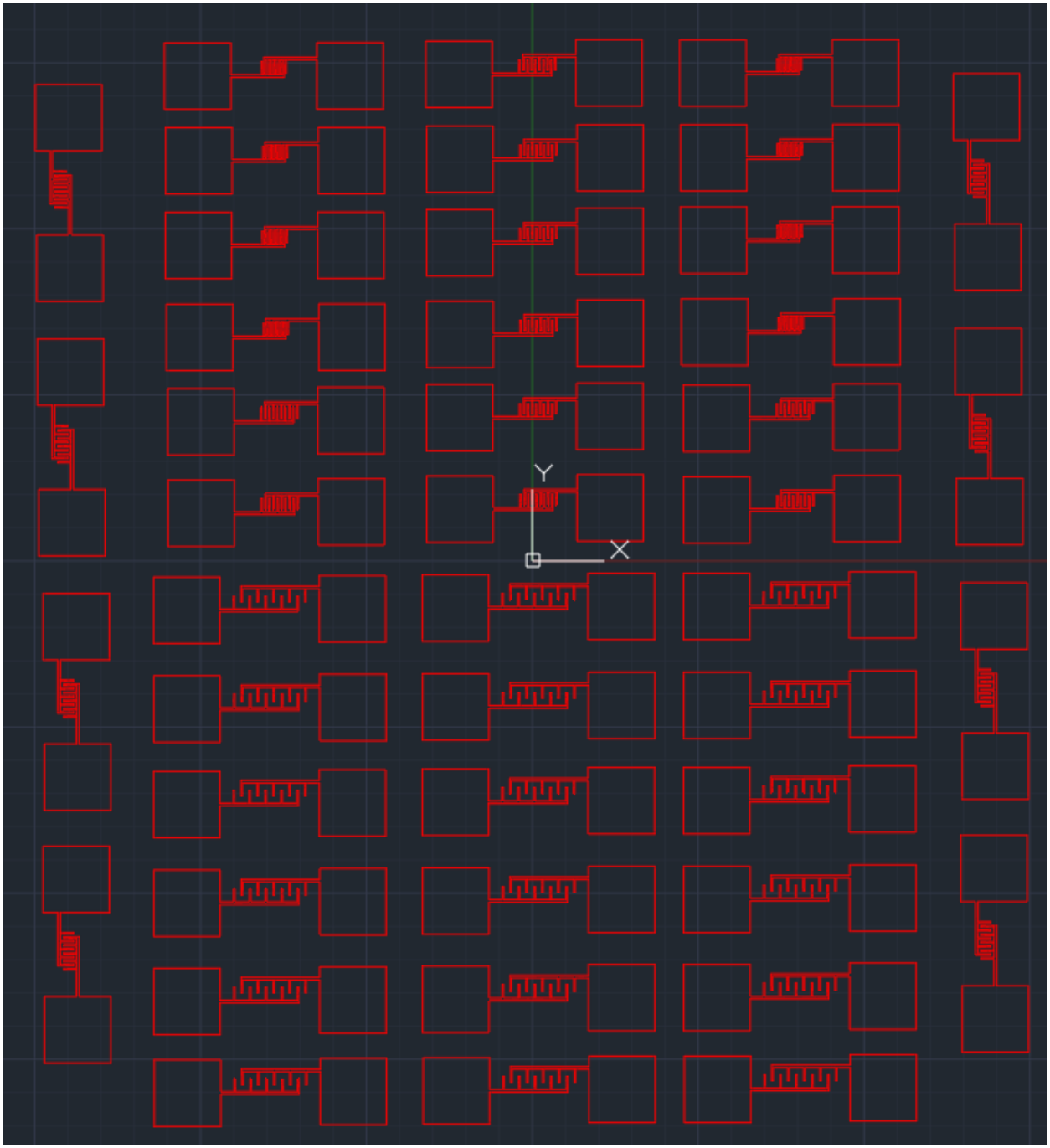

G.2: AutoCAD of small-interdigitated electrode microsupercapacitor.

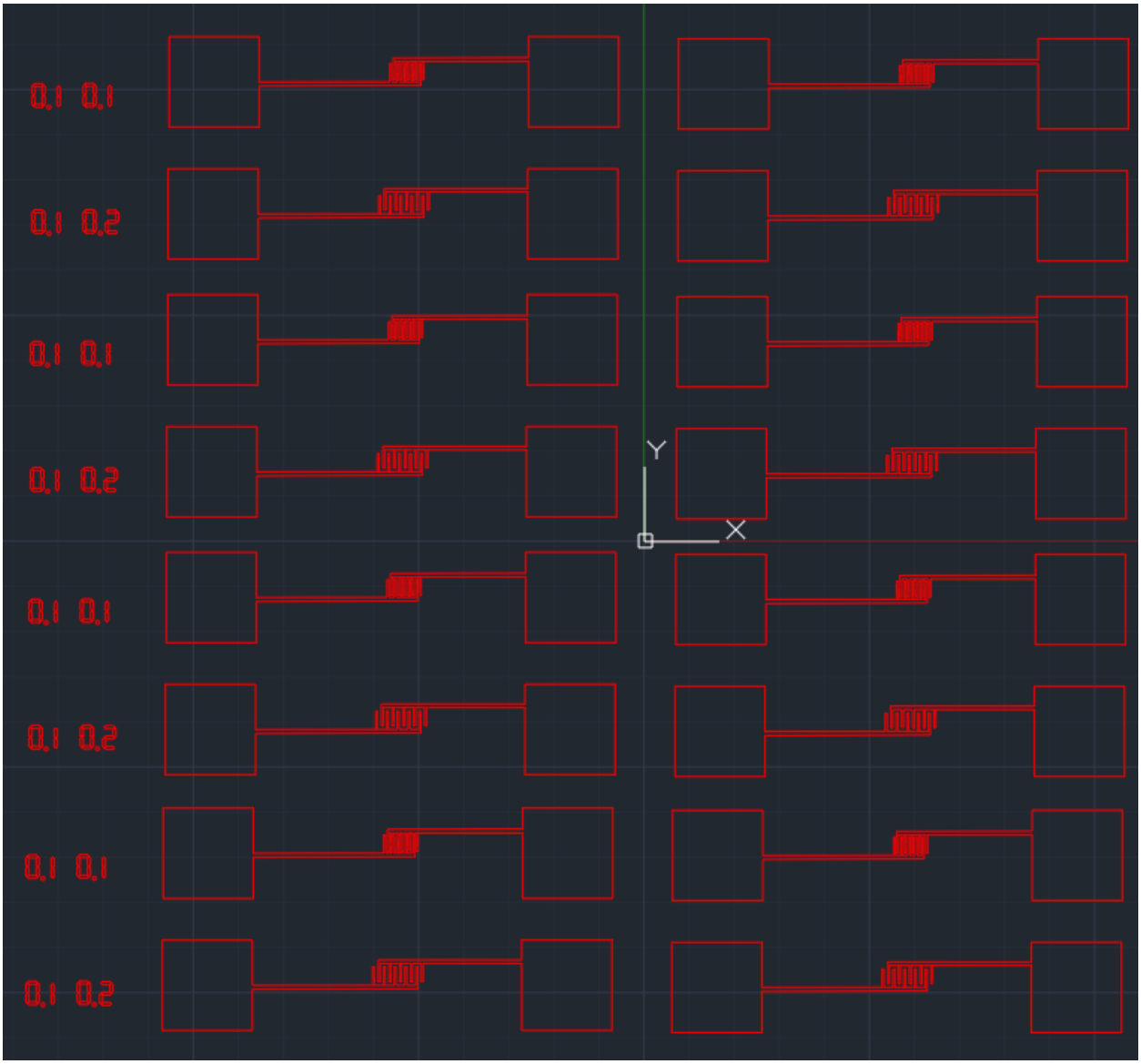

G.3: AutoCAD of small-interdigitated electrode long current collector microsupercapacitor.

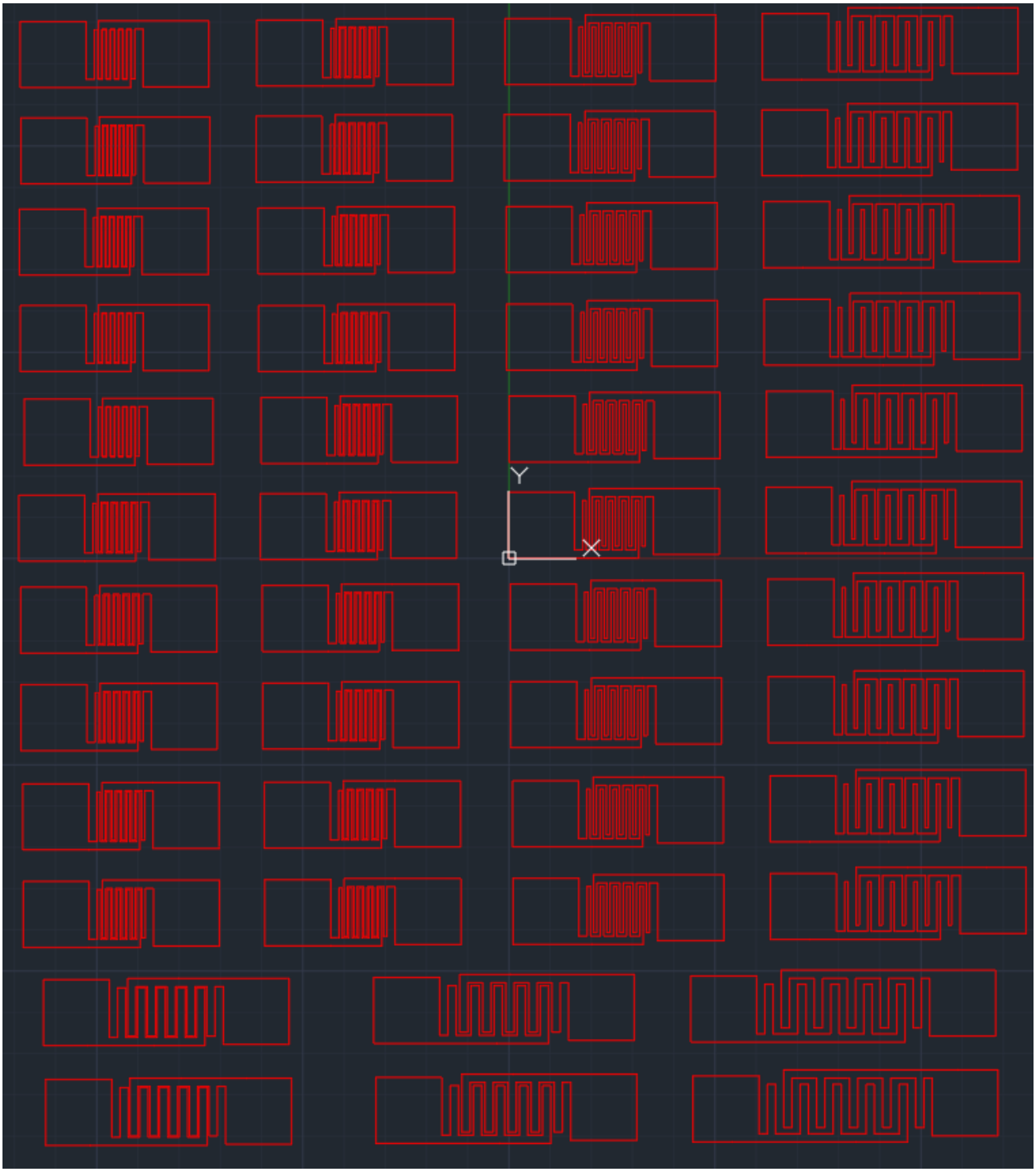

G.4: AutoCAD of large-interdigitated electrode microsupercapacitor.

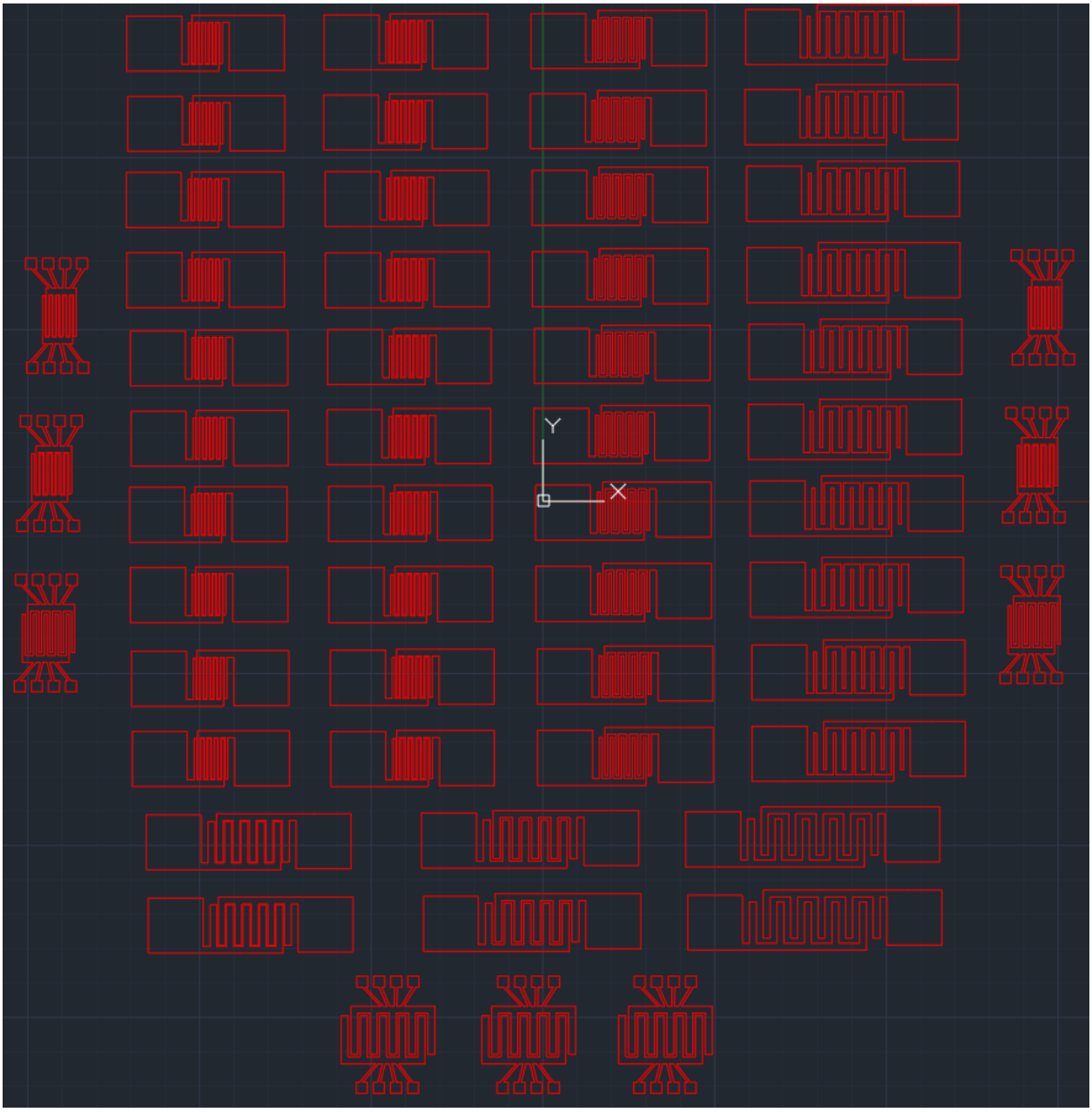

G.5: AutoCAD of large-interdigitated electrode microsupercapacitor and conductivity measurement pattern.

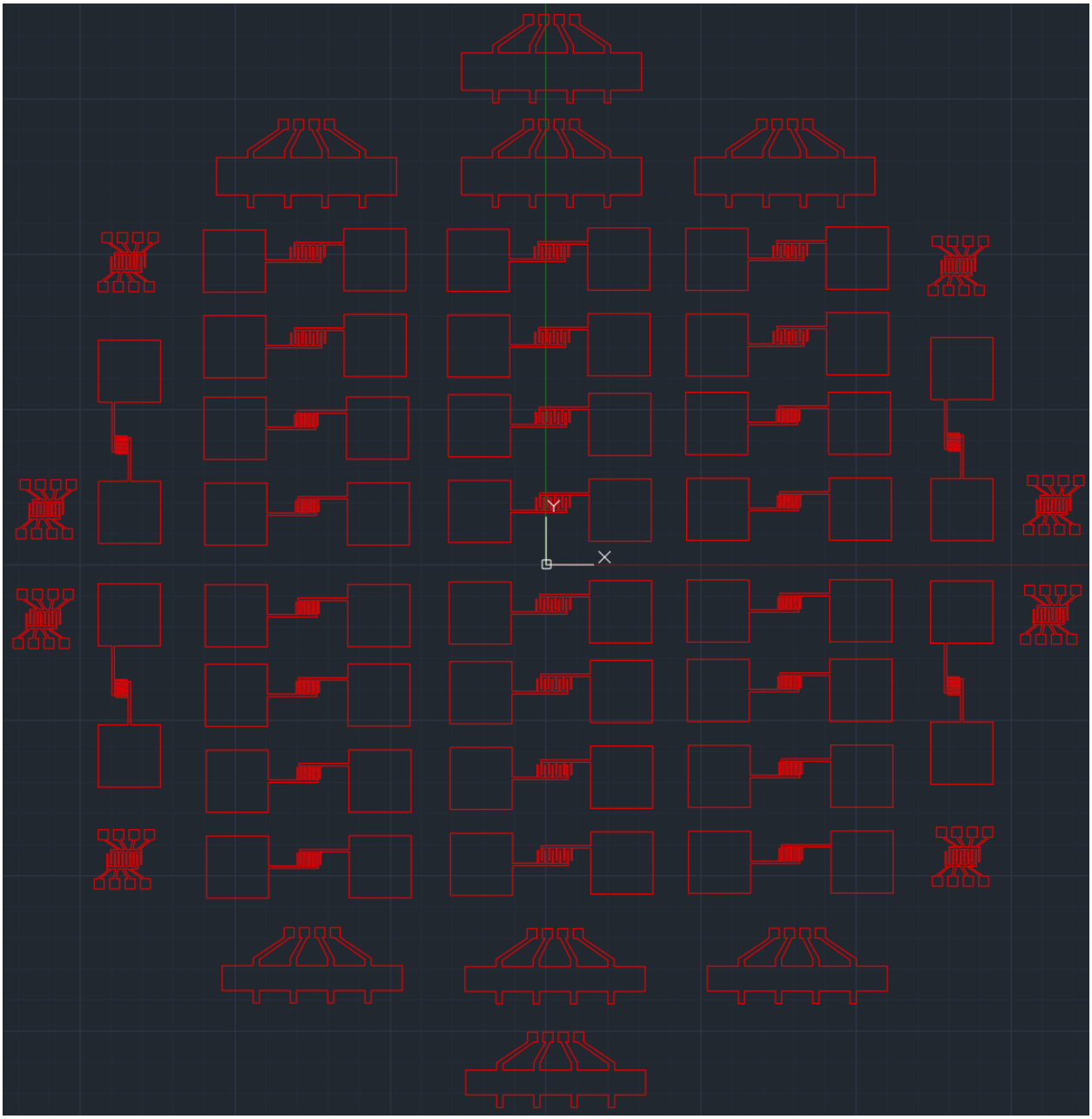

G.6: AutoCAD of small-interdigitated electrode microsupercapacitor and conductivity measurement pattern.

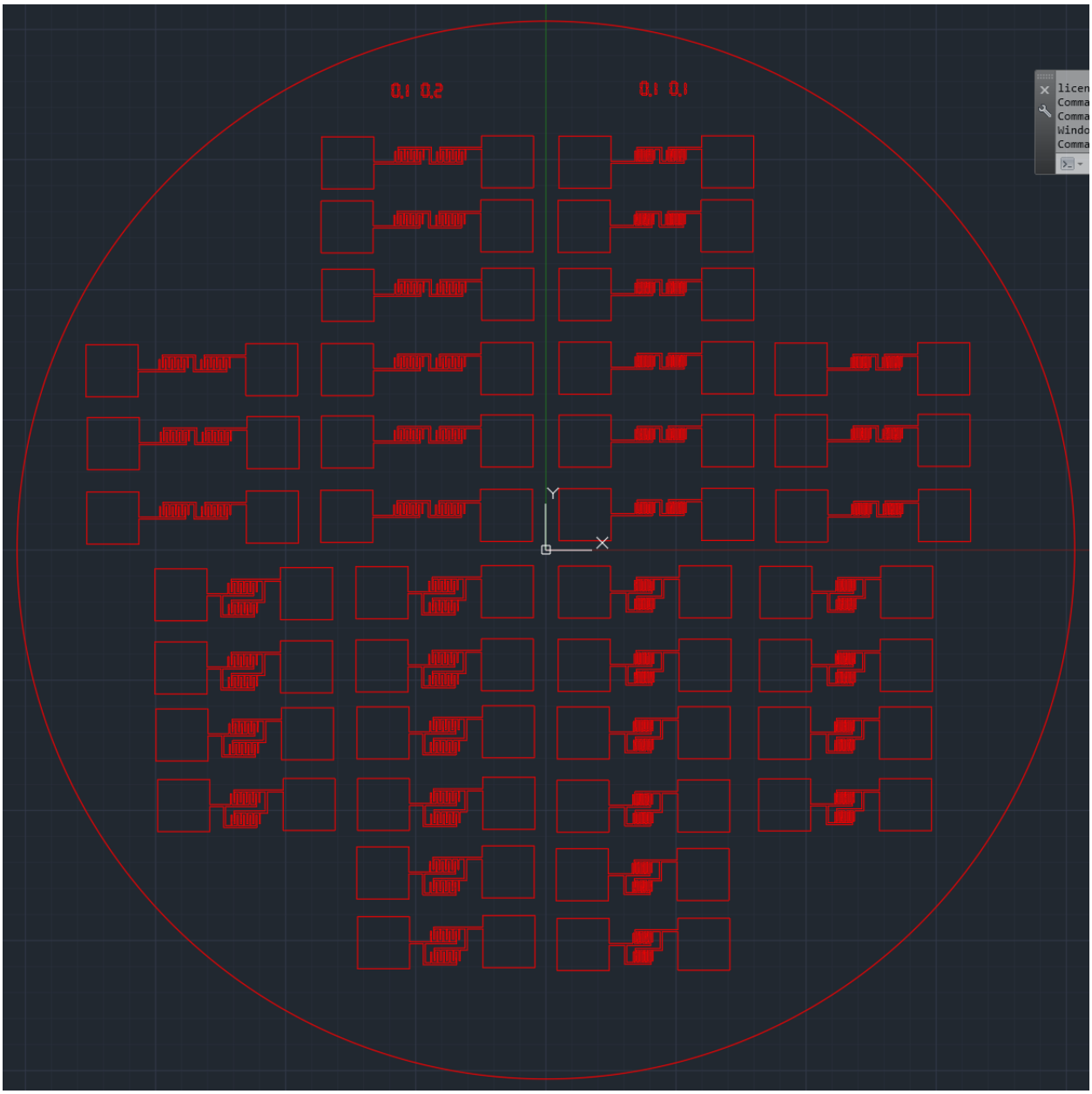

G.7**:** AutoCAD of large-interdigitated electrode microsupercapacitor in series and parallel pattern.

Appendix H Comb-shape Au-Al bi-electrode ZnO UV sensor

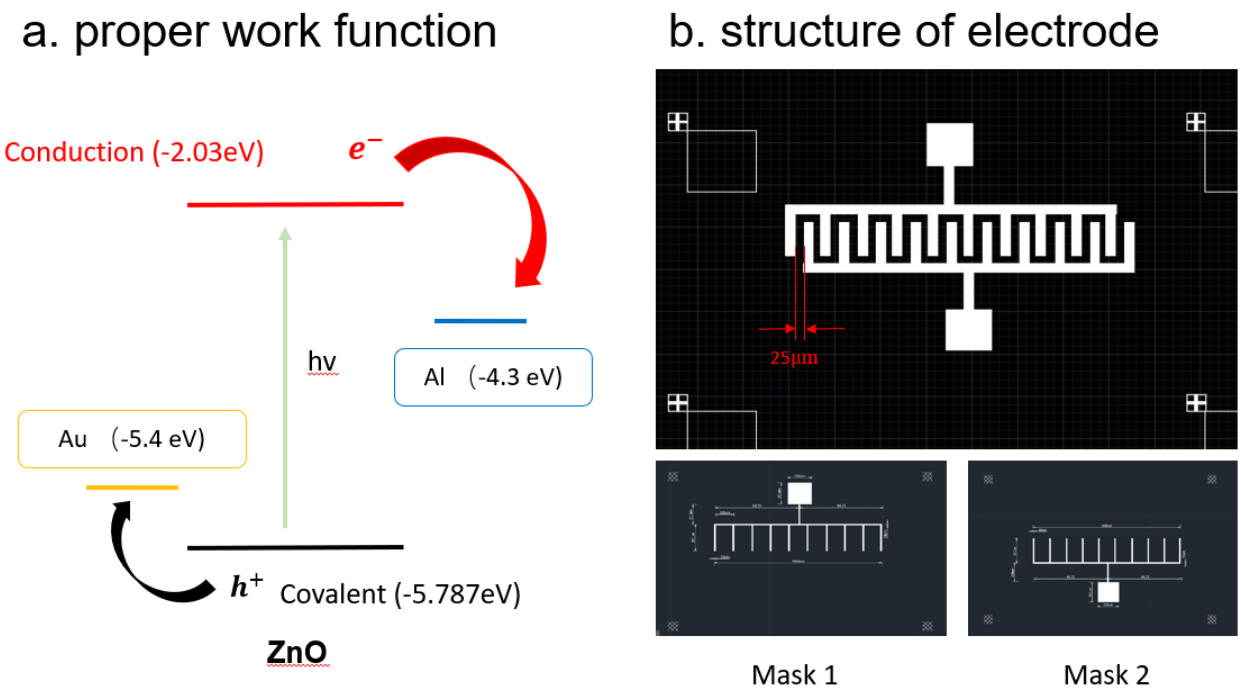

H.1: (a) Band structure of ZnO, Au and Al electrodes. (b) AutoCAD of interdigitated electrode.

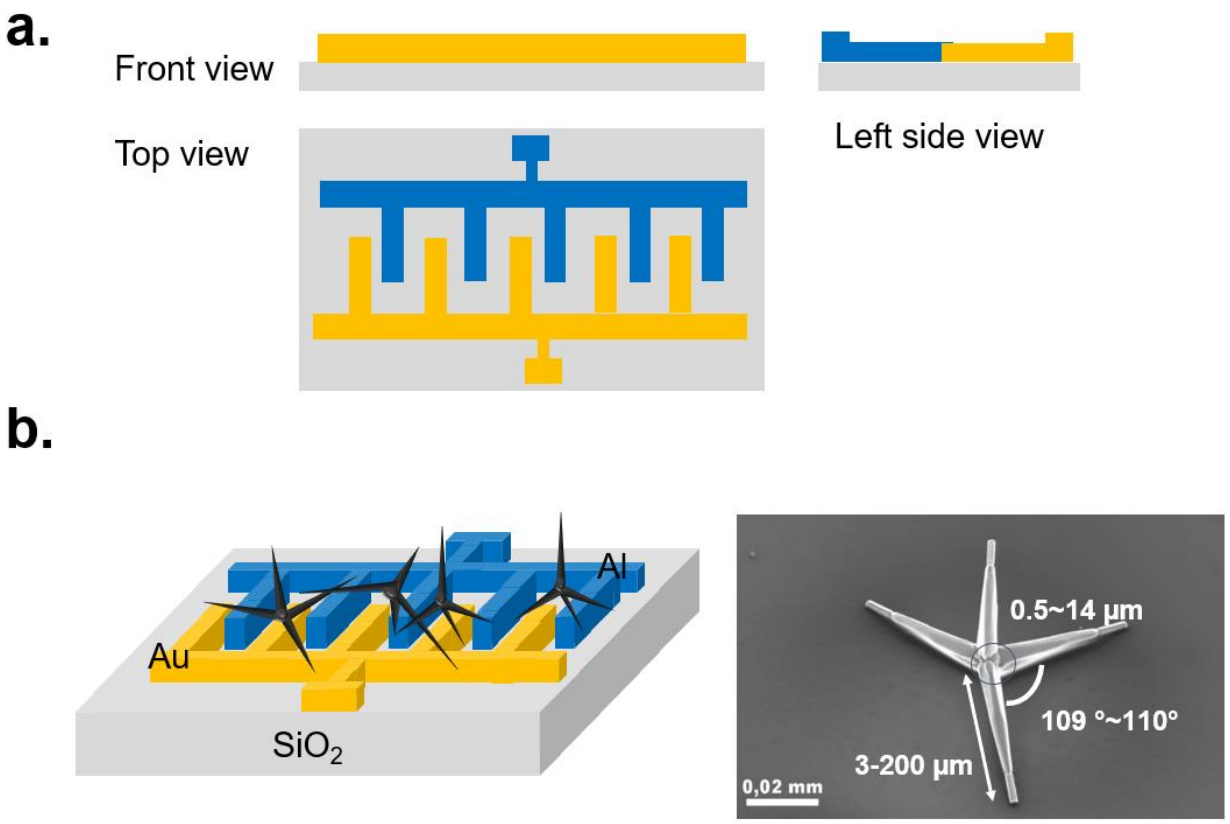

H.2: (a) Three views of UV sensor. (b) Schematic of UV sensor and SEM of ZnO tetrapod.

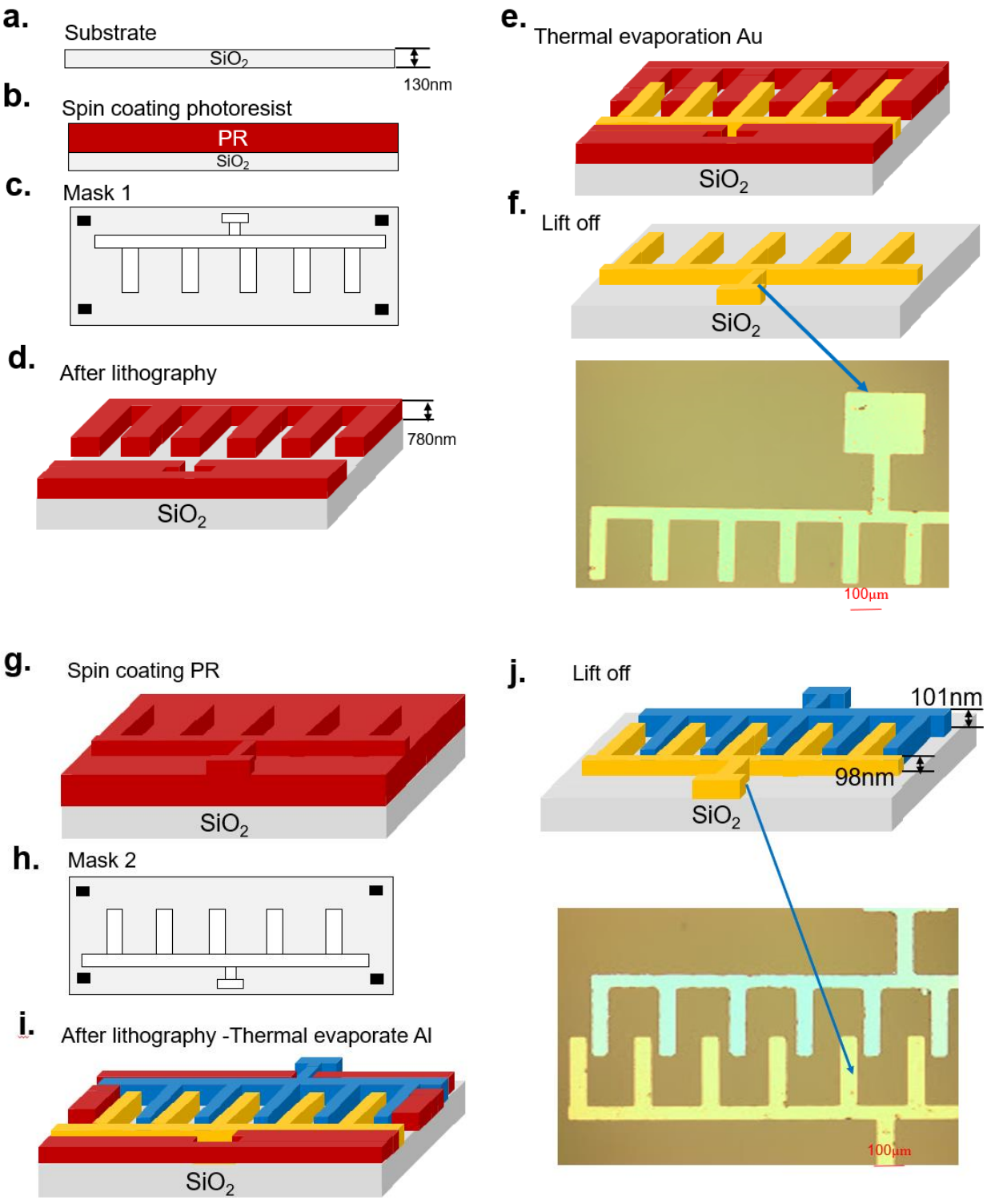
a.
Substrate
SiO2
130nm
b.
Spin coating photoresist
PR
SiO2
c.
Mask 1
d.
After lithography
780nm
SiO2
e.
Thermal evaporation Au
SiO2
f.
Lift off
SiO2
100μm
g.
Spin coating PR
SiO2
h.
Mask 2
i.
After lithography -Thermal evaporate Al
SiO2
j.
Lift off
101nm
98nm
SiO2
100μm

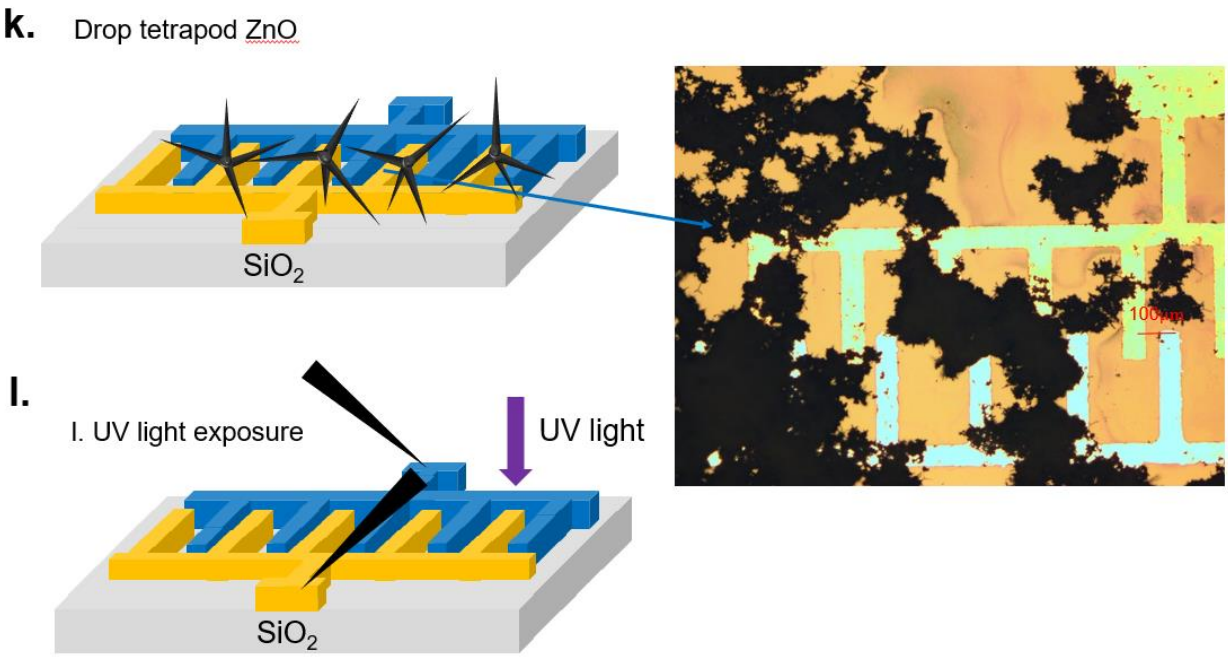

H.3: Flow process diagram of ZnO based UV sensor.

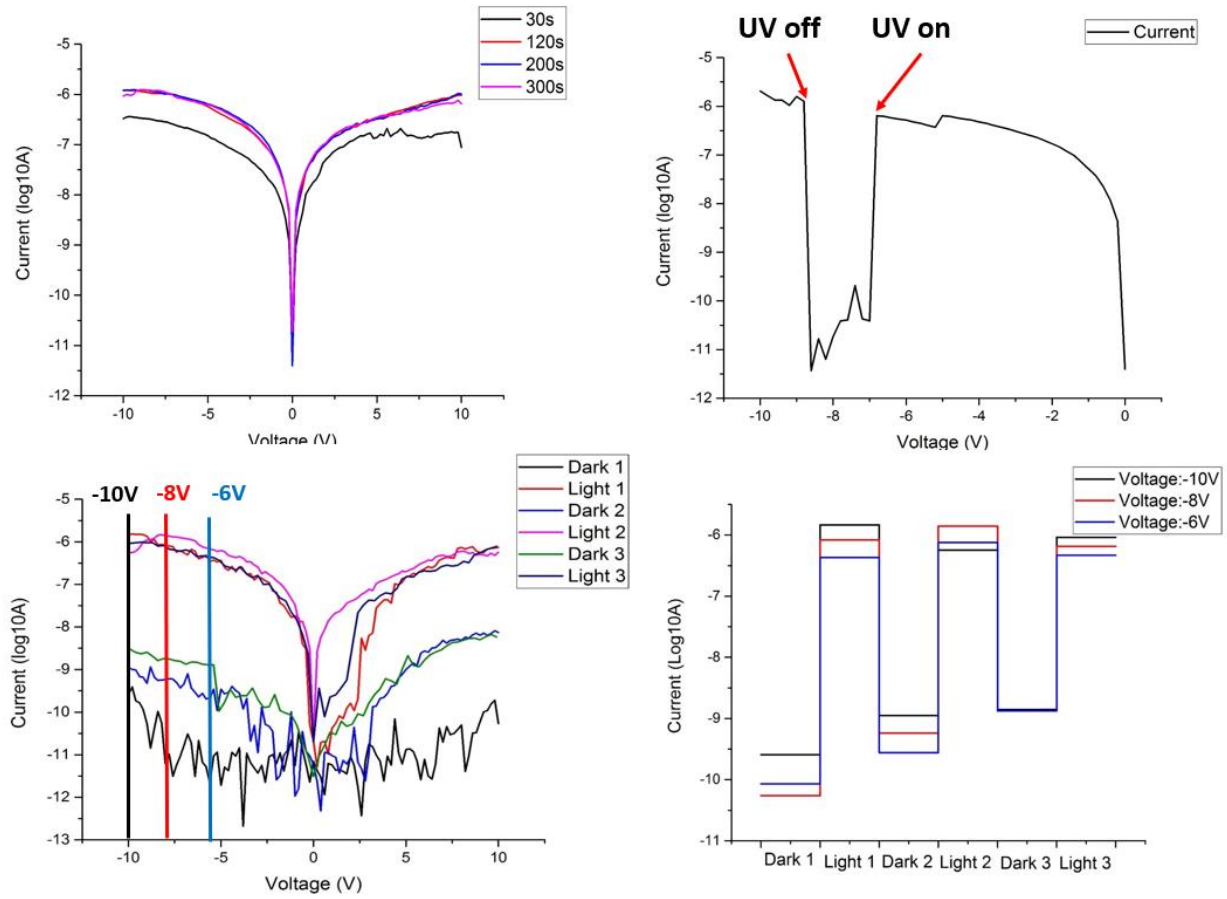

H.4: (a) Conductivity, (b) sensitivity and (c-d) recovery of ZnO based UV sensor.

Appendix I Nice pictures of rust and nanostructured conducting polymers

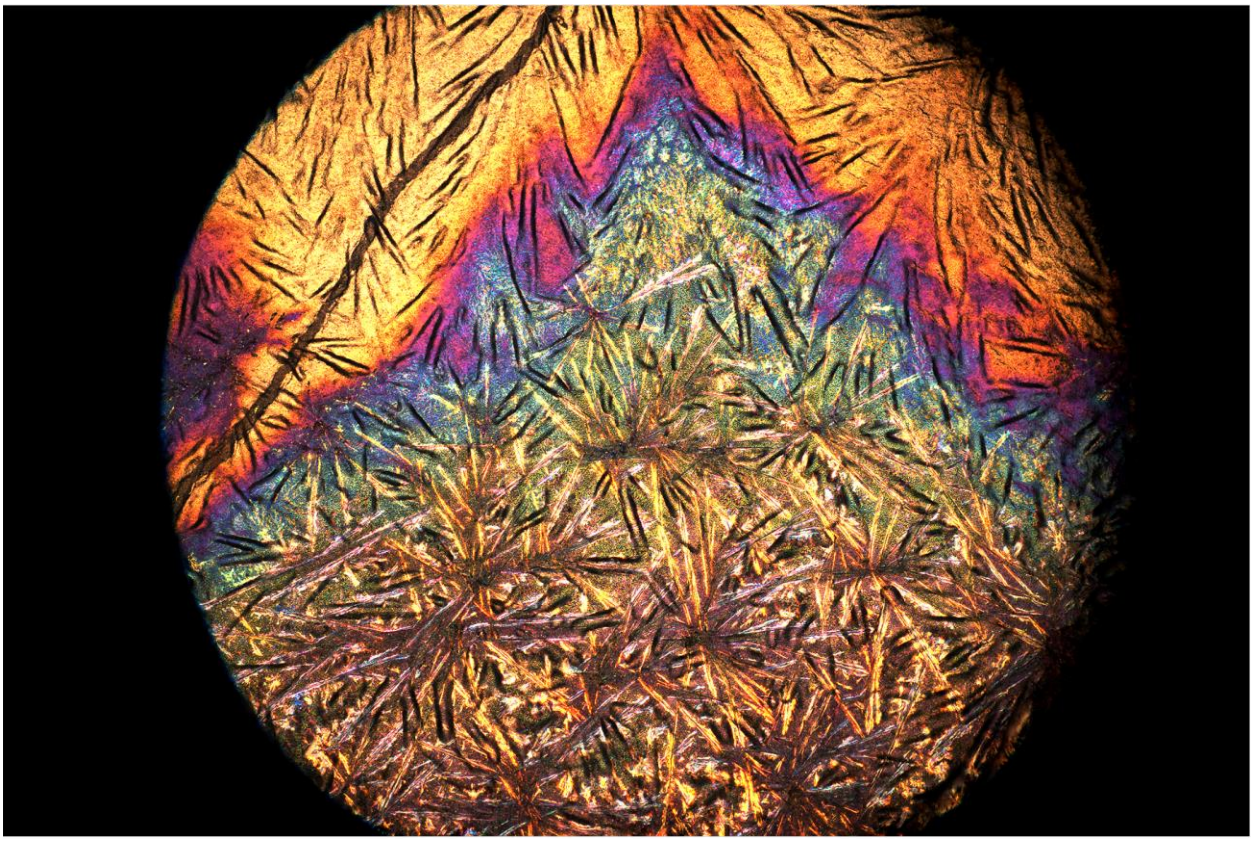

I.1: The Mountain. (Award 1st in 2019 spectra completion)

“The mountain” is composed of iron crystals and conducting polymer, or PEDOT, on a colorful film.

I.2: The Rose. (Award 2nd in 2019 spectra completion)

“The rose” is composed of conducting polymer (PEDOT) with 2D nanosheets and 1D nanofibers.

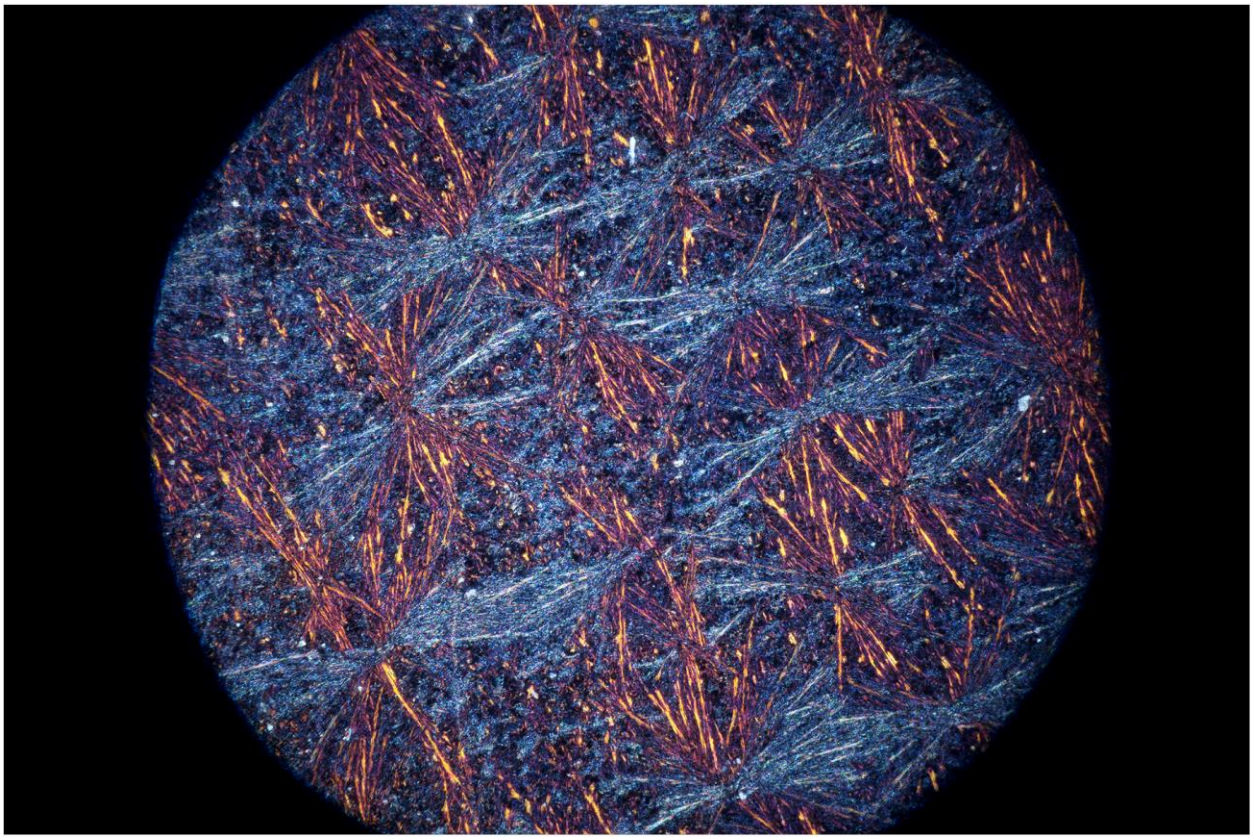

I.3: Symmetric nanofibers consist of PEDOT (blue) and iron (red).

I.4: A ink wash painting made of PEDOT nanostructures.

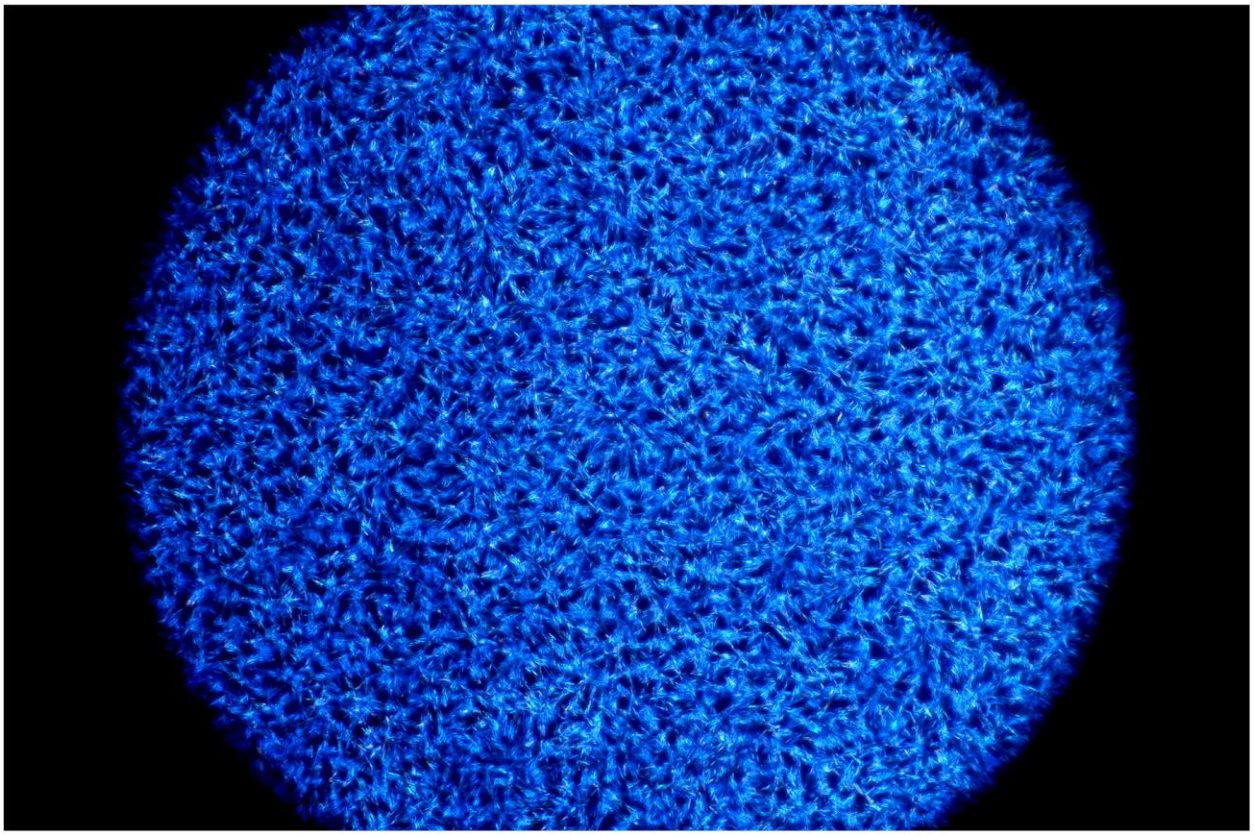

I.5: PEDOT nanofibers.

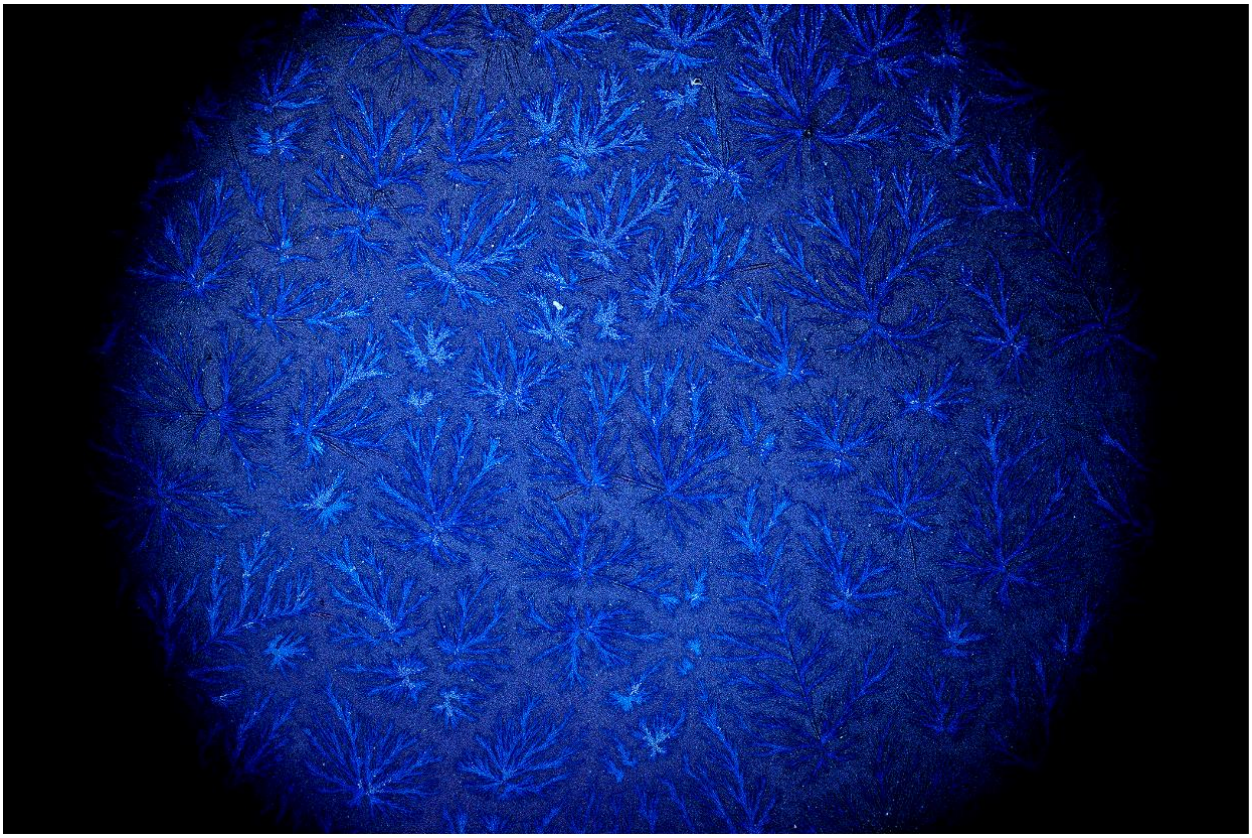

I.6: PEDOT nanofibers (1).

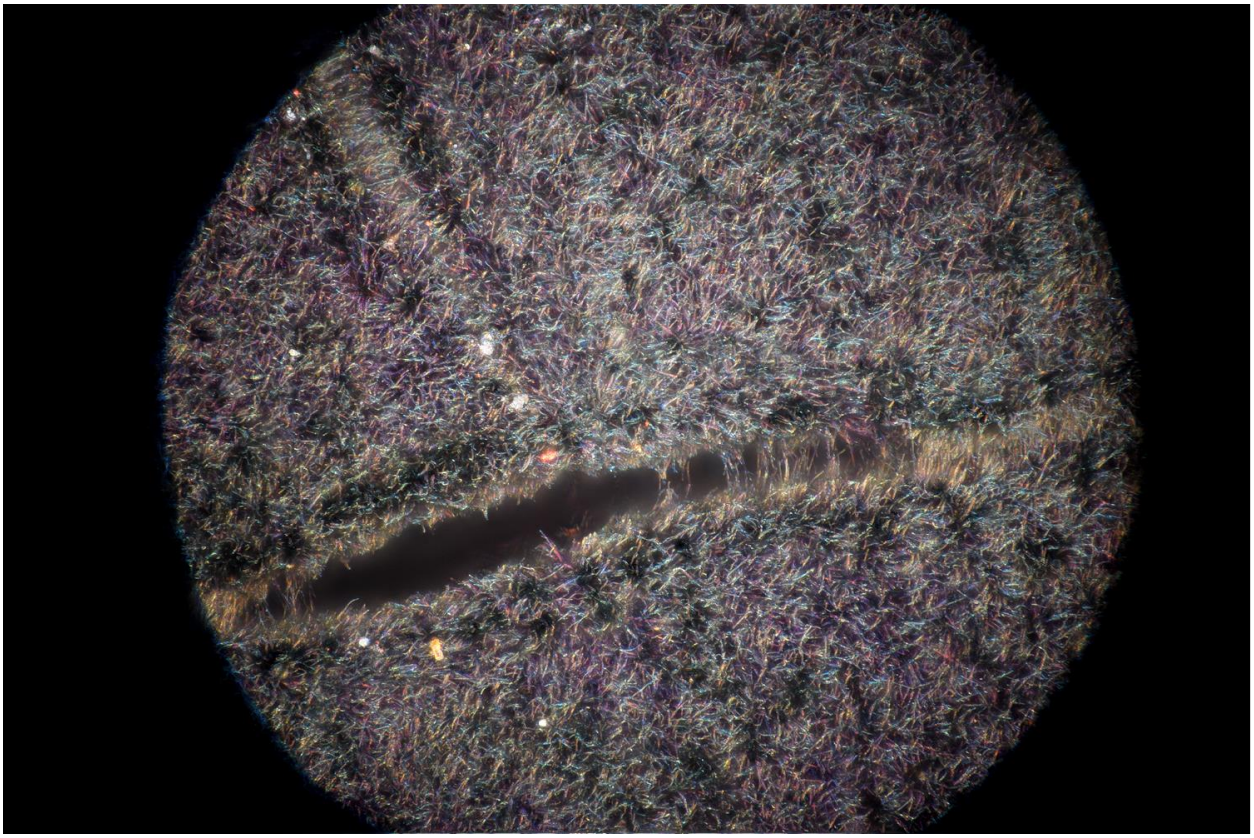

I.7: PEDOT nanofibers (2).

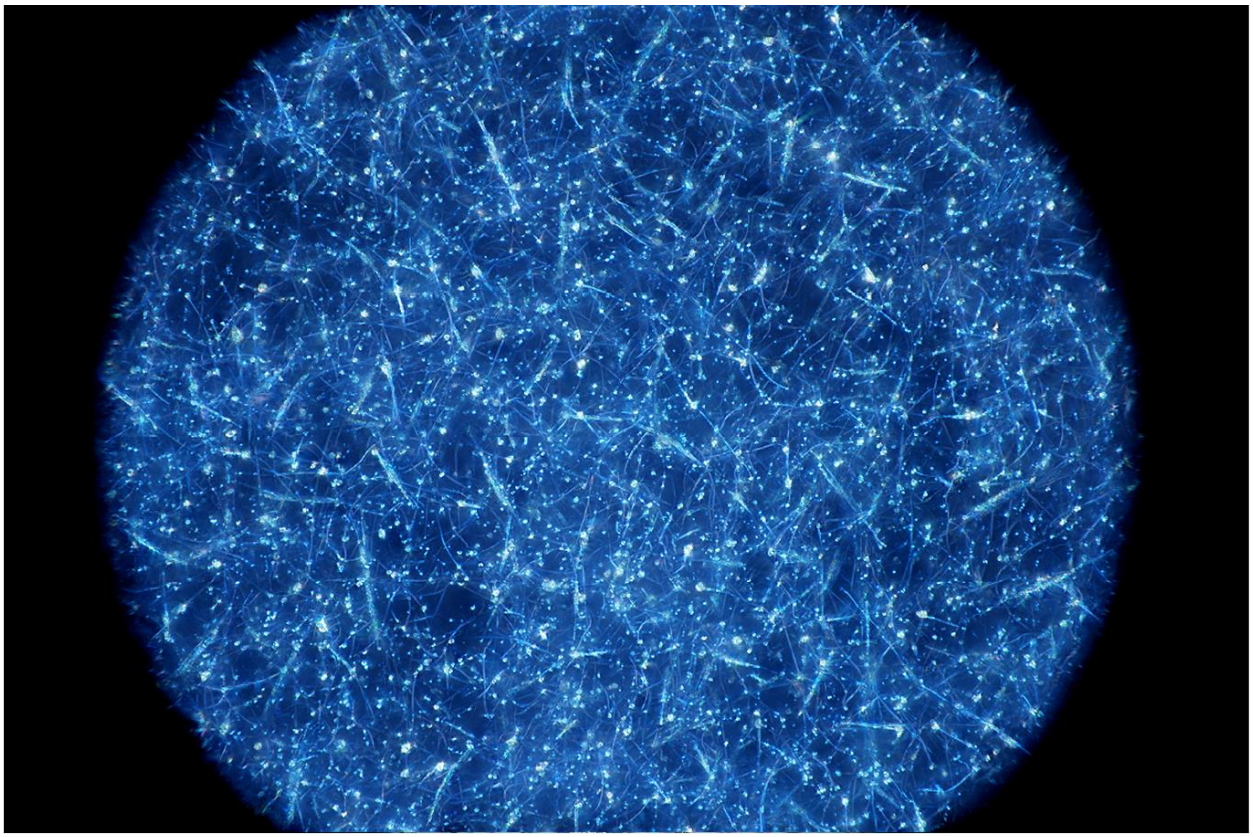

I.8: PEDOT nanofibers (3).

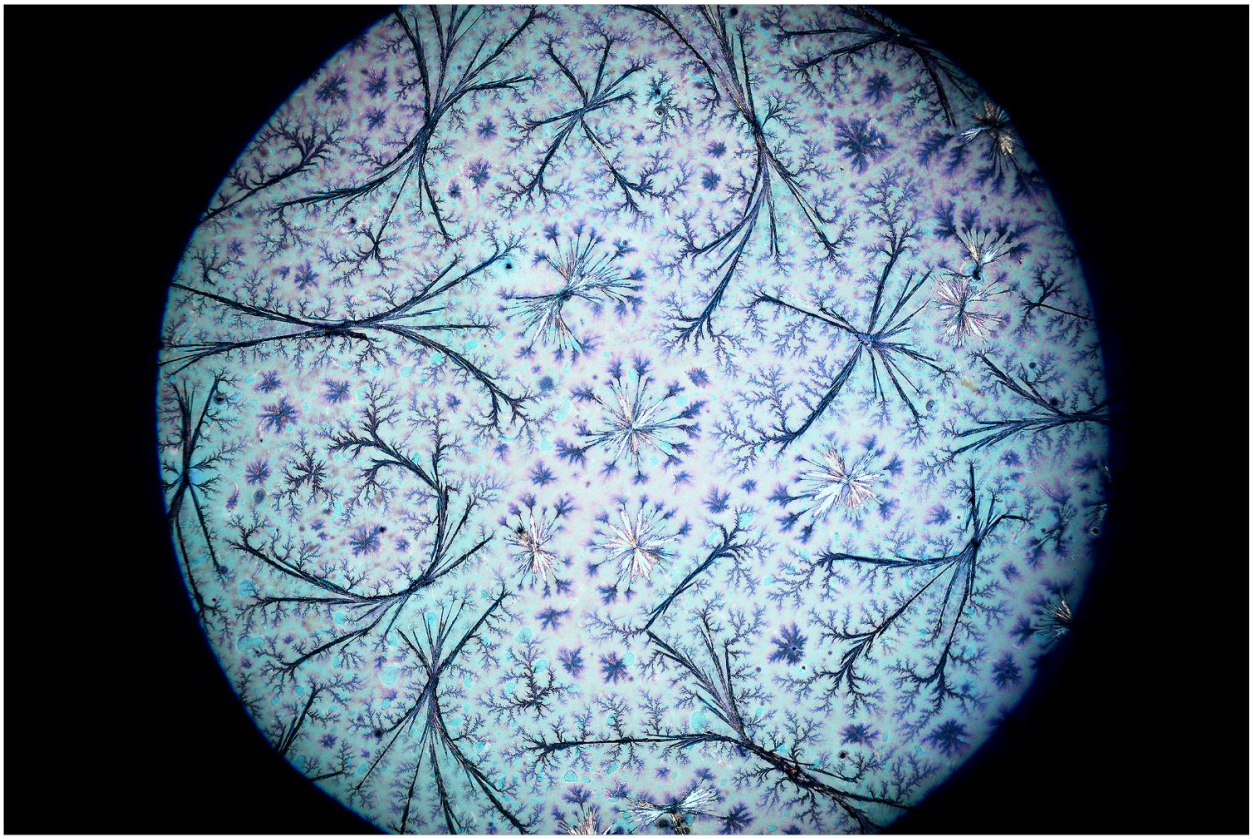

I.9: PEDOT nanofibers (4).

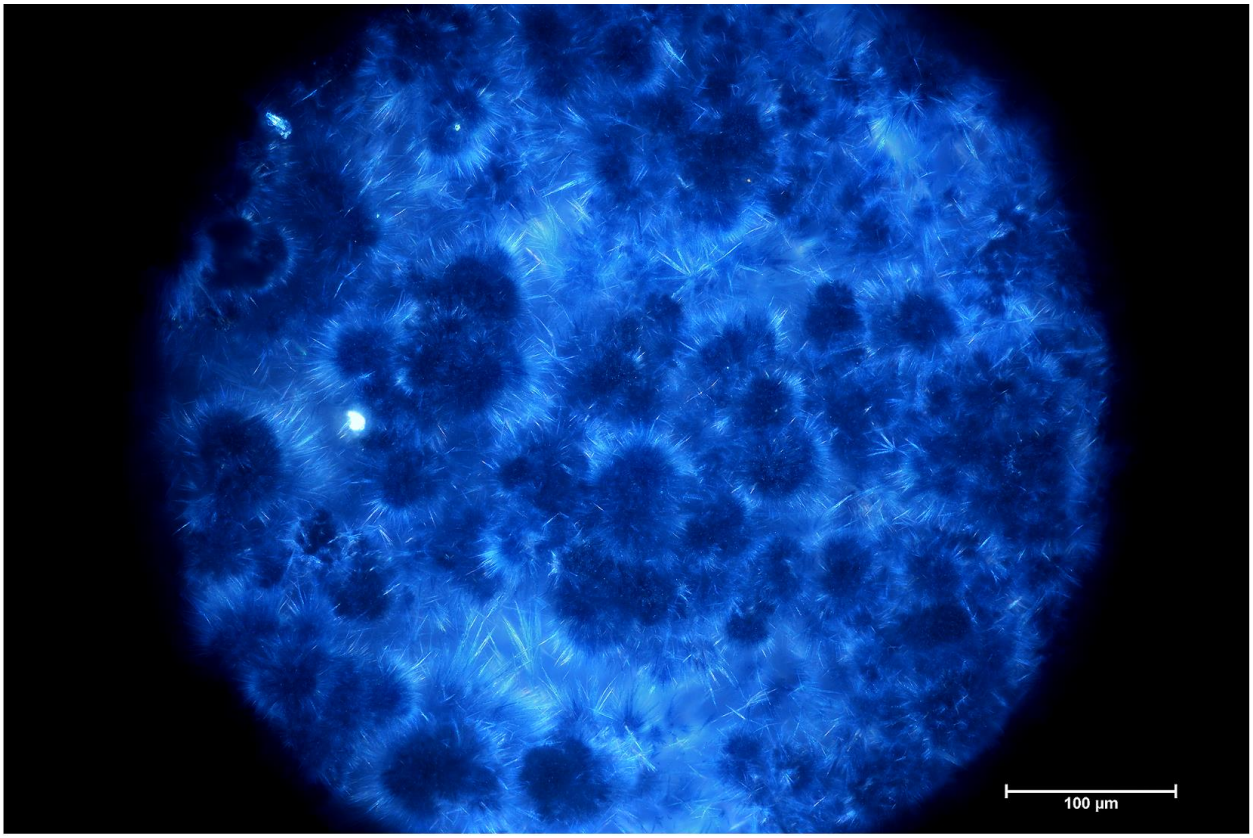

I.10: PEDOT nanofibers (5).

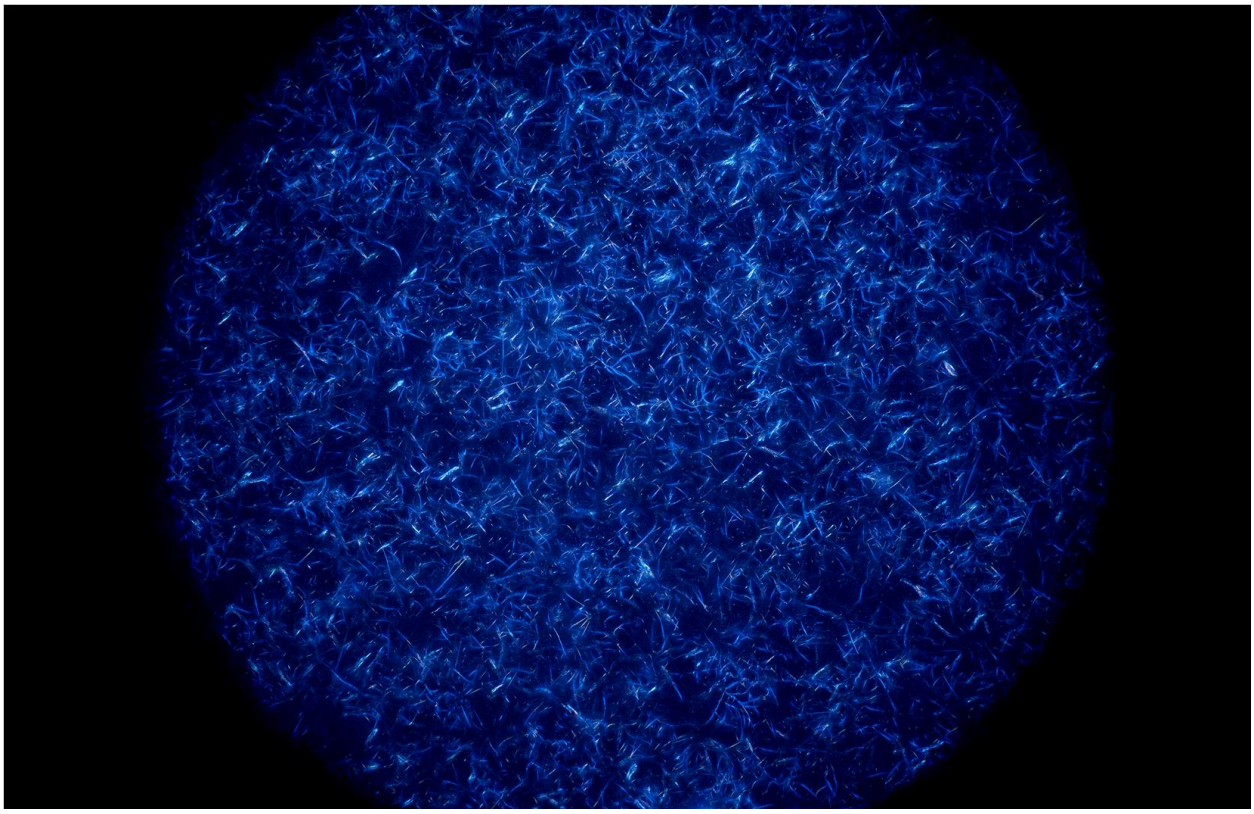

I.11: PEDOT nanofibers (6).

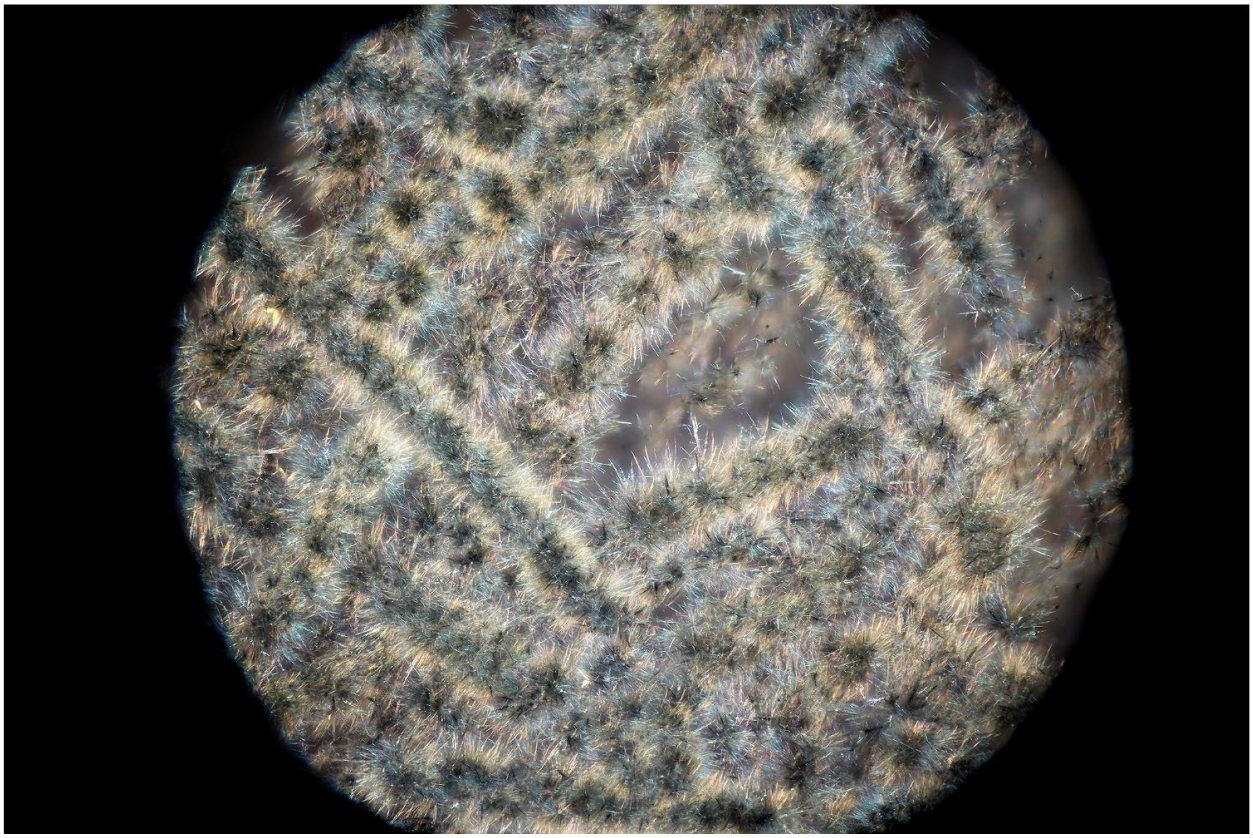

I.12: PEDOT nanofibers on hard carbon paper (1).

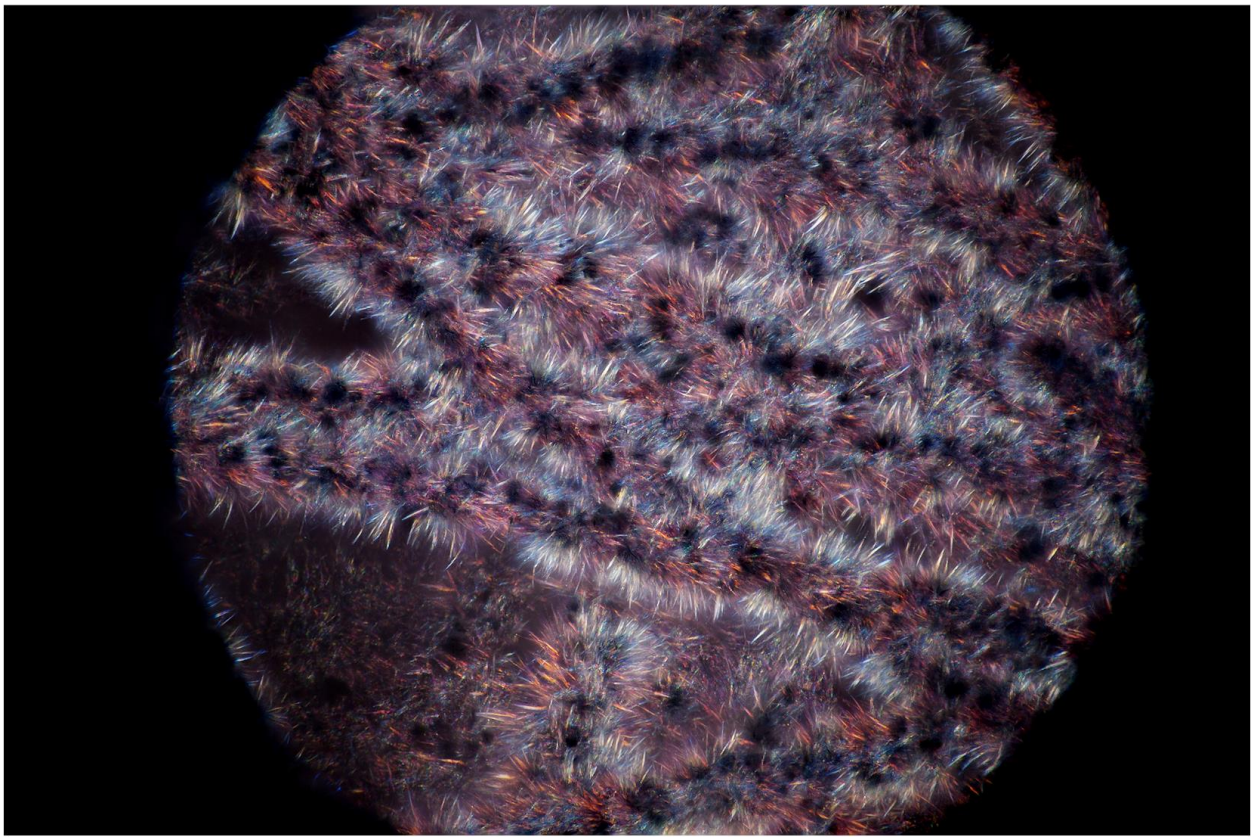

I.13: PEDOT nanofibers on hard carbon paper (2).

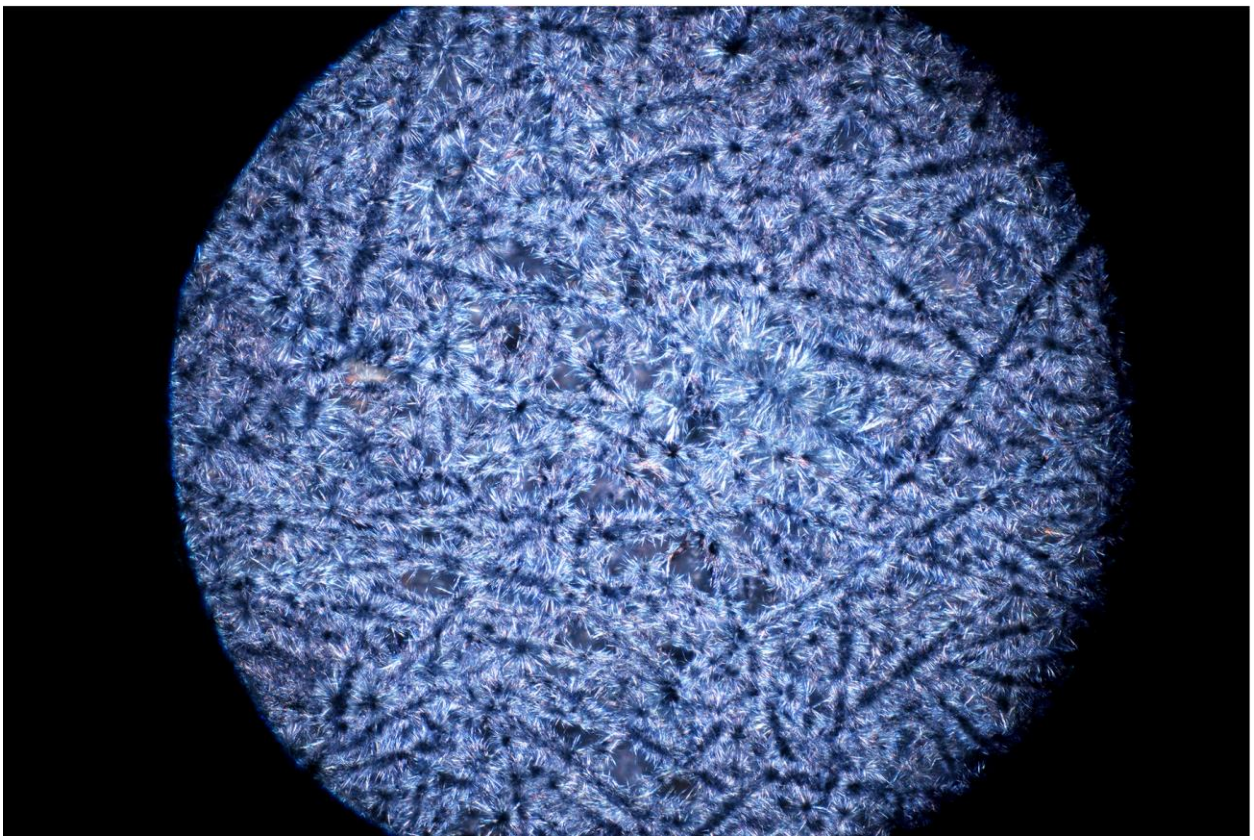

I.14: PEDOT nanofibers on hard carbon paper (3).

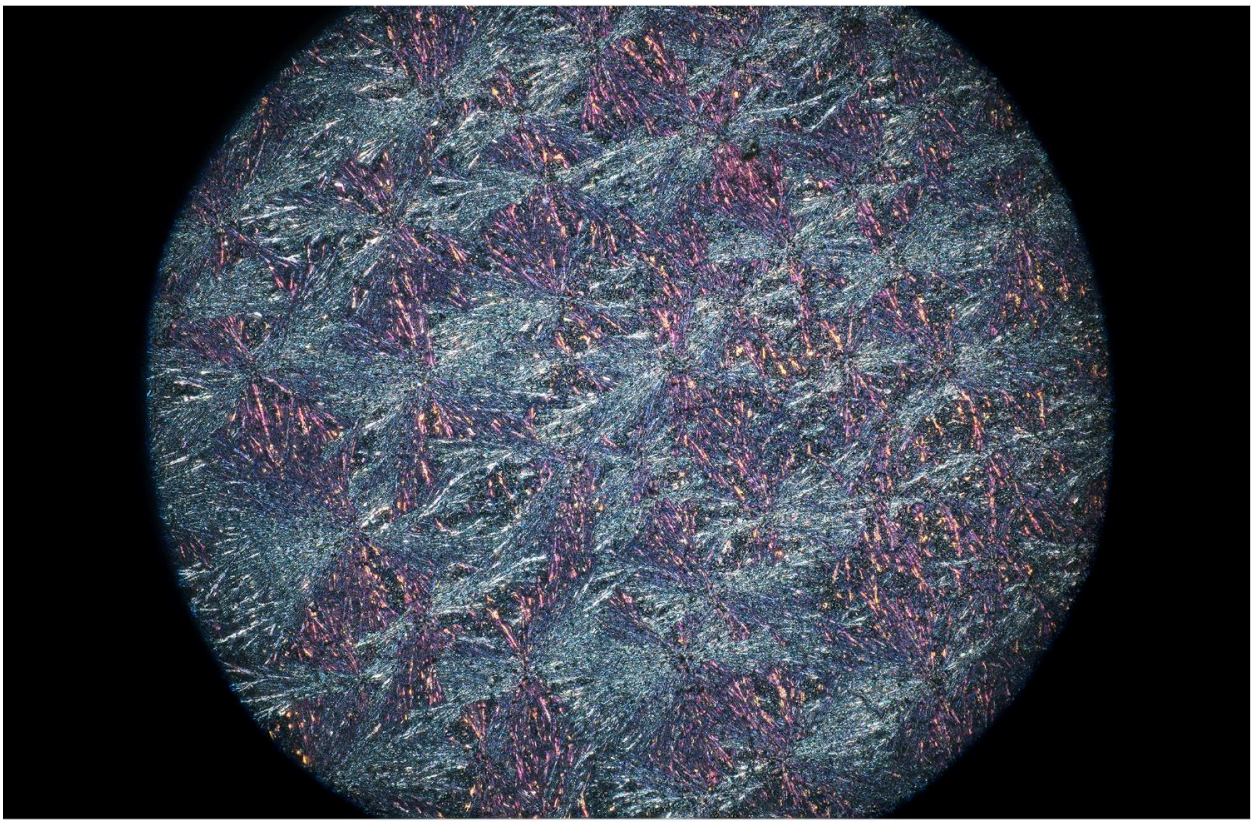

I.15: Symmetric nanofibers consist of PEDOT (blue) and iron (purple).

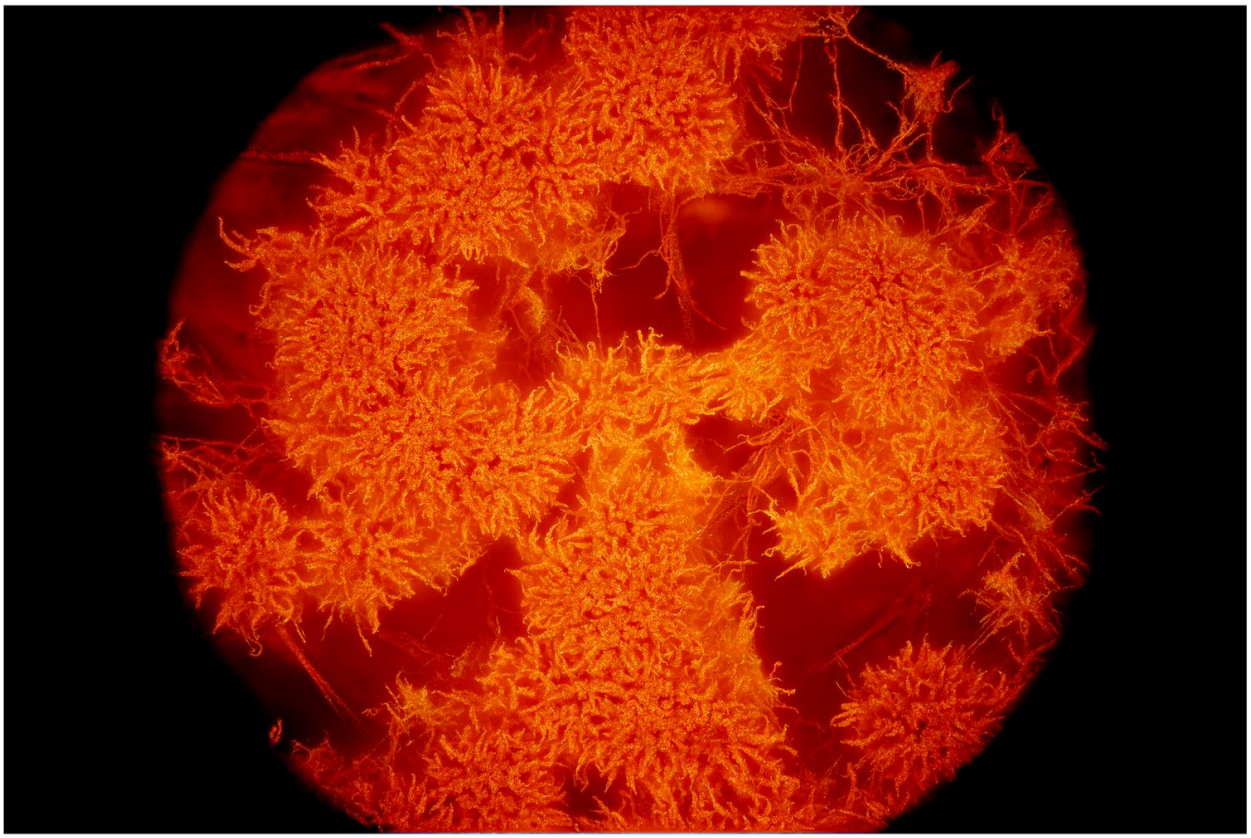

I.16: Iron oxide nanofibers.

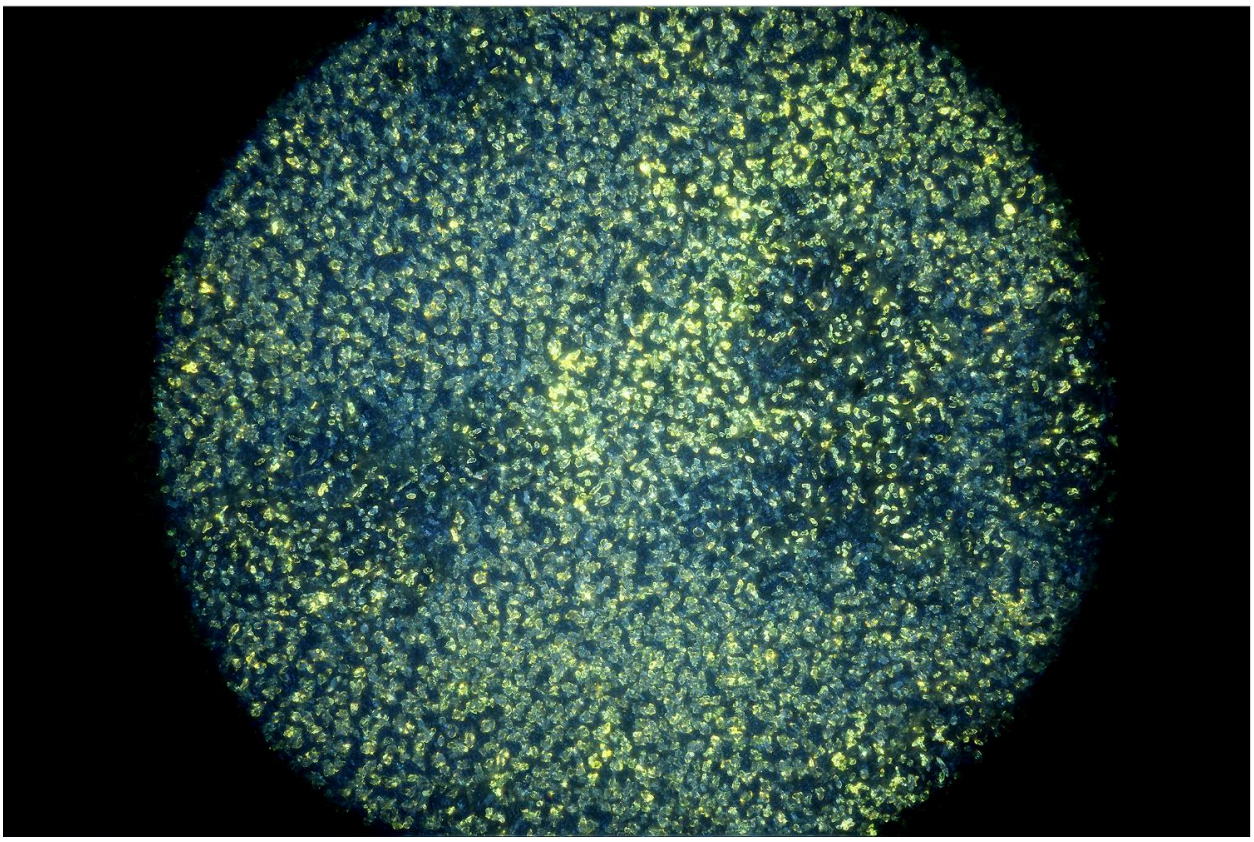

I.17: Yellow rust.

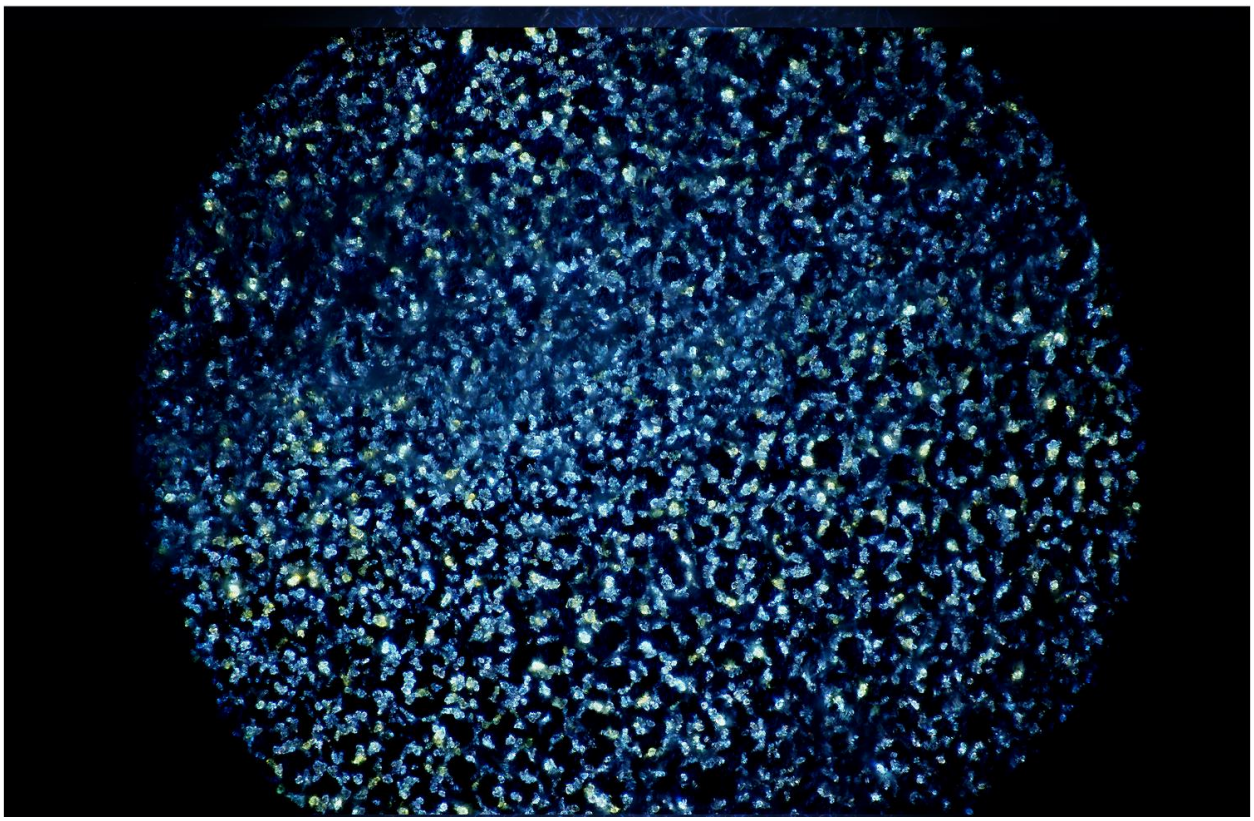

I.18: Green rust.

I.19: Red rust.

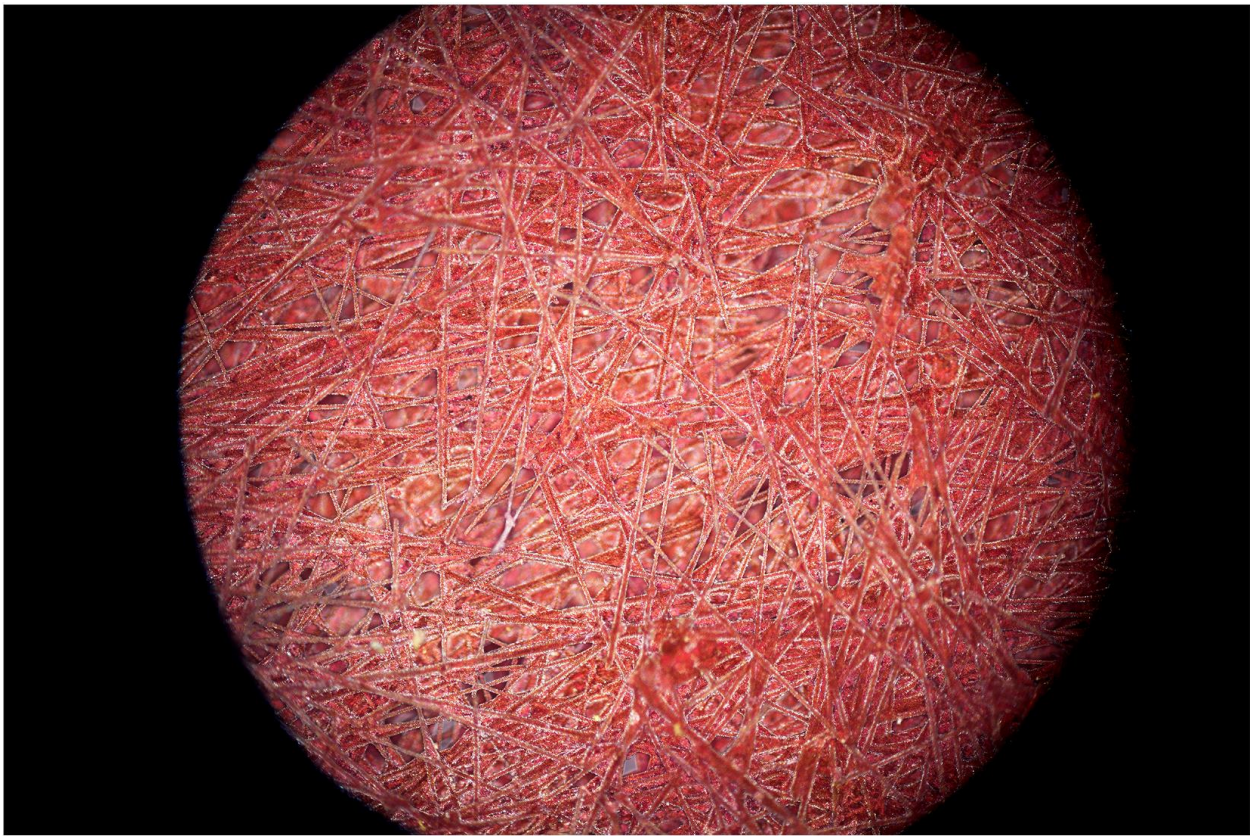

I.20: Iron oxide on hard carbon paper.

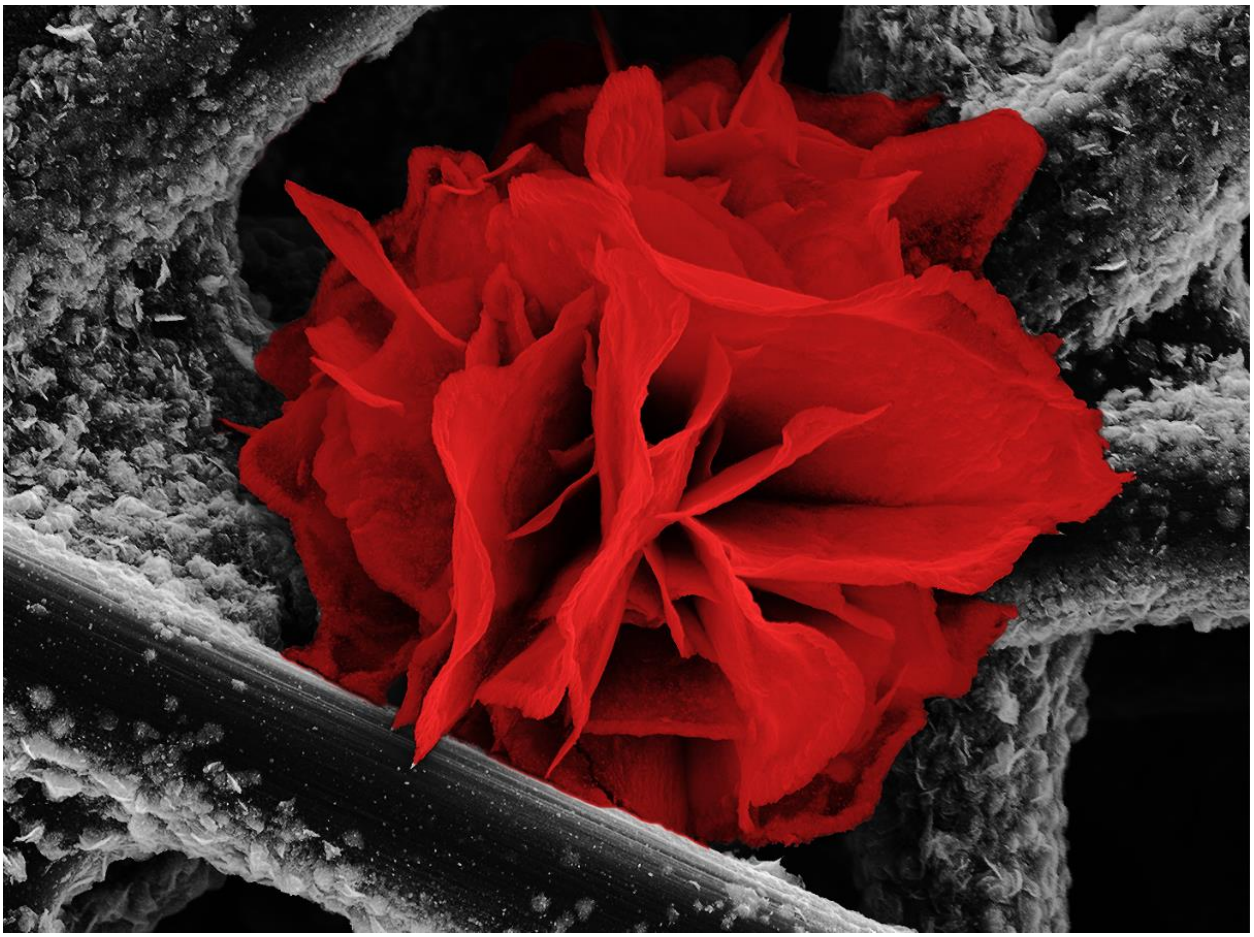

I.21: Iron oxide (flower) on hard carbon paper.